HCAL Technical Design Report

The HCAL Technical Design Report (CERN/LHCC 97-31, CMS TDR 2, 20 June 1997), is available on the HCAL TDR Page on the US CMS WWW Server. The final version of the document will be posted here, as will the eps files corresponding to the figures.

The Hadron Calorimeter Project Technical Design Report, 20 June 1997

HCAL Technical Design Report

Questions from LHCC Referees

Questions on the HCAL TDR from the LHCC referees were received on August 4, 1997. The written response to the referees questions was transmitted August 25, prior to the referees' August 28 meeting with CMS. The questions and answers are avialable below, or via anonymous ftp in the /pub/hcal_tdr/lhcc/ subdirectory on the uscms.fnal.gov server: ftp://uscms.fnal.gov/pub/hcal_tdr/lhcc/.

- Questions from the referees.
- Responsibilities for answers to referees' questions.
- Response to the referees questions (updated 25 Aug 1997):
  - Text: postscript (1074 KB), Adobe pdf (143 KB), Microsoft Word (183 KB)
  - Figures: postscript (1089 KB), Adobe pdf (224 KB), Microsoft Word (908 KB)

HCAL Technical Design Report

The HCAL Technical Design Report (CERN/LHCC 97-31, CMS TDR 2, 20 June 1997) was submitted at CERN on June 23, 1997. An initial printing of 100 copies was received on June 26. A final printing of approximately 1000 copies will be made after a number of minor errors and a few formatting problems are corrected.

The document is available as a series of Microsoft Word 6 files in the /pub/hcal_tdr/ subdirectory of the uscms.fnal.gov anonymous ftp server: <ftp://uscms.fnal.gov/pub/hcal_tdr/>. Postscript and pdf format versions will be posted as they become available.

Please send any corrections for the final printing to Terry Grozis at Fermilab, tgrozis@fnal.gov.

Html versions of the HCAL TDR chapters are available below. In addition, we will provide access to eps versions of all figures on an individual basis. This work is in process.

Access to the HCAL TDR area on uscms.fnal.gov

- via anonymous ftp: <ftp://uscms.fnal.gov/pub/hcal_tdr/>
- via a directory index on the WWW

The Hadron Calorimeter Project Technical Design Report, 20 June 1997

CERN/LHCC 97-31

CMS TDR 2

20 June 1997

20 June 1 CMS TDR 2

CMS

The Hadron Calorimeter Technical Design Report

CMS Spokesperson	CMS Technical Coordinator	CMS Hadron Calorimeter Project Manager
M. Della Negra	E. Radermacher	D. Green
CERN	CERN	Fermilab
michel.della.negra@cern.ch	ernst.radermacher@cern.ch	dgreen@fnal.gov

CMS Collaboration

Yerevan Physics Institute, Yerevan, ARMENIA

G.L. Bayatian, N.K. Grigorian, V.G. Khachatrian, A. Margarian, A.M. Sirunian,
S.S. Stepanian

Institut für Hochenergiephysik der OeAW, Wien, AUSTRIA

W. Adam, R. Fruehwirth, J. Hrubec, A. Kluge, M. Krammer, N. Neumeister, H. Pernegger, M. Pernicka,
P. Porth, D. Rakoczy, H. Rohringer, J. Scherzer, F. Szoncsó, G. Walzel,
T. Wildschek, C.E. Wulz

Byelorussian State University, Minsk, BELARUS

V.V. Petrov, V.S. Prosolovich

Institute of Nuclear Problems, Minsk, BELARUS

V.G. Baryshevsky, A.A. Fedorov, M.V. Korzhik, O.V. Missevitch

National Centre of Particle and High Energy Physics, Minsk, BELARUS

G.V. Basalyga, N.E. Chekhlova, V.A. Chekhovsky, O.V. Dvornikov, I.F. Emelianchik, A.P. Khomich, V.L. Kolpaschikov, A.S. Kurilin, V.I. Kuvshinov, A.V. Litomin, V.A. Mossolov, A.K. Panfilenko, A.V. Raspereza, S.I. Reutovich, N.M. Shumeiko, A.V. Solin, R.V. Stefanovich, V.J. Stepanets, S.V. Sushkov, S.S. Vetokhin, Y. Yurenya, V.B. Zalessky, F.E. Zyazyulya

Research Institute of Applied Physical Problems, Minsk, BELARUS

F.A. Ermalitsky, P.V. Kuchinsky, V.M. Lomako

Université Libre de Bruxelles, Brussels, BELGIUM

O. Bouhali, J.P. Dewulf, J. Sacton, J. Stefanescu, C. Vander Velde, P. Vanlaer

Vrije Universiteit Brussel, Brussels, BELGIUM

J. Lemonne, S. Tavernier, F. Udo, W. Van Doninck, L. Van Lancker, V. Zhukov

Université Catholique de Louvain, Louvain-la-Neuve, BELGIUM

K. Bernier, D. Favart, J. Govaerts, G. Grégoire

Université de Mons-Hainaut, Mons, BELGIUM

I. Boulogne, E. Daubie, Ph. Herquet, R. Windmolders

Universitaire Instelling Antwerpen, Wilrijk, BELGIUM

W. Beaumont, T. Beckers, J. De Troy, Ch. Van Dyck, F. Verbeure

Institute for Nuclear Research and Nuclear Energy, Sofia, BULGARIA

T. Anguelov, G. Antchev, I. Atanasov, D. Bourilkov, L. Dimitrov, V. Genchev, G. Georgiev, P. Hristov, P. Iaydjiev, I. Ivanov, L. Penchev, V. Penev, A. Shklovskaja, G. Sultanov, I. Vankov

University of Sofia, Sofia, BULGARIA

A. Gritskov, A. Jordanov, L. Litov, P. Petev, V. Spassov, R. Tsenov, G. Velev

Institute of High Energy Physics, Beijing, CHINA, PR

G.M. Chen, Y. Chen, B. Cheng, Y.F. Gu, Y.N. Guo, J.T. He, B.N. Jin, Z.J. Ke, J. Li, W.G. Li, X.N. Li, J. Liu, B.W. Shen, C.Q. Shen, P.R. Shen, X.Y. Shen, H.Y. Sheng, H.Z. Shi, X.F. Song, Y.Y. Wang, Y.R. Wu, R.S. Xu, B.Y. Zhang, S.Q. Zhang, W.R. Zhao, J.P. Zheng, G.Y. Zhu

Peking University, Beijing, CHINA, PR

Y. Ban, J.E. Chen, H. Liu, S. Liu, B. Lou, S. Qian, Y. Ye

University for Science and Technology of China, Hefei, Anhui, CHINA, PR

Q. An, Z. Bian, C. Li, Ch. Shi, L. Sun, X. Wang, Z. Wang, J. Wu, S. Ye, Z. Zhang

Technical University of Split, Split, CROATIA

N. Godinovic, M. Milin[1], I. Puljak, I. Soric, M. Stipcevic[1], J. Tudoric-Ghemo

University of Split, Split, CROATIA

Z. Antunovic, M. Dzelalija

University of Cyprus, Nicosia, CYPRUS

A. Hasan, P.A. Razis, A. Vorvolakos

Institute of Scientific Instruments, Brno, CZECH REPUBLIC

J. Dupak, P. Hanzelka, M. Horacek, A. Srnka

Charles University, Praha, CZECH REPUBLIC

M. Finger, T. Kracikova, A. Linka, J. Picek, M. Slunecka, M. Sulc

Czech Technical University, Praha, CZECH REPUBLIC

M. Laub, R. Nova'k, M. Vognar, J. Zicha

Institute of Computing Machines, Praha, CZECH REPUBLIC

M. Tomasek

Nuclear Research Institute, Rez, CZECH REPUBLIC

A. Janata

Institute of Chemical Physics and Biophysics, Tallinn, ESTONIA

R. Aguraiuja, A. Hall, E. Lippmaa, J. Lippmaa, R. Pikver, J. Subbi

Department of Physics, University of Helsinki, Helsinki, FINLAND

S. Lehti

HIP, University of Helsinki, Helsinki, FINLAND

O. Bouianov, N. Eiden, C. Eklund, L. Eronen, J. Hahkala, M. Heikkinen, V. Karimäki[2],
R. Kinnunen, J. Klem, M. Kotamaki, E. Pietarinen, H. Saarikoski, K. Skog, J. Tuominiemi

University of Jyväskylä, Jyväskylä, FINLAND

J. Äystö, R. Julin, V. Ruuskanen

Dept. of Physics & Microelectronics Instrumentation Lab., University of Oulu, Oulu, FINLAND

L. Palmu, M. Piila, K. Remes, R. Skantsi, E. Suhonen, T. Tuuva

Tampere University of Technology, Tampere, FINLAND

J. Niittylahti, O. Vainio

Laboratoire d'Annecy-le-Vieux de Physique des Particules, IN2P3-CNRS, Annecy-le-Vieux, FRANCE

G. Bassompierre, G. Bohner, J. Ditta, O. Drobychev, M. Forlen, J.P. Guillaud, J. Lecoq, T. Leflour, S. Lieunard, M. Maire, P. Mendiburu, P. Nedelec, L. Oriboni, J.P. Peigneux, M. Schneegans, D. Sillou, J.M. Thenard, J.P. Vialle

DSM/DAPNIA, CEA/Saclay, Gif-sur-Yvette, FRANCE

M. Anfreville, P. Besson, P. Bonamy, E. Bougamont, R. Chipaux, V. Da Ponte, M. De Beer, P. De Girolamo, M. Dejardin, D. Denegri, J.L. Faure, M. Geleoc, F.X. Gentit, A. Givernaud, Y. Lemoigne, E. Locci, J.C. Lottin, Ch. Lyraud, J.P. Pansart, J. Rander, Ph. Rebourgeard, J.M. Reymond, F. Rondeaux, A. Rosowsky, P. Roth, P. Verrecchia, G. Villet

Laboratoire de Physique Nucléaire des Hautes Energies, Ecole Polytechnique, IN2P3-CNRS, Palaiseau, FRANCE

J. Badier, M. Bercher, A. Busata, Ph. Busson, D. Chamont, C. Charlot, B. Chaurand, A. Debraine, L. Dobrzynski, L. Faurlini, O. Ferreira, H. Hillemanns, A. Karar, L. Kluberg, D. Lecouturier, P. Matricon, G. Milleret, P. Paganini, P. Poilleux, A. Romana, J.C. Vanel, C. Violet

Institut de Recherches Subatomiques, IN2P3-CNRS - ULP, UHA, Strasbourg, FRANCE

F. Anstotz, J.D. Berst, J.M. Brom, F. Charles, J. Coffin, J. Croix, F. Drouhin, W. Dulinski, J.C. Fontaine, W. Geist, U. Goerlach, J.M. Helleboid, T. Henkes, B. Hilt, Ch. Hoffmann, Y. Hu, D. Huss, F. Jeanneau, P. Juillot, P. Lorentz, A. Lounis, Ch. Maazouzi, V. Mack, J. Michel, A. Pallares, P. Pralavorio, C. Racca, Y. Riahi, I. Ripp, Ph. Schmitt, J.P. Schunck, B. Schwaller, Th. Todorov, R. Turchetta, A. Zghiche

Institut de Physique Nucléaire de Lyon, IN2P3-CNRS, Univ. Lyon I, Villeurbanne, FRANCE

M. Ageron, J.E. Augustin, M. Bedjidian, Y. Benhammou, V. Chorowicz, P. Cluzel, D. Contardo, R. Della Negra, P. Depasse, O. Drapier, H. El Mamouni, D. Essertaize, J. Fay, S. Gardien, R. Genre, M. Goyot, J. Guyon, R. Haroutounian, B. Ille, G. Jacquet, P. Lebrun, Ch. Lemoine, N. Madjar, J.P. Martin, H. Mathez, L. Mirabito, S. Muanza, P. Pangaud, M. Rebouillat, P. Sahuc, G. Smadja, S. Tissot, J.P. Walder, F. Zach

High Energy Physics Institute, Tbilisi, GEORGIA

N. Amaglobeli, I. Bagaturia, L. Glonti, V. Kartvelishvili, R. Kvatadze, D. Mzavia, T. Sakhelashvili, R. Shanidze, E. Tchikovani

Institute of Physics, Tbilisi, GEORGIA

I. Iashvili, A. Kharchilava, N. Roinishvili, V. Roinishvili, L. Rurua

RWTH, I. Physikalisches Institut, Aachen, GERMANY

W. Braunschweig, J. Breibach, W. Gu, K. Gundlfinger, W. Karpinski, Th. Kirn, T. Kubicki, Ch. Kukulies, K. Lübelsmeyer, D. Pandoulas, G. Pierschel, C. Rente, D. Schmitz, A. Schultz von Dratzig, J. Schwenke, R. Siedling, O. Syben, F. Tenbusch, M. Toporowsky, B. Wittmer, W.J. Xiao

RWTH, III. Physikalisches Institut A, Aachen, GERMANY

S. Bethke, O. Biebel, H. Faissner, H. Fesefeldt, D. Rein, H. Reithler, H. Schwarthoff, V. Sondermann, V. Tano, H. Teykal, M. Tonutti, J. Tutas, M. Wegner

RWTH, III. Physikalisches Institut B, Aachen, GERMANY

F. Beissel, V. Commichau, G. Flügge, K. Hangarter, J. Kremp, D. Macke, O. Pooth, P. Schmitz, R. Schulte

Humboldt-Universität zu Berlin, Berlin, GERMANY

Th. Hebbeker

Institut für Experimentelle Kernphysik, Karlsruhe, GERMANY

P. Blüm, W. De Boer, M. Feindt2, H. Gemmeke, D. Knoblauch, A. Menchikov, S. Meyer, Th. Müller, D. Neuberger, H.J. Simonis, W.H. Thümmel, H. Wenzel, S. Weseler

University of Athens, Athens, GREECE

L. Resvanis

Institute of Nuclear Physics "Demokritos", Attiki, GREECE

G. Fanourakis, S. Harissopulos, P. Kokkinias, A. Kyriakis, D. Loukas, A. Markou, Ch. Markou, I. Siotis, M. Spyropoulou-Stassinaki, S. Tzamarias, A. Vayaki, E. Zevgolatakos

University of Ioánnina, Ioánnina, GREECE

I. Evangelou, K. Kloukinas, P. Kolovos, N. Manthos, A. Pagonis, F.A. Triantis

KFKI Research Institute for Particle and Nuclear Physics, Budapest, HUNGARY

G. Bencze[2], A. Csilling, E. Denes, J. Ero[2], C. Hajdu, D. Horvath, D. Kiss, I. Manno, G. Odor, G. Pa'sztor, F. Sikler, A. Ster, L. Urban, G. Vesztergombi, P. Zalan, M. Zsenei

Kossuth Lajos University, Debrecen, HUNGARY

L. Baksay, T. Bondar, L. Brunel[2], S. Juhasz, G. Marian, P. Raics, J. Szabo, Z. Szabo, S. Szegedi, Z. Szillasi, T. Sztaricskai, G. Zilizi

Bhubaneswar Institute of Physics, Bhubaneswar, INDIA

S. Behari, B. Choudhary, D.P. Mahapatra, J. Maharana

Panjab University, Chandigarh, INDIA

S. Beri, M. Kaur, J.M. Kohli, J.B. Singh

Nuclear Physics Division, Bhabha Atomic Research Centre, Mumbai, INDIA

R.K. Chaudhury, S.B. Jawale, B. John, S.R. Kataria, R.S. Koppikar, A.K. Mohanty, S.V. Sastry, R.V. Srikantiah

Tata Institute of Fundamental Research - EHEP, Mumbai, INDIA

T. Aziz, Sn. Banerjee[2], S.N. Ganguli, S.K. Gupta, A. Gurtu, K. Mazumdar, R. Raghavan, K. Sudhakar, S.C. Tonwar

Tata Institute of Fundamental Research - HECR, Mumbai, INDIA

B.S. Acharya, Sd. Banerjee, S. Dugad, M.R. Krishnaswamy, N.K. Mondal, V. S. Narasimham

University of Delhi South Campus, New Delhi, INDIA

T. Chand, J. Cherian, R.K. Shivpuri, V.K. Verma

Università di Bari e Sezione dell' INFN, Bari, ITALY

M. Angarano, A. Colaleo, D. Creanza, M. De Palma, L. Fiore, G. Iaselli, F. Loddo, G. Maggi, M. Maggi, B. Marangelli, S. My, S. Natali, S. Nuzzo, A. Ranieri, G. Raso,

F. Romano, F. Ruggieri, G. Selvaggi, P. Tempesta, G. Zito

Università di Bologna e Sezione dell' INFN, Bologna, ITALY

A. Benvenuti, P. Capiluppi, F. Cavallo, M. Cuffiani, I. D'Antone, G.M. Dalla Valle,
F. Fabbri, P.L. Frabetti, G. Giacomelli, M. Guerzoni, S. Marcellini, P. Mazzanti,
A. Montanari, F. Navarria, F. Odorici, A. Rossi, T. Rovelli, G. Siroli, G. Valenti

Università di Catania e Sezione dell' INFN, Catania, ITALY

S. Albergo, V. Bellini, D. Boemi, Z. Caccia, P. Castorina, S. Costa, L. Lo Monaco,
R. Potenza, A. Tricomi, C. Tuve

Università di Firenze e Sezione dell' INFN, Firenze, ITALY

F. Becattini, U. Biggeri, E. Borchi, M. Bruzzi, M. Capaccioli, G. Castellini, E. Catacchini,
C. Civinini, R. D'Alessandro, E. Focardi, G. Landi, M. Meschini, G. Parrini, G. Passaleva, M. Pieri, A. Salamone, S. Sciortino

Università di Genova e Sezione dell' INFN, Genova, ITALY

P. Fabbricatore, S. Farinon, R. Musenich, C. Priano

Università de L'Aquila e Sezione dell' INFN, L'Aquila, ITALY

F. Cavanna, G. Piano-Mortari, C. Rossi, M. Verdecchia

Università di Padova e Sezione dell' INFN, Padova, ITALY

P. Azzi, N. Bacchetta, M. Benettoni, A. Bettini, D. Bisello, G. Busetto, R. Carlin, A. Castro, S. Centro,
E. Conti, M. Da Rold, M. De Giorgi, A. De Min, U. Dosselli, C. Fanin,
F. Gasparini, U. Gasparini, P. Guaita, I. Lippi, M. Loreti, R. Martinelli, A.T. Meneguzzo,
S. Paccagnella, M. Pegoraro, L. Pescara, P. Ronchese, A. Sancho Daponte, P. Sartori,
L. Stanco, I. Stavitski, E. Torassa, L. Ventura, P. Zotto, G. Zumerle

Università di Pavia e Sezione dell' INFN, Pavia, ITALY

V. Arena, G. Belli, G.L. Boca, G. Bonomi, G. Gianini, M. Merlo, S.P. Ratti, C. Riccardi,
L. Viola, P. Vitulo

Università di Perugia e Sezione dell' INFN, Perugia, ITALY

A. Aragona, E. Babucci, P. Bartalini, G.M. Bilei, B. Checcucci, P. Ciampolini, P. Lariccia, G. Mantovani, D. Passeri, P. Placidi, A. Santocchia, L. Servoli, Y. Wang

Università di Pisa e Sezione dell' INFN, Pisa, ITALY

F. Angelini, G. Bagliesi, A. Bardi, A. Basti, F. Bedeschi, S. Belforte, R. Bellazzini, L. Borrello, F. Bosi, C. Bozzi, P.L. Braccini, A. Brez, R. Carosi, R. Castaldi, G. Chiarelli, M. Chiarelli, V. Ciulli, M. D'Alessandro Caprice, M. Dell'Orso, R. Dell'Orso, S. Donati, A. Frediani, S. Galeotti, A. Giambastiani, P. Giannetti, A. Giassi, G. Iannaccone, M. Incagli, L. Latronico, V. Lebedenko, F. Ligabue, N. Lumb, G. Magazzu, M.M. Massai , E. Meschi, A. Messineo, L. Moneta, F. Morsani, M. Oriunno[2], F. Palla, G. Punzi, F. Raffaelli, R. Raffo, L. Ristori, G. Sanguinetti, P. Spagnolo, G. Spandre, F. Spinella, A. Starodumov, R. Tenchini, G. Tonelli, E. Troiani, C. Vannini, A. Venturi, P.G. Verdini, Z. Xie, F. Zetti

Università di Roma I e Sezione dell' INFN, Roma, ITALY

S. Baccaro[3], L. Barone, B. Borgia, F. Cavallari, I. Dafinei, F. De Notaristefani, M. Diemoz, A. Festinesi[3], E. Leonardi, A. Leone, E. Longo, M. Mattioli, M. Montecchi[3], G. Organtini, M. Puccini[3], E. Valente, A. Zullo

Dip. di Fisica Sperimentale & INFN, Torino, ITALY

M. Arneodo, F. Bertolino, R. Cirio, M. Costa, F. Daudo, M.I. Ferrero, S. Maselli, V. Monaco, C. Peroni, M.C. Petrucci, R. Sacchi, A. Solano, A. Staiano

Institute of Electronics and Computer Science, Riga, LATVIA

Y. Bilinski

Quaid-I-Azam University, Islamabad, PAKISTAN

P. Hoodbhoy, A. Niaz, I.E. Qureshi, K.N. Qureshi

Institute of Experimental Physics, Warsaw, POLAND

M. Cwiok, W. Dominik, A. Fengler, J. Krolikowski, I. Kudla, P. Majewski, K. Pozniak

Soltan Institute for Nuclear Studies, Warsaw, POLAND

M. Górski, P. Zalewski

Laboratório de Instrumentação e Física Experimental de Partículas, Lisboa, PORTUGAL

P. Bordalo, J. Da Silva, A. Ferreira, J. Gomes, R. Nobrega, S. Ramos, S. Silva

Joint Institute for Nuclear Research, Dubna, RUSSIA

S. Afanasiev, I. Anisimov, D. Bandurin, D. Belosludtsev, S. Chatrchyan, A. Cheremukhin, A. Chvyrov, A. Dmitriev, V. Elsha, Y. Erchov, A. Filippov, I. Golutvin, N. Gorbunov, I. Gramenitsky, I. Ivantchenko, V. Kalagin, V. Karjavin, S. Khabarov, V. Khabarov, Y. Kiryushin, V. Kolesnikov, V. Konoplyanikov, V. Korenkov, I. Kossarev, A. Koutov, V. Krasnov, A. Litvinenko, V. Lysiakov, A. Malakhov, G. Mechtcheriakov, I. Melnichenko, P. Moissenz, S. Movchan, V. Palichik, V. Perelygin, Y. Petukhov, M. Popov, D. Pose, R. Pose, A. Samoshkin, M. Savina, S. Selunin, S. Sergeev, S. Shmatov, N. Skachkov, N. Slavin, D. Smolin, E. Tikhonenko, V. Tyukov, V. Uzhinskii, N. Vlasov, A. Volodko, A. Yukaev, N. Zamiatin, A. Zarubin, P. Zarubin, E. Zubarev, C. Zubov

Petersburg Nuclear Physics Institute, Gatchina (St Petersburg), RUSSIA

N. Bondar, G. Gavrilov, Y. Gusev, O. Kisselev, O. Prokofiev, V. Rasmislovich, D. Seliverstov, I. Smirnov, S. Sobolev, V. Soulimov, G. Velitchko, A. Vorobyov

Institute for Nuclear Research, Moscow, RUSSIA

G.S. Atoyan, B. Bachtin, R. Djilkibaev, S. Gninenko, N. Goloubev, E.V. Gushin, V. Isakov, V. Klimenko, N. Krasnikov, V.A. Lebedev, V. Marin, V. Matveev, A. Pashenkov, V. Popov, V.E. Postoev, A. Proskouriakov, I. Semeniouk, B. Semenov, V. Shmatkov, A. Skassyrskaia, A. Toropin

Institute for Theoretical and Experimental Physics, Moscow, RUSSIA

S. Abdullin, E. Doroshkevich, V. Gavrilov, Y. Gershtein, I. Gorelov, V. Kaftanov, A. Khanov[2], V. Kolossov, D. Litvintsev, A. Nikitenko[2], A. Nikitin, S. Ouzounian, A. Papin, O.I. Pogorelko, V. Rusinov, V. Semechkin, Y. Semenov, N. Stepanov[2], V. Stoline, Y. Trebukhovsky, A. Ulyanov, A. Yumashev

Moscow State University, Moscow, RUSSIA

A. Belsky, V Bodyagin, A. Demianov, V. Galkin, A. Gribushin, O.L. Kodolova, V. Korotkikh, N.A. Kruglov, A. Kryukov, I. Lokhtin, V. Mikhailin, L. Sarycheva, A. Snigirev, I. Vardanyan, A. Vasil'ev, A. Yershov

P.N. Lebedev Physical Institute, Moscow, RUSSIA

E. Devitsin, A.M. Fomenko, V. Kozlov, A.I. Lebedev, S. Potashov, S.V. Rusakov

Budker Institute for Nuclear Physics, Novosibirsk, RUSSIA

V. Aulchenko, B. Baiboussinov, A. Bondar, S. Eidelman, V. Nagaslaev, T. Purlatz, L. Shekhtman, V. Sidorov, A. Tatarinov

Institute for High Energy Physics, Protvino, RUSSIA

V. Abramov, I. Azhgirey, S. Bitioukov, A. Dolgopolov, S. Donskov, A. Dyshkant, V. Evdokimov, P. Goncharov, A. Gorin, V. Katchanov, V. Khodyrev, A. Kondashov, A. Korablev, Y. Korneev, A. Kostritskii, A. Krinitsyn, V. Kryshkin, I. Manuilov, V. Medvedev, V. Obraztsov, A. Ostankov, M. Oukhanov, V. Petrov, V.V. Rykalin, P. Shagin, A. Singovsky, V. Solovianov, V. Sougonyaev, V. Soushkov, A. Surkov, V. Talanov, S. Tereschenko, L. Turchanovich, N. Tyurin, A. Uzunian, A. Volkov, A. Zaitchenko

Institute of Computing Machines, Zilina, SLOVAK REPUBLIC

R. Drevenak, V. Sluneckova

Centro de Investigaciones Energeticas Medioambientales y Tecnologicas, Madrid, SPAIN

M. Aguilar-Benitez, J. Alberdi, J.M. Barcala, J. Berdugo, C. Burgos, M. Cerrada, N. Colino, M. Daniel, M. Fernandez, A. Ferrando, M.C. Fouz, M.I. Josa, P. Ladrón de Guevara, J. Marin, F. Martin Suarez, J. Mocholi, A. Molinero, J. Navarrete, J.C. Oller, J.L. Pablos, L. Romero, J. Salicio, C. Willmott

Universidad Autónoma de Madrid, Madrid, SPAIN

C. Albajar

Universidad de Cantabria, Santander, SPAIN

J. Cuevas, C. Figueroa, I. Gonzalez, J.M. Lopez, J. Marco, F. Matorras, T. Rodrigo Anoro, A. Ruiz Jimeno, I. Vila

Universität Basel, Basel, SWITZERLAND

L. Tauscher, M. Wadhwa

CERN, European Laboratory for Particle Physics, Geneva, SWITZERLAND

P.A. Aarnio, D. Abbaneo, P. Antilogus, V. Arbet-Engels, E. Argante, P. Aspell, E. Auffray, P. Baillon, R. Barillère, D. Barney, W. Bell, D. Blechschmidt, Ph. Bloch, M. Bosteels, J. Bourotte, M. Bozzo, H. Breuker, A. Calvo, D. Campi, A. Caner, E. Cargnel, A. Carraro, A. Cattai, G. Cervelli, G. Chevenier, J. Christiansen, S. Cittolin, I. Crotty, B. Curé, C. D'Ambrosio, Th. de Visser, D. Delikaris, M. Della Negra, A. Desirelli, B. Dezillie, A. Elliott-Peisert, H. Foeth, A. Fucci, A. Furtjes, F. Gautheron, J.C. Gayde, H. Gerwig, K. Gill, W. Glessing, E. Gonzalez Romero, J.P. Grillet, J. Gutleber, C.E. Hackl, F. Hahn, R. Hammarstrom, M. Hansen, M. Hansroul, A. Hervé, M. Hoch, K. Holtman, M. Huhtinen, S. Ilie, V. Innocente, W. Jank, P. Jarron, A. Jusko, Th. Kachelhoffer, K. Kershaw, F. Klumb, A. Kruse, W. Kurzbauer, T. Ladzinski, Ch. Lasseur, J.M. Le Goff, M. Lebeau, P. Lecoq, N. Lejeune, F. Lemeilleur, M. Letheren, Ch. Ljuslin, B. Lofstedt, R. Loos, R. Mackenzie, R. Malina, M. Mannelli, E. Manola-Poggioli, A. Marchioro, M. Marino, J.M. Maugain, F. Meijers, A. Merlino, Th. Meyer, C. Mommaert, P. Nappey, T. Nyman, A. Onnela, S. Paoletti, G. Passardi, D. Peach, F. Perriollat, P. Petagna, M. Pimiä, R. Pintus, B. Pirollet, A. Placci, J.P. Porte, J. Pothier, M.J. Price, A. Racz, E. Radermacher, S. Reynaud, R. Ribeiro, J. Roche, P. Rodrigues Simoes Moreira, O. Runolfsson, D. Samyn, J.C. Santiard, B. Schmitt, M. Schröder, F. Sciacca, P. Siegrist, L. Silvestris, N. Sinanis, G. Stefanini, B. Taylor, A. Tsirou, J. Varela, F. Vasey, T.S. Virdee4, T. Wikberg, M. Wilhelmsson, I.M. Willers, G. Wrochna

Paul Scherrer Institut, Villigen, SWITZERLAND

O. Ayranov, W. Bertl, K. Deiters, P. Dick, A. Dijksmann, M. Fabre, Th. Flügel, K. Gabathuler, J. Gobrecht, G. Heidenreich, R. Horisberger, Q. Ingram, D. Kotlinski, R. Morf, D. Renker, R. Schnyder, H.Ch. Walter

Institut für Teilchenphysik, Eidgenössische Technische Hochschule, Zürich, SWITZERLAND

H. Anderhub, F. Behner, B. Betev, A. Biland, R. Della Marina, F.R. Di Lodovico, M. Dittmar, L. Djambazov, M. Dröge, R. Eichler, G. Faber, M. Felcini, K. Freudenreich, C. Grab, E. Hodin, H. Hofer, I. Horvath, A. Iglesias Lago, P. Ingenito, K. Lassila-Perini, P. Le Coultre, P. Lecomte, W. Lustermann, P. Marchesini, D. McNally, F. Nessi-Tedaldi, F. Pauss, D. Pitzl, M. Pohl, G. Rahal-Callot, D. Ren, J. Riedlberger, U. Roeser, H. Rykaczewski, H. Suter, D. Terribilini, J. Ulbricht, G. Viertel, H. Von Gunten, S. Waldmeier-Wicki

Universität Zürich, Zürich, SWITZERLAND

C. Amsler, F. Ould-Saada, Ch. Regenfus, P. Robmann, S. Spanier, S. Steiner, P. Truöl

Cukurova University, Adana, TURKEY

I. Dumanoglu, E. Eskut, A. Kayis, A. Kuzucu-Polatöz, G. Önengüt, N. Ozdes Koca,
H. Ozturk

Middle East Technical University, Physics Department, Ankara, TURKEY

A.S. Ayan, E. Pesen, M. Serin-Zeyrek, R. Sever, P. Tolun, M. Zeyrek

Institute of Single Crystals of National Academy of Science, Kharkov, UKRAINE

V.C. Koba, V. Trofimenko

Kharkov State University, Kharkov, UKRAINE

N.A. Kluban, V. Lebedev

National Scientific Center Kharkov Institute of Physics and Technology, Kharkov, UKRAINE

L.G. Levchuk, A.A. Nemashkalo, V.E. Popov, A.L. Rubashkin, P.V. Sorokin,
A.E. Zatzerklyany

University of Bristol, Bristol, UNITED KINGDOM

D.S. Bailey, R.D. Head, G.P. Heath, H.F. Heath, D. Newbold, R.J. Tapper

Rutherford Appleton Laboratory, Didcot, UNITED KINGDOM

E. Bateman, K.W. Bell, R.M. Brown, S.R. Burge, D.A. Campbell, D.J. Cockerill,
J.F. Connolly, J.A. Coughlan, L.G. Denton, P.S. Flower, M. French, R. Halsall,
W.J. Haynes, F.R. Jacob, P.W. Jeffreys, B. Kennedy, L. Lintern, J. Maddox, G. Noyes, G.N. Patrick, B. Smith, M. Smith, M. Sproston, R. Stephenson

Imperial College, University of London, London, UNITED KINGDOM

G. Barber, J. Batten, R. Beuselinck, D. Britton, W. Cameron, G. Davies, D. Gentry,
D.J. Graham, G. Hall, J.F. Hassard, J. Hays, K. Long, E.B. Martin, D.G. Miller, A. Potts, D.R. Price,
D.M. Raymond, C. Seez, L. Toudup, J. Troska

Brunel University, Uxbridge, Middlesex, UNITED KINGDOM

P. Hobson, D. Imrie, C.K. Mackay, J. Matheson, M. Osborne, S. Watts

Iowa State University, Ames, USA

E.W. Anderson, J. Hauptman, J. Wightman

Johns Hopkins University, Baltimore, USA

T. Anticic, B. Barnett, C.Y. Chien, M. A. Frautschi, D. Gerdes, D. Newman, J. Orndorff, A. Pevsner, X. Xie

Fermi National Accelerator Laboratory, Batavia, USA

M. Atac, E. Barsotti, A. Baumbaugh, U. Baur, A. Beretvas, M. Bowden, J. Butler, A. Byon-Wagner, I. Churin, D. Denisov, M. Diesburg, D.P. Eartly, J.E. Elias, J. Freeman, I. Gaines, H. Glass, S. Gourlay, D. Green, J. Hanlon, R. Harris, W. Knopf, S. Kwan, M. Lamm, S. Lammel, P. Mantsch, J. Marraffino, S. Mishra, N. Mokhov, J. Ozelis, A. Para, J. Patrick, A. Pla-Dalmau, R. Raja, A. Ronzhin, T. Sager, M. Shea, R.P. Smith, R. Tschirhart, R. Vidal, D. Walsh, R. Wands, E. Wilmsen, W.J. Womersley, W. Wu, A. Yagil

Virginia Polytechnic Institute and State University, Blacksburg, USA

H. Meyer, L. Mo, Th.A. Nunamaker

Boston University, Boston, USA

R. Carey, E. Hazen, O.C. Johnson, E. Kearns, S.B Kim, E. Machado, J. Miller, D. Osborne, B.L. Roberts, J. Rohlf, J. Salen, L. Sulak, J. Sullivan, W. Worstell

Northeastern University, Boston, USA

G. Alverson, H. Fenker, J. Moromisato, Y.V. Musienko, Th. Paul, S. Reucroft, J. Swain, L. Taylor, E. Von Goeler, T. Yasuda

Massachusetts Institute of Technology, Cambridge, USA

G. Bauer, J. Friedman, E. Hafen, S. Pavlon, L. Rosenson, P. Sphicas, K.S. Sumorok, S. Tether, J. Tseng

University of Illinois at Chicago (UIC), Chicago, USA

M. Adams, M. Chung, J. Solomon

University of Maryland, College Park, USA

A. Baden, A. Ball, R. Bard, S.C. Eno, D. Fong, M. Garza, N.J. Hadley, R.G. Kellogg2,
Sh. Kunori, M. Murbach, A. Skuja

The Ohio State University, Columbus, USA

D. Acosta, B. Bylsma, L.S. Durkin, J. Hoftiezer, R. Hughes, M. Johnson, D. Larsen,
T.Y. Ling, C.J. Rush, V. Sehgal, B. Winer

University of California at Davis, Davis, USA

R. Breedon, Y. Fisyak, G. Grim, B. Holbrook, W. Ko, R. Lander, F. Lin, S. Mani,
D. Pellett, J. Smith

Northwestern University, Evanston, USA

B. Gobbi, P. Rubinov, R. Tilden

Fairfield University, Fairfield, USA

C.P. Beetz, V. Podrasky, C. Sanzeni, T. Toohig, D. Winn

University of Florida, Gainesville, USA

P. Avery, R. Field, L. Gorn, J. Konigsberg, A. Korytov, G. Mitselmakher, A. Nomerotski, P. Ramond, J. Yelton

Rice University, Houston, USA

D.L. Adams, M. Corcoran, G. Eppley, H.E. Miettinen, Padley, E. Platner, J. Roberts,
P. Yepes

The University of Iowa, Iowa City, USA

N. Akchurin, A. Cooper, E. McCliment, J.P. Merlo, M. Miller, Y. Onel, R. Winsor

University of California San Diego, La Jolla, USA

J. Branson, H. Kobrak, G. Masek, M. Mojaver, H. Paar, G. Raven, M. Sivertz, R. Swanson, A. White

University of Nebraska-Lincoln, Lincoln, USA

W. Campbell, D.R. Claes, M. Hu, C. Lundstedt, G.R. Snow

Lawrence Livermore National Laboratory, Livermore, USA

L. Bertolini, J. Kerns, D. Klem, M. Kreisler, X. Shi, K. Van Bibber, T. Wenaus, D. Wright, C.R. Wuest

Los Alamos National Laboratory, Los Alamos, USA

R. Barber, Z. Chen, J. Hanlon, B. Michaud, G. Mills, A. Palounek, H.J. Ziock

University of California at Los Angeles, Los Angeles, USA

K. Arisaka, Y. Bonushkin, F. Chase, D. Cline, S. Erhan, J. Hauser, J. Kubic, M. Lindgren, C. Matthey, S. Otwinowski, J. Park, Y. Pichalnikov, P. Schlein, Y. Shi

Texas Tech University, Lubbock, USA

O. Ganel, V. Papadimitriou, A. Sill, R. Wigmans

University of Wisconsin, Madison, USA

W. Badgett, D. Carlsmith, S. Dasu, F. Feyzi, C. Foudas, M. Jaworski, J. Lackey,
R. Loveless, S. Lusin, D. Reeder, W. Smith

University of Minnesota, Minneapolis, USA

P. Border, P. Cushman, K. Heller, M. Marshak, R. Rusack, Ch. Timmermans

University of Notre Dame, Notre Dame, USA

B. Baumbaugh, J.M. Bishop, N. Biswas, R. Ruchti, J. Warchol, M. Wayne

University of Mississippi, Oxford, USA

K. Bhatt, M. Booke, L. Cremaldi, R. Kroeger, J. Reidy, D. Sanders, D. Summers

California Institute of Technology, Pasadena, USA

J. Bunn, Ph. Galvez, A. Kirkby, H. Newman, S. Shevchenko, R. Zhu

Carnegie Mellon University, Pittsburgh, USA

S. Blyth, A. Engler, Th. Ferguson, H. Hoorani, R. Kraemer, M. Procario, J. Russ, H. Vogel

Princeton University, Princeton, USA

P. Denes, V. Gupta, D. Marlow, P. Piroué, D. Stickland, H. Stone, Ch. Tully, R. Wixted

University of Texas at Dallas, Richardson, USA

R.C. Chaney, E.J. Fenyves, H.D. Hammack, M.R. O'Malley, D.J. Suson, A.V. Vassiliev

University of California, Riverside, USA

D. Chrisman, J.W. Gary, P. Giacomelli, W. Gorn, J.G. Layter, B.C. Shen

University of Rochester, Rochester, USA

A. Bodek, H. Budd, P. De Barbaro, D. Ruggiero, W. Sakumoto, E. Skup, P. Tipton

State University of New York, Stony Brook, USA

R. Engelmann, M. Mohammadi Baarmand, K.K. Ng, J. Steffens, S.Y. Yoon

Florida State University - HEPG, Tallahassee, USA

H. Baer, M. Bertoldi, V. Hagopian, K.F. Johnson, J. Thomaston, H. Wahl

Florida State University - SCRI, Tallahassee, USA

M. Corden, Ch. Georgiopoulos, K. Hays, T. Huehn, S. Youssef

University of Alabama, Tuscaloosa, USA

L. Baksay, B. Fenyi, J. Li

Brookhaven National Laboratory, Upton, Long Island, USA

C. Woody

Purdue University - Task D, West Lafayette, USA

A. Bujak, D. Carmony, L. Gutay, S. Medved

Purdue University - Task G, West Lafayette, USA

V.E. Barnes, G. Bolla, D. Bortoletto, M. Fahling, A.F. Garfinkel, A.T. Laasanen

Institute of Nuclear Physics of the Uzbekistan Academy of Sciences, Ulugbek, Tashkent, UZBEKISTAN

A. Avezov, N. Bisenov, A. Gaffarov, E. Gasanov, R. Gulamova, E. Ibragimova, K. Kim, Y. Koblik, D. Mirkarimov, A. Morozov, N. Rakhmatov, I. Rustamov, A. Urkinbaev, B. Yuldashev

1 Also at Institute Rudjer Boskovic, Zagreb, Croatia

2 Also at CERN, Geneva, Switzerland

3 Also at ENEA, S. Maria di Galeria, Italy

4 On leave of absence from Imperial College, London, United Kingdom

ACKNOWLEDGEMENT

The CMS Hadron Calorimeter Project would like to thank and acknowledge the important technical contributions made to this Technical Design Report by the following individuals:

M. Elongovan, P.R. Joseph, S.D. Kalmani, P. Nagaraj, L.V. Reddy, B. Satyanarayana Tata Institute for Fundamental Research (HECR), Mumbai, India

S. Bhattacharya, S.R. Chendvankar, M.H. Damania, M.R. Patil, N. Raja

Tata Institute for Fundamental Research (EHEP), Mumbai, India

A. Levin, V. Potapov, N. Skvorodnev, Yu. Orlov

Institute of High Energy physics, Protvino, Moscow Region, Russia

L. Bartoszek (consultant), J. Blomquist, S. Carlson, P. Deering, S. Hansen, J. Hoffman, S. Orr, Yu. Orlov, V. Polubotko, C. Rivetta, V. Sidirov

Fermi National Accelerator Laboratory, Batavia, Illinois, USA

Q. Shen

Purdue University, West Lafayette, USA

M. Kaya, D. Magarell, J. McPherson, E. Ozel, S. Ozkorucuklu, P. Pogodin

University of Iowa, Iowa City, USA

D. England, T. Haelen

Rochester University, Rochester, New York, USA

The Group is also indebted to the invaluable help given during the preparation of this report under the direction of Terry Grozis and aided by Patty Poole and Olivia Vizcarra of Fermilab.

Cover picture by S. Cittolin (CERN)

Table of Contents

CHAPTER 2

CHAPTER 3

CHAPTER 11

CHAPTER 12

CHAPTER 14

CHAPTER 15

1.1 OVERVIEW

1.1.1 The compact muon solenoid

The CMS detector[1] has been designed to detect cleanly the diverse signatures of new physics at the Large Hadron Collider. It will do so by identifying and precisely measuring muons, electrons and photons over a large energy range; by determining the signatures of quarks and gluons through the measurement of jets of charged and neutral particles (hadrons) with moderate precision; and by measuring missing transverse energy flow, which will enable the signatures of non-interacting new particles as well as neutrinos to be identified.

The CMS detector is shown in Fig. 1.1. It consists of a 4 Tesla Solenoidal Superconducting Magnet 13.0m long with an inner diameter of 5.9m. It is surrounded by 5 "wheels" (cylindrical structures) and 2 endcaps (disks) of muon absorber and muon tracking chambers, giving a total length of 21.6m and an outer diameter of 14.6m. This system forms the "Compact Muon Solenoid" which gives the detector its name. The Solenoid Magnet and everything located inside its cryostat are supported by the central wheel. Inside the magnet cryostat are placed three sets of charged particle tracking devices and a two-section calorimeter to measure particle energies (electromagnetic and hadron calorimeters). The cryostat, all detectors inside it, as well as the 5 muon wheels, are in a barrel (cylindrical) geometry and form the so-called "barrel" detectors. The endcap calorimeters are mounted on the inside of the two muon endcaps and are inserted into the ends of the cryostat.

The CMS tracker consists of a silicon pixel barrel and forward disks, followed by silicon microstrip devices again placed in a barrel and forward disk configuration. This silicon tracker system is surrounded by microstrip gas chamber (MSGC) planes with the same barrel and disk geometry. The tracker is located inside the calorimeter system and is suported by it. The CMS electromagnetic calorimeter barrel consists of about 100,000 rectangular crystals of $PbWO_4$, each 23 cm (25.8 X_0, 1.1 λ) in length and approximately 2cm ∞ 2cm in cross-section. Outside the crystal calorimeter, and supporting it, is the barrel hadron calorimeter, which rests on two rails in the cryostat vessel (on either side of the median plane). The combined response of the electromagnetic and hadron calorimeters provides the raw data for the reconstruction of particle jets and missing transverse energy.

1.1.2 The CMS hadron calorimeter

The combined CMS calorimeter system will measure quark, gluon and neutrino directions and energies by measuring the energy and direction of particle jets and of the missing transverse energy flow. This determination of missing energy will also form a crucial signature for new particles and phenomena, such as will be encountered in the searches for the supersymmetric partners of quarks and gluons. The hadron calorimeter will also help in the identification of electrons, photons and muons in conjunction with the electromagnetic calorimeter and the muon system. Thus the Hadron Calorimeter is an essential subsystem of the CMS detector, and will contribute to most if not all of CMS's physics studies.

The central pseudorapidity range $(|\eta| < 3.0)$ is covered by the barrel and endcap calorimeter system consisting of a hermetic crystal electromagnetic calorimeter (ECAL)

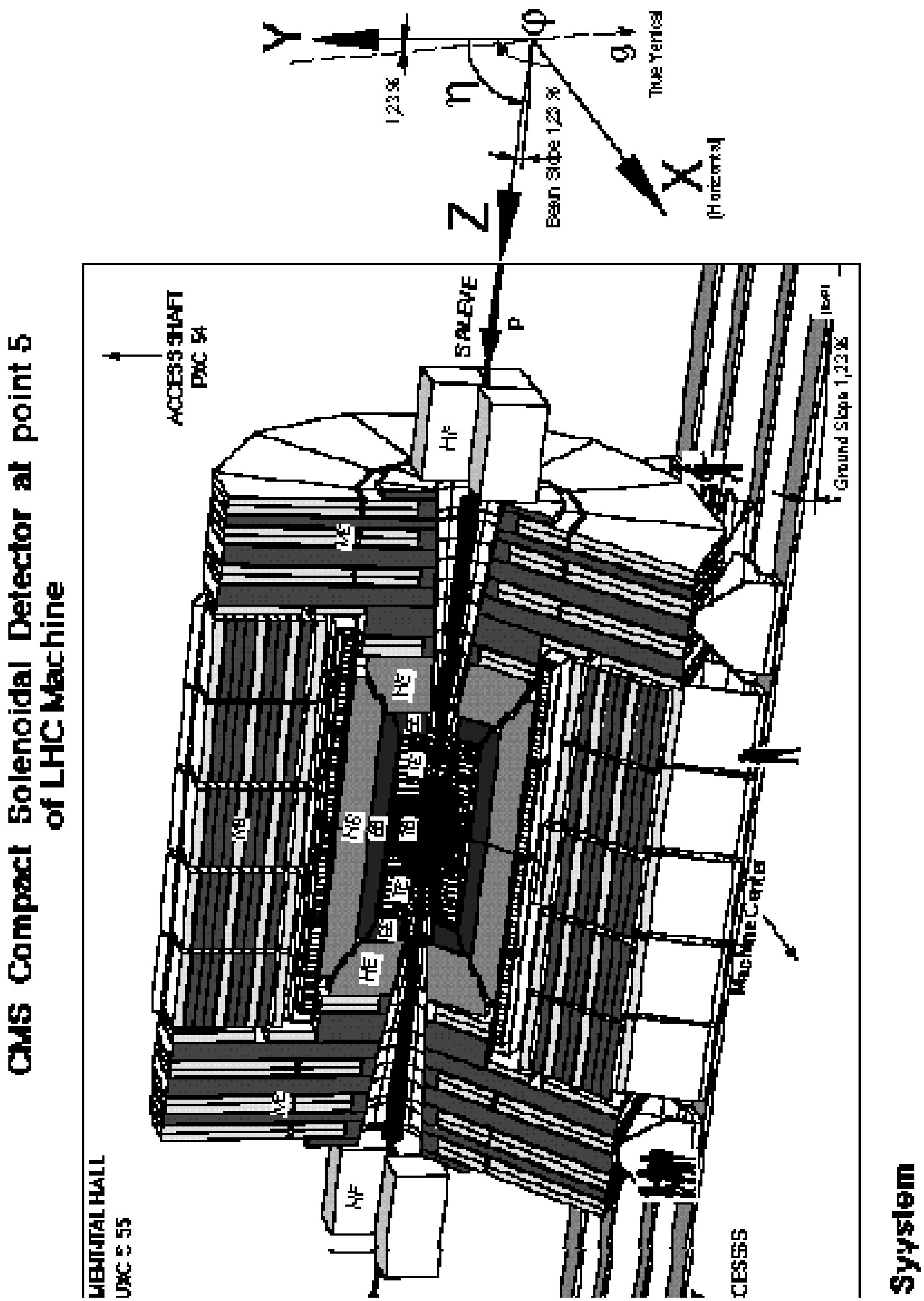

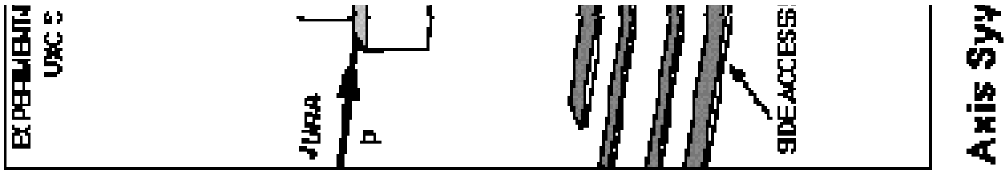

Fig. 1. 1: The CMS detector.

followed by the hadron calorimeter barrel (HB) and endcap (HE) as shown in Fig. 1.2. Both the barrel and endcap calorimeters experience the 4 Tesla field of the CMS solenoid and hence are necessarily fashioned out of non-magnetic material (copper alloy and stainless steel). The Central Hadron calorimeter is a sampling calorimeter: it consists of active material inserted between copper absorber plates. The absorber plates are 5cm thick in the barrel and 8cm thick in the endcap. The active elements of the entire central hadron calorimeter are 4mm thick plastic scintillator tiles read out using wavelength-shifting (WLS) plastic fibers.The barrel hadron calorimeter is about 79 cm deep, which at =0 is 5.15 nuclear interaction lengths (λ) in thickness. This is somewhat thin, as is the transition region between barrel and endcap. To ensure adequate sampling depth for the entire $|\eta| < 3.0$ region the first muon absorber layer is instrumented with scintillator tiles to form an Outer Hadronic Calorimeter (HO). These layers are shown in red in Fig. 1.2.

The choice of crystals for the EM calorimeter, as well as the thinness of the barrel calorimetry, places severe constraints on the hadron calorimeter design and tempers its peformance. A certain amount of ingenuity is required to optimize the calorimeter resolution and response. Constant vigilance during the design stage is also required in order that all necessary cable and service paths are kept to an absolute minimum to minimize hadronic energy leakage or absorption by unsampled material. Accounting for all energy is essential for an optimal missing transverse energy measurement.

To extend the hermeticity of the central hadron calorimeter system to pseudorapidity (η) of five (as required for a good missing transverse energy measurement), CMS employs a separate forward calorimeter (HF) located 6m downstream of the HE endcaps. The HF calorimeter covers the region $3.0 < |\eta| < 5.0$. It uses quartz fibers as the active medium, embedded in a copper absorber matrix. The HF will be located in a very high radiation and a very high rate environment. Because of the quartz fiber active element, it is predominantly sensitive to Cerenkov light from neutral pions. This leads to its having the unique and desirable feature of a very localized response to hadronic showers.

1.1.3 The CMS baseline barrel calorimeter

The hadron calorimeter barrel is a sampling calorimeter with 5cm thick copper absorber plates. The innermost and outermost plates are 7cm thick and are made of stainless steel for structural strength. The CMS baseline for the hadron barrel calorimeter comprises 13 copper plates plus the 2 stainless steel plates for a total of 15 sampling plates and a sampling depth of about 79 cm (5.15). There is good evidence that there may be adequate space inside the cryostat to increase the calorimeter depth by two additional copper plates by optimizing the use of space by the electromagnetic calorimeter and the tracker. If such space savings can be achieved, the hadron calorimeter could be increased in depth to 17 sampling plates for a sampling depth of about 89 cm (5.82). Throughout this Technical Design Report it is assumed that the 5.82 barrel calorimeter configuration will be the final CMS configuration (this viewpoint was endorsed by the CMS Technical Board and Management Board in March of 1997). Since the optimization of space utilization for both the crystal calorimeter and the tracker is still in progress the final calorimeter layout will have to await the Crystal Calorimeter and Tracker TDR's. The performance of the hadron calorimeter for both the 5.15 inner barrel configuration and the 5.82 inner barrel configuration are discussed in the appropriate calorimeter performance sections of this report.

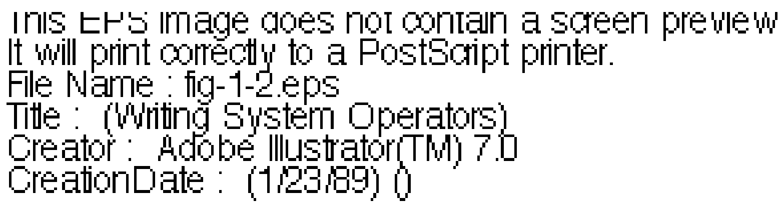

Fig. 1. 2 (see also C.S.): Section of CMS detector with HCAL shown in red.

1.1.4 The CMS forward calorimeter

The measurement of E_T^{miss} is essential for the study of top quark production and for Standard Model (SM) Higgs searches for mH ♠ 80 - 140 GeV and mH ³ 500 GeV in the H ∅ WW ∅ lνjj channels. It is also important in SUSY Higgs searches for A ∅ ττ ∅ eμ + E_T^{miss} and A ∅ ττ ∅ l±h± + E_T^{miss}, allowing the A mass reconstruction.

Forward jet detection is critical in the search for a heavy Higgs boson (mH ♠ 1 TeV), with the decay H ∅ WW ∅ lνjj, H ∅ ZZ ∅ lljj, at high luminosity, 10^{34} $cm^{-2}s^{1}$. The production of the Higgs boson in this mass range through the WW or ZZ fusion mechanism is often characterised by two forward tagging jets. The jets are energetic (<pL> ♠ 1 TeV), with a transverse momentum of the order of mW and they are produced in the pseudorapidity range 2.0 ² |η| ² 5.0. The detection of these tagging jets is needed in order to suppress the large QCD W, Z + jets background.

It is essential to have the capability to recognise and veto jets at forward angles in the search for direct Drell-Yan (DY) slepton pair production or the associate direct DY chargino-neutralino production, leading to final states with two or three isolated leptons, no jets and Etmiss. This is necessary to suppress the SUSY and SM backgrounds. With a coverage up to |η| ♠ 4.5, vetoing events containing a forward jet of E_T^{jet} ♠ 25 - 30 GeV will reject SUSY backgrounds by a factor 350 - 400 (SM background by a factor 9 - 10), with a 7% signal loss. In the case of slepton searches in two-lepton final states, the corresponding SUSY (SM) rejection factor, by veto on same type of forward jets, will be 30-50 (8 -10) with a loss in signal acceptance in the order of 10%.

In heavy ion collisions, the production rate of heavy vector mesons (Y, Y', Y") as a function of the global energy density in nucleus-nucleus interactions, will be measured and the energy density can be estimated from the transverse energy flow measured in the calorimeters.

1.1.5 The luminosity monitor

The CMS luminosity monitor detector will consist of the forward quartz fiber calorimeter as well as Roman Pots 300-400 m upstream of the low beta insertion.

1.2 PHYSICS REQUIREMENTS

The Standard Model (SM) is a very successful description of the interactions of the components of matter at the smallest scales ($<10^{-18}$ m) and highest energies (~ 200 GeV) available. It is a quantum field theory which describes the interaction of spin-1/2, point-like fermions, whose interactions are mediated by spin-1 gauge bosons. The bosons arise when local gauge invariance is applied to the fermion fields, and are a manifestation of the symmetry group of the theory, which for the standard model is SU(3) ∞ SU(2) ∞ U(1). The fundamental fermions are leptons and quarks. There are three generations of fermions, each identical except for mass. The origin of this generational structure, and the breaking of generational symmetry (i.e. the different masses of each generation) remains a mystery. Corresponding to the three generations, there are three leptons with electric charge -1, the electron (e), the muon (μ) and the tau (τ), and three electrically neutral leptons (the neutrinos ν_e, ν_μ and ν_T). Similarly there are three quarks with electric charge +2/3, up (u), charm (c) and top (t), and three with electric charge -1/3, down (d), strange (s) and bottom (b). There is mixing between the three generations of quarks, which in the SM is parametrized (but not explained) by the Cabibbo-Kobayashi-Maskawa (CKM) matrix.

The quarks are triplets of the SU(3) gauge group and so they carry an additional "charge", referred to as color, which is responsible for their participating in the strong interaction (quantum chromodynamics or QCD). Eight vector gluons mediate this interaction; they carry color charges themselves, and are thus self-interacting. This implies that the QCD coupling α_S is small for large momentum transfers but large for soft processes, and leads to the confinement of quarks inside color-neutral hadrons (like protons and neutrons). Attempting to free a quark produces a jet of hadrons through quark-antiquark pair production and gluon bremsstrahlung.

In the SM, the SU(2) ∞ U(1) symmetry group, which describes the so-called Electroweak Interaction, is spontaneously broken through the existence of a (postulated) Higgs field with non-zero expectation value. This leads to the emergence of massive vector bosons, the $W^\pm$ and the Z, which mediate the weak interaction, while the photon of electromagnetism remains massless. One physical degree of freedom remains in the Higgs sector, which could be manifest most simply as a neutral scalar boson H^0, but which is presently unobserved.

The basics of the standard model were proposed in the 1960's and 1970's. Increasing experimental evidence of the correctness of the model accumulated through the 1970's and 1980's. Deep inelastic scattering experiments at SLAC showed the existence of point-like scattering centers inside nucleons, later identified with quarks. The c and b quarks were observed and neutral weak currents (Z exchange) were identified. Tet structure and three-jet final states (from gluon bremsstrahlung) were observed in e^+e^- and hadron-hadron collisions, and the W and Z were directly observed at the CERN SPS collider. Following these discoveries, the last decade has largely been an era of consolidation. Ever more precise experiments have been carried out at LEP and SLC which have provided verification of the couplings of quarks and leptons at the level of 1-loop radiative corrections - $O(10^{-3})$. The top quark was discovered at Fermilab in 1995, and is found to have an unexpectedly large mass (175 GeV). Only two particles from the Standard Model have yet to be observed: ν_T (whose existence is strongly inferred from Z decays) and the Higgs boson. The latter is most important as it holds the key to the generation of W, Z, quark and lepton masses.

The successes of the Standard Model have drawn increased attention to its limitations. In its simplest version, the SM has 19 parameters - three coupling constants, nine quark and lepton masses, the mass of the Z boson which sets the scale of the weak interaction, four CKM mixing parameters, and one (small) parameter describing the scale of CP violation in the strong interaction. The remaining parameter is associated with the mechanism responsible for the breakdown of the electroweak SU(2) ∞ U(1) symmetry to U(1) of electromagnetism ("electroweak symmetry breaking" or EWSB). This can be taken as the mass of the Higgs boson the couplings of the Higgs are determined once its mass is given. Within the model we have no guidance on the expected mass of the Higgs boson. The current (June 1997) experimental lower bound from LEP2 is about 77 GeV, and the upper limit from global fits to electroweak parameters is about 470 GeV. As its mass increases, the self-couplings of the W and Z grow, and so the mass must be less than about 800 GeV, or the strong dynamics of WW and ZZ interactions will reveal new structure. It is this simple argument that sets the energy scale that must be reached to guarantee that an experiment will be able to provide information on the nature of electroweak symmetry breaking, which is the central goal of the Large Hadron Collider.

The presence of a single elementary scalar boson is distasteful to many theorists. If the theory is part of some more fundamental theory with a larger mass scale (such as the scale of grand unification, or the Planck scale) then radiative corrections will result in the Higgs mass being driven up to this large scale unless some delicate cancellations are engineered. There are two ways out of this problem which both result in new physics on the scale of 1 TeV. New strong dynamics could enter that provide the scale of the W mass or new particles could appear which would cancel the divergences in the Higgs boson mass. In any of these eventualities - standard model, new dynamics or new particles - something must be discovered at the TeV scale, i.e. at the LHC.

Supersymmetry is an appealing concept for which there is at present no experimental evidence. It offers the only presently known mechanism for incorporating gravity into the quantum theory of particle interactions and provides an elegant cancellation mechanism for the divergences affecting the Higgs mass, while retaining all the successful predictions of the standard model and allowing a unification of the three couplings of the gauge interactions at a high scale. Supersymmetric models postulate the existence of superpartners for all the presently observed particles. There are bosonic superpartners of fermions (squarks and sleptons), and fermionic superpartners of bosons (gluinos and gauginos χ_i^0, $\chi_i^{\pm}$). There are also multiple Higgs bosons: h, H, A and $H^{\pm}$. There is thus a large spectrum of presently unobserved particles, whose exact masses, couplings and decay chains are calculable in the theory given certain parameters. Unfortunately these parameters are unknown; but if supersymmetry has anything to do with EWSB, the masses should be in the region 100 GeV - 1 TeV.

An example of the strong coupling scenario is "technicolor" models based on dynamical symmetry breaking. An elegant implementation of these ideas is lacking. Nonetheless, if the dynamics has anything to do with EWSB, we would expect new states in the region 100 GeV - 1 TeV. Most models predict a large spectrum. At the very least, there must be structure in the WW scattering amplitude at around 1 TeV center of mass energy.

There are also other possibilities for new physics that are not necessarily related to the scale of EWSB. There could be neutral or charged gauge bosons with masses larger than the Z or W. There could be new quarks, charged leptons or massive neutrinos or quarks and leptons might turn out not to be elementary objects. While we have no definite expectations for the masses of such particles, the LHC must be able to search for them over its entire available energy range.

The fundamental physics goal of the CMS detector is then to uncover and explore the physics behind electroweak symmetry breaking. This involves the following specific challenges:

a) Discover or exclude the Standard Model Higgs and/or the multiple Higgs bosons of supersymmetry;

b) Discover or exclude supersymmetry over the entire theoretically allowed mass range;

c) Discover or exclude new dynamics at the electroweak scale.

The energy range opened up by the LHC allows us to search for other, perhaps less well-motivated objects:

a) Discover or exclude any new electroweak gauge bosons with masses below several TeV;

b) Discover or exclude any new quarks or leptons that are kinematically accessible.

CMS will have the possibility of exploiting the enormous production rates for standard model processes for studies such as:

a) The production and decay properties of the top quark, and limits on possible exotic decays;

b) b-physics, particularly that of B-baryons and B_s mesons.

CMS must also have the capability to find the totally unexpected. We can be sure, though, that new phenomena of whatever type will decay into the particles of the standard model. In order to cover the list above, great flexibility is required. The varied physics signatures of these processes require that CMS be able to reconstruct and measure final states involving the following:

a) charged leptons: electrons, muons and **taus**

b) **jets** coming from high-transverse momentum quarks and gluons

c) **jets** having b-quarks in them

d) **missing transverse energy** (E_T^{miss}) carried off by weakly interacting neutral particles such as neutrinos

e) the electroweak gauge bosons: photons, and Z and W bosons (in both their **dijet** and lepton plus **missing transverse energy** modes)

The CMS detector requires a hadron calorimeter to identify and measure the items noted in boldface above - jets, including those from b-quarks and taus, and missing transverse energy. In the design of CMS, considerable weight has been given to obtaining the best possible performance for muon identification and measurement and for the electromagnetic calorimetry (for photon and electron measurements). Our goal in designing the hadron calorimeter system is then to provide the best possible measurements of jets and missing transverse energy consistent with the chosen emphasis on muons and EM calorimetry, and to carry out an overall optimization of the detector so that the demands and performance of each subsystem match the physics goals of CMS.

In addition to the physics studies carried out with proton-antiproton collisions, CMS will search for the formation of quark - gluon plasma or other new physics in heavy ion collisions. Nuclei as heavy as lead will be collided in the LHC, and jets and muons will be used by CMS to probe the extremely high energy densities in the resulting nuclear matter. Hadronic calorimetry will again be central to such measurements.

1.3 THE CMS RADIATION ENVIRONMENT

1.3.1 Overview

The nominal luminosity of LHC, 10^{34} cm^{-2} s^{-1}, together with the 7 TeV beam energy, will create a very hostile radiation environment which all subdetectors will have to deal with. It has been known since the first LHC pre-studies, that the inner tracker and very forward calorimeters of LHC experiments will be confronted with unprecedented radiation levels. The endcap calorimeters and the muon spectrometer will also suffer from the environment. In CMS, due to the strong solenoidal field and the massive iron yoke, the barrel calorimetry and barrel muon spectrometry are the subsystems least affected by background and radiation damage effects.

We can distinguish three regions with quite different characteristics from the shielding point of view.

1. The main detector, up to | | = 3.0, where we have to deal with the pp-secondaries directly, but also with neutron albedo and hadronic punchthrough.

2. The region | | = 3.0-5.0 is covered by the HF. Cascades developing here affect the HF itself and its electronics, but any leakage would be of concern for the close by endcap muon system also.

3. At pseudorapidities beyond the acceptance of the HF comes the collimator, which protects the superconducting quadrupoles. Cascading in this region is the dominant source of radiation background in the experimental cavern outside of the detector.

Particles with $| \, |$ > 7.9 will not be captured in the experimental area.

1.3.2 Radiation damage

The hostile radiation environment implies that a lot of attention has to be devoted to selecting sufficiently radiation hard technologies. A significant part of LHC related R&D work has in fact concentrated on radiation hardness studies of detectors and electronics.

Silicon devices will be used in essentially all parts of CMS, either as electronic chips, as charged particle detectors or as photodiodes.

Similar dose-related damage effects have been reported for organic and inorganic scintillators, i.e. the $PbWO_4$ crystals of the CMS electromagnetic calorimeter and the plastic scintillators of the CMS central hadron calorimeter. In these cases the light transmission degrades due to the generation of color centers by the ionization (i.e. the plastic becomes less transparent). Thus the degradation of scintillators is also a function of the radiation dose.

Although in most cases significant annealing is observed, some fraction of the damage is never recovered and the detectors continuously degrade with increasing fluence or dose. The annealing effects make radiation damage a complicated function of both time and fluence. For instance, the calibration of a calorimeter might change due to both degradation during irradiation and simultaneous improvement due to annealing. If the annealing is very fast the calorimeter response can become luminosity dependent.

1.3.3 Induced radioactivity

While induced radioactivity is negligible at electron-positron colliders, it will be a major concern at LHC. We can assume that each inelastic hadronic interaction results in a residual nucleus, which can be almost anything below the target mass and charge. This residual can directly end up being stable, but more probably it will be radioactive.

Only some 30% of the interactions lead to formation of long-lived radionuclides, which we would really see as induced activity when entering the area. But this activity decreases relatively slowly after the end of irradiation, so that even long cooling times do not significantly improve the situation. A rough rule of thumb is that the effective half life of the remaining radioactivity is equal to the time which has elapsed after the end of irradiation.

1.3.4 Shielding requirements and materials

Inside of CMS shielding is dictated by the very limited space available. Therefore materials have been selected to provide the most efficient shielding in the smallest amount of space. An equally strong constraint on the choice of shielding strategy arises from the fact that the performance of the detectors cannot be compromised.

Outside the detector, around and beyond the HF, the constraints come mainly from cost and weight, although space restrictions have to be also taken into account for the HF shielding.

At LHC we are confronted with a radiation environment which includes essentially all types of particles. The energy distribution ranges from thermal neutrons up to the typical hadron energy around 1 GeV and ends in a high energy tail which extends to few TeV. This heterogeneous radiation environment implies that no shielding material alone will be the perfect one.

1.3.5 Minimum bias events

The radiation environment simulations are based on minimum bias events obtained from the DPMJET-II event generator[2]. DPMJET-II is the most recent of the Dual Parton Model generators, which are specially suited for simulation of minimum bias hadronic collisions. As one of the updates with respect to the best-known of its predecessors, the DTUJET93 generator[3], DPMJET-II includes a complete description of charm production.

1.3.6 Radiation transport codes

The radiation simulations are independent of the general detector performance simulations and are performed using simulation packages specially designed for radiation physics. FLUKA[4] is the baseline code for the radiation environment simulations of CMS, but MARS and GCALOR are also used for various dedicated studies.

Although FLUKA does not provide a user friendly geometry interface like GCALOR and is therefore not compatible with CMSIM, its use is motivated by more accurate and up-to-date physics models and the indispensable variance reduction possibilities.

1.3.7 Barrel and endcap calorimeter

Fig. 1. 3 gives an overview of hadron (E>100 keV) fluence and radiation dose in the CMS HB/HE region. At the end of the HE we can see some radiation streaming in the 3.44 cm wide gap, which is caused only by the approximate geometry. This gap is not present in reality and we can see that at large radii it leads

to slight overestimation of neutron fluence.

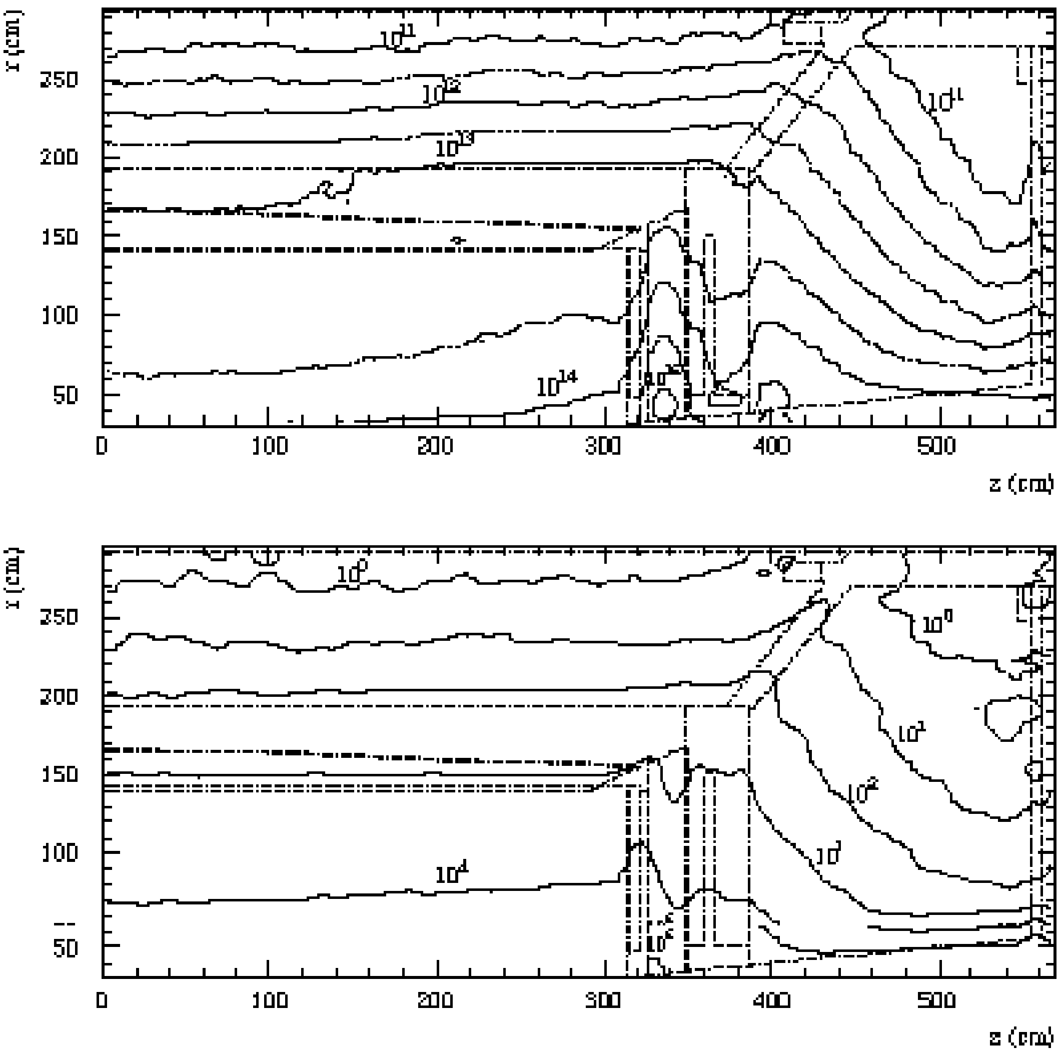

Fig. 1. 3: Fluence of hadrons (E>100 keV) in $cm^{-2}s^{-1}$ (upper plot) and radiation dose in Gy (lower plot) in the HB/HE region. The dose values have been smoothed by taking weighted running averages over neighbouring bins. Values are given for 5 10^5 pb^{-1}. The intermediate (dashed) contours in the fluence plot correspond to 3.16 10^n. The dotted lines indicate the geometry.

While Fig. 1. 3 is based on data obtained with a binning which is much coarser than the internal structure of the calorimeter, Fig. 1. 4 shows the dose in the HE for some fixed radii with a binning fitted to the internal structure. The alternation of absorber and scintillator layers in the HE becomes visible as a strong variation of the dose. This clearly indicates that a dose calculated in average material would underestimate the critical parameter, which is the dose in the plastic scintillators. Because most of the dose increase is due to recoil protons induced by low energy neutrons, simple corrections based on the variation of dE/dx cannot correct for the effect.

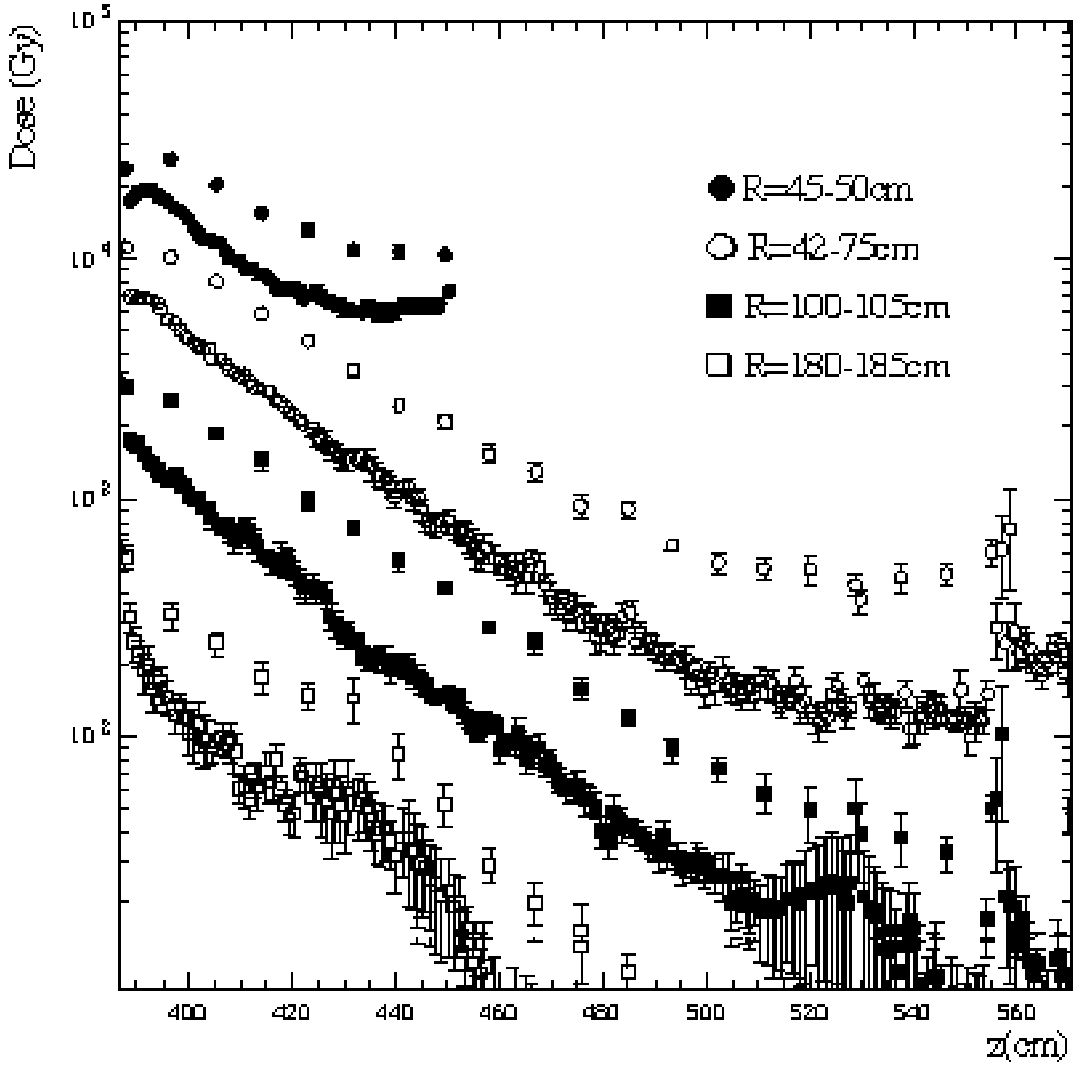

Fig. 1.4: Radiation dose for 5 10^5 pb^{-1} at fixed radii in the endcap HCAL. The error bars indicate only the statistical error of the simulations. The points with higher dose correspond to energy deposition in the scintillator layers.

In Fig. 1. 4 the effect of the calorimeter boundary at $|\eta|=3$ becomes significant at the smallest radii. The increase of dose as a function of depth is due to the particles entering the calorimeter from its $|\eta|=3$ boundary. At the end of the HE the dose increase is caused by the slot for the muon station ME1/1 and the crack left in the simulation model between the HE and the stainless steel back plate.

1.3.8 Forward calorimeter

HF is exposed to the most intense radiation of all CMS subdetectors. This is best seen if we consider that on average 760 GeV per event are incident on the two forward calorimeters, compared to only 100 GeV for the whole main detector. In addition, this energy is not uniformly distributed, but has a pronounced maximum at the highest rapidities.

The quartz fibres themselves can sustain significant radiation doses and hadron fluences. The hadron fluence and dose profiles in the HF are shown in Fig. 1.5**.** The lower energy cut for plotting the hadron fluence, including neutrons, is 100 keV.

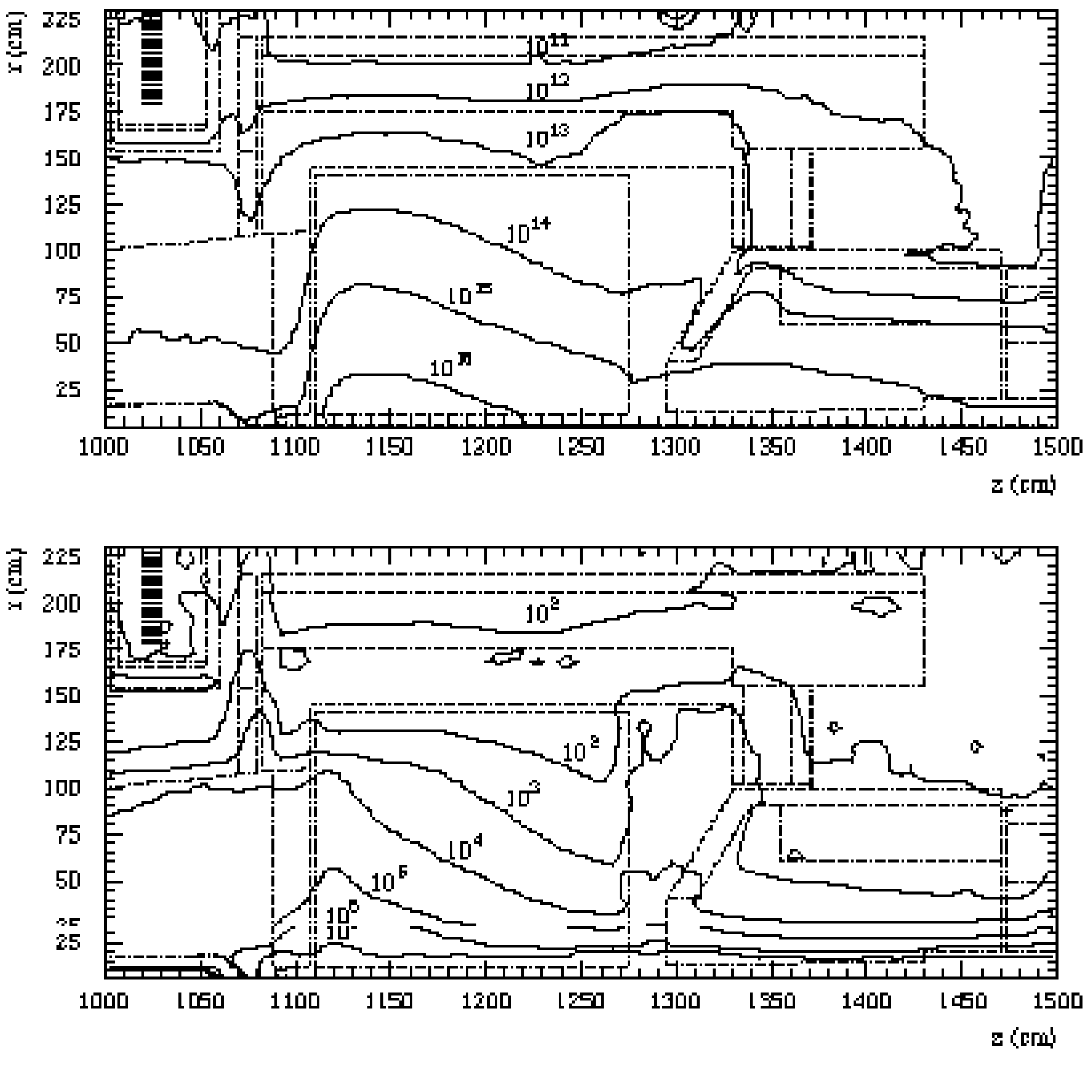

Fig. 1. 5: Fluence of hadrons (E>100 keV) in $cm^{-2}\ s^{-1}$ (upper plot) and radiation dose in Gy (lower plot) in the HF and its surroundings. The dose plot has been smoothed by taking running averages of the values, which slightly masks the dependence of dose on geometry details. Values are given for 5 10^5 pb^{-1}.

We can see from Fig. 1.5 that the shielding quite efficiently suppresses the hadron flux, and in particular the optimized interface between the endcap and the HF provides good shielding for the ME4 muon station. The polyethylene/iron layer around the back shielding plug protects the HF photomultipliers. The endplug efficiently suppresses both the dose and the neutron flux at the back of the calorimeter and smoothly joins with the rotating shielding. The shielding around the HF is most important for ME4. We can see that it suppresses neutron fluence and dose below the overall levels in the experimental area.

1.3.9 Radiation levels in scintillators

In Table 1. 1 the dose in the HE scintillators is collected along lines of constant rapidity. The raw data is obtained from equidistant radial bins and the values have been linearly interpolated between two bins. Corresponding data for the HB is shown in Table 1. 2. It has to be emphasized that the statistical significance of the given dose values in the outermost corner if the HE, around $|\eta|$1.5, is relatively poor.

We observe an increase of dose in the last scintillator layer. This is mostly due to the close-by slot for the endcap muon station ME1/1. The maximum dose at 2.8 is 26 kGy. Going even further up in pseudorapidity, the absolute dose maximum of 37 kGy is found in the second scintillator layer of the HE (after first absorber plate) at a radius of 40-45 cm.

Table 1. 1

Radiation dose (Gy) in the scintillators of the HE for an integrated luminosity of 5 10^5 pb^{-1}.

z (cm)	=1.5	=2.0	=2.8
388	570	3800	24000

Table 1. 2

Radiation dose (Gy) in the scintillators of the HB for an integrated luminosity of 5 10^5 pb^{-1}.

Radius (cm)	=0.1	=0.6	=1.1
198	190	250	300

The general "rule of thumb" that in hydrogen-containing regions of CMS the 100 keV threshold roughly splits the total neutron fluence in half, is supported by these HCAL fluences.

Activation and associated photon production are mainly low-energy phenomena, usually occurring only in the thermal regime. It should be understood that the actual thermal neutron fluence is only a small fraction of the difference between the total and the >100 keV fluence. In most parts of the HCAL the thermal neutron fluence is less than one percent of the total. But it should be noted that this low fluence is mostly due to the relatively small range of thermal neutrons in the HCAL material.

1.3.10 Radiation levels in HPD boxes

The HPD boxes were included explicitly in the simulation, although modeled as an annular ring in order to preserve the cylindrical symmetry. Their average density was assumed to be 2.4 g/cm^3. The composition was assumed to be a copper/plastic mixture. The energy spectrum for the HB boxes for photons and neutrons is shown in Fig. 1.6. Table 1. 3 shows the particle fluences and radiation dose in the barrel and endcap HPD boxes.

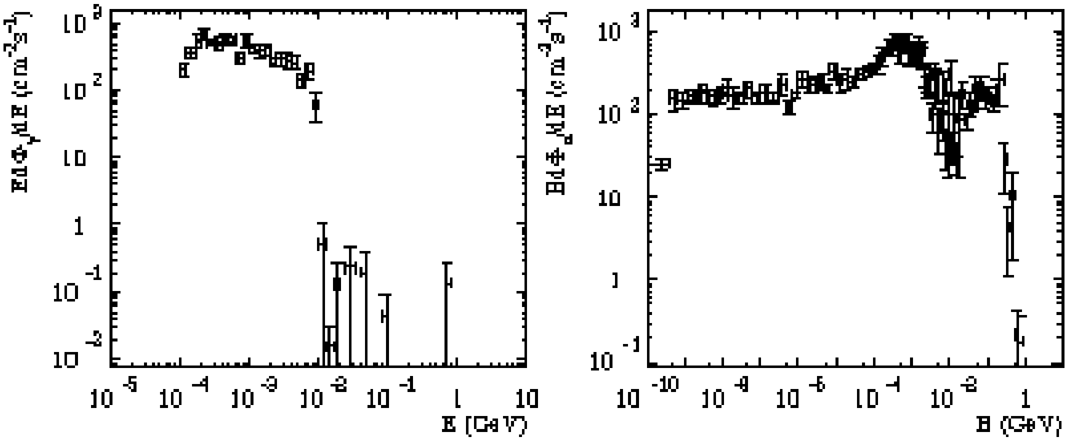

Fig. 1. 6 : Energy spectra of photons and neutrons in the barrel HPD box. Values are for LHC peak luminosity.

Table 1. 3

Particle fluence and dose in the HPD boxes. The hadron fluence is mainly neutrons above 100 keV and is the proper quantity for estimating silicon bulk damage. All fluences are given in 10^{10} cm^{-2} and the dose in Gy. All values are for 5 10^5 pb^{-1}.

	Barrel	Endcap
Total neutron fluence	28	7
Hadron fluence	13	2
Photon fluence	9	2
Dose	1.6	0.2

1.4 THE CMS HADRON CALORIMETER DESIGN SUMMARY

1.4.1 Requirements and design constraints1.4.1.1

Requirements

The design of the hadron calorimeter requires good hermiticity, good transverse granularity, moderate energy resolution and sufficient depth for hadron shower containment. We have chosen a lateral granularity of $\Delta\eta \times \Delta\phi = 0.087$ for $|\eta| < 2.0$ to match the electromagnetic calorimeter and the muon chamber structure. This granularity is sufficient for good dijet separation and mass resolution. The calorimeter readout must have a dynamic range from 5 Mev to 3 TeV to allow the observation of single muons in a calorimeter tower for calibration and trigger redundancy purposes as well as measure the highest possible particle jet energies that might arise in the search for new phenomena.

The physics program most demanding of good hadronic resolution and segmentation is the detection of narrow states decaying into pair of jets. The dijet mass resolution receives contributions from physics effects such as fragmentation and initial and final state radiation, as well as detector effects such as angular and energy resolution. When the jet p_T is small, mass resolution is dominated by physics effects. High p_T jets may arise from either the decays of boosted light objects or from decays of heavy objects. For the boosted case, angular resolution plays a more important role than energy resolution. Only in the case of back to back high p_T jets arising from the decay of heavy objects are the physics and angular effects suppressed to the point where energy resolution plays a significant role.The influence of hadron calorimeter transverse segmentation has been studied for hadronic decays of boosted W's and Z's. Segmentation coarser than $\Delta\eta \times \Delta\phi = 0.1 \times 0.1$ significantly degrades the mass resolution, particularly for W/Z p_T > 500 GeV/c, while the energy resolution has relatively little effect.

Test beam studies of the CMS calorimeter layout (including ECAL) indicate $\sigma_E / E = 100\% / \sqrt{E} \oplus 4.5\%$ is achievable between 30 GeV/c and 1 TeV. Detailed simulations of the cracks, dead material, etc of the calorimeter system have been made to obtain energy and missing E_T resolution as a function of η and ϕ.

The HF jet energy resolution and missing transverse energy resolution is well matched to that of the central calorimeter, as has been confirmed by test beam measurements and simulation studies.

1.4.1.2 Design constraints

The central calorimeters are located inside the CMS solenoid and cryostat. The 4 Tesla field permeates the entire calorimeter structure. The calorimeter support structure must be able to withstand the magnetic forces generated in the unlikely case of a quench of the superconducting solenoid magnet. The response of scintillator to charged particles in high magnetic fields has been measured and understood.

The 25ns time interval between beam crossings sets the scale for the time resolution needed in the calorimeter. The overall event rate of approximately 20 "minimum bias" intractions per crossing at LHC design luminosity sets the scale for unwanted backgrounds. The calorimeter must help distinguish the rare interesting events from this background and must have the granularity and time resolution to suppress multi-event pile up.

The radial depth of the barrel hadron calorimeter is restricted by the inner radius of the solenoid cryostat which limits its thickness to about 100cm. To maximize the number of hadronic intraction lengths in the barrel, a copper alloy is chosen as the absorber material.

1.4.2 The central hadron calorimeter design (HB/HE/HO)

Globally, the hadron calorimeter can be considered in two pieces: (a) a central calorimeter $(|\eta| < 3.0)$ in which we require excellent jet identification and moderate single particle and jet resolution; and, (b) a forward/backward calorimeter $(3.0 < |\eta| < 5.0)$ with modest hadron energy resolution but with good jet identification capability. The forward calorimeter is physically separated from the central calorimeter, its front face being located at ±11m from the interaction point.

The Central Calorimeter consists of the Hadron Barrel (HB) and Hadron Endcap (HE) calorimeters, both located inside the CMS magnet cryostat. An Outer Calorimeter (HO) is required in the barrel and endcap region to measure late shower development and ensure of total shower energy containment.

1.4.2.1 Structure

The central calorimeter is divided into a central barrel and two endcap calorimeter sections. The central barrel is divided into two half sections, each half section being inserted from either end of the barrel cryostat of the superconducting solenoid hung from rails in the median plane. Because the barrel calorimeter is very rigid compared to the cryostat, a special Belleville washer (spring) mounting system is used to ensure that the barrel load is distributed evenly along the rails.

A half barrel consists of 18 identical wedges, constructed out of flat absorber plates parallel to the beam axis. The body of the calorimeter is copper but the inner and outer plates are stainless steel. The endcap hadron calorimeter has the same 18 fold segmentation in ϕ. The copper plates are bolted together in a staggered gap/absorber structure to ensure that the calorimeter geometric layout contains no projective dead material for the full radial extent of a wedge. To allow the stacking of such plates without major tolerance build-up, they must be machined to better than 0.3mm in flatness over the entire length of the plate.

To maximize shower energy resolution (after the crystal ECAL) the inner barrel hadron calorimeter is segmented radially (in depth) into two different sampling hadron compartments (HB1 and HB2). There is an initial layer of sampling immediately following the ECAL electronics, and 17 layers of sampling ganged together into a single tower readout. Such an unusual distribution of sampling layers is the result of a response ratio e/h>2 induced by the crystal ECAL for the combined ECAL/HCAL system. The Outer Calorimeter with 2 coarse sampling layers is essential for full containment of hadron showers. Thus there are a total of 19 sampling layers in the barrel, except at = 0 where an additional absorber plate is inserted and sampled immediately outside of the magnet cryostat. All active readout scintillator tiles in each layer are divided into segments $\Delta\eta \times \Delta\phi = 0.087 \times 0.087$. This granularity gives good shower resolution and matches the trigger granularity of the electromagnetic calorimeter and of the muon system.

The two layers of scintillator of the Outer Calorimeter are divided into the same granularity of $\Delta\eta \times \Delta\phi = 0.087 \times 0.087$ as the barrel and envelop the entire first layer of the CMS muon iron absorber. This double layer of scintillator has an individual readout for each $\Delta\eta \times \Delta\phi$ segment (HB3). To wrap around the absorber effectively this scintillator double layer has a 12-fold symmetry to match that of the iron absorber. In the region $(0 < |\eta| < 0.4)$ an additional 15cm of steel are placed in front of the muon chambers. In this region The Outer Calorimeter consists of 3 sampling layers, since we must place a sampling layer immediately after the coil and before this additional absorber plate.

The Endcap Calorimeter (HE) is of monolithic construction, consisting of staggered copper plates bolted together into 10 degree sectors. The innermost and outermost plates along the beam direction are made of stainless steel for strength. Each monolith weighs about 300 tonnes. The HE outer radial perimeter is polygonal, corresponding to the 18 fold wedge structure of the barrel. The plates are bolted and then colleted against shear forces, layer by layer. Fig. 1.7 illustrates this structure. When completely assembled, the Endcap Calorimeter module is mounted onto its corresponding muon endcap. The scintillator trays are inserted before mounting.

Fig. 1.7: Bolted structure of the HE.

The endcap hadron calorimeter is also segmented in depth into two different sampling compartments (HE1 and HE2) with 80mm copper absorber thickness. Generally, there again is an initial sampling layer, followed by 18 layers ganged together into a single tower. However, the Endcap calorimeter has two special regions. The region at high eta, (2 < || <3), is a moderately high radiation area. To be able to re-weight the shower profile response as the scintillator response decreases as a result of radiation damage, the HE is divided into three readout sections (HE1, HE2 and HE3) consiting of (1 + 4 + 14) sampling layers. In a later discussion in this chapter we present a detailed discussion of how the HE can tolerate a certain amount of radiation damage by reweighting the scintillator response. Similarly the cable/service gap contains at least 10cm of non-uniformly distributed material, giving a non-uniform response; again, subdividing the readout into three enables one to reconsruct the shower profiles in the two towers shadowed by the cable/service gap and thus better estimate the energy lost in the material in the gap.

In the endcap region, the Outer Calorimeter has only a single sampling layers. It is essential in the barrel/endcap transition region (1.3 < || < 1.5) for full containment of hadron showers. It is embedded behind the first layer of muon chambers and is an integral part of the muon system. Thus there may be a total of 20 sampling layers in the barrel/endcap transition region. All active readout scintillator tiles in each layer are divided into segments of $\Delta\eta \times \Delta\phi = 0.087 \times 0.087$ as in the barrel (except at the highest region where the segmentation is made to match the granularity of the crystal calorimeter. This granularity gives good shower resolution and matches the overall trigger granularity of the electromagnetic calorimeter and of the muon system.

The effective barrel absorber thickness increases as the polar angle varies as $1/\sin\theta$. The barrel HCAL absorber thickness varies from 5.15λ at $|\eta| = 0$ to 9.1λ at $|\eta| = 1.3$. It follows that the stochastic resolution term in the barrel due to sampling depends only on the physically relevant variable $E_T = E \sin\theta$. A smooth transition is made to the endcap region at $|\eta| = 1.5$. However, two η segments in this region are traversed by a 100mm gap to provide cable and fiber paths to the outer detector. The total absorber thickness in the endcap averages about 10.5λ, to allow for the logarithmic increase in depth needed for the higher energy shower containment at fixed E_T. The electromagnetic calorimeter in front of HB/HE adds about 1.1 λ of absorber.1.4.2.2

Manufacture, shipping, assembly and installation

To facilitate construction, shipping, assembly and installation the barrel is divided into two halves, each half consisting of 18 identical wedge modules (weighing 27 tonnes each), for a total of 36 identical barrel modules. The absorber modules will be constructed at a site remote from CERN. Each half barrel will be pre-assembled at the manufacturing site to ensure its stacking tolerances. The half-barrel will then be disassembled and each individual wedge module will be shipped to CERN and equipped with scintillator trays in CERN Building 168. The final assembly will be in a horizontal orientation on a structural cradle that will also serve as lowering and installation fixture for each half barrel.

The outer CMS muon detector is divided into 5 barrel sections and 2 endcap sections. The central barrel section supports the solenoid and its cryostat vessel. The cryostat vessel in turn supports all barrel detectors that are mounted inside it (calorimeters and trackers). The remaining four barrel sections consist of the muon iron and the barrel muon chambers. The two CMS endcap sections support all of the endcap detectors (calorimeters, and the endcap muon system). The forward calorimeter is mounted independently.

The barrel hadron calorimeter halves are supported on rails attached to the inside of the cryostat vessel. This rail system is parallel to the beam axis and divides the cryostat vessel into two equal longitudinal sections (the upper section of the calorimeter pressing down on the rail, while the lower part hanging down from it). The barrel electromagnetic calorimeter sits on rails mounted on the lower segments of the barrel calorimeter, while the endcap electromagnetic calorimeter is mounted on the front face of its corresponding hadron endcap. The central tracking system, in turn, is mounted on rails attached to lower regions of the barrel em calorimeter.

Each HCAL half barrel will be transferred from its cradle to its resting position on the rails by pulling on a cable system anchored to the corresponding far end of the cryostat. The entire HB will be inserted into the cryostat for surveying in the surface hall, then removed and lowered into the experimental hall for re-insertion into the cryostat.

1.4.3 The central calorimeter optical system

The hadron calorimeter will consist of a large number of towers (~4300). In the barrel, inside the coil each tower will have 17 layers of scintillator tiles grouped into 2 samplings in depth. Outside the coil cryostat an additional two sampling layers of scintillator will be installed (HB3) around the muon absorber.

In order to limit the number of individual elements, the tiles in a given layer constitute a single mechanical unit called a "megatile". The eta-phi segmentation in the Barrel region $16(\eta)\times 1(\phi)$, and $16(\eta)\times 2(\phi)$, to match the staggered copper absorber structure of each barrel wedge. These 16 tiles or 32 tiles in one "megatile" layer of a wedge are organized into a single mechanical unit. The separate tiles are cut out of scintillator, the edges painted white, and the tiles are then attached to a plastic substrate with plastic rivets. The light from each tile is collected by a green Wave Length Shifting (WLS) fiber that is placed in a machined groove in the scintillator. After exiting the scintillator the WLS fiber is immediately spliced to a clear fiber that transports the light to the edge of the megatile. The clear fiber terminates into a multi-fiber optical connector at the megatile boundary. Multi-fiber optical cables carry the light from the megatiles to decoder matrix boxes where the fibers from the different layers comprising a η-φ depth segment are reorganized into towers, and the light from all the tiles making up a tower is optically mixed and sent to an optical transducer. The megatile along with the readout fibers will be packaged into scintillator trays (called "pizza pans") which will be inserted into the calorimeter absorber structure.

The advantage of this scheme is that the scintillator trays can be built and tested remotely from the installation area. Before the calorimeter absorber is lowered into the CMS pit and installed into the solenoid, the trays are rapidly inserted. Another advantage of the tray scheme is that in the unlikely event of catastrophic radiation damage to the scintillator, the trays can be removed and refurbished without removal of the absorber structure. Once in the experimental hall, optical fibers are connected between trays and the photodetectors.

A scintillator tray unit begins with a plastic cover plate of a thickness of 0.5 mm followed by the 4mm scintillator megatile wrapped in thin sheet of Tyvek 1073D (a plastic insulating material) for reflectivity and light tightness. The tiles are grooved to hold the WLS fibers. The top of the megatile is covered with 2mm white polystyrene. This plastic cover is grooved to provide routing for the fibers to the outside of the tray. The fibers rise out of the scintillator into the grooves on top of the white plastic. The white plastic layer is also grooved to accept tubes for the moving radioactive source.1.4.3.1

Choice of materials

We require the materials used in the CMS HCAL optical system to have a number of properties. The materials should have good long-term stability, be non-demanding in handling, and easy to machine. They should be able to survive the expected maximum radiation doses up to $|\eta| = 3.0$ (a total of ~ 0.2 Mrad in the barrel, 4 Mrad in the endcap) without the necessity of replacement. The total optical system should produce enough light to easily identify minimum-ionizing tracks penetrating the calorimeter (for use in muon identification as well as calibration/monitoring). Well controlled thickness (of the scintillator) and diameters (of the fibers) are critical to the optimal performance of the calorimeter. Attenuation lengths of the fibers also must be well-controlled.

Our baseline choice of material for the HCAL optical system satisfies these requirements. For the barrel, we will use Kuraray SCSN81 scintillator plastic. This material has been shown to be moderately radiation hard and have good long-term stability. For the WLS fiber, the baseline choice is Kuraray Y-11 double-clad fiber. The double cladding generates good mechanical properties as well as yielding ~ 1.5 times more light. The baseline clear fiber is Kuraray double-clad fiber.

It is well documented that the light yield from scintillator increases when embedded in a magnetic field [5]. Measurements at Fermilab and Florida State indicate that this effect saturates above 2T [6] for SCSN81 scintillator. This intrinsic brightening of scintillator in a magnetic field was confirmed in our 1996 test beam studies.

In addition to this intrinsic scintillator brightening, the CMS 4 Tesla field creates a geometric path length effect for soft electrons if the magnetic field is parallel to the absorber plates (barrel configuration). This increase in path length for soft electrons leads to an additional increase in the scintillator response by as much as 20% for electrons and about 10% for pions. This effect is well understood and is well simulated by Monte Carlo description of electron showers in high magnetic fields. By studying such simulations we have learned how to reduce such effects for hadrons to the 4% level. This effect is not tracked by any of our monitoring schemes and has to be determined by Monte Carlo calculations and controlled by our manufacturing procedures.

1.4.3.2 Production issues

To realize the tile/fiber technology, several developments were required. These developments, largely due to the CDF and SDC groups, include fiber splicing, mirroring, optical connectors and cables, and fundamental measurements of the tile-fiber optical system. Some of the results are discussed below.

Fibers are spliced together by controlled melting of the ends inside a restricting tube (thermal fusion). This technique has been optimized for factors such as long-term mechanical stability, strength to withstand repeated flexing, high optical transmission and very small variation in transmission for different splices. The mean value of the transmission through a splice (normalized to the uncut fiber) is measured to 91% with an r.m.s. of 1.8%.

Multi-fiber optical connectors were developed by the CDF collaboration. These connectors allow the optical signals to be treated similarly to electrical signals. The scintillator tile trays can be quickly connected and disconnected to multi-fiber optical cables that look strikingly like multi-conductor electrical cables. The optical connectors are made by precision injection molding of mechanically stable plastic. In this manner, all connectors are identical, and there is no need for pair-matching of the connectors. The reproducibility of the optical connector transmission for many make/break operations has been measured to be 0.6% with a mean transmission of 83% for a single fiber, and an overall variation of ~ 2 to 3 % for all fibers in the connector.

Variation in transverse uniformity of tiles in a tower or variation in tile-to-tile light yield for tiles in a tower will generate a contribution to the constant term in the calorimeter resolution. We have carried out detailed studies to identify the requirements on the optical system so that these variations do not contribute substantially to the constant term. We found that tile-to-tile variation of less than 10% is acceptable (see chapter 6). The CDF plug upgrade calorimeter group has built several thousand tiles. The measured finished tile to tile variation of the light yield from a set of over 16,000 of these tiles is found[7] to be 6.5%. This is adequate for a good hadron calorimeter.

The transverse uniformity of a tile is dominated by the placement of the WLS fiber. Based on knowledge from the CDF group, we expect our transverse non-uniformity to be a few per cent. This non-uniformity will not appreciably affect the resolution constant term.

1.4.3.3 Quality control

The scintillator trays will be built and tested remotely. The trays, optical cables, and decoder boxes will be shipped to CERN. There they will be installed in each individual wedge in Building 168. At this time, we must verify that all cables are correctly placed, good optical contacts are made, and that there are no broken or damaged components. We will determine this by using an integrated system of moving radioactive sources. This system allows a radioactive source to illuminate each tile in the system individually. By comparing the induced current to that expected, we can verify the integrity of the system.

The moving source system was developed for the CDF and SDC calorimeter projects. It consists of a set of tubes placed in the scintillator trays plumbed to a "source-mover". The source is inside a long flexible stainless steel tube. The source mover can (via computer control) push the source down any of the tubes and thus expose any of the tiles to the source. The same system will be used for the initial quality control testing at the remote site of the scintillator tray manufacturing. This quality control strategy is the same as used by CDF in their calorimeter upgrade project. Their experience gives us confidence that the strategy will work for CMS as well.

1.4.4 The central calorimeter photodetectors

The HB/HE photodetectors, which convert the optical signal from the fiber bundles corresponding to a tower, are required to have a linear dynamic range of 10^5 and operate in a uniform 4 T magnetic field. For calibration purposes, the detectors must have the capability of measuring the signal generated by a radioactive source as a DC current to a precision of 1%. In addition, the photodetectors are located inside the detector, adjacent to HB or HE itself, where service access is infrequent, thus placing an additional requirement on the mean time to failure. The useful lifetime of the photodetector must correspond to ten years of operation at a luminosity of 10^{34} cm^{-2} s^{-1}. A final requirement on the ratio of the signal to noise follows from the need to measure the signal from a minimum ionizing particle (m.i.p. ~ muon) in a single readout channel.

The proximity focused hybrid photodiode (HPD) is an image intensifier operated in the electron bombardment mode. Photoelectrons emitted from the photocathode are accelerated by an electric field and stopped in a silicon diode target where electron-hole pairs are produced generating the signal. In the device under our consideration, the 10 kV electric potential is uniform and the acceleration gap is 1.5mm to minimize magnetic field effects. Commercial devices are presently available in standard 18mm or 25mm diameter single channel versions. Prototypes have been made in which the diode is subdivided into pixels to make a cost effective multichannel device suitable for reading out fiber bundles corresponding to a number of calorimeter towers.

HPD's exhibit gain that is linear with applied voltage, being about 2000 at 10 kV. The gain has been measured to decrease by only 2% in the axial field of 3 T of the RD-5 magnet. The devices are linear to 2% over the required dynamic range of 10^5 and exhibit a fast response. The outstanding questions for these devices are the use of fiber optic windows, development of non-magnetic packaging, and further reduction of dark current.

The HPD has been chosen as the HB/HE baseline. Several manufacturers are under investigation (DEP and Hamamatsu).

1.4.5 Front end electronics

The electronic readout system of the HCAL will be based on the Fermilab KTeV QIE system for the front end electronics and the CERN FERMI system for readout electronics. The ADC has an effective a dynamic range of 5 MeV to 3 TeV.

The photodetectors and associated HV supplies, as well as their preamplifiers, will reside close to the HCAL detector itself, distributed around the outer radius of the $|\eta| = 1.3$ transition region from barrel to endcap. They would be attached to either the barrel or endcap and would be able to travel along with their own subdetector.1.4.5.1

Electronic system specification

The HCAL electronics can be divided into the front end amplification, ADC and readout systems followed by Level I and Level II trigger Digital Signal Processors. High Voltage, Low Voltage and Slow Control systems and monitors are also required.

From the photodetector to the ADC, we require for each HB and HE channel a photodetector (HPD pixel), amplifier (linear 16-bit range, 40 MHz, 2000 electron r.m.s. noise), shaper-range compressor, ADC channel, cable driver, cable, and cable receiver. At Trigger Level I we require an HB1+HB2+HB3 adder, threshold test electronics, muon bit test electronics, DSP to extract energy and crossing time, DSP to transform energy to E_T and a synchronous link to the rest of Level I. At Trigger Level II we require Level I latency pipeline, DSP to correct gain and subtract pedestals, timing and trigger control interface, derandomization of readout buffers, and control synchronization.1.4.5.2

Front end requirements

The front end requirements are set by the readout of the second HCAL tower longitudinal compartment (HB2), which contains the largest fraction of the hadron shower (on average). The requirements for the other two compartments (HB1 and HB3) can be less stringent, but for sake of uniformity of the electronics are identical to HB2.

The noise floor of the preamplifier and readout system is set by the requirement to cleanly recognize a muon or minimum ionizing signal. This capability is needed to provide independent and redundant information to the track and range signatures derived and matched to the tracker and external muon system. Taking the mean muon signal to be 10 photoelectrons, a threshold of 4 or more photoelectrons is 99% efficient. If this threshold is at 3 sigma of noise, the probability for a pedestal fluctuation to trigger is reduced to 0.25%. Equivalently, the pedestal r.m.s. should be less than 1 photoelectron (p.e.) for high tagging efficiency and low fake probability (2000 electrons r.m.s. after the HPD).

The upper end of the dynamic range is set by the expected maximum physics signal for the HB2 compartment. Because of the muon identification requirement, HCAL towers must be readout as energy, not transverse energy. Looking at the entire range of pseudorapidity coverage in HB and HE, considering the lateral size of hadron showers versus the actual tower size, longitudinal energy sharing, allowing for energy sharing between jet fragments, etc., we arrive at a target of 3 TeV as the maximum signal for the linear energy response of HB2. At 3 TeV, the constant term is dominant. Taking the constant term to be 5% and requiring the line shape to be valid 2 sigma above mean, sets a dynamic range of 15 bits or 33,000 photoelectrons to 1.

The resolution needed is determined by the constant term in the calorimeter response. Thus 8 bits of precision is more than satisfactory to reduce the quantization error to a negligible level.

The signal generated by a traveling radioactive source over each scintillator tile is a basic part of the calibration system. For the case of the HPD, this source signal is about 15 nA on top of a dark current of 5 nA. Calibration requirements require that a change in this current of better than 1% be measurable.

Charge injection is essential for diagnostics, complete system calibration and long term system monitoring. Stability, linearity and repeatability are all important for the charge injection system. These characteristics are tied to the source calibration requirements and call for a 0.5% stability.

Cross-talk between readout towers can occur due to unwanted electrical or optical couplings. If such couplings are linear and can be removed, then a 2% ceiling on cross-talk can be tolerated.1.4.5.3

Access, maintenance, operations

According to the current design, there is only very limited space to access the electronics for HCAL. Then the question arises: what fraction of dead channels will compromise the physics, especially the missing transverse energy measurement? Since repairs are tedious and lengthy, one has to understand the magnitude of the possible damage caused by dead channels.

We used a parameterized simulation program[8], and generated QCD dijets with partonic p_T greater than 2.5 TeV, as a physics source to estimate the missing transverse energy E_T^{miss}. To assess the effect of damage we randomly drop the energy in a given cell with either a 2% or 5% probability. The total E_T^{miss} is then compared to the case without any dead channels. We find that the impact is very small for 5% or less failures. To look at more "coherent" damage we require 5% or 10% dead channels in the barrel, endcap and the forward calorimeter. In this case we began to see a tail develop at high E_T^{miss} for 10% damage Fig. 1. 8. We conclude that up to 10% dead channels are acceptable.

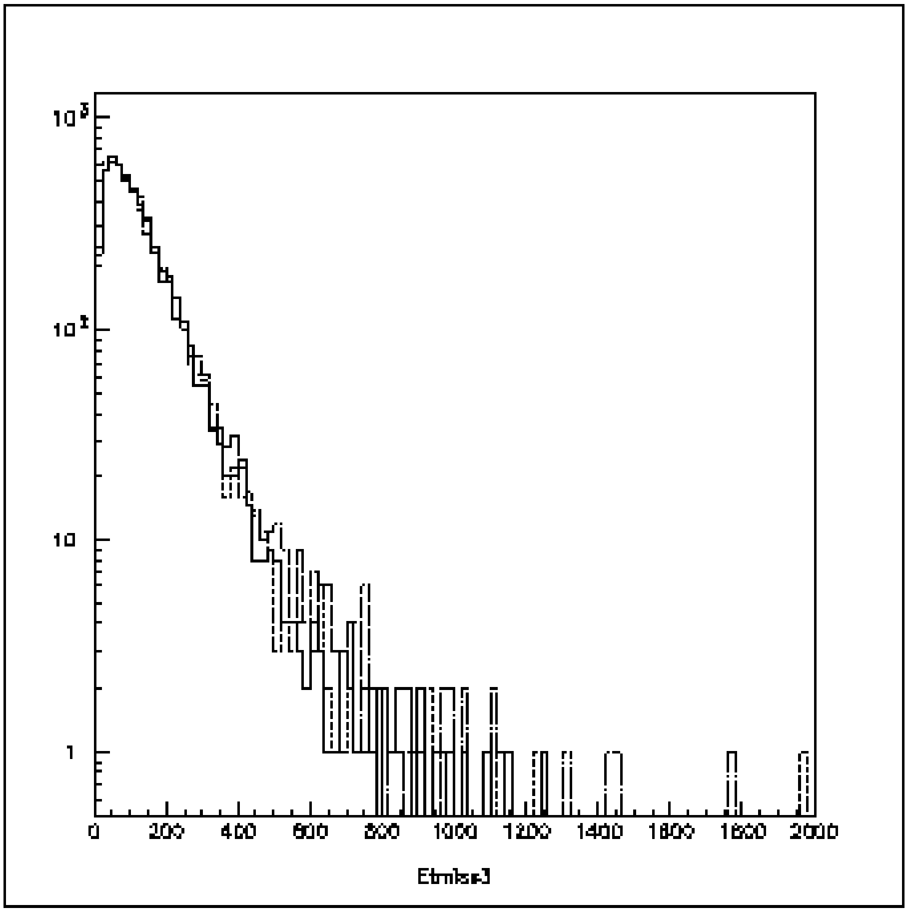

Fig. 1.8: Missing Et distribution for 0% dead channels (solid); 5% dead channels (small dashes); and 10% dead channels (large dashes).

1.4.6 Central calorimeter services

The barrel and endcap are serviced via the 100mm gap between the two subdetectors in the |η| = 1.3 region. This region also contains cables from the EM calorimeter and the tracking detectors.

Hadron Calorimeter related services include optical cables from the barrel and endcap megatiles and source tubes servicing each of the megatiles. Electronics and an occasional source driver box sit in a region close to the coil and also in the |η| = 1.3 region for both the endcap and the central barrel. The electronics boxes contain the tower optical mixing elements, photodetectors, the HV and LV distribution panels, tower preamplifiers, flash ADC's and digitizers (all functioning in a 4T magnetic field). The Electronic Boxes and Source Drivers are connected to the outside world via a cable path that snakes around the barrel and to the section around the central outer detector. The digitized photodetector signal, as well as power cables are routed through this path to electronics racks and power racks in the counting house.

1.4.7 Calibration and monitoring

Adequate performance of the hadron calorimeter requires that the response of the detector be uniform and stable in time at the level of few percent. The uniformity of response must, to first order, be assured by the construction and quality control. Experience of SDC and CDF shows that the uniformity of the tile fiber assembly can be maintained at 10% level for a large scale production. The assembly can be monitored by radioactive source and injecting light from UV lamps. Absolute calibration and linearity of the calorimeter will be established by exposing several modules to the hadron test beam. That calibration can be carried over to the CMS detector using radioactive sources. Both the QC/QA function and the transfer of test beam calibrations to other similar towers, imply the incorporation of source tubes crossing every scintillating tile, as in the SDC design. It is envisioned that the source tubes in most layers will be accessible only when the endcaps are withdrawn.

During the life of the experiment the response of the calorimeter may change as a result of radiation damage or aging. An over redundant system to monitor these changes and provide appropriate calibration must be envisaged.1.4.7.1

^{137}Cs radioactive sources

All layers of the hadron calorimeter will be equipped with thin 1mm diameter stainless tubes that will route Cs^{137} radioactive sources throughout the system. This is a system similar to the one used by CDF and proposed by SDC. We propose that an absolute calibration between wedges be maintained by the source tube system, without exposing each wedge in a test beam.

A wire with a point-like Cs source will be pushed through these tubes by remotely controlled system of drivers. A DC current induced by the source traversing the tower will provide an accurate measurement of the response of the entire measuring chain. The experience at CDF shows that this measurement can be maintained at the level of 1%. Change of response due to photodetector or electronics will show up as a change of the response of all tiles of a given tower and can be compensated by the adjustment of the overall calibration factor. Change of response due to radiation damage will lead to a change of the measured current that is dependent on the depth in the calorimeter.

A few layers of the barrel and endcap will be monitored during data taking to verify that nothing unexpected has occurred. The primary recalibration of each tile, however, will take place during long shutdown periods when access to the barrel and endcap source tubes is relatively easy.1.4.7.2

Laser light calibration system

The laser light system will be used to monitor the stability of the photodetectors and the associated electronics. It will also be able to monitor the linearity of the pulse height measurement chain and provide control of the timing of each channel. In addition, the laser system will be the primary radiation damage monitor during the data taking phase of the experiment.

The laser calibration system will consist of a triggerable nitrogen laser, a system of neutral density filters covering an adequate dynamic range and a light distribution system delivering the UV light to both the HPD pixel and to the scintillating tiles via quartz fibers. The intensity of the laser pulses will be monitored by directing a part of the light to a block of scintillator and measurement of the resulting light pulses by a PIN diode. The rest of the light will go through a system of neutral density filters covering a dynamic range of 4 orders of magnitude to a cascade of distributor/commutator boxes. To achieve 1% some 10,000 p.e.'s must be detected. The total laser power requirement is ~ $1–10^{-3}$ J taking into account the total number of towers, photodetector efficiency and allowing for reasonable losses of light in the distribution process.

1.4.7.3 Calibration using data

Suitably chosen calibration triggers can be used to monitor the overall stability and/or absolute energy scale of the hadron calorimeter. For example minimum bias events can be utilized to maintain the uniformity of response and its time stability. Vector - boson or photon + jet triggers can be used to provide calibration and the absolute energy scale, as will be discussed later.

1.4.8 Radiation damage

It is assumed that the integrated luminosity over the first ten years of LHC operation will not exceed $5x10^5$ pb^{-1}. The ten year integrated dose is thus estimated to be 0.3 kGy (0.03 Mrad) at the front corner of the HB (see Table 1.2). It is shown later that up to 30% damage in HB will not induce an unacceptable constant term in the energy resolution. In common with most commercial polystyrene based scintillators, SCSN81 together with K27 doped WLS fiber such as Kuraray Y11, suffers a light yield reduction of about 20% at 10 kGy (1 Mrad) and an unacceptable 60% at 50 kGy (5 Mrad). The baseline HB and HE design uses this combination.

The problem of radiation damage to the plastic is most severe in the endcap (HE). In this detector, the radiation field scales approxiamtely as $1/\theta^3$ so the region at low $|\eta|$ is less seriously affected. In the endcap region, up to $|\eta| \le 2$, our baseline is to use SCSN81 scintillator with Y11 doped fiber and 2 longitudinal segments. In this section the dose is <0.4 Mrad (see Table 1.1).

In the small angle region the dose is <2.4 Mrad (see Table 1.1). The longitudinal distribution of radiation damage has a characteristic length ~ λ, the nuclear interaction length. The total dose at the inner HE boundary is <2.4 Mrad over the lifetime of CMS. This dose falls off both with increasing angle and increasing depth. The energy deposition as a function of depth is shown below in Fig. 1.9. The exponential behavior is clear.

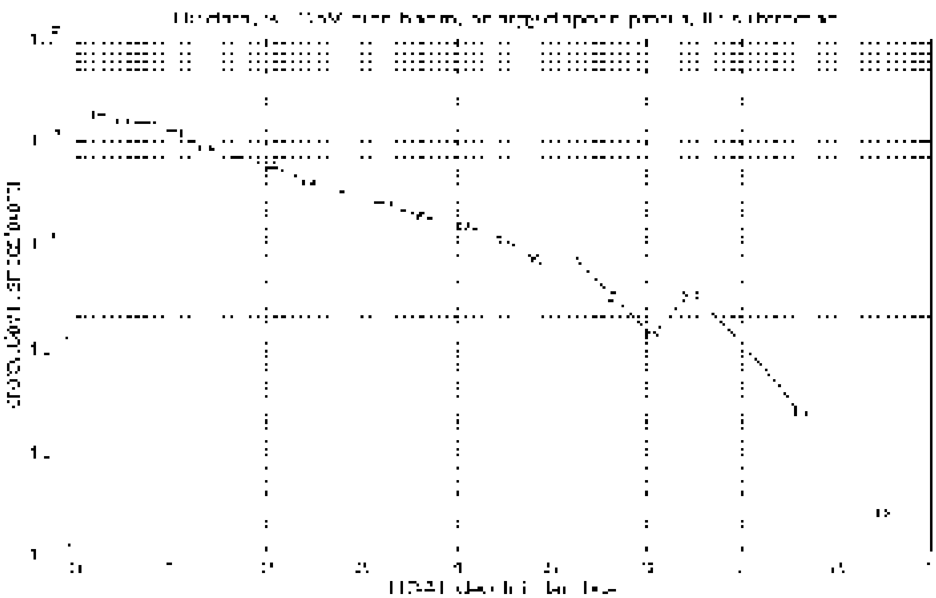

Fig. 1.9: Energy deposit as a function of depth for 30 GeV pions from the H2 test beam.

The loss of light output is related to dose, D , as ~ $\exp(-D/D_0)$, where D_0 for the Kuraray scintillator is ~ 3 Mrad. Therefore, a simple model for the radiation induced nonuniformity of HE is possible. Test beam data for 300 GeV pions from the H2 test with individual longitudinal readout is used. The individual layers were weighted by reduced light yields corresponding to different doses of radiation. The induced constant term as a function of dose is shown in Fig. 1.10, under the condition that the mean of the calorimetry is retained by recalibration of the HE1 and HE2 compartments.

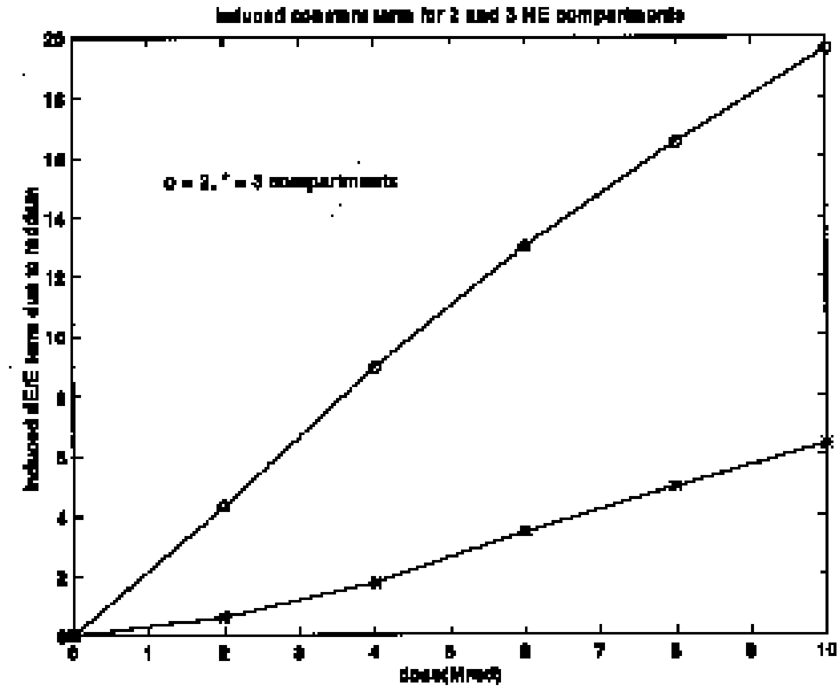

Fig. 1.10: Induced constant term in the energy resolution as a function of dose for 2 and 3 longitudinal compartments.

Clearly, for doses above about 2 Mrad, the induced constant term is comparable or exceeds the intrinsic constant term of the device. Therefore, for |η| < 2 the two compartments may simply be used for recalibration of the mean. However, for smaller angles in the HE towers a new strategy is needed. Two possible options can be considered. The first is passive, and consists of simply making a photographic mask which reflattens the depth response of the individual layers by throwing away light in the undamaged portion of the HE. A second approach is to further longitudinally segment the HE by adding new independent readouts. This approach does not require access to the detector nor does it require throwing away light, nor does it precluding the masking option.

The second alternative was studied for up to a 10 Mrad dose or a factor 4 worse than estimated as the real dose. A third compartment was added; HE1 a single layer, HE2 was the ensuing layers up to a depth ~ 2 λ in HE, and HE3 consisted of the remaining, largely undamaged layers. In this case the induced constant term at 100 kGy (10 Mrad) could be reduced to 6 % from the 20 % which was observed without extra longitudinal segmentation. Thus, a solution to the radiation damage problem, available at low cost, is to add a third HE segment to the readout in the region of highest damage. This precaution ensures that the HE performance is maintained over the lifetime of CMS.

1.4.9 The forward calorimeter design (HF)

Test beam results

The results of the test beam work with the HF hadronic and electromagnetic prototypes over the past two years forms the basis of the HF design:

a) The electromagnetic energy resolution using a quartz window PMT is 107%/$\sqrt{E}$, where E is the particle energy in GeV and the electromagnetic energy resolution is 137%/$\sqrt{E}$ if a glass window PMT is used.

b) The light yield is 0.87 photoelectrons/GeV for electromagnetic showers in the case of a quartz window PMT, and 0.53 p.e./GeV for a glass window PMT. For hadronic showers, the light yield depends on the energy. For example, 100 GeV pions give on the average 52 photoelectrons. For 1 TeV, the extrapolated data suggest that the average signal will be 610 photoelectrons.

c) The hadronic energy resolution contains an intrinsic component due to the fact that the Cherenkov mechanism responsible for the signal generation essentially selects only the π^o component of the developing showers. This irreducible resolution amounts to 25% at 100 GeV and if extrapolated from the test beam data, at 1 TeV, is 10%.

d) The calorimeter response was found to be dependent on the impact position of the incident particles. In a vertical scan with a narrow electron beam, the period of oscillation was found to correspond to the thickness of the grooved copper plates of which the prototypes were constructed. The effective sampling is slightly different when the particles enter the calorimeter at the position of the fibre (signal maximum), compared to where they enter between two fibres (signal minimum). This effect leads to a constant term in the energy resolution of about 1%.

e) The energy resolution of the quartz calorimeter contains contributions from the following components:

- Photoelectron statistics: For electromagnetic showers, this contribution scales like a/$\sqrt{E}$ where the coefficient a is determined by the sampling fraction. For the prototypes this equalled 1.07. This term is almost entirely responsible for the energy resolution. If the sampling fraction is doubled (i.e. 3% fibres in the absorber), then a goes down to 1.07/$\sqrt{2}$ = 0.76. For hadron showers, the situation is a little bit more complicated because of the non-linear response, but straightforward to calculate.

- Sampling fluctuations: These contribute to the resolution of fibre calorimeters as follows: /E = $a / \sqrt{E}$, with $a = 0.03 \times \sqrt{d / f}$ in which d is the diameter of the fibres in mm and f is the sampling fraction for minimum ionising particles[3]. For the tested HF prototypes, (d = 0.3 mm and f = 0.00488), the scaling constant a is thus about 25%. This formula allows to calculate the changes in the sampling fluctuations when the amount of fibre (f) and/or their thickness (d) are changed.

- A constant term, which results from the fact that the characteristic lateral shower dimension is of the same order of magnitude as the fibre pitch. This term can be estimated as follows. Using the measured lateral shower profile, one can determine the fraction of the signal producing shower contained in a cylinder with the fibre pitch as its radius. For hadronic showers in our prototypes, this fraction is 27%. The largest and smallest signal differ by 12% in the fibre matrix arrangement of the prototypes.

Layout

The HF calorimeters, located on both sides of the interaction point at 11.1 meters, cover the pseudorapidity range from 3 to 5. Each HF calorimeter consists of a large copper block that serves as the absorber. The embedded quartz fibers in the copper absorber run parallel to the beam and constitute the active component of the detector. Particles incident on the front face of the HF detectors produce showers in the copper/quartz matrix and a part of this shower (charged particles above the Cherenkov threshold) gives rise to Cherenkov light in the quartz fibers. This light forms the basis of energy measurement. The details of this device are presented in Chapter 5 and here we outline only the distinguishing features of this calorimeter here.1.4.9.1

Structure

The HF calorimeters are cylindrically symmetric around the beam line. The radius of the active part of the HF is 1.4 meters. The length, along the beam, is 1.65 m, or about 10 nuclear interaction lengths. This is largely sufficient to longitudinally contain the Cherenkov signal produced by hadrons of up to 1 TeV. The central region is open (25 cm in diameter) to allow for the beam pipe (20 cm in diameter).

In order to optimize for the energy resolution, for E and E_T flows and forward jets, the calorimeter has three segments in depth. This effective multiple segmentation within a monolithic copper absorber is achieved by using three different fiber lengths. We refer to them as Long (or EM, 165 cm long), Medium (or HAD, shorter by 22 cm from the front of the module) and Short (or TC, inserted 30 cm from the back face). Fig. 1.11 schematically shows one of the quadrants of the HF where only the top fiber layer is exposed.

The fibers are arranged into towers such that transverse dimensions are 5×5 cm^2 in the inner part ($|\eta| > 4$) of the HF, and 10×10 cm^2 in the outer region ($|\eta| < 4$), to maximize the forward jet detection and reconstruction capability over a huge pile-up background. The Short fibers serve as the active material of the tail catcher (TC) section and they are arranged in a coarser tower structure, 20×20 cm^2.1.4.9.2

Manufacture, shipping, assembly and installation

The HF calorimeters are constructed using a few relatively small size modules. Four different sizes of modules are envisioned to be the basic building blocks of the calorimeter. They have the following dimensions; ($w \times h \times l$) $600 \times 300 \times 1650$ mm^3 (32 units), $500 \times 300 \times 1650$ mm^3 (32 units), $300 \times 300 \times 1650$ mm^3 (16 units) and $600 \times 200 \times 1650$ mm^3 (8 units). These modules are constructed from copper plates with grooves and these plates are stacked together by diffusion welding such that the modules are self-supporting and mechanically sound. The quartz fibers are inserted into the holes (grooves) after a quadrant fabrication is mechanically completed. Each quadrant (as shown in Fig. 1.11) is composed of 11 basic modules that are mounted on a steel shell which provides structural support in assembly, installation and shipping. It also serves as a part of radiation shielding components when installed in the beam position.

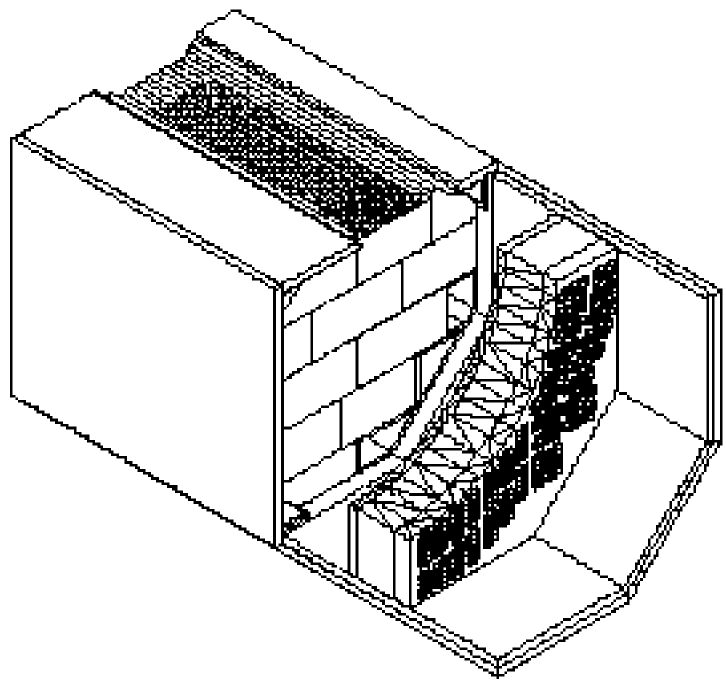

Fig. 1.11: An HF quadrant above shows that it is constructed from 11 modules. A top and a side steel plates are used during transportation and as a part of the assembly procedure. A cut-out of one of the top modules shows three different lengths of fibers inside the absorber that represent EM, HAD and TC

sections. The PMT boxes are mounted on the right of the shielding where the PMT foot-prints are shown.

The HF shipments are brought about a quadrant at a time, proceeding each stage of assembly completion. First, the absorber modules are put together in a structural steel shell in quadrants, tested and transported. This is followed by the insertion of quartz fibers into the holes and fiber bundling into towers, and shipped again in quadrants to the assembly site at CERN where the photodetectors and the other auxiliary components are mounted. Quadrants are assembled into halves (1/2 of HF arm) and then to full detectors in the same area (Building 168). Entire test assembly with the transporter platforms and the shielding blocks is also fulfilled in the assembly area before shipment to the CMS surface hall and installation in the experimental hall.

1.5 DESIGN PERFORMANCE (TEST BEAMS, LAB TESTS, SIMULATIONS)

During the R&D period of 1994 through 1996 considerable data was taken and a variety of tests were made for HB, HE and HF. Test beams of electrons, pions, protons, and muons were used in the H2 and H4 beamlines. In particular, the H2 data were taken at fields up to 3T in strength and in both "barrel" and "endcap" configurations. The combined CMS calorimetric system of ECAL+HCAL was tested in 1996. In addition to the beam tests, laboratory tests of the scintillator "brightening" phenomenon were made as were continuing radiation damage studies.

The HCAL group has attempted to also mount a complete set of simulations. Their purpose is both to assess the possible adverse impact of HCAL performance on physics searches in CMS and to serve as a method to allow extrapolations from test beam results to the HCAL baseline design.

A new effect was uncovered in the 1996 data taking period. In the barrel configuration, the effective e/π response ratio of the HCAL sampling calorimeter is a function of magnetic field. The effect is well understood, and the GCALOR Monte Carlo program gives a good representation of the data. Note that in the endcap this effect does not exist. In HE only scintillator brightening is observed to occur. The magnitude of the effect is tracked by both radioactive sources and muons. In HF there is no magnetic field so that the problem is localized to HB.

The existence of this effect has modified our calibration scheme somewhat, since it cannot be tracked at zero field. Hence, a plan to use in situ calibration using Z + jet final states and others is needed in order to establish the absolute calibration of the HCAL system. Since the sensitivity of the HCAL mean pion energy to space in the sampling gap is ~ 4%/mm, a QC plan to fix the scintillator package at a fixed location has also been adopted.

In summary, we have measured the relevant parameters of HCAL in test beams. In concert with an extensive Monte Carlo program, a good understanding of the response of HCAL exists, giving confidence that the performance of HCAL can be accurately predicted. Using the test beam results, we have explored a wide variety of Physics processes embodying new Physics beyond the standard model. For example, we do not find that the calorimetric performance degrades searches for SUSY, but that CMS is dominated by real backgrounds containing neutrinos.

1.5.1 Overview of physics performance

As explained earlier, the goals of the hadron calorimeter subsystem are to identify and measure hadronic jets and missing transverse energy. Physics processes for which these final state signatures are crucial include:

a) High mass (~ 1 TeV) standard model Higgs searches in $ll\nu\nu$, lljj and $l\nu jj$ modes.

b) Forward tagging jets for high mass Higgs production and strong WW scattering processes.

c) Supersymmetric Higgs searches in H and A ∅ $\tau\tau$ modes, h ∅ $\bar{b}b$ (produced by A ∅ Zh or H ∅ hh), and t ∅ b $H^{\pm}$ with $H^{\pm}$ ∅ $\tau\nu$.

d) Searches for supersymmetric particle production, which generally involve signatures consisting of missing transverse energy (arising from the escape of the lighest supersymmetric particle from the detector) plus jets and leptons.

e) Determination of the mass spectrum of supersymmetric particles will require reconstruction of invariant masses from combinations of jets (possibly b-tagged or anti-tagged) and missing transverse energy.

f) Discovery of technicolor states may require reconstruction of invariant masses of multijet systems such as ρ_T ∅ jj or ω_T ∅ γjj.

g) Discovery of compositeness would require the accurate determination of the cross section for high transverse momentum jets up to several TeV in E_T, and measurement of their center of mass angular distribution.

Many of these processes were investigated for the Technical Proposal[1]. Since that time, the physics performance of the CMS hadron calorimeter has been investigated both as part of ongoing studies within the physics group and as part of the effort to optimize the detector.

We have considered two performance benchmarks. For **missing transverse energy**, E_T^{miss}, we take the ability to discover and characterize supersymmetry as our benchmark. There is an unavoidable background to E_T^{miss} signals which results from the mismeasurement of QCD jets, and the production of heavy flavor within them (this dominates at relatively low E_T^{miss}, below about 100 - 200 GeV) and from the production of top and vector bosons, whose decays produce high-p_T neutrinos (which tends to dominate at higher E_T^{miss}). The background component from real neutrinos is irreducible and sets the scale for the measurement precision which is required to see new physics.

The finite pseudorapidity coverage of the detector introduces a mismeasurement of E_T^{miss}, as shown in Fig. 1.12; if the calorimeter coverage is reduced significantly below $|\eta| < 5$ then the rate for E_T^{miss} begins to substantially exceed the unavoidable background. For this reason, the CMS hadron calorimeter is designed to cover the whole range $|\eta| < 5$.

For the LHCC SUSY workshop held at CERN in October 1996, a number of studies were carried out using the fast parametrised Monte Carlo simulation CMSJET[9]. This simulation smears the energy of incoming particles according to assumed resolutions; for single hadrons in the HCAL these were $\sigma/E = 70\%/\sqrt{E(GeV)} \oplus 9.5\%$ (at $\eta = 0$), and in the HF, $\sigma/E = 172\%/\sqrt{E(GeV)} \oplus 9\ \%$. On the basis of these studies, we concluded that:

a) the CMS detector could discover squarks and gluinos up to masses of ~ 2 TeV, using a single charged lepton plus jets and E_T^{miss} signature. (This final state gives a greater reach than a pure E_T^{miss} or E_T^{miss} +jets search). Such masses are well above the maximum at which SUSY at the electroweak scale is felt to be reasonable.

b) CMS could observe sleptons, in leptons + E_T^{miss} final states, above the standard model and SUSY backgrounds up to masses of about 340 GeV;

c) CMS could observe chargino and neutralino production in leptons + E_T^{miss} final states, if nature lies in the region of parameter space where production cross section and branching ratio to leptons are significant. The lepton spectrum can be used to measure some of the neutralino masses.

A summary of the parameter space accessible to CMS is shown to Fig. 1.13.

The only concern is that the parametrized simulation may not provide a realistic model of the detector performance, particularly as far as E_T^{miss} is concerned. We have therefore evaluated[10] a number of very pessimistic scenarios for HCAL performance. As a baseline, we considered HCAL single-particle resolutions similar to those quoted in the Technical Proposal: $\sigma/E = 65\%/\sqrt{E(GeV)} \oplus 5\%$ (at $\eta = 0$), $\sigma/E = 83\%/\sqrt{E(GeV)} \oplus 5\%$ (in the endcaps), and in the HF, $\sigma/E = 100\%/\sqrt{E(GeV)} \oplus 5\ \%$. We then degraded this performance in the following ways:

a) increased sampling terms in the resolution: $100\%\sqrt{E(GeV)}$ in the barrel, $150\%\sqrt{E(GeV)}$ in the endcap and $200\%\sqrt{E(GeV)} \oplus 10\%$ in the HF;

b) assumed no measurement of electromagnetic energy takes place for 1.5 ² |η| ² 1.6 (an unsampled crack in the EM calorimeter);

c) assumed no measurement of any energy takes place for 3.0 ² |η| ² 3.1 (an unsampled crack between the HCAL endcap and the Forward Calorimeter HF);

d) degraded the HCAL response function to model 0.6 of material between the rear of the ECAL crystals and the front face of the HCAL, which introduces a low-side tail to the hadronic response with probability of losing an energy E_{loss}, $P(E_{loss}|E) \sim \exp(-E_{loss}/0.067E)$.

e) an alternative parametrization of a non-Gaussian low-side tail was also considered, chosen as a worst-case based on test beam data: 0.2% of events were shifted to the tail, and E_{loss} was distributed uniformly between zero and the incident energy.

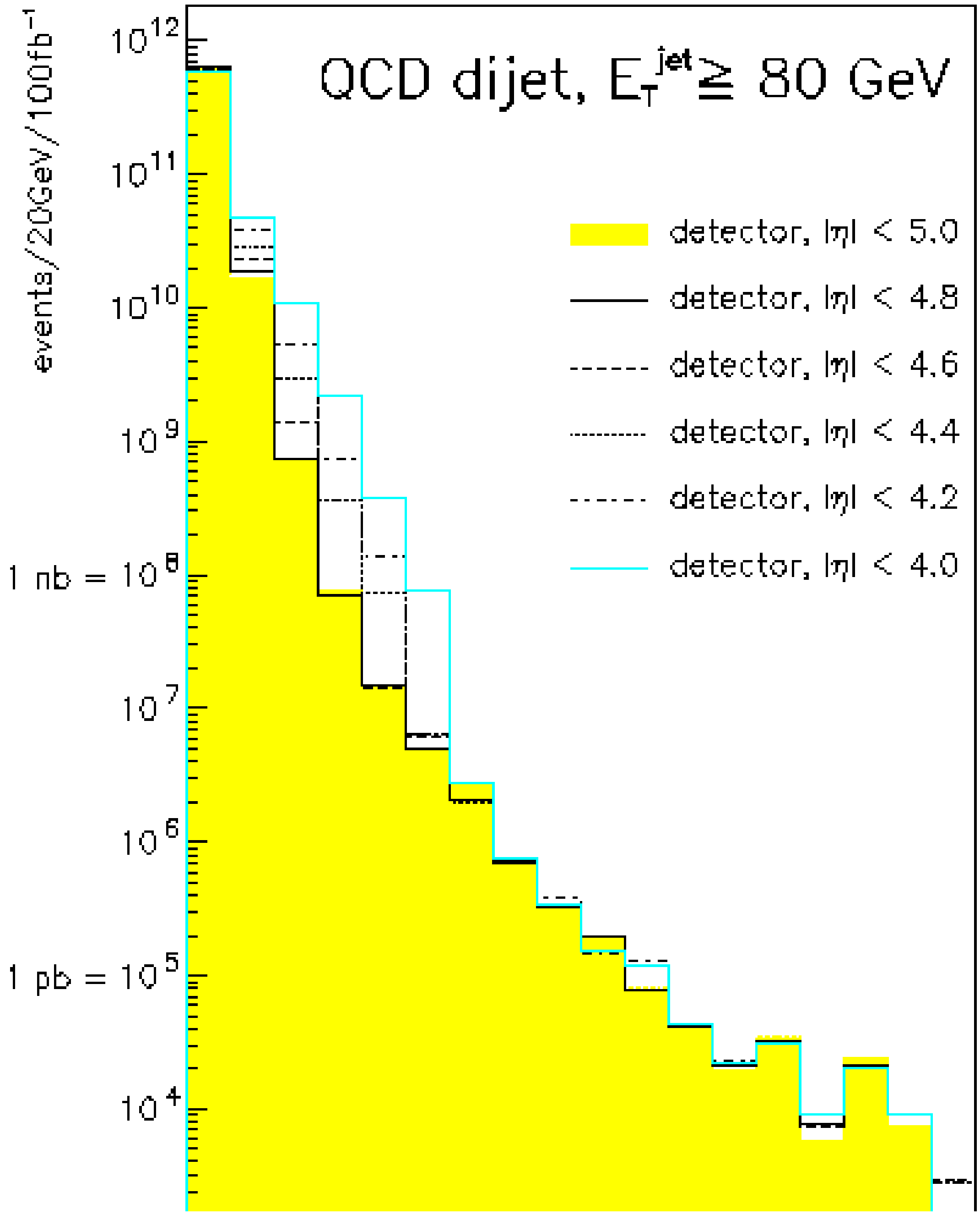

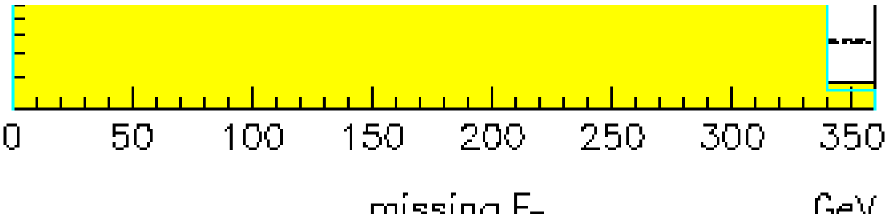

Fig. 1.12: Cross section at the generator level for E_T^{miss} from QCD dijet events, with $E_T^{jet} > 80$ GeV, showing the effect of varying pseudorapidity coverage.

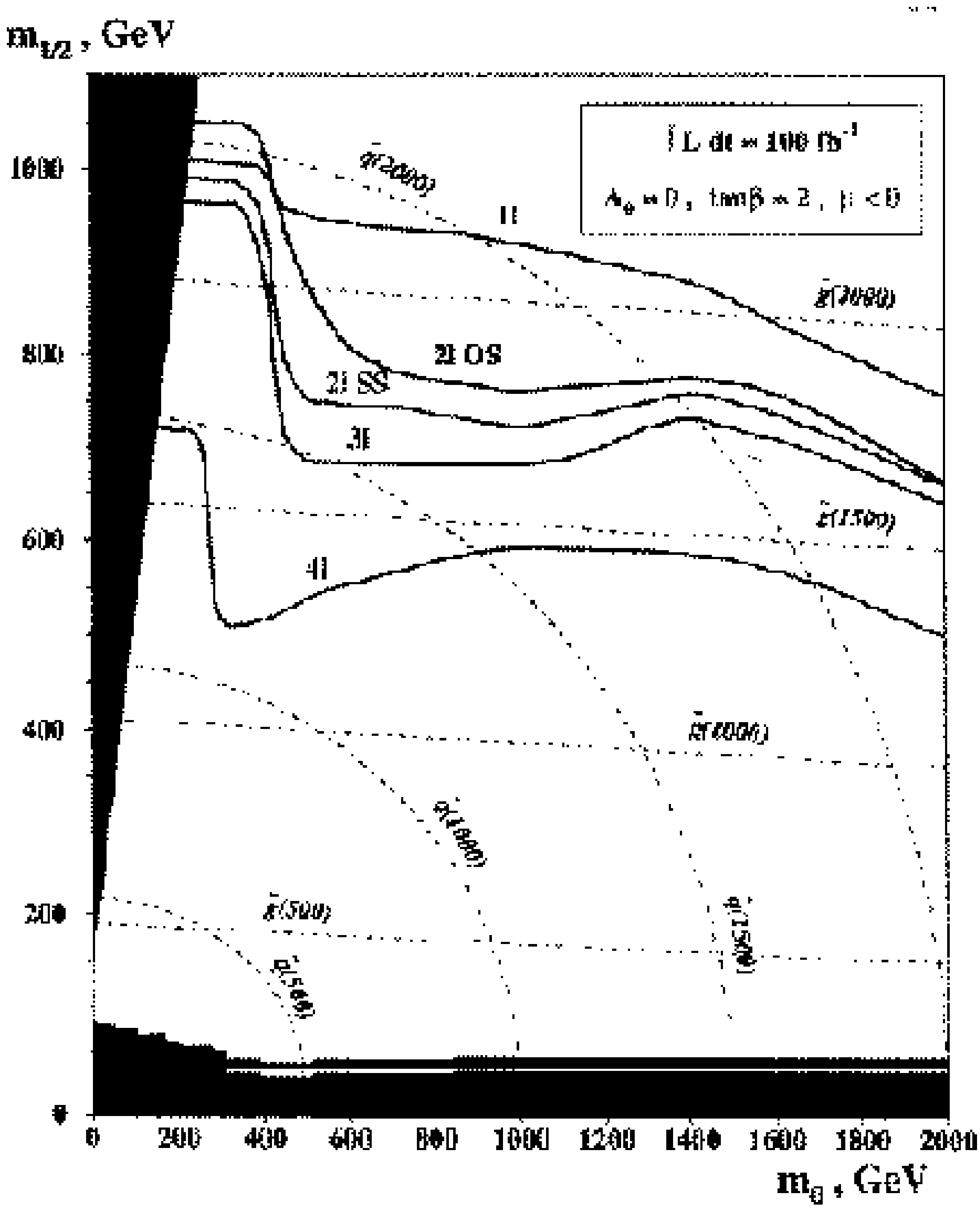

Fig. 1.13: Parameter space of the supergravity-inspired minimal supersymmetric standard model, m_0 vs

$m_{1/2}$, with lines showing the 5σ discovery reach for the CMS detector with 100 fb^{-1} of data. The searches required missing transverse energy, jets, and one lepton (1l), two leptons of same sign (2l SS) or opposite sign (2l OS), three (3l) or four (4l) leptons. Dashed lines are contours of constant squark and gluino masses, showing the CMS reach to be up to ~ 2 TeV, well beyond theoretical expectations for supersymmetry at the electroweak scale.[11]

We evaluated the effect of these scenarios on the observability of supersymmetry at CMS in the E_T^{miss} + jets channel. All of them are far worse than the performance we actually expect from CMS, yet none would actually prevent the discovery of supersymmetry. All tend to increase the background most at low values of E_T^{miss}, because this is the region dominated by mismeasurements of jets. The worsened, but still Gaussian, calorimeter resolutions would increase the luminosity required for an observation of SUSY by a factor of about 1.5. The pessimistically-modelled cracks have somewhat more serious effect, but by far the greatest impact comes from introducing non-Gaussian response functions. (The first parametrization considered increases the QCD background at E_T^{miss} ~ 150 GeV by two orders of magnitude). In the optimization of the HCAL detector, we have therefore placed considerable stress on the elimination of sources of non-Gaussian response, such as unsampled material between the rear of the ECAL and the front face of the HCAL.

We have also verified that the performance indicated by the HCAL test beam data is adequate for E_T^{miss}. In Fig. 1.14, we compare the cross section for QCD jet events as a function of E_T^{miss}, for the technical-proposal-like resolutions used as a baseline in the studies described above, and the result of a parametrization to the resolutions actually obtained from test beam data. The test beam performance is not quite as good as the earlier simulations, increasing the E_T^{miss} cross section by a factor of about two at moderate E_T^{miss}, this will not have a serious impact on the physics capabilities of the detector. As stated earlier, we have worked hard to remove sources of non-Gaussian response rather than striving to obtain the best possible resolution, since the impact on physics of a non-Gaussian response is much more severe.

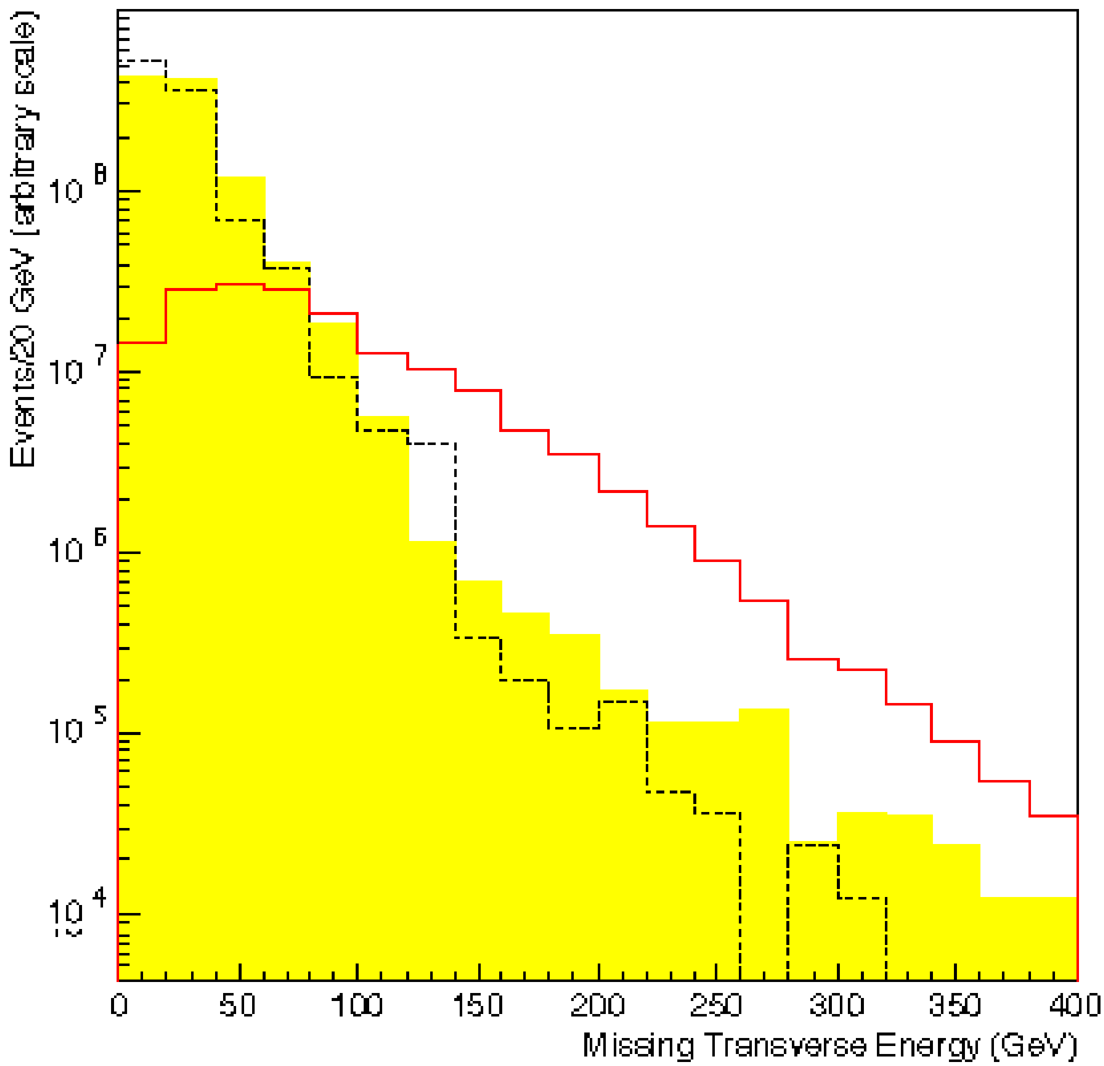

Fig. 1.14: Cross section for measured E_T^{miss} from QCD dijet events in CMS. The shaded histogram shows the result using single-particle resolutions taken from the test beam, while the open histogram is the technical-proposal single particle resolution. The second open histogram represents real physics background sources of neutrinos from W, Z and t decays. At least three jets were required, with $E_T > 100$, 80 and 60 GeV, and the E_T^{miss} was required to have an azimuthal angle from the leading jet between 20° and 160° to reduce the effect of mismeasurements. The physics backgrounds dominate for $E_T > 75$ GeV.

For **jet resolutions**, our performance benchmark is the ability to reconstruct the dijet decays of W and Z vector bosons. We have investigated this both in the context of a high-mass Higgs search, H ∅ WW ∅ lνjj, and in top decays (t ∅ Wb ∅ jjb). The latter process may be of interest as a calibration channel as well as for physics.

In the Higgs search[12] the W has significant transverse momentum. The W ∅ jj decay was therefore reconstructed from the calorimeter lego plot by finding a single large cluster (a cone of radius R = 0.8) containing two smaller jets (with a cone size of R = 0.15). The mass of the W was then estimated as the invariant mass of the whole large cluster, without attempting to assign energy between the two small jets. A requirement that the two jets have $(E_1 - E_2)/(E_1 + E_2) < 0.7$ reduces the W+jets background to the lνjj final state. Good resolution is obtained, with a FWHM of ~ 20 (30) GeV for m_H = 800 GeV without (with) minimum bias pileup. Since the dijet resolution is broadened by many unavoidable effects, such as out-of-cone showering, gluon bremsstrahlung, and combinatorics, our goal has merely been to avoid detector effects further degrading it. One example of such an effect would be the smearing introduced by the finite tower size of the calorimeter. Our studies indicate that, provided the tower size is smaller than about $\Delta\eta \infty \Delta\phi = 0.1 \infty 0.1$, the dijet resolution is not affected.

The top study[13] is complementary because the W is produced with lower transverse momentum and so two discrete jets are observed. Test-beam derived single particle resolutions were used. The simulation required between two and six jets with E_T > 20 GeV. The jets used to form the W were required to be more than R = 0.6 from either b-quark direction and to have an opening angle between 0.25 and 1.5 radians. They were then combined with one of the b-quarks to form a three-jet mass, which was required to be consistent with m_T (This last requirement gives a clean W for calibration purposes but would obviously not be appropriate for some top physics studies). Fig. 1.13 shows the resulting reconstructed m_W distribution, without minimum bias pileup; again, the FWHM is about 20 GeV. If minimum bias pileup events are included, this degrades to about 30 GeV as before.

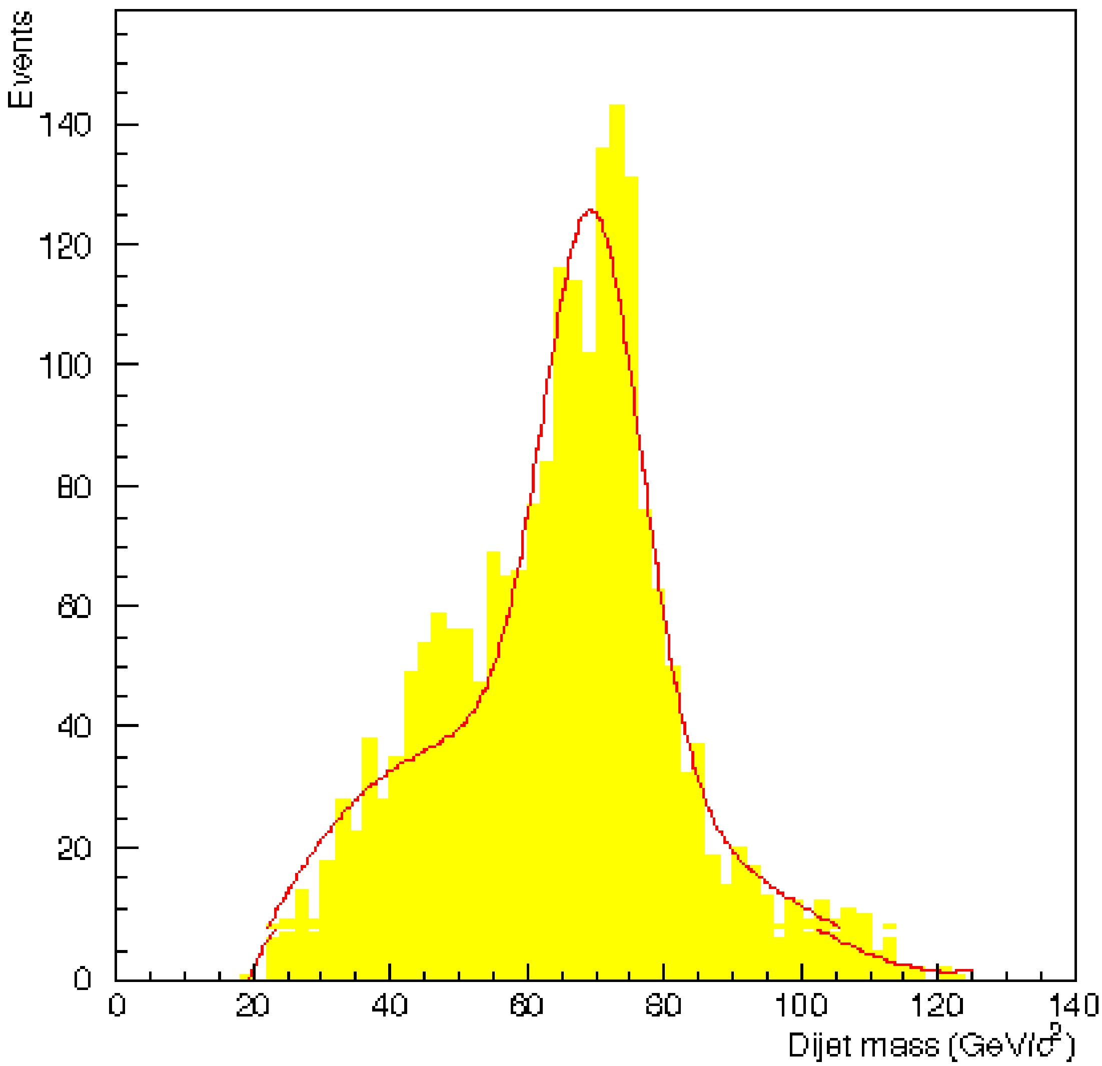

Fig. 1.15: Reconstructed dijet mass distribution from top decays showing the W peak. A jet cone size of R = 0.4 was used with no minimum bias pileup events.

In summary we believe that the HCAL design presented here can meet the physics goals of the CMS detector and is well-matched to the tasks required of it.

1.5.2 HB/HE test beam results

The CMS HCAL group has tested the performance of prototype HB sampling calorimeters with copper absorber/scintillator tiles and optical readout system using wave length shifter (WLS) fibers[14]. Each sampling layer of the HCAL colorimeter was read out separately, allowing for an simulation of variety of absorber configurations. The group has also in the same period tested HE and HF prototypes. The HF results are discussed in the next section.

During May 1995[15,16] we tested the prototype calorimeters in the CERN H2 beamline with the detector placed inside a large 3 Tesla magnet. The orientation of the magnetic field, with field lines perpendicular to the scintillator planes, corresponded to the Hadron Endcap (HE) configuration as shown in Fig. 1.16. In September 1995, we tested[17] the HCAL prototype in the H4 beamline (with no magnetic field present) with an ECAL detector consisting of a matrix of 7∞7 $PbWO_4$ crystals. The CMS combined calorimetric system of ECAL+HCAL was tested[18] in 1996 at the H2 beamline. This time, the 3 Tesla magnet was oriented in such a way that B field lines were parallel to the scintillator planes, corresponding to the CMS HCAL Barrel configuration. The H2 (1996) setup is shown in Fig. 1.17.

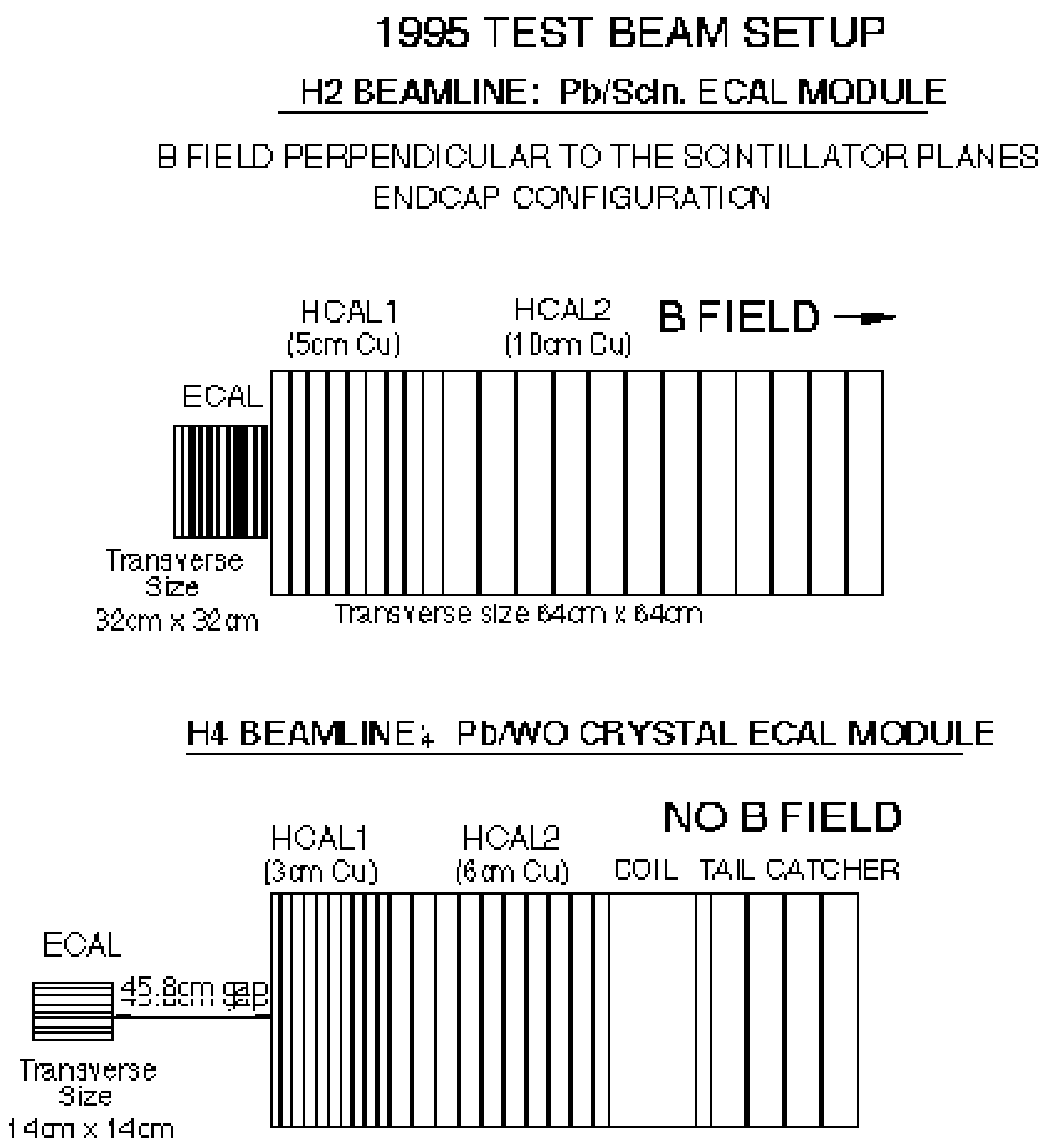

Fig. 1.16: 1995 H2 and H4 test beam setup.

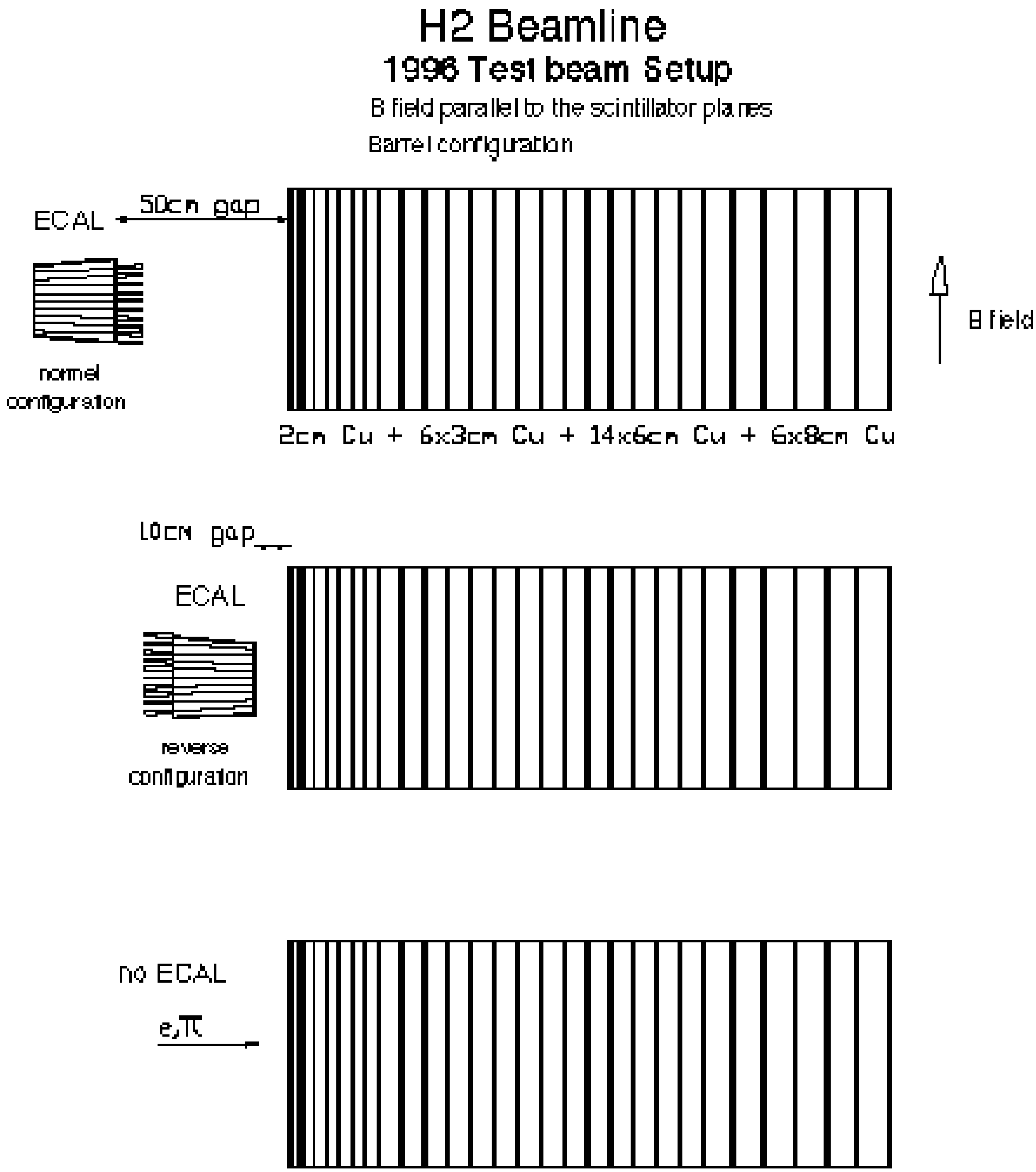

Fig. 1.17: 1996 H2 test beam setup.

In the following we summarize the results of HCAL Test Beam studies.1.5.2.1

HCAL absorber depth studies

The ECAL detector consisted of a 77 matrix of 2cm∞2cm $PbWO_4$ crystals. Approximately 95% of electron electron energy was contained inside a 33 crystal sum. The linearity of the ECAL response to electrons is shown in Fig. 1.18 while the electron energy resolution of ECAL is shown in Fig. 1.19. The resolution is well described by a 6% stochastic term (due to crystal photostatistics), 0.5% constant term (due to relative crystal-to-crystal calibrations) and 100 MeV/crystal incoherent electronic noise term.

Note that this performance is not the ultimate achievable for ECAL. It was simply made sufficient as to have no impact on the HCAL data.

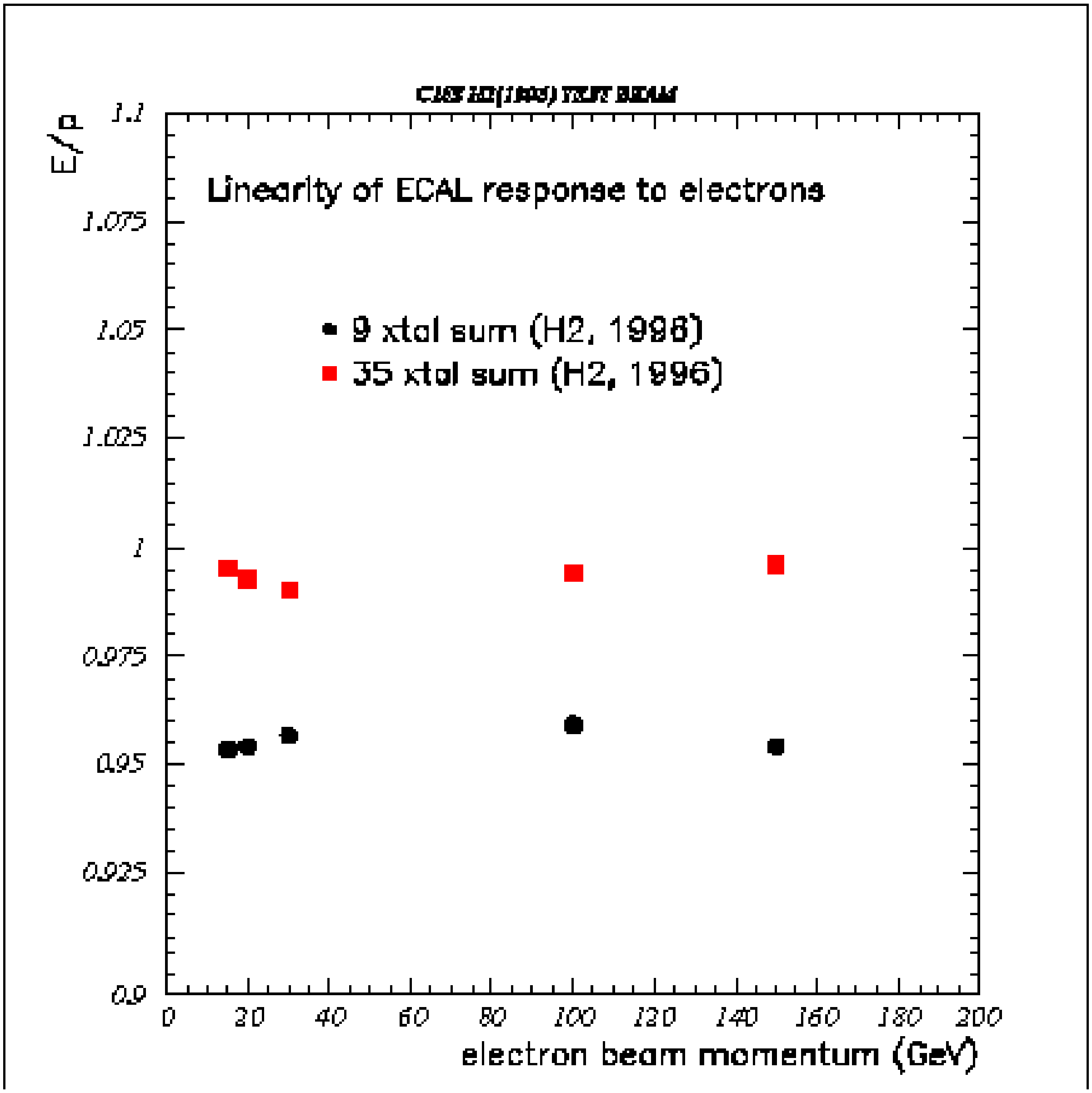

Fig. 1.18: Linearity of ECAL crystal detector to electrons.

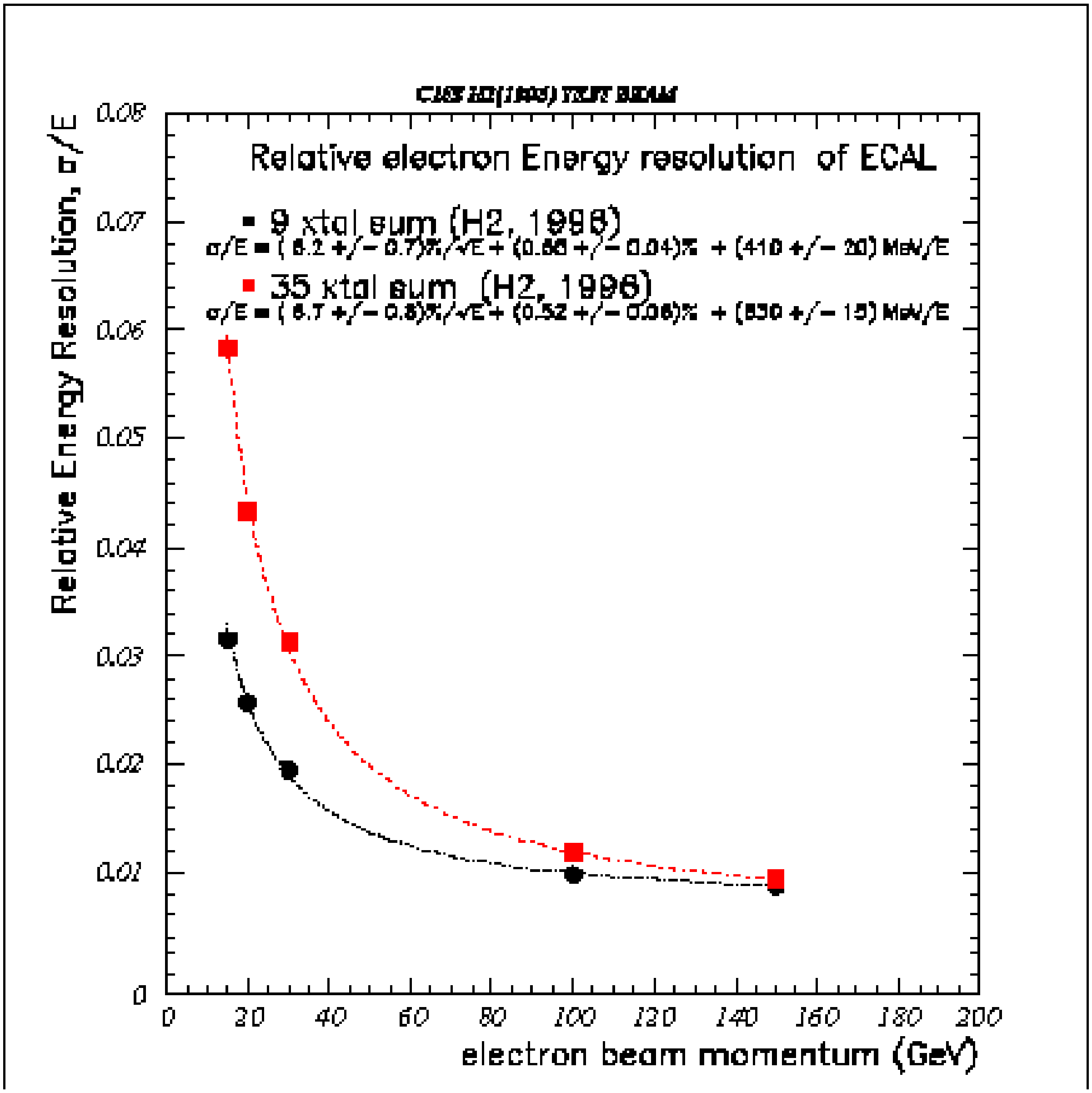

Fig. 1.19: Electron energy resolution of the ECAL detector.

The HCAL calorimeter was segmented into 27 layers, each read out independently by a photomultiplier. Relative calibration of individual HCAL layers was performed by equalizing the response of each layer to minimum ionizing particles. An average muon deposited approximately 4 GeV of energy in HCAL.

Fig. 1.20 shows the various sampling configurations simulated with the Test Beam apparatus. The "all layers" configuration corresponded to the case when all available samplings were included in the energy sum. A "baseline" HCAL configuration (assuming the inner HCAL radius of 1930 mm) used fourteen 6cm Cu samplings inside the magnetic coil, with a total equivalent of 5.2 interaction lengths inside the coil.

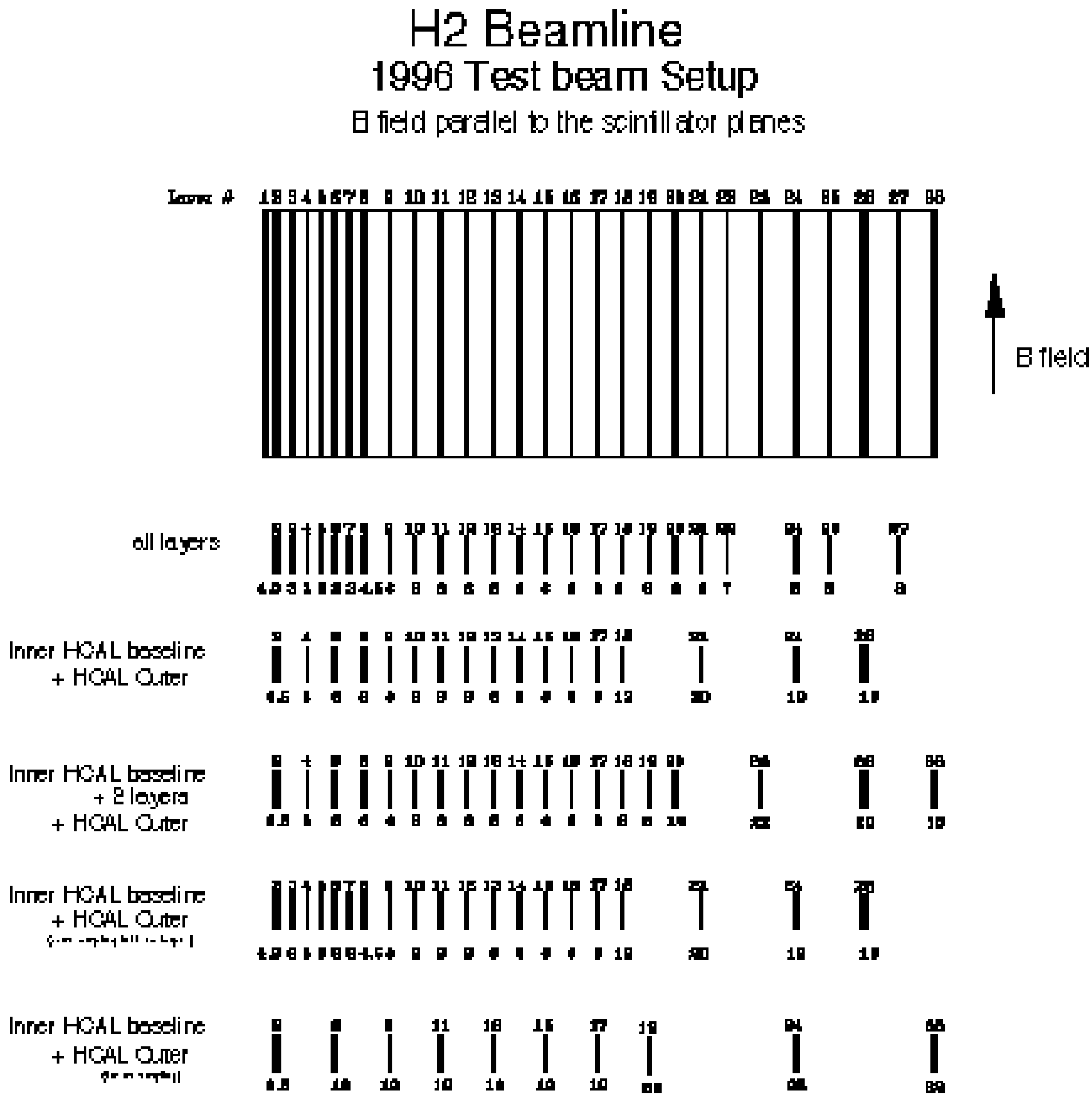

Fig. 1.20: Various sampling configurations simulated with the Test Beam apparatus.

Fig. 1.21 shows the average 50, 100, 150 and 300 GeV pion shower profiles as a function of calorimeter absorber depth. As shown in the figure, the average pion shower profiles extend significantly beyond 5.2 λ. In order to avoid the large energy tails of pions not fully contained by the HCAL inside the magnetic coil, we have added a HCAL Outer (HO) compartment. Note that the baseline of 5.15 λ HCAL + 1.1 l ECAL has $e^{-6.2}$ = 1/493 or a ~0.2% probability to not enteract in HB at all. The HO consists of 2 readout layers (3 in low eta region) and would sample energy immediately after the magnetic coil and between the iron plates of the Muon system.

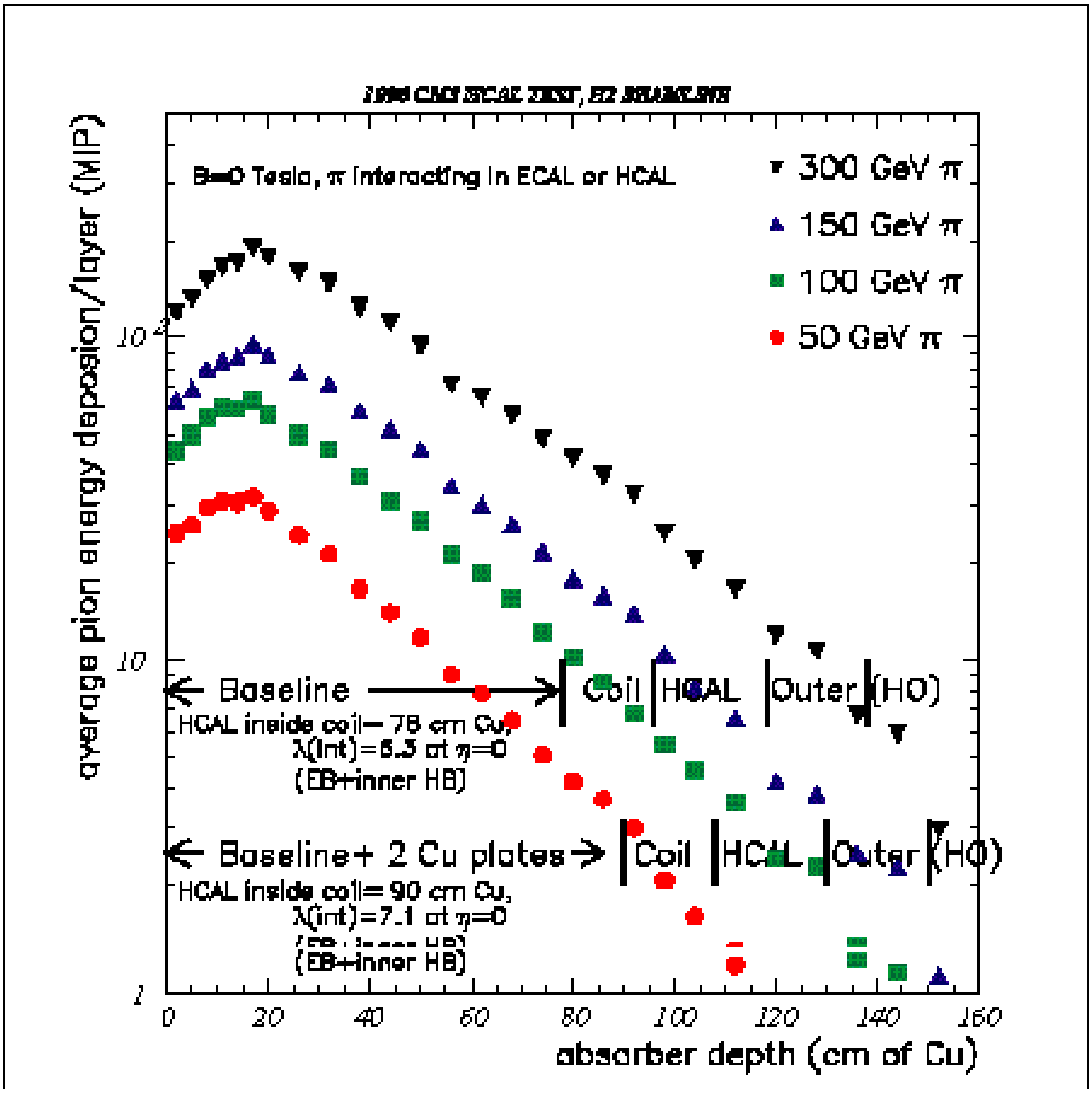

Fig. 1.21: Average 50, 100, 150 and 300 GeV pion shower profiles as a function of calorimeter absorber depth.

If an additional 2 layers of 6 cm Cu plates were added to the baseline HCAL design, the total depth of the HCAL inside the coil would increase to 5.9 λ. Fig. 1.22 shows the energy measured for 300 GeV pions for different HCAL sampling configurations: Baseline Inner HCAL, Baseline + 2 plates, Baseline + HO, and Baseline + 2 plates + HO. Adding the HO reduces the gaussian width as well as the non-gaussian low energy "leakage" tails in the energy distributions.

Fig. 1.23 shows the fraction of 300 GeV pions with energy reconstructed below 200 GeV (approximately 3 sigma below the mean). The fraction reduces from approximately 4% for the Baseline HCAL inside coil (total 5.2 λ), to less than 2% for the case of HCAL with 2 additional plates and HO (total 9.8 λ).

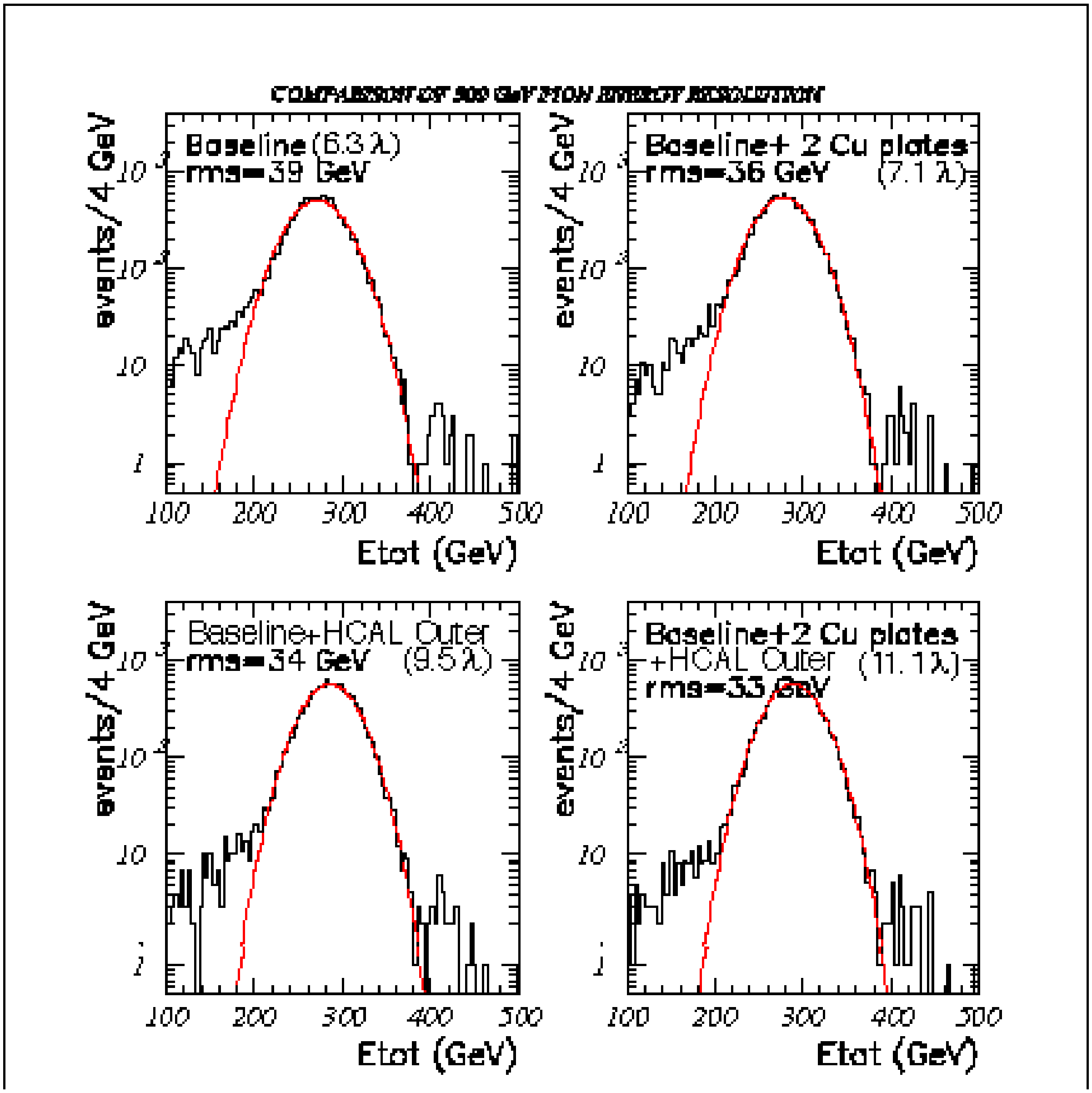

Fig. 1.22: Comparison of energy resolution (rms) for 300 GeV pions for different HCAL sampling configurations: Baseline Inner HCAL, Baseline Inner HCAL +2 plates, Baseline Inner HCAL + HO, and Baseline Inner HCAL + 2 plates + HO.

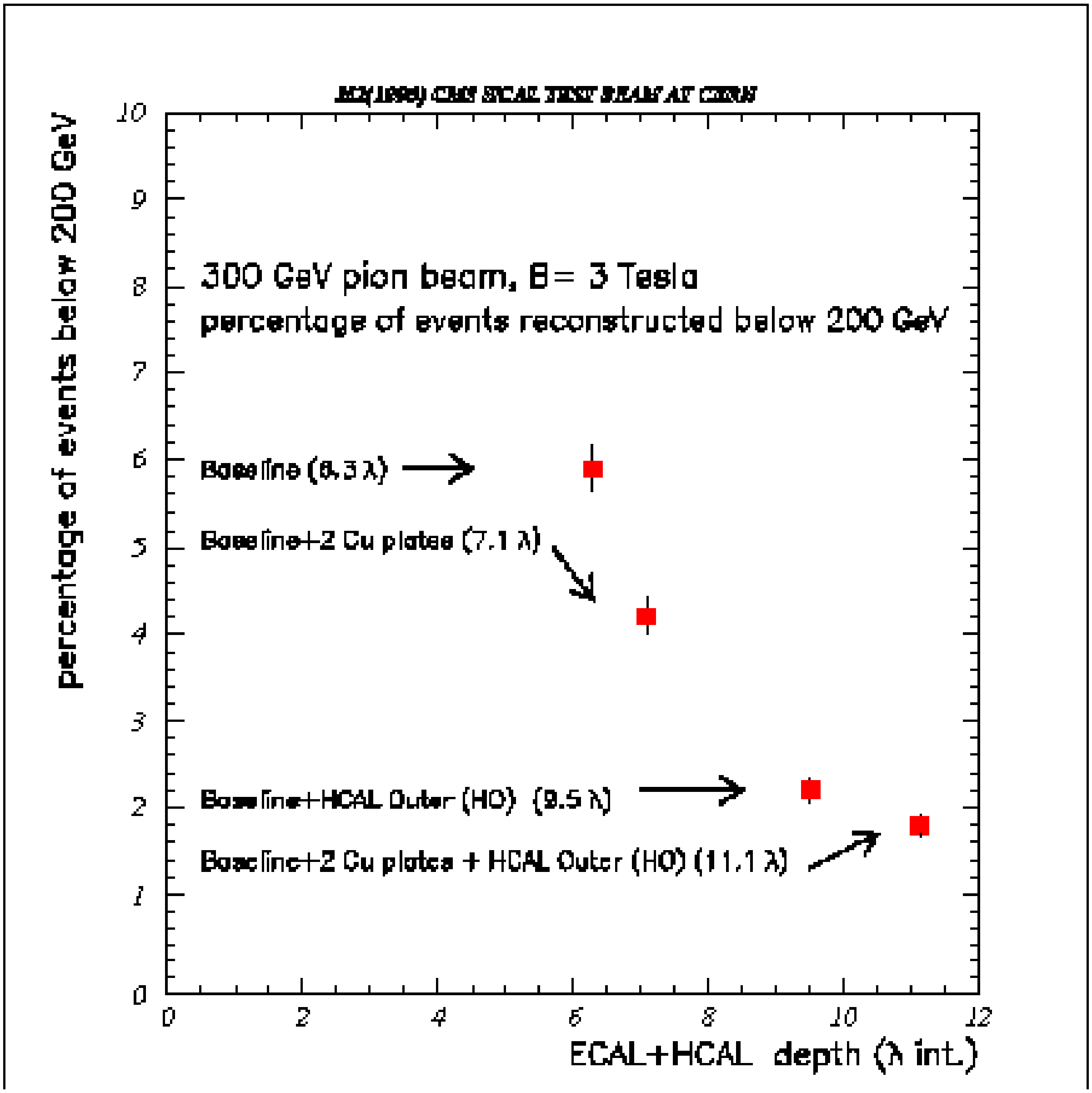

Fig. 1.23: Fraction of 300 GeV pions with reconstructed energy less than 200 GeV (approximately 3 sigma below the mean).1.5.2.2

Longitudinal segmentation studies

Fig. 1.24 shows the linearity of HCAL response to pions. The HCAL readout corresponded to Baseline Inner HCAL + HO. The absolute energy scale of ECAL was set using 50 GeV electrons. The absolute energy scale of HCAL was set using 50 GeV pions interacting only in the HCAL. For pions interacting in the HCAL, with a minimum-ionizing signal in the ECAL (circle symbols), the residual non-linearity of response of HCAL for data points between 20 and 300 GeV is less than 10%. However for pions interacting in either ECAL or HCAL (square symbols), the non-linearity is much larger.

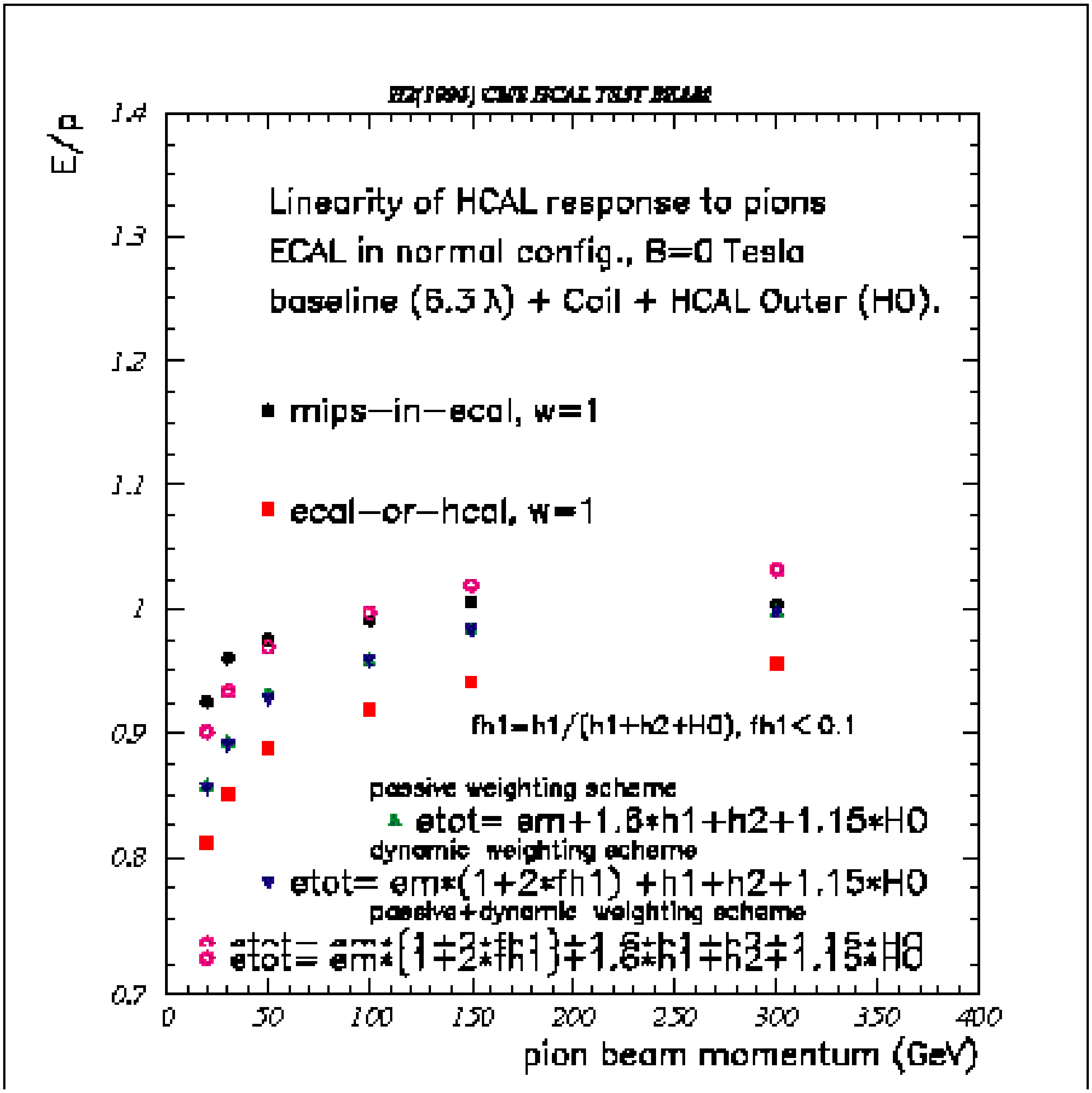

Fig. 1.24: Linearity of HCAL response to pions. The HCAL readout corresponded to Baseline Inner HCAL + HO. The absolute energy scale of ECAL was set using 50 GeV electrons. The absolute energy scale of HCAL was set using 50 GeV pions interacting only in the HCAL.

Fig. 1.25 shows the pion energy resolution of HCAL. For pions interacting only in the HCAL, with minimum ionizing signal in the ECAL, the energy resolution can be parametrized by a stochastic term of 91% and a constant term of approximately 4%. However for pions interacting in either ECAL or HCAL, due to the large e/h of the crystal ECAL, the energy resolution is significantly degraded: The stochastic term increases to 124%.

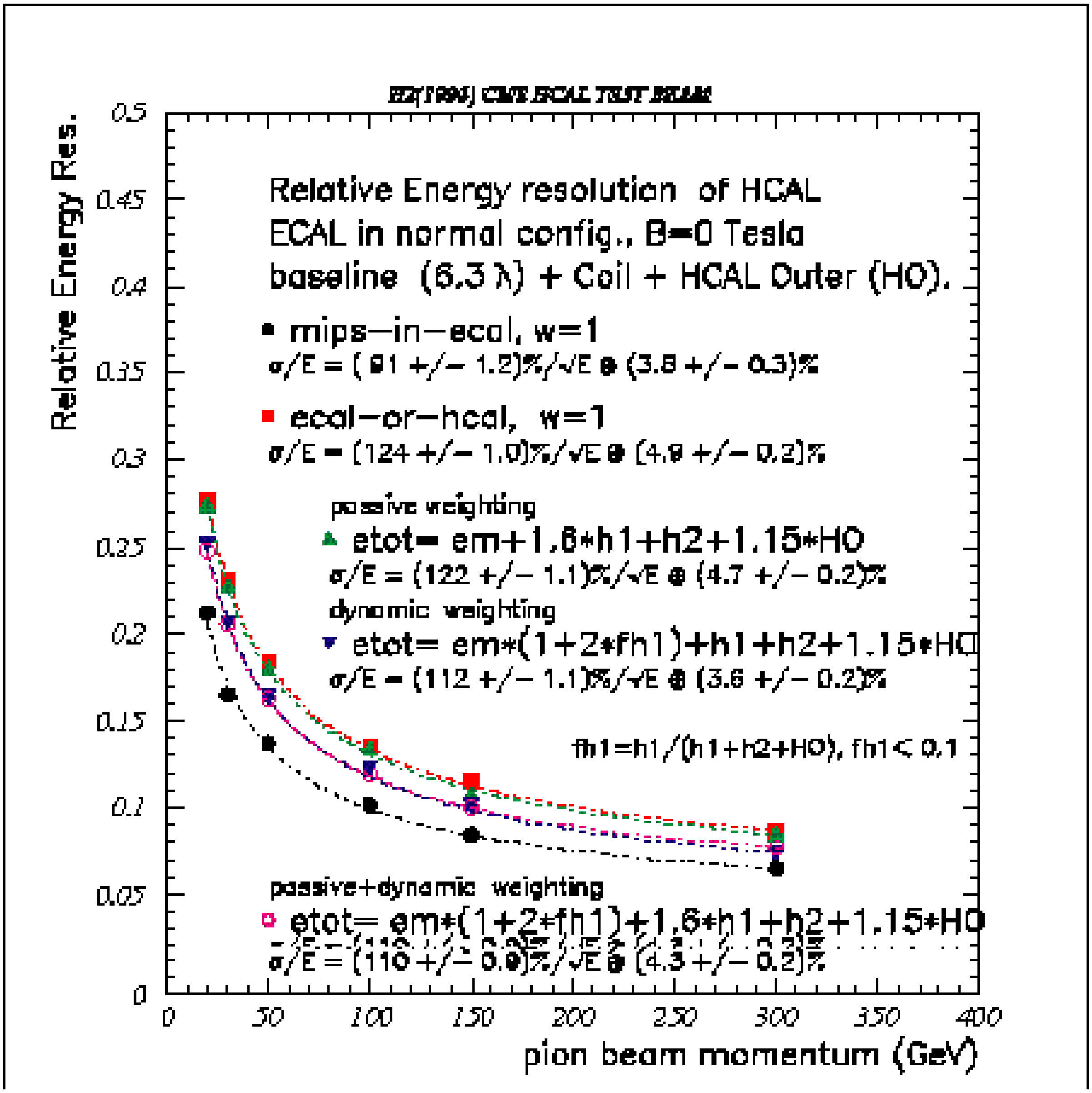

Fig. 1.25: Pion energy resolution of HCAL. The HCAL readout corresponded to Baseline Inner HCAL + HO. The absolute energy scale of ECAL was set using 50 GeV electrons. The absolute energy scale of HCAL was set using 50 GeV pions interacting only in the HCAL.

The Barrel HCAL calorimeter segment inside the CMS solenoid has two distinct longitudinal readouts H1 and H2. In studies done prior to the 1996 H2 beamline tests, no compelling argument to set the optimal partition between H1 and H2 was available. However, the 1996 Test Beam data showed that the optimal partition was that which was most useful in correcting for the large e/h response of the ECAL crystal calorimeter. The present baseline is to have the H1 compartment rather thin, while H2 constitutes the bulk of the inner HB. The reason for this choice is the following. The large e/h of ECAL means that, for hadrons interacting in ECAL, the ECAL response should be increased relative to the electron beam calibration of ECAL. However, this would mismeasure the electromagnetic energy of a jet of particles. Thus, one uses a thin H1 compartment just downstream of ECAL to estimate the energy deposit in ECAL for hadrons and weights it heavily. Thus, the basic function of H1 is to measure the low hadron response of ECAL and correct for it.

We have tested two possible approaches to correct the performance of the combined ECAL+HCAL calorimeters. In the first approach, called passive weighting, we reduce the non-linearity of energy response and the energy resolution by increasing the weight (α) of the first (H1) HCAL segment. Fig. 1.26 shows the dependence of E/p and $_{E}$/E as a function of the weight α. Clearly an overweighted H1, α ~ 1.6, is optimal.

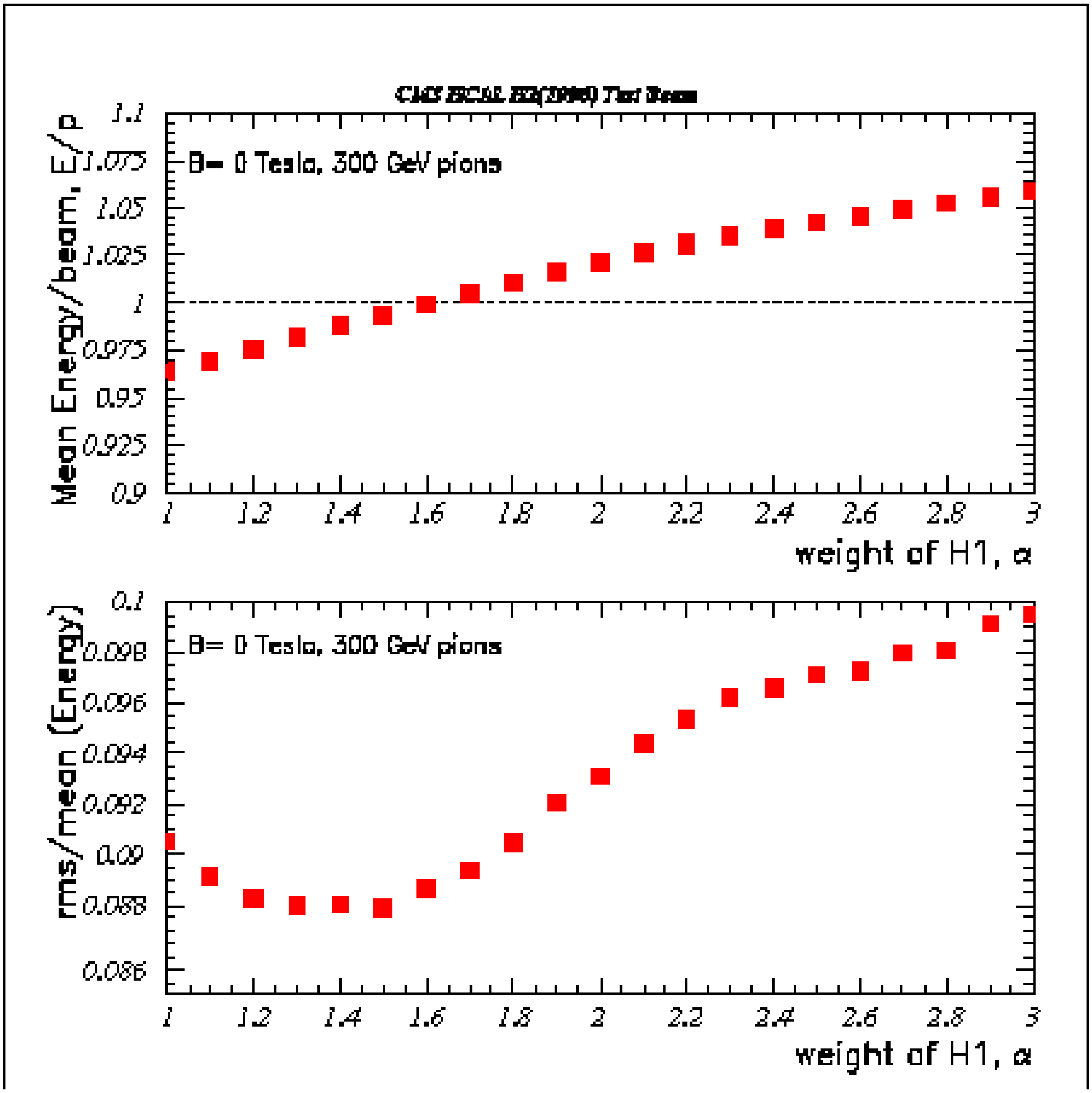

Fig. 1.26: Dependence of the E/p and rms (E)/E as a function of α, the weight assigned to the first HCAL compartment.

In the second approach we use a dynamic (event-by-event) correction. The energy ratio f(H1)=E(H1)/(E(H1)+E(H2)+E(HO)) effectively allows one to correct for the low ECAL response to pions interacting in ECAL. The correlation of total mean energy and f(H1) is shown in Fig. 1.27. Clearly, event by event improvements are indicated. The overall system response to pions can then be represented as the sum in quadrature of a 110% stochastic coefficient and a 5% constant term. One also finds a residual energy nonlinearity of only 10% for pions with energy between 30 and 300 GeV.

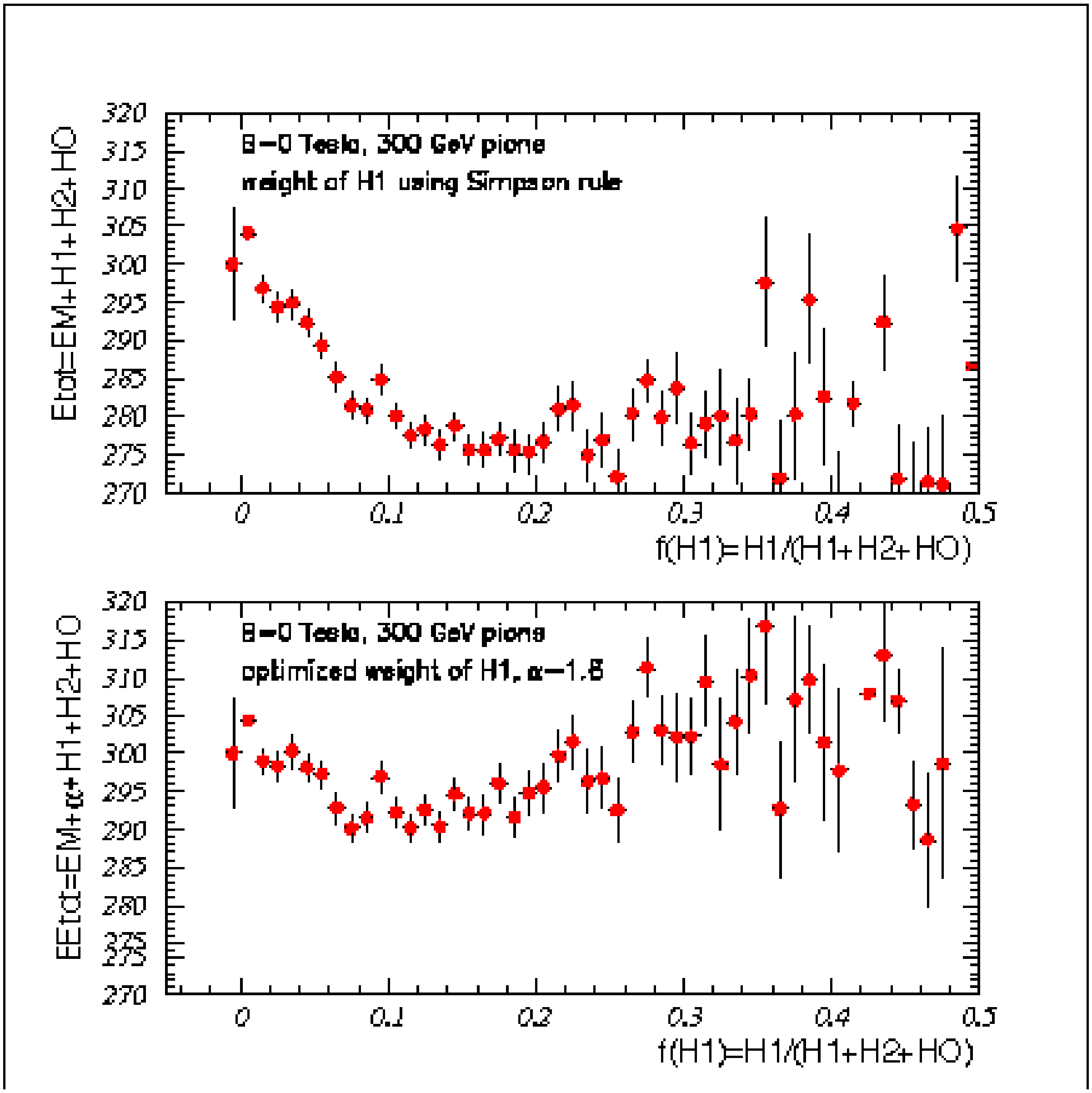

Fig. 1.27: Correlation between the total reconstructed energy, Etot and f(H1)=E(H1)/E(H1)+E(H2)+E(HO)).1.5.2.3

Monte Carlo simulation of the test beam results

Having optimized the depth and longitudinal segmentation of HCAL, it is important to establish a Monte Carlo model of HCAL which will then allow us to extrapolate and to explore other configurations not directly measured in the test beam.

GEANT simulations have been performed for various Test Beam setups. Several hadron shower generators are available in the GEANT framework and have been used in various studies for evaluating calorimeter design in CMS. In order to verify those simulations and to understand their limitations we used GCALOR to simulate the latest 1996 H2 Test Beam setup and take it as a reference to other generators. In the GCALOR simulation, details of ECAL and HCAL Test Beam geometry were implemented. Electronic noise and photo-statistics effects were simulated based on measured distributions of pedestals and electron and muon signals. Energy cut values in the GEANT simulation were set at its default values, 1 MeV for electrons and 10 MeV for hadrons.

The comparison of Test Beam data with GCALOR Monte Carlo simulations illustrates a good agreement. Fig. 1.28 shows the comparison of average longitudinal profile of 50 GeV pions.

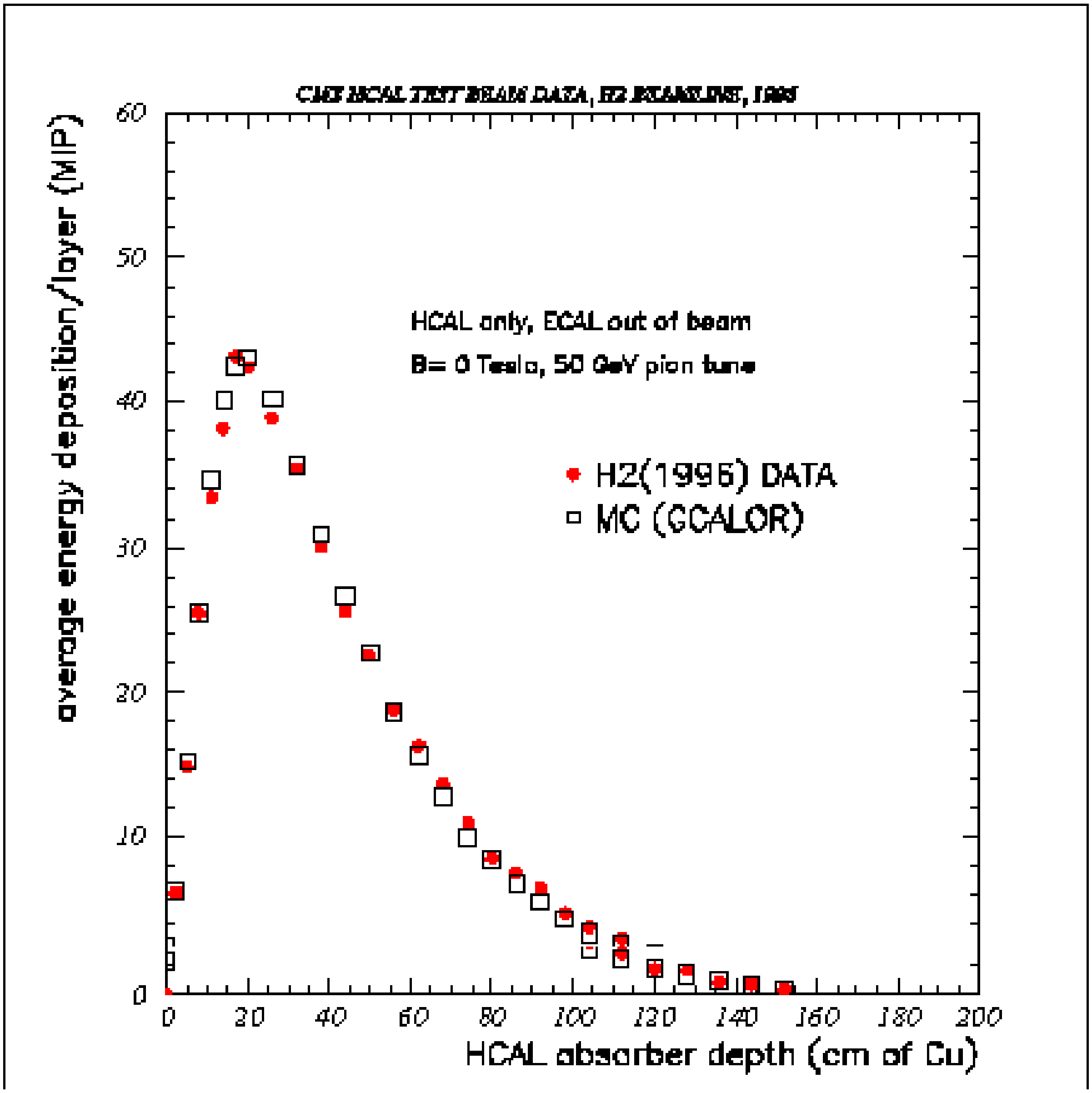

Fig. 1.28: Data vs GEANT comparison of average longitudinal profile of 50 GeV pions.

Fig. 1.29 shows the comparison of linearity of the combined ECAL+HCAL response to pions. Fig. 1.30 shows the comparison between the relative pion energy resolutions of the combined ECAL+HCAL system, after including all experimental effects. The simulated results are in good agreement with Test Beam data.

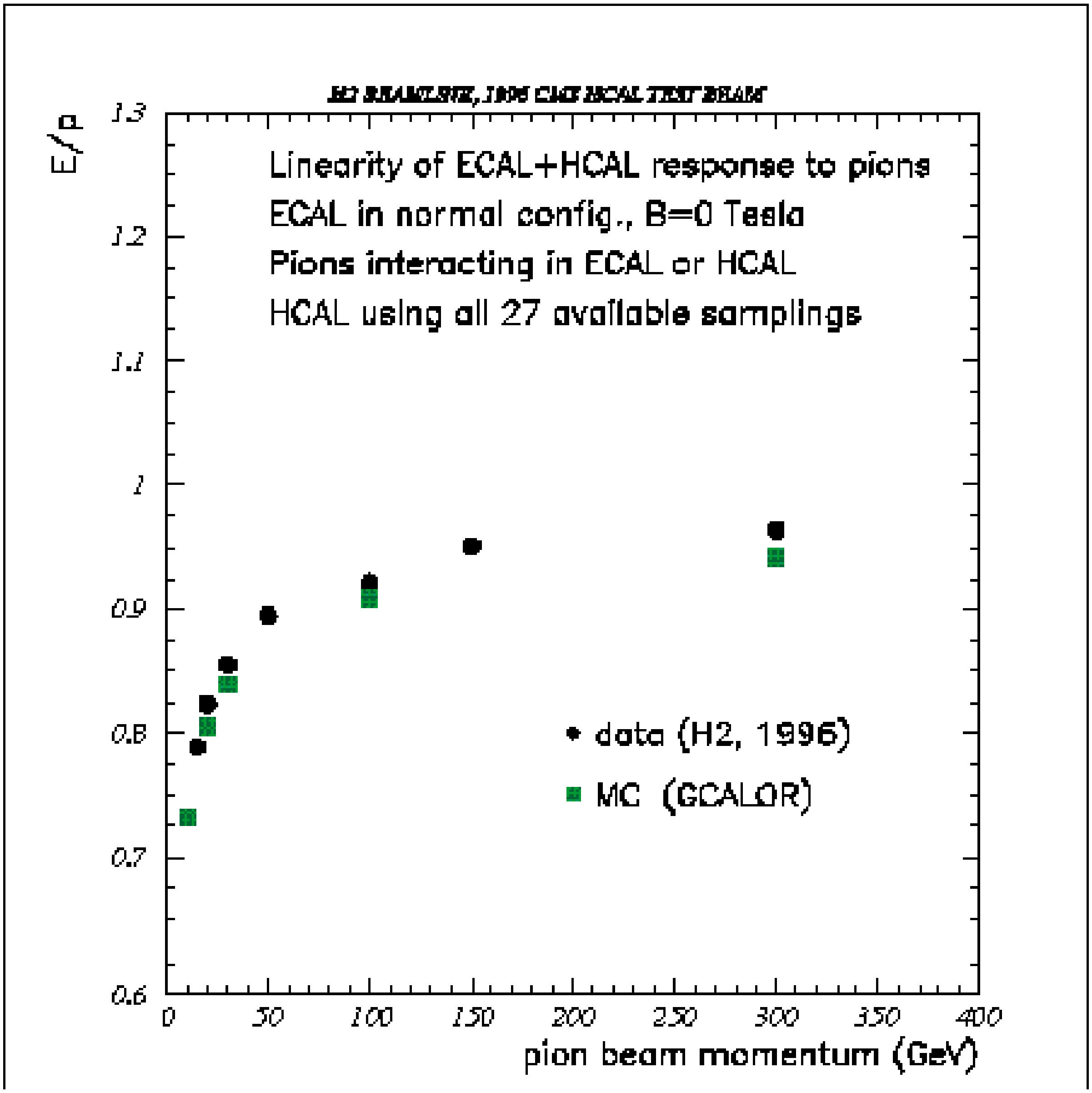

Fig. 1.29: Linearity of pion energy response in HCAL+ECAL combined system (pions interacting in ECAL or HCAL) and comparison with MC simulation.

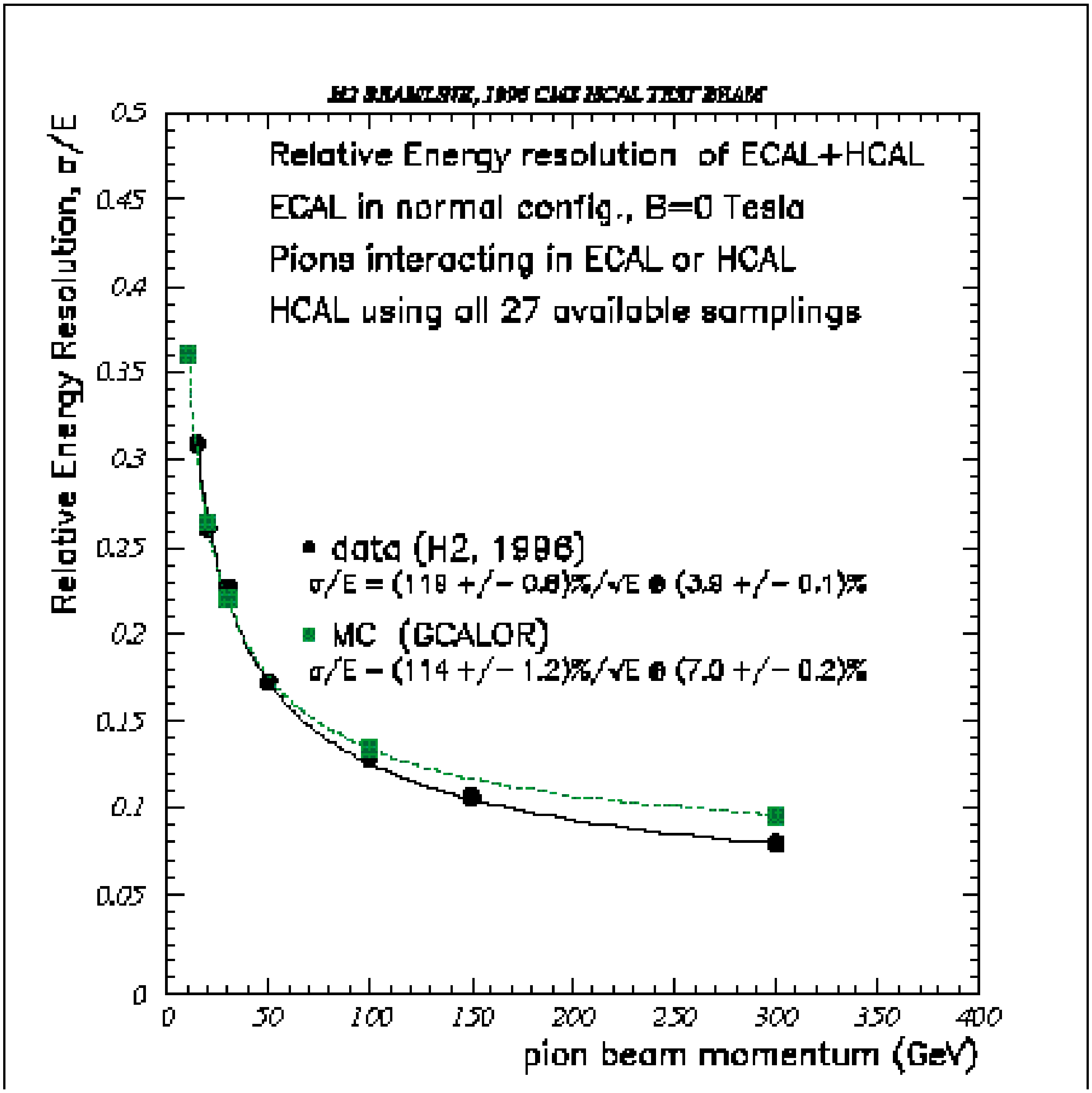

Fig. 1.30: Energy resolution of pions in HCAL+ECAL combined system (pions interacting in ECAL or HCAL and comparison with MC simulation.

Comparison between GCALOR simulation and other GEANT hadron simulators are shown in Fig. 1.31. GHEISHA was used in many of the following studies and gives a somewhat pessimistic resolution, while FLUKA and MICAP show much more optimistic resolution than GCALOR.

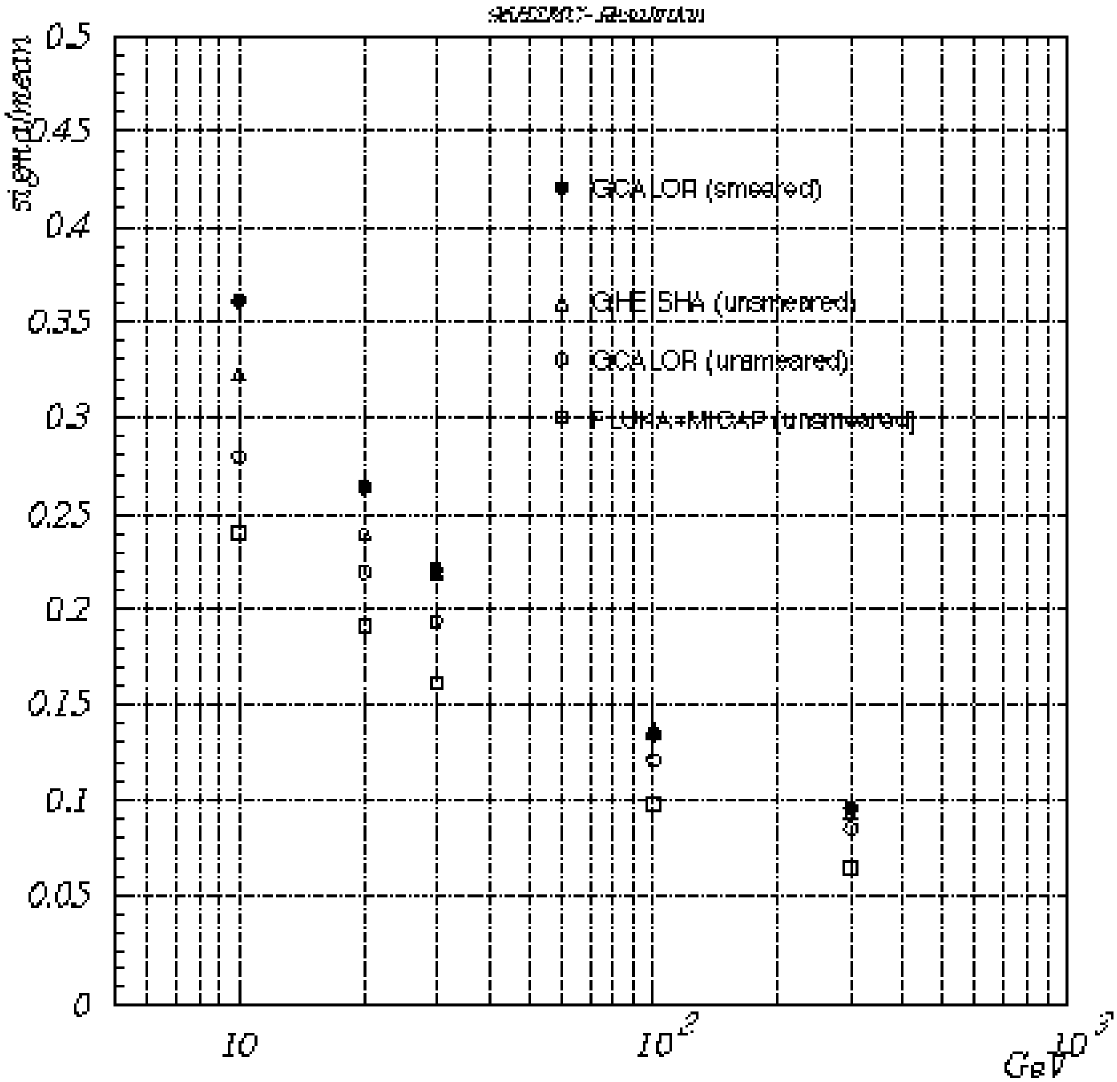

Fig. 1.31: Comparison of GEANT simulation of pion energy resolution of ECAL+HCAL, using various MC simulations (GHEISHA, GCALOR, and FLUKA-MICAP).1.5.2.4

Effect of magnetic field on the HCAL performance

The magnetic field changes the light yield of scintillator and affects the particle shower development. This latter effect depends on the field orientation. For a typical collider geometry, the axial magnetic field is parallel to calorimeter plates for the central part of the detector (Hadron Barrel or HB configuration) and is perpendicular to calorimeter plates in the large $|\eta|$ region (Hadron End Cap or HE configuration). One of the primary objectives of the HCAL Test Beam studies was to measure the dependence of calorimeter performance in the presence of perpendicular and parallel magnetic fields.

For the case of the magnetic field lines perpendicular to the scintillator planes (Endcap configuration), we observe an increase of the intrinsic light yield of scintillator of approximately 5%, relative to the case with no magnetic field. This scintillator brightening effect leads to an overall increased response of the calorimeter to muons, electrons and pions and can be well tracked by radioactive γ sources (wire sources). Fig. 1.32 shows the response ratio, relative to B=0 Tesla, of HCAL to pions, electrons and γ source as a function of field perpendicular to the scintillator planes.

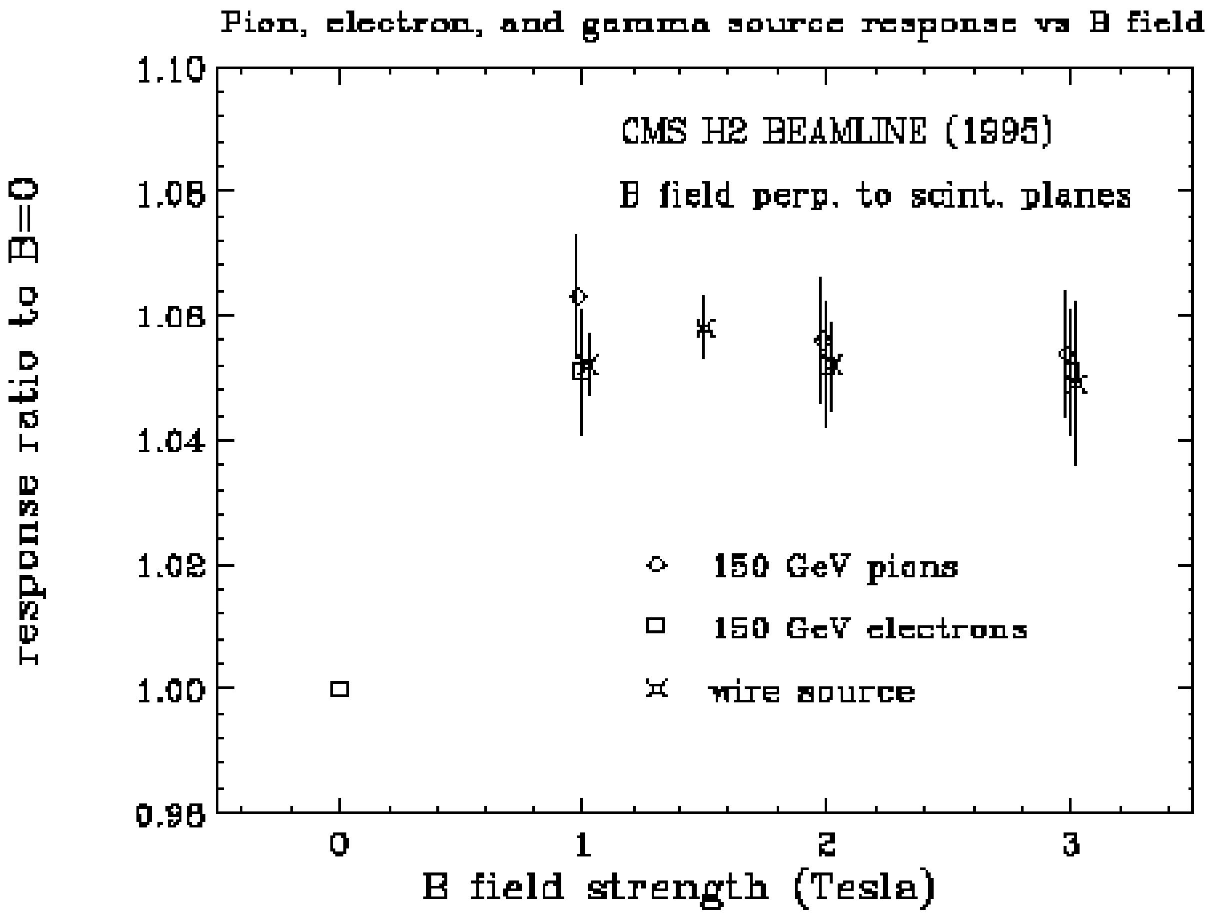

Fig. 1.32: Effect of B field on the average energy response of the tile/fiber calorimeter to pions, electrons (H2 data) and a calibration source. B field lines were perpendicular to the scintillator plates (HE Configuration).

Thus this configuration (B field perpendicular to scintillator planes) causes only increased scintillator light yield (~5%) and does not affect the shape of pion showers.

However, in the case of magnetic field lines parallel to the scintillator planes, an additional geometric effect leads to an increase of response of calorimeter to electromagnetic showers. Fig. 1.33 shows a comparison of average 50 GeV pion shower profiles, as a function of absorber depth. In the beginning of shower development, for pions in a B=3 Tesla field, the scintillator planes have an increased response relative to B=0 Tesla.

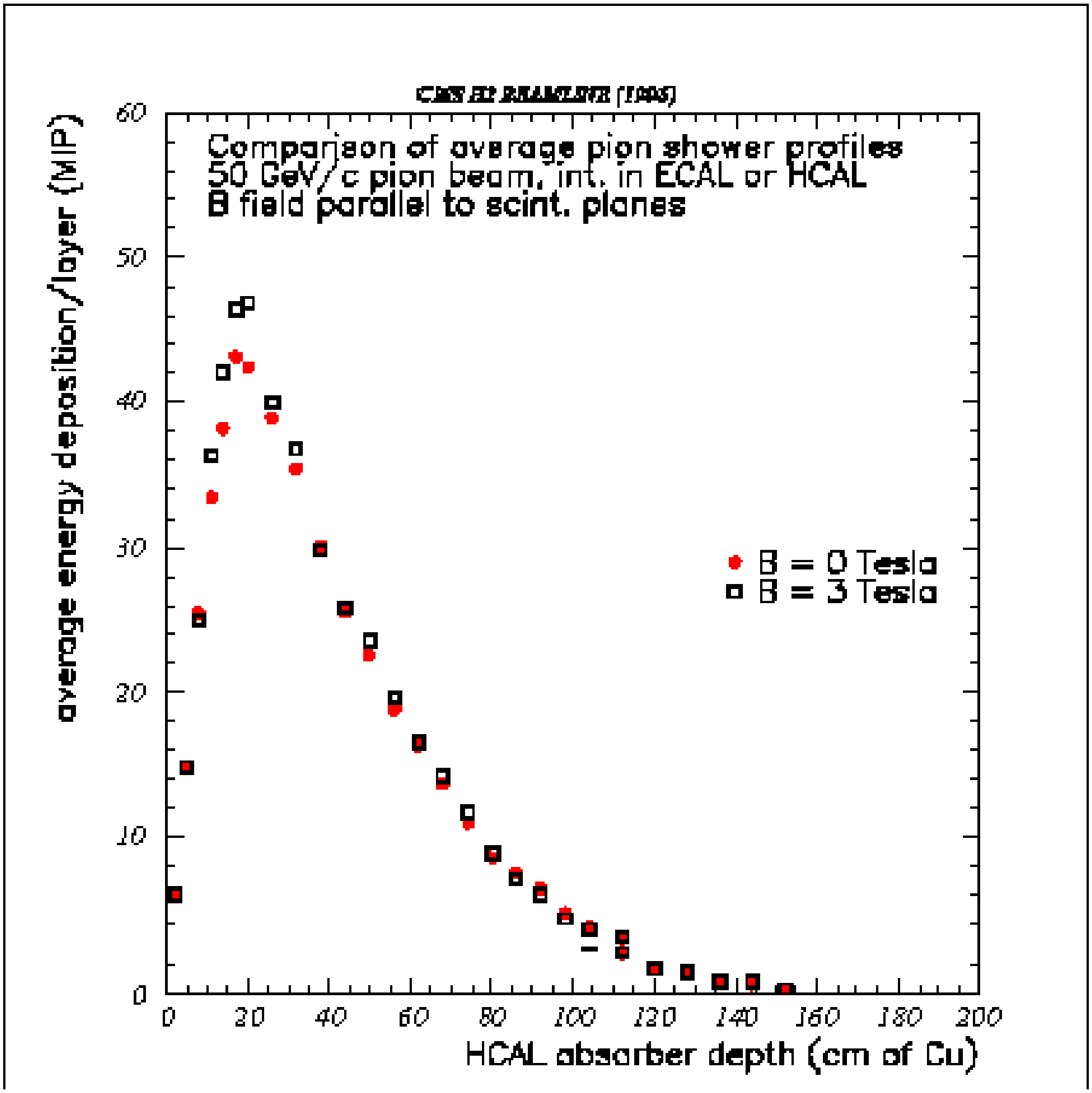

Fig. 1.33: Comparison of 50 GeV pion shower profiles with B=0 and B=3 Tesla magnetic field, with B field lines parallel to the scintillator plates (Barrel configuration).

The average increase of HCAL electron and pion response normalized to muons, as a function of B field, normalized to B=0 Tesla, is shown in Fig. 1.34. The 5% scintillator brightening effect cancels out since is has same effect on electrons, pions and muons.

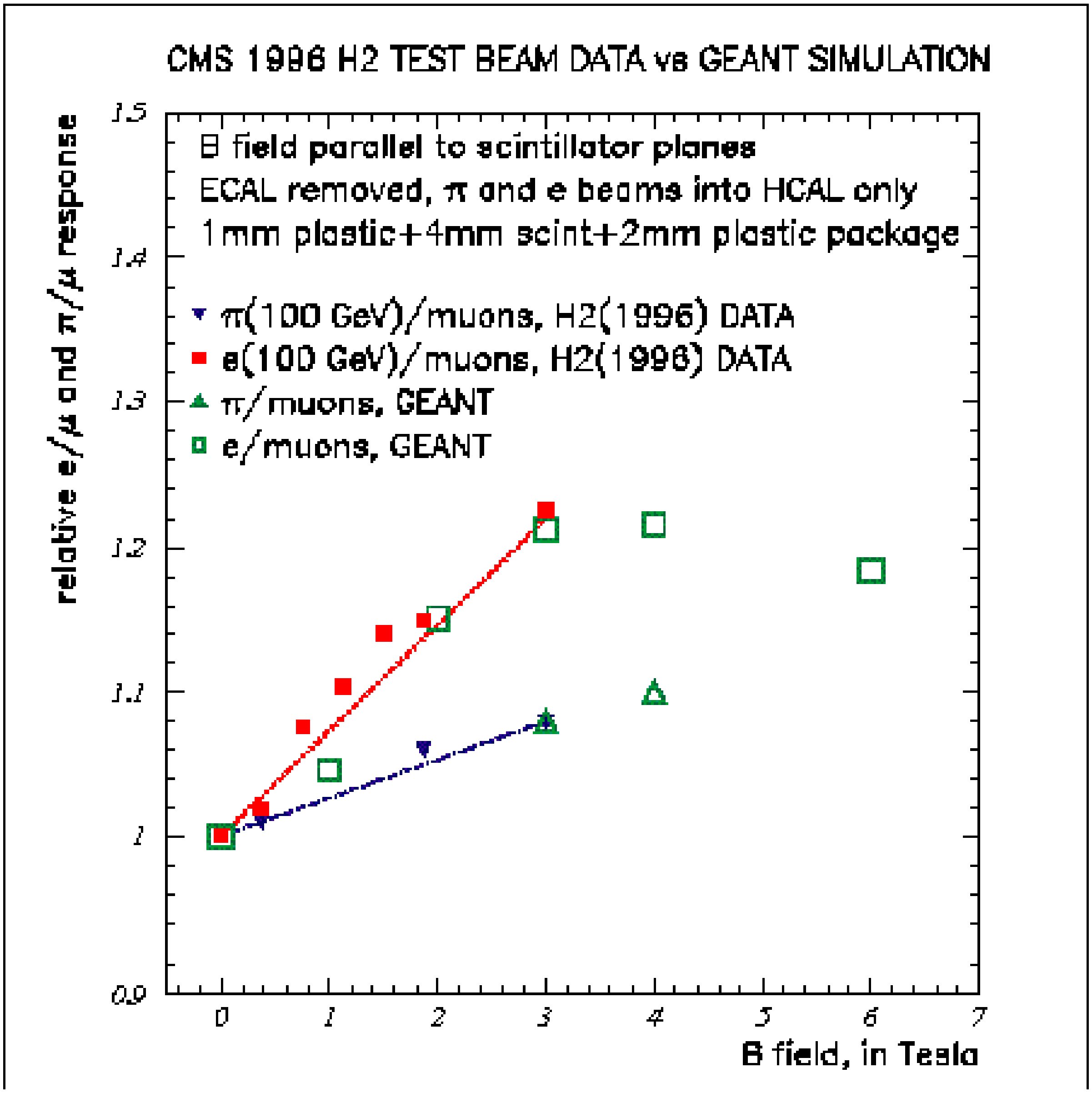

Fig. 1.34: Effect of B field on the average energy response of the tile/fiber calorimeter to pions, electrons (H2 data) (normalized to the muon response) and comparison with GEANT predictions. The ratio of hadrons to muons (lower curve) shows a smaller increase thus indicating the effect is a function of the electromagnetic fraction in the shower.

Subsequent simulation confirmed that this effect was due to the change of path length of low momentum electrons (between 1 and 10 MeV/c) through scintillator layer in a strong field and that only the electomagnetic components in hadronic showers contributed to this effect. Fig. 1. 35 shows a Monte Carlo study of dependence of this effect on the distance between the upstream absorbers and the scintillator packages placed in 9mm gaps between absorbers. The scintillator package consists of a 2mm plastic front cover plate, a 4mm scintillator and a 1mm plastic back cover plate. To set the scale, the radius of electron trajectory in a 4 Tesla field is ~0.8mm per 1MeV/c. Therefore as the scintillator moves away from the upstream absorber, in field parallel to the scintillator plane, low momentum electrons (a few MeV/c) no longer reach the scintillator.

This effect introduces a requirement for placement of scintillator package in gap between absorbers in HB. Since calibration data will be taken in the calibration beam line without a magnetic field, it will be very desirable to have minimal extrapolation from the calibration beam data (in 0 Tesla) to the CMS HB data (in 4 Tesla). In additon, gravity may push down the scintillator packages toward the front in absorber gaps at the top of HB and increase the HB response, while at the bottom of HB, it would push them toward the back and thus decrease the response. First we choose the tile orientation with the thicker plastic plate (2 mm thick) in front giving a larger distance between scintillator and front absorber. Then by forcing the package toward the back, we can limit the B field effect in HB to less than 2%.

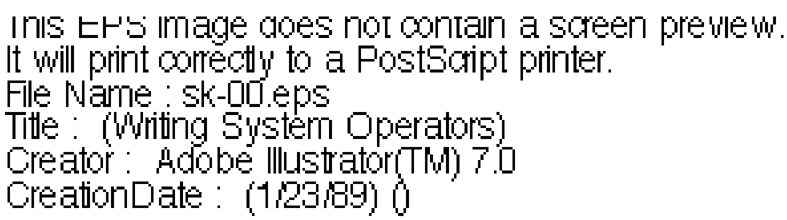

Fig. 1.35: Monte Carlo study on response of HB to 50 GeV pions in 4 Tesla field relative to response in 0 Tesla field with different air space between upstream absorber and scintillator package placed in 9mm gap between absorbers. The scintillator package consists of a 2mm plastic front cover plate, a 4mm scintillator and a 1mm plastic back cover plate.

1.5.3 HF test beam results 1.5.3.1

Description of HF prototypes

The HCAL group has built and tested two prototype modules for the forward calorimeter (HF). The first, a hadronic detector module, was 135 cm (8.5 nuclear interaction lengths) deep, with an instrumented lateral cross section of about 16∞16 cm^2. This area was subdivided into 9 square towers, Fig. 1.36. A tenth tower (T10), neighboring the central row of three, was also instrumented. In total, this module contained about 6000 fibers, with a total length of about 10 km. This calorimeter module was extensively tested in the CERN H4 test beam in 1995. The results have been submitted for publication in Nuclear Instruments and Methods.[19]

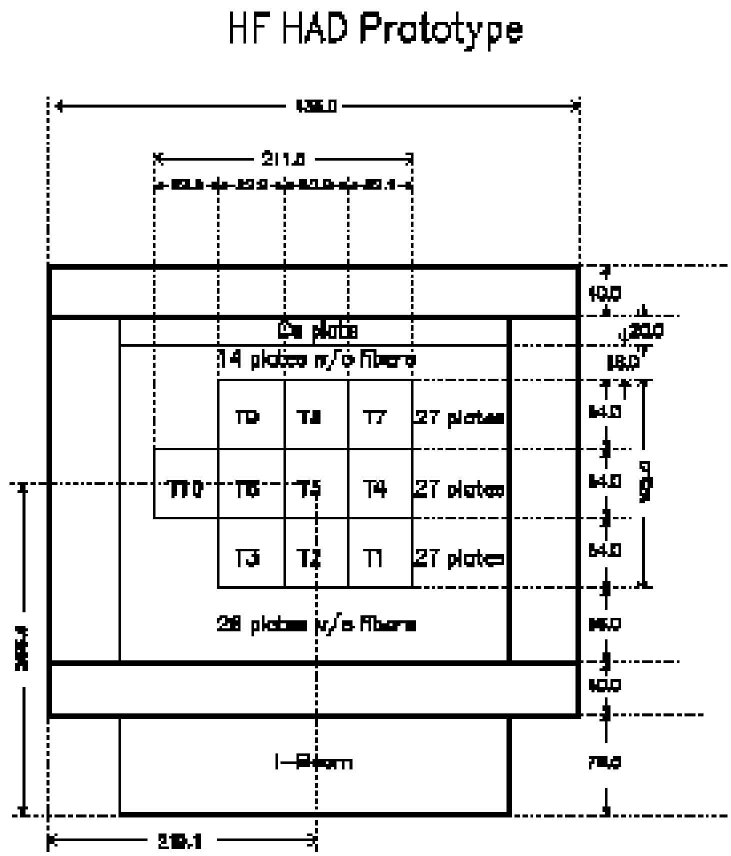

Fig. 1.36: Schematic end view of the HF hadronic prototype. All dimensions are in millimeters. The quartz fibers are embedded in copper absorber. By volume, quartz fibers constituted 1.5% of the detector.

The second, electromagnetic module had the same lateral structure as the hadronic module. It was about 34 cm (~23 radiation lengths) deep. The fibers emerged from the front face (towards the beam) and were aluminized at the open, downstream end. By mounting the readout in front of this detector, it could be joined flush to the hadronic module. This calorimeter was also tested, in the same H4 beam in 1996, both in stand-alone mode and in combination with the hadronic module. Some of the results are presented in the following.

During the beam tests, the calorimeter modules were exposed to electrons, pions, protons and muons of various energies, ranging from 8 GeV to 375 GeV. Dedicated tests were done to study various options for the location of the photomultiplier tubes, and to study pickup and cross talk in the fiber bundles emerging upstream from the electromagnetic module.1.5.3.2

HF hadronic prototype results

The light yield of this type of calorimeter is extremely small. We measured it to be less than 1 photoelectron per GeV. Fluctuations in the number of photoelectrons constituting the signals completely determine the electromagnetic energy resolution. In Fig. 1.37, this resolution is shown as a function of energy, for electrons from 8 GeV to 250 GeV. The data show no measurable constant term. When the calorimeter was read out by our standard PMT's (Philips XP2020), the resolution was found to be: (E) = $1.37\sqrt{E}$, commensurate with a light yield of 0.53 photoelectrons per GeV. When the same type of PMT was equipped with a quartz window, the signal increased by about 65%, to 0.87 pe/GeV, due to the larger fraction of the Cerenkov light that was detected. The energy resolution improved to $1.07\sqrt{E}$, reflecting smaller fluctuations in the larger number of photoelectrons.

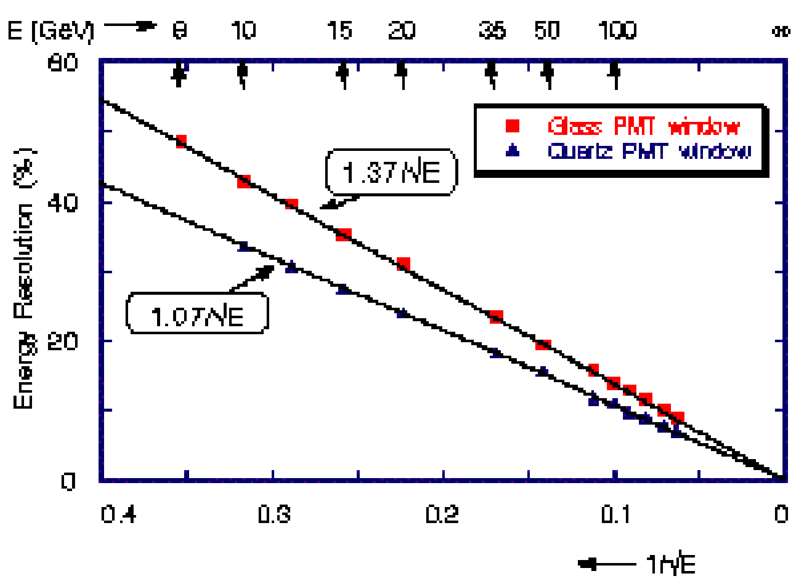

Fig. 1.37: The energy resolution for electrons as a function of electron energy, for readout with a XP2020 PMT (glass window) and with a XP2020Q (quartz window).

Although the light yield is extremely small, it is not a limiting factor for the resolution of the objects for which this calorimeter is intended: jets and energy flow at the 1 TeV level. With regular glass PMT's (the UV component of the signal is vulnerable to radiation and therefore will not be used in practice), we expect signals of about 500 photoelectrons at 1 TeV. Statistical fluctuations in that number amount to 4.5%, which is only a small contribution to the observed single particle resolution (10-12%) and is well below the intrinsic jet resolution.

The energy resolution for hadrons is shown in Fig. 1.38. Because of the asymmetric response function, the rms standard deviations are given, as opposed to the electron data which represent the results of Gaussian fits. The full circles show the energy resolution for pions, as a function of energy. The contribution from photoelectron statistics to these resolutions is represented by the triangles, and the *intrinsic resolution* (the squares) denotes the experimental resolution obtained after subtracting the contribution of photoelectron statistics in quadrature.

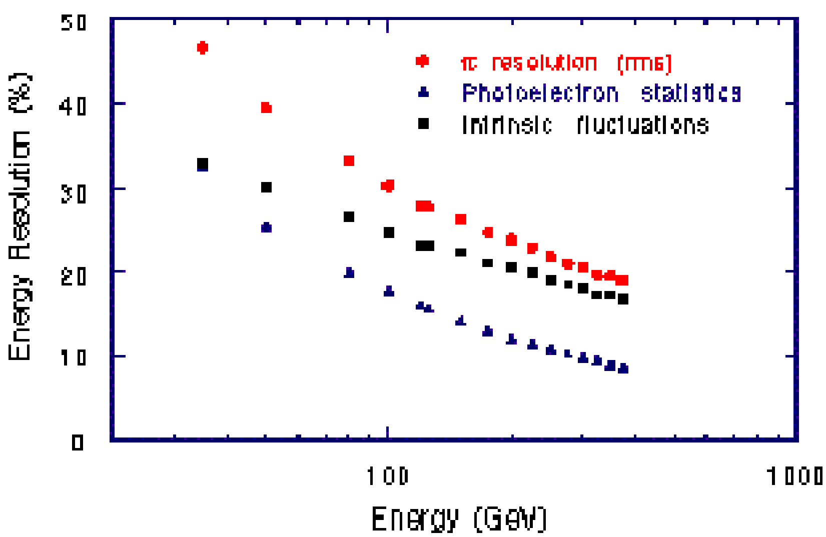

Fig. 1.38: The hadronic energy resolution (σ_{rms}) as a function of energy. The circles represent the raw data, the triangles the contribution of fluctuations in the number of photoelectrons, and the squares are the contributions from other sources.

These results show that the contribution of photoelectron statistics, although substantial in the low energy regime, rapidly diminishes at high energy and that therefore a large increase in the number of fibers would only have a miniscule effect on the energy resolution in the TeV regime. The results also show that the intrinsic resolution scales with the logarithm of the energy.[20]

The hadronic signals from this type of calorimeter are strongly dominated by the electromagnetic shower core. Apart from the asymmetric line shape already mentioned, this has several other consequences. First, the energy dependence of the average energy fraction carried by the EM shower component makes the hadronic response intrinsically non-linear. Second, the shower profiles derived from the Cerenkov signals are much narrower and also shallower than the profiles from detectors based on a measurements of *dE/dx*. This reflects the fact that the EM shower component is concentrated in a narrow core around the shower axis and that ^{0} production is limited to the first 4-5 interaction lengths in shower depth.

The signal for pions was measured relative to electrons and results are shown in Fig. 1.39. Since the available electron energies were less then 250 GeV, we extrapolated the electron energy dependence for higher energies. The intrinsic e/π of HF is rather nonlinear. We will use the relative normalizations of the longitudinal segments to require e/π = 1 at 1 TeV.

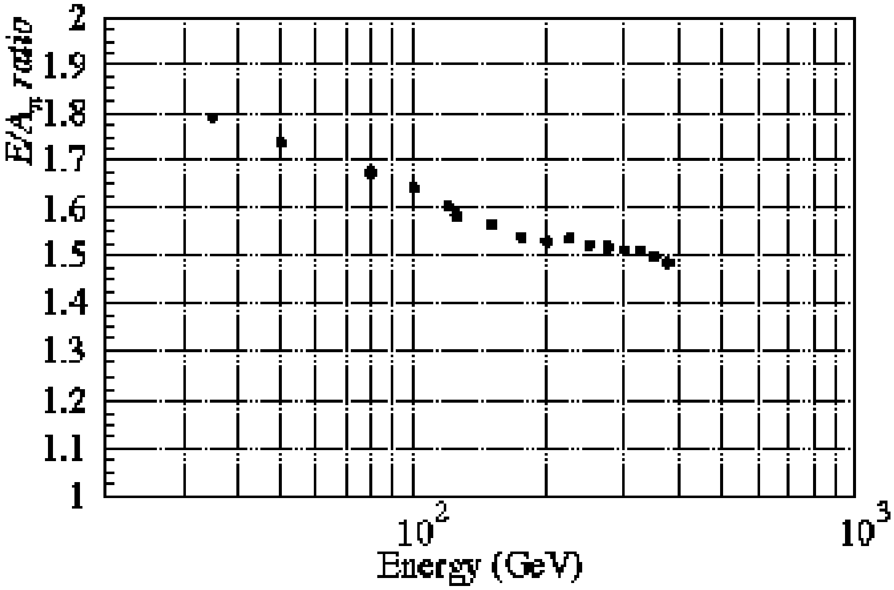

Fig. 1.39: e/ ratio of the hadronic module.

As with all fiber calorimeters, this detector is intrinsically very hermetic. There are no discontinuities in the calorimeter response at the boundaries between the towers. This is illustrated in Fig. 1.40, which shows the results from a scan with a narrow particle beam (80 GeV electrons) across the surface of the calorimeter. The response is uniform to within a few percent over the entire calorimeter surface. This figure also gives a good impression of the narrow lateral profiles of the showers in this calorimeter.

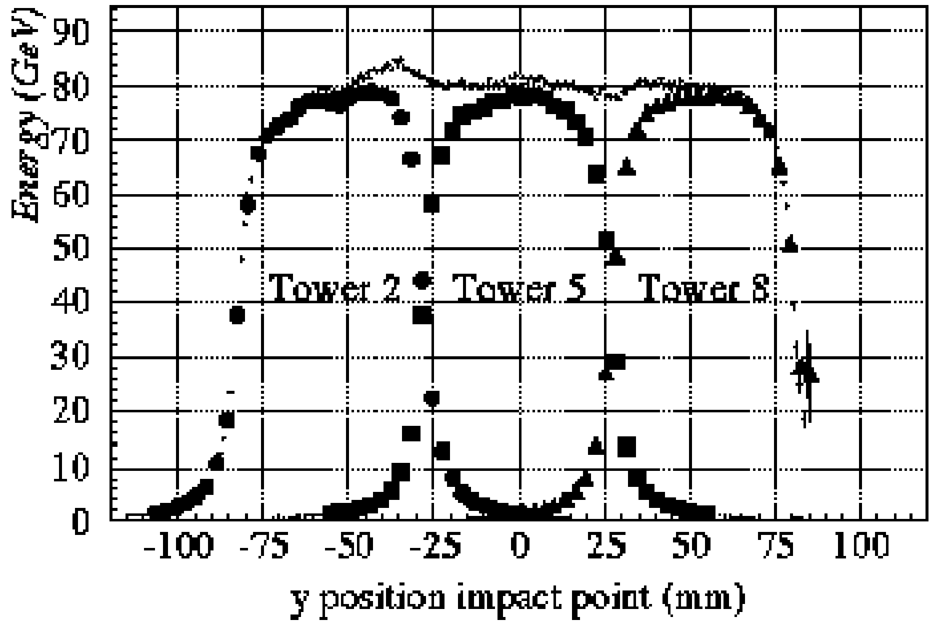

Fig. 1.40: The average calorimeter response to 80 GeV electrons as a function of their impact point. The results of a vertical scan in steps of 0.4 mm across the face of the detector. Shown are the average total calorimeter signal and the average signal in three individual towers as a function of electron impact position.1.5.3.3

HF hadronic and electromagnetic prototype results

The energy resolution for electrons was found to be /E = (155 ± 1)%/$\sqrt{E}$ + 6±0.2%. The larger constant term has its origins in a reflection non-uniformity of the mirrored ends of the electromagnetic section which was about ± 10%. The hadronic energy resolution is compatible with that of the single hadronic section at high energies (E > 300 GeV).1.5.4.4

HF signal timing measurements

We measured the time structure of the calorimeter signals, Fig. 1.41. This calorimeter is an extremely fast device. The entire charge produced by the Cerenkov photons is collected in about 5 ns, and this time is limited only by the transit time of the PMT. Typically 85% of the light, is reflected if the far end of the fibers are mirrored.

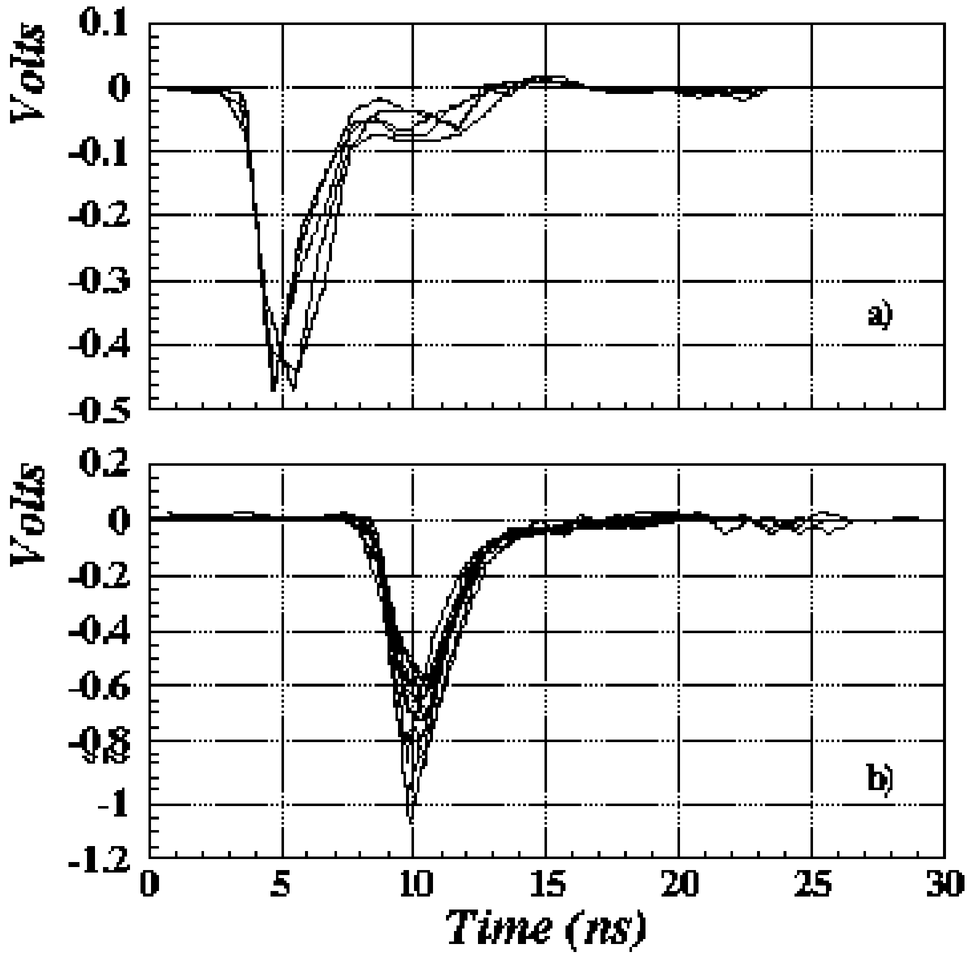

Fig. 1.41: The time structure of a typical electromagnetic shower detected in the detector before a) and after b) the mirrors were removed from the open end of the fibers. Two components in the top plot represent the Cerenkov light emitted in the forward and backward directions, respectively.1.5.3.5

Quartz fiber attenuation length measurements

The longitudinal uniformity of the hadronic prototype equipped with quartz core and flourine doped clad fibers was measured with 80 GeV electrons entering the detector sideways (90 degrees) at various positions. In this way, the light attenuation in the fibers can be measured. In these measurements, the signal observed from the front and from the back of the detector differed typically by less that 5%. The attenuation length in these fibers is thus very long, at least 15 m.1.534.6

Optical pickup measurements

The expected rate of charged particles, with β greater than βmin and arriving at the HF front face may range from 0.1 to 1 per cm2 and crossing.

Our earlier designs called for a configuration where the EM section would have its fibre bundles emerge from the front (close to the interaction point). During the 1996 test beam periods we tested this readout scheme by exposing straight bundles of fibers at different angles (90 and 45 degrees) behind various absorbers (air, polyethylene and iron).

Using GEANT we have simulated the experimental setup and found that, on average, about 1.6 charged particles (electrons and positrons) per event come with β greater than βmin and forming an angle of 45 ± 10 degrees with the bundle. This is equivalent to 0.02 cm-2 "Cerenkov particles", which is about an order of magnitude lower than the expected fluence at the HF entry face, per crossing, for the nominal LHC luminosity. Notice that, when traversing the bundle, each particle crosses, in average, 21 fibres.

Therefore, in our current design all the fibers are situated in the back of the copper absorber (♠ 10 λ) and are bundled only (to minimize the cross section) at the entrance of the air core light guides, near the PMTs, at a space location where the expected charged particle flux is several orders of magnitude smaller than at the HF front face.

1.5.4 HB/HE Simulation

Test beam data have been extensively used to study a response of the combined ECAL and HCAL system to single particles with various HCAL configurations in order to optimize the configuration. Normalized to this test beam data, GEANT simulations with detailed descriptions of the CMS detector geometry have been performed to extend the study to the CMS environment for further design optimization.

For good jet and missing E_T measurements the calorimeter has to be as hermetic as possible. Any holes due to cracks and dead material, or lack of stopping power i.e. insufficient depth for showers seriously spoil the measurements. We have made special attempts to reduce the energy leakage and keep a uniform response in the hadron calorimetry over a wide range of rapidity. In the following we will describe our GEANT[21] simulation and results from the simulations on shower leakage and the calorimeter response to single hadrons and jets in the rapidity range $|\eta|<3$.1.5.4.1

Simulation Program

The hadron calorimetry simulation was performed within the framework of the CMS general simulation program CMSIM. In addition to detector simulation with GEANT, CMSIM has interfaces to physics event generators and event reconstruction programs including a clustering code for jet finding.

The geometries used for the studies reported here are shown in Fig. 1. 42. TDR-0 corresponds to the baseline design and TDR-2 corresponds to the baseline plus two additional layers in HB. The ECAL consists of 23cm long crystals followed by a 2cm aluminum plate, a 4cm aluminum layer and a 2cm steel plates which represent respectively the crystal support structure, cooling, electronics, cables and a back plane in the ECAL mechanical structure. The HCAL consists of layers of a 5.0cm (7.9cm in endcaps) copper absorber followed by a gap with a scintillator package. The first and last absorbers are made of 7cm steel plates. Outside the solenoid two layers of HO are implemented in the muon system. The gap between HB and HE is 12cm wide and filled with 'cable material' (density 1.88g/cm^3) for the cables and pipes of the inner detector. In the endcap a preshower detector, made of 1.68cm lead with sampling Si layers, is placed in front of the ECAL. GHEISHA is used for hadron shower generation and energy cut values in GEANT are set to 1MeV for electrons and photons, and 10MeV for hadrons.

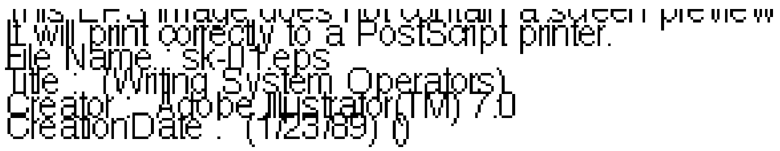

Fig. 1.42: Geometries in GEANT simulation: the baseline (TDR-0) and the baseline plus two layers in HB (TDR-2).

To study the response to jets we created shower libraries. A shower library stored the calorimeter system (ECAL+HCAL) response to single particles in 18-rapidity ∞ 6-energy bins for each HCAL configuration. Three thousand events were generated in each bin.1.5.4.2

Single particle response

The expected resolution in measurements of single pions energies between 4 and 300 GeV is shown in Fig. 1.43 for TDR-0. At a given incident energy the resolutions vary very little (<5% at 4GeV and <2% at 300GeV) in a wide rapidity range up to 2.8 and degrade beyond $|\eta|$=2.8 rapidly because of shower leakage through the inner edge of HE. (Note that the forward calorimeter (HF) was not included in this study.) Around the boundary between HB and HE at $|\eta|$=1.3~1.4 the resolution degrades by 1-2% due to energy loss in the 'cable' material in the crack region, and energy leakage through the relatively thin part of the calorimeter in the region of the crack. In the thinner or in the cracks region main issue is however not the Gaussian resolution but rather the population of the low energy tail. Overall, the single particle resolution is, by design, rather flat over the entire region $|\eta|$<3.

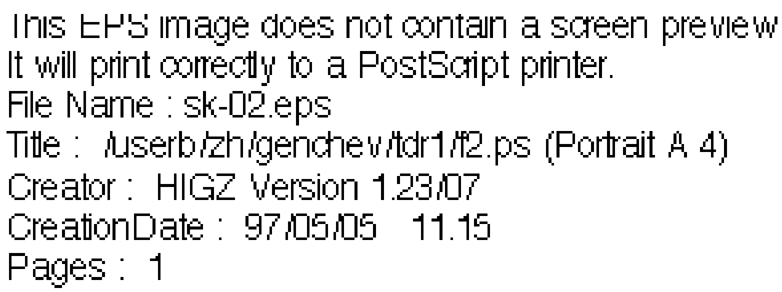

Fig. 1. 43: dE/E for single pions as a function of η.

The resolution for TDR-2 can be inferred from test beam data. At the GEANT simulation level the Gaussian resolution for TDR-2 is nearly identical to TDR-0. The simulated energy distributions for TDR-0 and TDR-2 are compared in Fig. 1.44 for 300 GeV single pions. Low energy tails are small in both cases and with two additional layers (TDR-2) an improvement can be seen in the central region η~0.0-0.3 and in the crack region η=1.3-1.4.

This EPS image does not contain a screen preview.
It will print correctly to a PostScript printer.
File Name : sk-03.eps
Title : /userb/zh/genchev/tdr1/g9.ps (Portrait A 4)
Creator : HIGZ Version 1.23/07
CreationDate : 97/05/04 19.46
Pages : 1

Fig. 1.44: Reconstructed energy distributions for 300 GeV pions.1.5.4.3

Jet response

The expected Gaussian resolution for jet E_T measurement fitted over the E_T 30 to 300 GeV range with a fixed cone size of $d\eta \infty d\phi = 0.74^2$ is shown in Fig. 1.45 for TDR-0. The degradation at the HB-HE boundary is less than 1%, and again the resolution is smooth and monotonic for $|\eta|<3$.

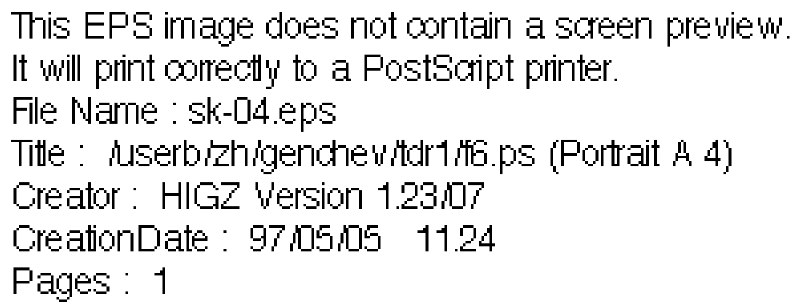

Fig. 1. 45: Jet energy resolution of HB and HE.

Reconstructed jet E_T distributions are shown in Fig. 1. 46 in the central part at η =0.1 for TDR-0 and TDR-2. Fig. 1. 47 shows reconstructed E_T distributions for E_T = 300GeV at four different rapidities.

This EPS image does not contain a screen preview.
It will print correctly to a PostScript printer.
File Name : sk-05.eps
Title : /userb/zh/genchev/tdr2/f9.ps (Portrait A 4)
Creator : HIGZ Version 1.23/07
CreationDate : 97/05/05 11.48
Pages : 1

Fig. 1. 46: Jet energy measurements at $\eta = 0.1$ for different E_T.

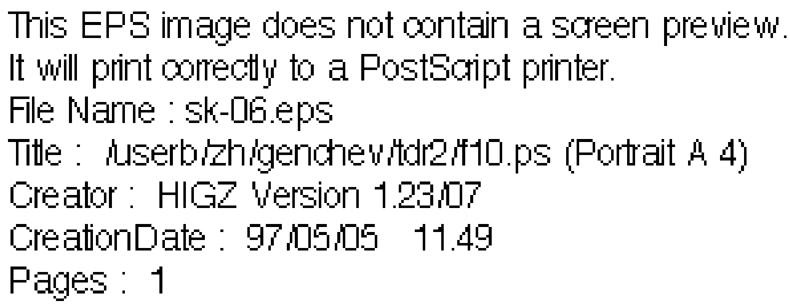

Fig. 1. 47: Jet energy measurements at E_T = 300 GeV for different η.1.5.4.4

HB-HE boundary

The geometry of the HB-HE boundary has been extensively studied with GEANT prior to the TDR designs.[22] The study showed that any projective cracks and dead material significantly damage the energy measurements and thus the missing E_T performance of the detector. In some designs the performance was very sensitive to the width of the cracks. The study concluded that in addition to HCAL, the ECAL should be hermetic with overlapping lips if possible. The present TDR design, with a crack at 53_ to the beam line, is the best solution among those considered, because the resolutions showed the least variation with rapidity and the slowest build-up of the low energy tail with increasing crack size.

Fig. 1. 48 shows distributions of reconstructed energies for 300 GeV pions with a baseline 12cm crack and for wider 15cm and 18cm cracks. Compared to TDR-0, TDR-2 shows narrower distributions on the low energy side of the peak for all three crack sizes and a significantly slower build-up of the low energy tail below 200GeV, which is about 3σ below the mean at 300 GeV incident energy.

This EPS image does not contain a screen preview.
It will print correctly to a PostScript printer.
File Name : sk-07.eps
Title : /userb/zh/genchev/tdr1/g20.ps (Portrait A 4)
Creator : HIGZ Version 1.23/07
CreationDate : 97/05/29 09.58
Pages : 1

Fig. 1. 48: Reconstructed energy for 300 GeV pions incident on the HB/HE boundary for different crack sizes in TDR-0 and TDR-2.1.5.4.5

ECAL-HCAL boundary

Shower particles from interactions in the crystals may spread in the space between ECAL and HCAL in the 4 Tesla field. In TDR-0 the distance between the back face of the crystals and the front face of HCAL is 27cm (56cm, 29cm) at η=0.0 (1.2, 2.2) along the particle direction. We have investigated the effect of this gap in various observables. Although this gap increases with rapidity in the HB region, our single particle and jet simulations show no significant degradation neither in the Gaussian resolutions nor in the low energy tails with increasing rapidity in the HB region.

To illustrate the effects of the magnetic field, Fig. 1. 49 shows distributions of reconstructed energies for 100 GeV pions with and without the 4 Tesla field. A small degradation (<1.5%) is observed in HB, while there is no significant degradation in HE. This effect of the magnetic field includes shower spreading in the HCAL-ECAL interface region as well as the path length effect in the HB absorber gaps discussed previously.

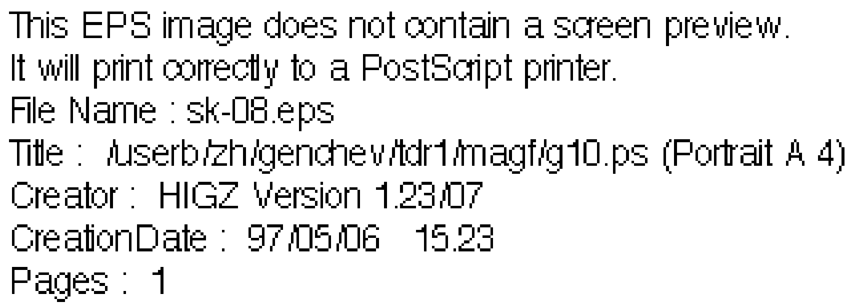

Fig. 1. 49: Reconstructed energy distributions for 100 GeV pions with and without 4T field.

1.5.4.6 HO simulation

The HB inside the solenoid is too thin to fully absorb the showers of most energetic particles expected. For $|\eta|<3$ HO provides at least 10λ as shown in Fig. 1. 50 to contain energetic showers and reduces the low energy tails in energy measurement. Fig. 1. 51 shows the reconstructed energy distributions for pions

(E_T=200GeV) in the muon ring (η=0.33-0.86) next to the central ring without HO and with HO1 and HO1+HO2, where HO1 is a HO layer before the first iron yoke and HO2 is a layer behind the iron yoke. A clear suppression of the low energy tail is seen with the addition of the two HO layers.

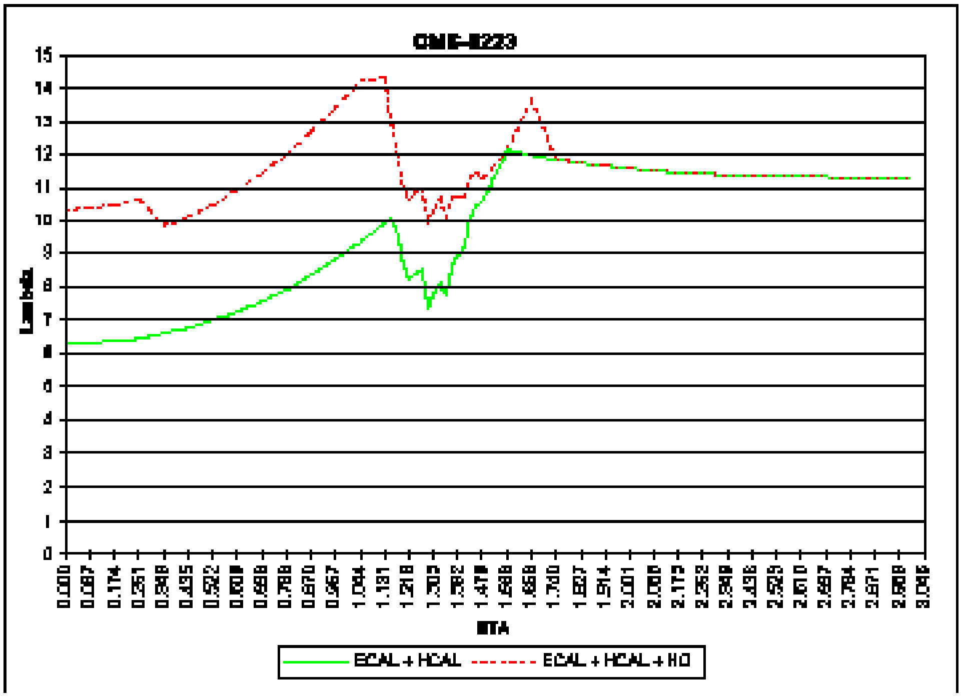

Fig. 1. 50: Interaction lengths for TDR-0.

This EPS image does not contain a screen preview.
It will print correctly to a PostScript printer.
File Name : sk-10.eps
Title : (Adobe Illustrator (R) Version 5.0 Full Prolog)
Creator : Adobe Illustrator(TM) 6.0
CreationDate : (3/7/1994) ()

Fig. 1. 51: Single π response with and without HO samples.

1.5.5 HF simulation

The quartz optical fibers are embedded in a matrix of copper absorber and run along almost parallel to the incident particle direction. Due to the optical properties of fibers the maximum amount of Cherenkov light is detected when the charged particle hits the fiber at an angle $\theta = \cos^{-1}(1/n\beta)$, where n is the index of refraction and β is the particle speed. For particles with $\beta \sim 1$ this angle equals $\theta \sim 45^o$ or $\theta \sim 135^o$. Light produced by particles entering fiber at other angles has very low probability to be detected[23]. Therefore such calorimeter mainly detects electrons and positrons copiously produced in shower development because these particles in contrast to hadrons and nuclear fragments are distributed isotropically even at the beginning of the shower independently of the initial particle direction. Thus a calorimeter based on Cherenkov effect in optical fibers detects hadronic showers predominantly through their electromagnetic component.

The basic design choice is the length of the fibers constituting the longitudinal HF compartments. As with other calorimeters, the HF EM compartment has a depth of 10-20 X_o. Having chosen the longitudinal partition, the weighting strategy for jets must be specified. The response to electrons and hadrons can be adjusted to make $e/\pi = 1$ at a given energy. Minimization of a jet energy resolution as a function of the EM and HAD calibrations allows us to fix these coefficients at an optimal point. There is an unavoidable residual energy dependence to e/π after this procedure is performed.1.5.5.1

Response to Jets

Tagging jets accompanying WW fusion have been generated using PYTHIA[24]25 in the pseudorapidity range $3 < |\eta| < 5$. Jets have been found using LUCELL jet finding algorithm within a cone $\sqrt{\Delta\eta^2 + \Delta\phi^2} < 0.5$ around the jet initiator. Jets were steered into the calorimeter. In this study we concentrated only on the effects of the shower to shower longitudinal fluctuations and their effect on the calorimeter characteristics. Therefore effects of the magnetic field or incomplete shower containment were neglected in order to simplify the procedure.

The calorimeter response to a jet was calculated using signals from SHORT and LONG fibers in two different ways:

- $E_J = N_{SH} + N_L$, that is LONG and SHORT fibers are readout by the same PMT;

- $E_J = \alpha N_{SH} + \beta N_L$. where weights α and β minimize the RMS of E_J under condition that $\langle E_T \rangle = E_T^{gen}$, this could be achieved using separate readout of SHORT and LONG fibers

Energy resolution for 1 TeV jets in the minimum point is 6.7 % whereas in the case when both fibers have the same length and run from end to end of the calorimeter it is about 9.3%, which occurs for any depth > X_o. Thus the optimal arrangement of sensitive media, though with lesser mean packing fraction allows us to achieve more than 30 % improvement in the jet energy resolution as shown in Fig. 1.52.

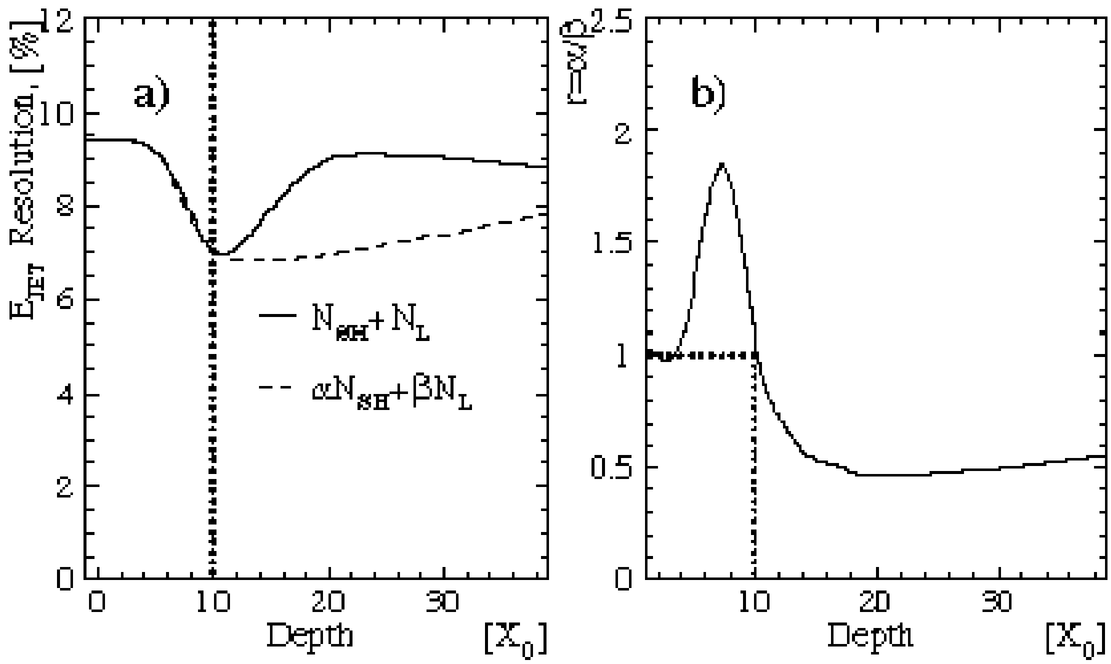

Fig. 1. 52: Jet resolution calculated if signals from long and short fibers are summed up (solid line) and if the signals from long and short fibers are weighted as described in the text (dashed line) as a function of depth; and b) r = α/β is the ratio of weights assigned to short and long fibers as a function of depth. *r*=1 at minimum.

The weighted resolution cannot be made less than minimum reached by the simple sum, but it can be kept at this level in the wider range of lengths *L*. Fig. 1. 52b shows the ratio of weights assigned to the SHORT and LONG fibers. At the point where jet resolution for the sum of LONG and SHORT fibers reached minimum this ratio should be equal to 1.

The jet response to a weighted sum for different jet energies as a function of the EM/HAD partition is shown in Fig. 1. 53. As with Fig. 1. 52, any depth > 10 X_o seems appropriate.

Fig. 1. 53 and Fig. 1. 54 show the result of the fits to the jet energy resolution for summed and weighted cases. The e/π ratio of the calorimeter is crucial to jet energy resolution. It is possible to compensate calorimeter based on Cherenkov effect in optical fibers by arranging fibers in such a way that packing fraction in the part of the calorimeter where the maximum of electromagnetic shower is deposited is less than in the rest of the calorimeter volume. It appears that we can achieve a 3% constant term for EM compartment depth >10 X_o.

Since the point of minimum jet energy resolution is at the same time the point where the calorimeter becomes almost compensating the short fiber length can be determined in the beam tests. Having found the optimal configuration it is possible to use single readout from long and short fibers, halving the number of electronic channels. This looks very attractive since it would decrease substantially the overall calorimeter cost. Since the position of the jet energy resolution minimum as a function of depth *L* is sensitive to jet energy and also is affected by fiber radiation damage, which occures at the maximum of EM shower, we suggest a separate readout scheme for long and short fibers. Choosing *L*=15-20 X_0 it is possible to avoid these problems using weighted sum of long and short fibers. Radiation damage in long fibers will lead only to re-adjustment of weights.

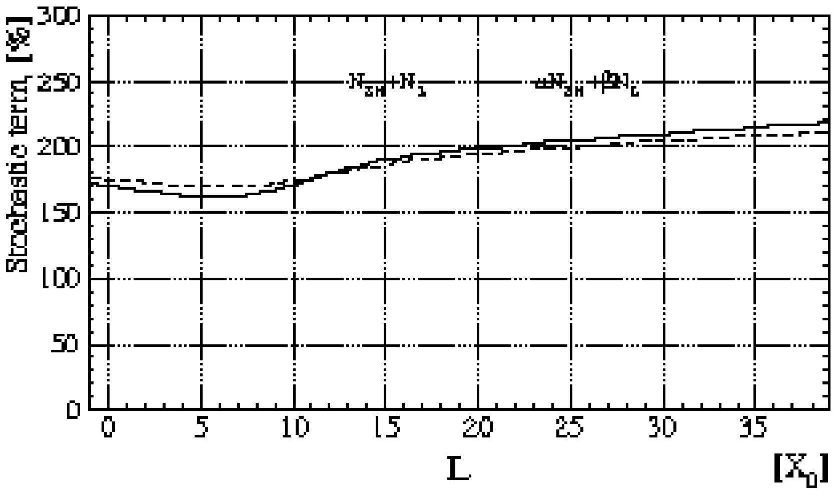

Fig. 1. 53: Jet resolution function - stochastic term versus short fiber depth.

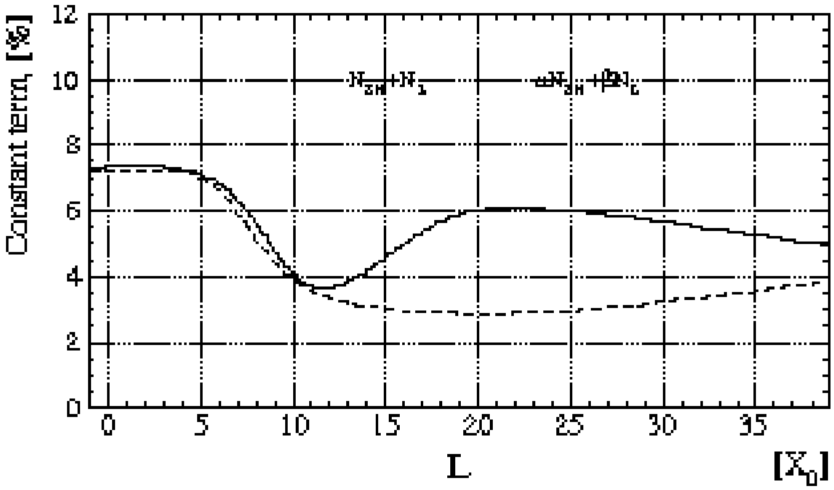

Fig. 1. 54: Figure 10. Jet resolution function - constant term versus short fiber depth.

1.5.5.2 The HE/HF interface: η dependence of the energy resolutions

The HE/HF interface is located at |η| = 3 where the coverage of HF starts. HE and HF are separated by about 7 m and use different techniques for energy reconstruction; HE utilizes scintillation light whereas the HF relies on the Cherenkov effect in the active medium of the calorimeter. We have studied the energy resolution performance at this transition region by simulating single particles and jets at and around this η region (2 < |η| < 5) using GEANT.

The expected energy resolution for various pion energies (10 - 800 GeV) is shown, in Fig. 1. 55, as a function of pseudorapidity. As can be seen, there is no significant effect in the HE/HF transition region

(|η| =3). Aside from the expected difference in energy resolutions on either side of the crack (the intrinsic resolution of HE is better than that of HF), no surprising effect, such as a dramatic and rapid degredation in resolution due to change from HE to the HF, is observed. The worsening of energy resolution at |η| around 5 is due to incomplete shower containment.

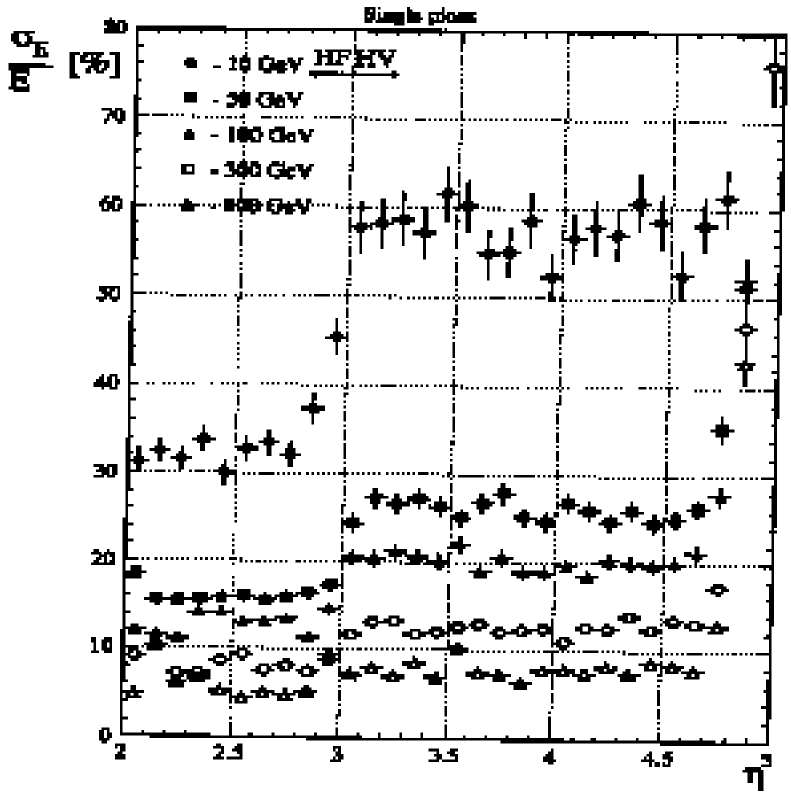

Fig. 1. 55. Energy resolutions for single pions in the energy range of 10 to 800 GeV as a function of η are given above. The HE/HF interface is located at |η| =3.

We have generated 1 TeV forward tagging jets using PYTHIA[24]. Jets are produced in qq→ H qq reaction through VV→ H→ VV fusion process. The particles in jets generate cascades in the HE and the HF. Jets were reconstructed and comparison was carried out between the generated and the simulated signals. We display in Fig. 1.56 the E_{rec}/E_{gen}, E_{res}, $E_{t,rec}/E_{t,gen}$ and $E_{t,res}$ as a function of η. The results indicate that the overall response will drop by about 20% in amplitude in η = 3. The performance at HF, however, is stable up to η = 4.5. Beyond that, the performance worsens due to small angle leakage. The energy resolution remains at the level of 5% in the HE region, increases smoothly to about 10% at η = 3 and decreases to 8-9% in the HF domain up to η = 4.5. As with the HB/HE interface, a monotonic variation in the mean response and the resolution (at high E_T) is maintained in the HE/HF boundary.

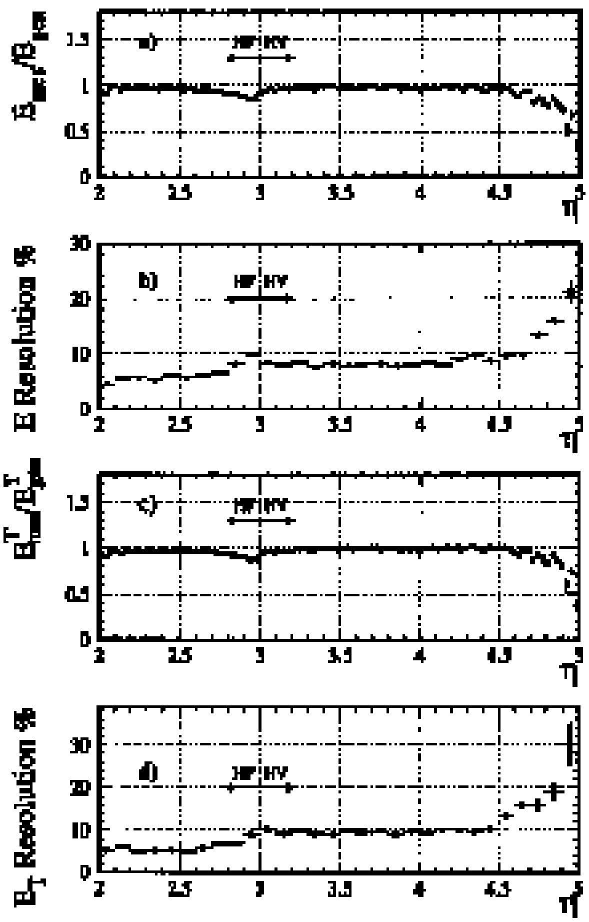

Fig. 1. 56: a) Normalized energy response; b) energy resolution, c) normalized transverse energy response; and d) transverse energy resolution for 1 TeV tagging jets as a function of η.1.5.5.3

The effect of radiation damage on the HF performance

Pure silica, the material of the fiber core, is known to resist high radiation doses with minimal deterioration in its optical properties. The radiation hardness of quartz optical fibers also crucially depends on the cladding around the quartz core since the cladding material makes total internal reflection possible.

We convoluted the expected radiation levels in the HF (see chapter 5) as a function of η with the attenuation known and studied the influence of the fiber transparency loss on the energy resolution for jets after 10 years of LHC operation. We use the same 1 TeV jet sample as in the previous section in our calculations here[25]. The results are given in Fig. 1. 57 and they show the jet energy resolution as a function of η, for quartz/quartz fibers (top) and quartz/plastic fibers (bottom) for two cases: with (black circles) and without (open circles) a 10 years equivalent dose. The jet energy resolution practically does not change in the case of the quartz-quartz fibers while a significant deterioration starts to set in for quartz-plastic fibers at about $\eta = 4$. This is the primary reason that our design calls for quartz-quartz fibers in the region $|\eta| > 4$.

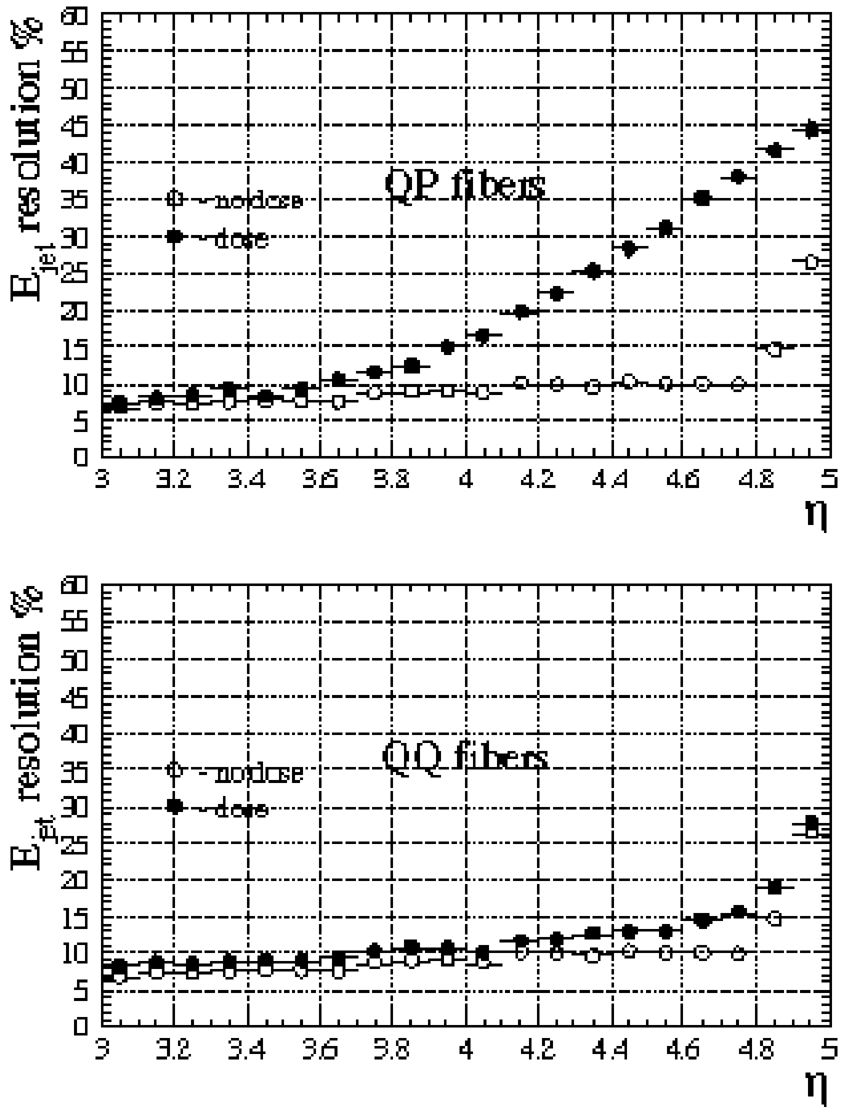

Fig. 1. 57: Energy resolutions for 1 TeV jets as a function of η, the quartz/plastic fibers (top) and the quartz/quartz fibers (bottom), are shown. Full circles in both figures correspond to radiation dose in fibers after 10 years of LHC operation.

1.5.5.5 Jet tagging and reconstruction: transverse granularity

The overall aim of this study is to find the optimal transverse granularity needed for forward tagging jet identification and reconstruction with simultaneous maximization of the pileup suppression. The working hypothesis is that the jets we are interested in are in the range 500 GeV ² E_{jet} ² 3 TeV, with E_{Tjet} 30 GeV[26].

Monte-Carlo generation of the pileup background

We have simulated background events using ISAJET.[27] We have considered a centre of mass energy per pp collision of 14 TeV, a σ_{pptot} = 100 mb, a luminosity of 10^{34} cm^{-2} s^{-1} and an interbunch crossing time of 25 ns. This corresponds to an average number of pp collisions per crossing equal to 25, Poisson distributed.

In addition we made the conservative hypothesis that the pp background collisions consist of a mixture of 60 mb minijets (qq qq, p_T^{jet} > 5 GeV) and 40 mb minimum bias events.

The generated multiplicity distribution per LHC crossing has a mean value of ♠ 5700 with rms ♠ 1200. Here, γs are considered as stable particles. The multiplicity distribution of particles reaching the HF sensitive areas has a mean value of ♠ 1050 (per HF arm), with rms ♠ 320. More details about the expected pileup background can be found in the references.[28,29]

Monte-Carlo generation of the tagging jets

High mass Higgs events of the type qq WW(ZZ) Hqq, with m_{Higgs} = 800 GeV/c^2 were generated using PYTHIA[24].

On the average, the mean value of the energy of the particles inside a jet is much higher (<E> ♠ 60 GeV, rms ♠ 115 GeV) than for background particles[28]23 in HF (<E> ♠ 8.1 GeV, rms ♠ 13 GeV). This is one of the crucial jet features for the jet finding over the pileup background. The second important point concerns the collimation of the energy in a jet: on the average, ♠ 50% of the jet energy is concentrated in a radius of 5 cm. Due to the spread (although small) of the particles in a jet, the strong magnetic field and the central hole in the HF, not all the particles in a jet can reach the HF sensitive areas. The mean value of the multiplicity distribution of the tagging jets at the IP is ♠ 27 and ♠ 20 at HF. This loss of particles induces already an error in the reconstruction of the jets: the distribution of the misdetermination of the jet energy (at the level of particle energies) in terms of {[E_{jet}(IP) - E_{jet}(HF)]/E_{jet}(IP)} has a mean value of ♠ 2% with an rms of ♠ 4%. In ♠ 2.5% of the cases, the energy lost accounts for more than 10% of the jet energy at the IP.

Monte-Carlo generation of the showers

The analysis that follows is done using one of the arms of the HF.

We have generated showers, using GEANT 3.21[21]. FLUKA[30] was used for the hadronic interactions. An E_{cut} of 10 keV was imposed on all particles in the showers. For cascade simulation, the HF is seen as a copper block of dimensions 3000x3000x1650 mm^3 (with a central hole of dimensions 30030035 mm^3), with quartz fibers embedded on it. The packing fraction is 1.5% by volume.

Every particle in a crossing which reaches the HF sensitive area gives rise to a shower. For cascade generation the impact point of the particle in the calorimeter and its three momentum are used as initial parameters, together with the particle identifier.

Under these conditions, we have made a full simulation of 200 background crossings and 1261 "tagging" jets in the HF.

The average transverse profile of a tagging jet is very narrow in space. On average, a significant fraction (♠ 30%) of the total jet light concentrates in a single 55 cm2 tower. Note that the extent of the jet in rapidity is the same as in HB or NE.

The fraction of the energy containment in a jet, as a function of the tower transverse size (assumed square), is given in Fig. 1. 58 for three η regions. The jet extent in η space is essentially independent of η, so that a common segmentation is used in all CMS calorimetry, unless the hadronic shower size exceeds this segmentation as in HE at $|\eta|$~3.

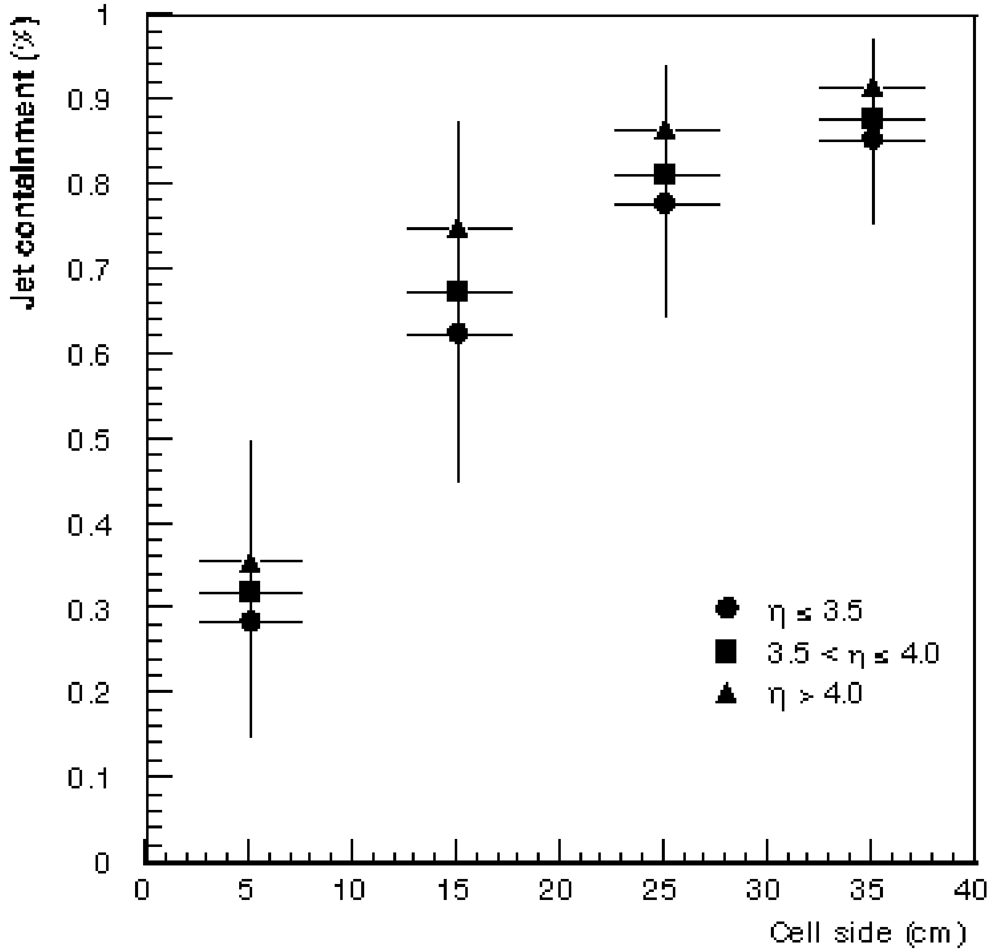

Fig. 1. 58: Jet shower containment (in %) as a function of the tower side dimension (see text), for three η regions.

A typical transverse profile of a jet event over a background crossing is shown in Fig. 1.59. The "min bias" energy flow and the tagging jet are distinct.

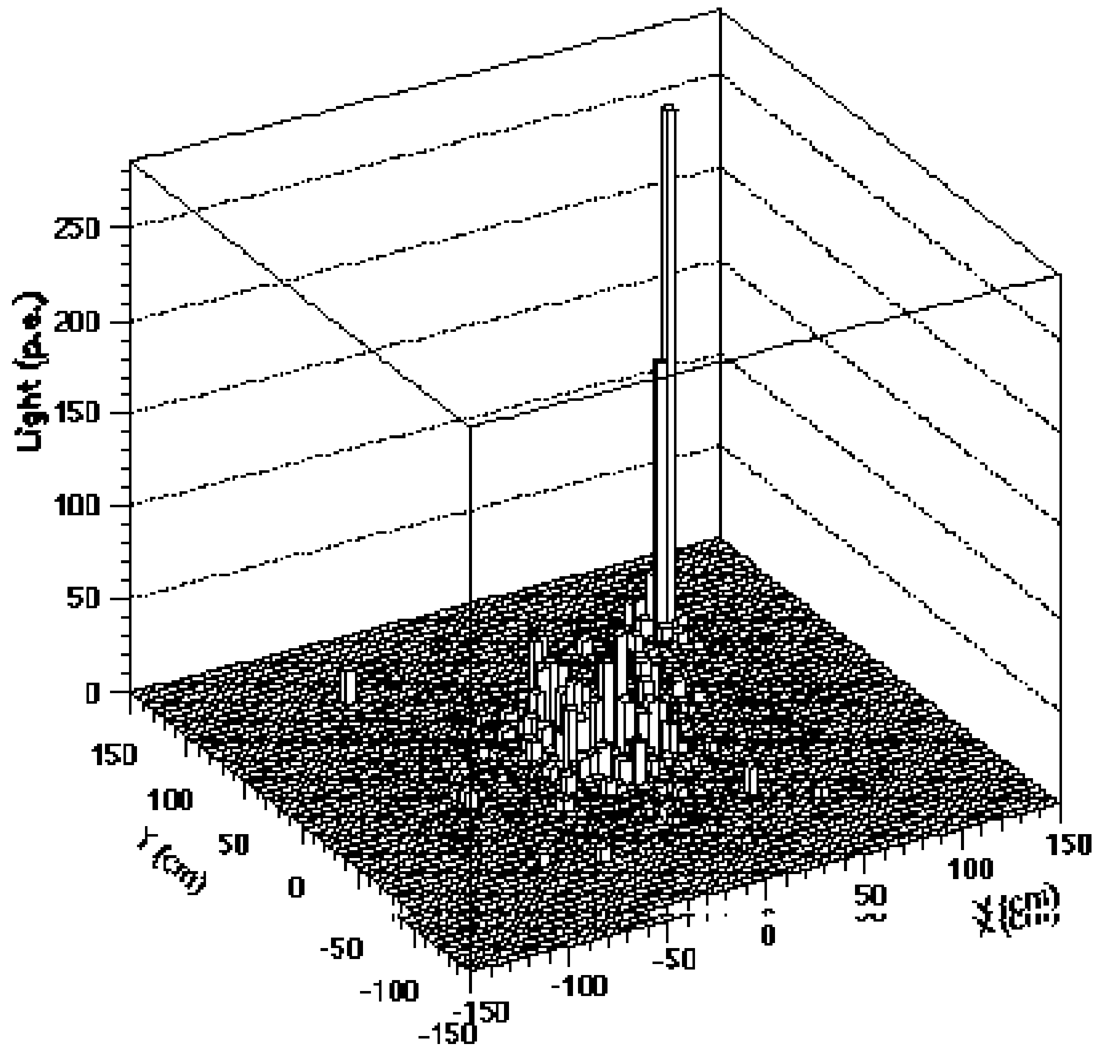

Fig. 1. 59: Transverse profile of a crossing containing a tagging jet.

Jet tagging and reconstruction

We have designed a simple tagging algorithm that allows to detect a jet and make a first calculation of Ejet and $E_T$jet. The algorithm allows a high level of suppression of the pileup background.

The jet tagging is related to the issues of transverse granularity and energy and angular resolutions in the reconstruction of single jets, as well as in dijet systems.

The algorithm includes the following steps:

- Find a maximum among the light collected (S) in the considered towers of the HF. The number of physical towers depends on the transverse granularity used.

- Check whether $S > S_{cut}$ and $S_T > S_{T,cut}$.

If these two conditions are fulfilled, we assume that a seed central tower (CT) of a tagging jet candidate is found.

- Go back to 1) and repeat the operation for other possible maxima.

Stop the cycle when no additional candidate is found or a maximum number of candidates has been obtained.

If the list contains at least one candidate:

- Choose as CT seed of the tagged jet the tower having the maximum S_T.

- Reconstruct the jet by summing up the content of the 33 towers around the maximum.

We assume that the jets we are looking for have E > 500 GeV and E_T > 30 GeV, which are typical lower values for tagging jets in the heavy mass Higgs production and for veto when looking for sleptons. The calibration constant is ♠ 0.4 p.e./GeV (in the assumed experimental conditions) and the maximum allowed number of jet candidates in a given crossing is set to 5.

Transverse granularities

We have applied the above algorithm using various transverse granularities, with the aim of determining the optimal one. This criterion guided our baseline choice of granularity.

Pileup background rejection power

A strong rejection power is mandatory. We have first applied the method described above to crossings containing only background (the 200 crossing sample fully simulated in the HF), looking for the E_{cut} and $E_{T,cut}$ that have to be applied to obtain 100% rejection in the investigated sample of pileup background events. The rejection power is only sensitive to the applied $E_{T,cut}$. On the other hand, the use of large surface granularities (as 1515 cm^2) leads to no rejection power (at least for $E_{T,cut}$ < 30 GeV).

Jet tagging

We now mix each fully simulated jet in HF with each of the background crossings to form a sample of 252200 CMS crossings containing one jet per crossing at HF.

Different transverse granularities for HF lead to different efficiencies in jet tagging. The optimal granularity, that maximizes the jet finding efficiency (♠ 55.4%) with simultaneous suppression of the background, is that of towers of 5x5 cm^2 for $|\eta|$ ³ 4, 10x10 cm^2 for $|\eta| < 4$. In what follows we will use this transverse granularity for jet finding and reconstruction over the pileup background.

Jet reconstruction

The tagged jets are reconstructed by summing up the light content of the 33 towers around the maximum, after applying the jet finding algorithm with the $E_{T,cut}$ that allows background suppression. The energy of the jet is defined as

$$E^{jet}(GeV) = 1/0.46\infty_i S_i(p.e.),$$

where i runs from 1 to 9 and S_i(p.e.) is the light collected in tower i.

The jet "impact point" in HF is defined as the centre of gravity of the 9 towers. The X^{jet} and Y^{jet} coordinates allow to reconstruct E_T^{jet} and the transverse angle Θ^{jet}. The reconstructed jet energy and $E_{T,}$, compared to the generated values, show a mean consistent with zero and an 18% (E^{jet}) and 17% (E_T^{jet}) fractional rms. The fractional azimuthal distribution is centered at zero with an rms = 2 degrees.

Two jet reconstruction in Higgs production

We have used PYTHIA to generate events of the type qq' WW(ZZ) Hjj' with m_{Higgs} ♠ 800 ± 200 GeV/c^2. The inclusive η distribution of the jets is given in Fig. 1. 60. Note that about half of the tagging jets are in HF and half in HE. Therefore, the HE/HF boundary must be very well understood.

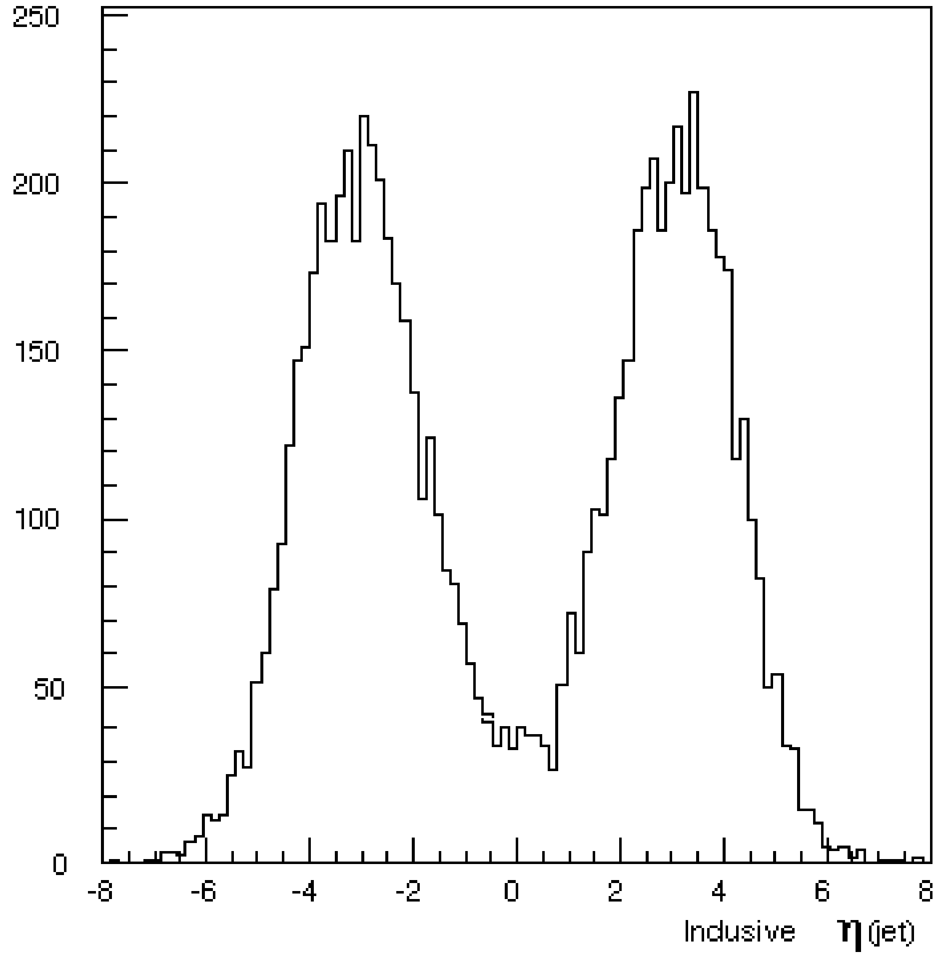

Fig. 1. 60: The inclusive η distribution of the tagging jets in the Hqq' sample.

We have considered the events having a forward and a backward jet in the region $3 < |\eta| < 5$ and smeared the jet energy and the jet transverse angle according to the resolutions found earlier. The resolution of the combined jets is correlated with $E_T^{jj'}$ (generated). The $E_T^{jj'}$ error has a 72% stochastic term and an 8% constant term.

Under these conditions, the error in the reconstruction of the $p_T^{jj'}$ of the dijet system, balancing the typical p_T^{Higgs} = 130 GeV/c, in an Hqq event, will be better than 15% (♠ 20 GeV/c).

1.6 LUMINOSITY MEASUREMENT AT CMS

1.6.1 The measurements required

A precise knowledge of the proton-proton luminosity at the CMS interaction region is an essential ingredient in the measurement of absolute cross sections in the experiment. Monitoring the instantaneous luminosity is also important for making corrections to the data for detector effects related to the number of interactions per beam crossing. A luminosity working group was formed in 1994 with representatives from several associated areas within CMS. The responsibilities of the working group include the following topics:

- absolute luminosity measurements

- relative luminosity monitoring over time

- monitoring of beam-gas backgrounds and backgrounds during beam tuning and scraping

- providing real-time luminosity information to CMS and the LHC machine

- development of detectors for luminosity and background monitoring as needed.

- physics topics associated with detectors used for luminosity monitoring.

Several guidelines have been established for the luminosity measurements:

- The group will aim to measure the luminosity at CMS with a precision of better than 5%. This precision is chosen to match approximately the precision which theorists expect to achieve in predictions for hard scattering cross-sections at LHC energies by the year 2005.

- There should be sufficient redundancy in the detectors and techniques for luminosity monitoring to allow for consistency checks and the situation when one monitoring technique is not operational.

- Separate luminosity measurements must be made for all 2835 bunch crossings.

Several techniques are under study for determining the absolute luminosity. The first is called "counting zeros". Here, two sets of luminosity monitors, symmetrically located on each side of the IP, count the fraction of times a given bunch crossing results in no detected particles on either side. The luminosity is inferred from the rate of such zeros. This technique is used by the D0 and CDF experiments at the Fermilab Tevatron collider and leads to an uncertainty of order 5%. This method is only appropriate if the rate due to σ_I leads to a significant fraction of zeros. Thus it is used only up to ~0.01 of the design luminosity. The second is the Van der Meer method in which the proton-proton interaction rate is measured while the beams are displaced transversely through each other. This method was used successfully at the ISR with continuous beams and at the Fermilab Tevatron collider with bunched beams. A third possibility is to use the trigger tower sums as a "current" of rate. This technique could then be used at design luminosity and we could transfer the measurement to it at low luminosity from the "zeros".

This chapter also describes the monitoring of relative luminosity over time and accelerator backgrounds using overlapping techniques. Both HF and the Level 1 Calorimeter Trigger are used in relative luminosity monitoring.

Calibrating the luminosity system will require both low-luminosity running, where there will be an average of one interaction per bunch crossing, and running the LHC at a center-of-mass energy of 1.8 or 2.0 TeV, so that the calibration can be cross checked with certain measured cross sections at the Fermilab Tevatron. The former will happen as a matter of course, since the LHC start-up luminosity will be a factor of 10 to 100 lower than the design luminosity of 10^{34} cm^{-2} s^{-1}. The latter is also feasible, according to discussions with LHC machine physicists.

1.6.2 Absolute luminosity measurements

Two techniques are presently foreseen to determine the absolute luminosity. 1.6.1.1

Counting zeros method

The counting zeros technique works as follows. Two sets of luminosity monitors, symmetrically located on each side of the IP, count the fraction of times a given bunch crossing results in no detected particles on either side. The luminosity is inferred from the rate of such zeros.

The counting zeros technique is used by the D0 and CDF experiments at the Fermilab Tevatron collider and leads to an uncertainty of order 5%. A modified version of this technique is expected to yield similar precision at CMS at low luminosity.

The probability of having an empty crossing, a "zero", where the forward/backward counters detect no particles is given by:

$$P(0) = e^{-n_2/2} \times (2e^{-n_2/2} - e^{-n_1})$$

where n_2 is the average number of forward/backward coincidences and n_1 is the average number of one-side hits. n_1 and n_2 are related to the instantaneous luminosity, L, according to

$$n_1 = L\tau(\varepsilon_1^{sd}\sigma^{sd} + \varepsilon_1^{dd}\sigma^{dd} + \varepsilon_1^{hc}\sigma^{hc})$$

and

$$n_2 = L\tau(\varepsilon_2^{sd}\sigma^{sd} + \varepsilon_2^{dd}\sigma^{dd} + \varepsilon_2^{hc}\sigma^{hc})$$

In these expressions, τ is the LHC machine revolution period, σ^{dd}, σ^{dd}, and σ^{hc} are the cross sections for single-diffractive, double-diffractive, and hard-core scattering, respectively. ε_2^{sd}, ε_2^{dd}, and ε_2^{hc} are the acceptances for forward/backward coincidences from these processes, and ε_1^{sd}, ε_1^{dd}, and ε_1^{hc} are the acceptances for single-side hits.

The counting zeros technique for measuring absolute luminosity relies on knowing the above components of the total cross section at the center-of-mass energy of 14 TeV. Measuring these cross sections is part of the physics program of the proposed FELIX experiment.

Fig. 1. 61 shows the probability of recording a zero per bunch crossing as a function of instantaneous luminosity, assuming a proton-proton total cross section of 100 mb. One sees that for luminosities in the range 10^{32} to 10^{33}, which is the anticipated luminosity range during the first 2 years of LHC operation (similar to the present situation at the Fermilab Tevatron), the probability of obtaining a zero is not negligible.

Fig. 1. 62 shows the time between zeros as a function of luminosity for full, 50%, and 10% acceptance luminosity detectors. At start-up luminosity, the HF array yields a counted zero as frequently as every microsecond, yielding a luminosity measurement with negligible statistical uncertainty in a fraction of a second.

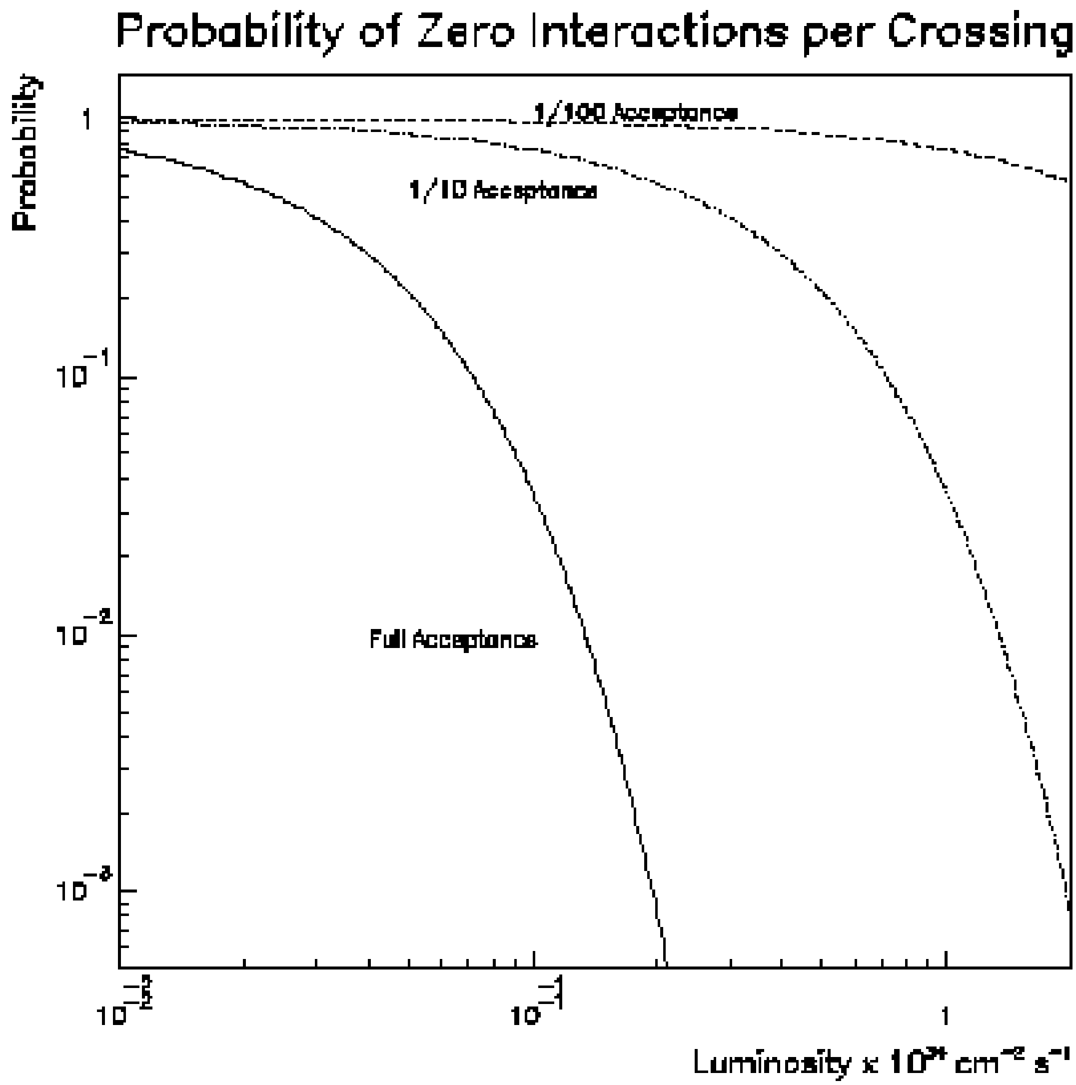

Fig. 1. 61: The probability of recording a zero (no particles detected in the forward and backward luminosity counters) vs. instantaneous luminosity.

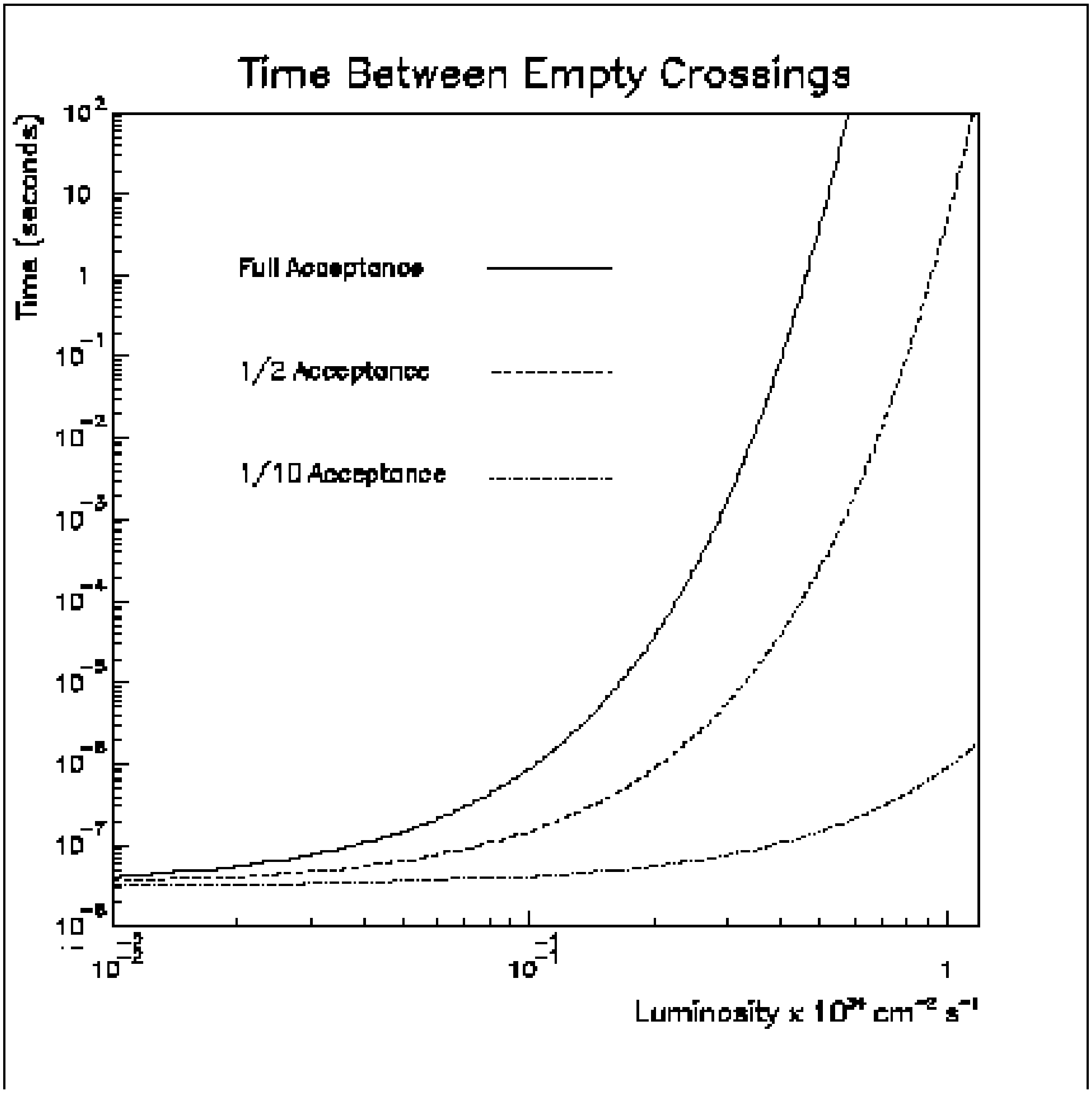

Fig. 1. 62: The average time between recorded zeros vs. instantaneous luminosity.1.6.1.2

Van der Meer method

The Van der Meer method is a promising candidate for a measurement of the absolute luminosity. With bunched beams as in the LHC, the Van der Meer method involves calculating the luminosity according to the formula

$$L = N_1\ N_2\ f/h_{eff}\ w_{eff}$$

where N_1 and N_2 represent the number of particles in the two protons beams, f is the LHC machine revolution frequency, and h_{eff} and w_{eff} are the effective height and width of the beam overlap region at the interaction point. The two beam currents are determined precisely by the accelerator, and f is known exactly. h_{eff} and w_{eff} are measured by displacing the beams with respect to each other, separately in the horizontal and vertical directions, while monitoring the proton-proton interaction rate with one or several relative luminosity detectors as a function of the beam displacement. Difficulties may arise because the small transverse beam sizes (σ's of order 15 μm) will require the control and monitoring of beam displacements with μm precision. It is expected that Van der Meer scans would be performed on an occasional basis at relatively low luminosity and would serve to calibrate relative luminosity monitors for continuous measurements. The feasibility of controlled Van der Meer scans is being studied by LHC machine physicists, and discussions between CMS and the LHC machine are being coordinated by LEMIC (the LHC Experiment - Machine Interface Committee).

1.6.3 HF as the luminosity monitor for couting zeros

The HF detectors are on each side of the interaction region, covering the pseudorapidity range of approximately $3 < |\eta| < 5$, and will be used in the counting zeros technique.

The HF elements have the following characteristics: good and well-determined acceptance for detecting hard-core scattering, very tight (i.e. sub-ns) timing resolution in the high-rate environment, high efficiency for single minimum ionizing particles, a large dynamic range and radiation hardness.

Hits in the HF towers will be used to count the number of front-back coincident events, the number of front-only or back-only events, and the number of neither-side-hit events for each of the bunch crossings. These rates, the acceptances of the counters for hard-core scattering, single diffractive and double-pomeron-exchange scattering, and measured (by CMS and other experiments) cross sections for these processes at $\sqrt{s}$ = 14 TeV will combine to yield the luminosity for each bunch crossing. The HF towers will be used for several other purposes. They will monitor interaction rates during separated beam scans (Van der Meer method), which will aid in the absolute luminosity calibration. They will also provide real-time accelerator diagnostics during scraping, beam tuning, and throughout a physics store (run).

During the first few years of LHC running, the anticipated luminosity will be a factor of 10 to 100 lower than the design luminosity of 10^{34} cm^{-2} s^{-1}, although the number of bunches will be the design value of 2835. Rates in the HF towers during low luminosity running will calibrate other luminosity tools for transfer to higher luminosities. Other tools include the rates of easily-identified and reconstructed physics process. Rates for W, Z, and high-p_T J/ψ production are candidate physics processes for luminosity monitoring.

An important step in calibrating the HF towers will be to run the LHC at a lower center-of-mass energy where the total pp cross section and its components (hard-core, elastic, single-diffractive, ...) have been accurately measured. For example, it will be possible to run the LHC as low as 2 TeV, albeit with reduced luminosity, so that the luminosity calibration can be cross checked with the measured cross sections at the Tevatron. (Note that the cross sections in proton-proton and proton-antiproton collisions are approximately equal for the above processes at 2 TeV.)

1.6.4 Relative luminosity monitoring using HF

Luminosity measurement by HF is intended mainly to serve two purposes; one is to provide input to accelerator tuning during the initial phases of LHC operation and the other is to monitor luminosity during data taking. The constraints on this system are the following:

- it is required that the system is ready to function in day one of LHC start up,

- it is independent of other systems, *i.e.* it can operate in a stand-alone mode,

- it is able to measure relative luminosity within 10% accuracy, and

- the data output from this system can easily be transmitted and interpreted.

The principle idea is to measure pile up events as an average current from a group of HF towers. The average energy deposition and its rms for a minimum bias event can be measured and connected to the low luminosity zero measurement at some appropriate luminosity.

The rms and the average photoelectrons for a given bunch crossing are determined from the following relationships.

$$(rms) = G^2 \mu (rms)^1 + G^2 \mu <E>^2 + G\mu <E>$$

$$N_{pe} = G\mu <E> \quad (1)$$

The average energy deposition and rms of the energy deposition in one tower for a minimum bias event are $<E>$ and $(rms)_1$, while μ is the average number of proton-proton interactions per bunch crossing and *G* is the number of photoelectrons per GeV of deposited energy in the calorimeter (~ 0.5 pe/GeV). For the outer ring towers, for example, at high luminosity, $(rms)/<N_{pe}>$ is about 2.9. For a group of 16 towers and <5% accuracy, 0.9×10^3 bunch crossings are needed.

Each tower is assumed to be calibrated prior to the HF installation and that each tower is gain monitored during data taking with the aid of LEDs and a laser system to maintain gains of each photomultiplier within 5% .

References

[1] The Compact Muon Solenoid. Letter of Intent. CERN/LHCC 92-3, LHCC/I 1, 1 October 1992.

[2] J. Ranft, Phys. Rev. D51 (1995) 64.

[3] P. Aurenche et al., Computer Physics Commun. 83 (1994) 107.

[4] P.A. Aarnio et al, CERN TIS-RP/168 (1986) and CERN TIS-RP/190 (1987)

A. Fasso et al., Proc IV Int. Conf. On Calorimetry in High Energy Physics, La Biodola, Sep 20-25, 1993, Ed. A. Menzione and A. Scribano, World Scientific, p. 493 (1993).

[5] S.Bertolucci et al., Nucl. Instr. and Meth. A254 (1987) 561.

D.Blomker et al., IEEE Transactions on Nuclear Science, Vol. 37/2(1990) 220.

J.P.Cumalat et al., Nucl. Instr. and Meth. A 293 (1990) 606.

[6] V. Abramov, Nucl. Instr. and Meth. A 374 (1996) 34.

[7] See: CDF End Plug Hadron Calorimeter Upgrade, P. de Barbaro at al, IEEE Trans. on Nucl. Science, vol 42, #4, p510-517).

[8] J.Freeman and W.Wu. FNAL-TM-1984 (August 1996).

[9] S. Abdullin, CMS-TN/94-180.

[10] I. Gaines et al., CMS-TN/96-058.

[11] S. Abdullin, at LHCC SUSY Workshop, CERN, October 1996.

[12] I. Gaines et al., CMS-TN/95-154.

[13] J. Freeman and W. Wu, Fermilab-TM-1984, 1996.

[14] *Scintillator Tile-Fiber Calorimeters for High Energy Physics: The CDF End Plug Upgrade, Selected Articles*., edited by P. de Barbaro and A. Bodek, University of Rochester preprint UR-1309, October 1994.

[15] P. de Barbaro et al., *Construction and Quality Control of Scintillator Tiles with WLS Fiber Readout for the 1995 CMS Test Beam Hadron Calorimeter*, University of Rochester preprint UR-1430, July 1995.

[16] K. Michaud et al., *Comparison of the 1995 H2 Test Beam data with the Geant Simulation of the CMS End Cap Calorimeter*, University of Rochester preprint UR-1432, CMS TN 95-116.

[17] P. de Barbaro et al., *Performance of the CMS Hadron Barrel Calorimeter Prototype using the 1995 Test Beam data*, CMS TN/96-077.

[18] Nucl. Instr. & Meth. Article in preparation.

[19] N. Akchurin et al., Beam Test Results from a Fine-Sampling Quartz Fiber Calorimeter for Electron, Photon and Hadron Detection, submitted to Nucl. Instr. Meth. Also CMS/TN 97-XXX.

[20] O. Ganel and R. Wigmans, Nucl. Instr. Meth. A365 (1995) 104.

[21] "GEANT" R. Brun et al., CERN DD/EE/84-1 (1987). See also CERN Program Library Long Writeup W5013 (1993).

[22] CMS Note 1996/020, D. Denegri and V. Genchev, "Study of the CMS hadron calorimeter barrel/endcap trtansition region".

[23] D. Litvintsev, CMS/TN 95-098.

[24] "PYTHIA: The Lund Monte Carlo for Hadronic Processes" H.U. Bengtsson and T. Sjostrand, Sep. 1991.

[25] "Study of degradation of the quartz HF response due to fiber radiation damage", D. Litvintsev, CMS/TN 96-106.

[26] "Jet tagging and reconstruction over the expected pileup background in the CMS quartz fibres very forwardcalorimeters" A. Ferrando et al., CMS IN/97-xxx, May 1997.

[27] F. Paige and S. Protopopescu, BNL 38774 (1986).

[28] "Incoming particle rates, irradiation and power dissipation in the CMS very forward calorimeters due to the pileup bacckground" C. Burgos et al., CMS TN/95/035, March 1995.

[29] "Particle fluxes in the gaps of gas of the CMS iron/PPC very forward calorimeters due to the pileupbackground" A. Ferrando et al., CMS TN/95-036, RD37 TN/95-5, March 1995.

[30] "FLUKA92" A. Fasso, A. Ferrari, J. Ranft, P.R. Sala, G.R. Stevenson and J.M. Zazula, Proceedings of the Workshop on Simulating Accelerator Radiation Environments, Santa Fe, USA, January 1993.

Table of Contents

2.1 MECHANICAL OVERVIEW

The CMS Central Calorimeter, consisting of the barrel (HB) and endcap (HE) calorimeters, sits inside the CMS solenoid vacuum tank. HB covers the η range 0 < |η |< 1.3 and extends radially between r = 1.806 and r = 2.95 meters, while the HCAL endcaps (HE) cover the pseudorapidity range 1.3 < < 3.0 . Both components share many features. They use scintillator/fiber as the active detectors are made of the same absorber material, and share many similarities of construction.

The presence of the 4 tesla magnetic field places unusual requirements on the calorimeter absorber. First, it should be non-magnetic to eliminate magnetic forces on it, and to avoid distortion of the uniform central field in CMS. Second, it should have a short interaction length to best take advantage of the limited space. It should have a relatively low z to limit multiple scattering of muons. It should be a structural material, because it must support itself as well as all other interior components in the CMS central detector. Finally, it must be affordable. These requirements led us to choose a copper alloy as the absorber material. Copper has an interaction length of about 15 centimeters, compared to 17 cm for iron. Thus we can pack substantially more interaction lengths into the same region by using copper. We chose a copper alloy, 90-10 brass (90% Cu, 10% Zn) due to its better machinability compared to pure copper.

The HB is a cylindrical structure created by connecting 18 calorimeter "wedges" into half-barrels. Each wedge subtends 20 degrees of φ, and extends from the CMS detector mid-plane about 4.3 meters in z and weighs 25.7 metric tonnes (tonne). Fig. 2. 1 shows the overall view of the HCAL half barrel. Fig. 2. 2 shows the cross section of a single 20 degree wedge. The side view of the wedge is shown in Fig. 2. 3. The wedge is composed of copper alloy absorber plates that are bolted together into the wedge structure. Machined slots in the plates create slots for the scintillator trays. These 9mm thick slots are regions of constant radius that extend the full z length of the wedges. The wedge is composed of 31 copper alloy plates that are bolted together to make the body of the wedge. In addition, for strength, the inner and outer plates are made from stainless steel. The wedges are bolted to each other with bolts that are located in the front and back stainless steel plates.

The HCAL will sit on rails attached to the inner shell of the vacuum tank of the superconducting coil. The 2 horizontal wedges of each half barrel will have a mating rail structure that will rest against the rails of the vacuum tank.

The HCAL design is unusual in that brass is used as a structural element. Because there is not much experience using this material structurally, we have chosen a cautious design path. We have made a variety of finite element analyses of the calorimeter structure, using different assumptions on boundary conditions and other details. We have chosen the models that predict the largest forces in our structure (worst case models). In all cases, we design using the yield strength of soft copper, rather than cold worked material. Using that yield strength, we have designed the calorimeter to have a factor of 2 safety margin.

Each half-barrel is supported on two rails attached to the vacuum tank in the median plane (3 o'clock and 9 o'clock). The weight of each half-barrel is distributed uniformly along the length of the rails using a plunger/disk spring system. In turn, each supermodule of the crystal electromagnetic calorimeter (ECAL) is supported from the innermost stainless steel plate of an HB wedge via a 4 point suspension system attached to guide rails machined into the stainless steel plate of the corresponding wedge. The CMS tracker is supported on the innermost stainless steel plate by a four-point mounting frame, also attached to the plate in the median plane.

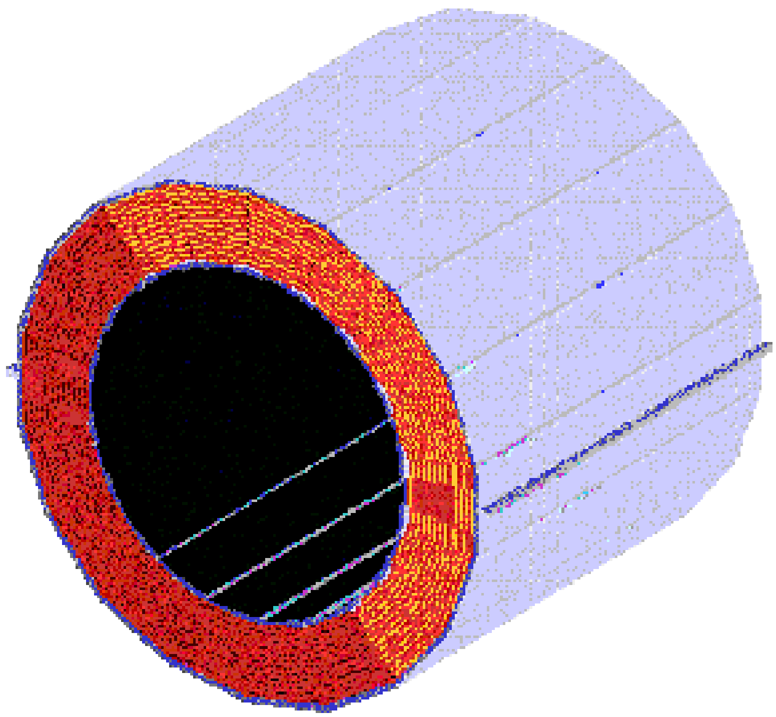

Fig. 2. 1: An isometric view of the HCAL half barrel.

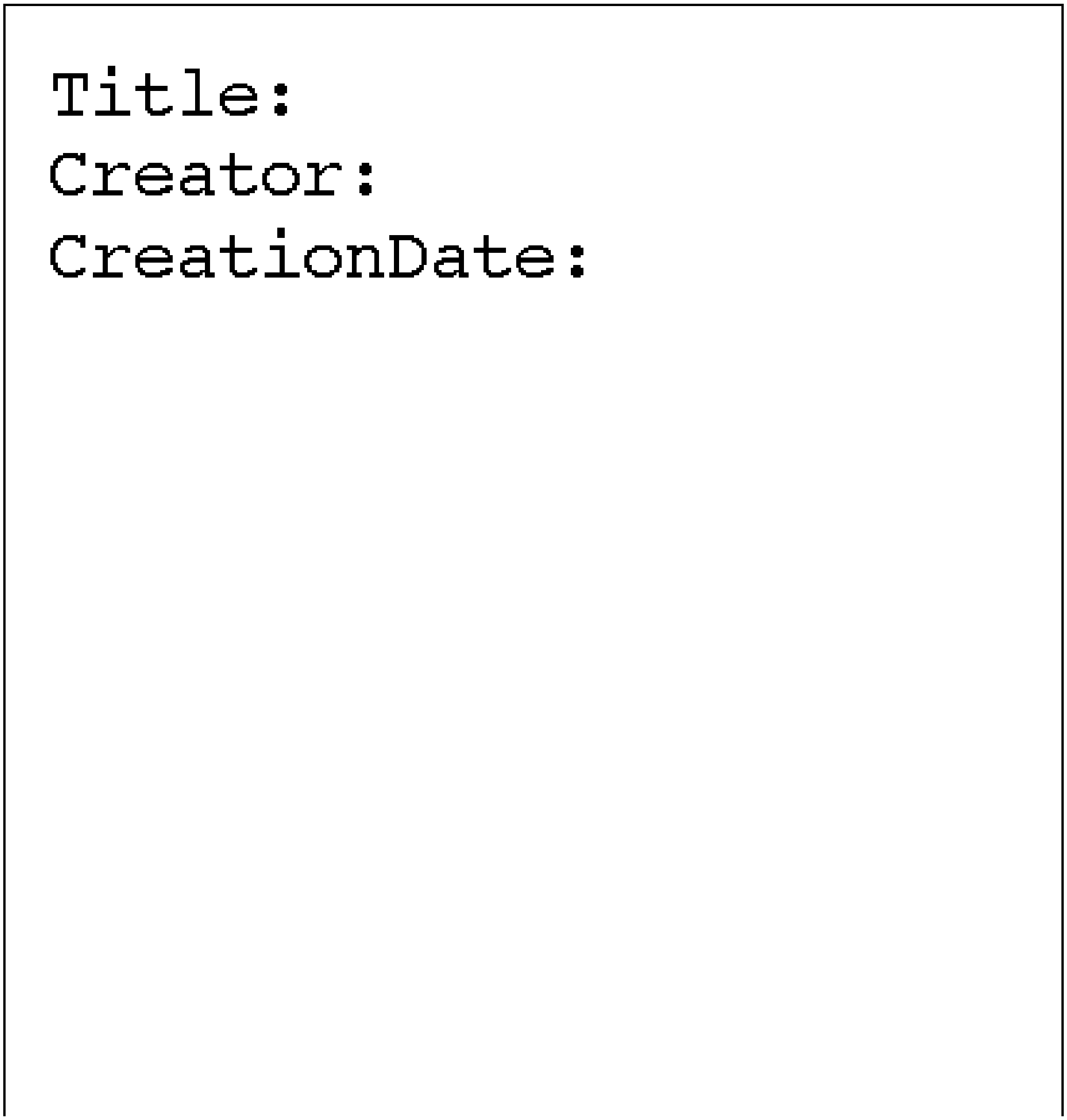

Fig. 2. 2: The cross section of a HCAL wedge.

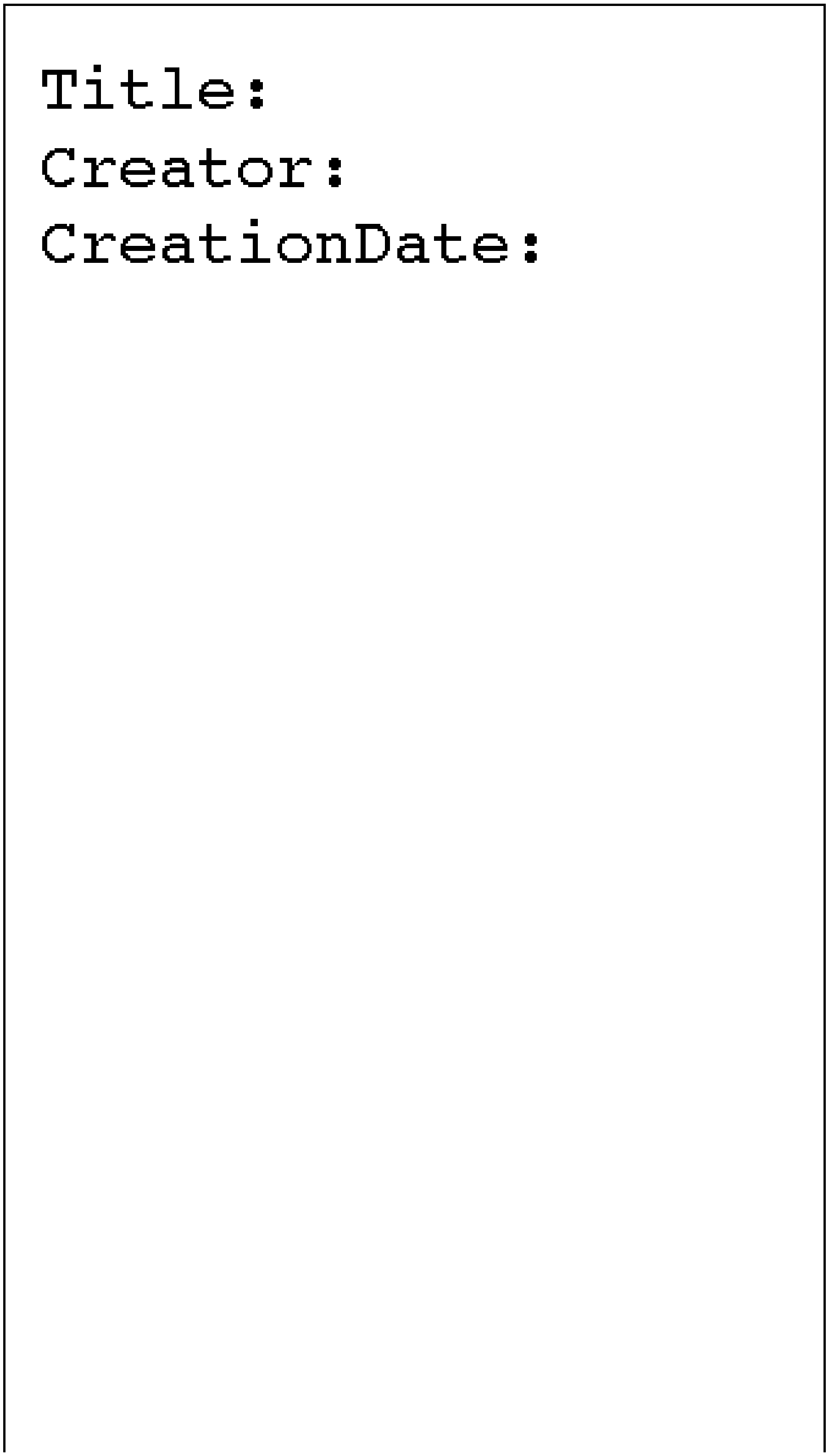

Fig. 2. 3: The side view of the HCAL wedge.

There is a unified CMS numbering system. The CMS global coordinate system is as follows (See Fig. 1.1):

- y is nearly vertical, x is horizontal and points inward to the center of the LHC rings, and Z is aligned with the beam. This results in y being inclined at 1.23% from the true vertical plane as the plane of the LHC is not horizontal.

- The azimuthal angle φ is increasing from the x axis toward the y axis, while the pseudorapidity increases (decreases) with increasing (decreasing)z.

The HCAL half-barrel at positive z is labeled +1, while the negative Z barrel is labeled -1. The wedges are numbered 1 through 18 for each half-barrel, starting with 1 at the X axis and proceeding counterclockwise towards positive y.

Each HB wedge contains 17 active layers of scintillator trays, starting with the first one between the front (or inner) stainless steel plate and the first brass absorber plate. This one is numbered 1, and the last layer, outside the outer stainless steel plate, is numbered 17. There is an additional layer in front of the inner stainless steel plate, labeled 0. It is possible that there be even an additional scintillator layer inside the ECAL, immediately in front of the ECAL strong-back plate. If so, this layer will be labeled -1.

2.2 STATIC LOADS

Each HB wedge weighs about 25.7 tonnes (metric). The ECAL supermodule weighs 4 tonnes (metric). The total weight of the tracker is approximately 4 tonnes (metric). The combined weight of the HCAL barrel plus components supported by the HCAL barrel is then about 1130 tonnes (metric).

2.3 DYNAMIC LOADS (ASSEMBLY/INSTALLATION)

We are designing the HCAL structure to have a factor of 2 safety margin above the static load. Therefore all dynamic loads must be less than this absolute allowed loading. This requirement places constraints on the crane in the assembly hall, the gantry that will lower the half-barrels into the collision hall, and the insertion tooling. In addition, this also places constraints on the shipment of the wedges from the absorber factory to CERN.

The entire weight of the HCAL rests on the rails on the inner shell of the vacuum tank. Therefore it is essential to ensure the integrity of the welds that connect the rails to the vacuum tank. Each weld will be x-rayed to check for defects. The welds are designed to have a safety factor of 2 to the yield strength of stainless steel.

2.4 TOOLING

Specialized tooling is required for the construction and installation of the HCAL barrel. A plate lifting fixture is needed for manipulating the plates. An assembly table is needed during the process of stacking the plates into wedges. A wedge lifting fixture is needed to allow the lifting and rotation of wedges for construction of the half-barrels. A cradle and spider support mechanism is needed for assembly of each half-barrel. An insertion/extraction tool is needed to insert and remove the half-barrels from the vacuum tank.

In addition, tooling is required for quality control of the absorber structure. A load test fixture is needed to test the mechanical integrity of each wedge, starting with the first prototype wedge.

2.5 ECAL REQUIREMENTS

The crystal electromagnetic calorimeter barrel (ECAL) is constructed out of supermodules, each ECAL supermodule matching an HB wedge. As indicated earlier, the ECAL barrel is supported from the HCAL barrel supermodule by supermodule. The ECAL barrel supermodule is supported by a rail system integrated into the design of the HCAL front stainless steel plate. The requirement that ECAL be supported by the HB (inner) front plate places requirements on the HB front plate flatness and placement in the CMS global coordinate system. The ECAL needs to be in the form of a cylinder centered within 2mm of the r=0 of CMS and coaxial to the beam line. The ECAL supermodule-to-supermodule placement needs to be controlled to less than 1mm. These requirements can be translated into requirements on the HCAL global placement, the HCAL front plate flatness, and the HCAL rail system.

2.6 VACUUM TANK REQUIREMENTS

The HCAL half-barrels are much more rigid than the vacuum tank rails upon which they rest. A sophisticated weight distribution system has been designed which is described later in this chapter. In addition, a clearance of 5 cm is required between HB maximum radial extent and the vacuum tank minimum inner radius.

2.7 TRACKER MOUNTS AND REQUIREMENTS.

The Tracker weight of 4 tonnes (metric) will be carried on the HCAL structure. Two supports on each end will carry the load from the tracker to plates that are attached to the front face of the HCAL at z beyond the extent of the ECAL. The supports will be at +- 30 degrees in from the -y direction. These supports will trap the ECAL supermodules interior to them in z. Therefore the design of the tracker support will include the addition of temporary supports so that one of the permanent supports can be removed. This will allow maintenance of the freed ECAL supermodule if necessary.

2.8 WEDGE DESIGN

2.8.1 Overview

The HCAL is composed of 36 wedges. There are 4 special wedges of 2 types, those at 3 and 9 o'clock. These wedges have the rail structure mounted in the back plate. The remaining 32 wedges are identical. Figure 2.2 shows the cross section of a "typical" or "regular" wedge, while Fig. 2. 4 shows the cross section of one of the 4 special wedges that provide the support structure for rail mounting.

Each wedge has an inner stainless steel plate, followed by 31 brass plates, ending with an outer stainless steel plate. The wedges are bolted together across the inner plates and the outer plates. The phi edges of the wedge will have thin "skins" installed, to retain the scintillator packages. The wedge structure will have a "cutout" at the large z large r end to contain the photodetector/electronics box. To avoid eddy currents in the HCAL in case of a fast discharge of the solenoid, the stainless steel inner and outer plates will have an electrical isolation coating applied to them. (Note that the brass plates of adjacent wedges do not touch.) Forces transverse to the wedge (and bolts) are distributed along key bars (shear keys) inserted snugly into each plate. 18 wedges are bolted together to form a half-barrel. Stainless steel ties, inserted and bolted into machined slots in the outer plates take up any shear forces present. The inner plate has aluminum ties bolted on to take up shear forces. The 2 half-barrels rest on rails inside the vacuum tank. The half-barrels are not connected together.

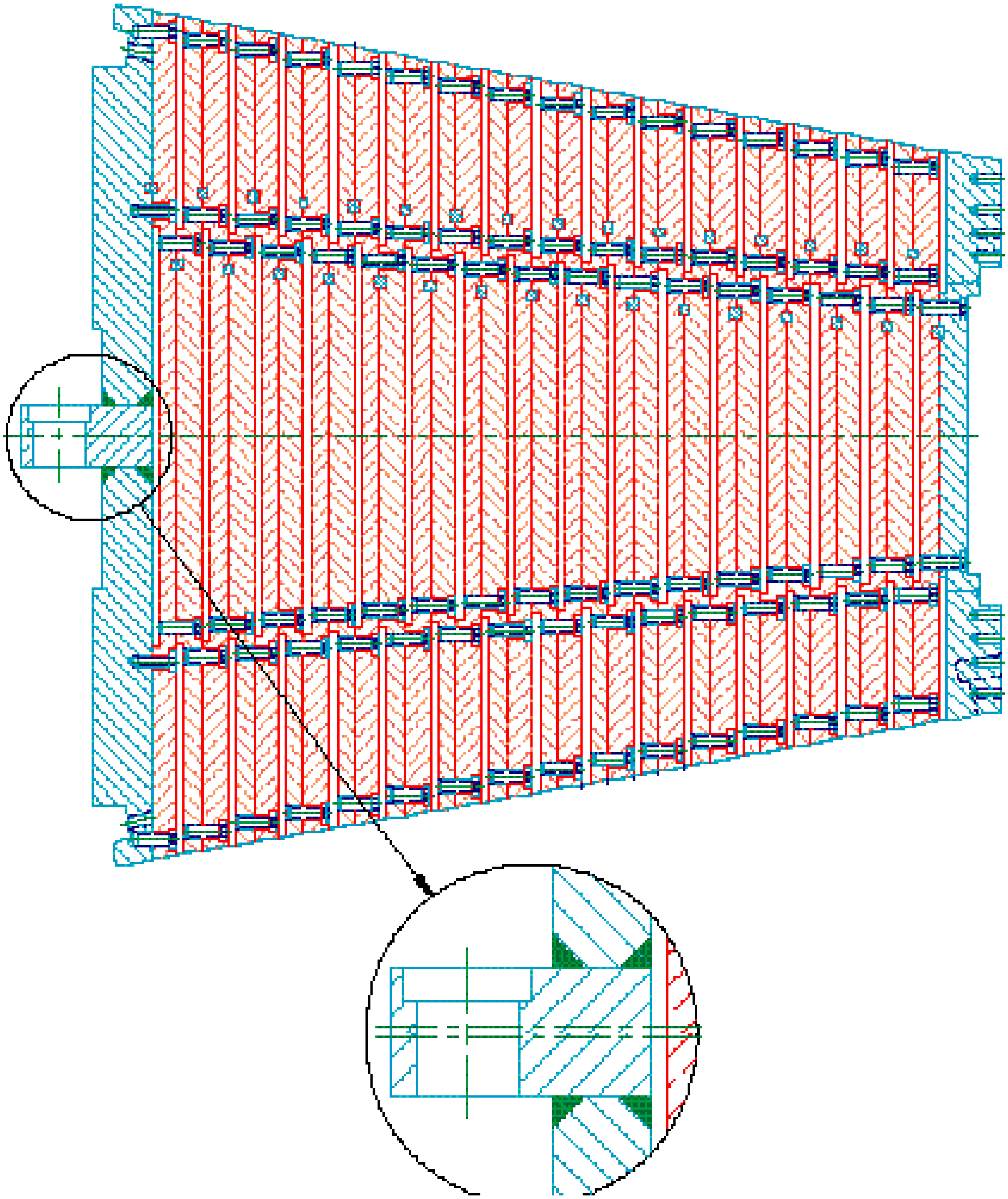

Fig. 2. 4: The "rail" wedge

We have chosen 90% Cu/10% Zn brass for our absorber material. It has roughly the same density for the same price as 99% Cu. We performed a market survey to see what materials were commercially available in the form we required. We solicited proposals regarding material choices from copper foundries in the United States, Europe, Russia, and China. Our first choice was Phosphor-Bronze, a very strong material. Unfortunately, this material was available from only one vendor, and was three times as expensive. Our second choice, 90-10 Brass, C22000, was available from a number of vendors.

Issues regarding the choice of brass are its availability in proper form, strength, density, machinability, and potential for creep.

C22000 has a yield strength of 70 MPa (10 ksi), (1 ksi = 1000 lb/in^2 = 1000 psi) 1000 psi) and a ultimate strength of 260 MPa (37 ksi). It has a machinability rating of 20 where C36000 free-cutting brass is 100 and pure copper is 20. It has a fair machinability. C22000 has a density 3% less than pure copper. Its nuclear interaction length is 15 cm.

We are concerned with the possibility of long term creep of the brass material. We have searched the literature regarding creep in brass or copper. At the loads we anticipate, creep is not an issue at room temperature. However it is prudent to experimentally verify this result. We are preparing a creep experiment to test this prediction.

2.8.2 Plate layout

The inner and outer plates are 7cm thick stainless steel. The interior plates are 2.9cm thick and are composed of C22000 brass. Brass ingots are cast, then hot rolled to the approximate dimensions of the plate. Finally, the faces of the plate are machined, to form the 9mm slots for scintillator trays, and to add the bolt holes, threading, and slots for keying. Fig. 2. 5 and Fig. 2. 6 Fig. 2. 6show the layout of the stainless steel front and back plates. Fig. 2. 7 and Fig. 2. 8 show the layout of the 2 types of brass plates which allow for inner and outer scintillator trays respectively.

Title: From AutoCAD Drawing "\\Violet\CMS.PPD\USERS\POLUB\TDI
Creator: AutoCAD
CreationDate: 5497 11:33:50

Fig. 2. 5: Wedge outer stainless steel plate

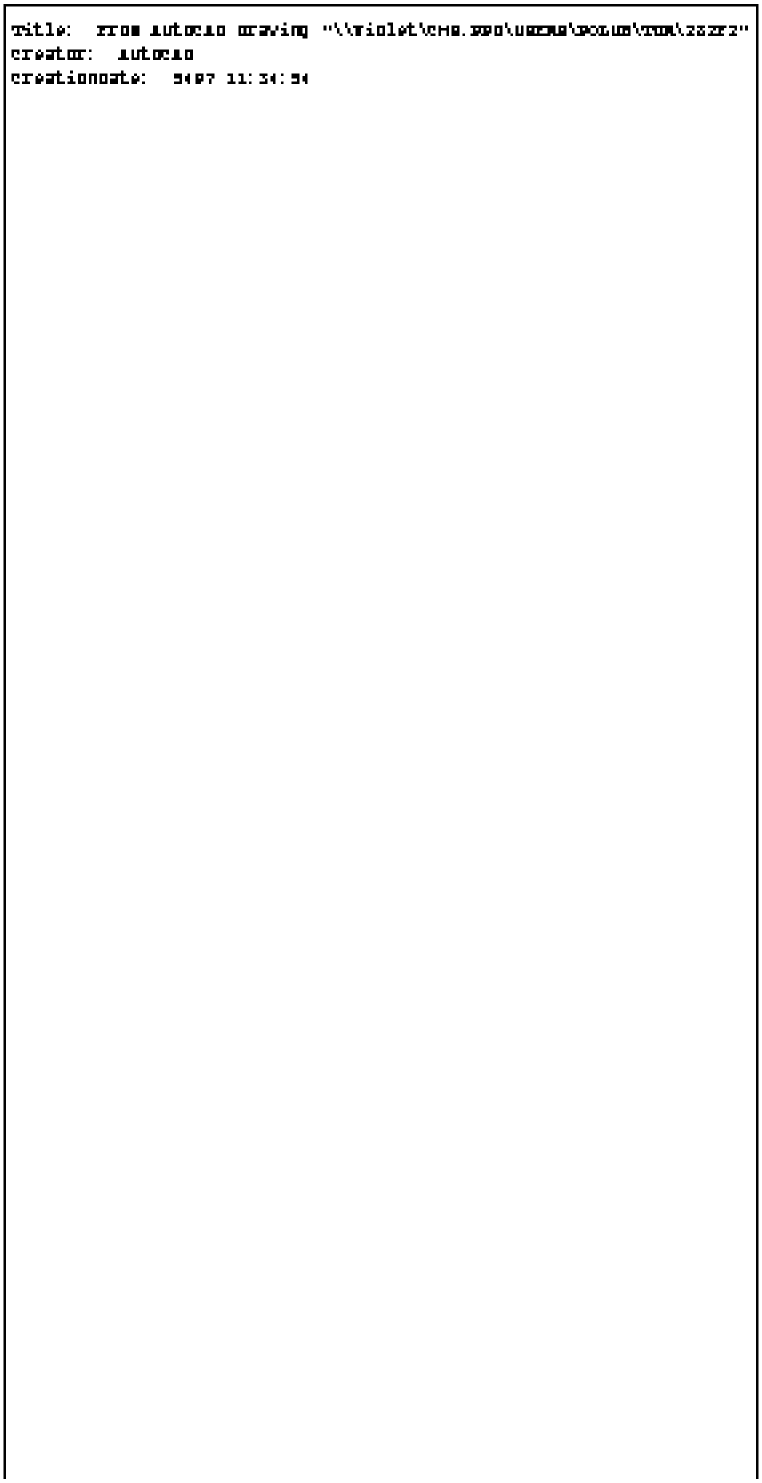

Fig. 2. 6: Wedge inner stainless steel plate

Title:
Creator:
CreationDate:

Fig. 2. 7: Figure Brass absorber plate

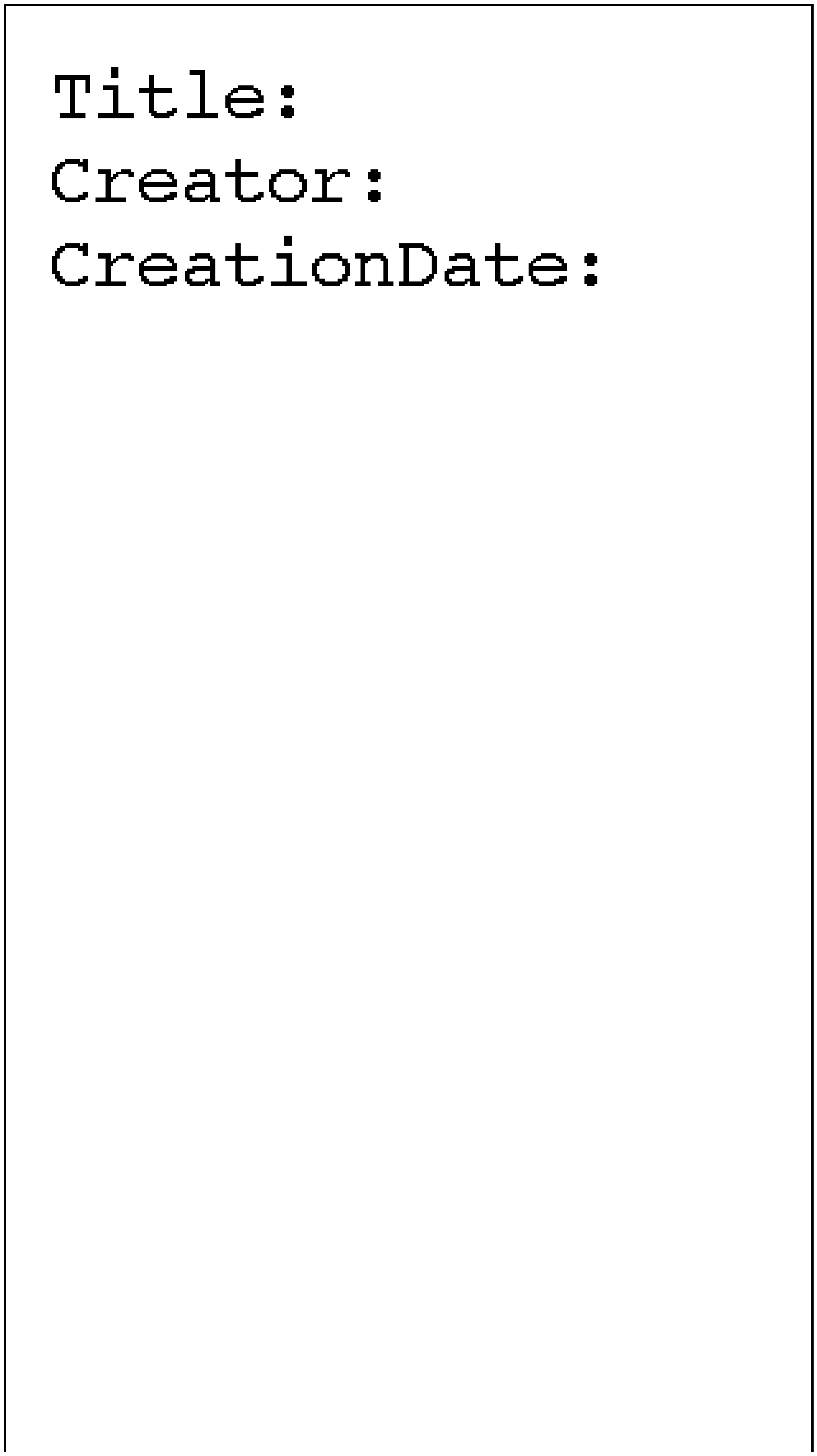

Fig. 2. 8: Brass absorber plate

2.8.3 Bolts and bolt patterns

The absorber plates are bolted together with M16x2 low head stainless steel bolts. Fig. 2. 9 shows the bolt geometry.

As seen in Figs. 2.7 and 2.8, the plates are bolted together along 4 rows. Each row has bolts at 20cm centers. There are 2000 bolts per wedge, and about 72,000 bolts in the total HB structure. To supply a preload to the plates (to prevent them from separating due to the forces on the wedges in the barrel structure), the bolts are torqued to 170 N m (125 foot-pounds) of force, supplying 51.7 kN (11600 pounds) of preload per bolt. (The threads of the bolt will be lubricated with silicone.) There is a maximum separating force of 25.8 kN (5790 pounds) per bolt in the barrel structure. Thus the 51.7kN (11600 pounds) preload gives a factor of 2 safety margin.

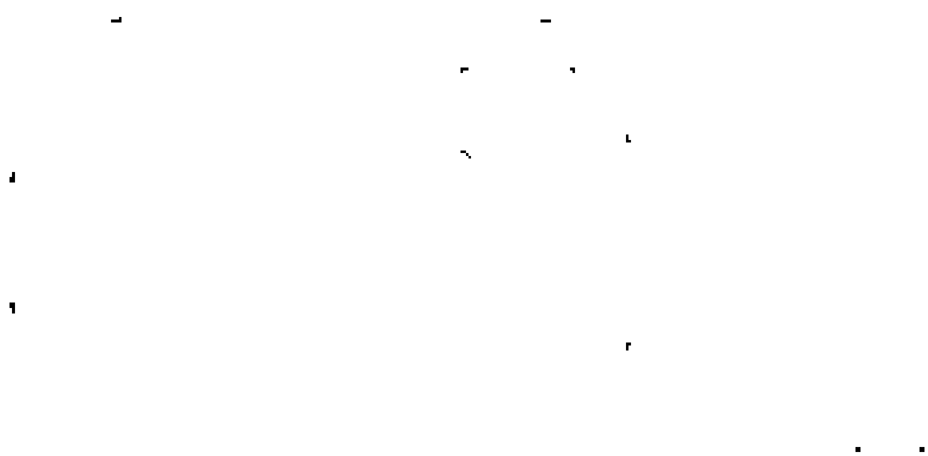

Fig. 2. 9: Bolt design2.8.3

Bolt analysis

The strength of the bolted connection depends on the bolt strength, the strength of the brass plate under the bolt head, and the strength of the threaded plate the bolt connects into. The FEA calculation of the maximum force on any bolt is 25.8 kN (5790 lbs.). We require a safety factor of 2, so the maximum force = 51.7 kN (11600 lbs.).

The force on the material under the bolt head is

$$P = \pi D h \tau \quad (1)$$

with D the diameter of the bolt, h the thickness of the plate under the bolt, and τ the allowable shear stress of the material, 5 ksi for soft copper.

- For our plate and bolt design, D = 23.8mm (15/16"), h = 20.3mm (0.80") and thus P = 52.6 kN (11,800 lbs.) for a safety factor of more than 2 . 2.8.3

Bolt tests

Bolt tests on the efficacy of the head socket (torque test) and the strength of the bolt (tensile test) are being carried out at the University of Mississippi and at an ASTM certified testing lab - MMA Laboratories, Inc., Newtown, PA. For our research and development work we have selected American standard size 5/8"-11 UNC bolts because they are readily available. The tensile stress area for the 5/8"-11 bolts is 146 mm^2 (0.226 in^2) whereas for M16x2 bolts it is 157 mm^2 (0.243 in^2). This gives us an additional margin of safety on the bolt. All tests so far have been carried out on thin head 5/8 inch diameter, #11 rolled threads , 2 inch long bolts fabricated from 304 stainless steel and from Nitronic 50. Two bolts of stainless steel and three of nitronic were tested and the results are presented in Table 1.1.

Tensile Strength

Table 1.1

Elongation vs yield

Type	Sample	Before	After	Difference (%)	Yield (N)
304 SS	1	58.62 mm	58.73 mm	0.0019	84183
304 SS	2	58.62 mm	58.79 mm	0.0029	82400
Nit 50	1	58.47 mm	58.57 mm.	0.0017	91197
Nit 50	2	58.42 mm	58.52 mm	0.0017	91732
Nit 50	3	58.55 mm	58.63 mm	0.0014	88027

Testing was performed in accordance with ASTM-A370-95. The yield point is not the point where the bolt fails, but corresponds to the point where the bolt becomes permanently deformed and will not recover totally elastically. These tests are being duplicated at the University of Mississippi. It should be noted that the bolts are stronger than the bolt base material, which was also tested by the lab. We ascribe this additional strength to work-hardening that occurs when the thread is rolled. The bolts are able to withstand the required 51.7 kN (11600 lbs.) of force.

Torque test

To achieve the 51.7 kN (11600 lbs.) preload, the bolt must be torqued to 170 N m (125 foot-pounds) of torque. We tested the bolt design to verify that this torque is achievable. The torque tests are carried out using a modified ASTM F880 procedure. The bolt is threaded into a hardened steel fixture until the bottom of the head is nearly flush with the fixture. Then a hardened steel bolt is threaded from the bottom of the fixture until it bears against the bolt under test. A hex key bit is inserted to the full depth of the bolt socket and the torque applied with a torque wrench. The Nitronic 50 bolts have a socket strength of greater than 197 N m (145 ft-lbs.). The 304 SS bolt sockets fail at about 190 N m (140ft-lbs.). Although this is greater than the needed 170 N m (125 ft-lbs.), we are modifying the bolt design. We will change the Allen socket for a Torx socket, which can withstand more torque.

Thread tests

We plan on bolting the bolts into threads cut into the absorber plate. Since this is a soft material, we need to know at what point the bolt or the threading will fail. We obtained samples of hot-rolled copper from Non-Ferrous Metals Company, Sofia, Bulgaria (a potential vendor for the HCAL absorber). Hardened steel bolts are fitted through a 19 mm (3/4 inch) thick piece of the copper alloy and then threaded into a hole tapped into a second piece of copper alloy thereby clamping the two pieces together. Standard feed holes and threads are used (either UNC ½-13 or UNC 5/8-11). The bolts are then torqued until thread failure. It was noted that about 13.6 N m (10 ft-lbs) before thread failure a noticeable change in the way the bolt was reacting to the torque occurred. We attribute this to the copper flowing around the bolt into the non-threaded section.

The results of the test are given in Table 1.2.

Table 1.2

Maximum torque on bolts - test results

Bolt Diameter	Torque (N m) at which Cu threads failed
9.5 mm (3/8")	not tested
12.7 mm (1/2")	171 (126 ft-lbs.)
12.7 mm (1/2")	181 (133 ft-lbs.)
12.7 mm (1/2")	171 (126 ft-lbs.)
15.9 mm (5/8")	228 (168 ft-lbs.)
15.9 mm (5/8")	238 (175 ft-lbs.)
15.9 mm (5/8")	239 (176 ft-lbs.)

The maximum torque's for the 5/8" threading are considerably larger than the required 170 N m (125 ft-lbs.) needed to supply the 51.7 kN (11600 lbs.) preload. In addition, the brass should have better mechanical properties than the copper. Tests on brass are under way.

2.8.4 Shear keys ,keyways, and shear pins

The shear forces between the wedge absorber plates cannot be held by the friction induced by the bolt preload, as it is too small. Shear forces will be taken by keys, as shown in Fig. 2. 4.

The keys are 12.7 mm (0.5 inches) square in cross section. The keyway extends the whole length of the wedge. The keys are press fit into the lower plate keyway. Each key is 20cm long, and the keys are placed continuously for the full length of the wedge.

In calculating the forces on the keys, we will conservatively assume that the friction force = 0 and that the keys will have to take up all of the shear force. The maximum shear force F is applied to the joint between the outer SS plate and the first inner absorber plate. The maximum shear force is exerted on the horizontal wedges, at 3 and 9 o'clock. From the FEA analysis, the maximum force on a bolt is 25.8 kN (5790 lbs.), with the distance between two bolts of 200mm (7.87"). The allowable shear stress for soft copper, τ_{max}, is 35 MPa (5 ksi).

τ_{max} =F_{max}/A = 5970/(0.57.87) = 1.52 ksi (10.6 Mpa), (2)

This well below the allowed limit. In reality, the key will be made of cold drawn material which will have an even larger τ_{max}. The stress in the plate is small. The normal stress is σ.

σ = F_{max}/A = 5970/(0.257.87) = 3.0 ksi (21 Mpa) (3)

Again this is well below the maximum allowed stress in copper of 70 Mpa (10 ksi). The technique for installing and loading the keys during the wedge assembly process is described in the section on wedge assembly.

The keys and keyways structure take the shear forces in the phi direction. We also need a pin to take shear forces in the z direction, along the long length of the wedge. The wedges are built and always remain in the orientation with the long axis of the wedge parallel to the floor. Then there are nominally no shear forces in the z direction. However, for safety, and to serve for plate alignment during assembly, we will place one shear pin between each pair of plates.

2.8.5 Calorimeter FEA summary

The FEA model used for the wedge is 2-dimensional. We justify this approximation because the wedges are continuously attached together, and continuously supported. The bolts were modeled as point hinges between plates (i.e. like spot welds). The plates were free to rotate about the point attachments. In addition, the absorber plates were allowed to penetrate each other. These simplifying assumptions were used because it is a "worse case". In actuality, the bolt head and nut will supply some torque to prevent plate rotation. Thus this model will have more deformations than the final wedge.

The two simplifying assumptions above were justified by studying their effects via finite element models. To test the effect of the "spot weld" treatment of the bolts between absorber plates, we made a model where the absorber plates were "welded" together along their length. This model was more rigid than the "spot weld" model. Therefore we chose the spot weld model because of its more pessimistic predictions.

To test the effect of absorber plate penetrations, we made a FEA model of the barrel structure where the absorber plates could not penetrate each other. In this model we found that the forces on the plates were small. Therefore we elected to use the model where the plates can penetrate.

The wedges make contact with each other only at the inner and outer stainless steel plates. We studied two models of the inter-wedge attachment. The first model had the inner and outer SS plates welded to the neighboring wedges along the full length of the wedge. The other model of wedge attachment had SS plates are attached by hinges. The plates could pivot about those points. We found that the maximum tensile force on the bolts connecting wedge plates was 1.6 times larger for the hinged model than for the welded model. The maximum tensile forces on bolts connecting wedges was very close in the two models 78.9 kN (17688 lbs.) for hinged, 79.7 kN (17863 lbs.) for the welded.

Therefore we made our default model one where the absorber plates are connected by spot welds, and can penetrate each other. The adjacent wedges are connected by hinges. This model will give us pessimistic results. The model is shown in Fig. 2. 10. The brass absorber plates do not touch. The force vectors on the front of the calorimeter represent the 4 tonnes (metric) ECAL modules.

The deformations on the calorimeter are shown in Fig. 2.11. The values are in polar coordinates, centered in the nominal center of the barrel. The maximum deflection is in the vertical Y-Z plane, and is about 1.3mm (0.05"). The scintillation slots also suffer distortion. The maximum closing down of a slot is 0.4mm, Fig. 2.12. This is large enough that we will need to take it into account in the preparation of scintillators for those slots.

The stresses on the plates are low, 42 MPa (6000 psi), with σ_y = 70 MPa (10000 psi), as shown in Fig. 2.13. and Fig. 2.14 . The maximum stresses are found in the horizontal rail wedges at the connection between the stainless steel outer plate and the first copper plate. A maximum bolt load of 25.8 kN (5790 lbs.) occurs in this region.

We have also compared this FEA to other studies. One study treated the bolts similarly, but was 3-dimensional. We found consistent results between these 2 models.

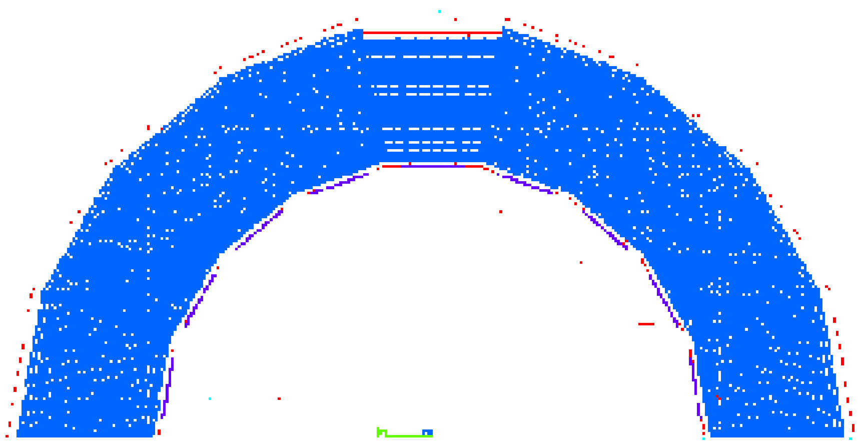

Fig. 2. 10: Barrel structure FE model

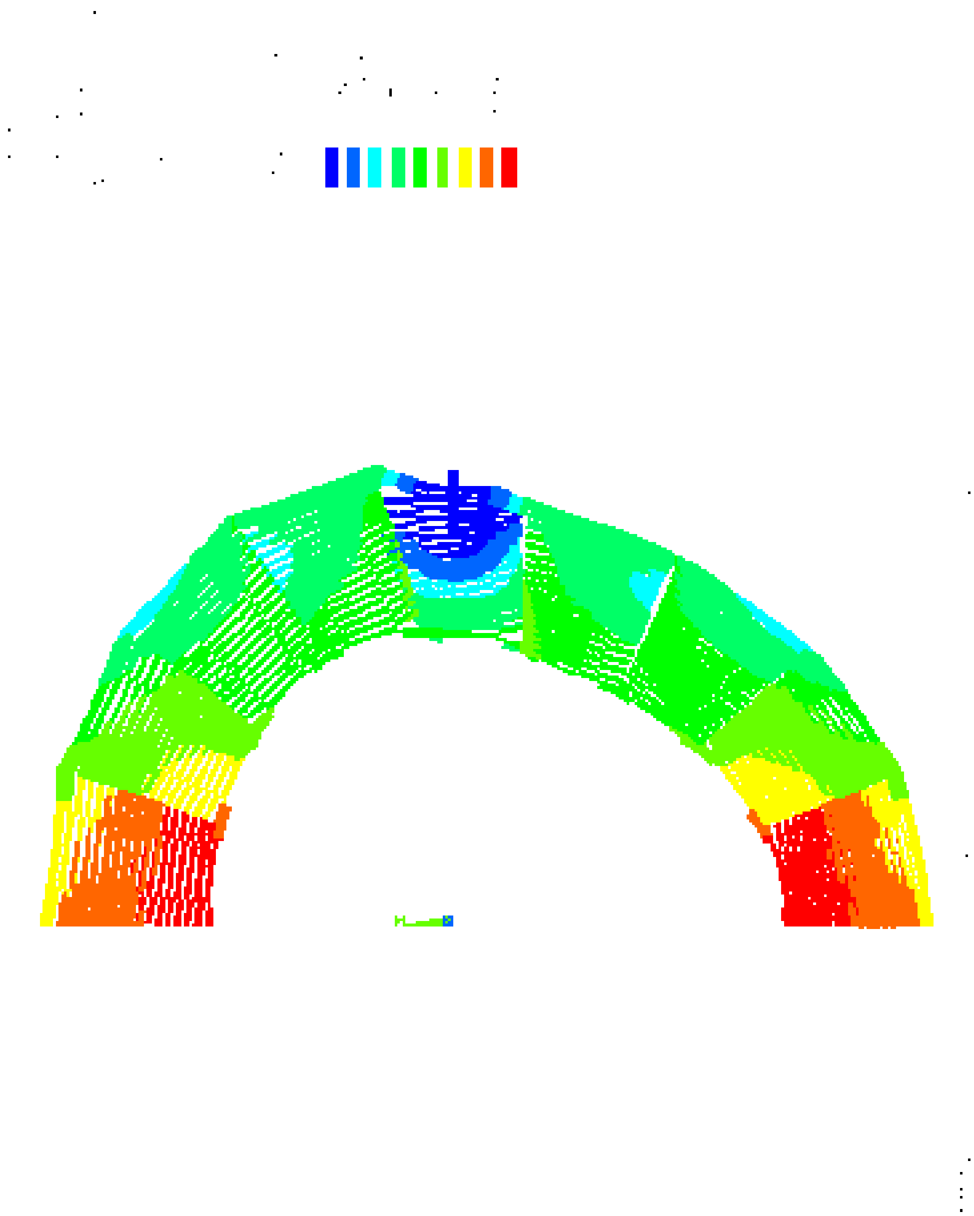

Fig. 2. 11: Total Displacement (mm)

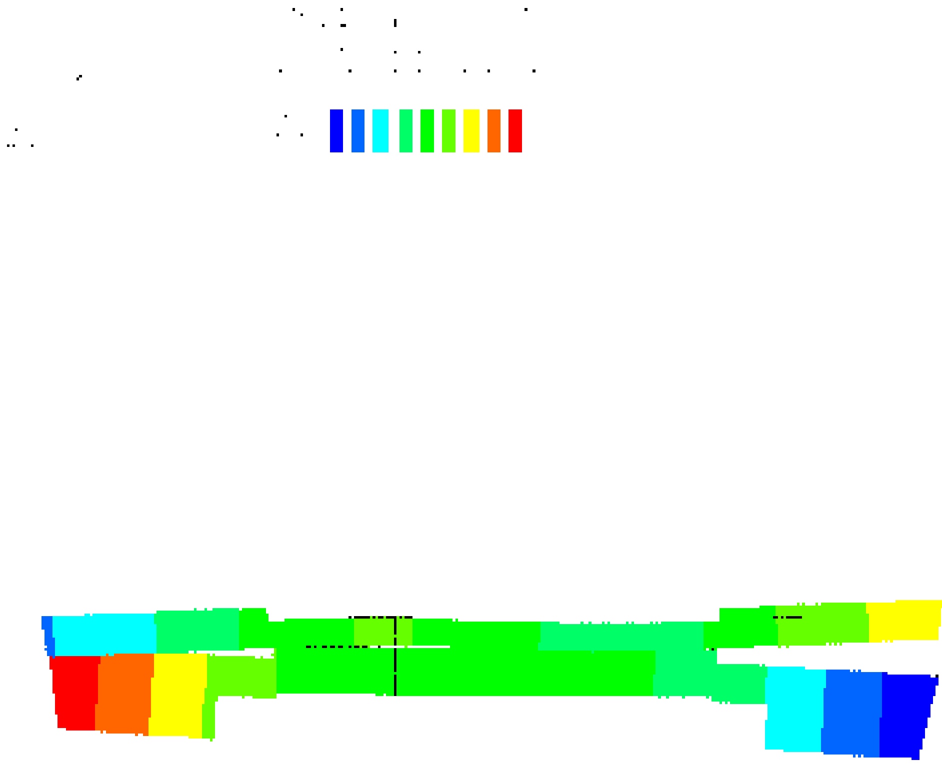

Fig. 2. 12: Plate displacement (mm)

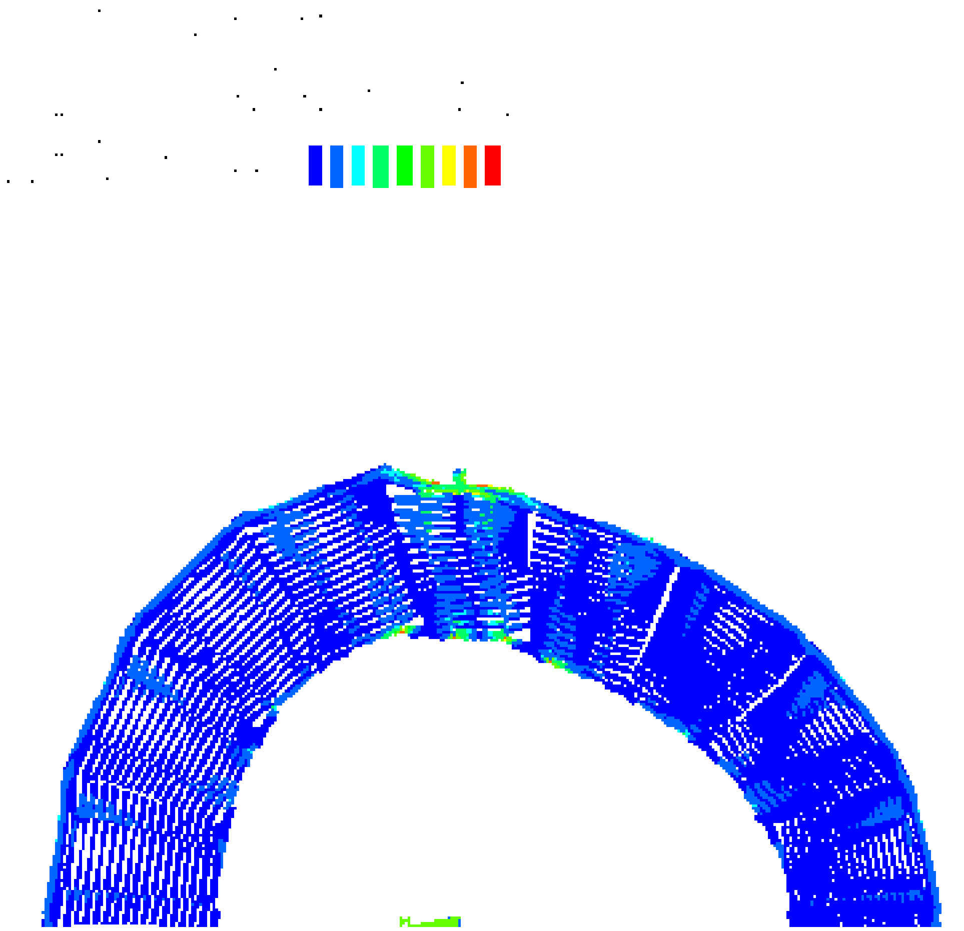

Fig. 2. 13: Plate stresses (MPa).

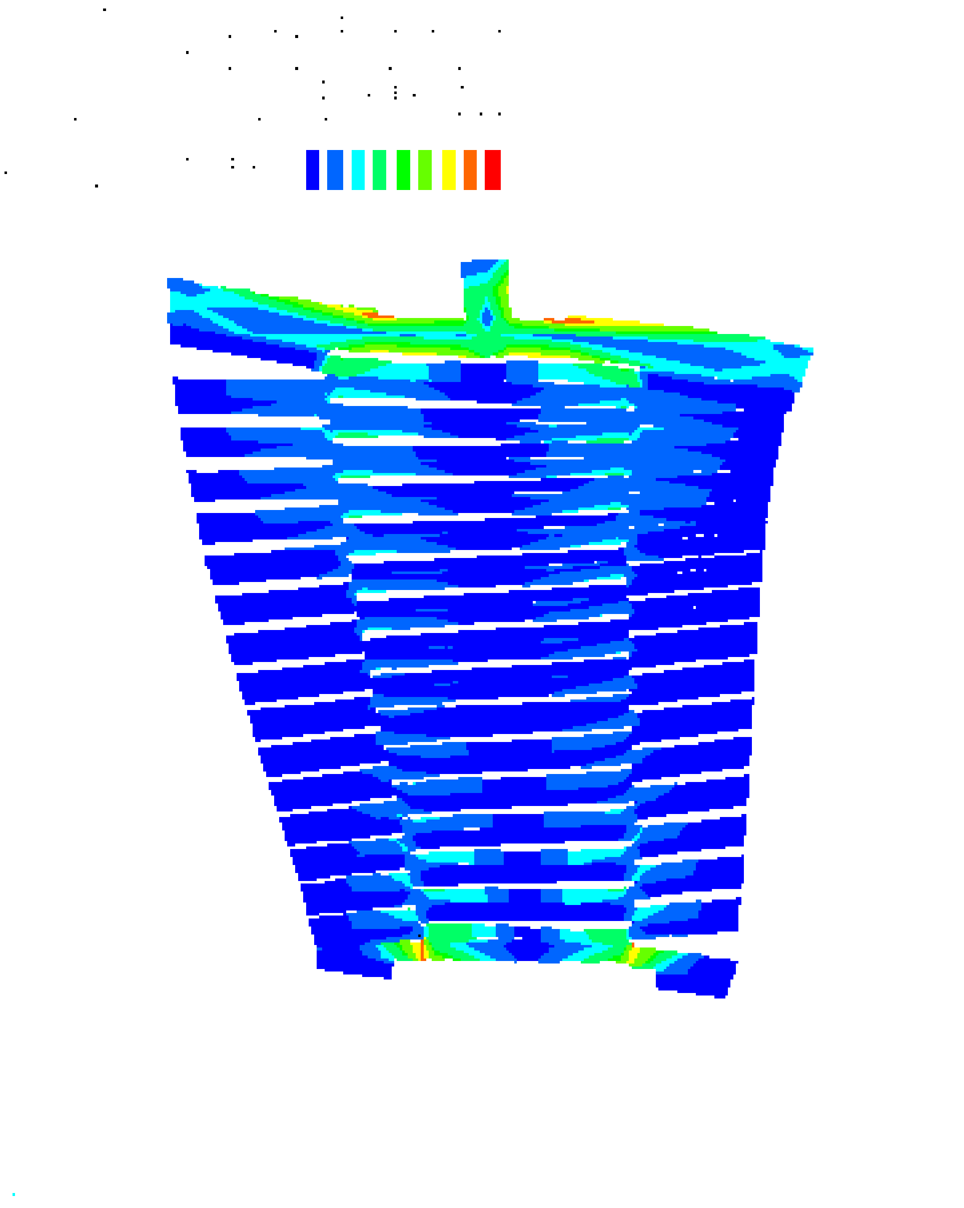

Fig. 2. 14: Wedge Plate Stresses (Mpa).

Table of Contents

2.8.6 Prototype Wedge

During 1997 the HCAL group will construct a full size wedge prototype. This prototype will be instrumented with scintillators and tested with cosmic rays. Finally it will be taken to the H2 test beam at CERN for more extensive testing. Part of the HCAL project is to construct a test beam motion table so the wedge can be scanned through the H2 test beam.

The wedge is assembled from back to front, starting with the stainless steel back plate. The back SS plate is attached to a flat assembly plate, as shown in Fig. 2.15. Shear keys and the alignment/shear pin are positioned into place. (The top of the key is has a 1mm radius and the upper plate keyway is oversized by 0.5mm, to allow an easy fit.) Then the next brass absorber plate is positioned into place onto the alignment pin, then lowered onto the shear keys. The plate is pushed transversely (according to the direction of gravity that this wedge will experience in the completed barrel), to engage the key in the oversized upper keyway. Then the plate is bolted down with M16 bolts. Keys and the alignment pin are installed on this plate, then the next absorber plate is positioned, and so on until the wedge is completed.

Special tooling required for stacking the wedge are the assembly table, shown in Fig. 2.15, and a plate lifting fixture, shown in Fig. 2.16. The plate lifting fixture is designed such that the plate is not deformed during the lifting and assembly process. The plates are required not to be elastically distorted by more than 0.2mm during the lifting process. This constraint arises because the key ways will not fit together if the plates sag too much during lifting.

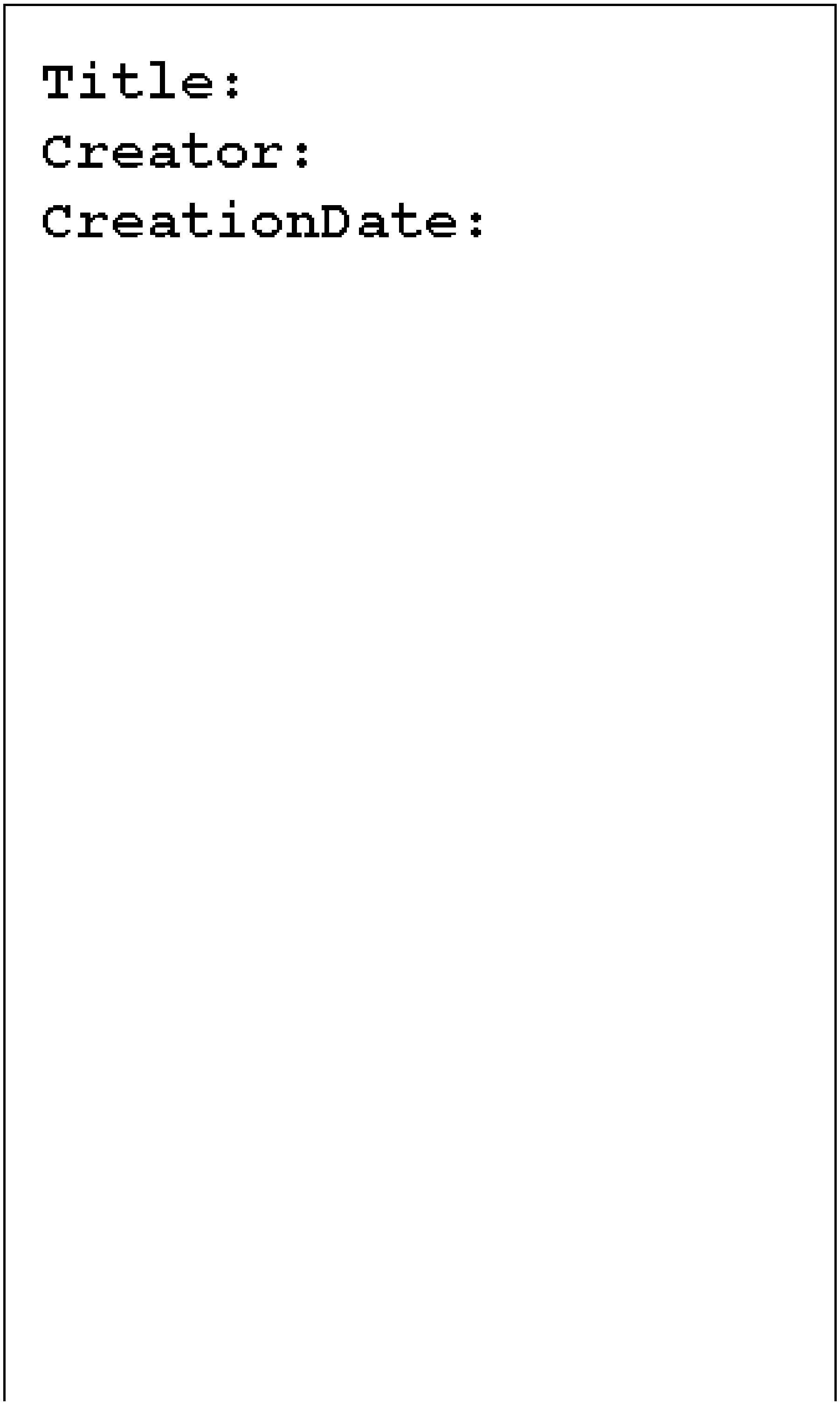

Fig. 2.15: Wedge Assembly Table (dimensions are in inches).

2.8.6.2 Plate lifting fixture

The HCAL absorber plate lifting fixture is used to facilitate HCAL wedge assembly. Its purpose is to lift individual absorber plates and position them on top of one another so that they may be bolted together. The philosophy behind the assembly procedure is to maintain each individual absorber plate to a high degree of rigidity so that it may be accurately positioned with respect to it's neighbor's shear key. Once the absorber plate lifting fixture is bolted to each absorber plate it acts as a rigid spine, stiffening an otherwise flexible plate. The fixture is bolted to the plate in sixteen locations to ensure a maximum deflection in the plate of less than 80 microns (0.003 inches). This maximum deflection was calculated based on a 20mm minimum cross-section of the copper absorber plate. Stresses induced in the copper plate were equally low, on the order of 1.4 MPa, where the yield stress for copper is about 70 MPa.

Calculations were also done for the stainless steel outer and inner radius absorber plates. On a plate with a 63.5mm cross-section, a maximum deflection of 46 microns (0.0018 inches) was obtained. Stress values in the plate were 0.6 MPa, compared to a yield stress in stainless steel of 210 MPa.

The maximum bolt forces were calculated based on the reaction forces at the points were the plates were fastened. The maximum values obtained were around 2500 N (560 lbs.) Since we will be using the existing M16 threaded holes in the absorber plates to attach to the lifting fixture, this is clearly within the acceptable range.

The lifting fixture itself is constructed of an American Standard I-Beam (15 42.9) (designation 15 42.9 means the I-beam is 15 inches (381 mm) in depth and weighs 42.9 lbs/ft (64 kg/m)) with four similar I-beam outriggers welded to it. Fig. 2.16 shows the plate lifting fixture.

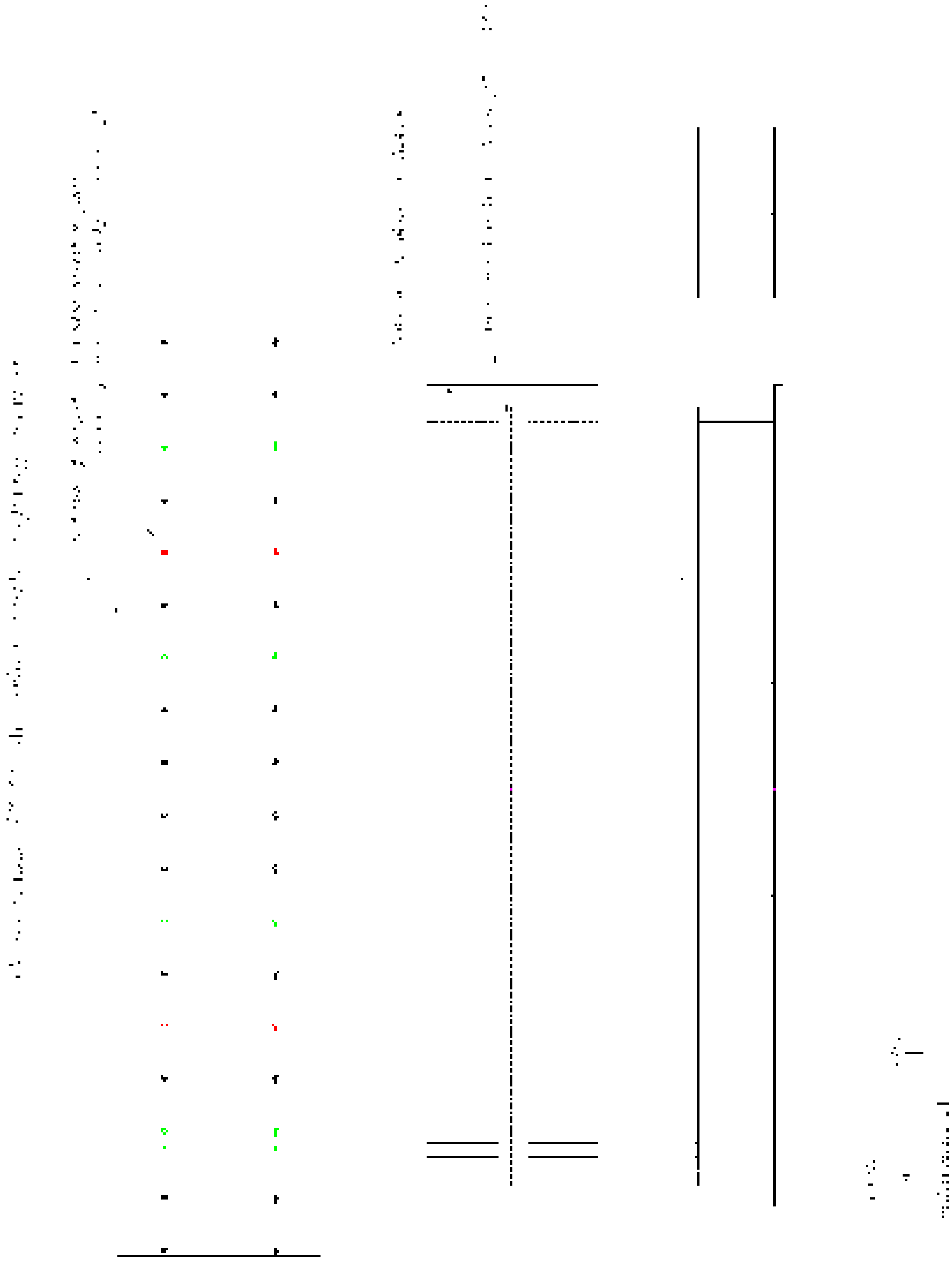

Fig. 2.16: Plate lifting fixture

Machined steel plates, 40mm (1.5 inches) thick, are bolted to the outrigger section of I-beam and shimmed flat with respect to each other. Slots are machined in the plates in order for them to accept the bolting pattern of all the absorber plates.

The lifting fixture was designed for rigidity so its deflection under maximum load is only on the order of 25 microns (0.001 inches).

The total deflection of all components in the wedge assembly is about 100 microns (0.004 inches). This requirement is imposed by the assembly procedure and is necessary to position the absorber plates on their shear keys. The plate lifting fixture deflection gives a factor two better positioning tolerance than the 200 microns required in order to ease wedge assembly.

Wedge test loading fixture

The HCAL barrel wedge load fixture, Fig. 2.17, is designed to simulate the load conditions that an HCAL rail wedge will encounter in its final assembled state. The rail wedge in the HCAL barrel assembly is the wedge that sees the greatest stresses and for that reason it is the one that should be simulated. Since the first prototype wedge is to be a "common" non-rail wedge, provisions for adding a "rail" to it must be accommodated. Bolting and pinning a "rail" to the outer stainless steel absorber plate will be done before the wedge is structurally tested. At the wedge to wedge connection locations in the stainless steel inner and outer radius, the prototype wedge will be attached to the load fixture by a series of mechanical actuators. These actuators will allow loading of the wedge to provide comparable deflections to those obtained in the finite element analysis results.

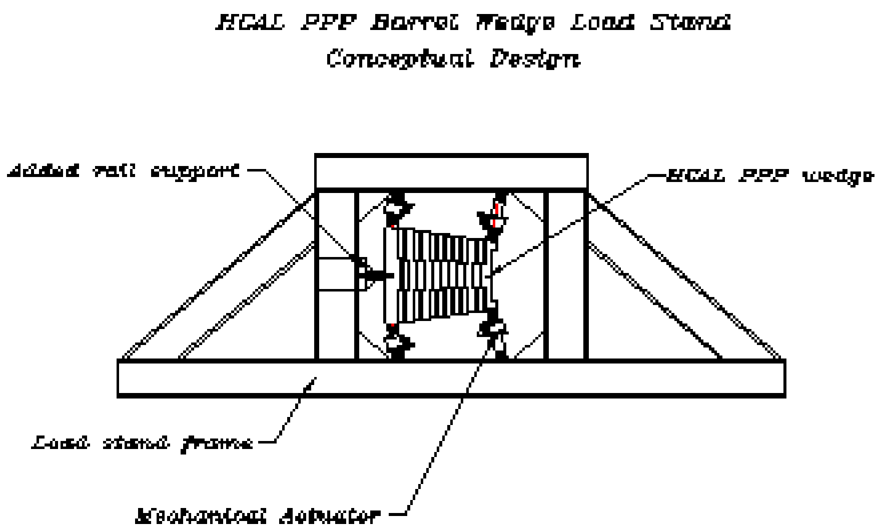

Fig. 2.17: Wedge test loading fixture

As part of our overall quality control, each wedge will be tested for structural soundness at the manufacturing site. The wedges will be loaded by the load test fixture, and deformations measured.

Test Beam Motion Table

The wedge will be placed in the H2 test beam at CERN. In order to move different parts of the wedge into the beam, a motion table is required. The table will also be capable of azimuthal motion so that the beam can be placed in each projective tower of the wedge. The 2 degrees of motion are achieved by: motion via a vertical axis fixed to the floor; φ motion via rotation about a horizontal axis that is part of the motion table. The angle of rotation φ is ± 20º. Ultimately, the HCAL group will build 2 prototype wedges. The motion table will be designed to be able to support both of these wedges of the HCAL barrel. In addition, the table will be able to accommodate a 40 degree sector prototype of the HE endcap hadron calorimeter. It will also accommodate prototypes of the ECAL barrel and endcap calorimeters. Thus a full 40 degree sector of the CMS central calorimeter can be held on the motion table. Fig. 2.18 shows the layout in the H2 beam line. The position of the CMS prototype calorimeters are shown in 2 configurations: one where the beam is traveling at η=3, and the highest η edge of the calorimeter is just out of the beam; and the other position where the beam is at =0, and the lowest η edge of the calorimeter is just outside the beam. Fig. 2.19 shows the isometric view of the motion table loaded with 2 HB wedges, the HE prototype, and ECAL EB and EE prototypes. Also shown are the muon chamber and the muon return flux iron.

The platform also rotates around the vertical axis y. The rotation angle is 90º. The rotation around the y axis (90º) will take 30 minutes maximum and the rotation around the φ axis will take 15 minutes maximum. Accuracy of positioning around both axis is ±1 mm. Both motions will be controlled by computer. The turntable will have computer-readable position indicators.

Title: From AutoCAD Drawing "C:\Polub\TDR\fig13"
Creator: AutoCAD
CreationDate: 5397 14:57:22

Fig. 2.18: Layout of motion table in H2 test beam area. Dimensions in mm.

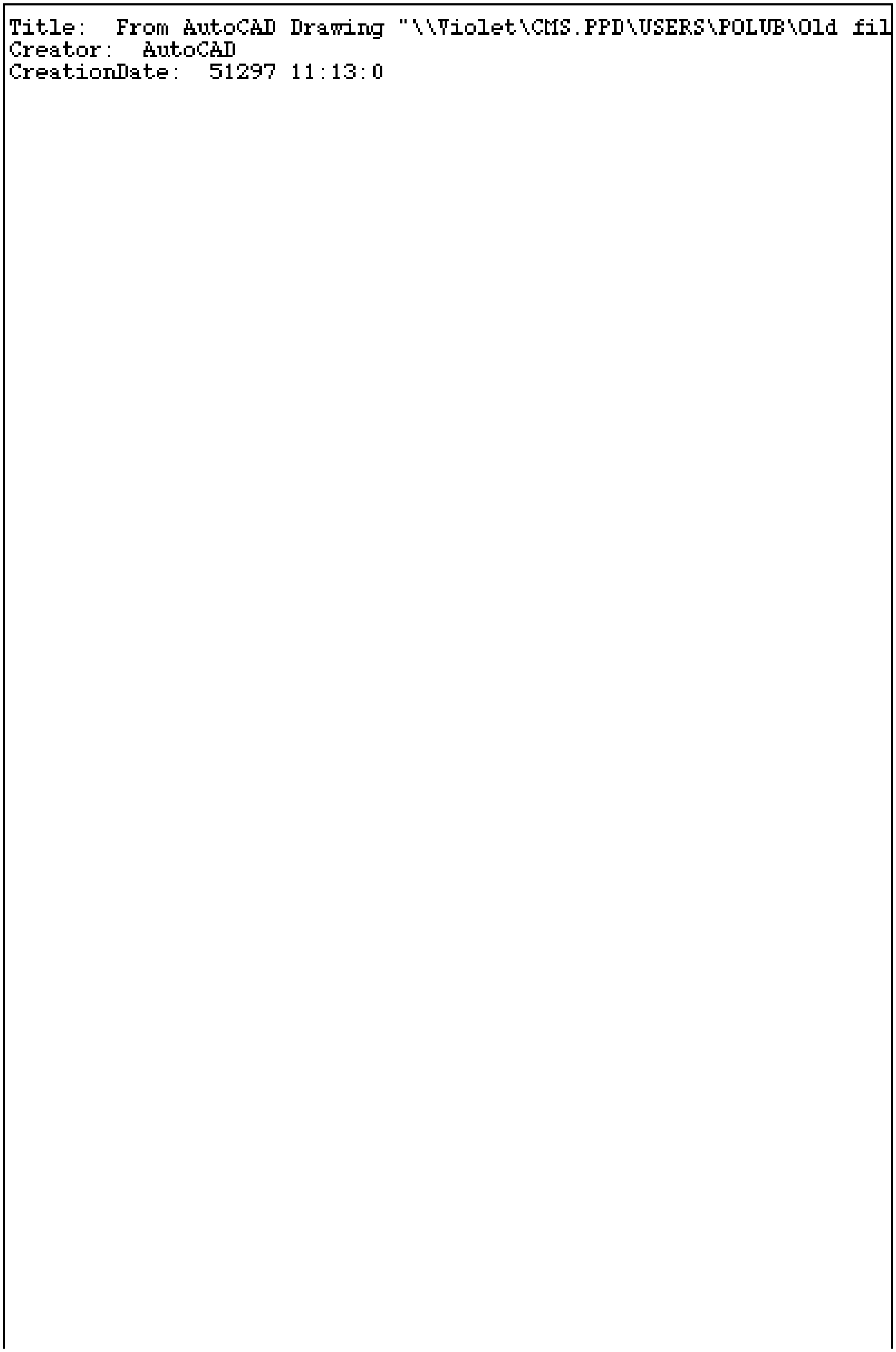

Fig. 2.19: Side view of motion table showing calorimeters.

2.9 WEDGE CONSTRUCTION QUALITY CONTROL

The internal structure of the wedge cannot be measured after assembly. We will test the rigidity of each wedge after construction to verify its mechanical integrity. We will use the wedge test loading fixture at the absorber factory, installing each wedge into the load fixture and applying reference loads. Then we will measure the deflections of the wedge. This allows us to test the internal structure of the wedge.

The dimensions of the wedge are critical. We will insert scintillator tray templates into each slot to verify go/nogo. Each wedge will be surveyed to assure that its dimensions are within tolerance. Finally the entire barrel half-rings will be assembled at the factory to verify that the completed structure is within tolerance. The support cradle and spider tooling will be reused for final assembly at the CMS assembly hall. The half barrels will be assembled in the nominal configuration with the symmetry axis horizontal. The half barrels will be surveyed, and any corrective machining or shimming will be done. Finally the half barrels will be disassembled and the individual wedges and tooling shipped to CERN.

2.10 BARREL DESIGN

2.10.1 Overview

Each HCAL half-barrel consists of 18 wedges, bolted together at the inner and outer radii. The bolted-together stainless steel front plate and back plate polygons act as structural members to minimize the deflections. The half-barrels rest on rails attached to the vacuum tank inner wall, at 3 and 9 o'clock.

2.10.2 Wedge layout

The wedges are attached together by brackets which are bolted to the back face of the SS outer radius plate. The bracket is designed to take and shear forces between the wedges. At the inner radius, the wedges are bolted together through slots machined in the SS inner plate.

2.10.3 Bolt patterns

Fig. 2.20 shows the detail of the outer stainless steel plate. The notches for the cross-bolting of wedges are also shown as well as the bolting together of two wedges Fig. 2.21 shows a detailed view of the inner stainless steel plate. The wedges are bolted together using M20 bolts between adjacent wedges at the inner plate, brackets between adjacent wedges at the outer plate.

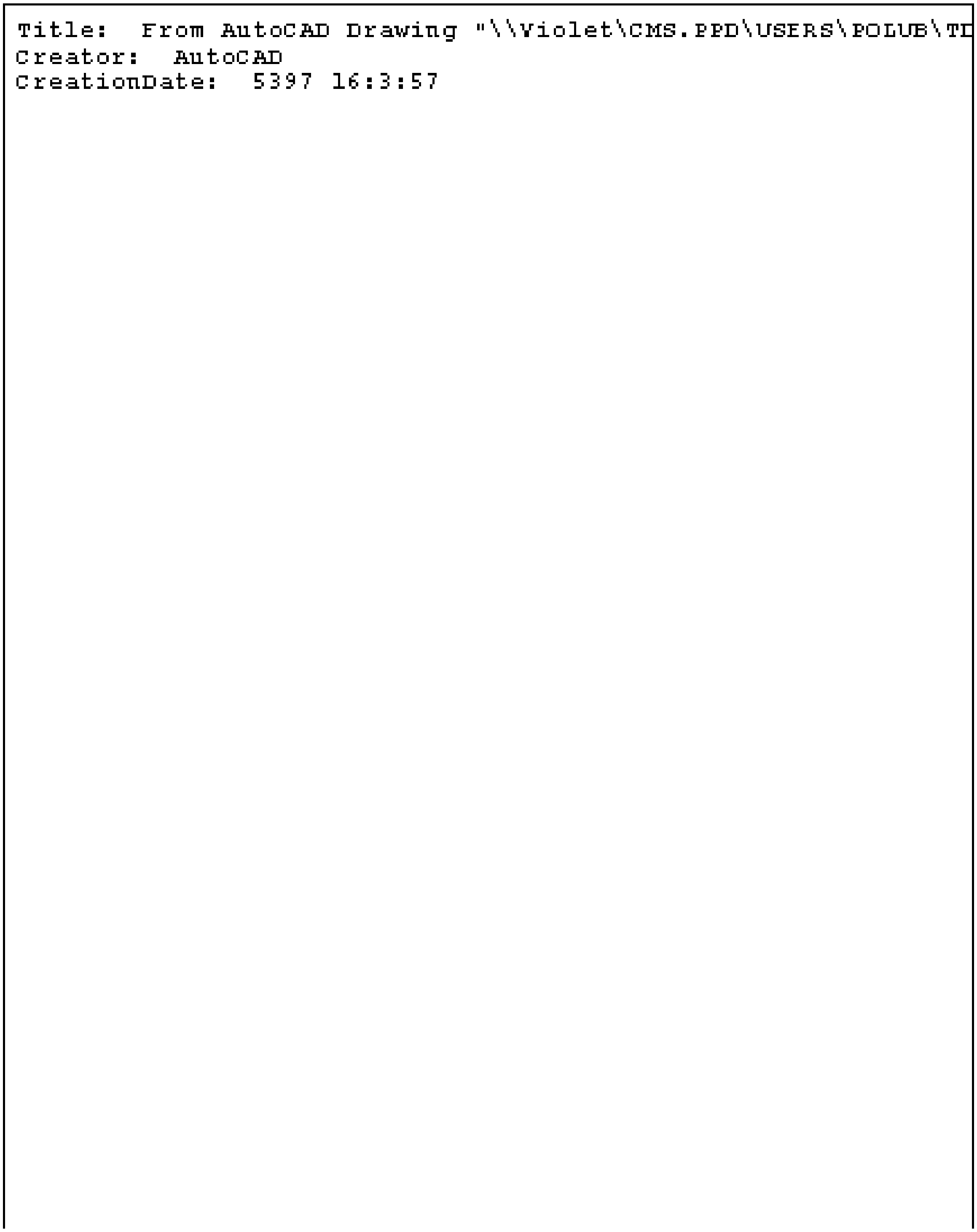

Fig. 2.20: Detail of outer SS plate, showing attachment brackets

Title: From AutoCAD Drawing "C:\Polub\TDR\fig_vis
Creator: AutoCAD
CreationDate: 5397 14:38:22

Fig. 2. 21: Detail of inner SS plate, attachment brackets

2.11 BARREL MOUNTS (RAILS)

The HCAL half-barrels reside inside the CMS vacuum tank, resting on rails welded to the inner stainless steel wall of the vacuum tank. The half-barrel is much more rigid than the vacuum tank inner wall. Thus, a non-uniform load distribution would be expected on the rails, with most of the load being taken at the minimum and maximum z extent of the half-barrel. To make the half-barrel more compliant, a load distribution system has been designed.

The weight of the half barrel is carried to the vacuum tank through the wedges at the 3 o'clock and 9 o'clock positions. These wedges have a support structure built into them to mate with the rail structure on the vacuum tank.

2.11.1 Cryostat/rail FEA

The HCAL half barrel rests on the two rails welded to the inner wall of the vacuum tank. The forces and deflections on the rails are of great interest to us. To understand this system, we made a finite element model of the rails, the vacuum tank, and the vacuum tank attachment to the muon support iron. The model is shown in Fig. 2.22. We modeled ½ of the vacuum tank taking advantage of its mirror symmetry about the midplane. We modeled the worst case scenario as if the vacuum tank rails were as far apart as the vacuum tank drawing tolerances allow. In this case the HCAL applies the maximum torque on the rails. The rails are split at the midplane. A coarse model of the vacuum tank and rails was formed. In this model, the 2 rail halves (on either side of the midplane) are not fixed at the midplane. The rail welds were not modeled in detail. Rather they were treated as two strips, one on top of the rail, and one below. The calorimeter barrel halves had no contact during the deformation. The vacuum tank and rail deflections were calculated using the coarse model. The results are shown in Fig. 2.23 and Fig. 2.24.

To understand the effects on the stresses due to the muon system support, 2 models were created: one with ribs connecting the central barrel wheel to the vacuum tank (See chapter 9 of the Magnet TDR), and the other with no ribs and constraints in the contacts between the ribs and the outer shell. The details of the central barrel wheel attachment had no effect on the rail and inner vacuum tank stresses. This is as expected. The flange disk connecting the outer and the inner vacuum tank shells isolates the inner shell from distortions of the outer shell.

A refined submodel was created with a detailed description of the welds, Fig. 2.25 . The refined submodel was used to calculate stresses on the rails, welds, and inner shell of the vacuum tank. Fig. 2. 26 shows stresses in the inner shell of the vacuum tank, which are small. Fig. 2.27 shows stresses on the rail material. The stresses are again small. Fig. 2.28 shows the rail deflection within the length of the half-barrel. This deflection must be accommodated by the plunger/Belleville washer system.

The results of the FEA study are:

a) There was no effect of the details of the muon system attachment.

b) The inner shell deflections, Fig. 2.23 and Fig. 2.24, were within +- 10mm.

c) The total rail deflection over the length of the half-barrel was 2.4mm, but the relative deflection was only 0.6mm. The relative deflection is important for the calculation of the stroke of the suspension plungers. Fig. 2.28 shows how the rail cross section moves as a result of the calorimeter load.

d) The stresses in the rail material (SS 304) were well below the limit of elasticity, σ_y = 245 MPa (35ksi). As shown in Fig. 2.27, the maximum rail stress was 97 MPa (14ksi).

e) The maximum stresses in the rail welds are acceptable, as shown in Fig. 2.29 and Fig. 2.30 . Ignoring the stress concentration at the upper radius of the rail (important only for fatigue issues which are irrelevant here), the stress in the weld is about 90 MPa (13 ksi). This is less than ½ of the maximum allowed stress of 210 MPa (30 ksi). Thus our safety factor on this weld is 2.3.

f) The stresses in the inner shell are shown in Fig. 2. 26. They are well within allowable limits.

As pointed out earlier, the inner vacuum tank/rail is a critical component of the HCAL support. Therefore an independent FEA analysis was performed to check the results presented above. There was good consistency between the two analyses, giving us confidence that these results are correct.

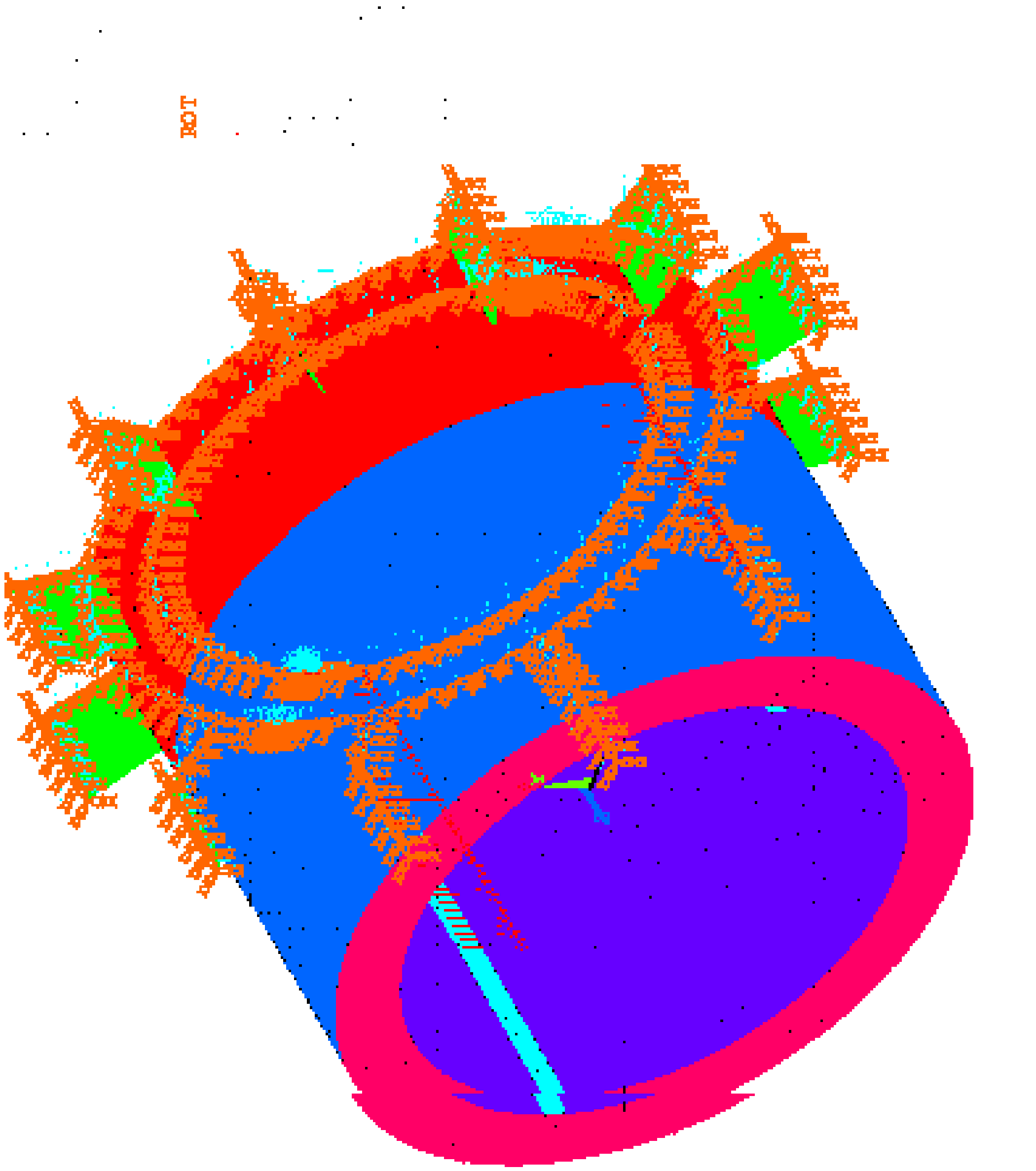

Fig. 2.22: Coarse FEA model of vacuum tank

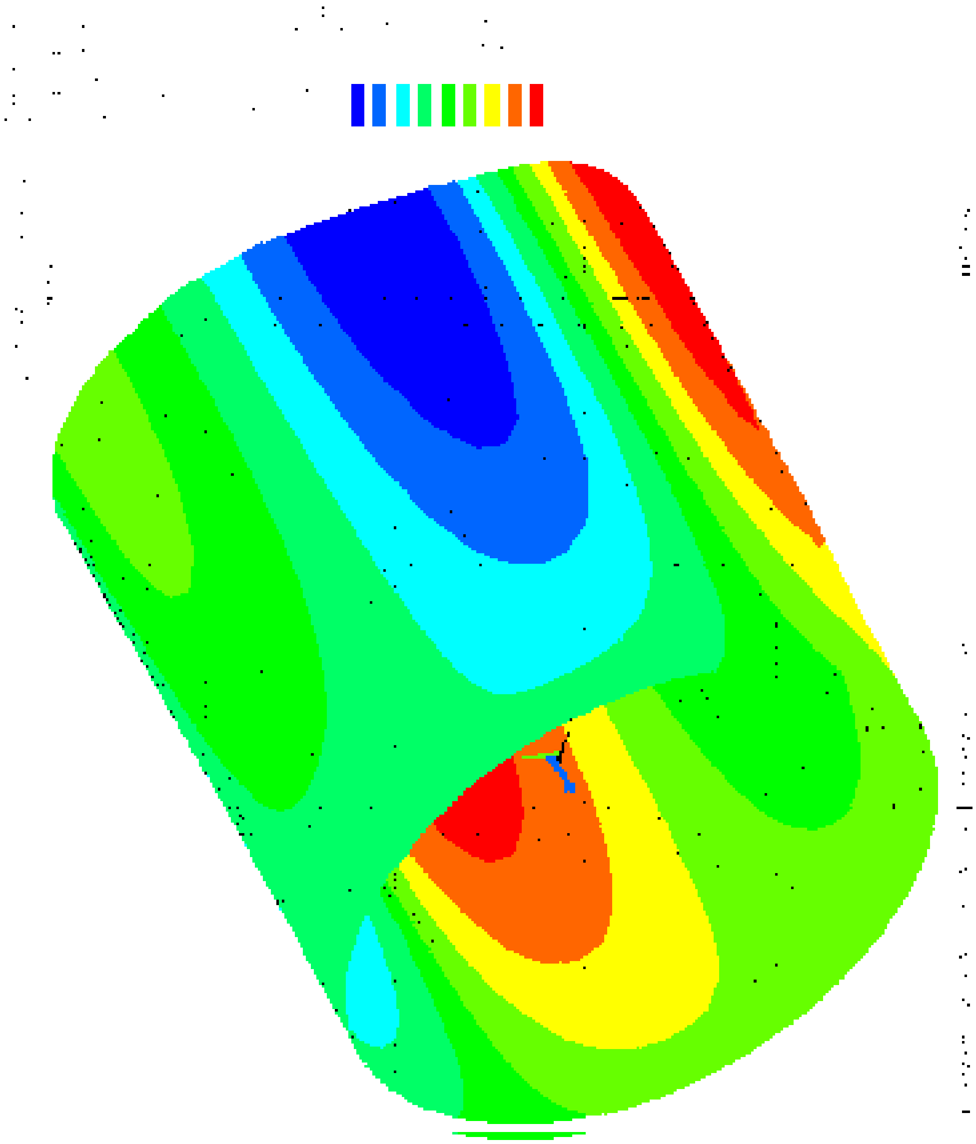

Fig. 2.23: Cryostat inner shell deformation in a cylindrical coordinate system (mm).

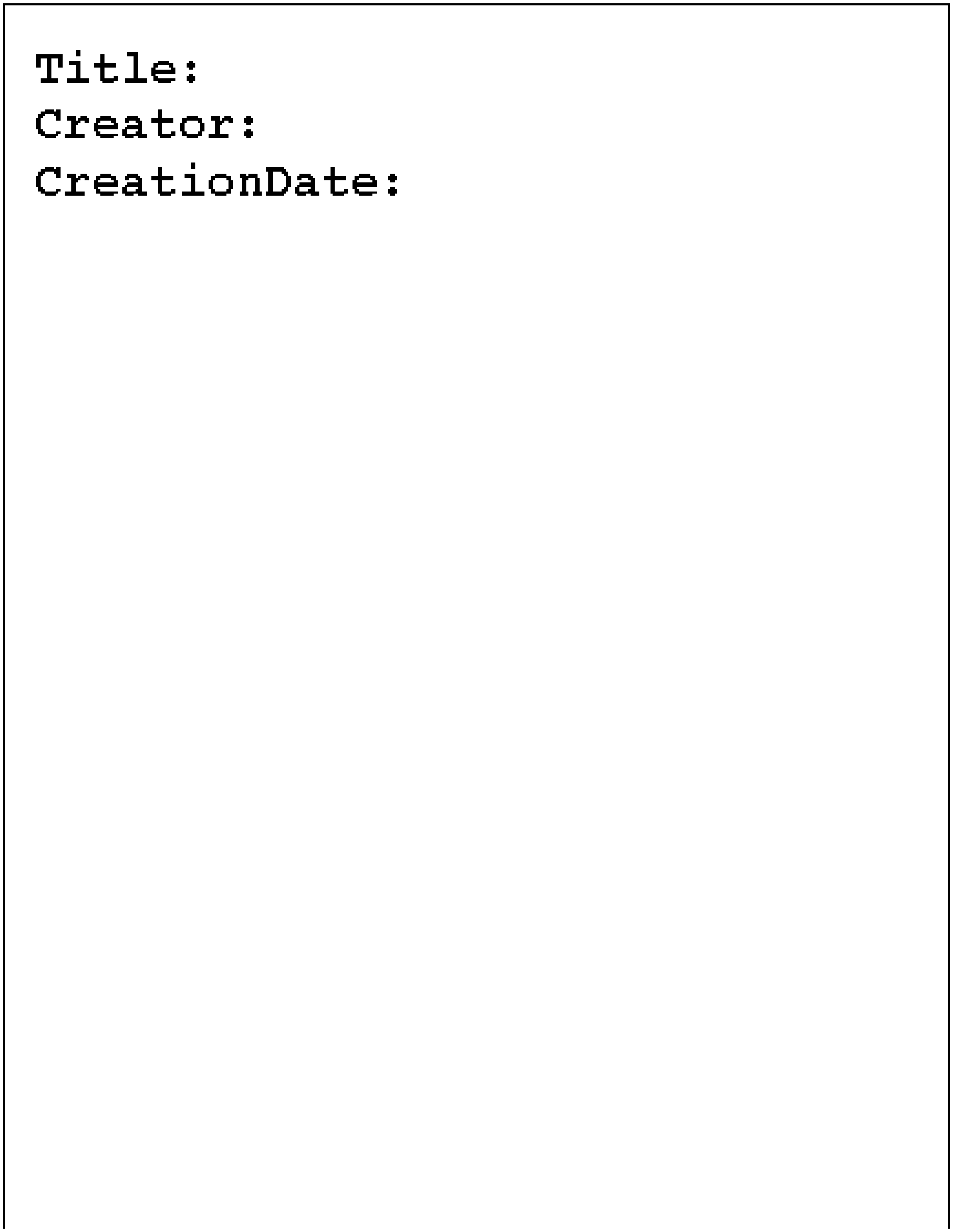

Fig. 2.24: Distortion on inner shell of vacuum tank

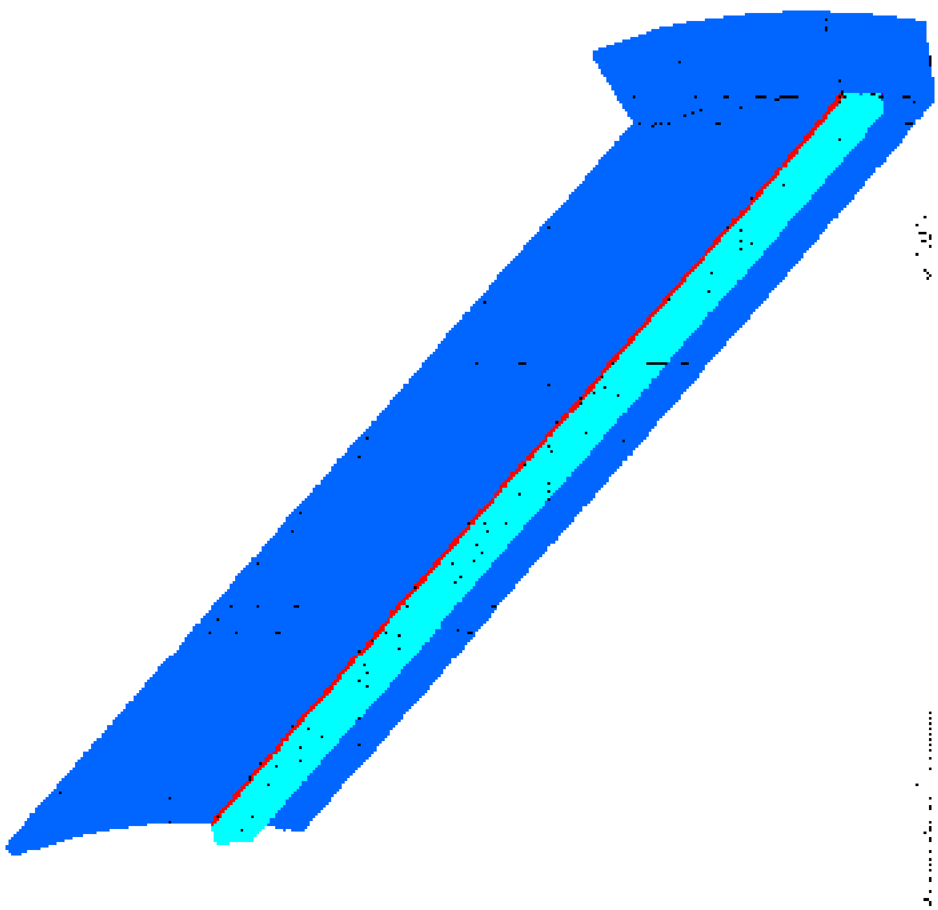

Fig. 2.25: Rail submodel

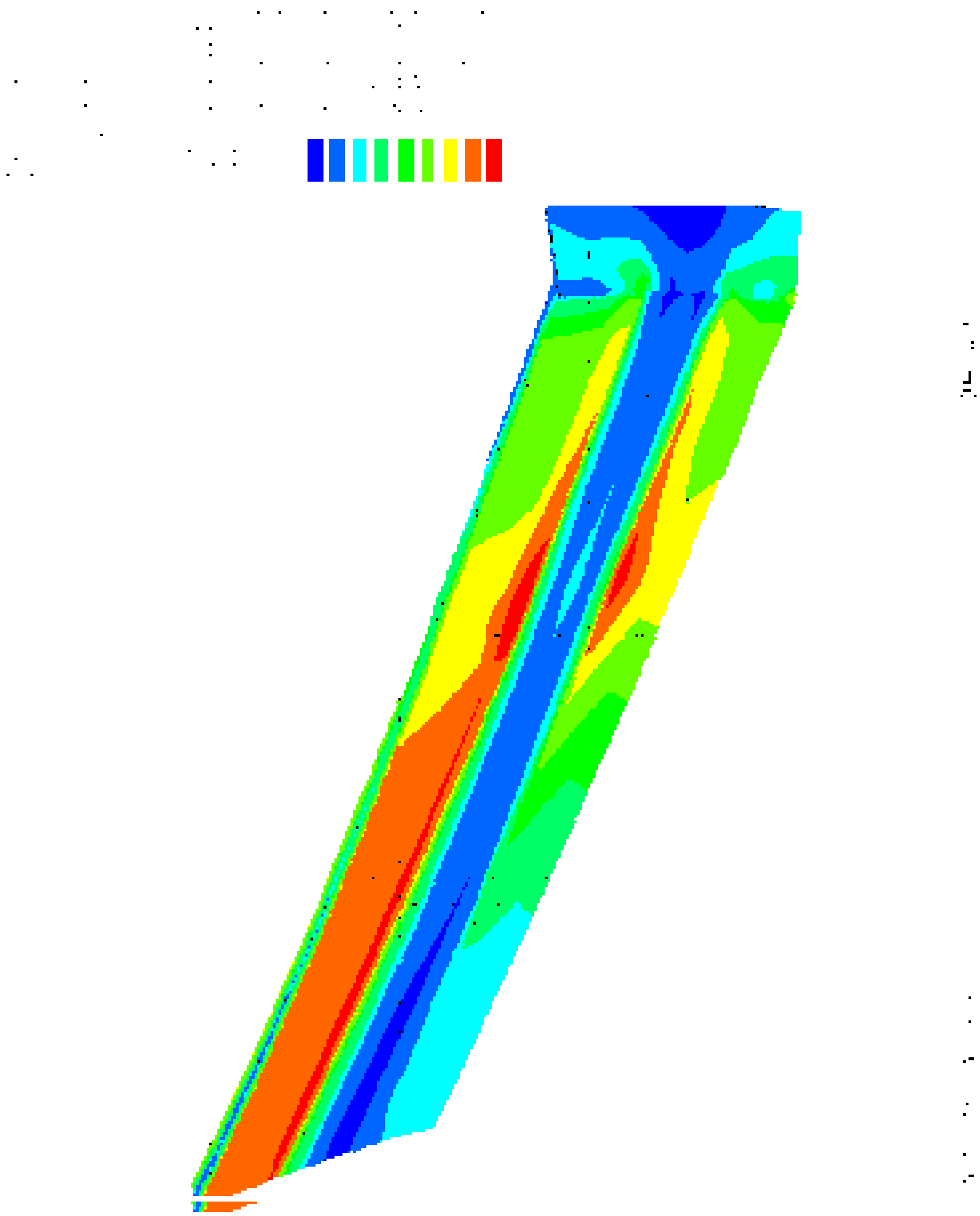

Fig. 2.26: Stresses in the inner shell of the vacuum tank (MPa).

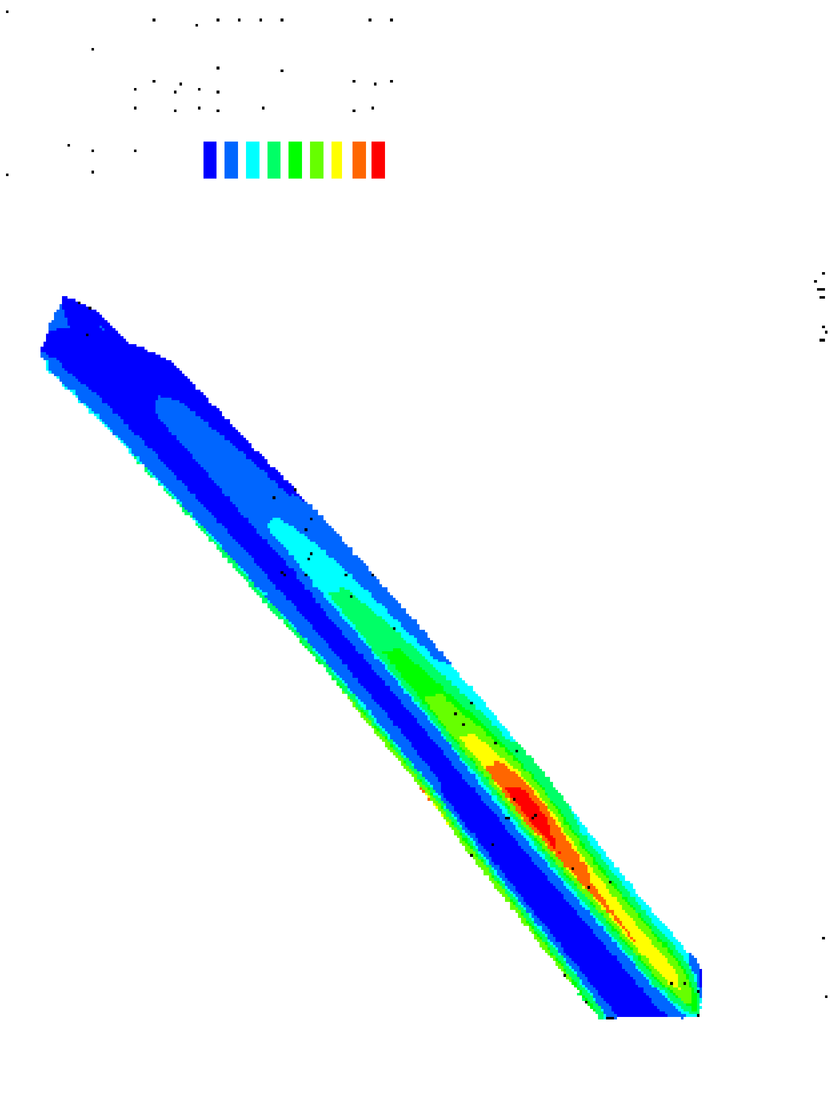

Fig. 2.27: Stresses on rail (MPa)

Title:
Creator:
CreationDate:

Fig. 2.28: Rail deformations showing sag and twist.

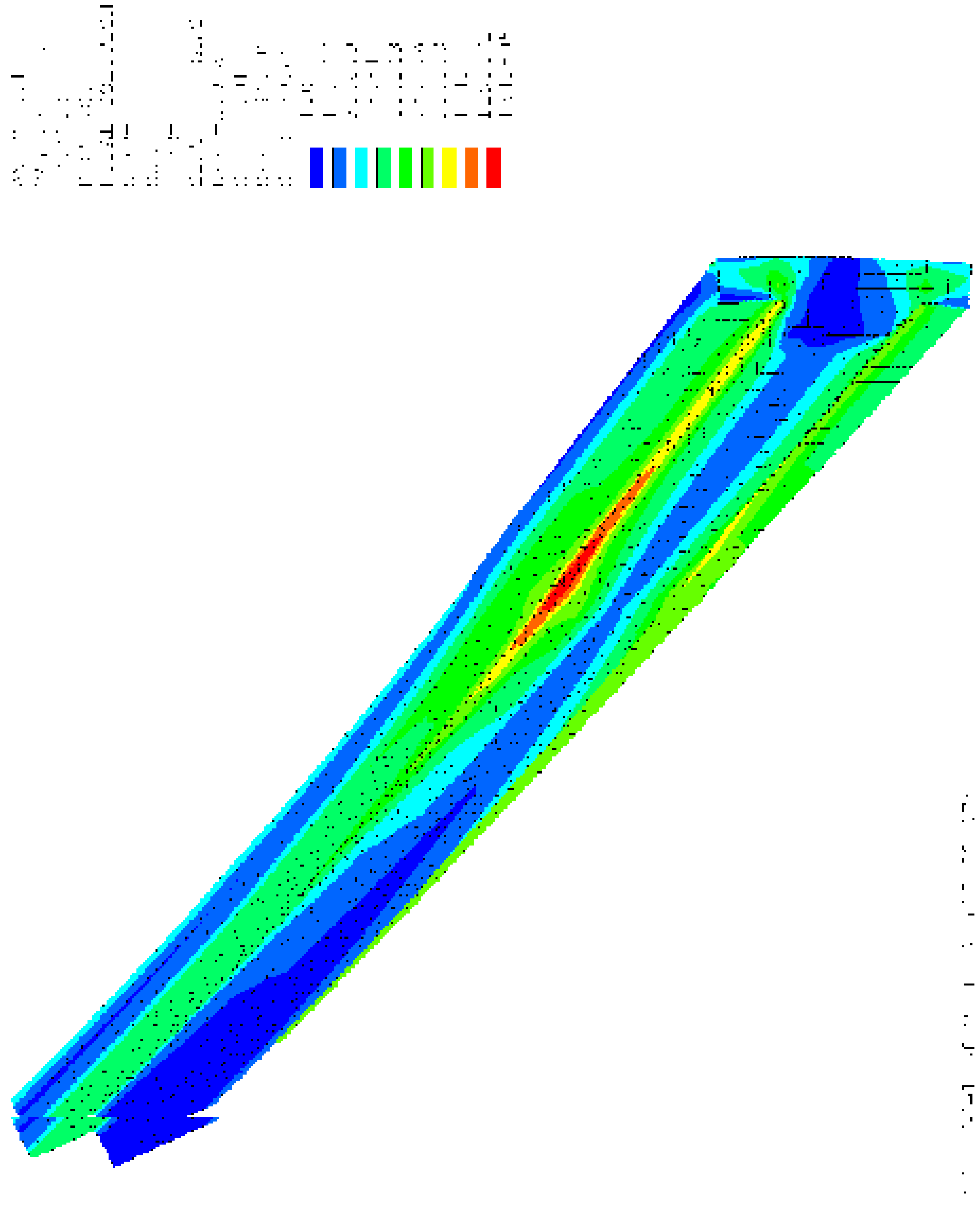

Fig. 2.29: Stress on rail weld along its length (MPa)

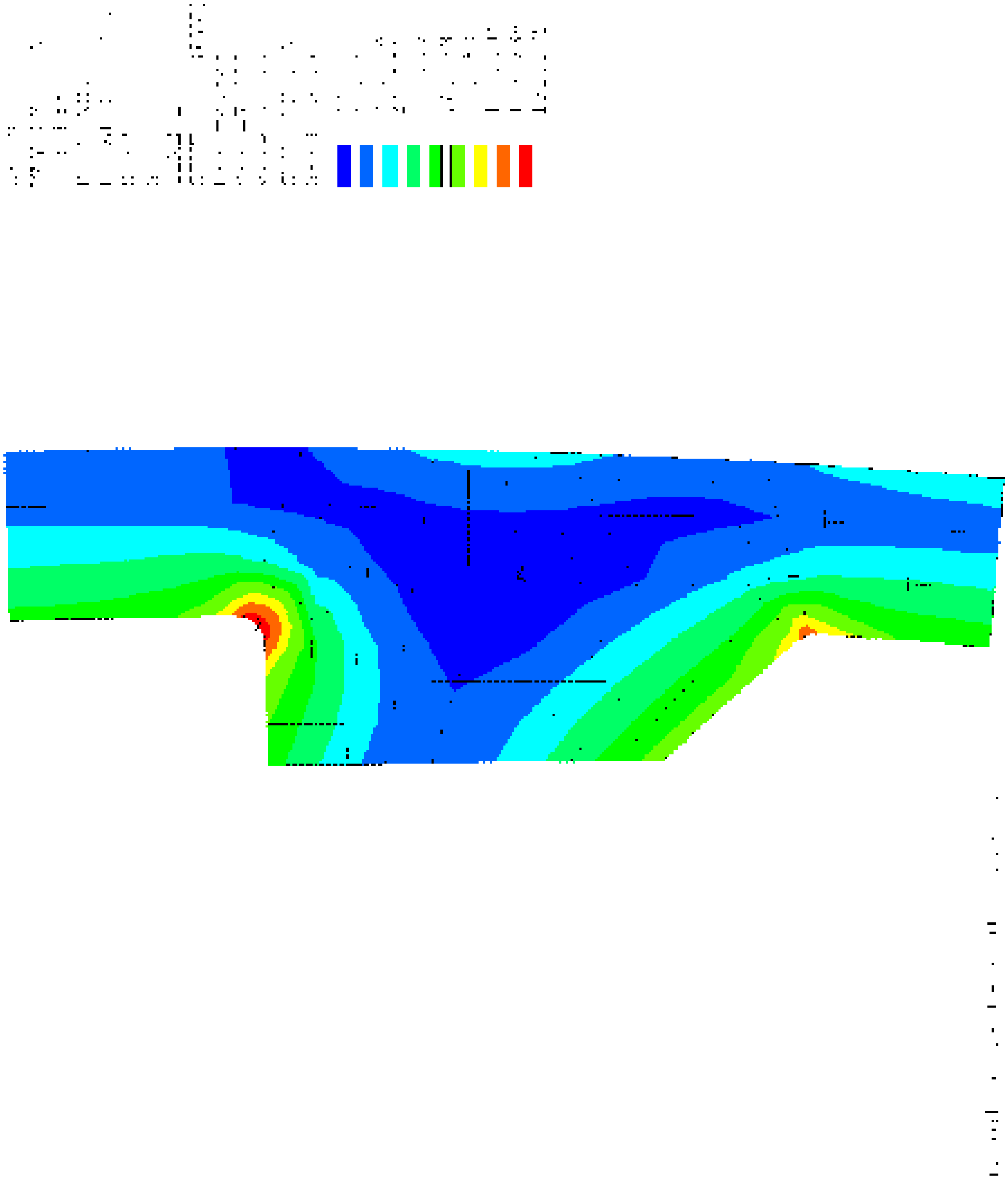

Fig. 2. 30: Stress in cross section of top weld of rail to vacuum tank inner shell (MPa)

2.11.2 Forces and deflections

The rails deflect by 2.4mm as the HCAL half barrel is installed into the vacuum tank. Of this, 1.8mm is an overall drop in the vacuum tank height, and 0.6mm is due to local deformation. The weld stresses are acceptable.

2.11.3 Calorimeter support system

The calorimeter half barrel is guided and supported by the rails welded to the vacuum tank inner shell. The rails have a relative deflection of 0.6mm under the weight of the half barrel. The half barrel is provided with a layer of compliance to compensate for the rail deflection and rail non-flatness. For this purpose, each side of the half barrel has a row of spring preloaded plungers. See Fig. 2.31.

The barrel is suspended on disk springs that exert force on the plungers. These plungers transmit the load to sliding pads connected to the plungers through hemispherical surfaces. The pads are made of bronze and have a Teflon coating on the sliding surface.

Fig. 2.32 shows details of the support system. The rail support system consists of the barrel rail (1) welded to the outer SS of the wedge (not shown). The rail houses bronze bushings (2). Plungers (3) have on their lower end the sliding pads (4) with hemispherical backs. This hemispherical back allows the pad to follow any distortions in the vacuum tank rails. Disk springs (5) are mounted on the top end of the plungers. A retainer ring (6) limits the plunger stroke downward, and prevents the plunger from falling out of the bushing. The disk springs limit the plunger stroke upwards. The disk springs push against the top bar (7). The top bar is connected to the barrel rail by bolts (8) and spacers (9).

The barrel weight is transmitted through the barrel rail (1), bolts (8), top bar (7), springs (5), plunger (3), and pad (4) to the vacuum tank rail (10) which is welded to the inner shell of the vacuum tank (not shown).

The size and number of disk springs determine the plunger stroke and the rigidity of the spring set. We have considered a variety of spring combinations and have chosen the one shown in Fig. 2.31. The optimal spring set consists of commercially available springs with OD 70mm and spring thickness of 5mm.

The maximum load on the spring set is 133.8 kN (310^4 lbs.) (springs are flat). The maximum load on one plunger is 75.8 kN ($.710^4$ lbs.) The stiffness of the set is 22.5 kN/mm (12.810^4 lb/in.) The stroke after the dead weight of the calorimeter is applied is 2.6mm which is sufficient to cover the deflection and non-flatness of the rail.

Title:
Creator:
CreationDate:

Fig. 2.31: Barrel support mechanism. Dimensions in mm.

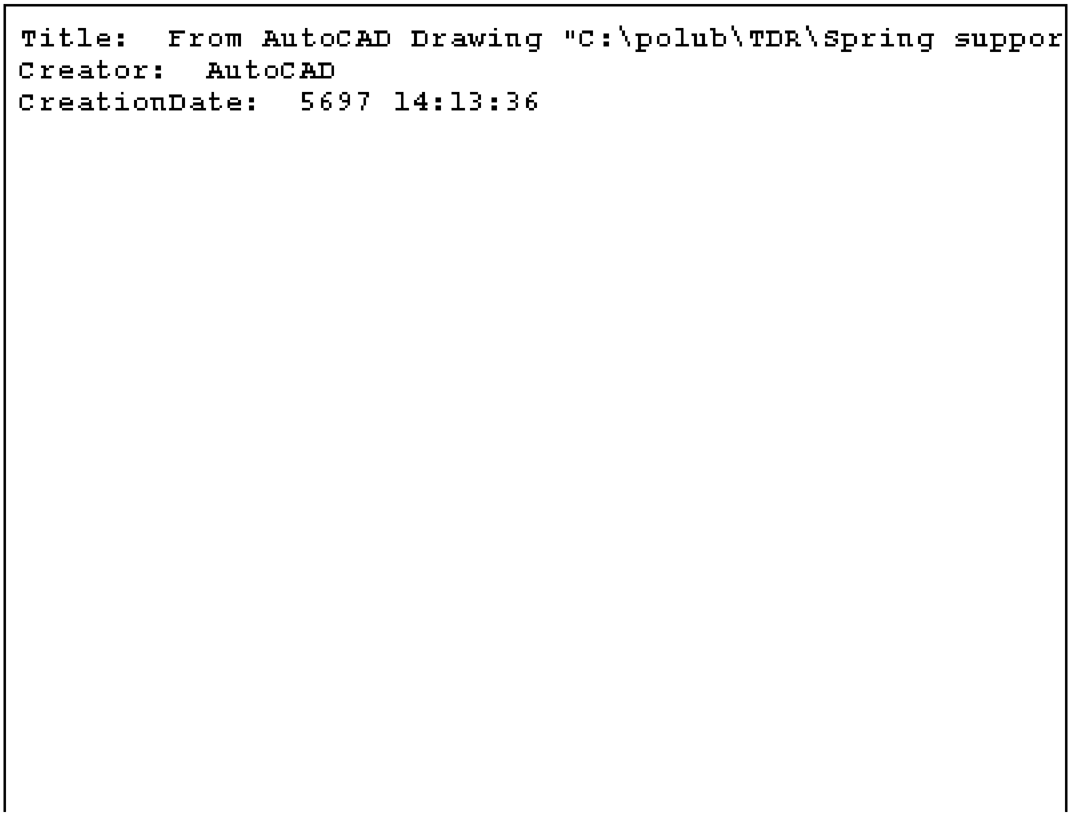

Fig. 2.32: Details of plunger/spring mechanism.

We will calculate the specific pressure for the load =2F=21.710^4 lb=151.1 kN. The doubled load will compensate for the uneven pressure on the pad as a result of the friction in the hemispherical pad support; and compensate for the rail non-flatness. The specific pressure is σ = 2F/A , where A is the sliding pad area and equals 70110 mm^2.

σ = 15400/(70110) = 19.6 Mpa. (4)

CERN has performed a test for us using a 0.3mm thick Teflon pad for the sliding surface. These test results show that the material will stand σ = 46.6 MPa which is more than twice our requirement of 19.6 MPa.

We will use the same material and gluing technique as used in the CERN test. In addition, we plan to perform our own test to study the complete rail support design. We will check the disk springs (maximum load and stiffness), the functionality of the hemispherical supports, and the coefficients of static and dynamic friction.

The rail test fixture is shown in Fig. 2.33 Shown are the base, and the sliding rail, constrained on the sides by rollers. The rail sits on the sliding surface of the base, and is loaded by two plungers. The rail is driven by the hydraulic cylinder. A force gauge will measure the friction force and the pad load.

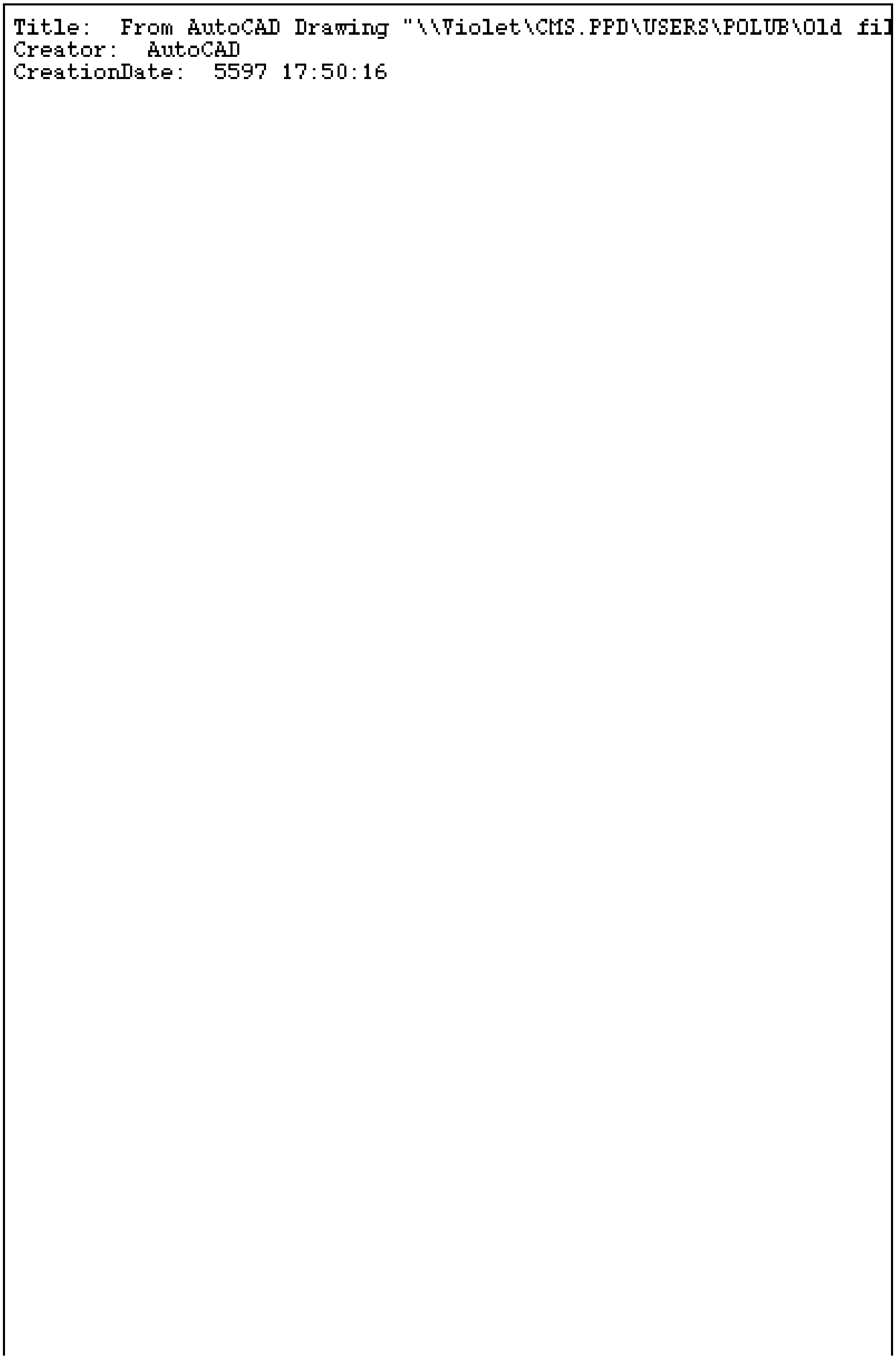

Fig. 2.33: Rail mechanism test fixtures

2.11.4 Calorimeter support FEA

The barrel rails, shown in Fig. 2.34, are welded to the outer SS 304 plate of the calorimeter wedges at 3 o'clock and 9 o'clock. A 3D finite element model was created in order to study the stresses in the rails and welds. The results are shown in Fig. 2.35. The maximum stresses are approximately 140 MPa (20 ksi).

The barrel support system (as shown in Fig. 2.31 including plungers, pads, support bars, and disk springs) is a heavily loaded system. This loading is due to both the high weight of the calorimeter and the confined space for the support system.

We have studied stresses in the barrel support using a finite element model, shown in Fig. 2.36. Results are shown in Fig. 2.37. The maximum stresses in the top bar, area "a", are caused locally by the bolt head as the bolt bends. These stresses can be ignored because area "a" is small and the local contact stress can be much higher than the limit of elasticity, σ_y = 245 MPa (35 ksi) for SS 304. The stresses in other areas are less than 140 MPa (20 ksi). The stresses on the bottom plate, Fig. 2.38, less than 112 MPa (16 ksi).

The load capacity of a M30 bolt is F= σ_{yA} , where σ_y = 280 MPa(40 ksi) for rolled thread, and A is 561 mm^2, (0.833 in^2) the tensile stress area for M30 bolts. The load capacity is F = 148.5 kN (33,312 lbs.), a satisfactory capacity, since our nominal load is 75.8 kN (1.710^4 lbs).

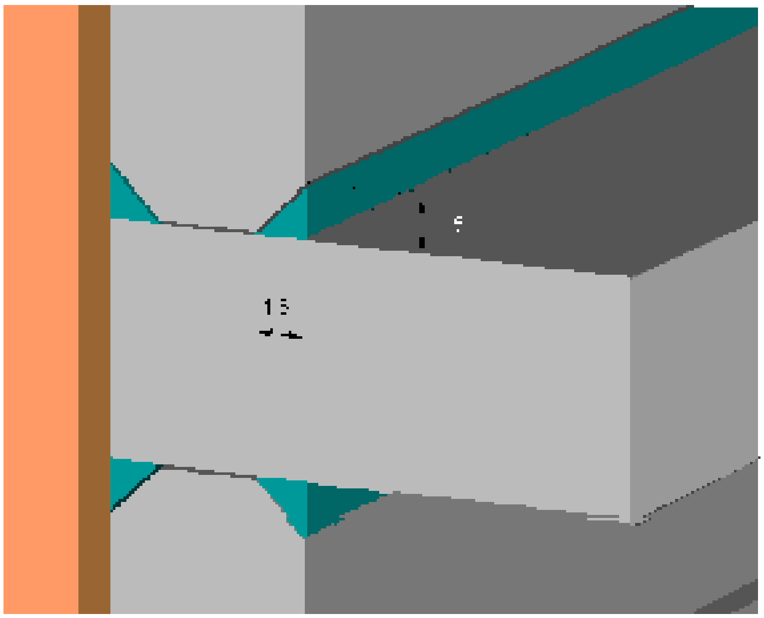

Fig. 2.34: Rail, weld on outer SS plate of 3'oclock wedge

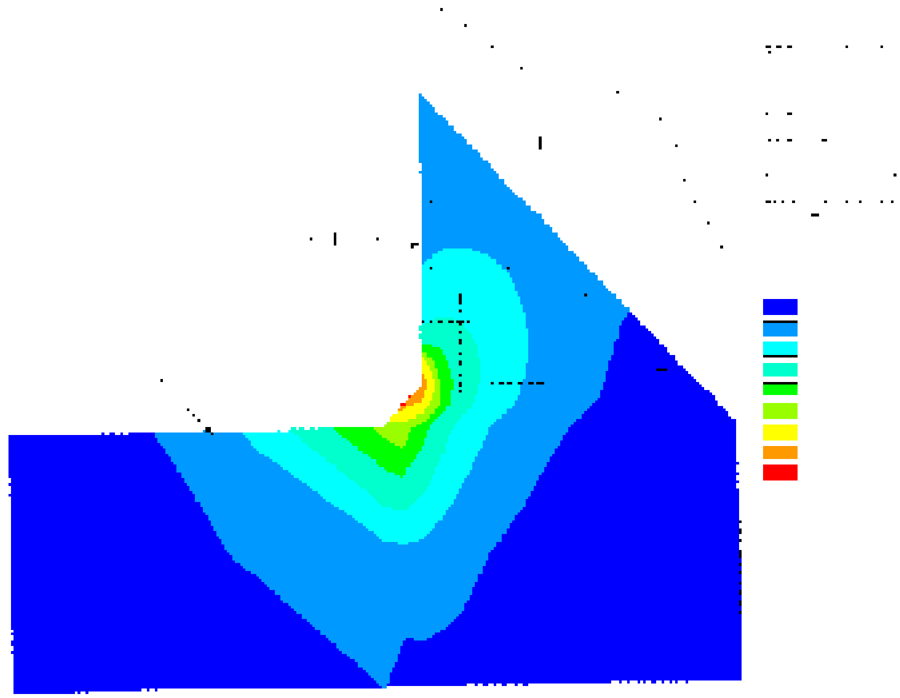

Fig. 2.35: FEA stresses on top weld of rail (Mpa)

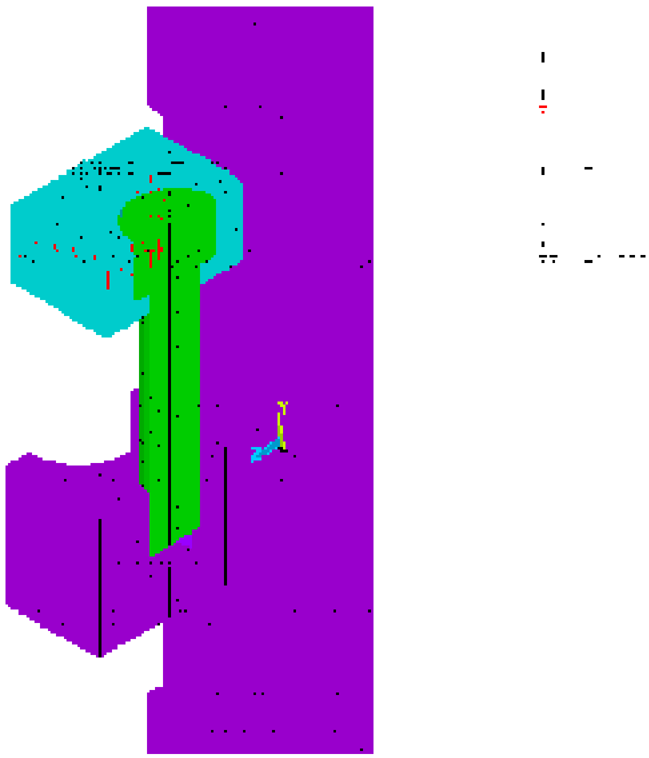

Fig. 2.36: FEA model of wedge support system

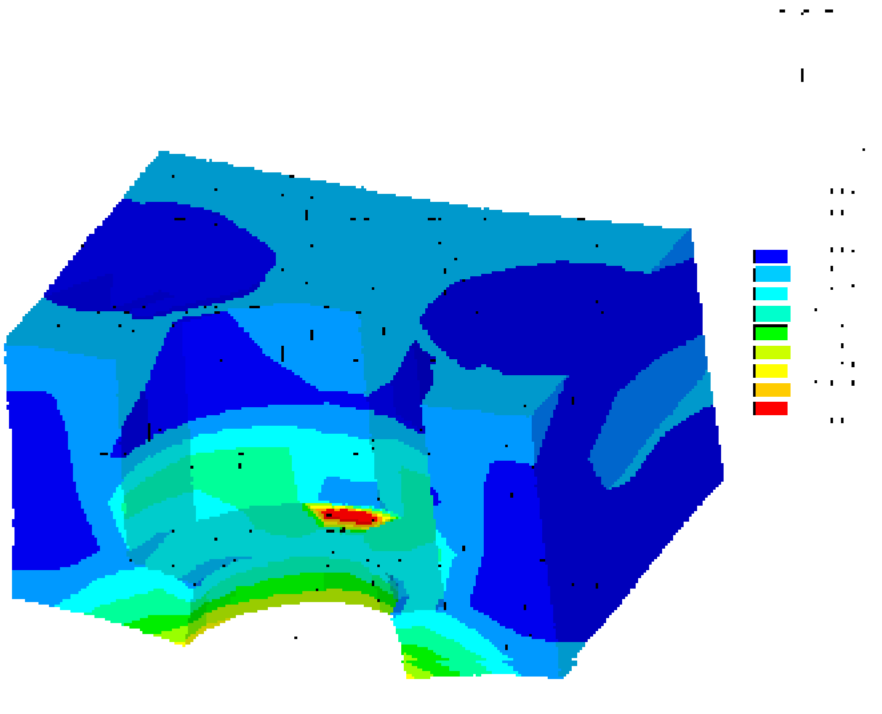

Fig. 2.37: Results of wedge support system FEA top (MPa)

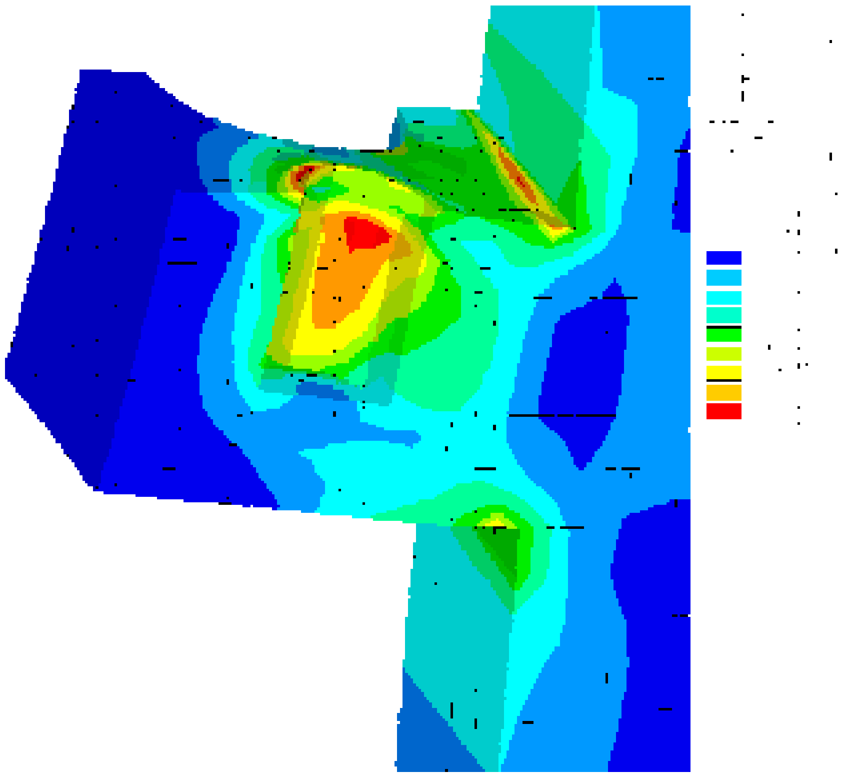

Fig. 2.38: Results of wedge support system FEA bottom stress (MPa)

Table of Contents

2.12 BARREL ASSEMBLY

2.12.1 Overview, constraints, specifications

The HCAL barrel consists of two halves, HB+1 and HB-1 each weighing approximately 465 metric tonnes (510 English tons) each. The final assembly of these halves must reside within a dimensional envelope specified by the parameter drawing. A quarter view of HCAL is given in Fig. 2.39.

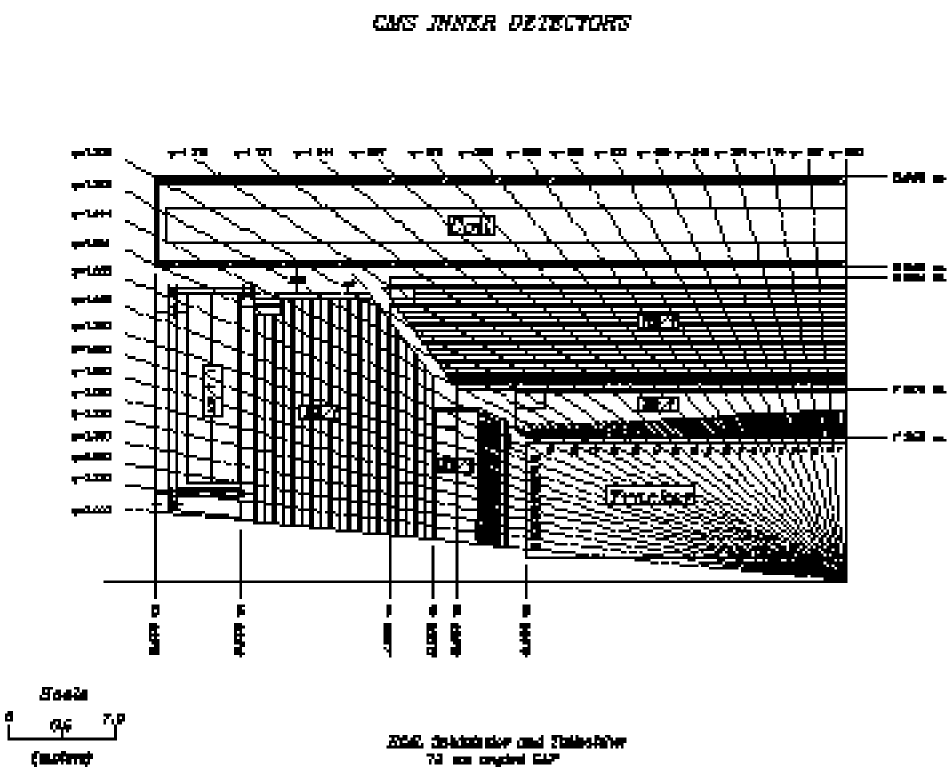

Fig. 2.39: CMS Inner Detector Parameters Drawing

Each barrel half, HB+1 and HB-1, is comprised of eighteen nominally identical wedges. Two of these eighteen wedges are the support or rail wedges. The wedges will be assembled at a factory whose site will be determined by competitive bid.

2.12.2 Assembly scenario2.12.2.1

Factory assembly

Assembly at the factory of HB+1 and HB-1 is a necessary step in the QA/QC process to guarantee a suitable final product. Three months will be allowed for the factory assembly of HB+1, the first HCAL barrel half, and one month for HB-1.

The HCAL barrel wedges will be measured and dimensioned after final machining at the factory. After each wedge has been measured and verified, the wedges will then be "pre-assembled" in a CAD program to determine which order graphically provides the "best" fit when assembled. This order will be primarily dictated by the position of the support wedges in order to ensure that they will be located as close to their ideal position as possible.

Once the computer assembly model is complete, each physical HCAL barrel half will be assembled in its entirety. This procedure will mimic the planned assembly sequence that will take place in the surface hall SX5.

A tolerance study for the purposes of assembly was conducted using the allotted machine tolerances for the wedges. The machined tolerance of the wedge's inner and outer stainless steel plates, and hence its geometrical envelope is +/- 0.15 millimeters (+/- 0.006 inches). The study focused on a worst case scenario in which the inner radius chord of each wedge was +0.15 millimeters over its nominal dimension and conversely the outer radius chord was -0.15 millimeters under. In this case, the last wedge in the assembly must be machined out of nominal tolerances to fit. This case would require three different wedge sets of scintillator; One set for all the nominally identical wedges, and one set for each of the two special machined-to-fit wedges. This is necessary either to avoid gaps in the coverage or simply fit into the absorber structure, depending if the special wedge is oversized or undersized. In this case, the scintillator tile production for the special wedges must wait until both HB's are completed in the factory. The goal is to have all nominally identical wedges to avoid this. Tolerance buildup is indicated in Fig. 2.40.

To account for this variation in the wedges during to the manufacturing process, shims may be added between the wedges to ensure a better overall geometrical agreement with an ideal barrel shape. These shims, if necessary, would be used in wedges where the wedge to wedge connection stress is at a minimum. The support rail wedges would not be shimmed with respect to their neighboring wedges. This is done so as to maintain the best possible contact surface between the wedges in the region where the majority of wedge to wedge contact stress exists. Upon completion, the HCAL barrel halves will be surveyed and checked against the dimensional envelope parameter to make sure they satisfy all QA/QC requirements. Once these specifications have been met, the wedges will be marked in order to allow the procedure to be exactly duplicated in future assembly. This implies that the factory has access or must be provided with the necessary surveying equipment. Each of the barrel halves will then be disassembled for shipping to the temporary storage site at CERN, Building 168. Three months will be allowed for shipping time as the site of the factory is as of yet undetermined.

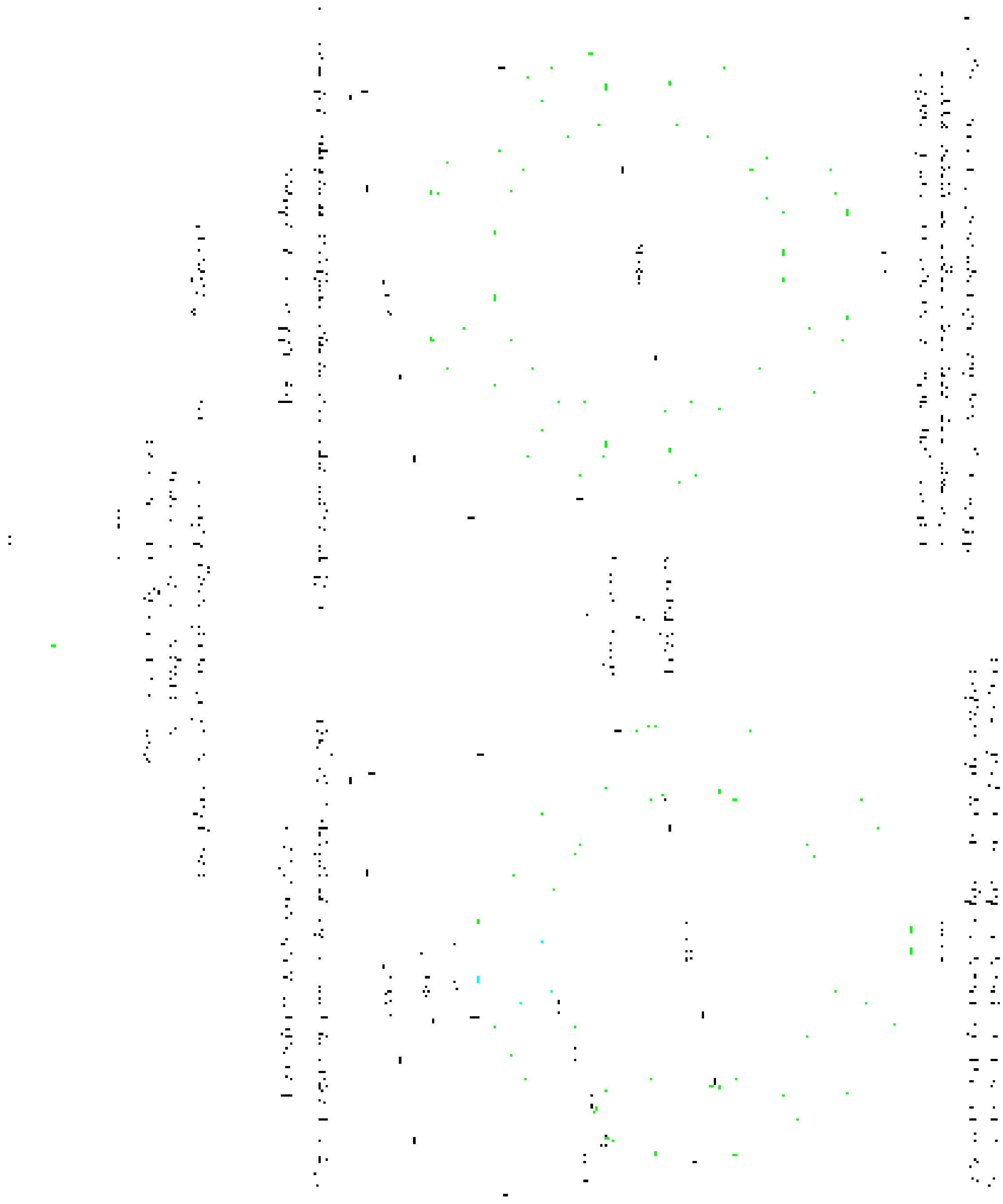

Fig. 2.40: Wedge tolerance buildup .

Building 168 at CERN, see Fig. 2.41, is where the HCAL barrel wedges will be instrumented with scintillator and stored until needed for barrel assembly in the surface hall SX5. The wedges arrive singly at Building 168 by truck. Spacers are then attached to the wedge to make it compatible with a wedge handling fixture. Each wedge weighs about 25.7 metric tonnes (28.3 English tons).

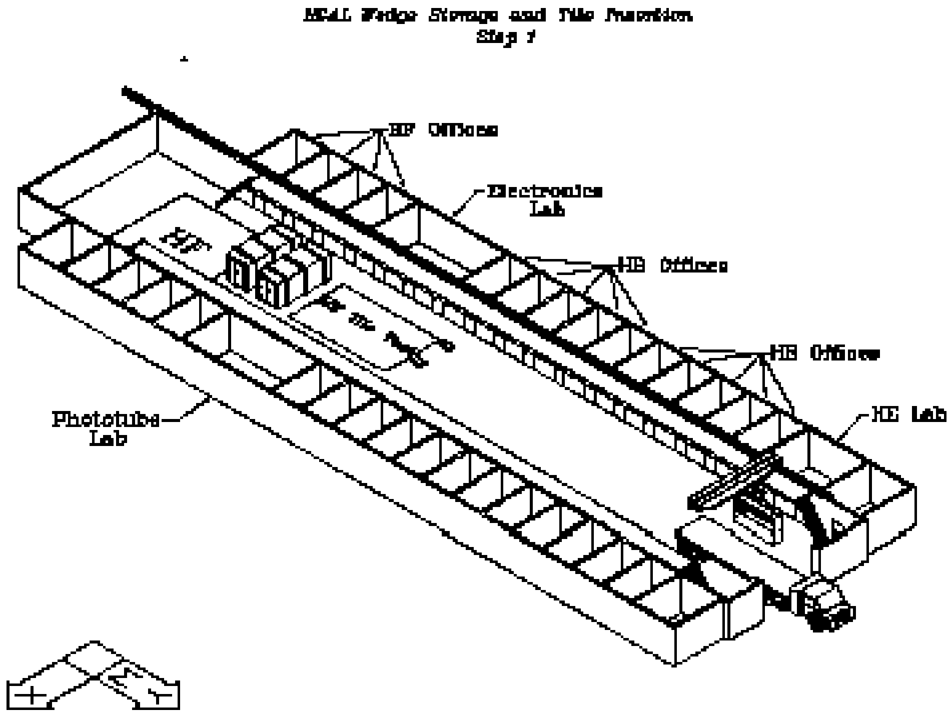

Fig. 2.41: First absorber wedge arriving in Bldg. 168.

A simplified wedge handling fixture is proposed to transport a completed wedge to its storage position on the floor. Since the wedges don't need to be rotated during storage, a less complex lifting fixture may be used to move them. This simplified lifting fixture may also alleviate some of the constraints imposed by the 5 meter hook height of the storage building. The barrel wedges will be stacked on the floor outside diameter side down and two wedges high. This is an acceptable working height for loading the scintillator packages into the wedge's slots. The storage capacity in the building's current layout fits one HCAL barrel half comfortably. Depending on the space requirements of the HE, HF, and HO groups, enough space to accommodate both halves of the HCAL barrel may exist. Currently there is a 9 month interval from the completion of HB+1 and the need of the first wedge of HB-1 at the surface hall SX5. *(See Fig. 2.42 through 2.45 for HCAL Wedge Storage and Tile Insertion Steps 2 through 5.)*

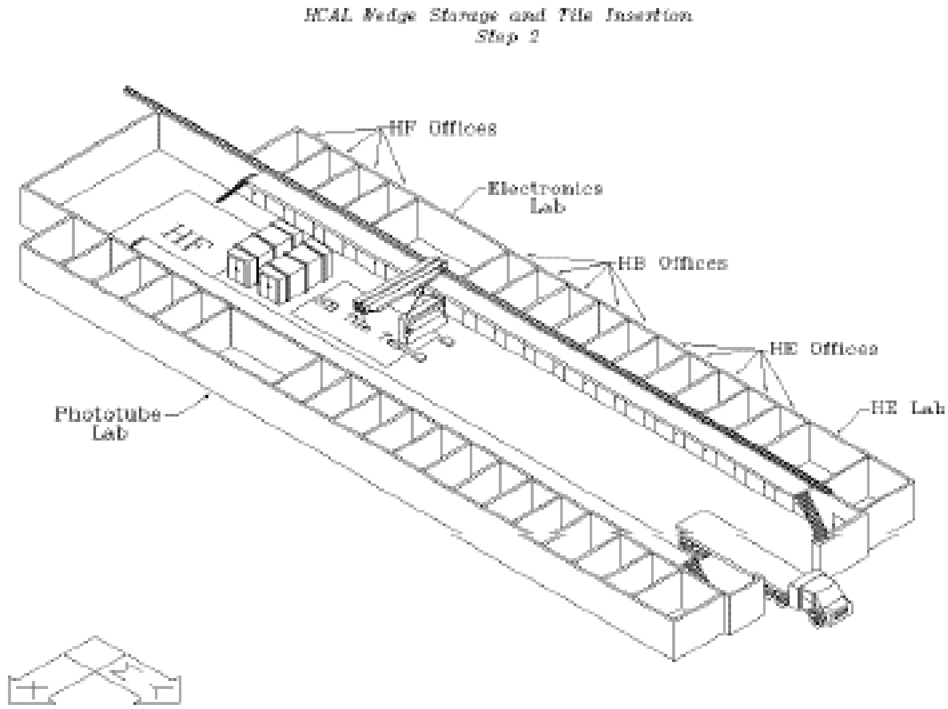

Fig. 2.42: HCAL wedge storage and tile insertion step 2.

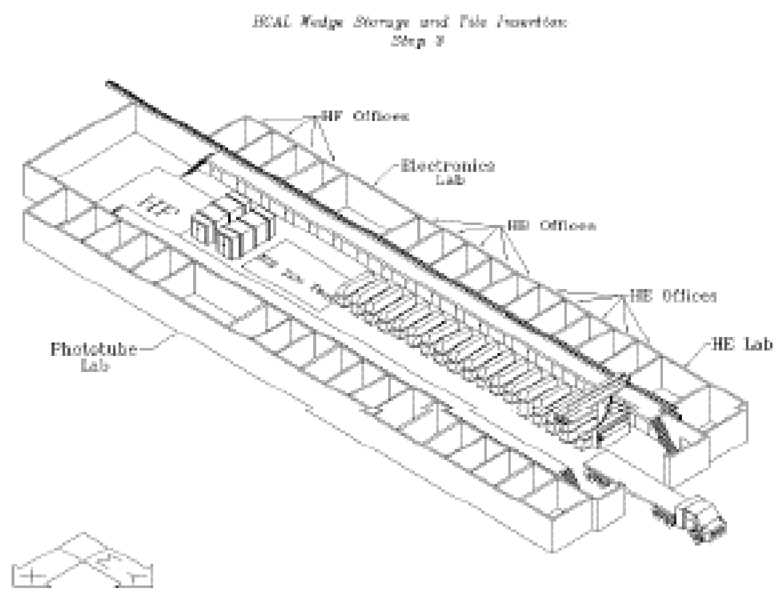

Fig. 2.43: HCAL wedge storage and tile insertion step 3.

The scintillator tiles will arrive stored in two sea containers, each holding one complete half-barrel worth of scintillator. A special lift table will be used to unload the tiles from the sea container and insert them into the stored wedges

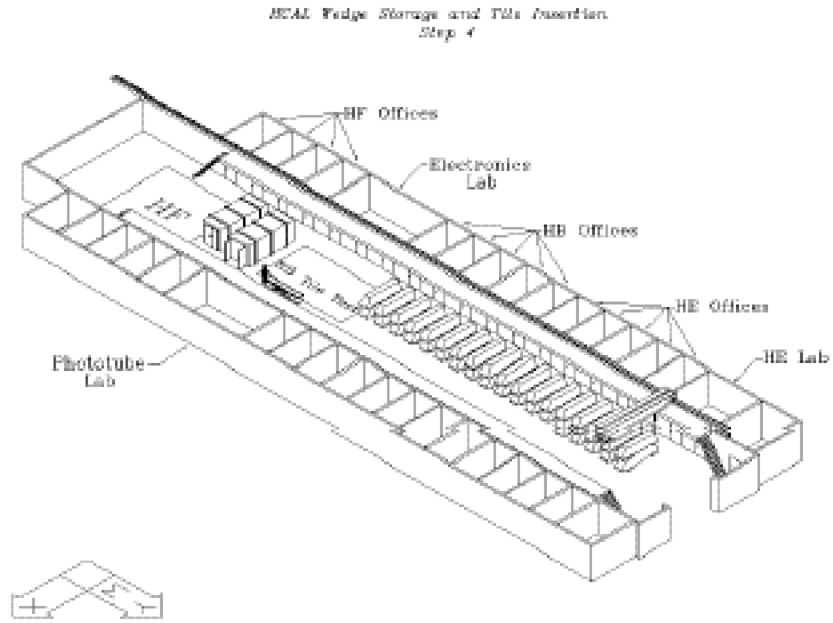

Fig. 2.44: HCAL wedge storage and tile insertion step 4.

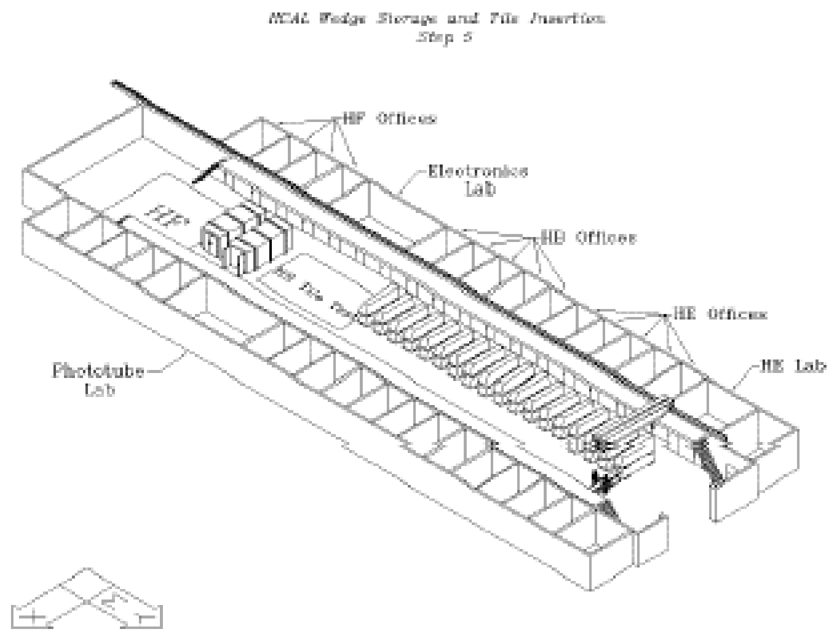

Fig. 2.45: HCAL wedge storage and tile insertion step 5.

Testing and laboratory facilities, set up in Building 168, will be required to test the scintillator tiles upon their arrival and later after they are inserted into the wedges.2.12.2.3

Surface hall assembly

The HCAL Barrel Wedges will arrive individually at the Surface Assembly Building by truck from storage in Building 168. Attached to the wedges while in transit will be the HCAL wedge handling fixture. This fixture may be the ALEPH wedge handling device. The eleven steps for HCAL assembly in the above ground assembly hall (SX5) are shown in Fig. 2.46 through Fig. 2.56 respectively.

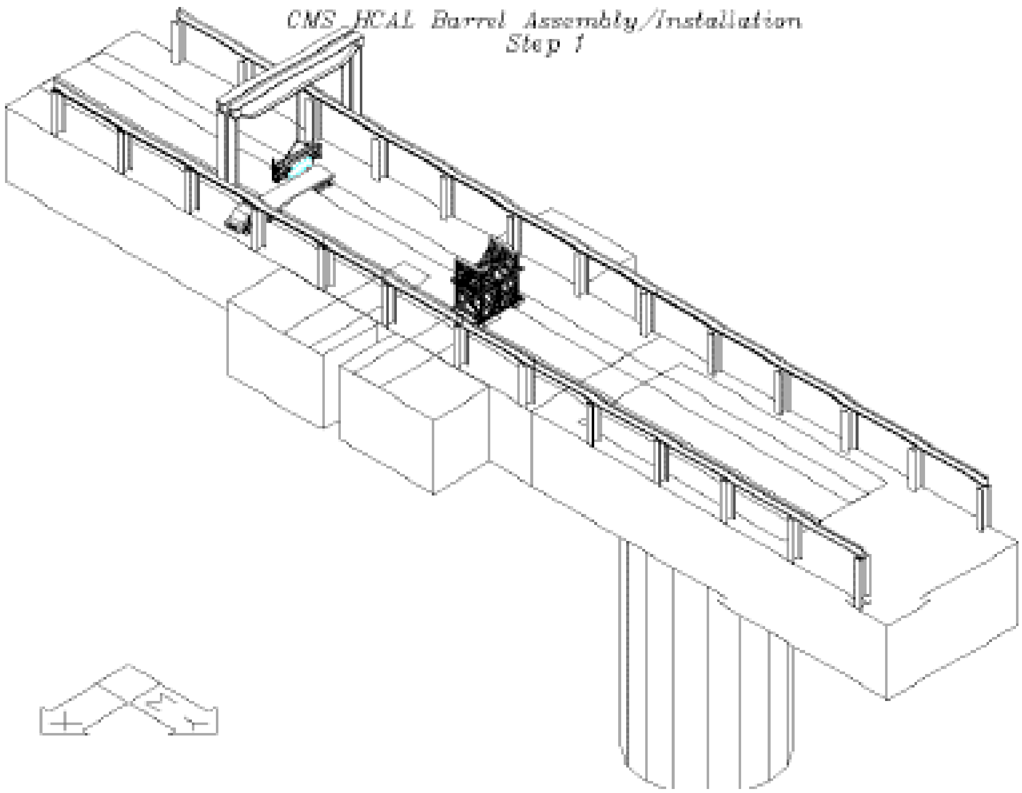

Fig. 2.46: CMS HCAL barrel assembly/ installation step 1.

The first HCAL barrel half, HB+1, has been allotted approximately 8 months of assembly time in the surface hall SX5. The construction time may be shorter depending on the learning curve which was established at the factory trial assembly stage. The HCAL HB+1 barrel cradle will be positioned to proper height before the arrival of the first HB+1 wedge. Currently both halves of the barrel, HB+1 and HB-1, will be assembled at beam height (approximately 8.5 meters). This is due to the fact that the trial insertion of the HB+1 and HB-1 barrels into the vacuum tank precedes the availability of the 2500 tonne gantry crane. Scaffolding will be erected to allow access to the wedge to wedge bolt connections. The position of first wedge is predetermined on the cradle by a set of pins. After lowering the first wedge into position, it will be fixed to the cradle. The first wedge will be surveyed into place and recorded as a fiducial. All subsequent wedges will be assembled with respect to the first wedge. The pins which locate the first wedge will be removed so that they will not interfere with the installation of subsequent wedges. (See Fig. 2.47)

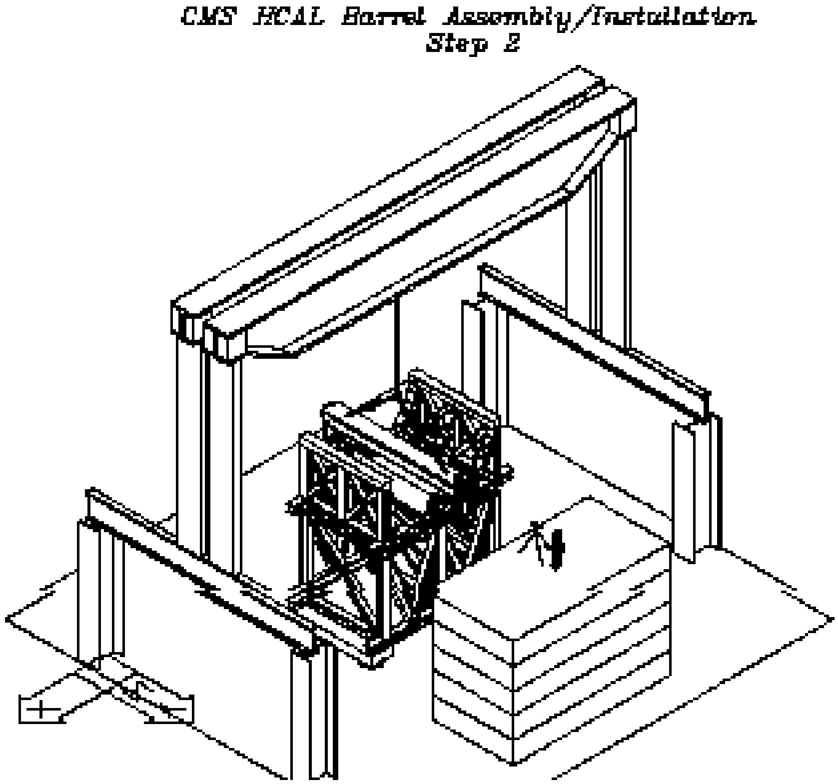

Fig. 2.47: MS HCAL barrel assembly / installation step 2.

Wedges will be assembled in the same sequence as predetermined during the factory trial assembly procedure. The second wedge will be positioned, shimmed if necessary, and then bolted to the neighboring wedge. All inner radius connection bolts and all but a few outer radius connection bolts may be installed and a final survey check performed. Bolts are tightened but with no pre-load at this stage. The outer radius bolt slots that may not be accessed due to cradle interference, will be addressed later. (See Fig. 2.48)

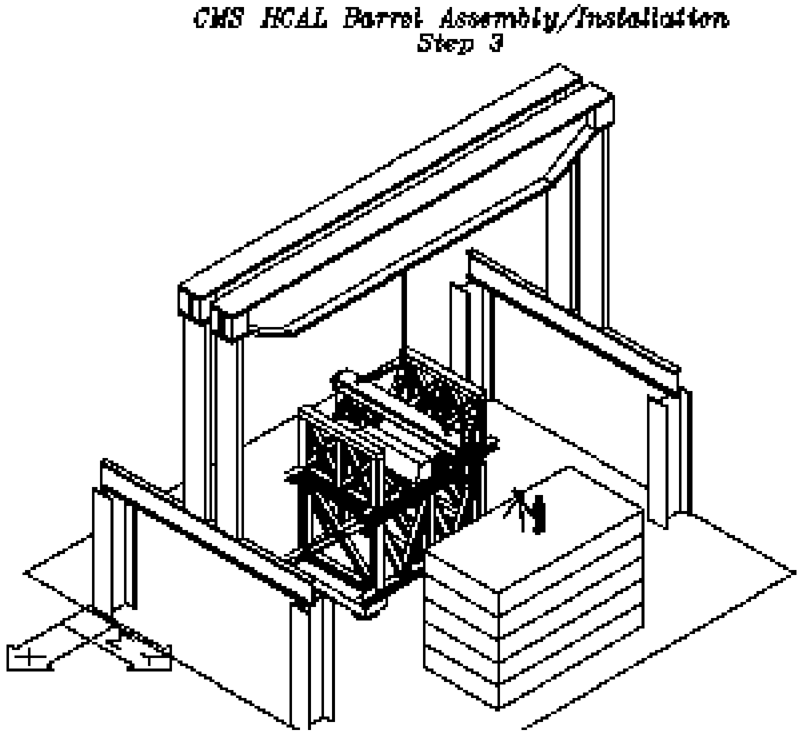

Fig. 2.48: CMS HCAL barrel assembly / installation step 3.

This procedure will continue, alternating sides with respect to first wedge until both support or "rail" wedges are in place. Surveying the rail wedges to verify acceptable dimensions is important before continuing construction. (See Fig. 2.49)

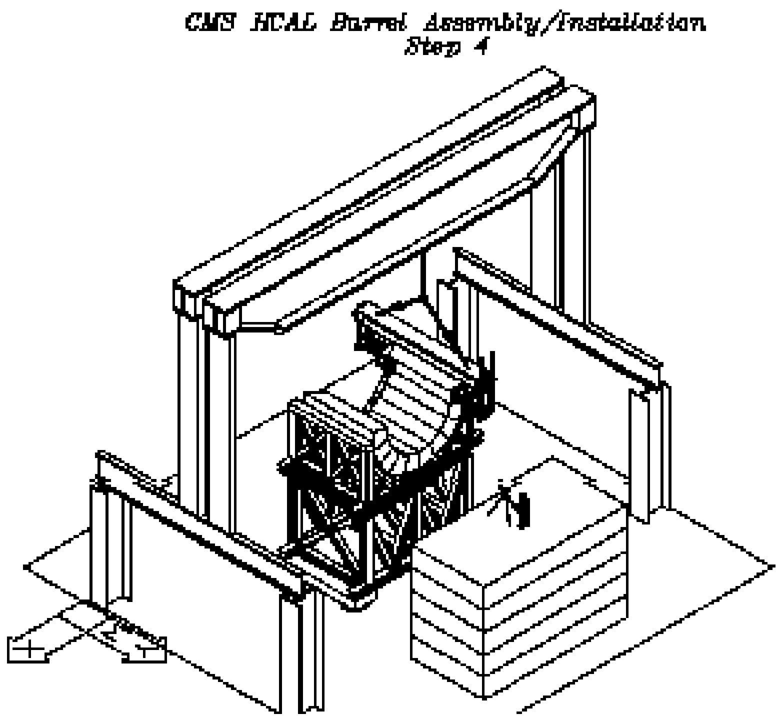

Fig. 2.49: CMS HCAL barrel assembly / installation step 4.

Once the rail wedges are surveyed in place, the assembly spiders are inserted before construction resumes. The two assembly spiders are placed at each end of the barrel and surveyed into the proper location. (See Fig. 2.50)

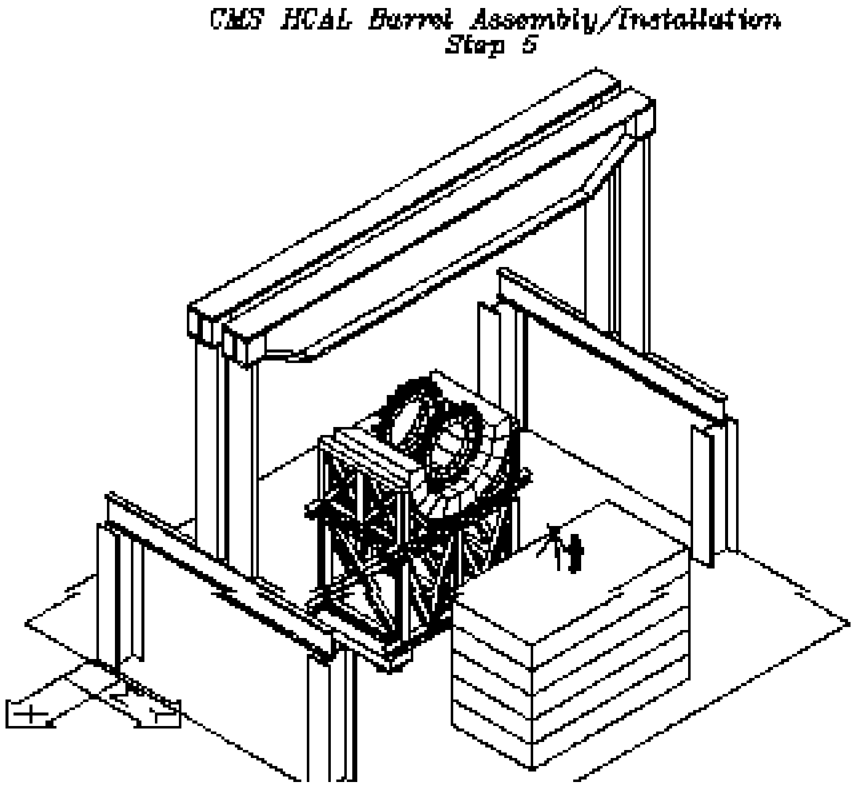

Fig. 2.50: CMS HCAL barrel assembly / installation step 5.

The spider's mechanical actuators are adjusted through the use of an air impact hammer. The position of these actuators with respect to the inner radius dimensional target will be verified by surveying. The spiders will be tied together with connecting rods to ensure lateral stability. Wedge assembly continues alternating from side to side using the spiders to maintain proper inner geometry and counteract the gravity load. (See Fig. 2.51)

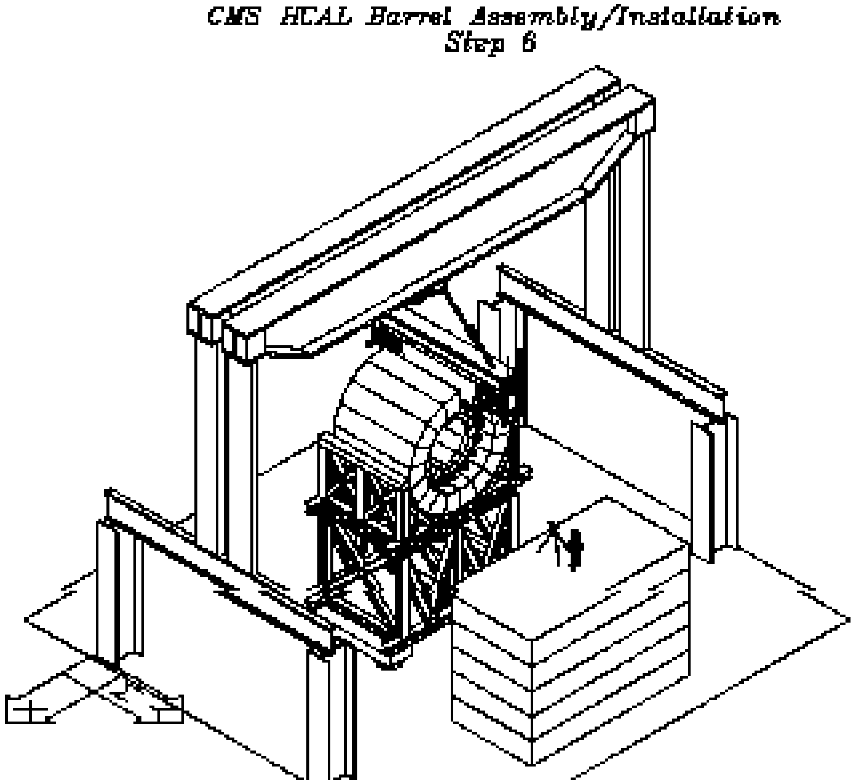

Fig. 2.51: CMS HCAL barrel assembly / installation step 6.

Insertion of the last wedge in a half barrel may require a different approach than that of the others. If needed the spiders may be used to jack open the barrel to force the gap for the last wedge to enlarge. The necessity of this procedure will already have been determined in the factory trial assembly. As an alternative, allowing the spiders to remain at a fixed inner radius may be desirable. In this case, auxiliary spreader bars may be introduced. The spreader bars will force the remaining wedge gap to enlarge to facilitate the insertion of the last wedge. This gap could give as much as 2.2 millimeters of lateral clearance. Once the last wedge is positioned at the correct inner radius by the spider and bolted to its neighboring wedge, the spreader bar can be relaxed to allow the final gap to close. Once the final gap has closed and the wedge to wedge connection is made, the half barrel assembly will be ready for its remaining connections to be bolted. (See Fig. 2.52 through Fig. 2.54, CMS HCAL Barrel Assembly / Installation Steps 7-9).

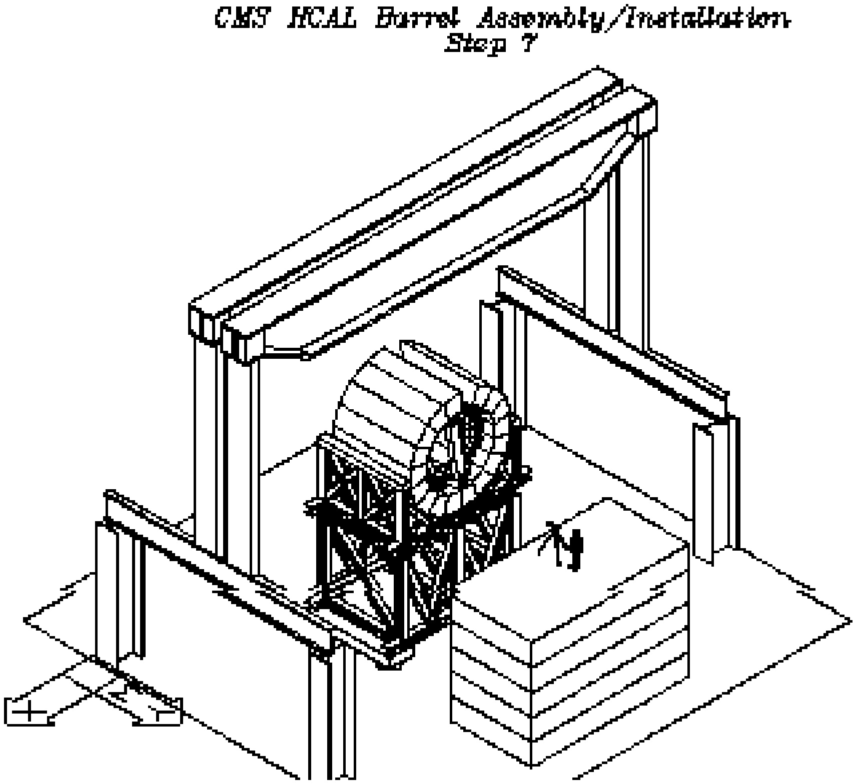

Fig. 2.52: CMS HCAL barrel assembly / installation step 7.

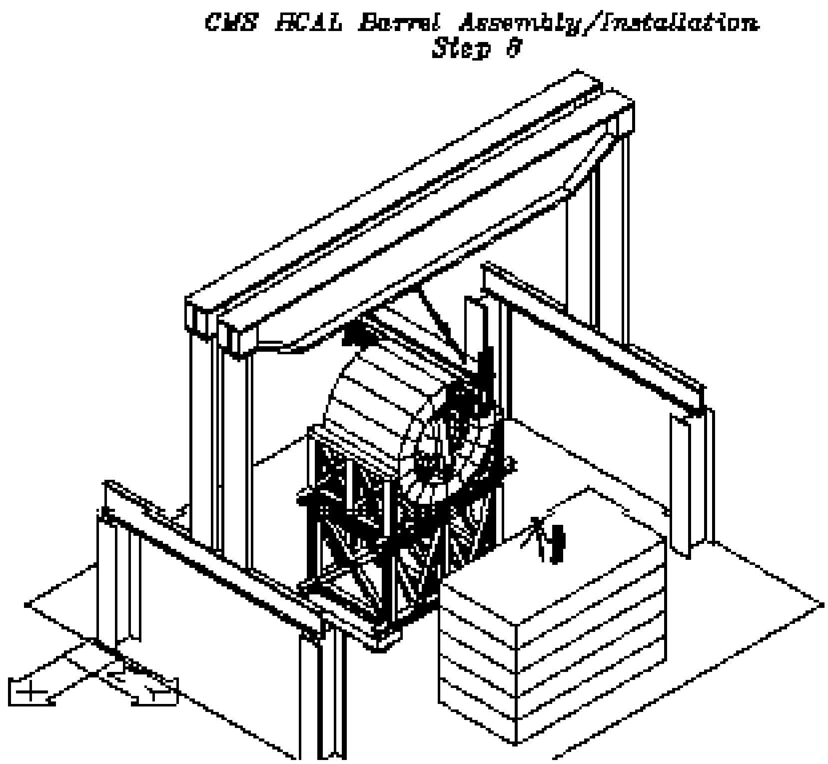

Fig. 2.53: CMS HCAL barrel assembly / installation step 8.

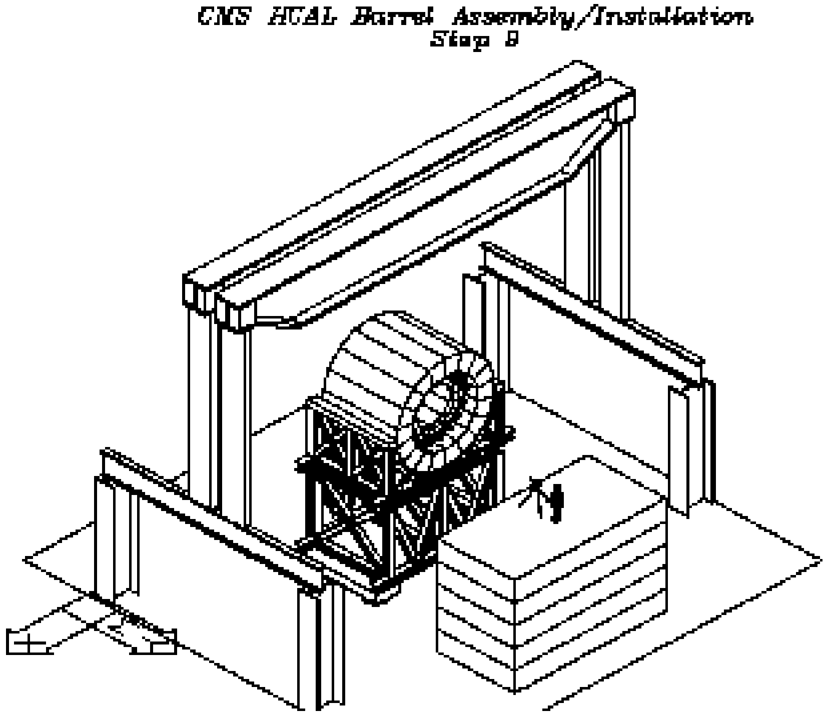

Fig. 2.54: CMS HCAL barrel assembly / installation step 9.

The lower barrel wedge supports will be retracted on the cradle so that barrel will rest on the rail system. The barrel will then be translated on the rails far enough to allow access to the remaining outer radius bolt slots and insert bolts that were inaccessible due to the cradle. Once all bolts are in place a final tightening sequence will be applied to achieve the desired pre-load. If necessary the barrel will then be translated back to its original position to tighten the last bolts. The barrel will be lowered onto the lower cradle wedge supports and stored in this position.

The completed HB+1 half barrel will be moved into its storage alcove in the surface hall SX5. The HB storage alcoves are 17 meters long, 10 meters wide, and 12 meters high. HB+1 and HB-1 will fit into their alcoves with the aid of removable sections of Surface Hall crane rail. The length of the storage alcoves allows for the possibility of scintillator insertion and removal. This is important in the event that the decision is made to insert the scintillator tiles after the absorber structure has been assembled. The alcoves need to be set up for scintillator testing to verify that the tiles survived the assembly process.

The same assembly sequence applies to HB-1 which will take place approximately 9 months later. The five weeks of time allotted for HB-1 assembly is significantly less than for HB+1. Regardless of the prior experience with HB+1, it is felt that this assembly schedule will require additional shift work to complete. (See Fig. 2.55 CMS HCAL Barrel Assembly / Installation Step 10).

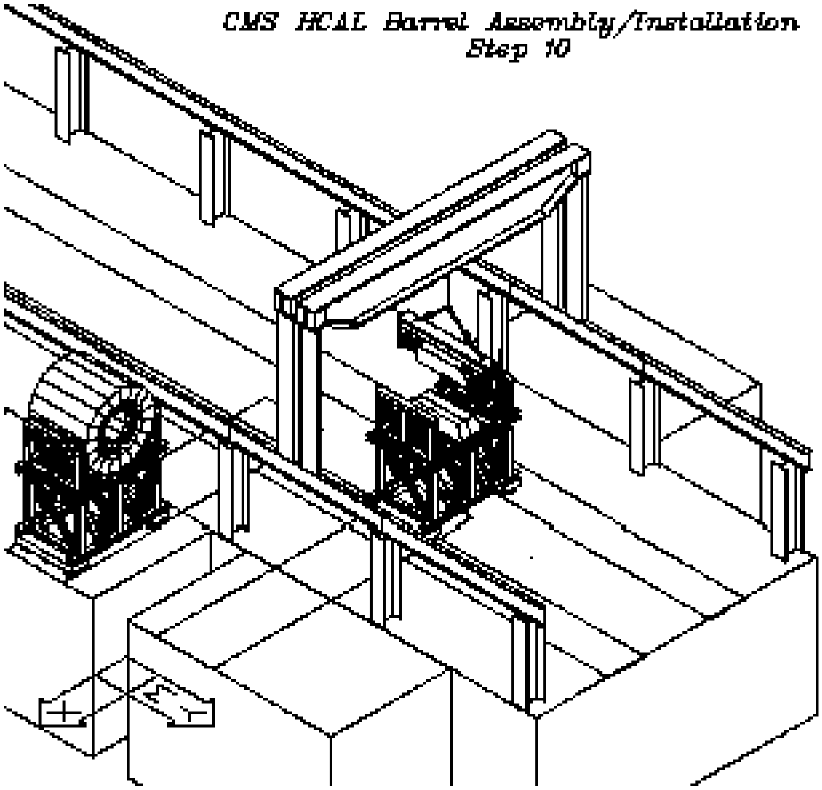

Fig. 2.55: CMS HCAL barrel assembly / installation step 10.

Before lowering the HCAL barrel halves into the Underground Hall, a trial insertion of HB+1 and HB-1 into the vacuum tank will take place. HB+1 and HB-1 will be moved from their storage alcoves and positioned on either side of the central iron barrel ring and the vacuum tank. Each set of HB cradle rails will be lined up with the corresponding rails in the vacuum tank. Once the rails have been aligned, the cantilevered ends of the vacuum tank will be supported to minimize deflection during HCAL Barrel insertion. Each barrel half will be pulled into the vacuum tank via a cable system operating at the level of the rails.

Insertion of the two HB barrels inside the vacuum tank will strain the vacuum tank to its final shape, allowing the adjustment of the position of the coil with respect to the iron yoke during the surface magnetic test (see chapter 18 of the Magnet TDR). In addition, after the trial insertion is complete the deflection of vacuum tank and HB's will be measured. This is to allow for the shimming of the HB supports upon removal so that upon insertion in the Underground Hall will yield a more concentric HCAL barrel shape. (See Fig. 2.56 CMS HCAL Barrel Assembly / Installation Step 11)

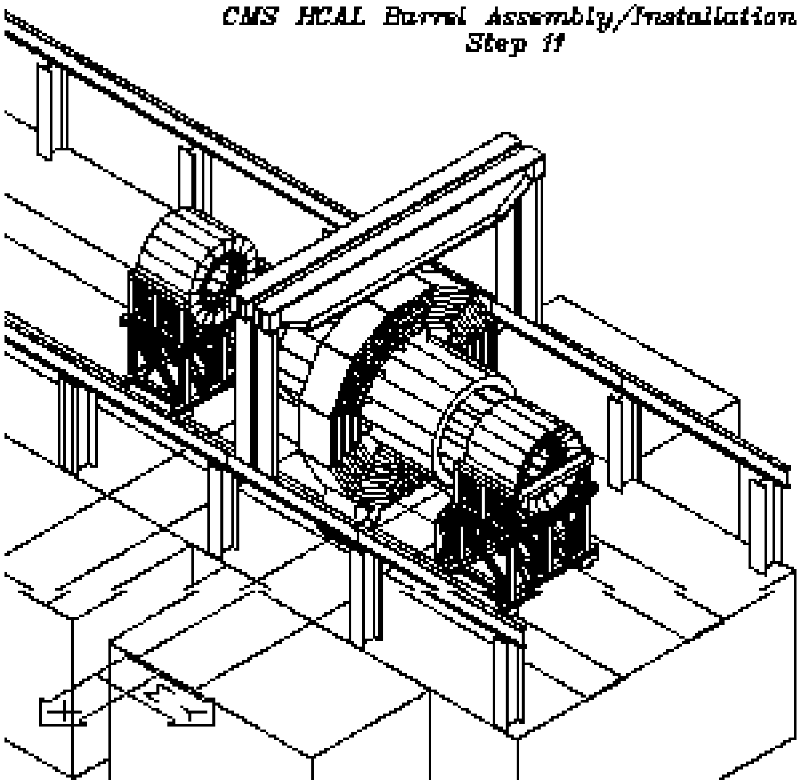

Fig. 2.56: CMS HCAL barrel assembly / installation step 11.

2.12.3 Tooling design

HCAL Barrel Installation Fixture

During the HCAL barrel installation, the cradle in which each half-barrel sits will be securely anchored to the central iron ring and vacuum tank. This will prevent any tipping of the cradle due to the moments experienced during barrel insertion. A stiffback, similar to a large I-beam will be fastened to the opposite end of the vacuum tank at the level of the barrel rails. Two come-alongs will be attached to the stiffback and will be used to pull the barrel into the vacuum tank. A total of 60 tonnes will be required to insert the barrel into the vacuum tank. This value assumes a friction coefficient of 0.1 between the barrel support pads and the rail and also take into account the 1.23% incline of the hall into consideration. Although it would be desirable to pull each come-along will equal force, this is unlikely to occur in reality. Therefore this implies that both come-alongs will each be rated for at least 60 tonnes, so that each is capable of initiating movement of the barrel mass. The stiffback will transfer this load into the edge of the vacuum tank.

Cryostat Support Post

The vacuum tank support post's role is to limit the deflection caused by the cantilever load of the HCAL half barrels during insertion. A set of triangulated I-beams will support the vacuum tank at both ends, under the end flanges.

OPAL Wedge Rotating Fixture

The OPAL wedge rotating fixture or similar device will be used to orient the HCAL barrel wedges for half barrel assembly. The OPAL wedge rotating fixture is designed in such a manner as to be wedge length independent. It has two independent stands to which the ends of the wedge connect via an attachment fixture. Each stand has a bearing and bearing housing providing the rotational adjustment. The wedge attachment fixture is a plate which is temporarily bolted and pinned to the face of the wedge in the region of the inner and outer radius stainless steel support plates. A special fixture will be designed for the 53 degree chamfered end of the wedge so that the attachment fixture plates will be parallel to each other.

A rod with a flange protrudes from this plate at the calculated center of gravity of the wedge. Once the end flange fixtures are secured to the wedge, the crane will lift the wedge to the height of the two stands where the rod end flange will be bolted to the stand's bearing flange. The wedge is now set up for rotation. The wedge may be rotated manually or with a bit of mechanical assistance to the desired angular orientation. Predetermined stops at the desired angles will have been drilled into the stands back plate and been fitted with removable pins. The wedge is then lifted vertically by four support points, two at each end connected by a spreader bar. The wedge is now in the "rough" angular position required for assembly. One support point on each end will be held by a remotely adjustable length link. These two support links or straps will have small degree of vertical adjustment capability in order to provide fine angular adjustment during assembly.

HCAL Barrel Cradle

The two HCAL barrel cradles will serve as the assembly and storage platforms for HB+1 and HB-1. Additionally, they will serve as the insertion interface for the vacuum tank and the barrel halves. (See Fig. 2.57 HCAL Barrel Cradle.)

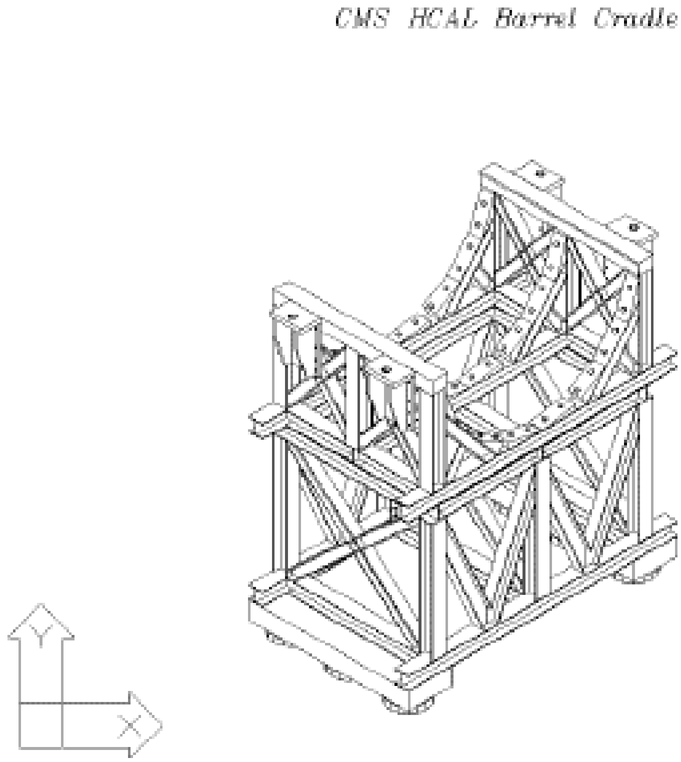

Fig. 2.57: HCAL barrel cradle.

The HCAL barrel cradle will be designed to support each of the wedges below the rail wedges individually during barrel assembly. Each of these wedges will be supported by four independent mechanical actuators which will be surveyed into position before the wedges are attached to them. Mechanical spiders will be use to complete the rest of the barrel above the rail wedge. Once the barrel is completed, the cradle rails on which the support wedges rest will be raised sufficiently so as to support the entire weight of the HCAL barrel half. The cradle rails will have vertical and lateral translation capabilities. In addition, pitch along the beam axis will be incorporated to allow for any angular misalignment with the vacuum tank rails in this plane. This angular misalignment may pre-exist or be a result of the load transfer during insertion of the barrel halves into the vacuum tank.

Four 136 tonne (150 English ton) mechanical actuators, two for each rail, will provide the vertical adjustment of the cradle rails. The actuators have a 36:1 worm gear ratio so will be self-locking when under load. Each rail will be driven by a stepper motor which will control the two actuators associated with that rail. The actuators and the motor are connected via a coupling system that allows synchronous movement of the actuators. In the event that a pitch correction is required, the transmission shaft to one actuator contains a removable flexible disc coupling. Once this coupling is removed, it allows independent adjustment of the other actuator. This actuator will be connected to the cradle by a pivot, and has a constant velocity joint incorporated in its transmission shaft to allow for the angular displacement of the shaft during the pitch adjustment of the rail. The conceptual design for the rail adjustement is given in Fig. 2.58.

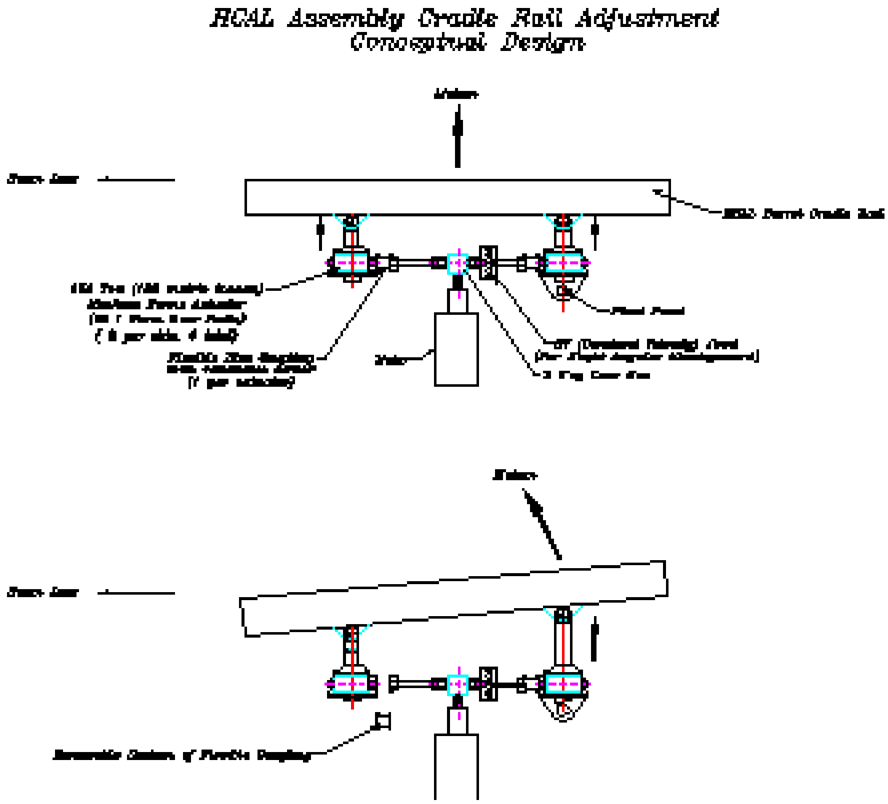

Fig. 2.58: HCAL assembly cradle rail adjustment conceptual design.

The lateral adjustment of the rail is required to accommodate the tolerances of the vacuum tank construction and the ultimate position of the rail welded to it. The entire vertical adjustment system and rail will be resting on an adjustable skidpad with respect to the cradle. The lateral adjustment will be performed by a manual screw mechanism and locked in a similar fashion.

The end of the cradle rails will be tapered and match correspondingly tapered rails in the vacuum tank as shown in Fig. 2.59. The taper is designed to facilitate the smooth transition of the load by the barrel rail support pads from the cradle rails to the vacuum tank rails. At least one full barrel support pad will be in contact will both rails over the transition region at all times. This feature will aid in maintaining rail to rail alignment. The edges of the rail will be chamfered in the transition region to further improve the forgiveness of the rail mating and to aid in the longevity of the Teflon coated barrel support pads.

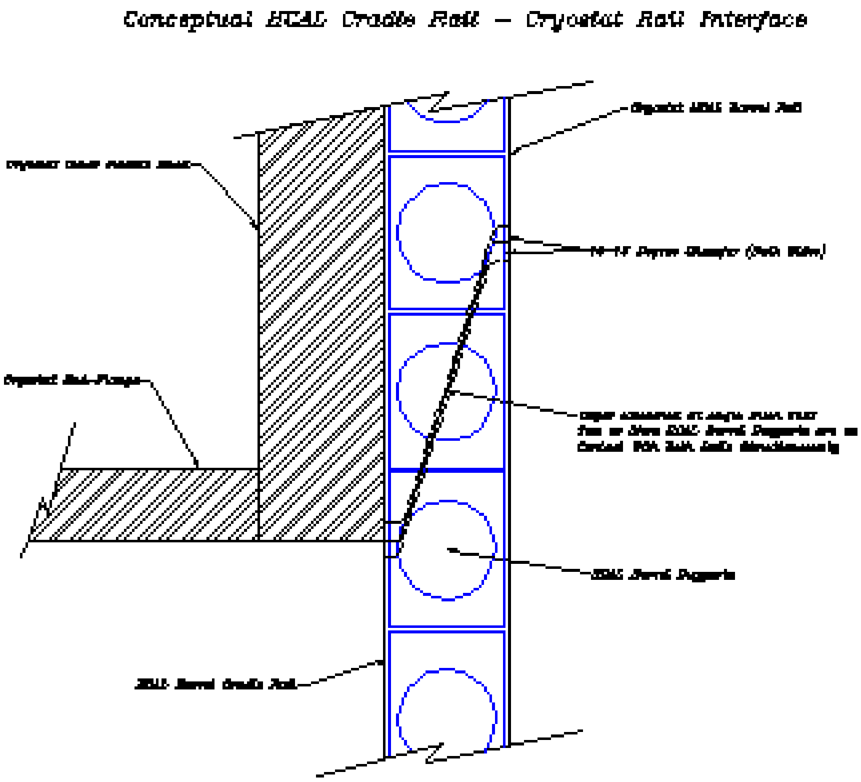

Fig. 2.59: Cradle Rail End Detail.

The entire HCAL barrel cradle moves on a series of airpads which are connected to the bottom of the support stand. These airpads allow the cradle to translate in any direction and move over non- smooth surfaces such as rough concrete (See Chapter 10 of Magnet TDR).

The HB+1 cradle must be constructed in such a fashion as to allow it to be dismantled into sections not exceeding 3.5 meters wide by 6.0 meters long by 7.0 meters high. This requirement is dictated by the size of the transfer tunnel through which the sections must pass in order to be removed from the Experimental Hall to the surface. Once the central iron barrel ring and vacuum tank are installed in the Experimental Hall, they effectively block passage to the main access shaft PX56 leading to the surface hall SX5. The transfer tunnel will help alleviate this restriction by providing passage to the auxiliary access shaft PM54. The HB+1 cradle will be fabricated of several sections which are bolted together each section having a size which does not exceed the transfer tunnel limits. It is not clear at this point if the HB-1 cradle will be constructed in the same manner. The HB-1 cradle does not have the same restrictions imposed on it as it will be accessible by the surface hall SX5 cranes without having to go through the transfer tunnel. Due to the increased cost of a sectional and bolted design, the HB-1 cradle may simply be a monolithic welded structure but still retain the adjustment capabilities for barrel assembly.

HCAL Barrel Assembly Spiders

Assembly spiders are fabricated from a double collar of steel box beam to which is attached 18 screw actuators, as illustrated in Fig. 2.60.

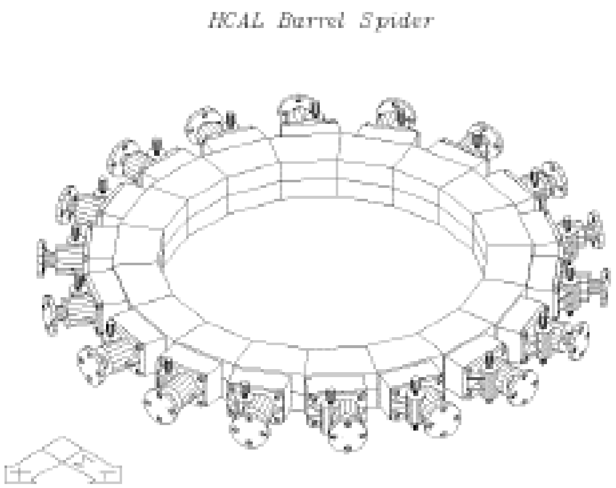

Fig. 2.60: HCAL Barrel Spider

The box beams are American standard 12" x 6" x 0.5" (305mm x 153mm x 13mm) rectangular structural tubing. The double collar will be continuously welded along its seam. The actuators are adjusted with an air impact tool. It takes 48 revolutions of the actuator's input shaft for a 25mm raise. Each actuator is rated at 32 tonnes (35 English tons) The ratio of the actuators was selected such that they allow for fine adjustment and are self-locking under load. Since a pair of spiders will be used for the barrel assembly, the combination will have 2.5 times the rated load capacity for handling a wedge.

HCAL Barrel Assembly Spreader Bar

The HCAL barrel spreader bar consists of one 45.5 tonne (50 English tons) capacity screw actuator and one manually adjustable screw with pad placed at opposite ends of a W610 x 155 I-beam (W24 x 104 US standard). The spreader bar is shown in Fig. 2.61.

Fig. 2.61: HCAL barrel spreader bar.

A preliminary finite element analysis was done to determine the performance of the spreader bar. Under full load (45.5 tonnes), an overall displacement of 2.5 mm (0.98 inches) was realized. The main component of translation we are interested in for assembly is the one in the lateral or "x" direction according to the model.

This component resolved to be about 2.2 mm which will be used as extra clearance for installing the last wedge. The clearance allows for an additional 6 mm of vertical travel for the last wedge.

The barrel is modeled such that the lower half (below the rail) is supported by the cradle and the upper half (above the rail) is free. The localized stress induced by the spreader bar in the wedge where the force is applied is reasonable. The stress here peaks at 106 MPa (15.37 ksi) which is artificially high due to the localized application of the load. In reality one can expect lower stress values.

The reaction force due to the spreader bar load is greatest at the rail support point with a maximum value of about 78 kN (17500 lbs). Again this value is artificially high because of its localized nature. Nevertheless, it is still an acceptable value for the rail.

2.13 BARREL INSTALLATION

2.13.1 Overview, constraints, specifications

The greatest constraint for HCAL barrel installation is the project schedule and timeline. It requires that HB+1 is complete and lowered into the Underground Hall before the central iron barrel ring and the vacuum tank are lowered.

2.13.2 Installation scenario

Once the HCAL barrel halves are ready to be lowered into the Underground Hall, special lifting fixtures will be attached to the sides of the cradles. Since the HCAL barrel weighs around 465 tonnes (510 English tons) and the capacity of the gantry crane is 2500 tonnes, only half of the gantry's cables will be used to lower the HCAL barrels. (See Fig. 2.62 and Fig. 2.63 CMS HCAL Barrel Assembly / Installation Steps 12-13).

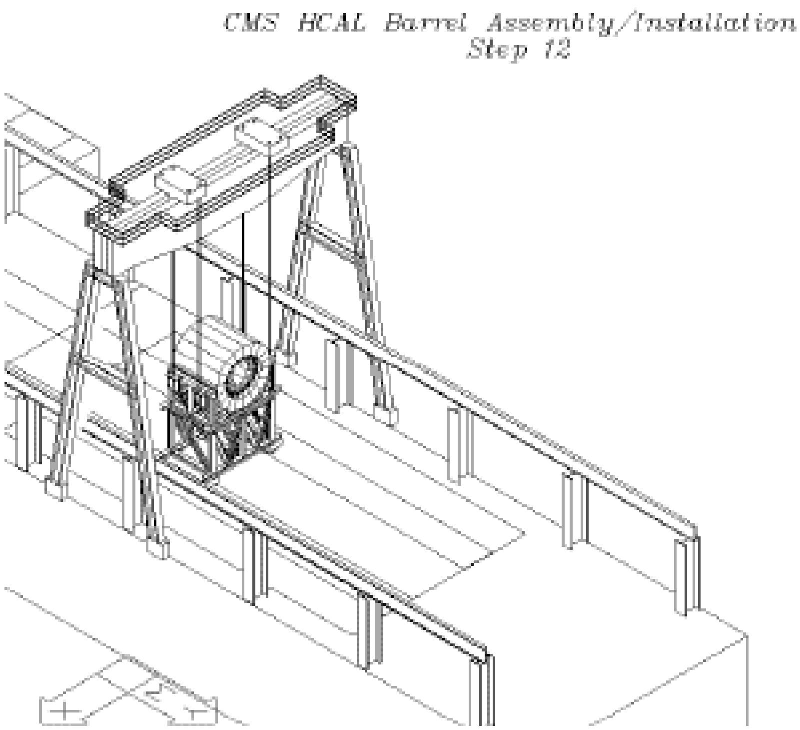

Fig. 2.62: CMS HCAL barrel assembly / installation step 12.

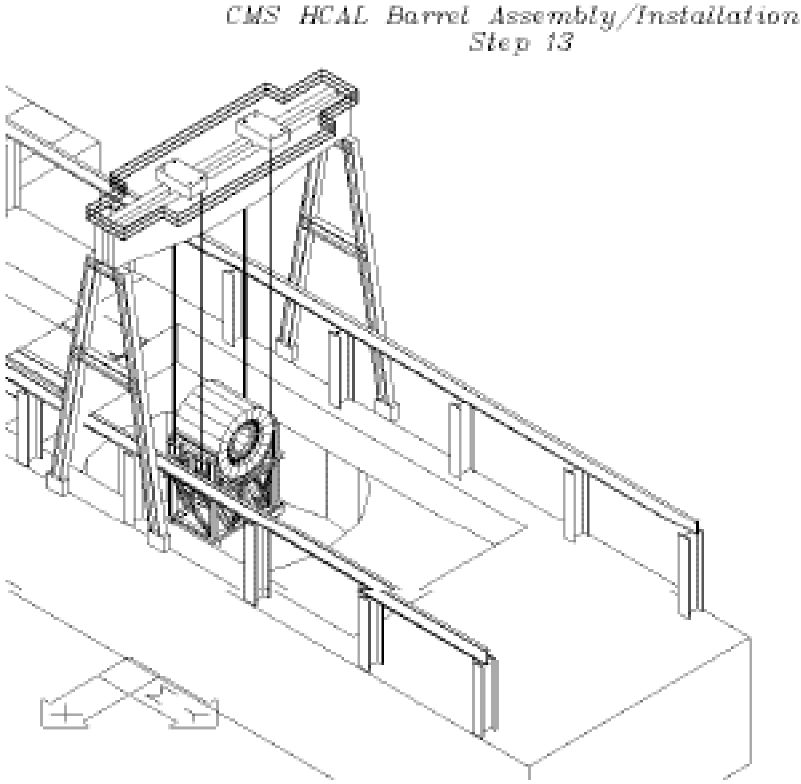

Fig. 2.63: CMS HCAL barrel assembly / installation step 13.

The HCAL barrel will be lowered into the Underground Hall with its lower half supported by the cradle. This will be done to provide an additional margin of stability during the gantry crane rigging procedure. The assembly spiders will remain in the barrels during the lowering process as well. Once HB+1 has been lowered into the Underground Hall, the barrel half must be raised in its cradle and supported on its rail system. The remainder of the outer layer of barrel scintillator will be installed at this stage before insertion into the vacuum tank. Because this procedure is on the critical path for assembly, it is an important step to be included in the Underground Hall activity timeline. The shimmed and fully instrumented barrel will then be inserted into the vacuum tank via the cable come-along device that was used in the surface hall SX5.

The assembly spider will remain in the half barrels during their insertion into the vacuum tank and will be removed upon proper placement of the half barrel. The removal of the spiders will be accomplished by selectively retracting the mechanical actuators and placing a roller bearing surface on the pads. The bearing pads will then be extended back to the inner diameter of the half barrel to provide a rolling surface to facilitate removal.

Once HB+1 has been installed in the vacuum tank, dismantling of the HB+1 cradle may begin. The pieces must be less than 3.5 meters wide, 7 meters high, and 6 meters long so that they will fit through the transfer tunnel. The pieces will be transported through the transfer tunnel to a location under crane coverage from the surface hall SX5 through the auxiliary access shaft PM54. The pieces of the HB+1 cradle will then be lifted from the Underground Hall to be disposed of in the surface hall SX5. The pieces of the cradle should not exceed 80 tonnes.

HB-1 will be lowered into the Underground Hall during the time that HB+1 is being inserted into the vacuum tank. HB-1 will be installed in the vacuum tank in similar fashion to HB+1. The HB-1 cradle will be able to be removed through the main access shaft PX56 in its entirety. If the HB-1 cradle weighs more than 80 tonnes, the 2500 tonne gantry crane may be used to bring it up to the surface hall SX5.

2.14 ECAL SUPPORTS AND ECAL SAMPLING TILES

The ECAL consists of 36 "supermodules", one for each HCAL wedge. The supermodule will be supported by the front plate of the HCAL wedge. The ECAL has a 2 cm thick stainless steel back plate. Anti-friction pads attached to the stainless steel plate provide a "4-point" suspension for the ECAL. This suspension minimizes the distortion on ECAL due to its attachment to HCAL.

It is anticipated that the HCAL half-barrels will be installed into the cryostat in the surface assembly building where they will be surveyed. The survey will be used to make correction machining on the spacers of the supermodules to insure that they are in the right locations after installation onto HCAL.

Analysis of test beam data has shown that the combined ECAL + HCAL has a large e/h which degrades the combined calorimeter linearity and energy resolution. It has been found that making a separate readout immediately behind the ECAL (labeled H1), and using the ratio of H1/Htotal (Htotal is defined to be the sum of H1 plus the remaining layers in the HCAL tower, labeled H2) can largely correct for this problem. Therefore a scintillator readout immediately behind ECAL is required. Fig. 2.64 shows the placement of this scintillator layer. It is anticipated that the ECAL supermodule will be attached to HCAL, and then the scintillator will be installed.

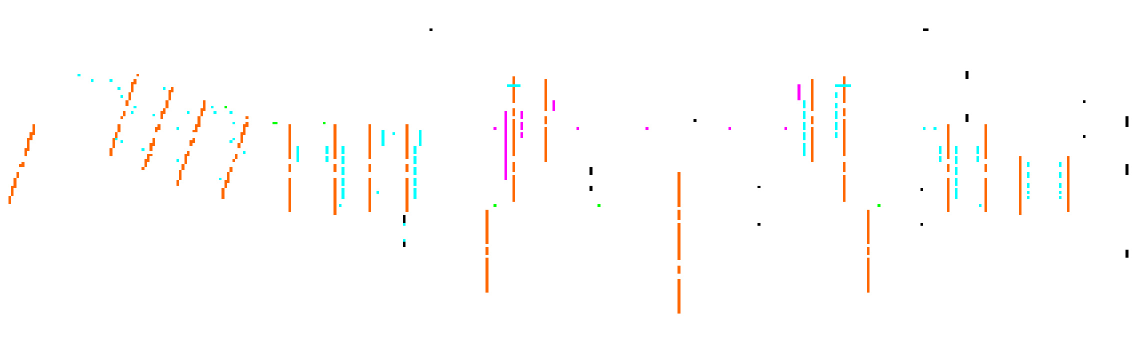

Fig. 2.64: Detail of ECAL attachment to HCAL. Also shown are the scintillators between HCAL and ECAL. Dimensions in mm.

2.15 TRACKING SUPPORTS

The tracker is connected to the HCAL barrel through the cradle, Fig. 2.65. The cradle is connected to the inner stainless steel plates of the barrel by four brackets shown on each end of the cradle. The brackets sit in z beyond the extent of ECAL. If the ECAL supermodule trapped by the bracket needs to be removed, temporary tracker supports will be installed, and the permanent bracket will be removed. Thus all ECAL modules can be accessed without removing the tracker.

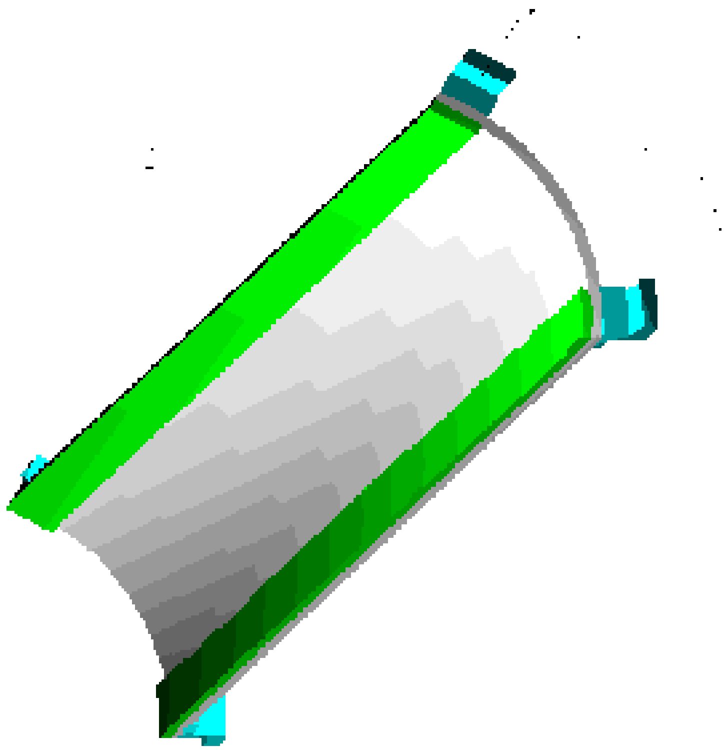

Fig. 2.65: Tracker support cradle.

Table of Contents

SAMPLING TILES 1732.15 TRACKING SUPPORTS 174

3. HE MECHANICAL DESIGN AND CONSTRUCTION

3.1. OVERVIEW AND REQUIREMENTS

3.1.1 Overview

The endcap hadron calorimeter (HE) covers a rapidity region between 1.3 and 3.0 with good hermiticity, good transverse granularity, moderate energy resolution and a sufficient depth. A lateral granularity (x) was chosen 0.087 x 0.087. The hadron calorimeter granularity must match the EM granularity to simplify the trigger.

The basic requirements of the HE design are the following:

- nonmagnetic material for absorber;

- minimal of the absorber to have maximum absorption length;

- total calorimeter length about 10 to provide sufficient containment of high energy jets;

- sampling must be adequate to the required energy resolution;

- minimal dead zones to measure missing energy.

The basic structure of the endcap calorimeter is the same as for the barrel calorimeter. A crystal electromagnetic calorimeter (EE) of 27 X_0 is placed in front of HE. The total depth of the HE calorimeter (not counting the electromagnetic calorimeter) is about 10 absorption lengths (19 active layers). The absorber sampling thickness is 8 cm. The absorber material is brass (90% Cu+10% Zn), the front and back plates are made of stainless steel to increase strength. The absorber plates are bolted together to form a single monolithic structure, with gaps for scintillator insertion. This structure is conceptually similar to the barrel structure, although differing in engineering details because of the endcap geometry and mounting scheme. The entire HE monolith is fastened from its back stainless steel plate to a 10.0 cm front plate of the Endcap Muon absorber steel (YE1).

The EE electromagnetic calorimeter is attached to the front face stainless steel plate of HE (1.16 times thicker than the brass plate for an interaction length equivalent to that of the brass absorber). The total thickness of the front plate is determined by the dead material introduced by EE cables, electronics etc. (about 0.1). So the thickness of the plate may be reduced by this amount in order not to introduce additional layer of scintillators. The EE is a highly non-compensating calorimeter that introduces nonlinearity of energy response and degrades the energy resolution. To correct these effects in some degree a weighting technique may be used. In this case the expected energy resolution is $E/E = 105\%/\sqrt{E}$ 4%. The weighted response of the initial layer(s) of the hadron calorimeter is used separately applying a correction taking into account the ratio $E_{H1}/(E_{H1}+E_{H2})$.

Each end cap is an 18 sided polyhedron that covers and closes one end of the barrel calorimeter. The HE is constructed of plates, separated by staggered spacers, that are perpendicular to the beam axis. The basic geometrical parameters of the HE are shown in Fig. 3.1.

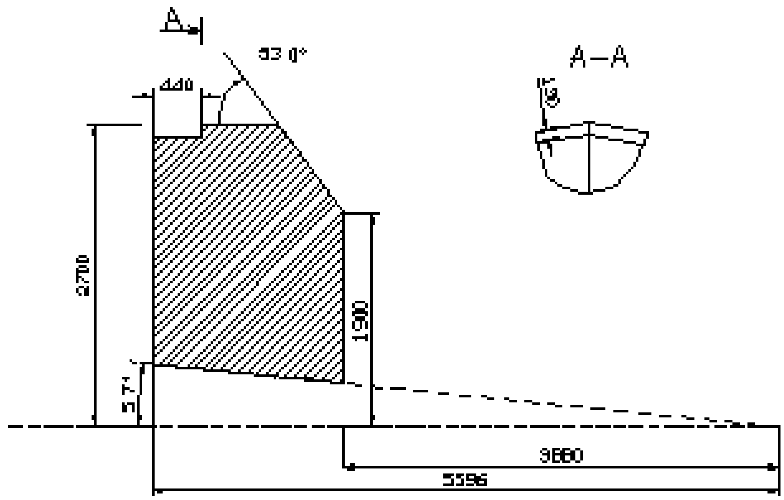

Fig. 3.1: Basic parameters of HE.

Fig. 3.1: Scintillating plates are mounted on aluminum plates forming trapezoidal tray ("pizza pan") structures which are installed in the gaps of the endcap absorber. The construction allows easy access to the pizza pans and provides a rigid structure.

3.1.2 Engineering design requirements

The basic design guidelines are:

- the absorber must be made of brass plates with minimal gaps (0.5 mm) in ;

- mechanical assemblage of the absorber plates with bolts ;

- design must provide for the required insertion of megatiles and easy removal;

- back flange is made of stainless steel;

- dimensions of the absorber plates in ϕ must correspond to minimal cost, minimal waste and maximum machinability;

- absorber design and all interface elements must satisfy the safety requirements to sustain about 300 tonnes and provide stable position of endcap in space during all operation time;

- safe operation during access to EE and HE and to the interior of the detector;

- provide the required precision of muon chambers ME1 alignment, with the possibility to replace separate chambers without interfering with other end cap systems;

- HE design and the interface zone must correspond to the requirements of the standard assembling procedures and time schedule at the CERN assembly hall on the surface;

- the cost must be within the allocated sum;

- the safety factor for the most loaded elements (taking into account all combined stresses) must be greater than 2;

- the calculations of stresses and deformations must take into account dynamical forces equal to 0.15g.

3.2 HE ABSORBER GEOMETRY

The endcap hadron calorimeter covers the rapidity region between 1.3 and 3.0 and is an 18 sided polyhedron in shape. The HE consists of the absorber plates with 19 sampling gaps filled with scintillator trays. The scintillator response signal is transferred via optical cables to megatiles decoder boxes in which the signals from tiles forming a single (x ϕ) tower are optically mixed together. The decoder box also contains the readout photodetectors, the frontend amplifiers, as well as the initial signal digitizers. This figure shows a cut through the vertical plane of the HE cross section in y-z plane. Fig. 3.2 presents the endcap segmentation (HE and EE) in ϕ and Fig. 3.3 shows the longitudinal structure of HE.

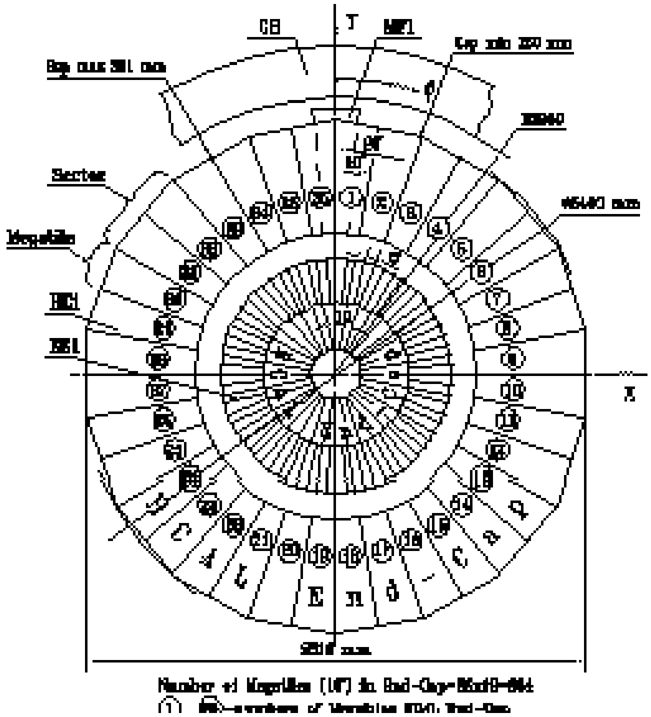

Fig. 3.2: End cap segmentation.

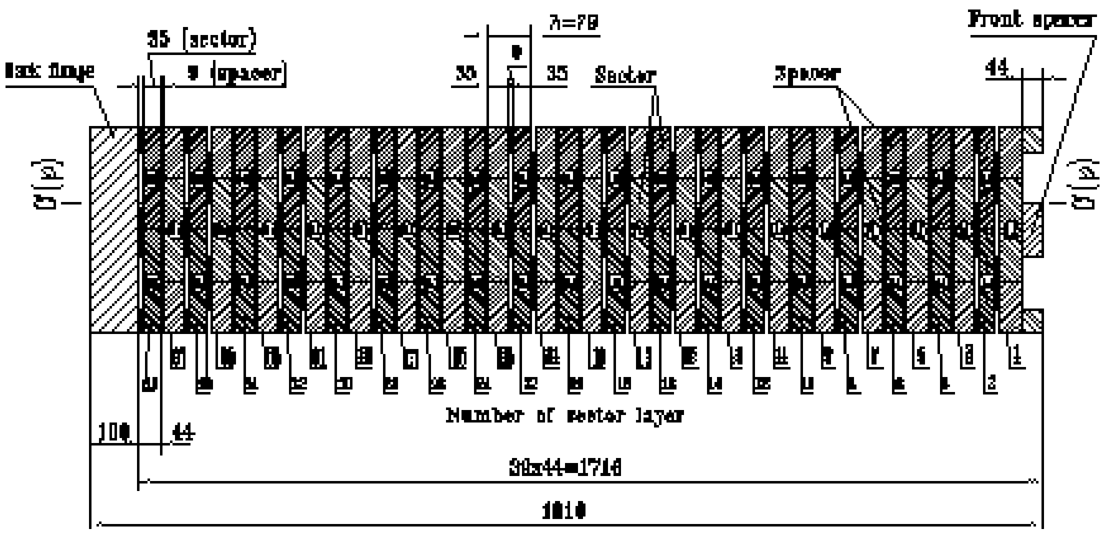

Fig. 3.3: Longitudinal structure of HE.

3.3 HE ABSORBER DESIGN AND MANUFACTURE

The HE design with mechanical connection of elements is presented in Fig. 3.4. Absorber elements and spacers are connected with bolts M24x2 with cylindrical head. To eliminate a relative shift of absorber elements in the vertical plane under the shear forces due to the HE weight, a large number of collets with diameter 36mm are used for interplate connection and stabilization.

The calorimeter is formed by assemblage of sector and spacer elements. Each layer consists of 18^0 brass sectors 35 mm thick. The sector layers are separated by 18 brass spacers 9 mm thick covering 10^0 in ϕ for the scintillator insertion gaps.

From the production point of view the following requirements were taken into account:

- to cut the cost of the absorber plates produced by industry the sector plate cover 20^0 in ϕ;

- minimization of the absorber plate dimensions allows to use standard industrial equipment with required precision of machining;

- to control the quality of all industrially produced absorber elements a control assemblage is planed;

- an analysis of sector absorber production from rolled plates with width 600, 1060, 1200, 1250 and 1500 mm shows that the most economical option is 20^0 sectors;

- several producers of rolled plates were considered: Bulgaria (produces plates up to 1060 mm wide); Orsk plant OTM, Russia (produces plates up to 1200 mm wide); "Krasnyi Vyborzhets" plant in St.Petersburg, Russia (produces plates up to 1500 mm wide); metallurgical plant in Bendzin, Poland; KGHM Poland copper; firm "Outukumna", Finland.

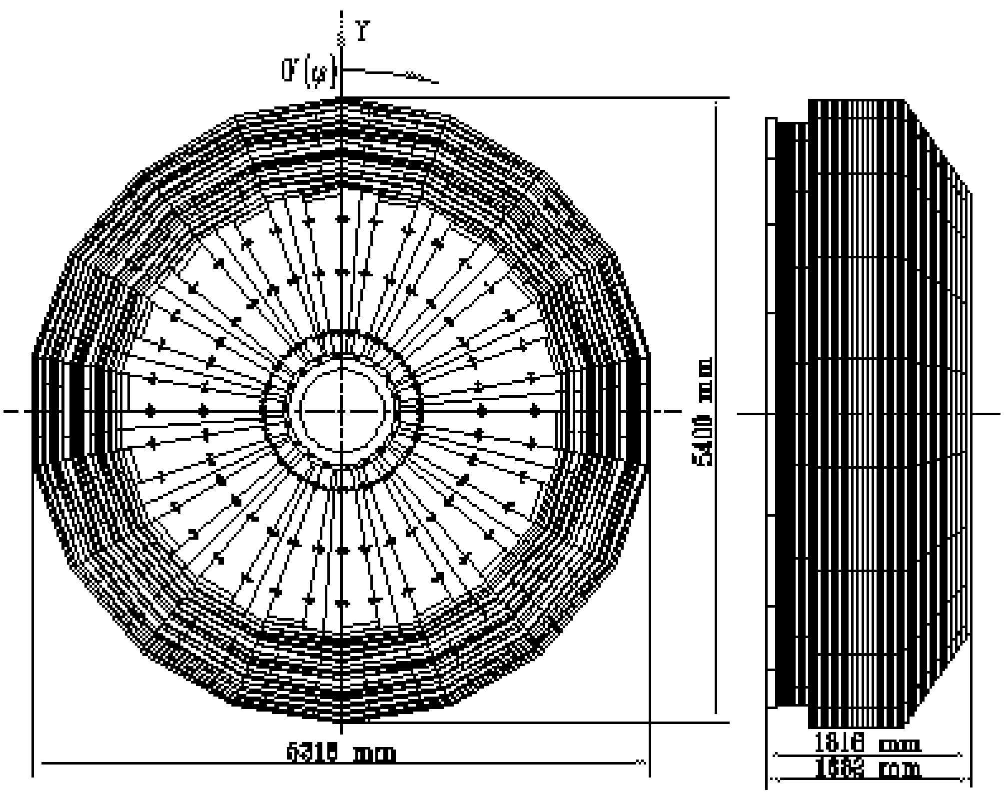

Fig. 3.4: Absorber of the HE.

3.3.1 Sector and spacer layout

The HE absorber consists of alternating layers of sector and spacer plates connected with bolts and collets (see Fig. 3.5). The arrangement of the even and odd layers is shown in Fig. 3.6. The numbering of the layers starts from the layer closest to the interaction point and is shown in Fig. 3.7. The layer numbering scheme is the same as that in the barrel, namely that the layer immediately following the innermost stainless steel plate is numbered as layer one, while the layer following the outermost stainless steel plate is layer 19. Plates in front of the innermost stainless steel plate of HE will be numbered zero (and -1). The geometry of the sector and the spacer is presented in Fig. 3.8.

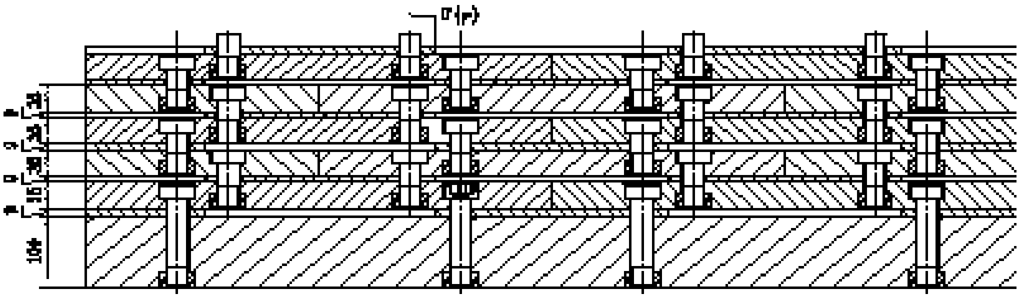

Fig. 3.5: Scheme of HE layer joints.

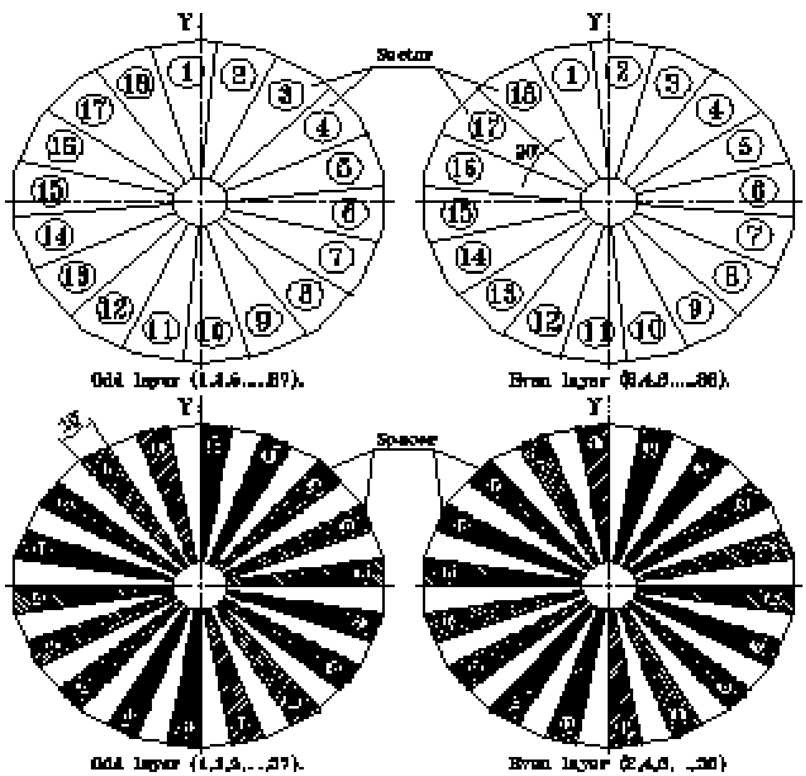

Fig. 3.6: Sector and spacer arrangement in odd and even layers.

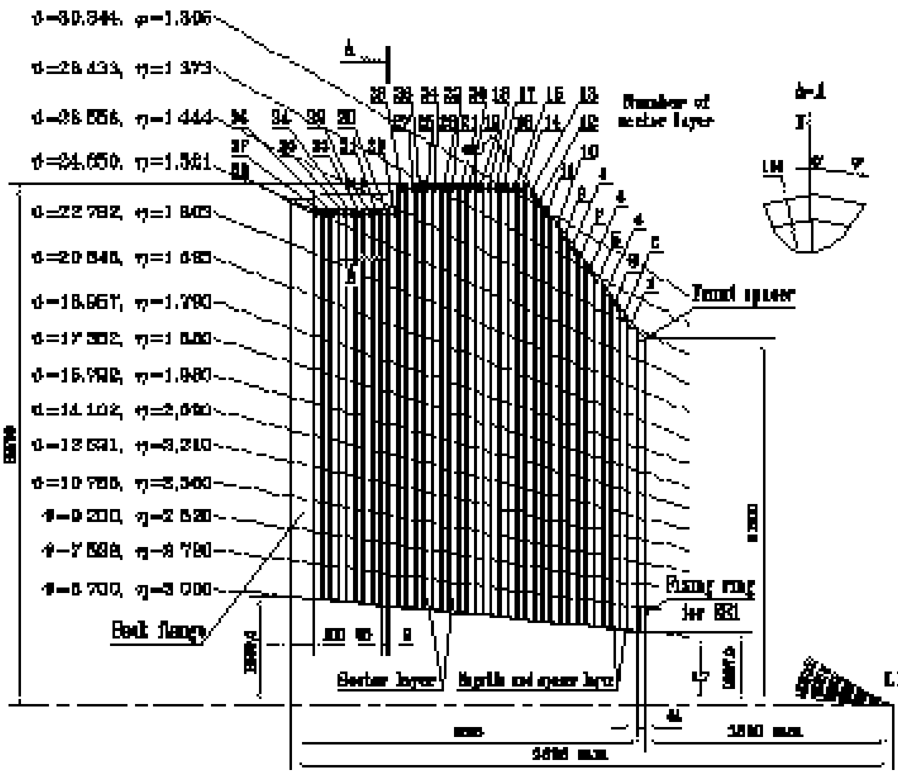

Fig. 3.7: Longitudinal section of HE absorber.

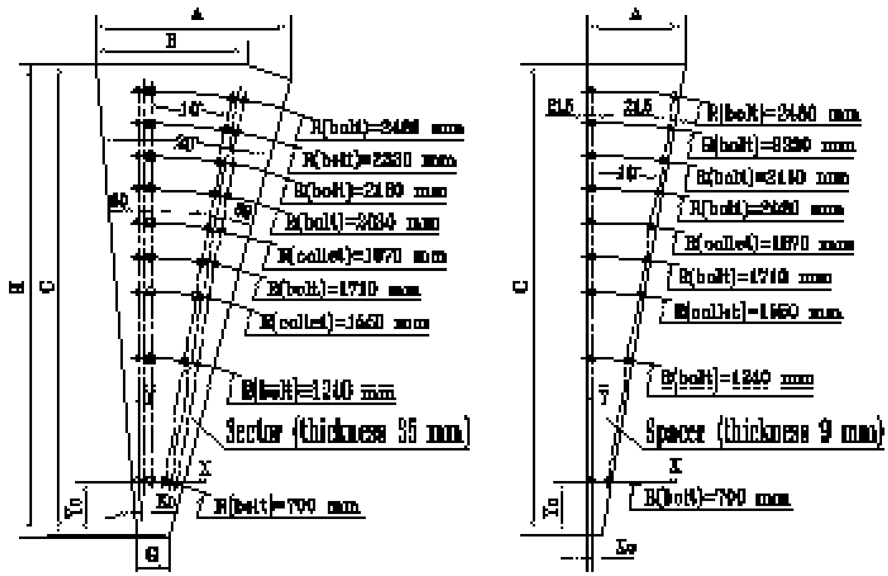

Fig. 3.8: Geometry sector and spacer.

3.3.2 Fastening elements of HE

All absorber plates are connected with bolts and collets. The general layout is shown in Fig. 3.5. The collet design is shown in Fig. 3.9, while Fig. 3.10 presents the bolted connection.

The number of fastening elements along the z-axis (HE depth) is optimized (see Fig. 3.11). The most loaded layer # 38 (next to the back flange) has 468 bolts M24x2, the less loaded layer #1 has 216 bolts. The number of collets with diameter 36 mm and cross section 756 mm^2 is 72 in the last layer. The layers assemblage is made with torque indication wrench that allows to increase static load on the bolts by a factor of 2.

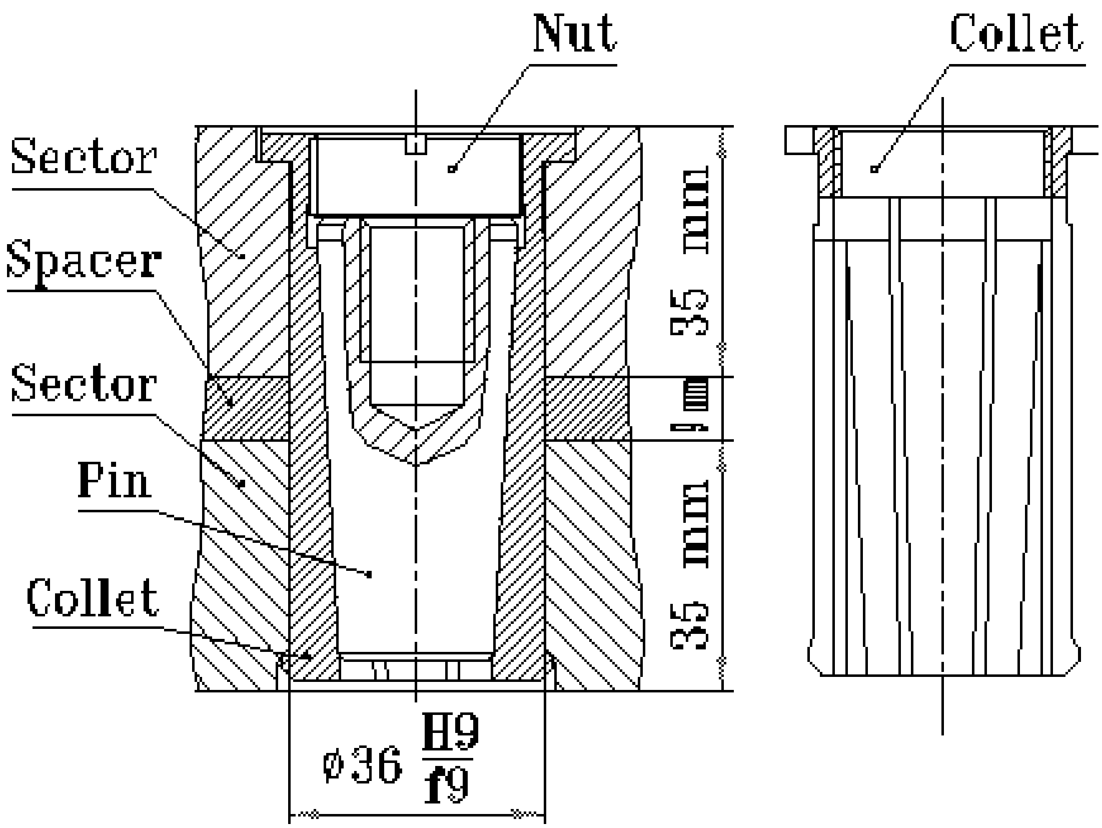

Fig. 3.9: Collet connection.

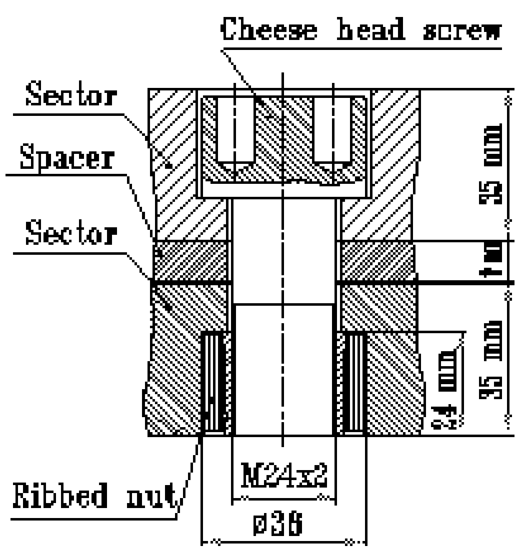

Fig. 3.10: Bolted connection.

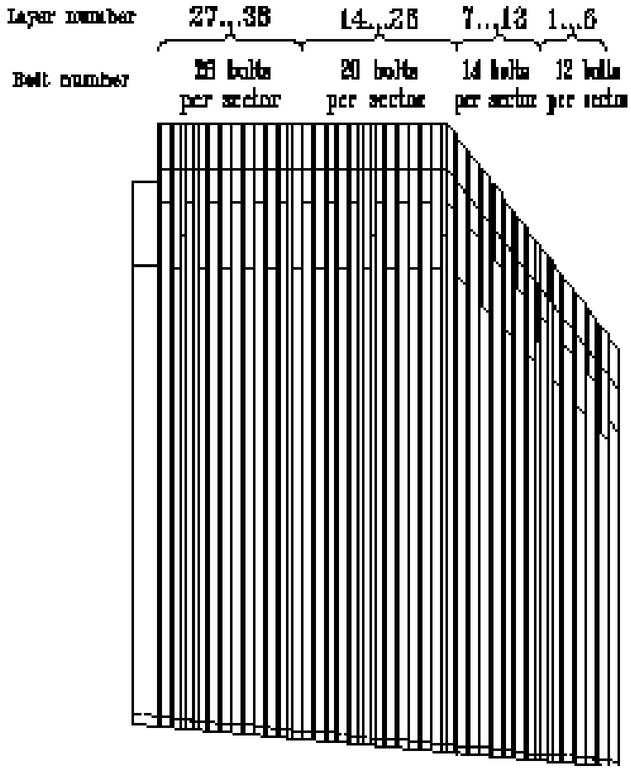

Fig. 3.11: Minimised number of bolts in z direction.

3.3.3 Forces, stress, deflection

The input data for the calculations are:

- the schematic location of the center of gravity and weight of the endcap components including the endcap crystal EE and its mounting frame (Fig. 3.12);

- the material of the bolts, nuts and collets is brass (yield limit equals to 2.94×10^2 MPa);

- the sector material is brass;

- the bolt and collet dimensions are presented in Figs. 3.9 and 3.10.

Strength analysis of the bolt joints

The rating scheme is based on the layout presented in Fig. 3.13. The calculation results of the stress values and the safety factor are presented in Fig. 3.14.

The absorber material and construction elements (bolts and nuts) were tested with a machine made by Instron. The machine could develop a force of up to 20 tonnes. The main results of this testing are the following:

1. Force for the beginning of the plastic deformation for M24*2 bronze BrX1 bolt Fpl = 14.2 tonnes. That is

much more than the required load Fa = 5767 kg.

2. The bolt elongation before bolt break down = 6 mm (15% of length).

3. Force for break down of bolt thread = 16 tonnes.

4. Force for break down of absorber material (for copper) under bolt head surface = 17.5 tonnes. For brass, the required force is 1.5 to 2 times more.

Thus the materials (brass for absorber and bronze for connecting elements) meet all requirements.

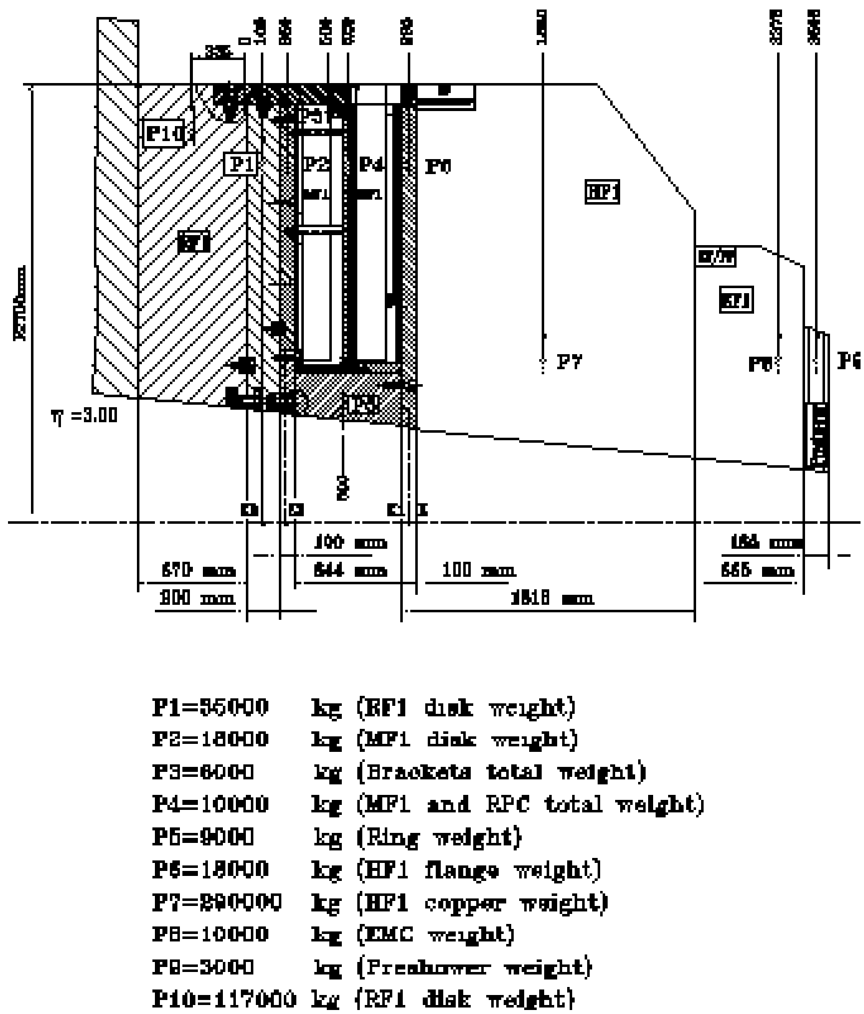

Fig. 3.12: Weights and center of gravity of the end cap components.

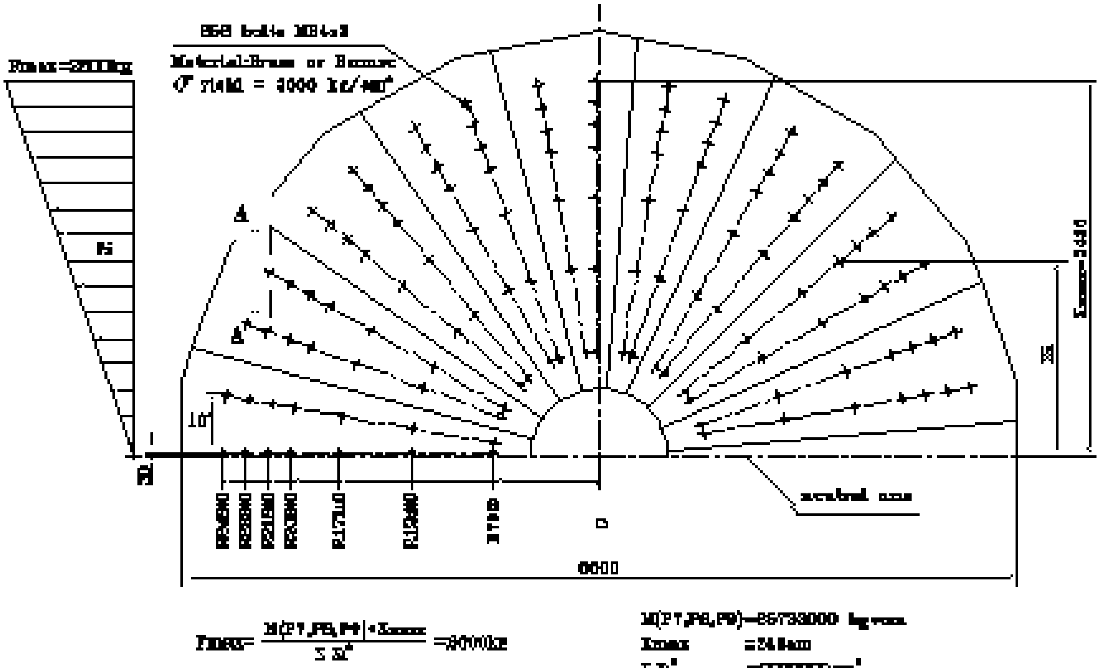

Fig. 3.13: Strength analysis of the HE sector bolt joints.

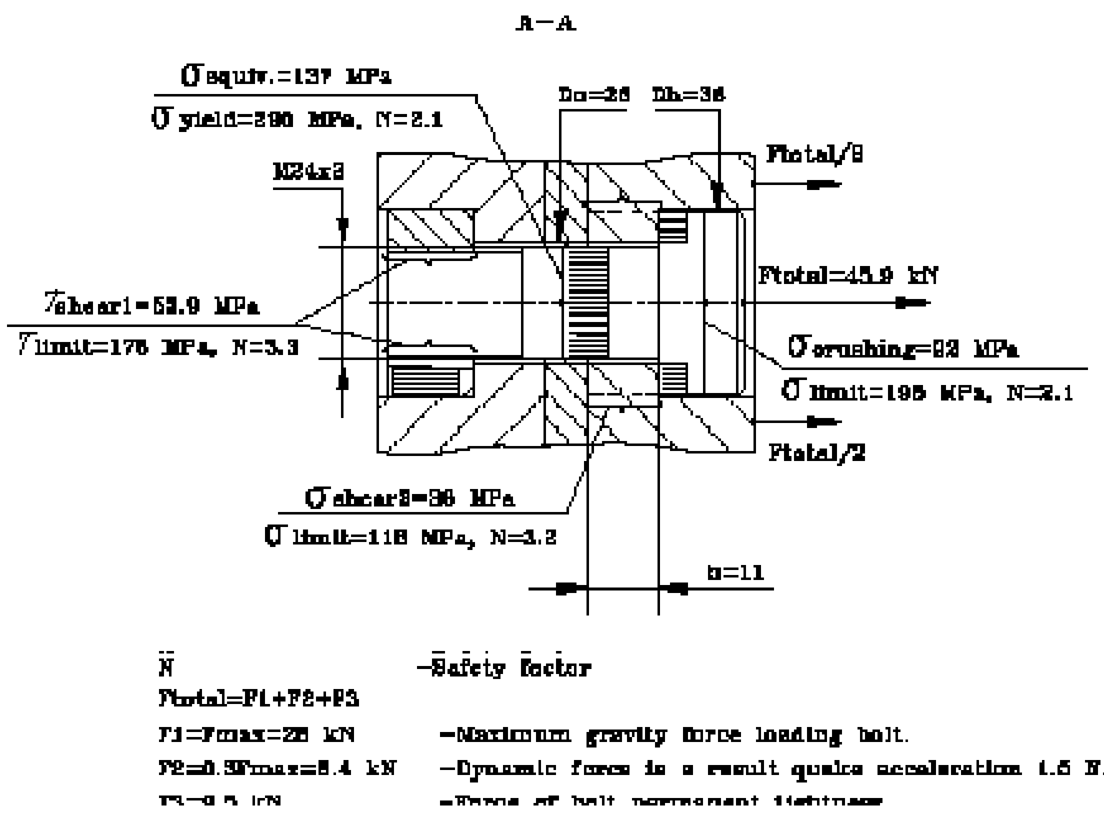

Fig. 3.14: Stresses of the HE sector bolt joint.

Strength analysis of the collet joints

The layout of the HE collets is shown in Fig. 3.15. The calculation results of the stresses and safety factors are presented in Fig. 3.16.

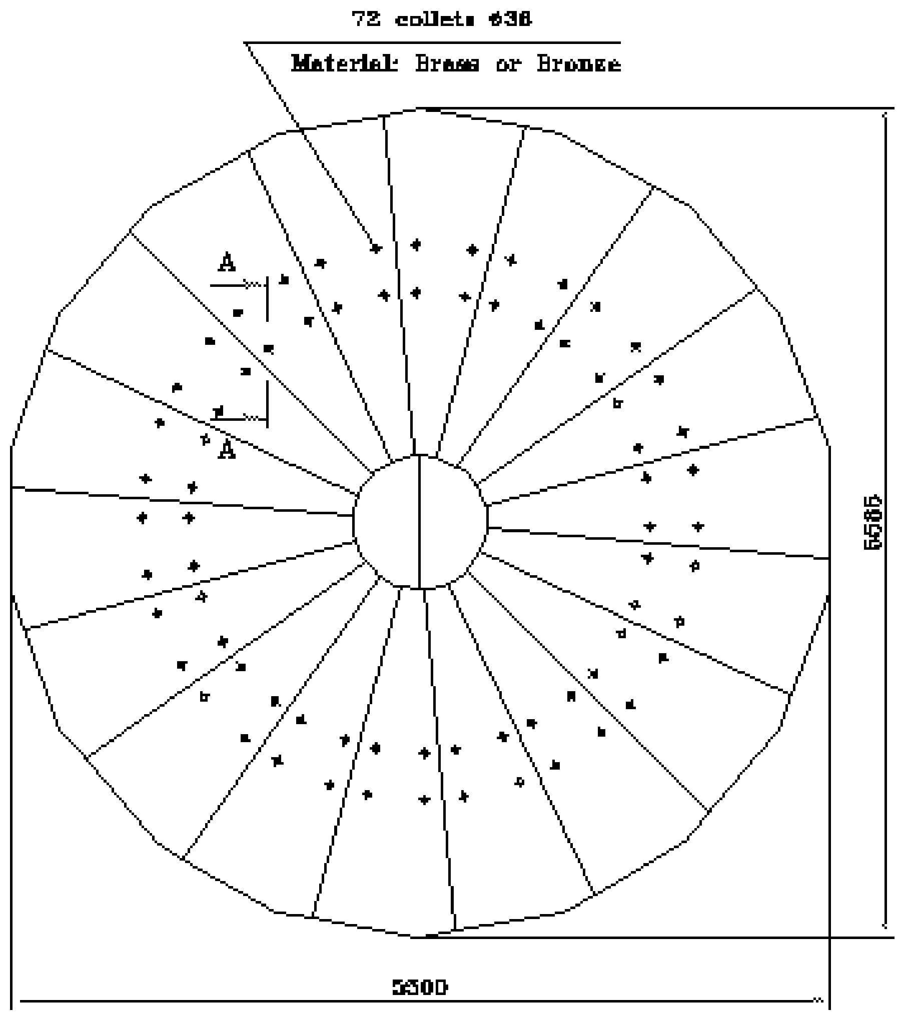

Fig. 3.15: Layout of the HE collets.

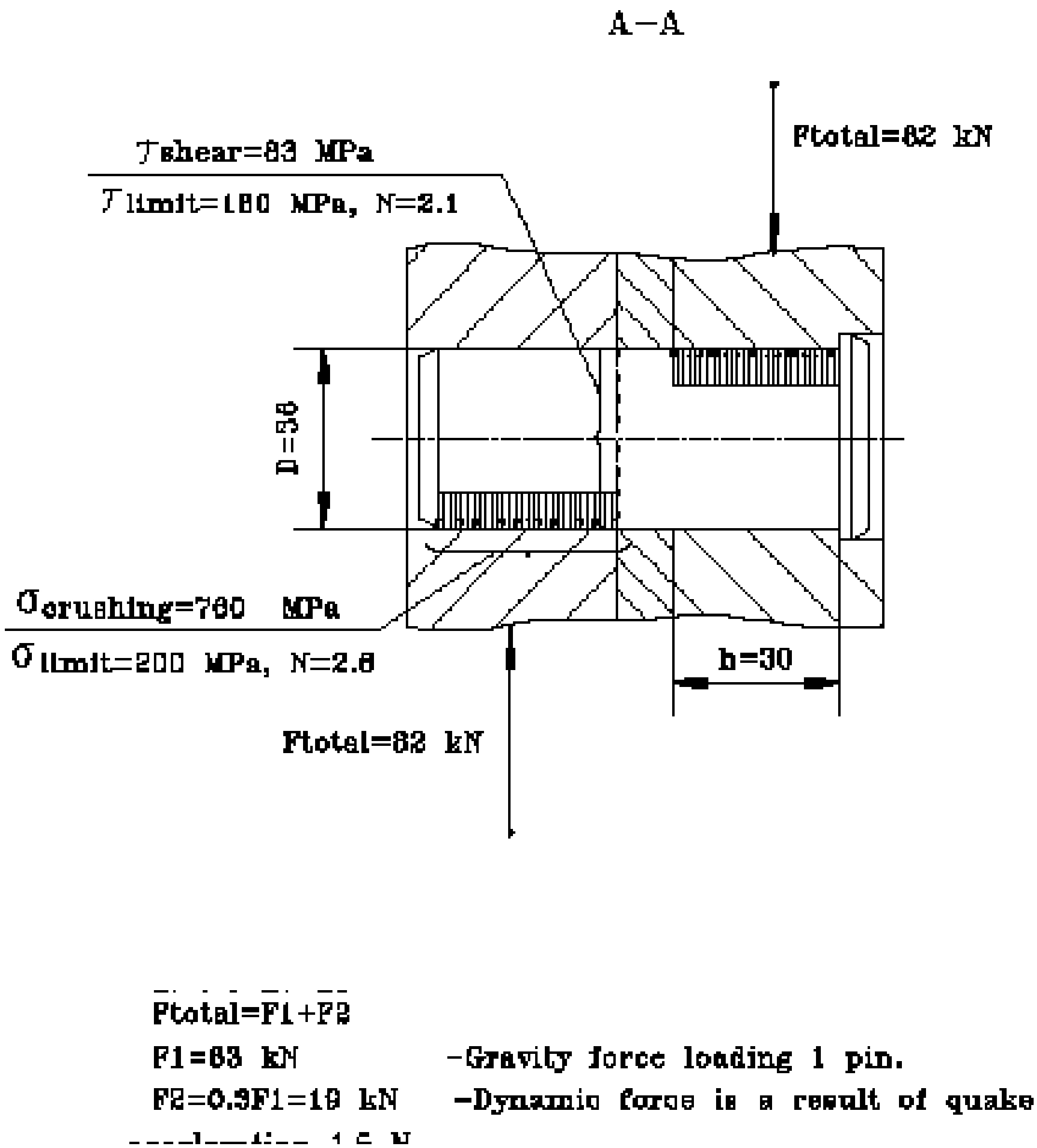

Fig. 3.16: Stress analysis of HE collet.

3.3.4 Finite element analysis of HE

The Finite Element Model

The ANSYS finite element program was used to model the HE for the purposes of determining bolt loads, plate stresses, and deflections under normal static operational conditions. This model is shown in Fig. 3.17. Eight node solid elements modeled all components, and a total of 80 k nodes and 40 k elements were used in the model.

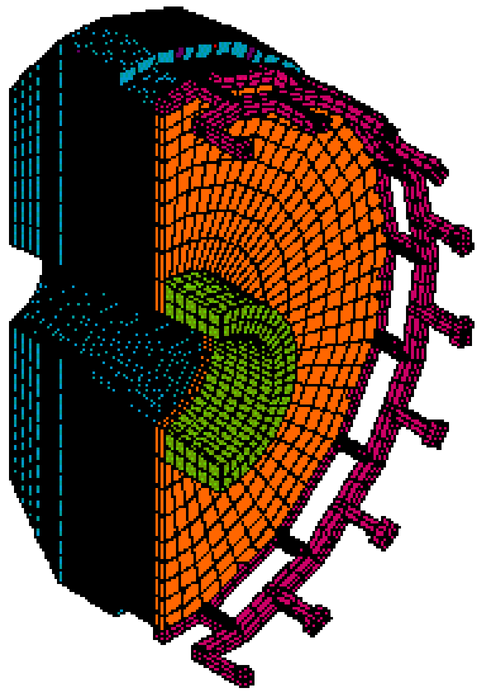

Fig. 3.17 (see also C.S.): ANSYS FE model of HE.

The entire HE, with the exception of the backflange and inner ring, is made of discreet 20 degree sector and spacer plate segments. The segments are connected to each other by 24 mm diameter bronze bolts and collets. The backflange and inner ring are 360 degree annuli.

Fig. 3.18 is a close-up of a typical sector/spacer plate connection. Because the spacer plates are through bolted to the sector plates, and the sector plates stagger azimuthally by twenty degrees between each layer, the load path is a zig-zag through the plates in z, and the bronze bolts and collets are responsible for transmitting the forces back to the support points. The modeling of this load path in precise detail is impossible given the large problem size which results. Instead, the "bolts" were represented by spring elements along the radial edges of the sector/spacer plate junctions. Although the actual bolt will pass through two sector plates and sandwich the intermediate spacer plate, the finite element model places "bolts" only at one of the sector/spacer interfaces; the other interface is merged into a continuous line. This will not change the calculated bolt loads, since the load at each merged interface must pass through a spring-simulated "bolt" to reach the support points.

The collets, which serve a shear function only, were modeled at the same points as the bolts by applying two additional spring elements acting in the radial and azimuthal directions.

The number of spring elements on a radial connection line does not represent the exact number of bolts in each sector. There are a minimum of 13 bolts along each radial bolting line at the most heavily loaded locations; the model uses 11 bolts along every line, except near the support, where 10 are used. The force output from the program was taken at face value to represent a single bolt, with the resulting conservatism ignored.

The stiffness of the bolted joint, which is input to the model as the stiffness of the springs, was estimated with a

2-d axisymmetric model of a typical joint.The bolt was modeled as brass, 24 mm in diameter, and the recessed holes for bolt head and nut were included in the model. The bolt was thermally preloaded to 90% of the 300 MPa yield strength of the bolt material, and a load applied to the joint which acted to separated the bolted components. The resulting deflection was used to calculate the bolt stiffness input to the 3-d finite element model. This stiffness was 1.46×10^{6} N/mm.

Stiffness for the spring elements representing the collets, and resisting only shear forces, was set at an arbitrary 1×10^{6} N/mm.

The HE is supported from the endcap iron plate YN1. Three HE steel components are responsible for this support. The 100 mm thick backflange is attached at its inner radius to the inner ring (IR) , which keys and bolts to YN1. The backflange is attached at its outer radius to the FF plates, which have had substantial material removed to allow access to the MF1 chambers. In the actual structure, vertical shear is taken entirely by the connection of the inner ring to YN1. This was simuated by constraining the vertical motion of the end of the ring. Overturning moment is taken by the FF plates, which are radially bolted into YN1. This was simulated by constraining the z-motion of the ends of the stirrup plates.

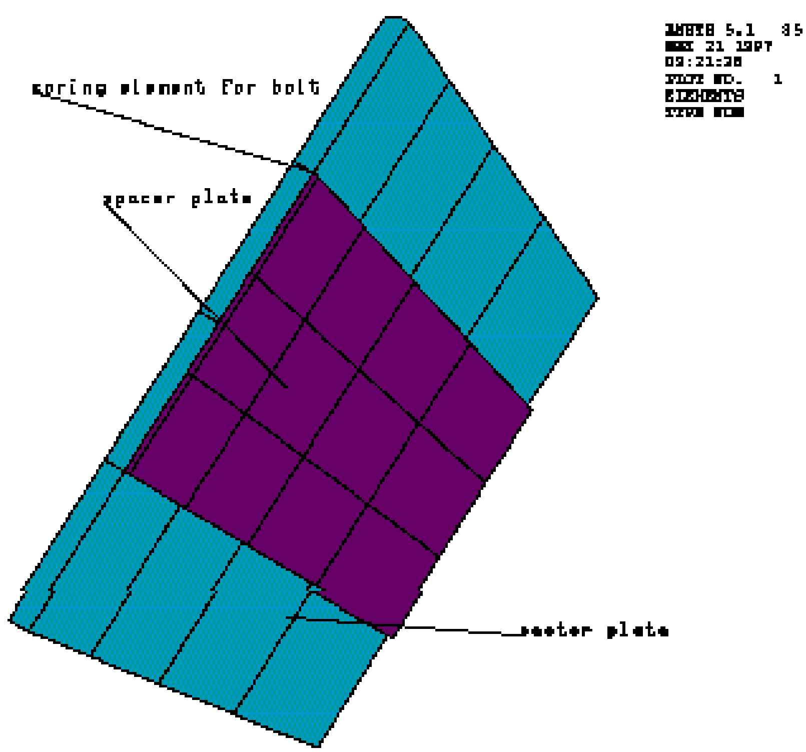

Fig. 3.18 (see also C.S.): Close-up of a typical sector/spacer plate connection.

The EE, which has a mass of 10000 kg, bolts to the upstream end of the HE. This mass loading was simulated by using a point mass element located at a z (relative to the i.p.) of 3365 mm. The mass element was supported from the upstream end of HE by two massless and very stiff spar elements. Therefore, while the details of the support effects on the upstream end of HE are not precisely modeled, they are almost certainly simulated in a way which will increase the local loading on HE, and produce the correct mass and moment effects.

Working stresses for the bolts and collets were taken as 2/3 of the 300 MPa yield strength for bolt tension or 200 MPa, and 1/3 of 300 MPa for both bolt and collet shear stress, or 100 MPa.

Establishing working stresses in the copper is problematic, as the current specification states only that the ultimate tensile strength is 200 MPa. If the procedures of the ASME Boiler and Pressure Vessel Code, Section VIII, Div. II, Appendix 4, are applied, then the maximum allowable membrane stress is 1/3 of the ultimate, or 66 MPa, and the maximum allowable stress for combined membrane plus bending is 1/2 ultimate, or 100 MPa.

Bearing stresses in the copper at the bolted joint are allowed to reach 3/4 of the ultimate stress, or 150 MPa.

The working stress of the stainless steel of the backflange, inner ring, and stirrup plates were taken as 138 MPa. This value is for SA-240 SS304 stainless steel as specified in the ASME Boiler and Pressure Vessel Code, Section VIII, Div. II.

Loading

The loads considered in this analysis were dead weight and earthquake/handling accelerations of 0.15 g. They were applied in the following load cases:

- Dead weight plus 0.15g additional downward force for earthquake/handling.

- Dead weight plus 0.15 g additional force parallel to beam axis for earthquake/handling.

The azimuthally symmetric geometry means that earthquake forces acting horizontally and perpendicular to the beam axis can produce bolt stresses and support reaction which are not higher than those from load case 1. Therefore, the one-half symmetric model is adequate to consider all earthquake effects.

Results

Fig. 3.19 and 3.20 shows the deformed shape of the HE for load cases 1 and 2, respectively. The maximum deflection calculated by the model was at the mass element representing the EE. This deflection was 1.3 mm. This deflection is relative to the stirrup plate and inner ring supports, and does not include any deflection in the YN1 plate.

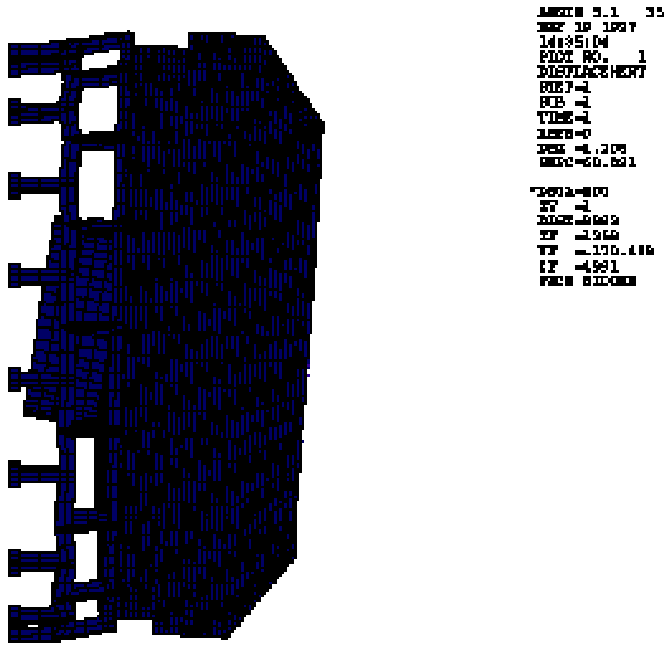

Fig. 3.19 (see also C.S.): The deformed shape of the HE for load case 1.

The bolt tensile stress for both load cases was obtained by dividing the spring force calculated at each "bolt" location by 354 mm^2, the tensile stress area of a 24 mm diameter bolt. The maximum tensile bolt stress calculated by this means was 198 MPa for load case 1, and occurs at layer 38, nearest the supports. This is consistent with the location of the maximum cantilever moment. The maximum tensile stress is below the allowable of 200 MPa, and does not take into account that there are actually 13 bolts along a radial line, and not the 10 "bolts" modeled along the line in the finite element model in this most highly loaded region.

Shear stresses, which are taken in the HE by both the bolts and collets, were evaluated with the finite element model by assessing the vertical shear force distribution in the model, and applying the forces to the actual bolt and collet areas available. This was done at the most highly sheared location, which is layer 38. The cross section was divided into ten horizontal strips, and the shear force calculated. The most heavily sheared regions are at the top and bottom of the circular area, which each see a shear force of 7.24×10^5 N over an area of 14.22 x 10^5 mm^2, or an average shear (if the spacer and sector plates were continuously connected) of 0.51 MPa. The area available for shear from the bolts is the number of bolts in the layer times the bolt stress area, or 468 x 353.87 = 1.66×10^5 mm^2. The total area of the layer is 1×10^7 mm^2. Scaling by the ratio 100/1.66, the average shear stress on the bolts in these most highly stressed regions is 31 MPa. This is well below the allowable of 70 MPa, and neglects the contribution of the collets.

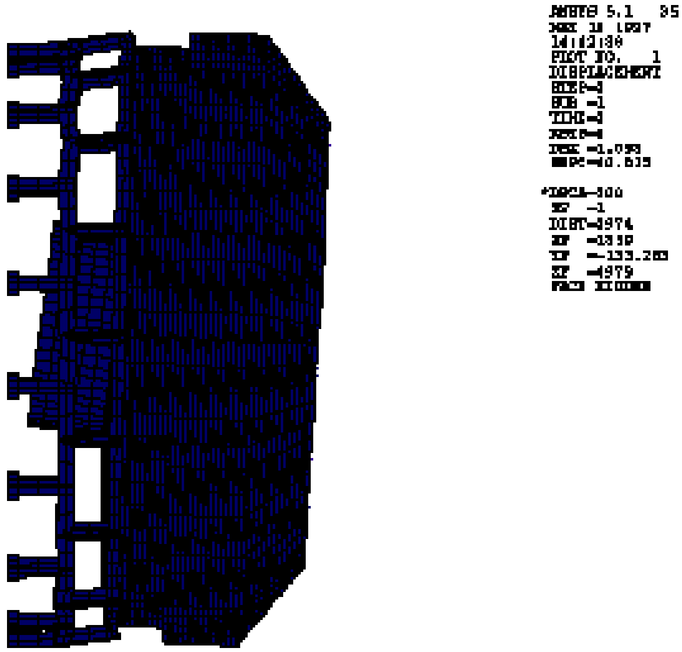

Fig. 3.20 (see also C.S.): The deformed shape of the HE for load case 2.

The copper from which the sector and spacer plates are made is softer than the brass bolts, having an ultimate strength of 200 MPa. This material must take the bearing stress produced by bolt preload and external loading. A calculation of the bearing stress under the bolt head due to preload can be made by applying the preload force to the bearing area. For a preload of 270 MPa and a bolt stress area of 353.87 mm^2, a force of $9.55x10^4$ N is required. If the contact area at the bolt head is 680 mm^2, the resultant average bearing stress on the copper under the bolt head is 140 MPa. This is below the ultimate strength of the copper material.

Bearing in the hole resulting from shear can be calculated by taking the average shear force per bolt calculated above and applying it to the bearing area of the hole. If the hole against which the bolt shank bears is 31 mm long and 24 mm in diameter, the projected bearing area is 372 mm^2 (for single shear) For a shear force of 51 x 353.87 = $1.8x10^4$ N, the resultant bearing is 48 MPa. This is below the ultimate strength of the copper material.

The 2-d finite element bolting model, which was used to find the stiffness of the joint for input to the spring elements in the 3-d model, can also be used to look at the actual distribution of external force between the bolt and the clamped materials. The purpose of preloading is to stiffen the joint by compressing the material, and ensuring that its compliance is a part of overall joint behavior. Fig. 3.21 shows the joint, preloaded to 270 MPa, with an external force of 70 kN applied as a shear at the outer boundary of the top sector plate. The results show that the axial bolt stress, averaged over the bolt area, increases from 270 MPa to 280 MPa under this load. Though this loading method is a simplification of the actual 3-dimensional load path, the results show that the preloaded joint effectively involves the clamped materials in its overall load response.

The maximum membrane stress in the copper is 48 MPa for load case 1, and occurs at a bolted spacer/sector plate junction in layer 38. At this same location, the maximum membrane plus bending stress is 68 MPa. Both of these stresses are below those allowable established from the specified ultimate tensile strength.

The stresses in the back flange, stirrup plates, and inner ring are shown in Fig. 3.22 for load case 1. The maximum stress is 65 MPa, which is well below the allowable of 138 MPa.

Conclusion

The bolted sector/spacer plate connection has sufficient strength to allow support of the HE from the stirrup plates and inner ring attached to YE-1, for the condition of dead weight plus 0.15 g vertical or horizontal earthquake or handling accelerations. This analysis shows that both the shear and tension bolt loads are well within the capacity of the design. The collets were not explicitly considered, and any additional shear capability resulting from the material clamping friction was also neglected. The tensile bolt loads were calculated using 20 bolts per sector at layer 38, rather than the 26 called for in the design. Shear stress was calculated by extracting shear distributions from the model and applying them to the actual number of bolts in the design.

The 2-d joint study show that the properly preloaded joint will allow external load sharing between the clamped materials and bolt. Bearing stresses in the joint, when averaged over the available bearing area, are below the working stress limits in bearing for the copper material.

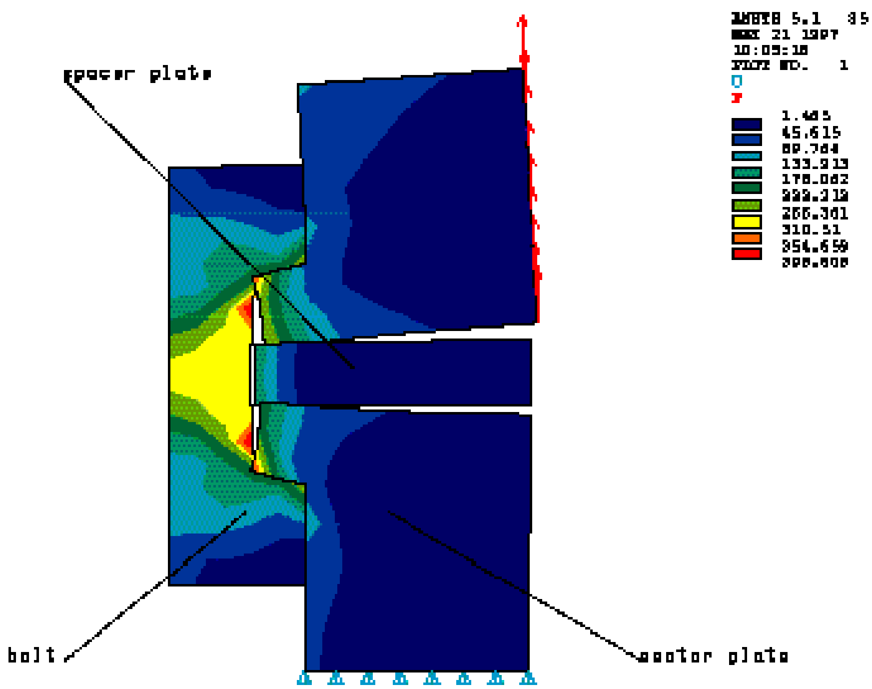

Fig. 3.21 (see also C.S.): Joint preloaded to 270 MPa, with an external force of 70 kN applied as a shear at the outer boundary of the top sector plate.

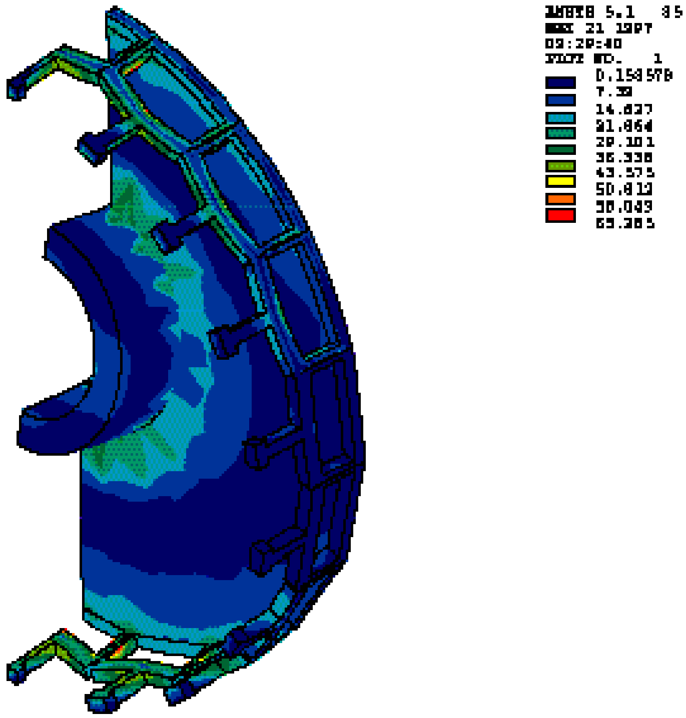

Figure 3.22 (see also C.S.): The stresses in the back flange, stirrup plates, and inner ring.

Electrical/magnetic isolation

In case of emergency switch off of the superconducting magnet a drop of the magnetic field from 4 T to zero magnetic field can occur. The changing magnetic field will lead to eddy currents in the endcap which will increase the electromagnetic forces in the HE absorber and as a consequence to additional load on the bolted joints. To minimize (eliminate) such forces the sector and spacer elements have a two layer electrical isolation to minimize (prevent) current flow. The first layer is an oxide layer on the absorber, while the second one is an enamel covering.

3.3.5 Materials

Mechanical requirements

Bolt, nut, pin, sector and spacer(collet) material is brass L90 (density is 8.78 g/cm^2, ultimate strength is 2.4x10^2 MPa, yield limit is 1.2x10^2 MPa, ultimate strength is 2x10^2 MPa, Brinel hardness (HB) is 50 units, relative extension is 45%).

Chemical requirements

Brass L90: Cu - 89.5%, Zn - 10%, admixture - 0.5%.

The geometry requirements

- Nonflatness - 0.5 mm per 1 m.

- Roughness - R_z 6.3.

- Thickness tolerance: 35 +0, -0.5 mm; 9 + 0, -0.2 mm.

3.3.6 Manufacturing procedures

Production of HE copper plates has the following steps:

- hot rolling of plates and machining of the sector parts (thickness, contour);

- hole drilling for bolts and pins, the distances between the holes are based on calculation of temperature variation in fabrication shop relative 20^0 C;

- machining of the spacer contour;

- drilling of the holes for bolts and pins;

- fitting of the coordinate holes;

- checking and documenting of the sectors and spacers;

- machining, checking and assembly of the HE back flange;

- machining, checking and documenting of the fastening elements of HE;

- control assembly and inspection of the HE absorber including the support ring for EE installation (at a factory);

The procedure has been agreed with engineers of the machinery plant which will make the absorber.

Quality control and assurance

The control is realized in to two steps. The first steps is the control of the sector and spacer plates obtained from producer. It includes the control of technical documentation, markers of elements, surface quality, dimensions of plates, mechanical and chemical analysis of the material,

The technical standards of input control are the following:

- technical requirements, quality certificate for the consignment of brass;

- control of plate markers, stamps of the producer in accordance with technical documentation: brands of brass, consignment number, melt and rolled good numbers, stamp of quality control service;

- surface quality control of plates - visual control to check the absence of cracks, grooves and hollows up to 0.5 mm deep;

- dimension control of plates (measurement precision is 1 mm) according to Euronorm standards;

- chemical analysis of brass, the deviation must be within the range mentioned above;

- mechanical control according Euronorm standards, deviation must be within the range mentioned above.

The second step (after production of all HE elements) includes the control of dimensions, machining quality, quality of protective cover according to the technical documentation for all absorber elements (sectors, spacers, flanges). After production each sector and spacer must have a marker with layer number and ϕ position.

Quality assurance is provided by way of technical control at all production stages, metrological attestation of the used apparatus and by calibration of the measuring devices according to methods of Euronorm standards.

All parameters of machining (precision, surface roughness, tolerances on thread holes etc.) are controlled in accordance to Euronorm standards.

A quality certificate of the manufacturing firm must accompany all the components with the following information:

- assortment certificate copy;

- item dimensions with accuracy not worse than 14 quality;

- signature and stamp of technical inspection division leader.

A quality certificate must be drawn up for the check assembly with a purchaser representative attendance.

Quality certificate shall be drawn up after the check assembly has been done and sent to the purchaser with the components in one parcel. The manufacture must have all the certificate copies kept for three years.

Preassembly of the HE absorber at the factory

The Endcap calorimeter HE will be preassembled at the factory with the goal of the technological development of the absorber assembly, quality control of the produced absorber elements, correction of the mistakes made during previous production stages.

Preassembly is realized on the factory floor (at the nominal factory) which can carry weight above 30 tonnes/m^2, the total absorber mass is about 290 tonnes. A crane with carrying capacity 10-15 tonnes must be used.

The assembly set includes two half disks 100 mm thick of the back flange, 6684 sectors 35 mm thick, 684 spacers 9 mm thick, a set of 13824 bolt joinings, a set of 2500 collet joinings.

The control scheme consists of nut pressing into the holes of the back flange half disks, back flange assemblage, pressing of the M24 nuts into sector holes, assemblage of the first layer of the absorber installing 18 spacers and 18 sectors, mounting bolts and collets, fixation of the bolts with torque indication wrench (the force is 4000 kg), assemblage of the second layer and so on up to the last absorber layer, assemblage, positioning and fastening of the centering ring to joint EE, the control of the assembled absorber, disassemblage of the absorber and the back flange, painting of the sectors and spacers, control of the painting, packing and control of the packing, transportation of the absorber elements to CERN (according to Euronorm standards).

3.3.7 Absorber prototype

An Endcap sector prototype will be designed and constructed before the HE design is finalized. The prototype consists of a full scale sector covering 30^0 in ϕ equipped with 38 megatiles and 2 decoder boxes including laser and radioactive source control. It's production and assemblage is planed to be completed at the second part of 1997 year. The results of the assemblage will be used to finalize the requirements of the absorber design. The design of the prototype is shown in Fig. 3.23.

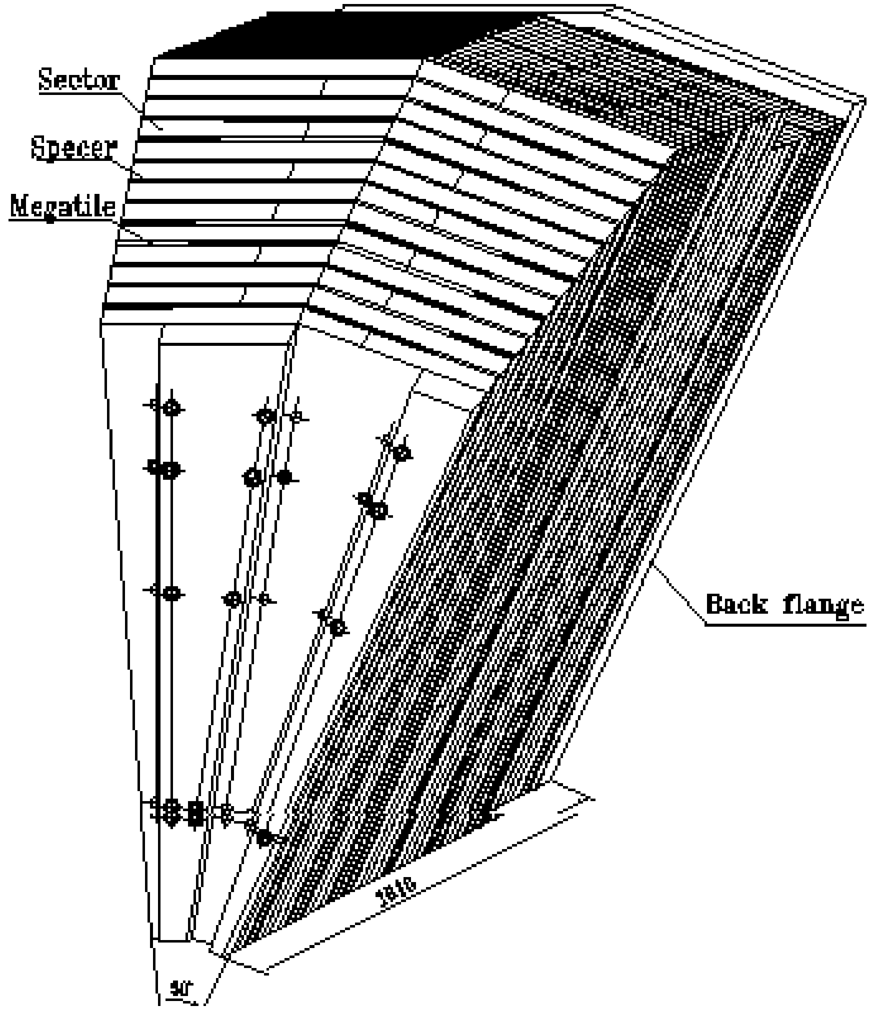

Fig. 3.23: The design of the prototype HE.

3.4 INTERFACE OF HE AND THE ENDCAP MUON SYSTEM

3.4.1 HE and ME interface

The design of the interface support system is shown in Fig. 3.24 and 3.25. It consists of the following elements:

- stainless steel internal support ring (see Fig 3.26);

- back flange disk 100 mm thick made of low carbon steel (see Fig. 3.27);

- intermediate disk 70 mm thick made of aluminum alloy D16T;

- 18 fastening frames made of stainless steel and placed around the outer surface the interface zone (see Fig. 3.28).

An internal support ring is connected to the back flange of HE (see Fig. 3.29) by 18 bolts M36. The fastening frames are fastened to the back flange by 18 keys with dimensions 40x40x210 mm, from the other side it is connected to the flange of nose YE1 by 18 keys with dimensions 80x80x250 mm.

Muon chambers ME1 are placed and positioned on the internal disk with 20^0 intervals in ϕ. On the outer surface of the internal ring, on the lateral side of the back flange and on the flange disk of nose YE1 a polyethylene radiation protection is placed. On the back surface of the back flange resistive plate chambers (RPC) are set. The layout of the first layer of muon chambers is shown in Fig. 3.29. The design of the 100 mm back flange disk is presented in Fig. 3.30.

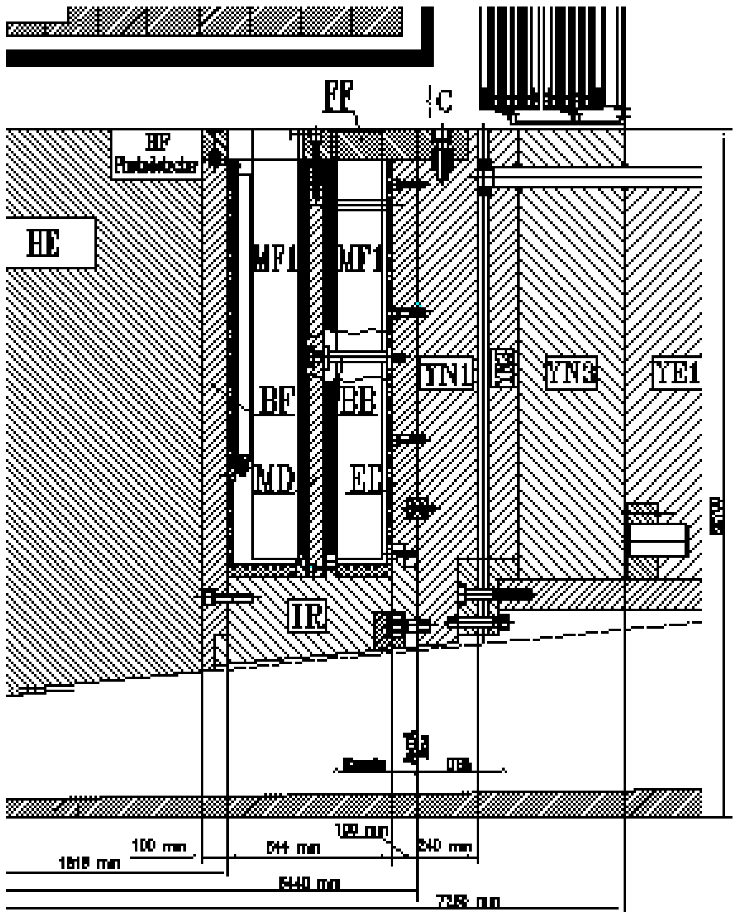

Fig. 3.24: Interface of HE, MF1, RPC and nose of YE1.

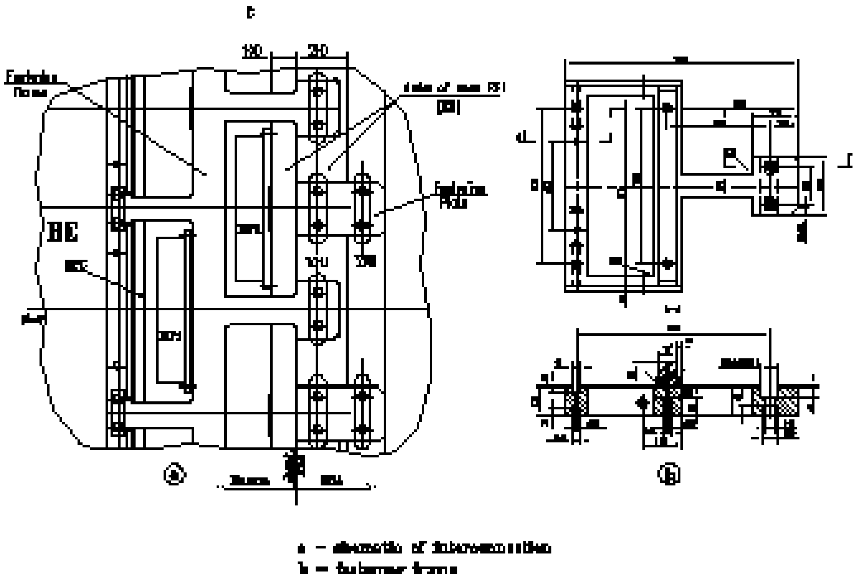

Fig. 3.25: Fastening frame for interconnection of HE and disc of YE1 nose.

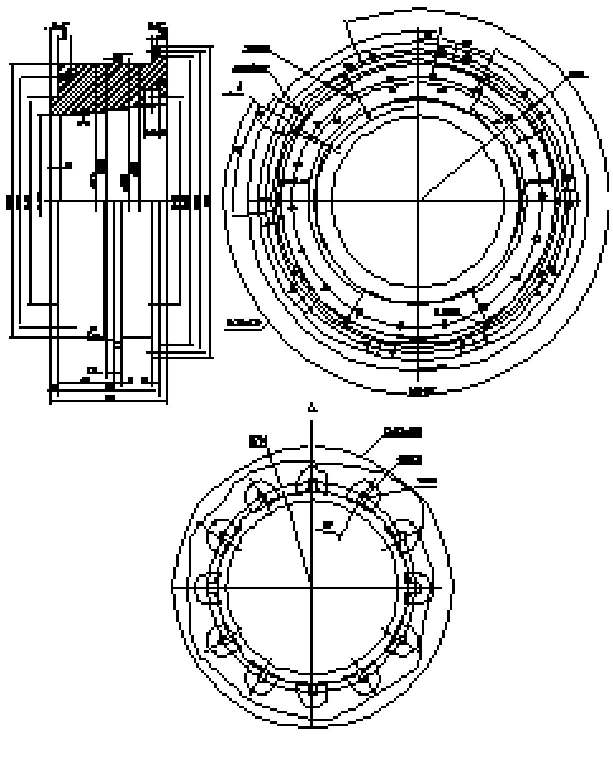

Fig. 3.26: Inner support ring.

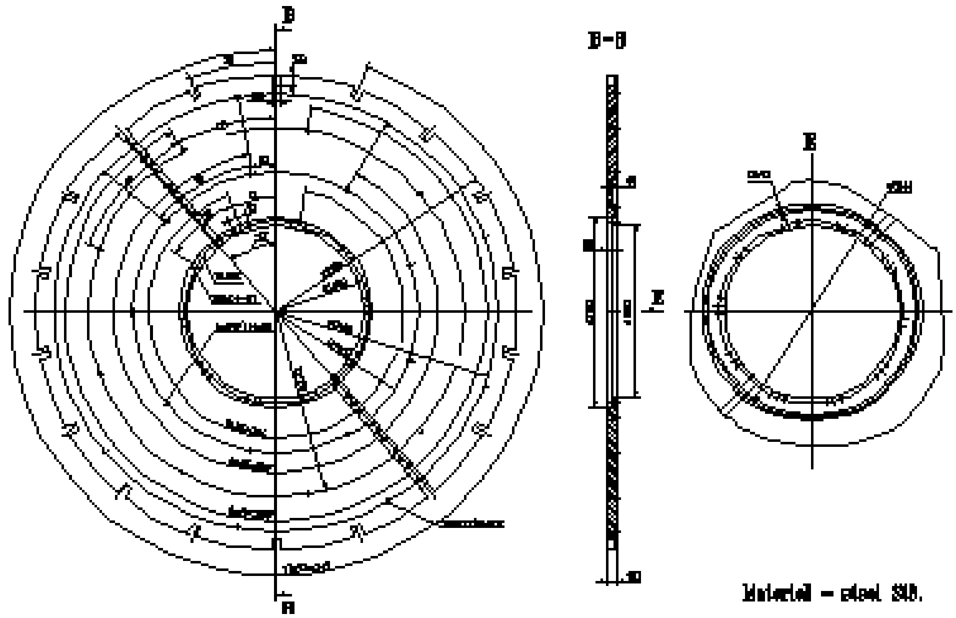

Fig. 3.27: End disk of YE1 nose.

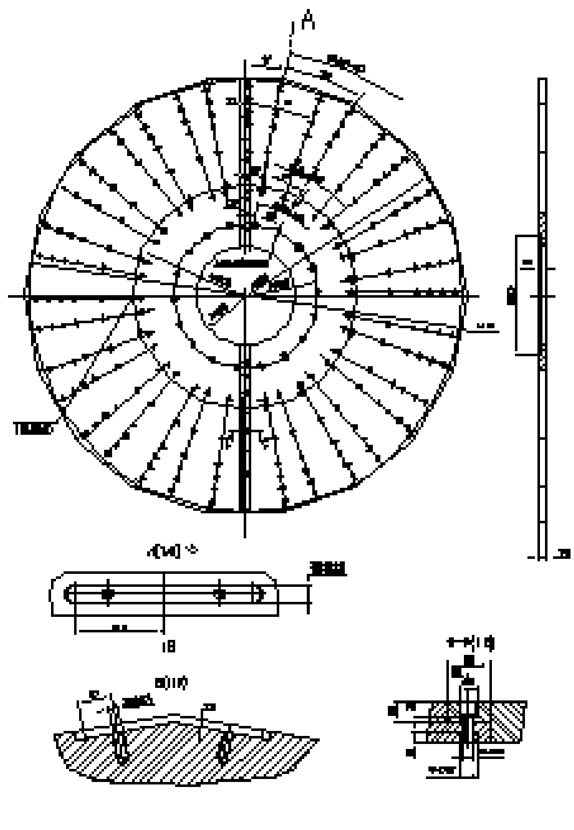

Fig. 3.28: Back flange of HE.

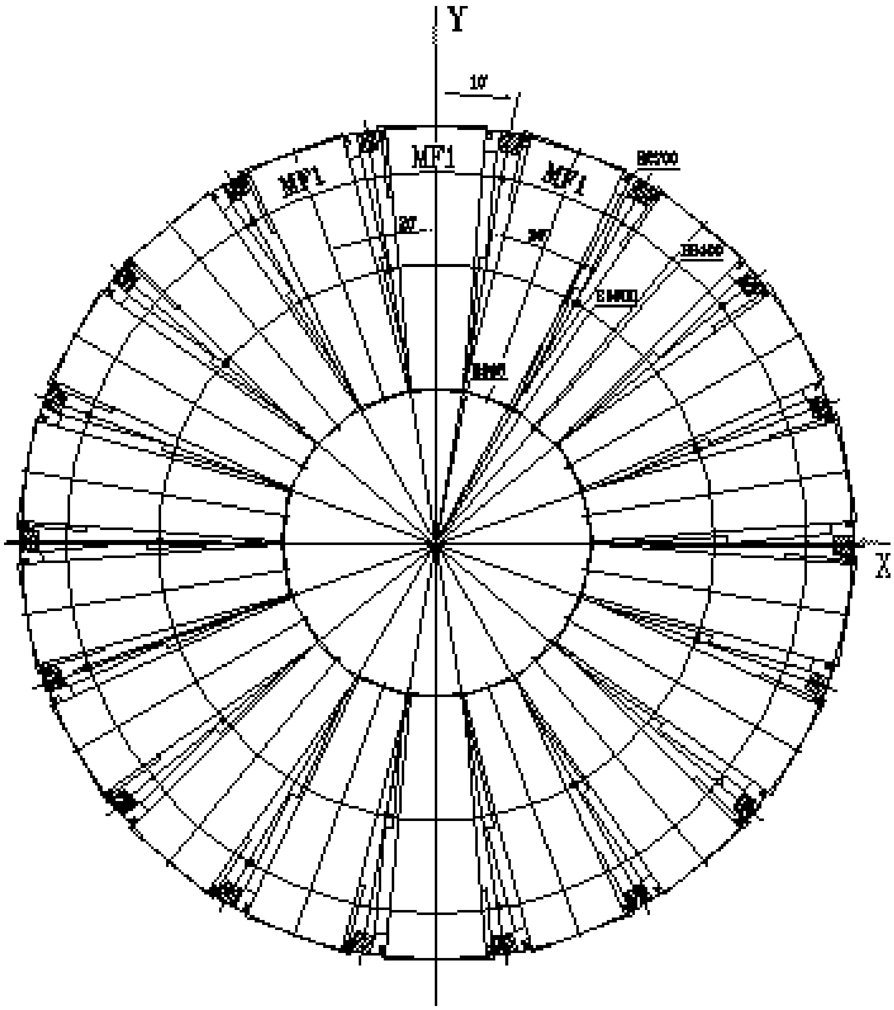

Fig. 3.29: Layout of the first layer of the muon chambers.

3.4.2 General requirements

The proposed design of the interface zone must satisfy the following requirements:

- stable spatial position of endcap calorimeters;

- ensure the pre-determined spatial position of ME1;

- assemblage and disassemblage of ME1 and the RPC system without destruction of the mechanical structural elements;

- optimal cable and cooling system laying;

- place for polyethylene radiation protection;

- assemblage and disassemblage of all endcap calorimeters.

3.4.3 Fastening elements

The basic fastening elements have been enumerated above. To prevent the collapse and/or deformation of the back flange from the 100 mm YE1 nose under electromagnetic force the back flange is fastened with 37 bolts M24x2 to the YN1 disk 240mm thick.

3.4.4 Forces, stresses, deflections

The input data are shown in Fig. 3.12. The materials used for the calculations are:

- material of the key (Figs. 3.30 and 3.31) is steel 40x13, steel 20;

- material of the bolt (Fig. 3.32) is steel 65G;

- material of the top bracket (fastening frame) is stainless steel 12x18H10T (Fig. 3.33).

The results of the stresses and safety factors are presented in Figs. 3.30 - 32. The top bracket maximum deformation is shown in Fig. 3.33.

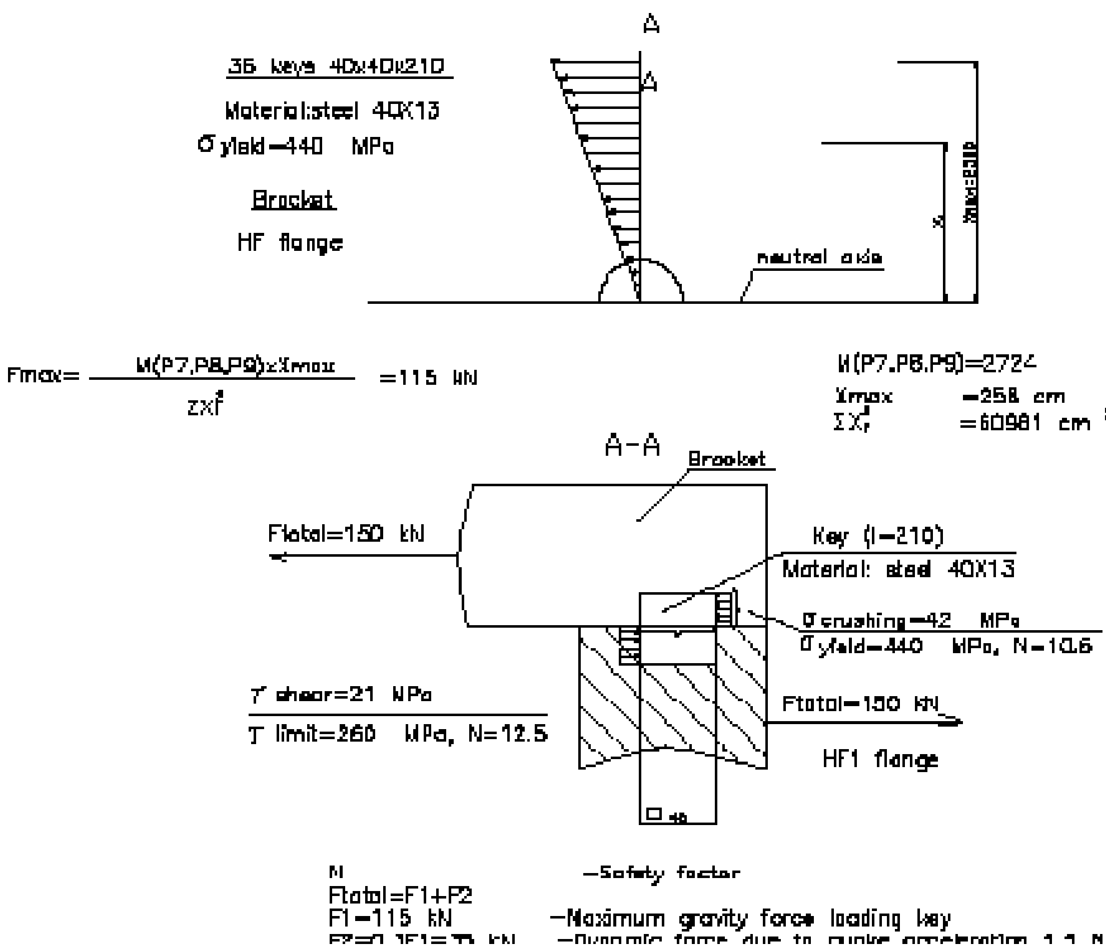

Fig. 3.30: Stresses of the key jointing HE flange and bracket.

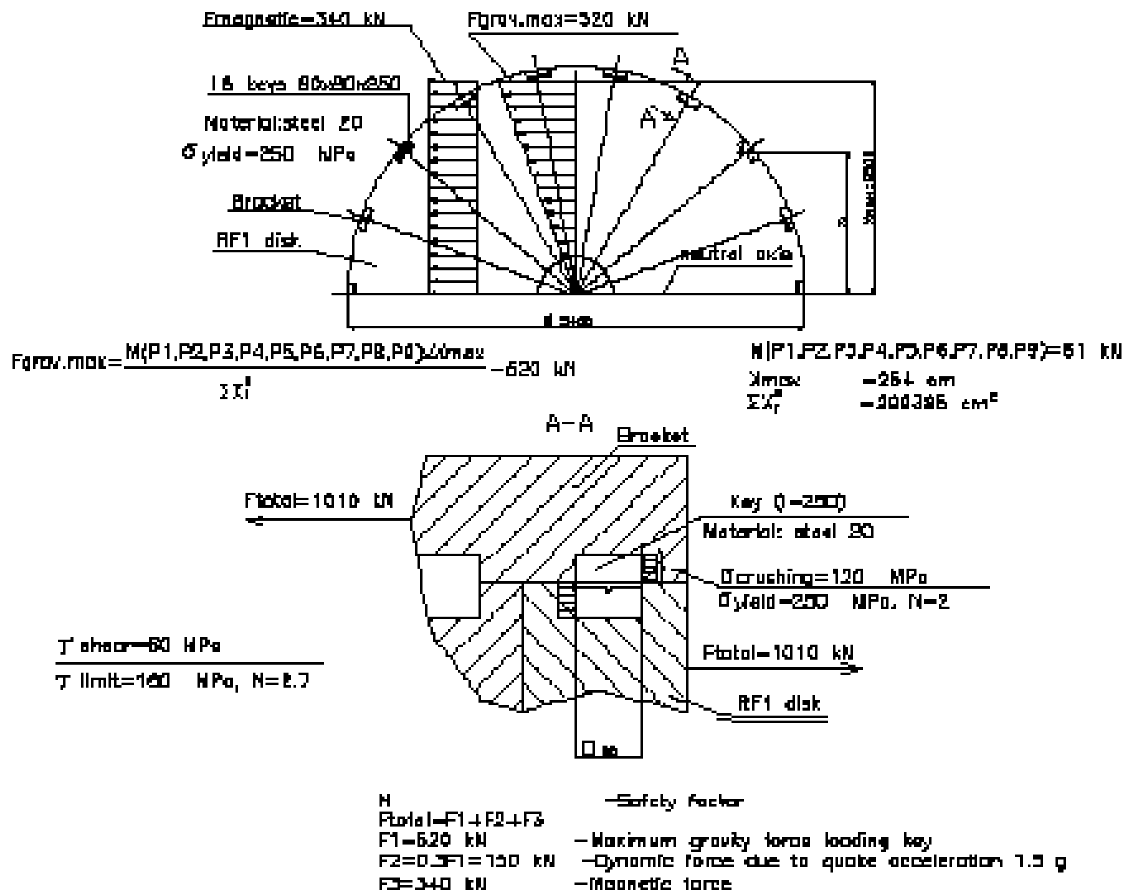

Fig. 3.31: Stresses of the key jointing YE1 disks.

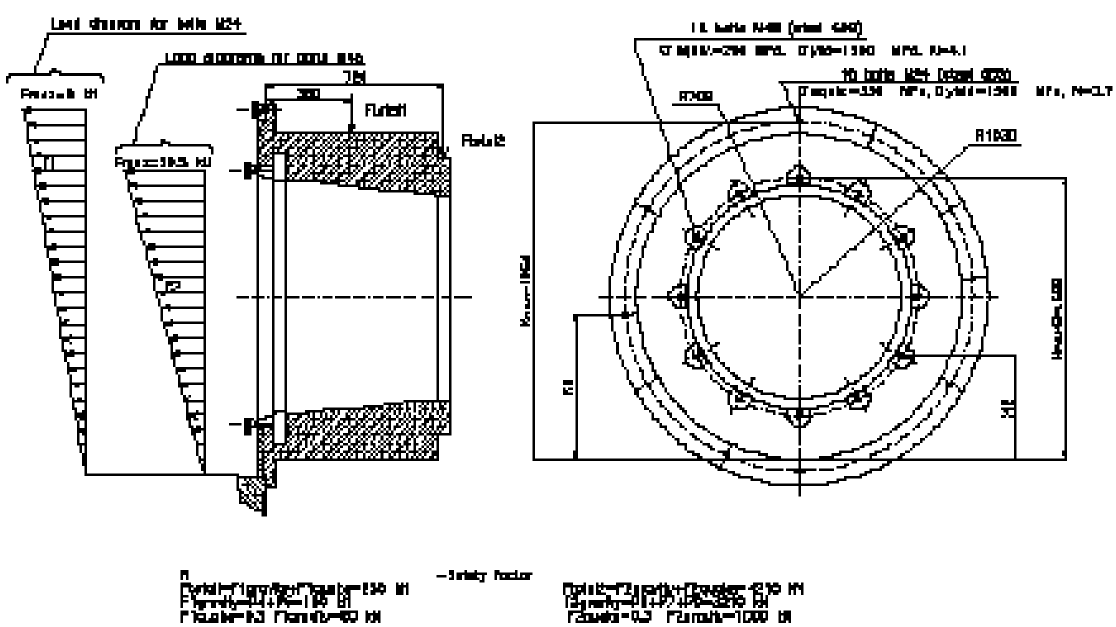

Fig. 3.32: Strength analysis of the bolts fastening ring to YE1.

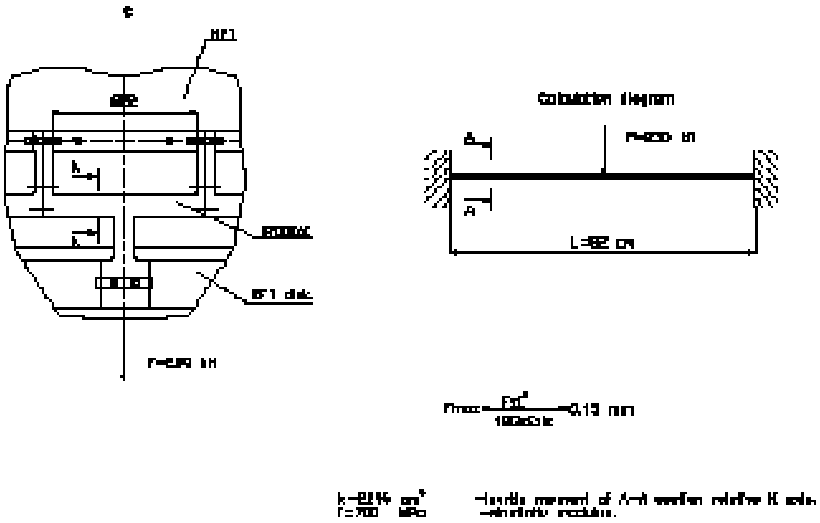

Fig. 3.33: Analysis of the top bracket maximum deformation.

3.4.5 Interface of HE and EE.

To position HE and EE a centering support ring is placed on the HE forward absorber plate. The ring is made of stainless steel 08X18H10T. On the outer surface of the support ring EE is fastened by 18 bolts M24 (see Fig. 3.34). The centering support ring is shown in Fig. 3.35.

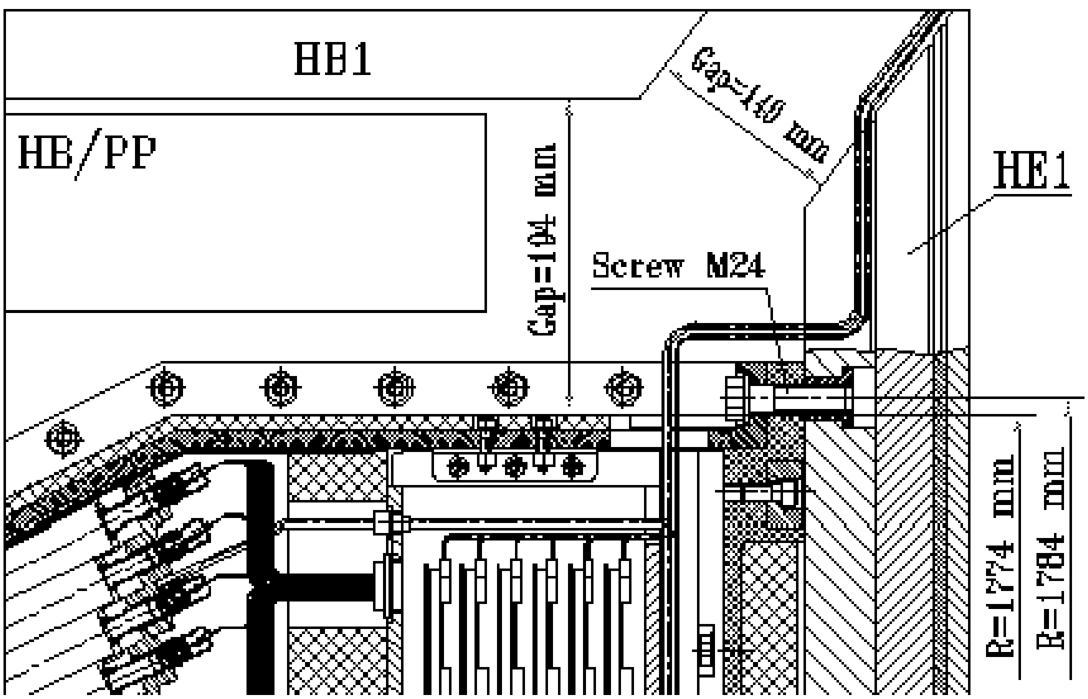

Fig. 3.34: Interface of EE to HE.

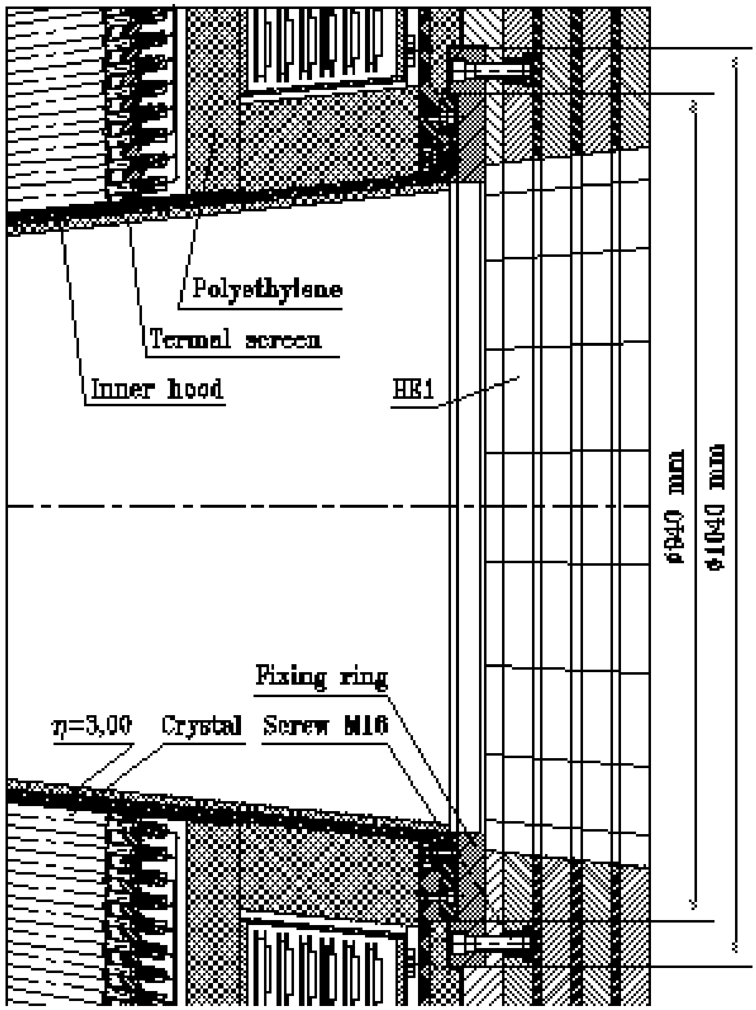

Figure 3.35: The centering support ring of HE and EE interface.

3.5 ENDCAP CALORIMETER ASSEMBLY

3.5.1 Assembly scenario

At CERN in the surface assembly hall HE, ME1, RPC, back flange disk (ED) and disk of the nose YE1 are assembled as a single block and then they are connected to YE1 nose. The assemblage is carried out in horizontal position with subsequent turn of the block on 90^0 and connection to YE1. Then it is lowered in the experimental hall where EE and preshower are mounted on HE and form a single unit.

The scenario of the assemblage is the following:

- in the surface hall a platform shown in Fig.3.36 is mounted from concrete blocks 5200 mm high and with cross section 7 x7.4 m^2;

- 4 technological supports shown in Fig. 3.37 with small hydraulic jacks are installed on the top of the platform (see Fig. 3.38);

- the disk YN1 shown in Fig. 3.39 (weight is 40 tonne and thickness is 240 mm with special cuts to fasten rotational tooling) is installed on the technological supports using arm presented in Fig. 3.40;

- Fig. 3.41 shows the disk ED (weight is 18 tonne and thickness is100 mm) installation on the surface of the YN1 disk (fastened by 37 bolts M36x4);

- internal support ring IR (weight is 5 tonne) is mounted on YN1 (see Fig. 3.42) and positioned by pins M48;

- the bearing base (BB) shown in Fig. 3.43 is mounted on the surface of the disk ED;

- Fig. 3.44 shows the intermediate disk (MD) with 36 steering plates for ME1 and Fig. 3.45 shows MD mounting and fastening using the temporary support shown in Fig. 3.46;

- assemblage of RPC on the HE back flange;

- the back flange (weight is 17 tonne) is mounted on the landing surface of the internal support ring (see Fig. 3.47);

- Eighteen fastening frames are mounted along the perimeter of the interface zone and bolted by torque indication wrench (see Fig. 3.48);

- Fig. 3.49 shows HE absorber assembly;

- Fig. 3.50 shows installation and assembly of scintillator trays with optical and quartz cables and radioactive source tubes;

- installation and assembly of the decoding boxes;

- testing of the control systems;

- installations, alignment and testing of 36 ME1 chambers;

- Fig. 3.51 shows installation of a frame (see Fig. 3.52) on the top of HE and fastening of two plates (see Fig. 3.53) to the disk YN1 and to the frame plates;

- installation of supports for rotation shown in Fig. 3.54 is made in two steps: 1) lifting of the assembled system with hydraulic jacks and 2) installation of supports;

- the whole structure with the support is presented in Fig. 3.55;

- Fig. 3.56 shows rotation of endcap calorimeter on 90^0;

- Fig. 3.57 shows installation of hydraulic jacks for endcap aliment;

- Fig. 3.58 shows moving of YE1 to endcap;

- connection of YE1 and endcap with stud-bolts and super-nuts is shown in Fig. 3.59, the rotation support is removed;

- YE1 and end cap is moved to the pit and lowered into the hall;

- EE installation and assembly with cables and cooling pipes;

- preshower installation and assembly of cables and cooling pipes, Fig. 3.60 shows the final assemblage.

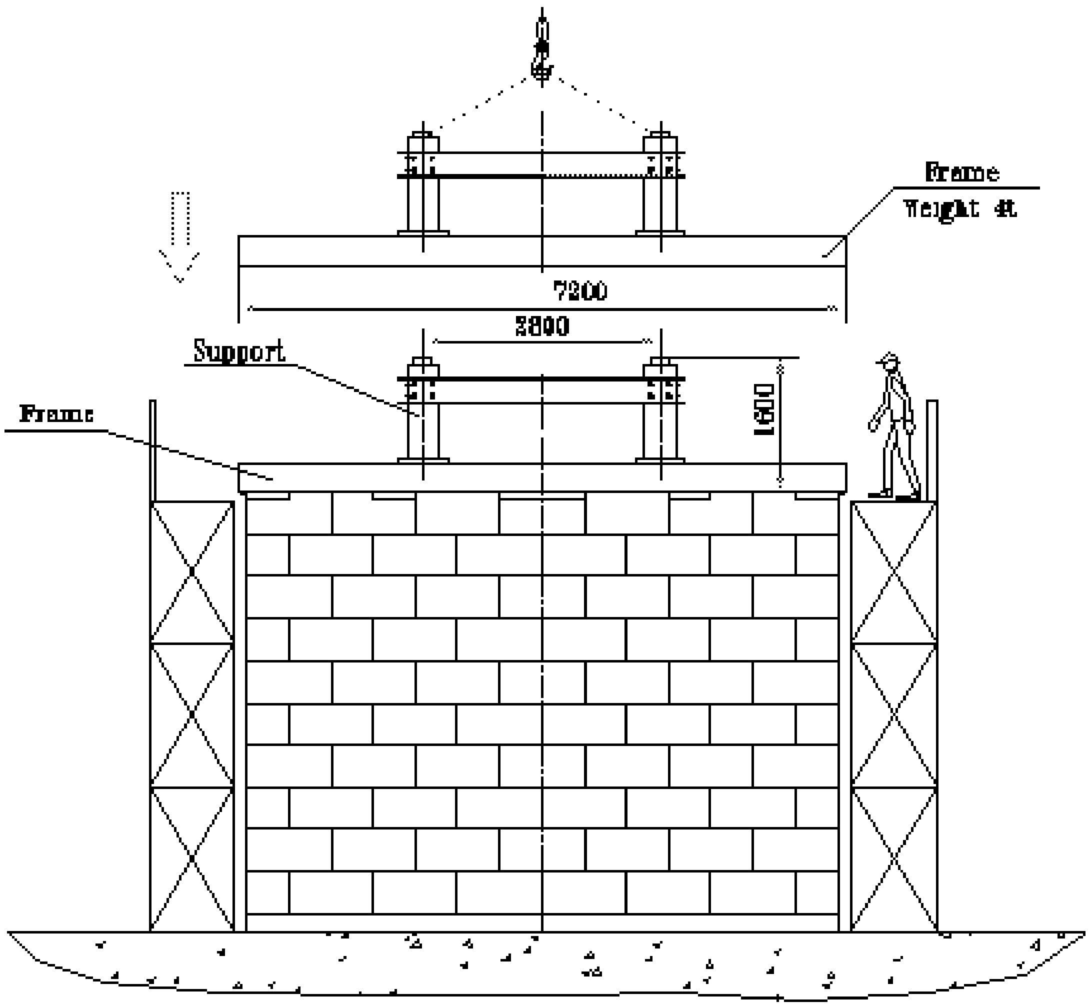

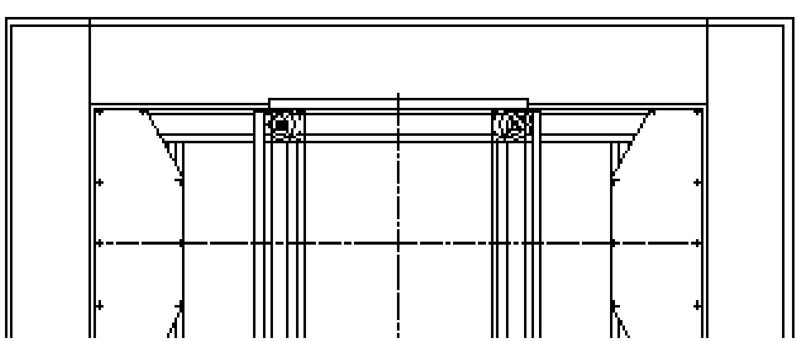

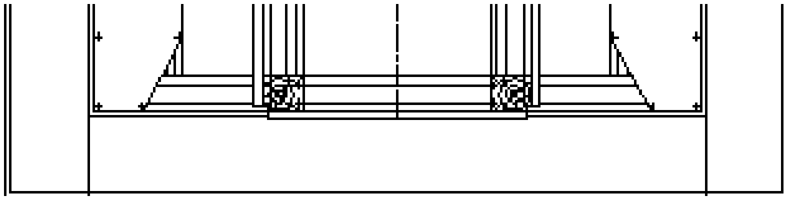

Fig. 3.36: Support structure for the assemblage.

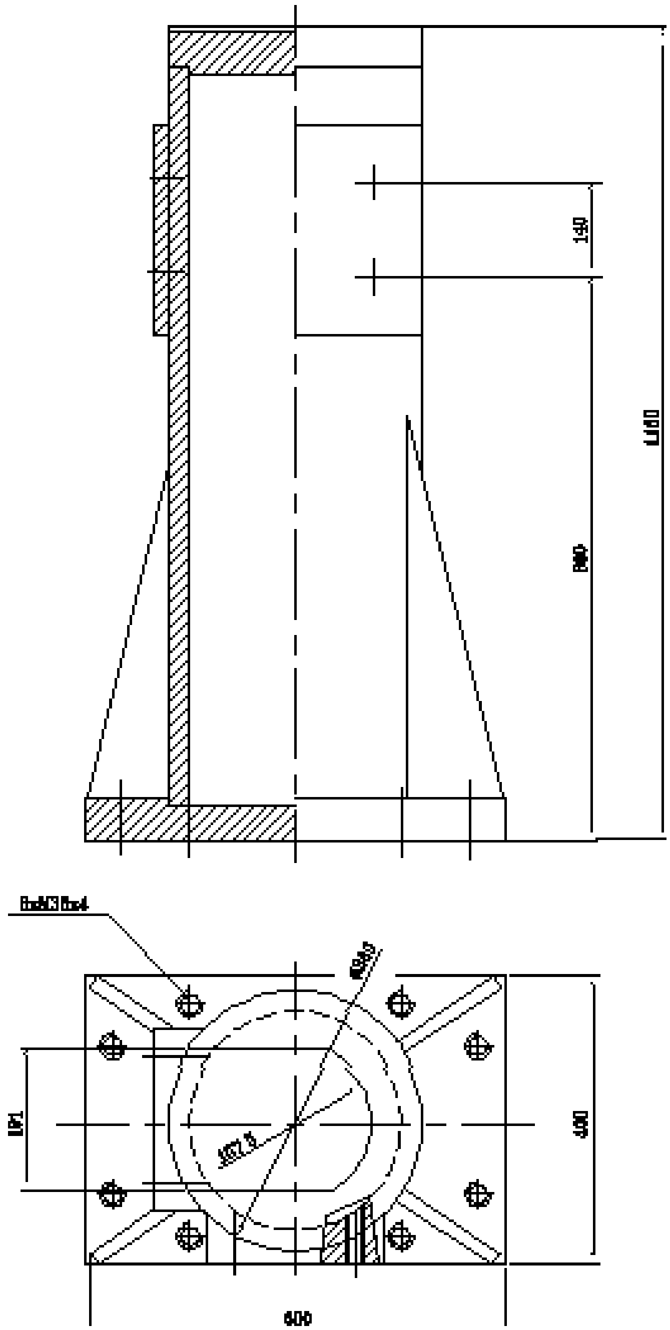

Fig. 3.37: Support tube.

.

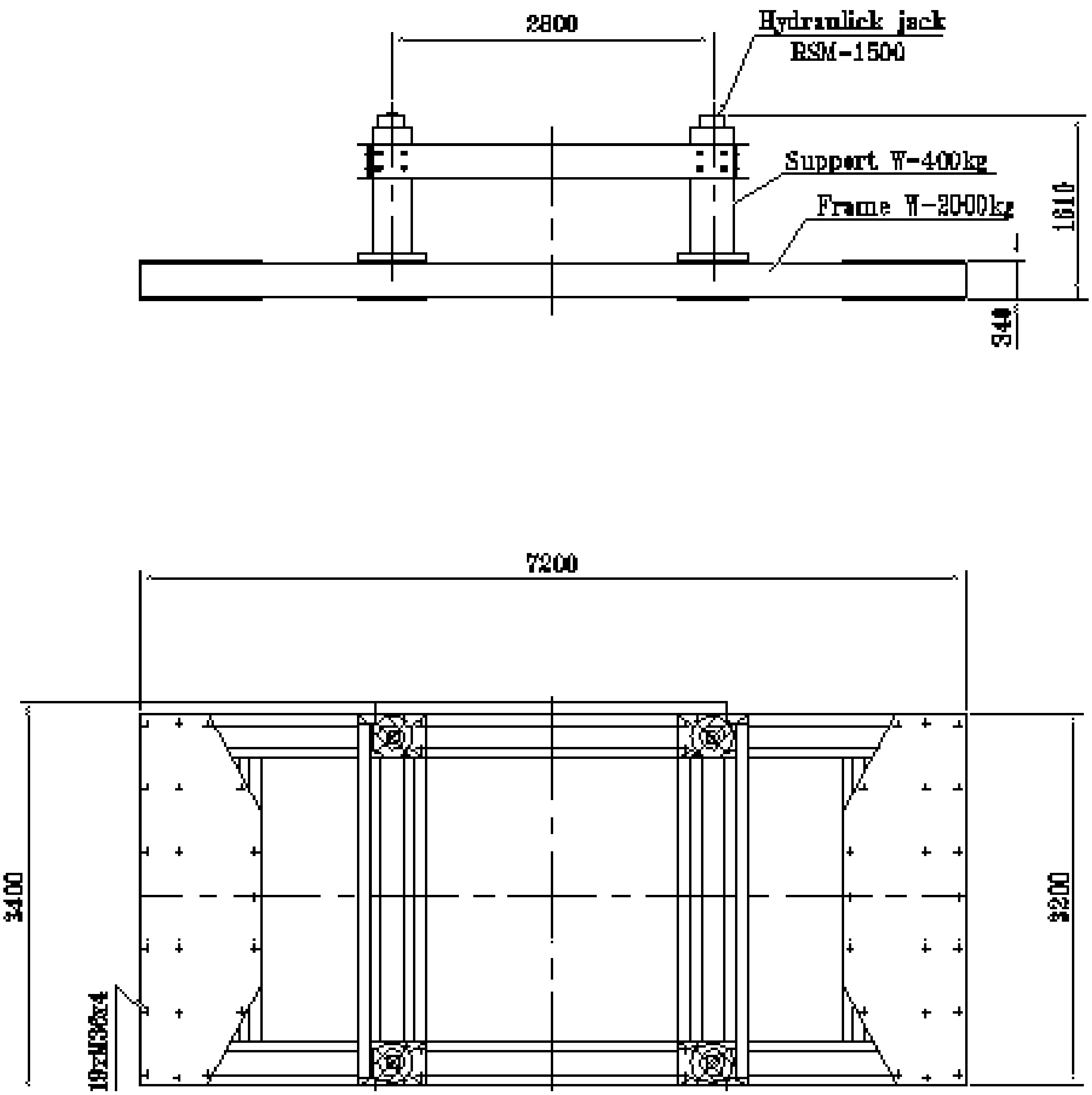

Fig. 3.38: Support table

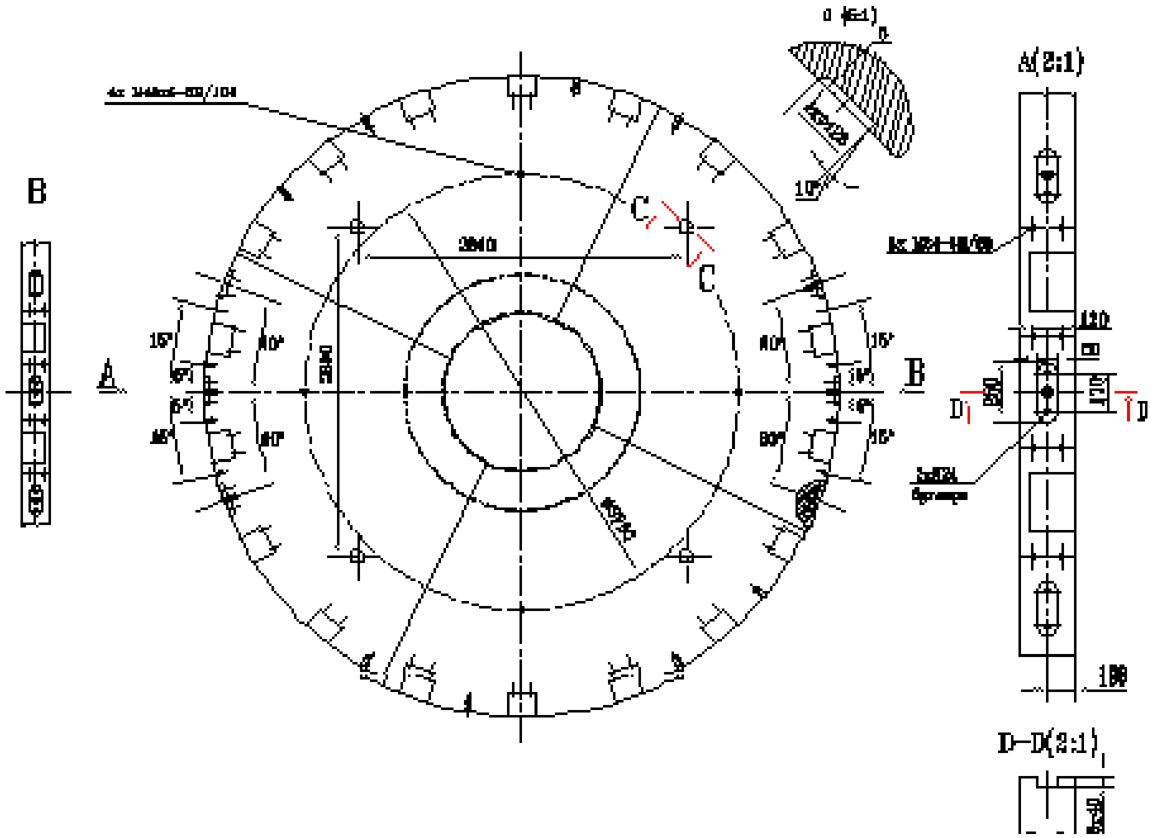

Fig. 3.39: Disk YN1

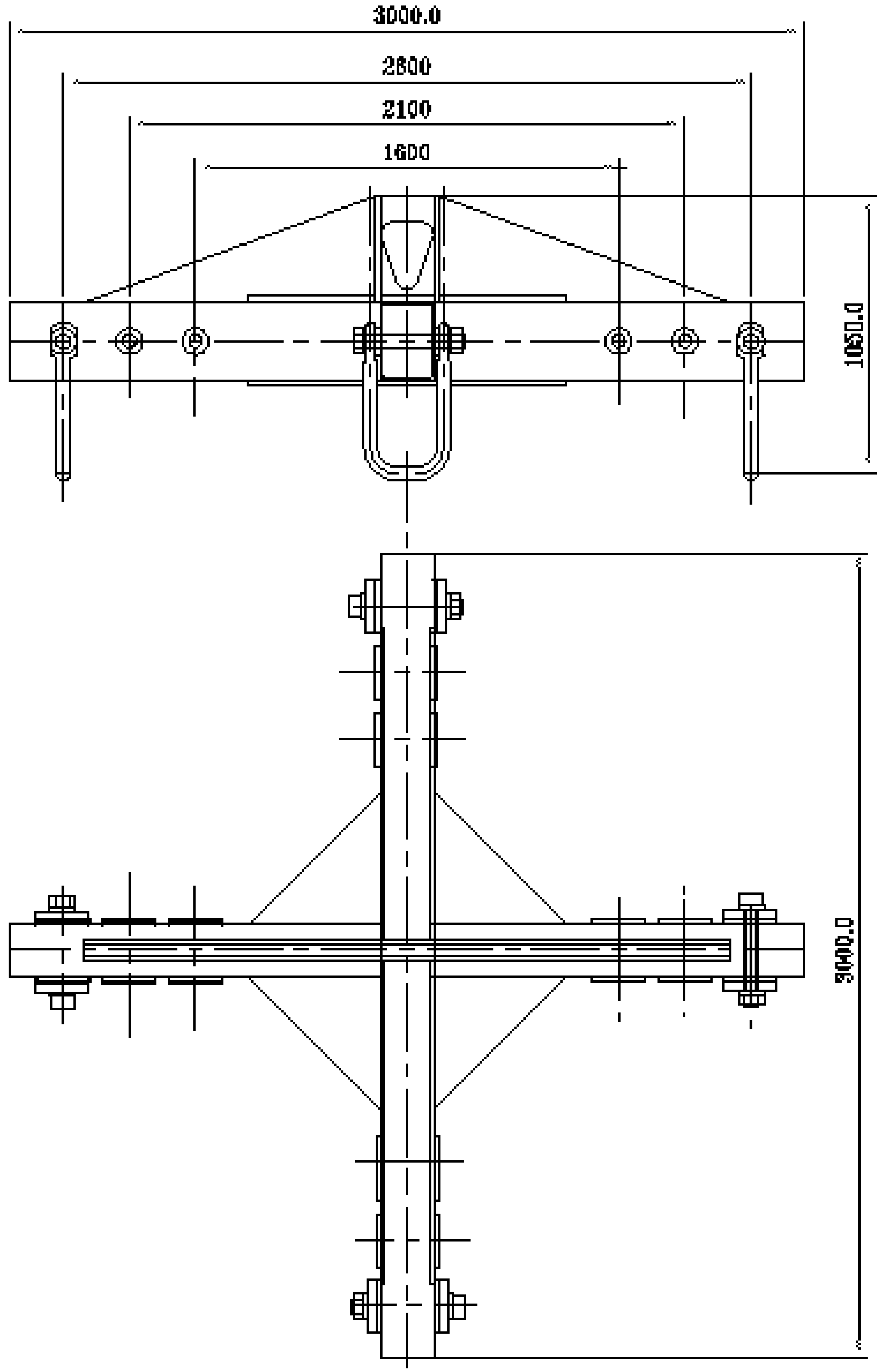

Fig. 3.40: Arm for the assemblage.

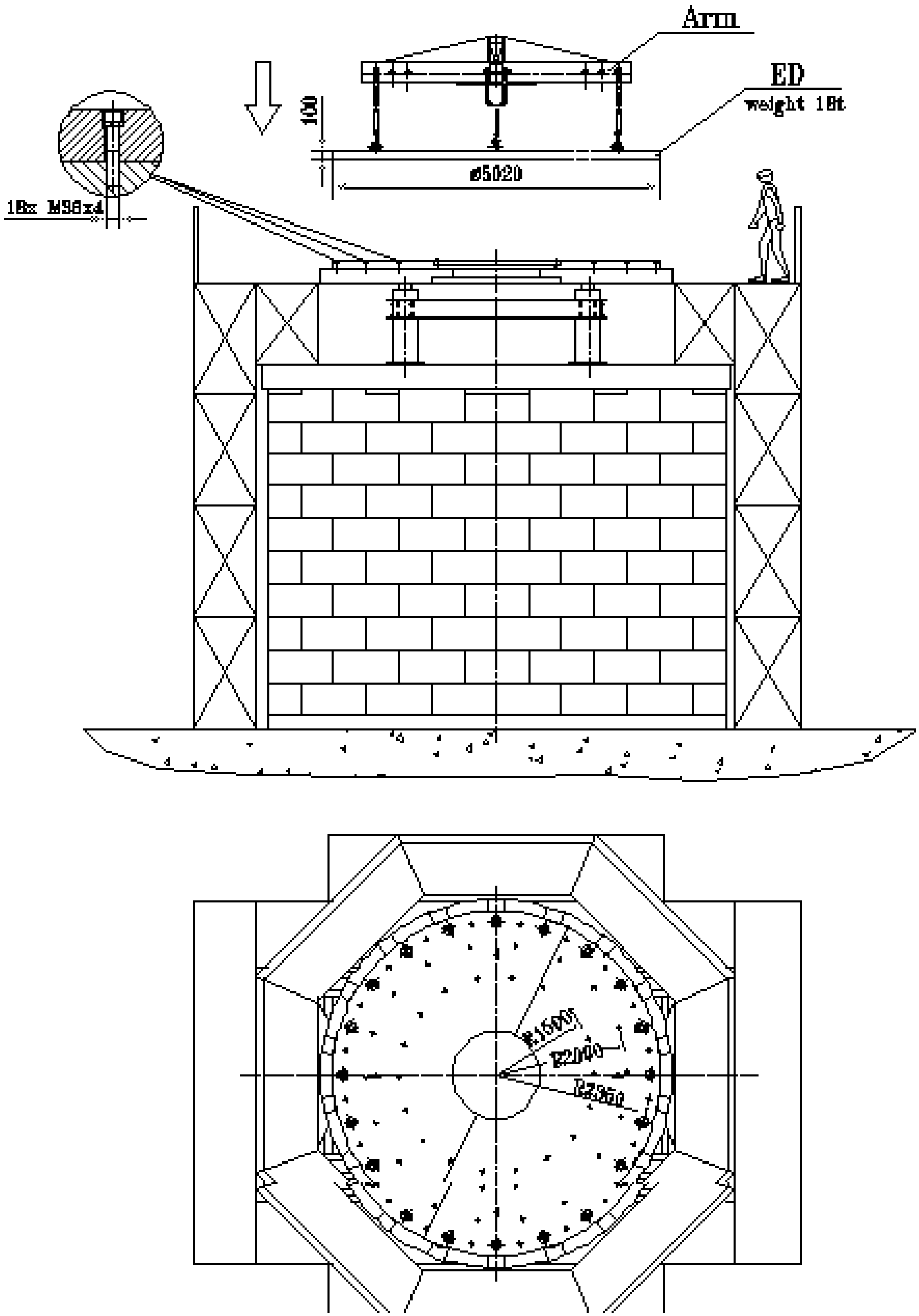

Fig. 3.41: Installation of disk ED on YN1.

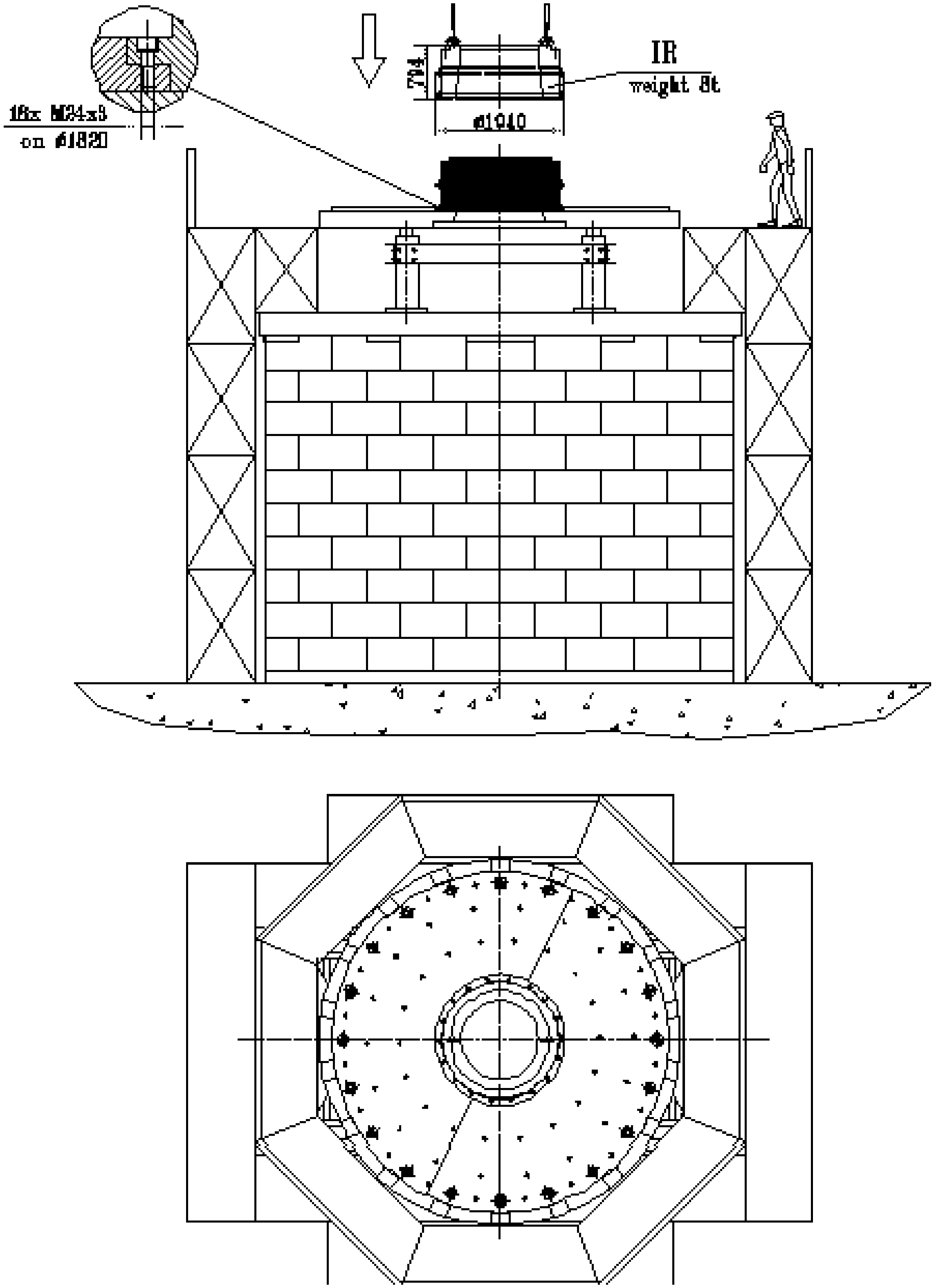

Fig. 3.42: Installation of internal support ring (IR)

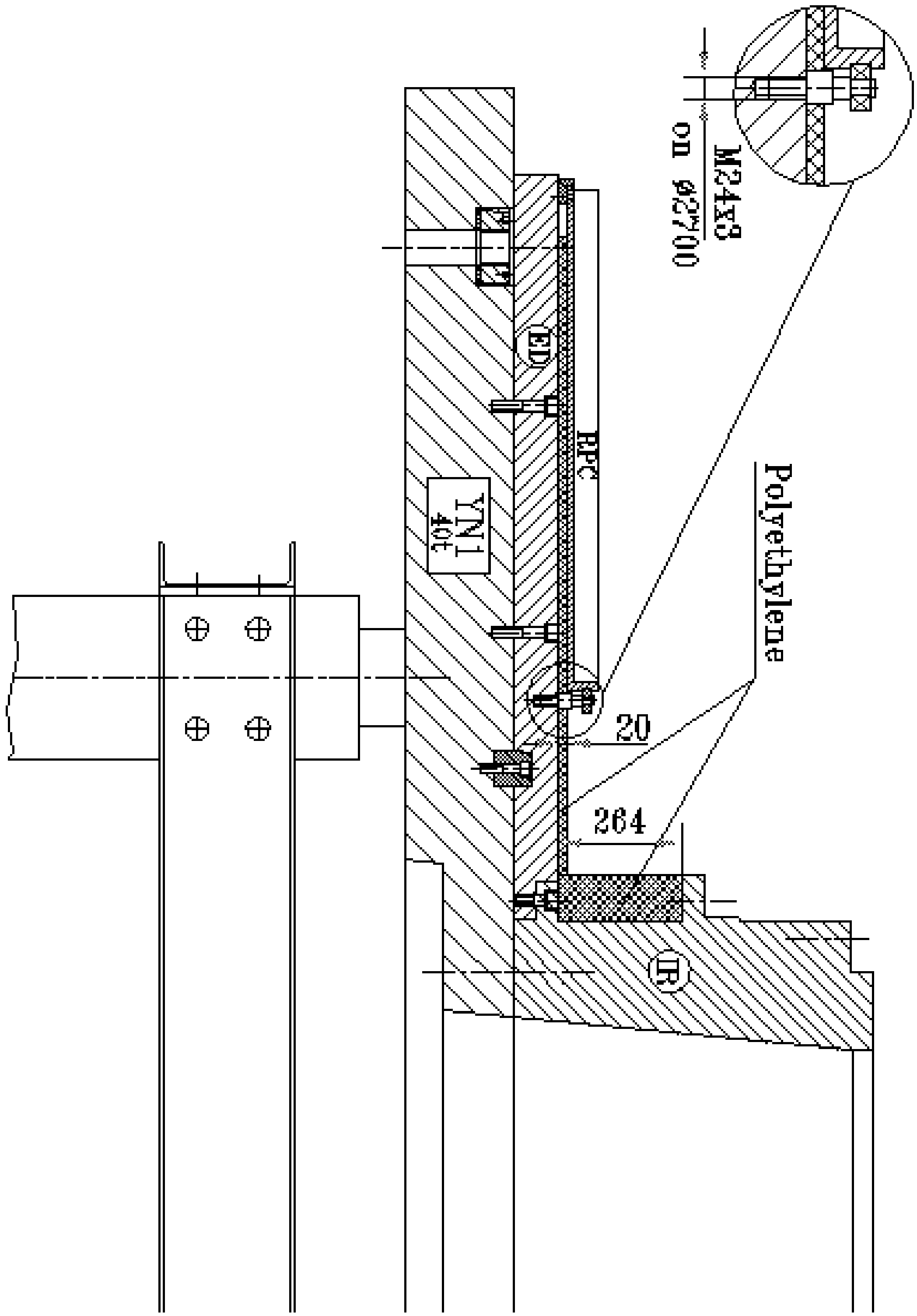

Fig. 3.43: Bearing base is connected to ED and IR.

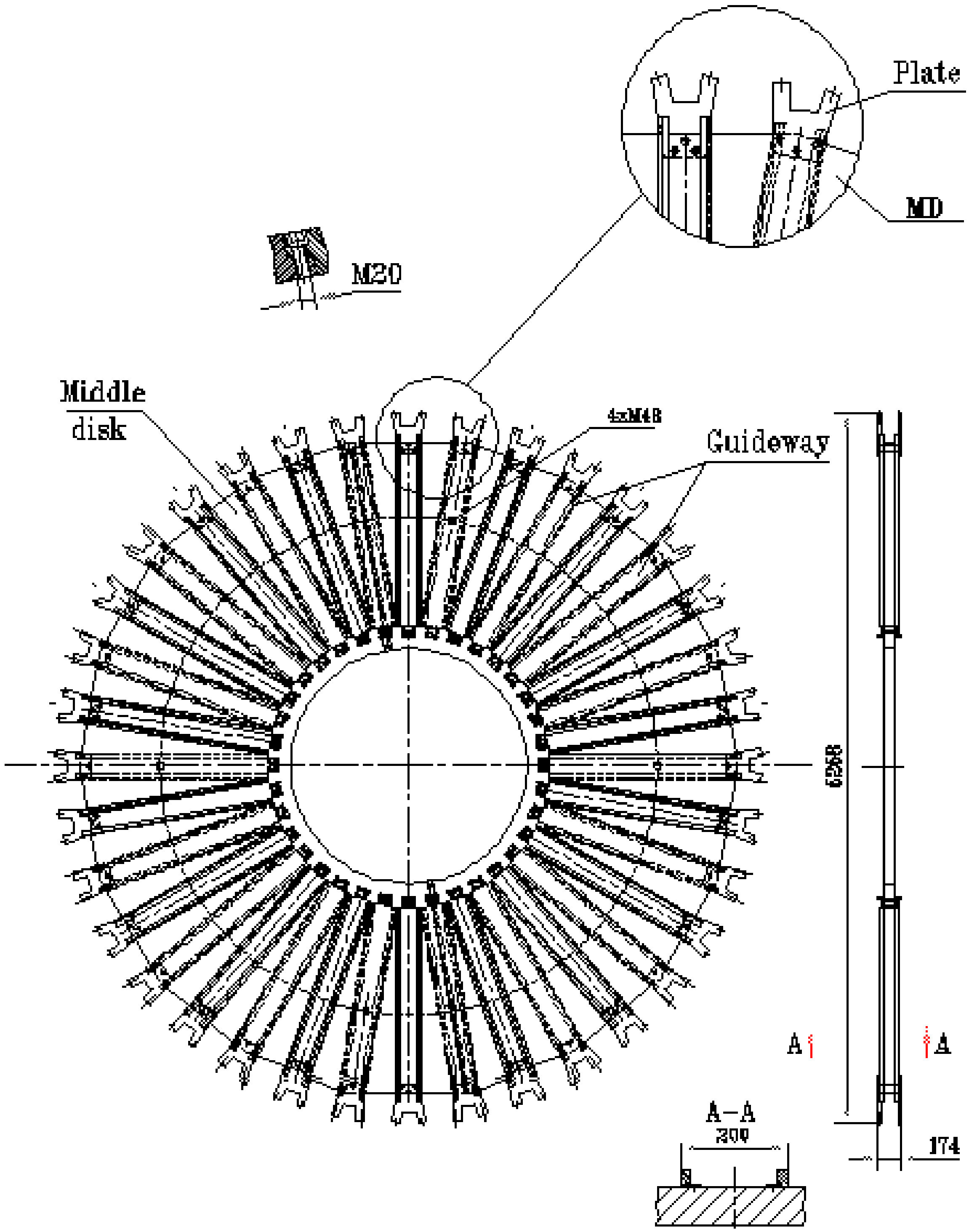

Fig. 3.44: Middle disk for installation of ME1.

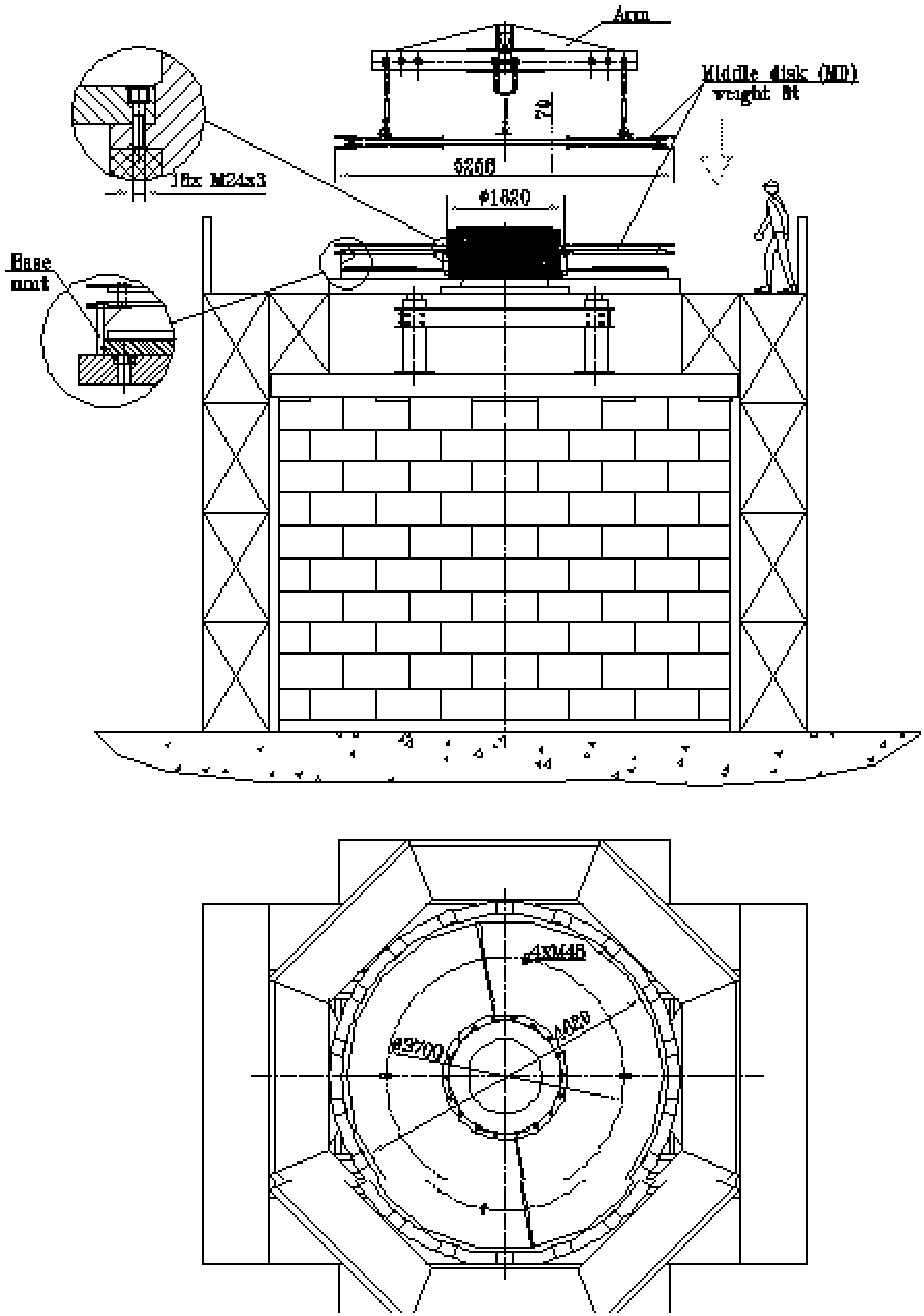

Fig. 3.45:.Installation of middle disk.

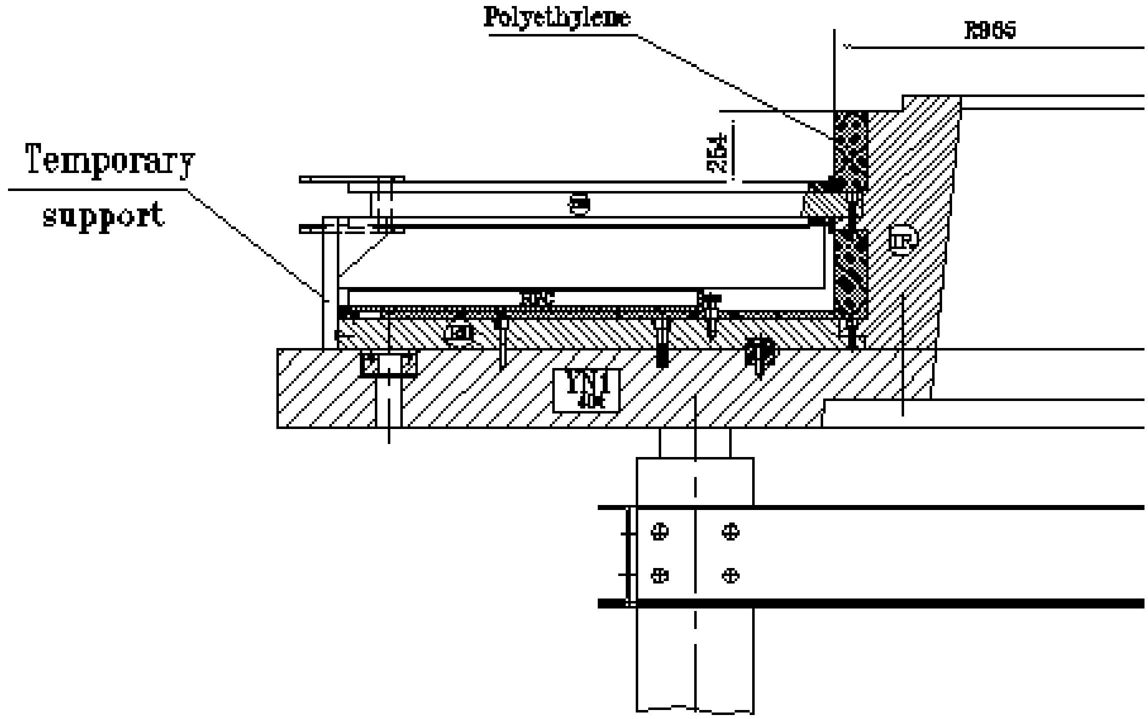

Fig. 3.46: Installation of temporary support.

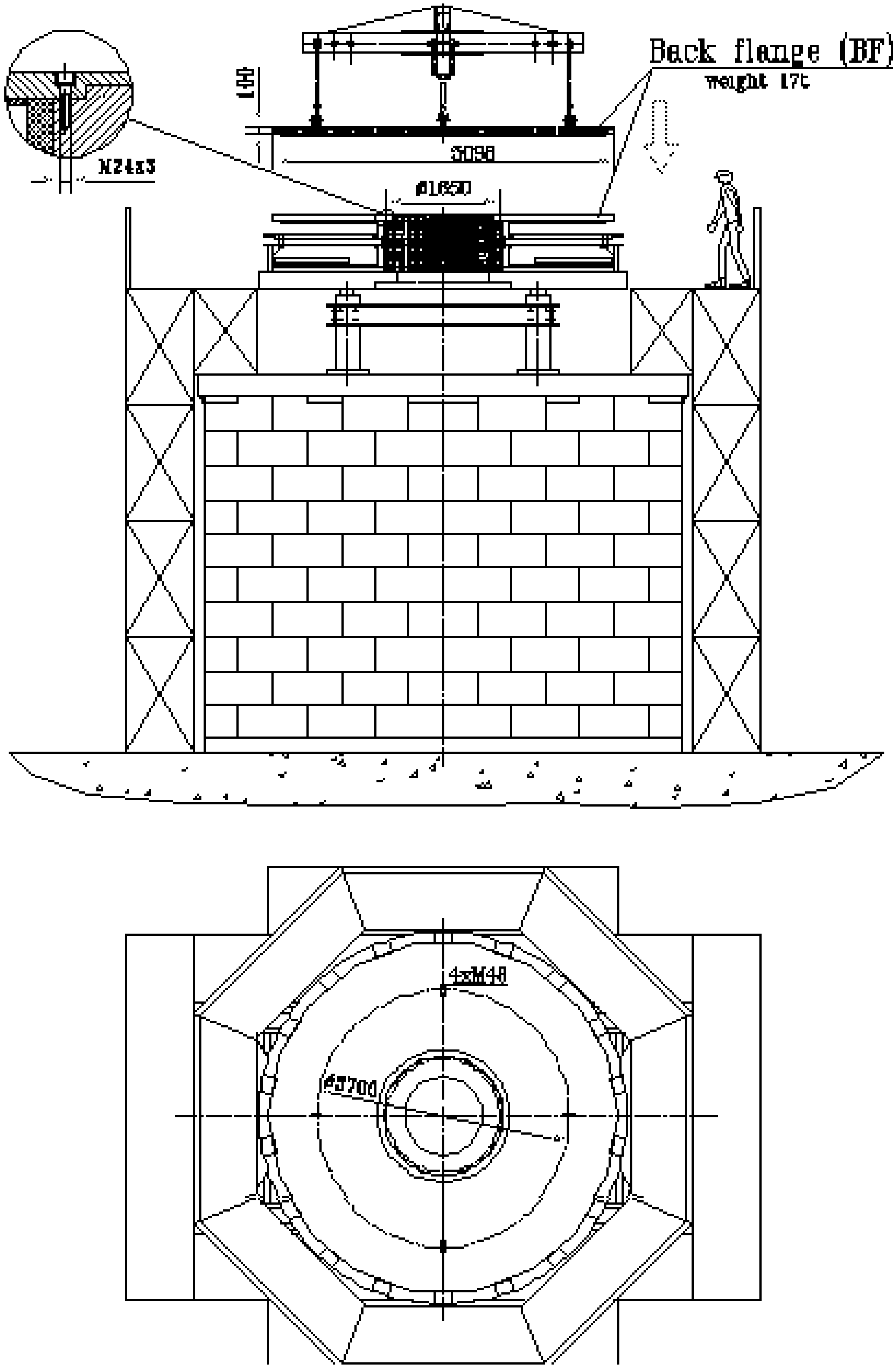

Fig. 3.47: Installation of HE back flange.

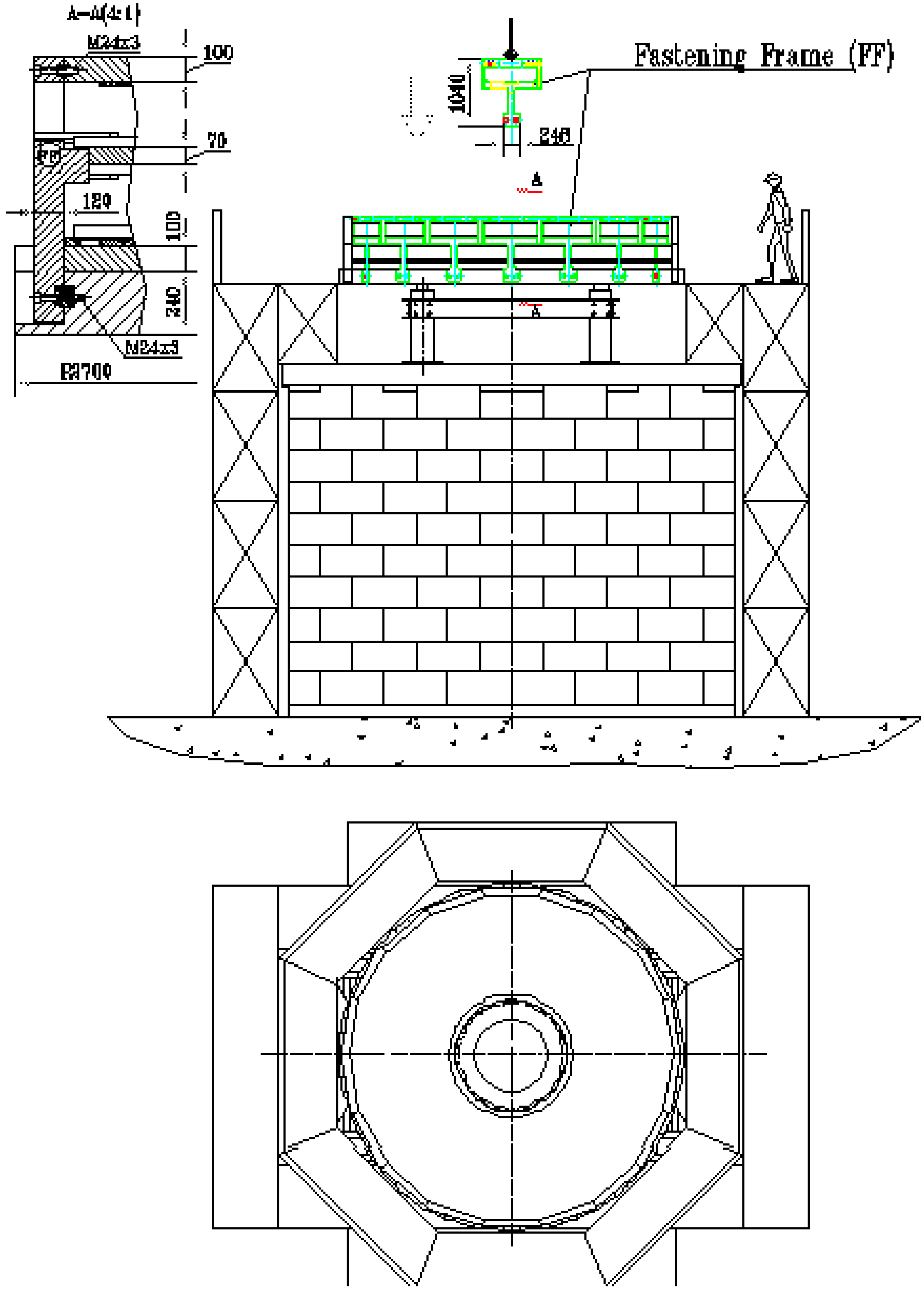

Fig. 3.48: Mounting of fastening frame.

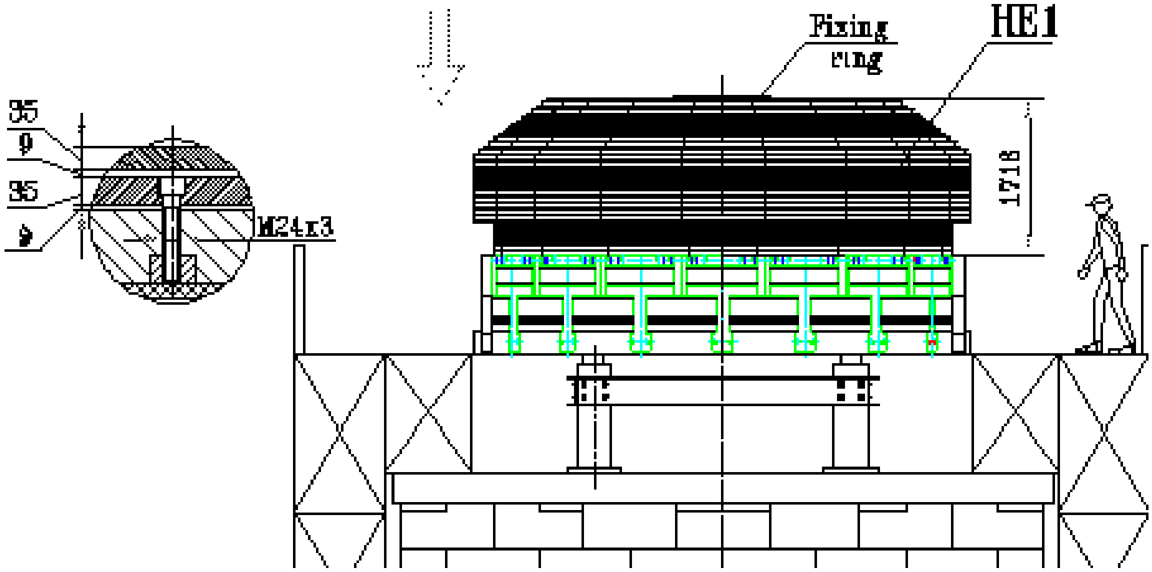

Fig. 3.49: Assembly of the HE absorber.

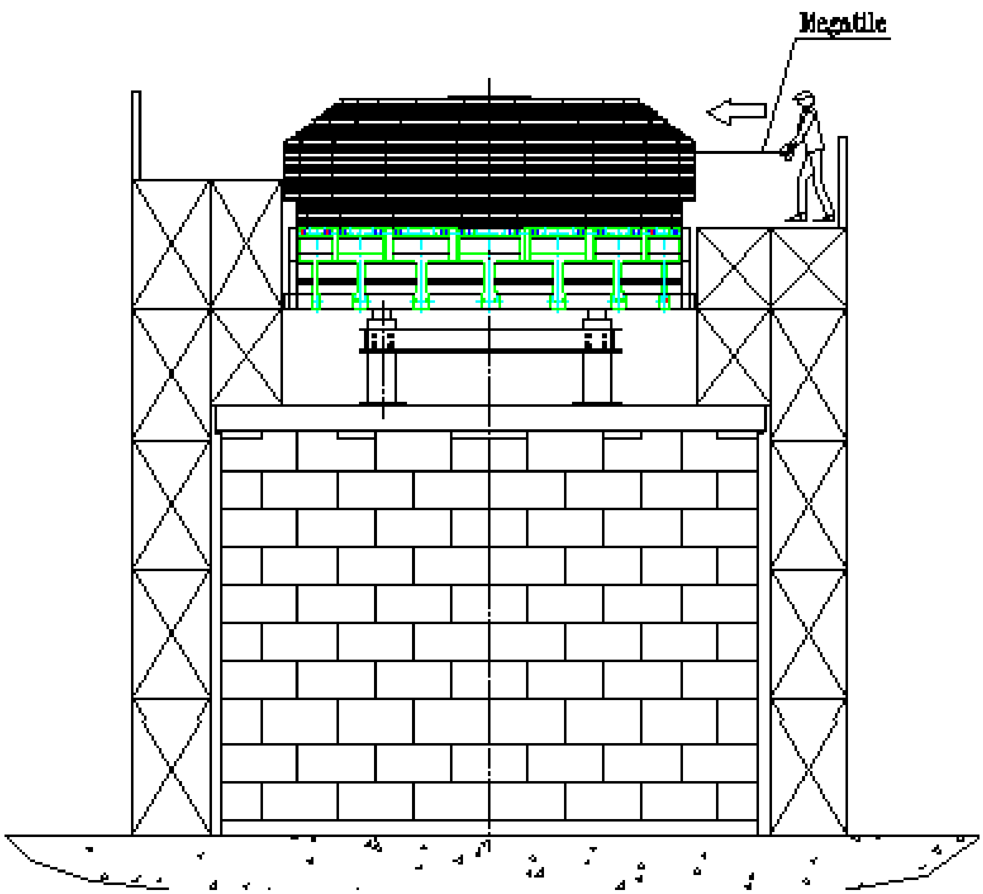

Fig. 3.50: Installation of megatiles.

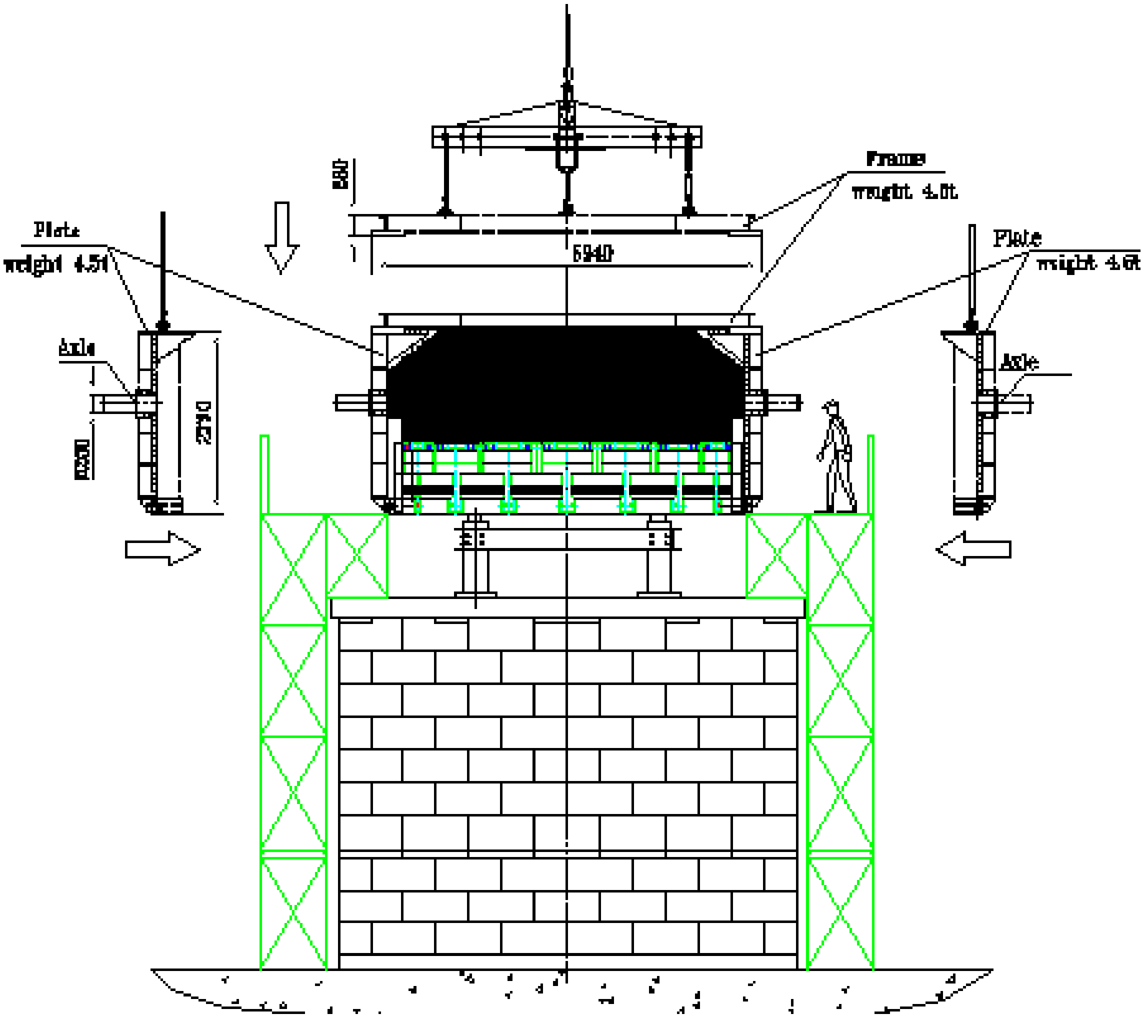

Fig. 3.51: Installation of tooling for HE rotation.

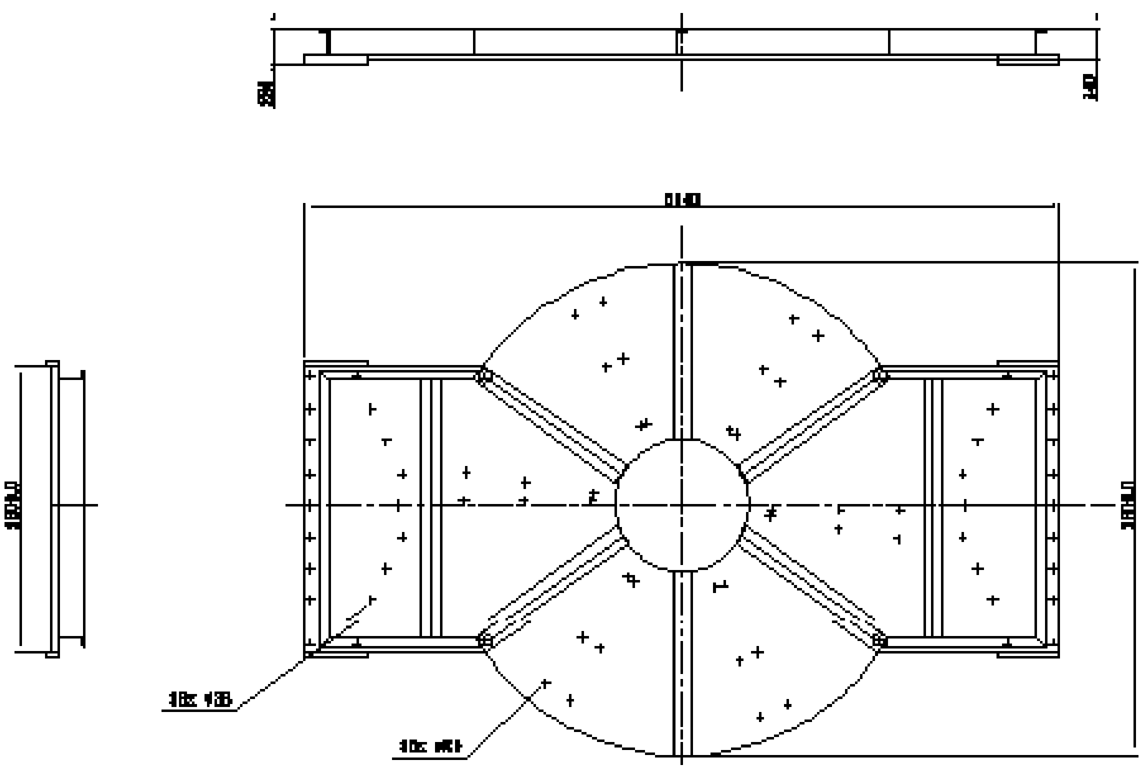

Fig 3.52: Top plate of the tooling for HE rotation.

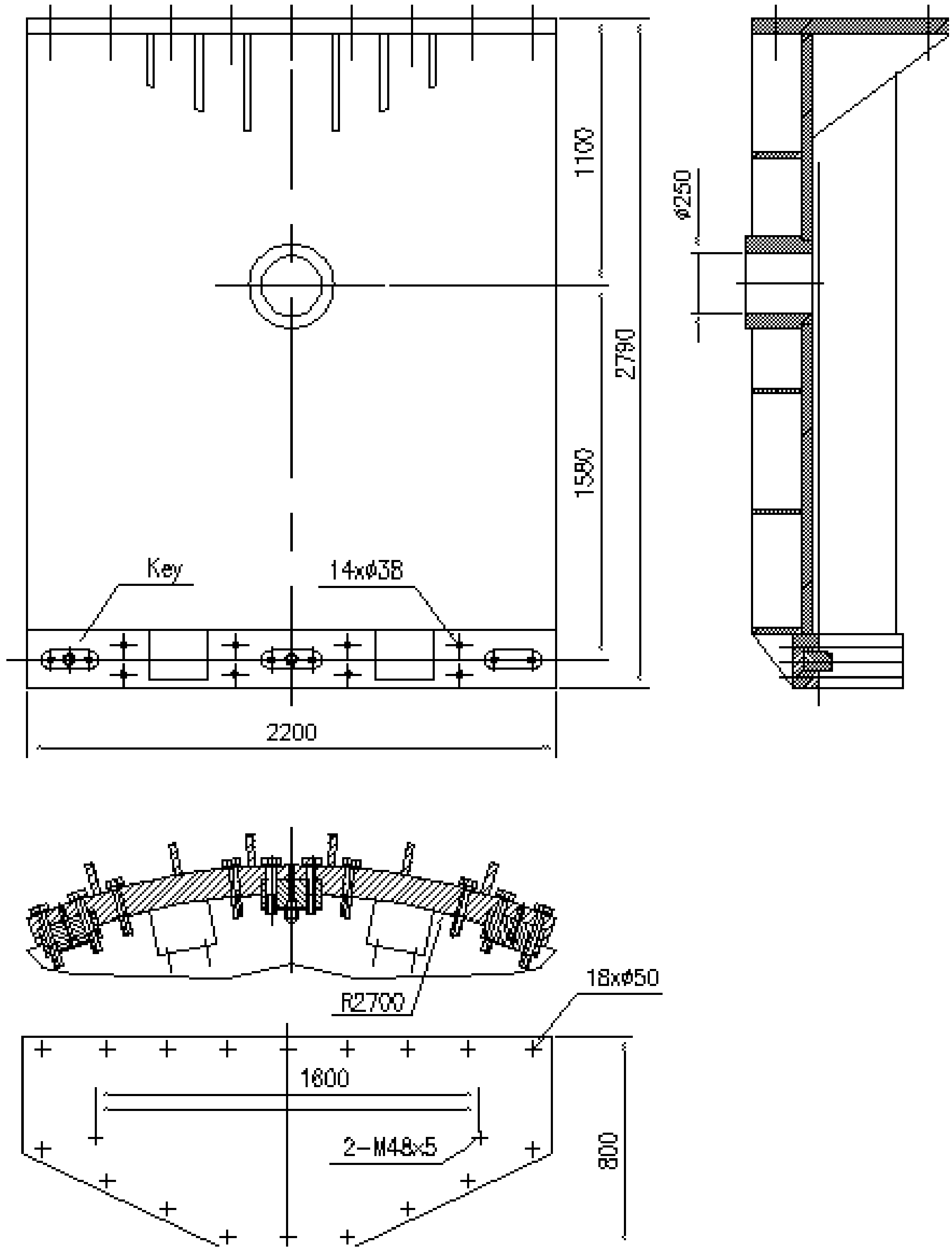

Fig. 3.53: Side plate of the tooling for HE rotation.

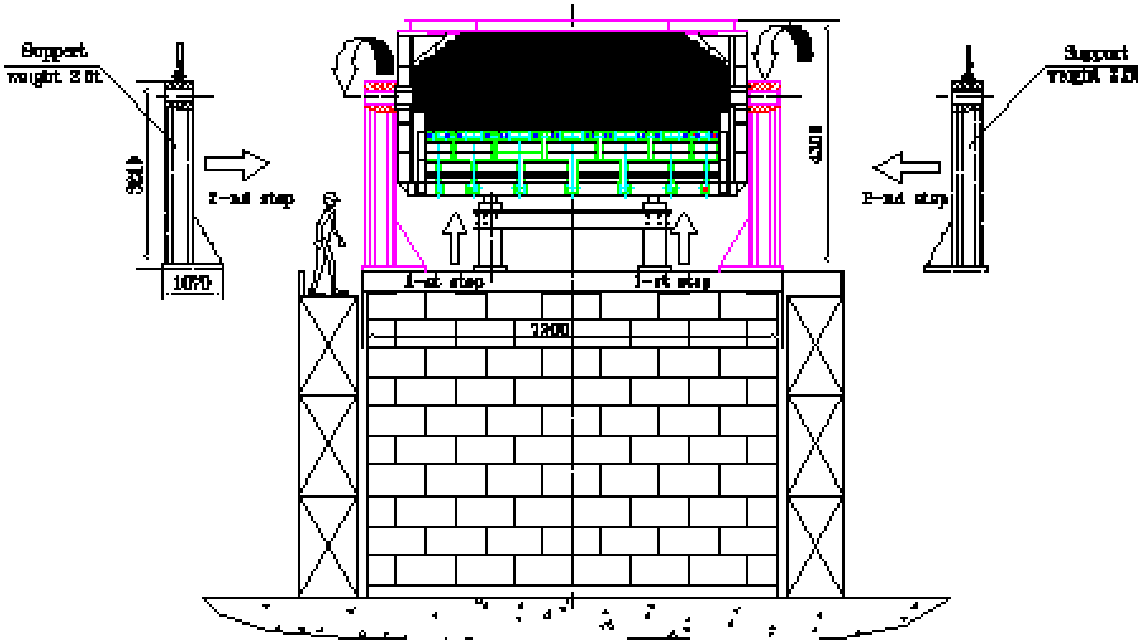

Fig. 3.54: Installation of support for HE rotation.

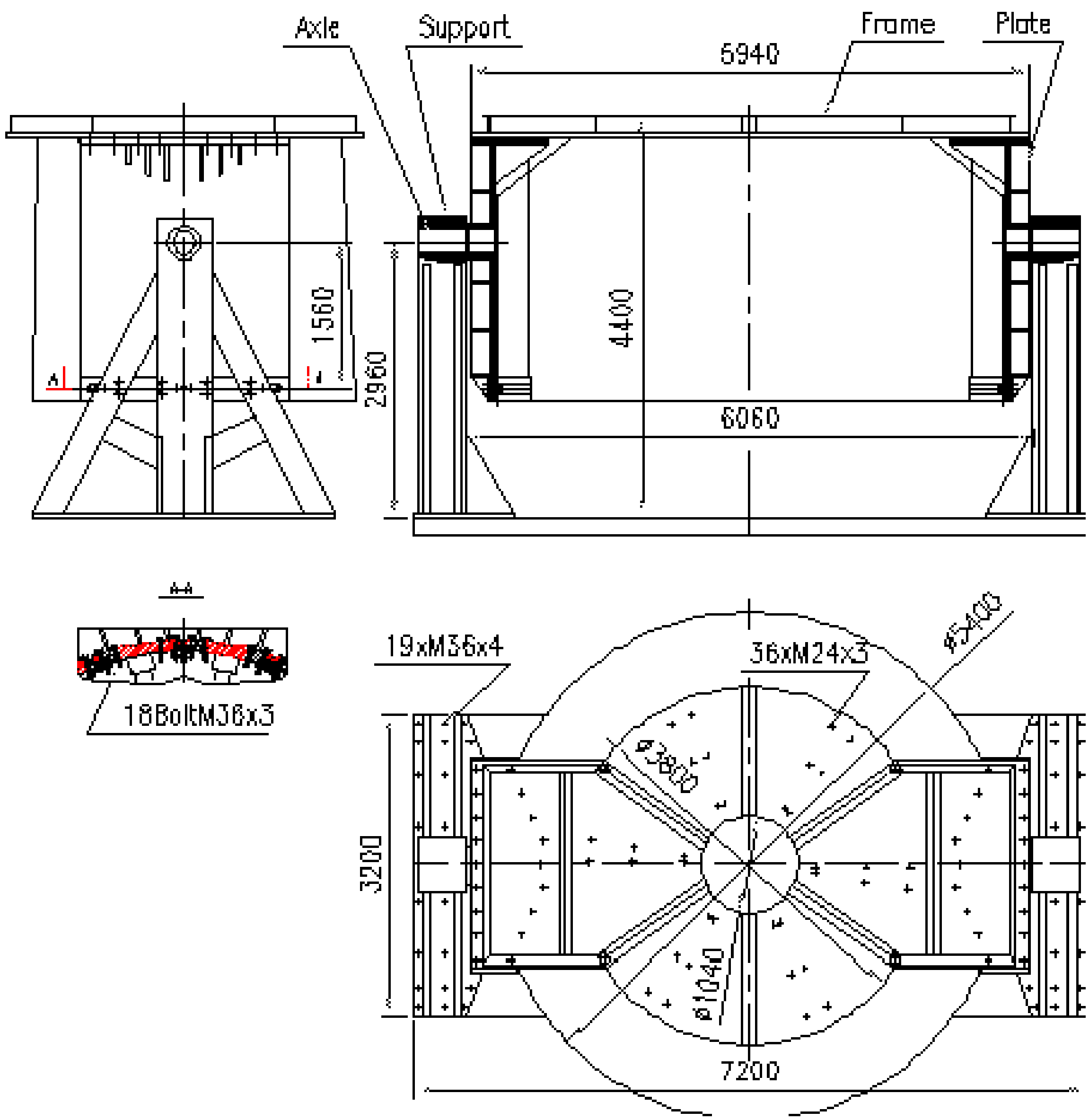

Fig. 3.55: The assembled tooling for HE rotation.

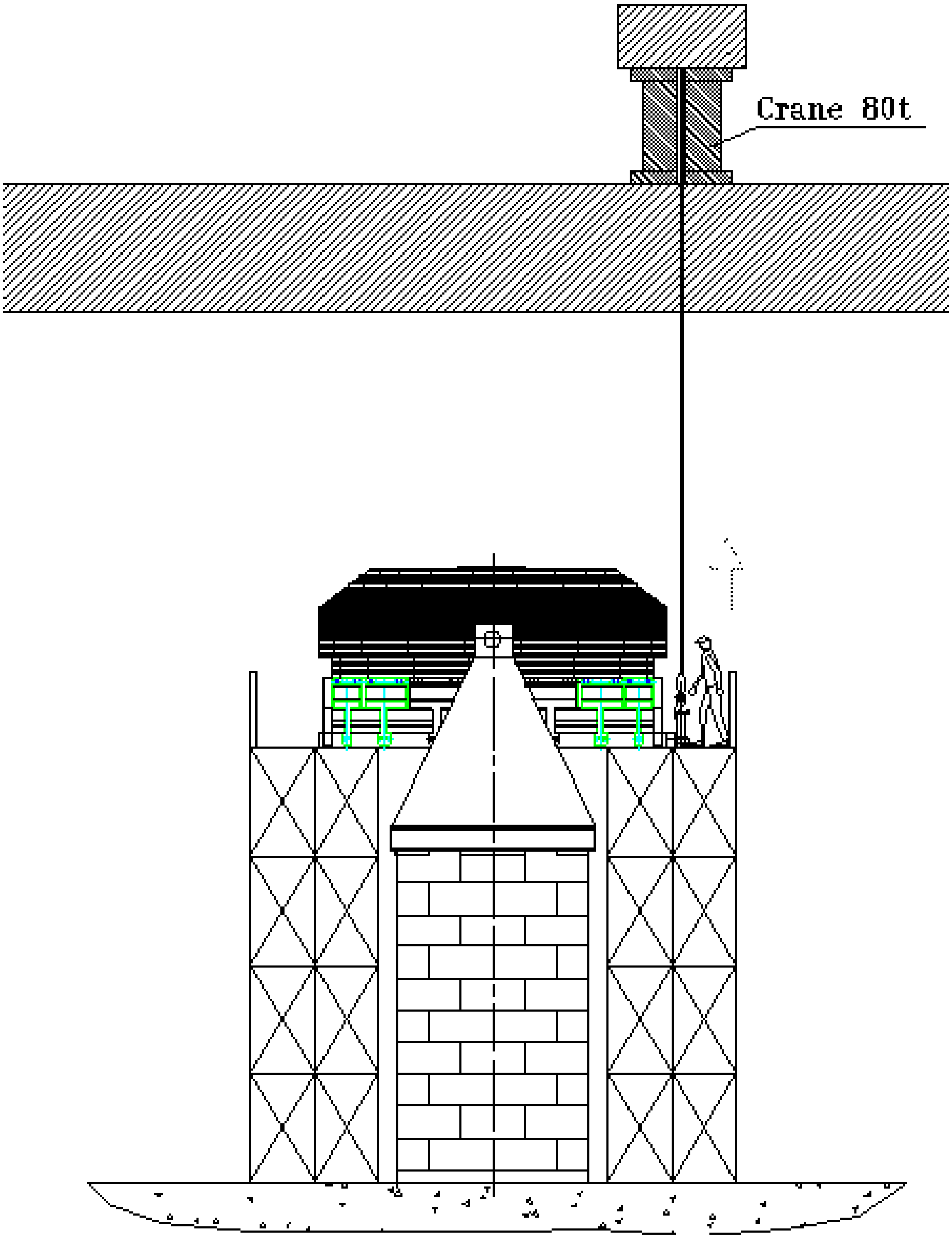

Fig. 3.56: Removal of support tubes and rotation of HE.

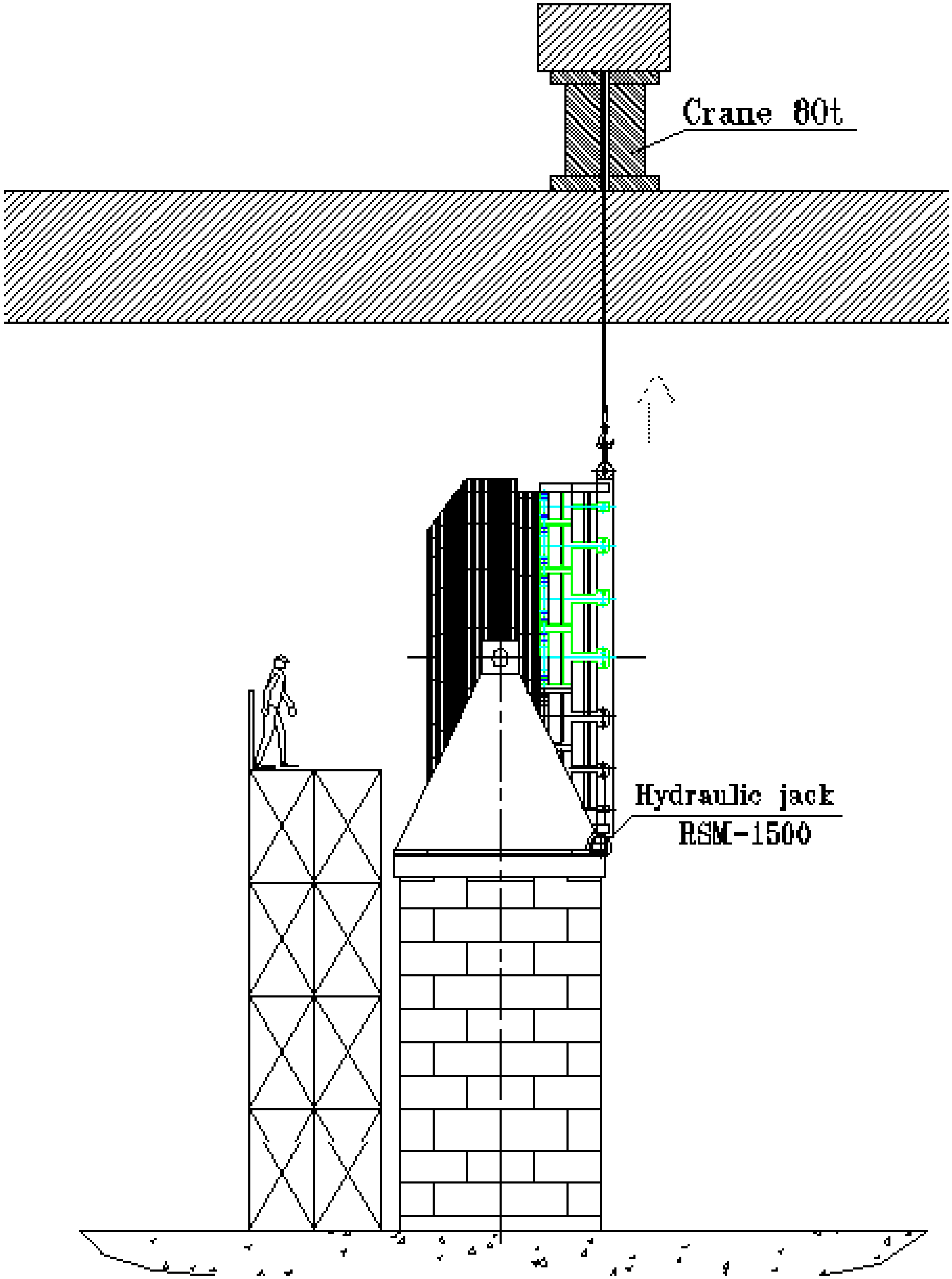

Fig. 3.57: Installation of hydraulic jacks for HE alignment.

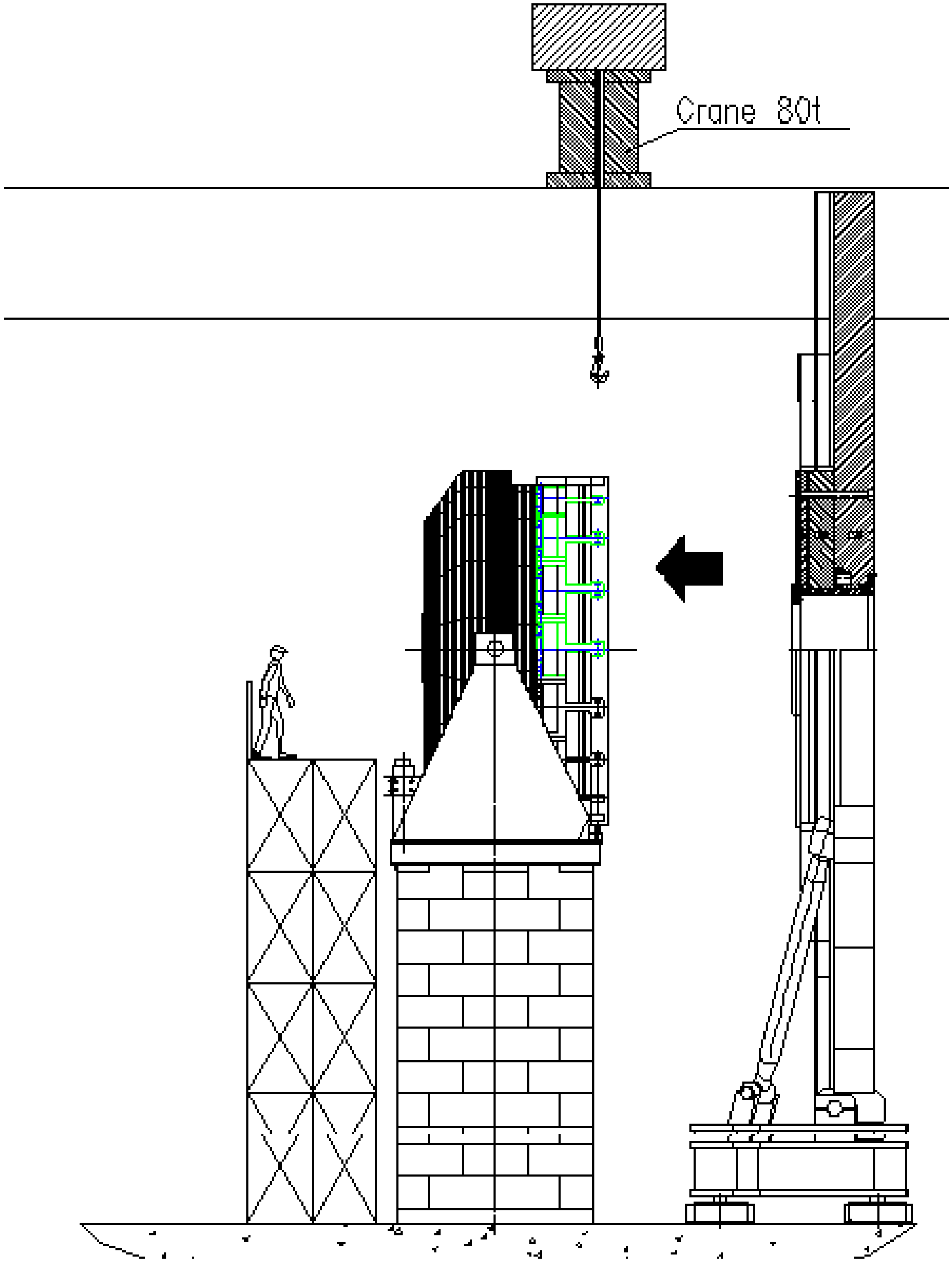

Fig. 3.58: Moving of YE1 to HE.

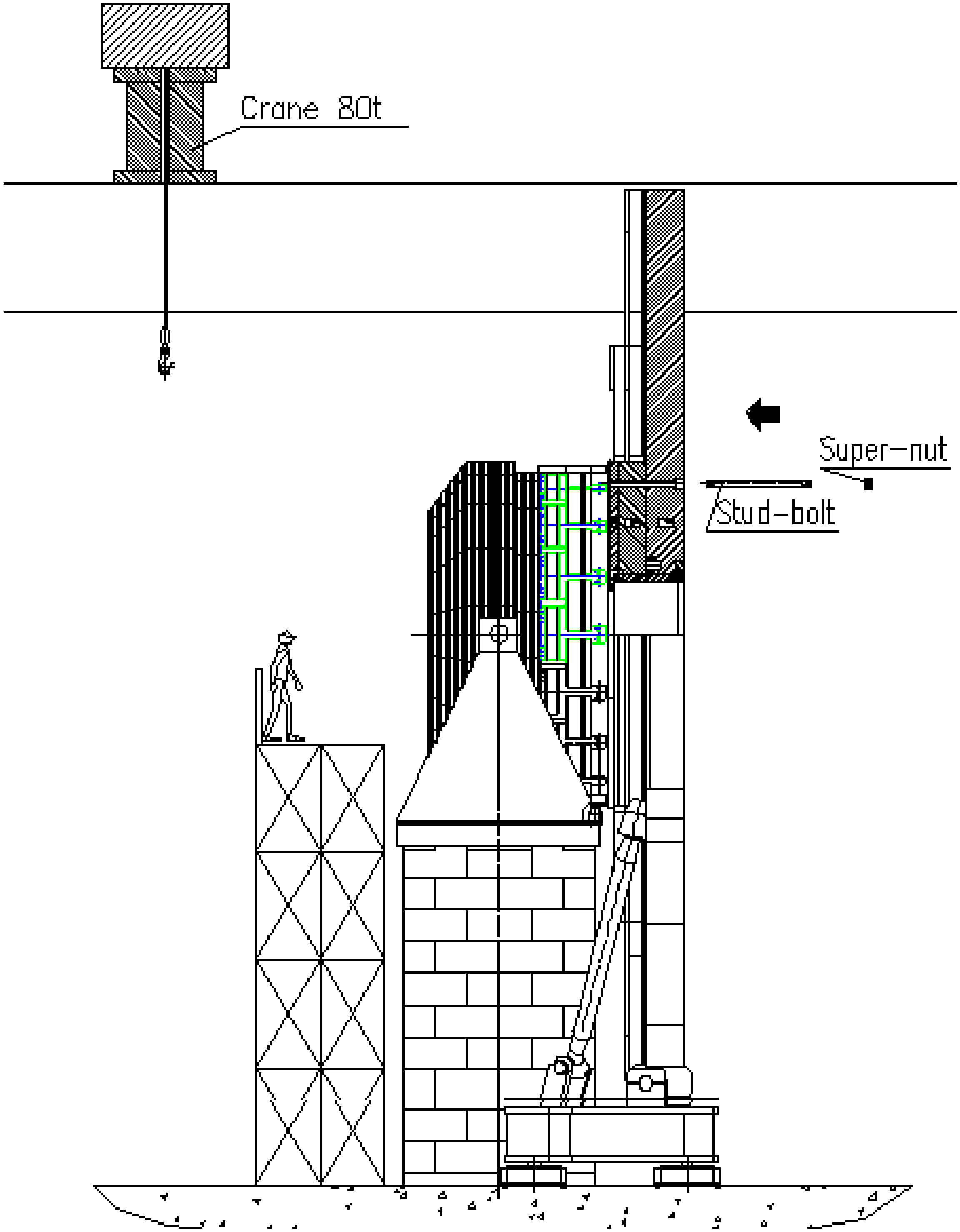

Fig. 3.59: Connection of YE1 and HE.

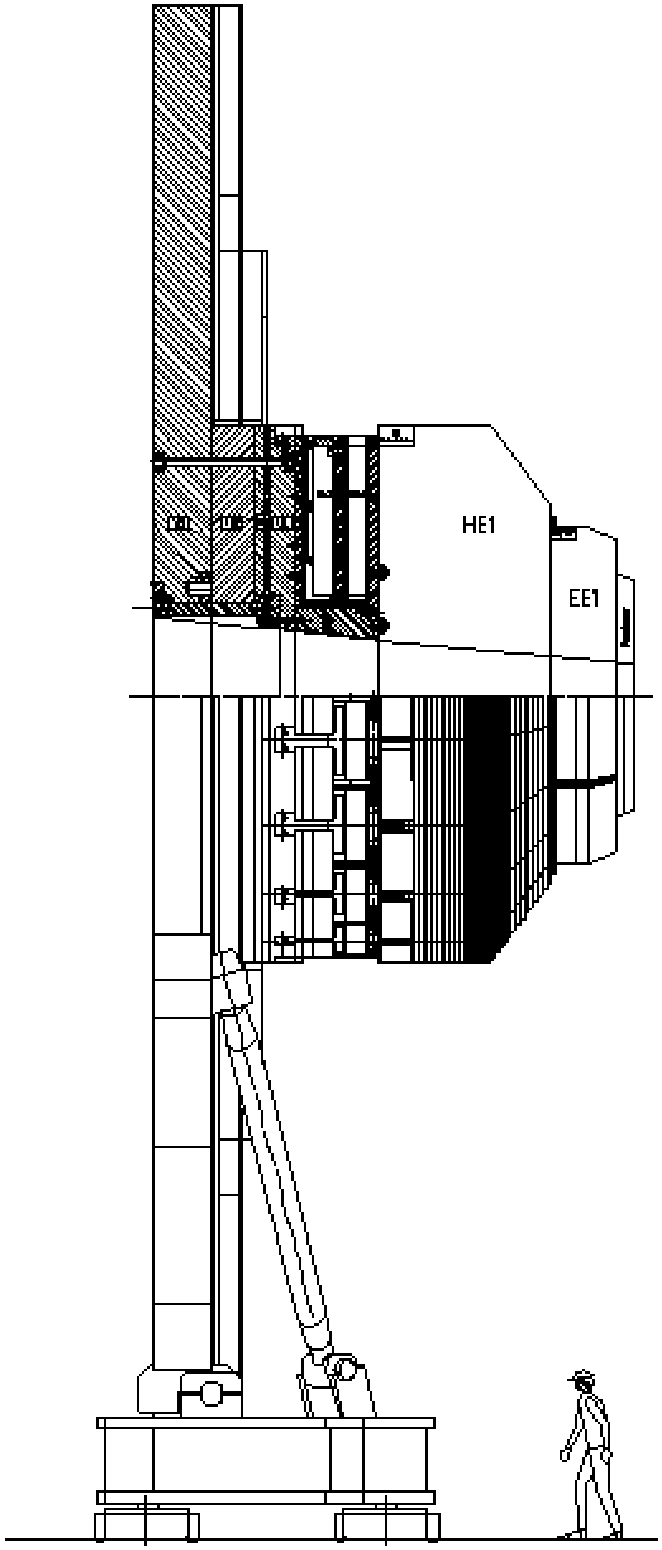

Fig. 3.60: Assembled unit.

3.5.2 Factory preassembly

The preliminary assemblage of the endcaps consists of two stages: preassembly of the HE absorber and preassembly of the interface support structure. The first stage has been described in chapter 3.3.5.2, the interface support structure assembly is presented in chapter 3.5.1.

3.5.3 Facilities requirements (CERN assembly hall)

1. For the disk (back flange, disks MD, ED, YN1) assembly a space on the floor must be 8 m x 8 m;
2. storage area 7 m x4 m for disks and back flange;
3. storage area 6 m x 20 m for sectors and spacers;
4. storage area 3 m x 15 m for megatiles and detector boxes;
5. storage area 3 m x 12 m for muon chambers;
6. storage area 3 m x 5 m for inner ring and fastening frames;
7. assembly floor space about 10 m x 10 m for endcap calorimeter;
8. conventional tooling for repairs and assembly: lathes, drills and mills;
9. platforms to work at 4 m height;
10. power tools with corresponding instruments: saw and other hand-held tools;
11. at least 2 personal lifts to work at 9 m height.

3.5.4 Tooling design

For mounting and assemblage special handling fixtures described in chapter 3.5.1 will be designed and produced. Standard vacuum lifters (two pad litters) will be used for absorber assembly (sector mounting, 400 tonne). The final assembly of the end caps (HE + EE + preshower + ME1 zone) will be carried out on the vertical supports with 4 hydraulic jacks. To turn the end caps on 90^0 2 rotational supports will be designed and produced. To connect the end cap calorimeters to YE1 nose 2 special transport blocks will be used.

3.6 ACCESS, MAINTENANCE AND OPERATION

The full access to the endcaps (EE, HE, RPC and ME1) is possible only during a long shut down of LHC operation. During this time all repair work must be done including the replacement of radiation damaged scintillators. The radioactive source tube control system will be used to check the performance of the active elements. For such access, the endcap muon absorber with the attached YE1 disks is moved 10m along the z-axis from the IP. Because the endcaps are at large height above the Experimental Hall floor (the distance between the floor and beam height is 8m) service space trusses must be used for access to the HE and the rest of the Endcap system.

Table of Contents

4. MECHANICAL DESIGN AND STRUCTURE (OUTER CALORIMETER HO)

4.1 OVERVIEW

The CMS hadron calorimeter (HCAL) consists of four parts. These are the inner barrel calorimeter (HB), located inside the magnet covering the central rapidity region of up to $|\eta| \leq 1.4$; endcap calorimeters (HE), for $1.4<|\eta|<3.0$, and forward calorimeters (HF) for $3.0<|\eta|<5.0$. In addition, since the space inside the solenoid is not sufficient to contain the hadronic showers completely, it is necessary to extend the barrel hadron calorimeter outside the solenoid. This part of the calorimeter which is located outside the coil is referred to as the outer calorimeter (HO-B).

The HO-B consists of two layers of scintillator tiles located on either side of the first layer of return yoke (YB1) which acts as the absorber (30 cm thick) for the outer calorimeter. The scintillation light from the tiles is collected using WLS fibres embedded in grooves in the tiles. These WLS fibres are spliced to clear fibres and the clear fibres transport the light to the photo detectors located at the outer boundaries of the barrel muon system.

In order to simplify the installation of the HO-B scintillator layers, several scintillator tiles will be packed into a single mechanical unit called the scintillator tray. For ease of installation, each tray will be one ϕ slice wide (5 in ϕ). However along the Z (η) direction, they will cover the entire span of a muon ring i.e. 2.53 m. The trays will be held by sheet metal C-channels welded onto the return yoke YB1 using "L" shaped brackets.

4.2 STATIC LOADS AND CONSTRAINTS

The weight of individual HO-B scintillator trays will be in the range of 25 to 30 kg only. Each tray will be supported by two sheet metal C-channels for the entire lengths of 2.53 m along the Z direction. Hence the weight per unit length on the tray support structure will be less than 15 kg/meter.

4.3 DYNAMIC LOADS AND CONSTRAINTS

Since the weight of the trays is less than 30 kg and they will be directly hanging from the return yoke, dynamic load will not be a serious issue for these trays.

4.4 MUON SYSTEMS REQUIREMENTS

AND CONSTRAINTS

The outer calorimeter is geographically located inside the barrel muon system and hence is constrained by the geometry and construction of the muon system. Fig. 4.1 shows the position of the return yoke and the rings of muon stations in the overall CMS setup. The outer calorimeter layers are placed behind the muon station 1 and in front of the muon station 2 so that they occupy the space on either side of the iron yoke YB1. Radial position of the front faces of the two layers are 4.57 m and 4.89 m respectively (Fig. 4.2) and a radial thickness of 15 mm has been allocated for each of them.

The scintillator layers should map to the five rings of muon station and the optical fibres should be taken out through the space between the rings to the photo detectors placed at the outer end of the ring (at a radius of 7.43 m). The rings are 2.536 m long and are symmetrically positioned with respect to the centre point. The separation of ring 1 from the central ring 0 is 0.2 m and that between rings 1 and 2 is 0.12 m. The muon rings have 12-fold symmetry along ϕ and 75 mm thick stainless steel beams hold successive layers of iron for the return yoke.

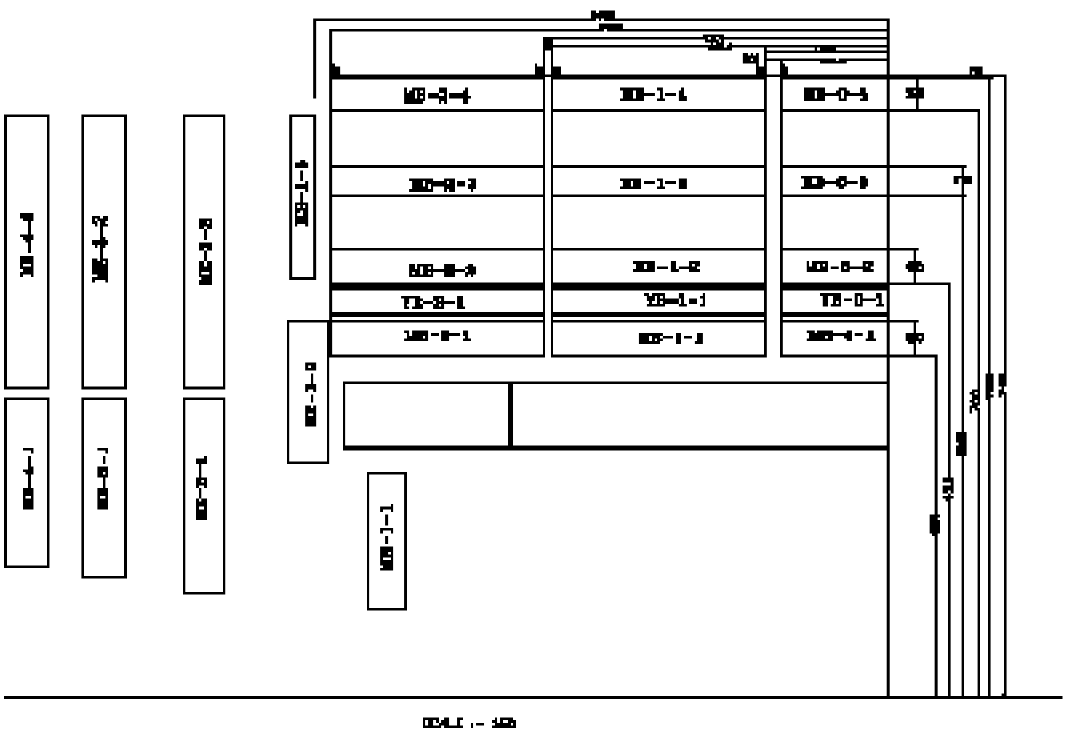

Fig. 4.1: Cross-sectional sketch of the magnet return yoke (YB1), muon detector (MB) and outer hadron calorimeter.

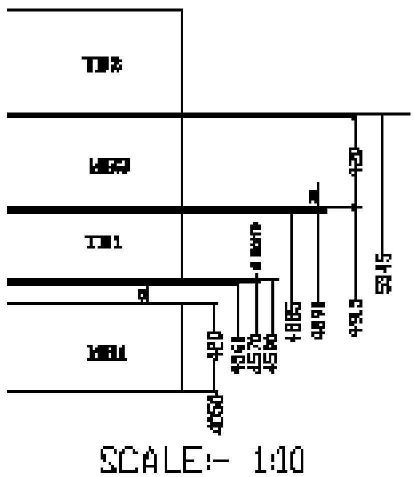

Fig. 4.2: Radial position of the two HO-B scintillator layers.

The sizes of the scintillator tiles are supposed to map to the inner layers of hadron calorimeter to make towers of granularity 0.087×0.087 in η and ϕ. The space between successive muon rings in the η direction and the space occupied by the stainless steel beams in the ϕ direction are not available for HO sampling and this will constrain the shape and sizes of some of the tiles for the outer calorimeter. In addition, the mechanical structures needed to position the scintillator trays will further reduce the sizes of the tiles as discussed in chapter 6.

4.5 OUTER CALORIMETER DESIGN

4.5.1 Frame layout

The scintillator trays are held to the magnet return yokes YB /-2,-1,0,1,2/ 1 by C-channels (0.5 mm thickness, 16.1 mm height, 10.5 mm breadth, and 2.536 m length) made out of sheet metal. The magnified view of two C-channels supporting a tray on one side is shown in Fig. 4.3. The C-channels point along the direction and are spaced such that the scintillator trays can be inserted into them. The spacing between the centres of the C-channels holding a tray varies between a minimum of 0.267 m and a maximum of 0.571 m depending on the position of tray along . At one end of 30 sector in the outer layer it has been decided to combine a 123 mm wide scintillator tray belonging to the bend of the magnet with the previous 448 mm wide tray as a straight, extended portion in order to simplify the construction. In this arrangement the tray extends beyond the bend in the magnet iron. The support for this tray on the spoke side will be a specially shaped sheet metal channel since both the spoke and the iron yoke are inclined to the tray in an inconvenient angle.

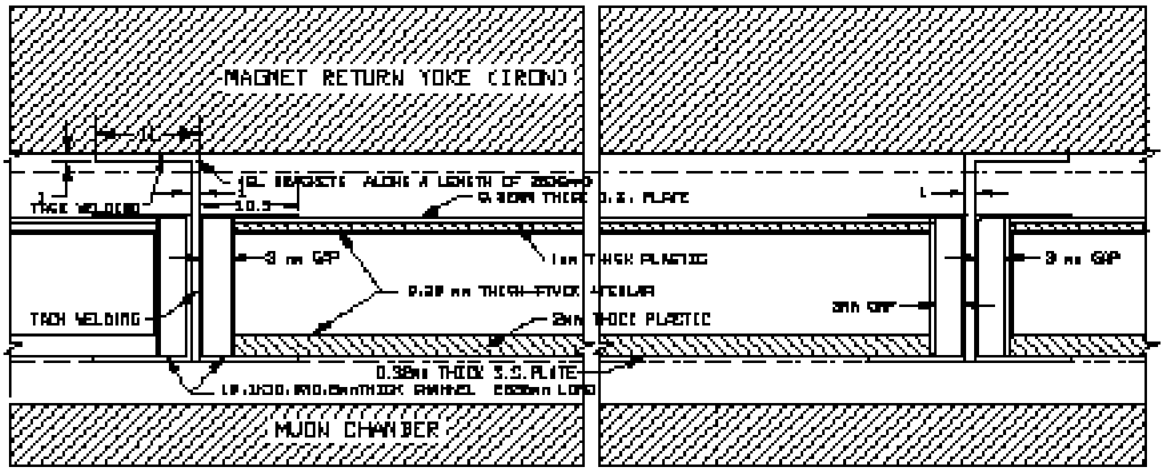

Fig. 4.3: Cross-sectional view of a HO-B scintillator tray and its support structure.

The channels are attached to the iron yoke by 1 mm thick, 2 cm broad "L" shaped brackets made of sheet metal of length 20 mm (with six brackets for a length of 2.536 m corresponding to a ring). The length of the bracket at a particular point depends upon the deviation of the magnet yoke surface from the standard. The shorter portion of this bracket is tack welded to the magnet yoke iron. The C-channels are tack welded to the longer arm of this bracket (brackets in the middle of a -section holding C-channels on both sides) after adjusting the C-channel in its proper position with a jig. This is necessary in order to keep the trays flat in a plane, to avoid bendings due to the slope variation in the surface of the magnet return yoke caused by the manufacturing process and to ensure that that the 5 mm "no-go" zone on the muon chamber side is not encroached. This jig will have markings or slots along its width to indicate the position of the L-bracket and C-channels. This jig will help in positioning the L-bracket of length 20 mm to make solid and flat contact with the magnet return yoke and make both the tray and the L-bracket stay clear off the "no-go" zone on the muon chamber side. We will have jigs of two different widths for two layers of the outer hadron calorimeter.

Other than these C-channels which are attached on both sides of the iron yoke through L-brackets, no other separate frame structure is necessary to hold the scintillator trays.

4.5.2 Bolt patterns

Since the L-brackets which hold the C-channels are tack welded there will not be any bolts in the supporting structure. However, the tray assembly itself is held by special brass bolts which are described in the tray assembly section. The L-brackets are welded to the magnet yoke with consecutive L-brackets along the length of 2.536 m having the welded side of the brackets facing opposite directions. By orienting alternate welded sides in opposite directions we will have a better balance.

4.5.3 Forces, stresses and deflections

The tray is supported along its whole length by rigid sheet metal C-channels anchored to the iron yoke of the magnet. Therefore there will not be any bending along the length of the tray weighing a maximum of 30 kg for the widest tray. Along the width (a maximum of 563 mm) of the tray, however there will be bending amounting to a maximum of 0.2 mm for the widest tray caused mainly by the 10 mm thick scintillator. Other trays will have less bending due to narrower width. The separate and independent buckling of the 0.3 mm stainless steel plate will be controlled by the brass screws and custom made nuts.

4.5.4 Assembly and installation

Specialised tooling is required for the installation of the hanging structure which consist of sheet metal C-channels onto the YB1 and also to insert the finished scintillator trays to their respective positions. In order to attach the C-channels to their correct positions, a jig will be made for each of the two layers. Before welding, the individual C-channels will be attached in pre-fabricated slots in the jig. The entire jig will then be positioned on either side of the return yoke (There will be two separate jigs for layer 1 and layer 2 as the positions of the C-channels are different for the two layers) by using two guiding slots on the support beams on either side of the 30 ϕ sector. The individual C-channels will then be spot welded onto the iron using "L" brackets. After the welding process is over, the C-channels will be detached from the jig and the jig will be removed keeping the C-channels hanging from the iron. The entire process will then be repeated for all the twelve ϕ sectors of a muon ring and for the five rings. A lifting fixture is needed for lifting and positioning the jig in the guiding slots before the welding of the C-channels onto the return yoke. Individual trays will be inserted in the slots of the C-channels at a later stage. A separate lifting fixture will be needed to lift and insert the trays.

4.5.5 Prototype sector

During 1997, we will construct two outer calorimeter layers to cover one HB wedge (20 in ϕ). The trays will be similar in size and design as per the HO-B specification. After fabrication and assembly the trays will be tested for their minimum ionising particle (mip) capabilities using cosmic ray muons at Bombay during early 1998 and finally will be taken to CERN during summer 1998 and will be attached behind the prototype barrel wedge for test beam studies.

4.5.6 HO-E overview, constraints, specifications and requirements

The outer calorimeter HO-E is geographically located inside the outer ring of the first endcap muon station and hence is constrained by the geometry and construction of the muon chambers making up the ME2 muon chamber ring. In fact the scintillator trays making up the HO-E system will be mounted within aluminium frames that will be attached directly to the ME2 support frames and will reside within the ME2 chamber space. There will be 36 trapezoidal trays captured within the muon chamber support frames, each subtending 10 of and the pseudorapidity range of 1.2<||<1.5. Optical cables attached via optical connectors to the scintillator trays will route the scintillator response to the outer radius of the endcap muon absorbers. Decoder and electronic boxes will be located at this outer periphery of the muon absorber .

Table of Contents

5.1 OVERVIEW AND REQUIREMENTS

5.1.1 Introduction: physics aims

The very forward calorimeter (HF) covers the pseudorapidity range $3.0^{2}|\eta|^{2}5.0$. The front face of HF is located at ±11.1 m from the interaction point (IP). There are two main objectives with this detector: to improve the measurement of the missing transverse energy (E_T^{miss}) and to enable identification and reconstruction of very forward jets. In some cases, these jets are the distinguishing characteristic of several important physics processes, in others, they are background signatures. With the addition of the HF calorimeters, the total coverage increases to $|\eta|$ ♠ 5, and this reduces the fake (instrumental) E_T^{miss} by an order of magnitude in the 20-120 GeV energy range over that derived from HB+HE alone.

5.1.2 The HF environment: physics requirements

The physics aims outlined in the previous section have to be fulfilled in a very demanding and hostile environment. To start with, a bunch crossing occurs every 25 ns. With the LHC operating at a luminosity of 10^{34} $cm^{-2}s^{-1}$, and assuming a total *pp* cross section of 100 mb (25 *pp* collisions per bunch crossing), the average particle multiplicity at the IP per crossing is about 5700 (rms=1200). This corresponds to a rate of $2.3\infty10^{11}$ s^{-1}, equivalent to 280 particles/crossing/rapidity unit, or $1.1\infty10^{10}$ particles/s/unit of rapidity. The most populated region is the inner part of the HF ($4.5<\eta<5$), with an incoming rate of particles of about $9.6\infty10^{9}$ Hz equivalent to a flux of about $6.0\infty10^{6}$ cm^{-2} s^{-1}. This particle flux will produce absorbed doses that will reach values close to 100 Mrad/year. Therefore, the detectors must be able to survive in an exceptionally high radiation field.

Particles incident on HF will initiate showers leading to large neutron fluxes in the calorimeter absorber (close to 10^{9} cm^{-2} s^{-1} at shower maximum) and to the activation of the absorber material. Thus, the detection technique employed by the HF should be insensitive to neutrons and to low energy particles from the decay of activated radionucleids. As a result of this activation, the inner parts of the HF will be a source of radiation (after 60 days of LHC operation and one day of cooling down) up to about 10 mSv/h. Thus the detector must be robust and require minimal maintenance.

5.1.3 The technique: quartz fibre calorimetry

A charged particle, traversing a quartz fibre with a velocity greater than the speed of light in quartz, emits photons due to the Cherenkov effect. The opening angle of the Cherenkov cone, Θc, is related to the speed of the particle, β, and the index of refraction n.

$\cos \Theta c=1/n\beta$ (1)

There is a threshold value ($\beta min=1/n$), below which there is no Cherenkov radiation. The light yield, in photons, due to the Cherenkov effect, depends on α, the fine structure constant, λ, the wavelength of the emitted light, x, is the path of the particle through the medium and z, is the charge of the incident particle.

$d^2N/dxd\lambda=2\pi\alpha z^2(\sin^2 \Theta c /\lambda^2)=2\pi\alpha z^2/\lambda^2[1-1/\beta^2n(\lambda)^2]$ (2)

The amount of light observed by a detector positioned at one end of the fibre depends on the velocity of the particle, on the incident angle, and on the distance between the particle trajectory and the center of the fibre. It also depends on the fibre core and cladding refraction indices, on the spectral transmission range of the fibre and on the spectral quantum efficiency of the light detector.

The particles entering the absorber of a calorimeter produce showers of particles. Those among them which enter a quartz fibre with β close to one are essentially electrons. The electrons producing light in a quartz fibre are roughly those entering the fibre with an angle of ♠45_±10_[1].

The immediate implication is that the apparent shower development in quartz fibre calorimeters is dramatically different from the one observed in *dE/dx* calorimeters. The showers appear to be very narrow and, in the case of hadrons, short. A typical transverse shower size for both EM and HAD showers is characterised by the Moliere radius of the absorber.

The Cherenkov effect is insensitive to neutrons (because they have no charge) and to activation products if they lie below the β threshold. In addition, the Cherenkov effect can be considered instantaneous. Therefore there is no other limitation than the photodetectors and electronics which slow down the detector response. Hence, the charge collection is accomplished in much less than 25 ns with the present design.

The HF will be constructed as a block of copper with embedded quartz fibres, running parallel to the beam axis. The photodetectors and associated electronics will be located at the outer parts of the calorimeter, where the radiation doses are lower and these components are easily accessed.

5.2 HF-RADIATION ENVIRONMENT

5.2.1 Shielding requirements and constraints

The large amount of hadronic energy absorbed in the HF inevitably leads to the generation of an immense neutron flux inside of the HF. We observe hadronic leakage from the rear face even after ten interaction lengths. Fortunately, most of the punchthrough is contained within the shielding or is directed towards the end wall of the cavern and does not directly impact any other subdetector. Some of these particles will cross the photomultipliers and front-end electronics. The protection of these devices is the primary reason for quite substantial shielding at the back of the HF. This shielding is also beneficial to the endcap muon system, since the energy carried by the punchthrough particles is converted into neutron and photon albedo at the end wall of the experimental hall, and so indirectly influences the ME4.

For the ME4, radial leakage from the HF is more of a concern than punchthrough. Particles emerging from the HF side faces could directly impinge on the CMS endcap. A substantial effort has been devoted to optimising the shielding configuration around the HF.

The neutron albedo from the HF front face has been shown to be of no importance for the central tracker but, if unshielded, would be an important source of background in the high η region of the endcap muon spectrometer. A 20 cm thick polyethylene slab lining the HF front face is sufficient to suppress the neutron albedo below the level of the neutron flux generated by interactions in the beam pipe.

An important channel for neutron leakage from the HF directly into the ME4 has been blocked by introducing a 10 cm thick borated polyethylene slab into the endcap/HF interface. The interface itself is designed to be flat, with a clearance not exceeding 3 cm. The lateral faces of the HF are surrounded by 70 cm of shielding elements, of which the innermost 30 cm are steel, followed by 30 cm magnetite concrete with a density of 3.65 g/cm^3. The shielding is completed with a 10 cm thick layer of borated polyethylene. A cylindrical shape shielding is advantageous because of savings in total weight. A shielding structure with square cross section, for example, would leave in the corners some parts of the ME4 directly exposed to the HF.

At the back of the HF we have to deal with the interface to the rotating shielding and shielding the photomultipliers. Behind the HF we have a relatively massive shielding block starting at z=12.95 m. The inner boundary of this block is conical and follows the η=5.3 line. The block has an outer radius of 100 cm and consists of steel and magnetite concrete. Its outer surface is covered by 10 cm of borated polyethylene. The interface to the rotating shielding is provided by a 40 cm of shielding block which is a separate entity that is installed after both the HF and the rotating shielding are in place. The crack between the HF shielding and the rotating shielding shown to be critical. A flat connection is possible if the clearance does not exceed 3 cm. Assuming 3 cm clearance, the rotating shielding starts at z=1496 cm. In addition to its main task of reducing the background in the experimental cavern and ME4, the thin section of the rotating shielding plays a non-negligible role in shielding the HF photomultipliers. The optimization of the rotating shielding design in view of the ME4 is still in progress. Here we use the best design so far, consisting of three radial layers: 30 cm of steel starting at r=20 cm, followed by 30 cm of magnetite concrete and a 10 cm of borated polyethylene, giving an outer radius of 90 cm.

The photomultipliers are stacked between the cylindrical shielding block and the outer lateral shielding described above. To suppress the fluence of punchthrough particles, a special shielding consisting of 5 cm steel, 25 cm borated polyethylene and 10 cm steel is placed between the HF and the photomultipliers. The light from the fibres is fed to the photomultipliers through air-core light mixers that are located in small holes in this shielding.

5.2.2 Results of radiation simulations

We have calculated the particle fluences and radiation dose in a glass plate representing the photomultiplier windows. The results are collected in Table 5.1 and the radial dependence of fluences and dose are shown in Fig.5. 1 and Fig.5. 2. Along with the FLUKA results, we provide some values obtained with the MARS code. In general, we observe very good agreement. The increase of the MARS neutron fluence estimate with respect to FLUKA at large radii may be explained by the significantly longer scoring bins (along z) used in MARS.

Table 5. 1

Particle fluences in cm^{-2} and dose in Gy in the position of the photomultipliers of the HF. All values are for an integrated luminosity of 5∞10^5 pb^{-1}.

	FLUKA	MARS
All neutrons	2.8×10^{12}	-
Neutrons *E* > 100 keV	2.3×10^{12}	2.9×10^{12}
Thermal neutrons	8.3×10^{9}	-
Charged hadrons	3.8×10^{10}	2.0×10^{10}
Dose	70	-

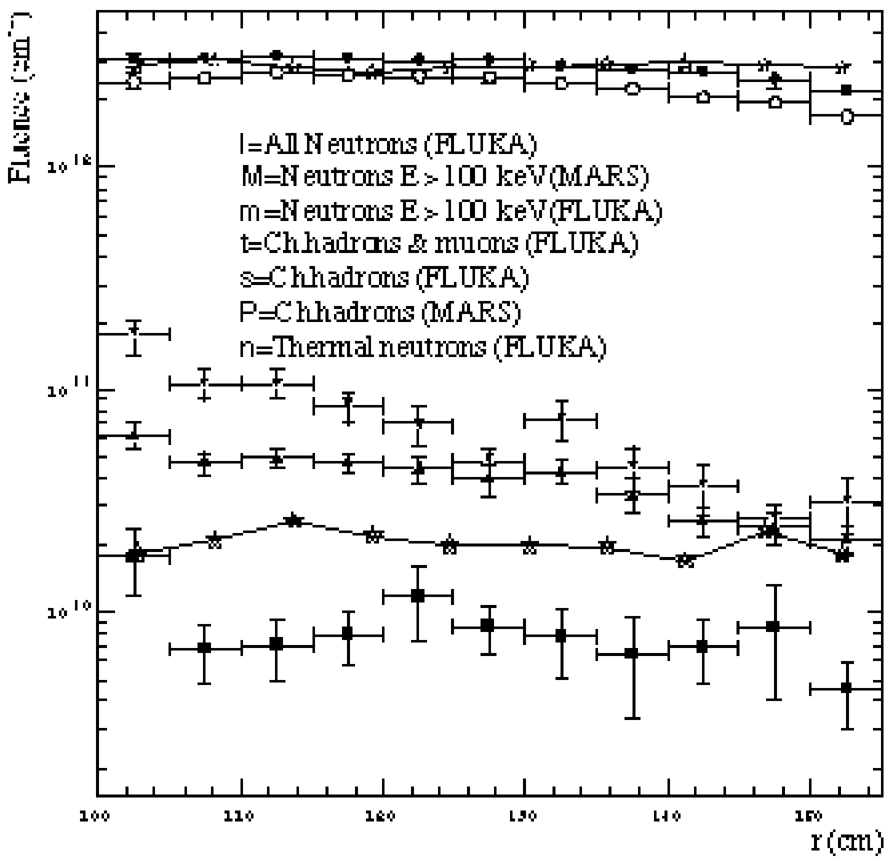

Fig. 5. 1: Fluence of different particle types at the position of the photomultipliers as a function of radius. Values are for 510^5 pb^{-1}. The legend (top to bottom) refers to largest to smallest values.

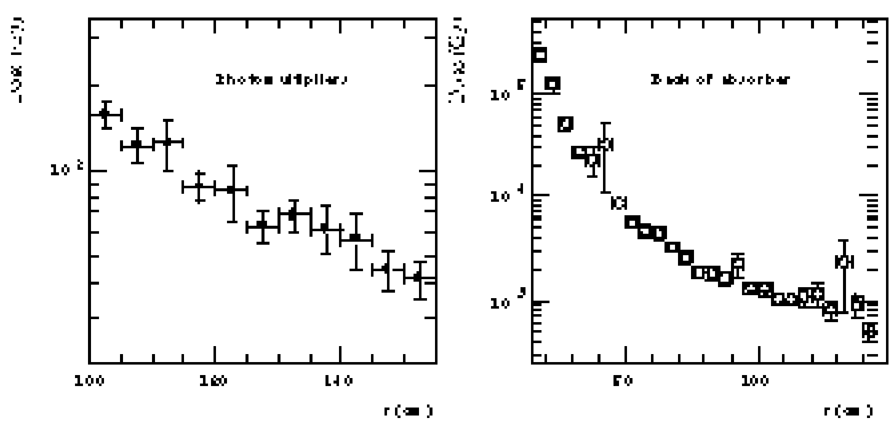

Fig. 5. 2: Radiation dose in the photomultiplier windows (glass) and just behind the absorber (air) as functions of radius. Values are for 510^5 pb^{-1}. Fig.5. 3 and Fig.5. 5 show the photon and neutron spectrum in the position of the photomultipliers and behind the HF absorber. We observe that, as expected, the polyethylene has removed a significant amount of the neutrons around 1 MeV and therefore lowered the potential bulk damage to silicon devices. When interpreting the photon spectra, it should be remembered that photons emitted in radioactive decays are not included in the simulation. Fig.5. 2 and Fig.5. 4 show the dose and particle fluences as a function of radius just behind the HF absorber. We can observe a variation by several orders of magnitude between the innermost and outer radii. Fig.5. 5 shows the photon and neutron spectrum just behind the HF absorber averaged between radii of 20 cm and 60 cm. The neutron spectrum shows the typical shape inside or on top of pure

metal, with very few thermal neutrons (probably backscattered from the polyethylene on the shielding plug) and a very pronounced 1 MeV evaporation peak. The smaller peak around 100 MeV is the more significant one, since these neutrons are very penetrating. Note that the increase of the absolute values with respect to Fig.5. 3 is not an effect of the polyethylene shielding of the photomultipliers alone, but mostly caused by the different radial range considered.

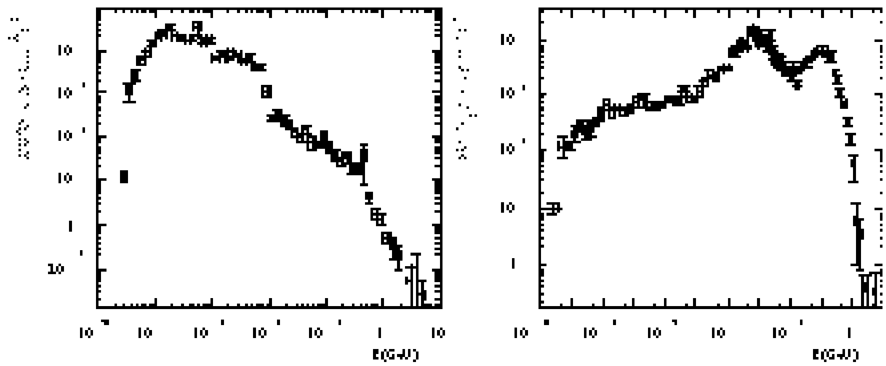

Fig. 5. 3: Energy spectra of photons (left) and neutrons (right) in the position of the photomultipliers. Values are for LHC peak luminosity.

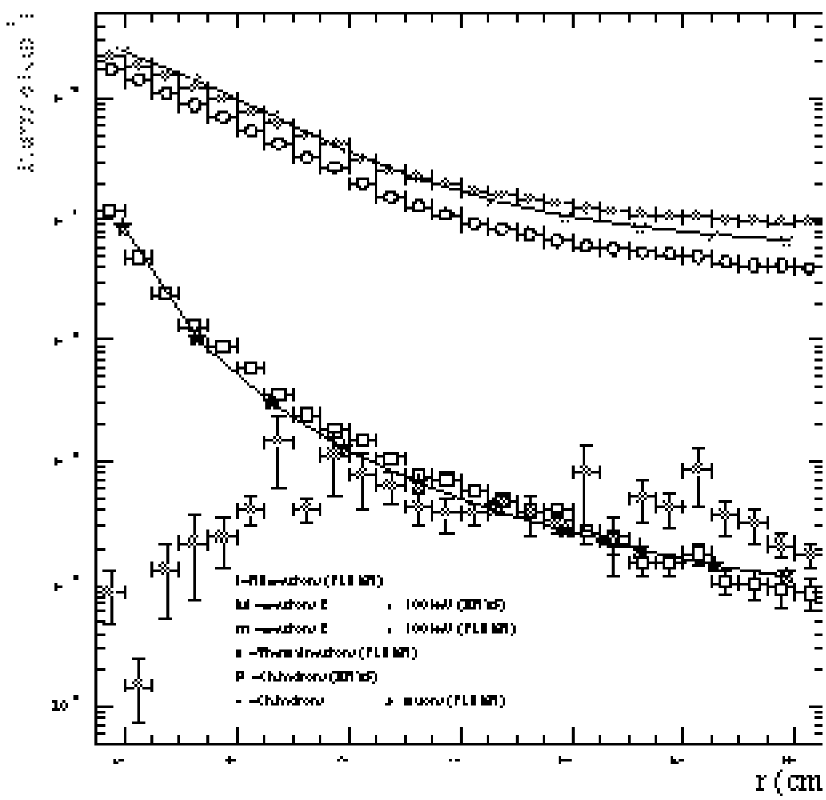

Fig. 5. 4: Fluence of different particle types just behind the absorber as a function of radius. Values are for 5 ∞ 10^5pb^{-1}. The muon contribution to the charged fluence, quoted for FLUKA, is only a few tenths of a percent so the pure charged hadron curve would be almost indistinguishable from the present one. The legend (top to bottom) refers to largest to smallest values.

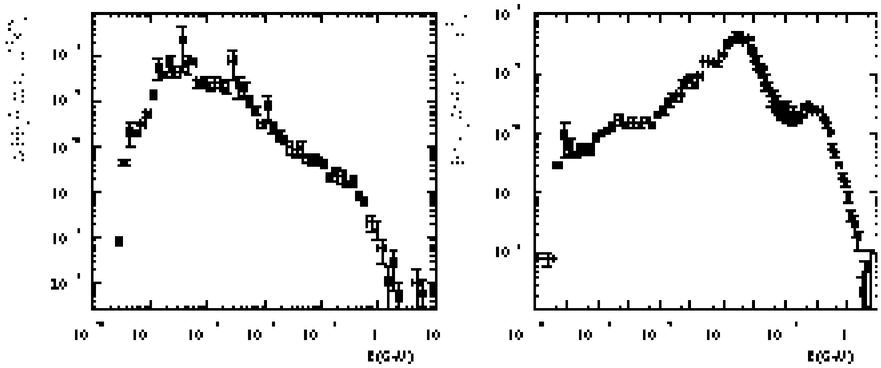

Fig. 5. 5: Energy spectra of photons (left) and neutrons (right) just behind the HF absorber averaged over radii *r*=20 cm to *r*=60 cm. Values are for LHC peak luminosity.

One important issue is where to place the electronics racks needed by the HF. Since the cable length from the photomultipliers to these racks has to be minimised, the most suitable position is just outside the lateral shielding of the HF. Fig.5. 6 shows the fluence of different particle types in this position as a function of the longitudinal (z) coordinate. The large increase of fluence at z = 1080 cm is caused by the 3 cm wide crack between the endcap and the HF shielding. An inspection of the curves shows that most of the bulk damage in silicon devices will be caused by neutrons with energies above 100 keV. The contribution by other hadrons is relatively small.

Radiation dose is probably the more important parameter for the electronics racks. The dose as a function of z is shown in Fig.5. 7. The dose just inside the borated polyethylene shielding is shown alongside the dose in the air just outside the shielding. As expected the dose in the polyethylene is higher, which can be attributed to recoils from *(n,p)* reactions. The dose in silicon itself should be close to that in air. In the rack, we can expect a certain amount of cables and other plastic items to accompany the silicon devices. Therefore, the two values should provide a proper estimate of the uncertainty in dose due to the material composition of the racks.

Both the fluence and dose have a soft minimum between z = 12 m and z = 12.5 m which thus is the preferred position for the racks. Beyond z = 13 m we observe a clear increase of fluences and dose, which is caused by the end of the absorber and therefore significantly reduced lateral shielding. Fig.5. 8 shows the energy spectra of photons and neutrons on top of the lateral shielding of the HF. While nothing unusual can be observed in the photon spectrum, the neutron spectrum is remarkably hard. The deficiency of thermal neutrons is explained by the borated polyethylene which forms the top part of the shielding. The fact that the 1 MeV evaporation peak has almost disappeared tells us that the shielding provides a very efficient neutron attenuation in the energy range where hydrogen is effective. The neutrons at about 100 MeV cannot be stopped, except with very massive shielding for which we have neither the space nor the possibility of support.

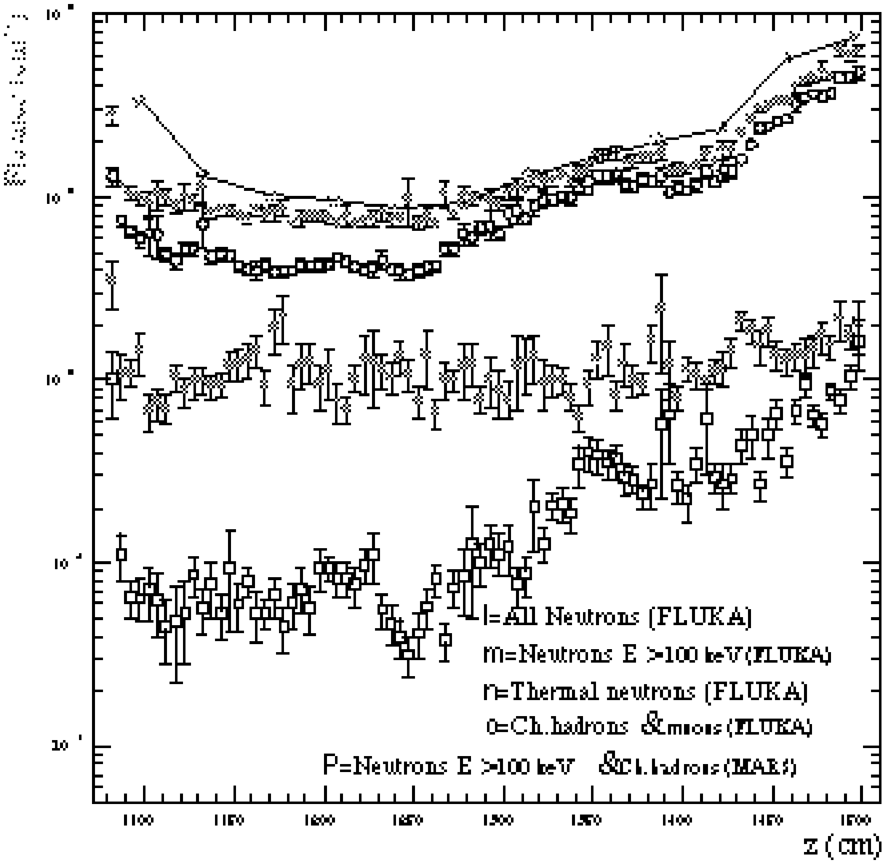

Fig. 5. 6: Fluence of different particles around the HF lateral shielding as a function of z-coordinate. Values are for $5\infty10^{5}$ pb^{-1}. The legend (top to bottom) refers to largest to smallest values.

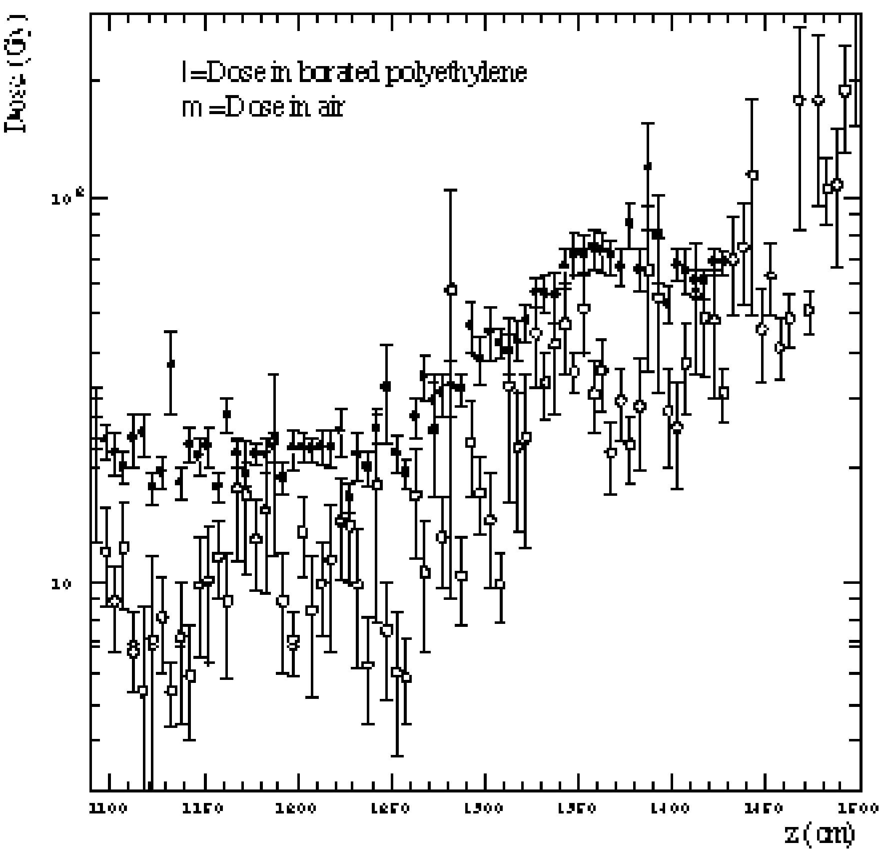

Fig. 5. 7: Radiation dose around the lateral shielding of the HF as a function of *z*-coordinate. The large error bars in the air values are caused by the low density, which reduces the number of energy deposition events. Values are for $5\infty10^5$ pb^{-1}. The legend (top to bottom) refers to largest to smallest values.

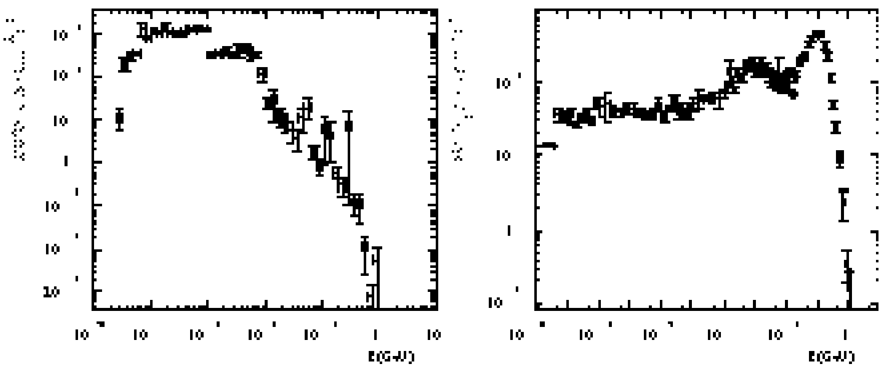

Fig. 5. 8: Energy spectra photons (left) and neutrons (right) around the HF lateral shielding where electronics racks are positioned. Values are for LHC peak luminosity.

5.3 TRANSPORTER PLATFORM

The transporter platform is designed to fulfill the following functions and meet the listed requirements:

a) transportation of the HF between the garage position and the foot of the elevation system;

b) adequate strength in supporting the weight of the HF and its shielding elements (~310 tonnes) as it is raised/lowered to/from beam position;

c) 25 cm motion on the horizontal plane for each half of the HF to facilitate installation of the HF around the beam pipe and eventual maintenance of the HF itself when in the garage position;

d) 30 cm motion along beam direction when the HF is raised to the beam height to ease installation of the detector between the endcap muon system and the rotating shield arms;

e) sufficient surface for the installation of the HF endplug shielding and 40 cm shielding collar between the HF shielding and the rotating shielding;

f) mechanical interface elements between the hydraulic jacks and support frames;

g) rolling mechanism that is consistent with the construction, assembly and installation plans of the HF detector;

h) mechanical structure that conforms to the radiation shielding requirements;

i) alignment system that is integrated to the HF detector system and the rest of the experiment.

The details of the transporter table are shown in Fig. 5.9 through Fig. 5.12. Fig. 5.9 shows half of HF positioned on the transporter platform. The transporter platform is equipped with four airpad feet at each corner. This type of airpad is also used for the CMS magnet elements and has been successfully tested recently. Fig. 5.10 illustrates the details of the horizontal motion of the detector on the platform. A pair of channels is located on top of the table to guide the rollers that are shown in Fig. 5.11. The motion along the beam direction is accomplished in a similar manner along the channels at the bottom of the table. Fig. 5.12 shows both side view details of the transporter table.

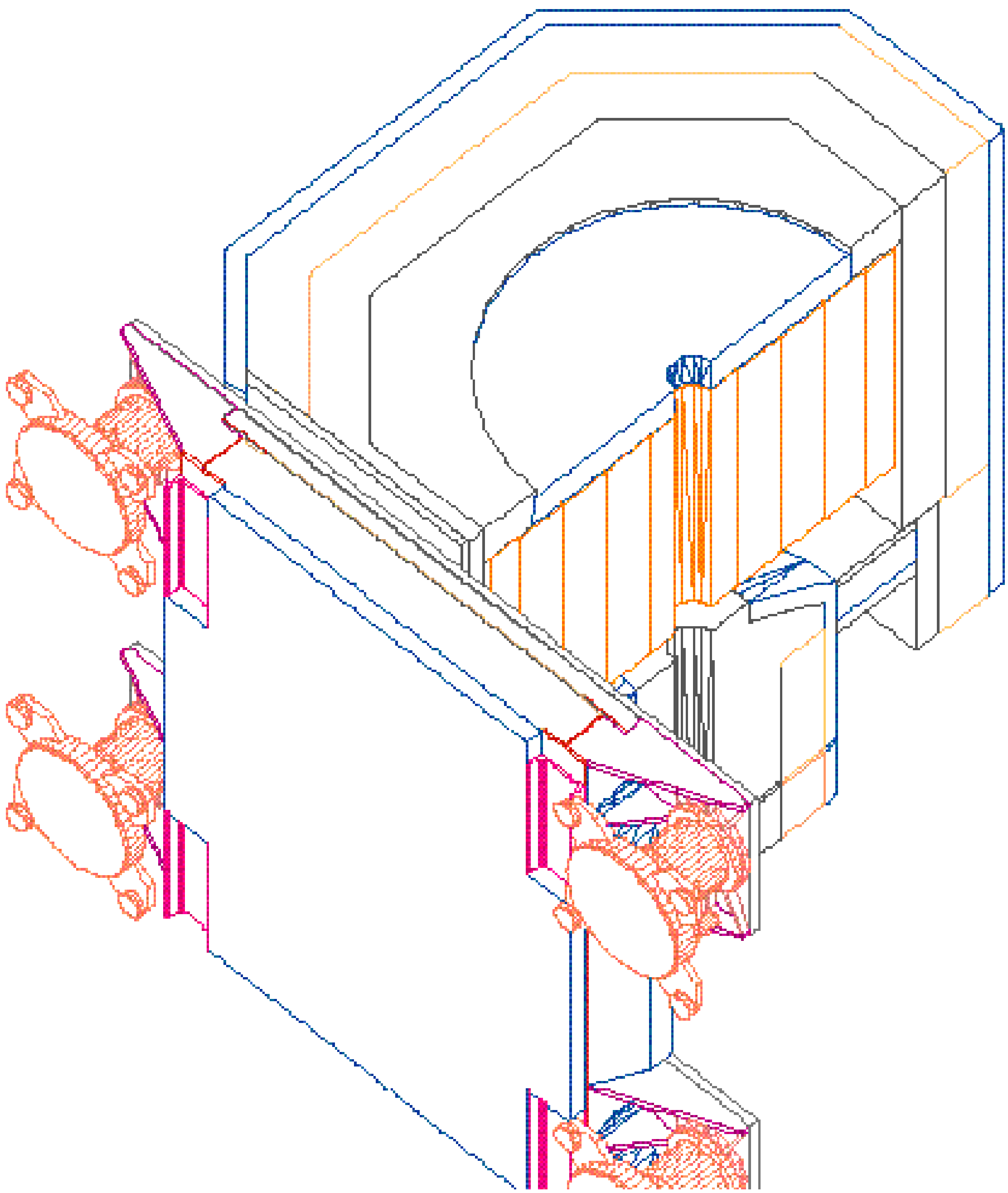

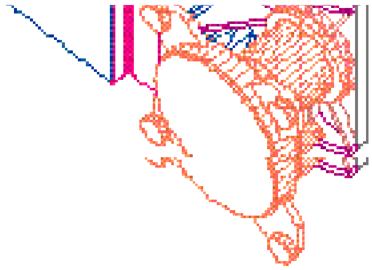

Fig. 5.9 (C.S.): The bottom view of the transporter table is shown above. The half of the HF detector and the endplug shielding are positioned on the table. The motion of the table is accomplished by four airpad feet located at its corners.

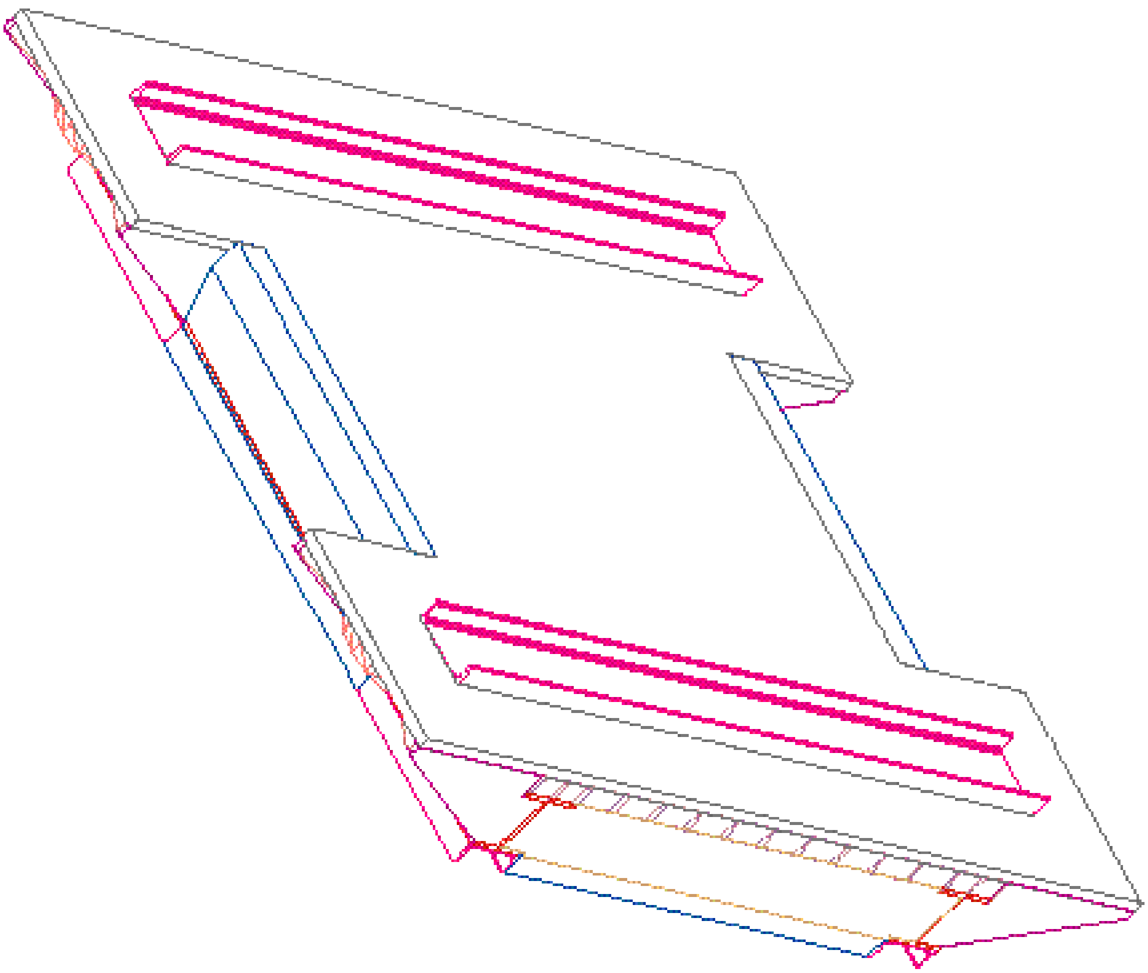

Fig. 5.10 (C. S.): The top view of the transporter table shows the channels for the horizontal motions; left

and right movement of each detector half (channels located on top of the table) and the motion along the beamline (channels positioned at the bottom of the table).

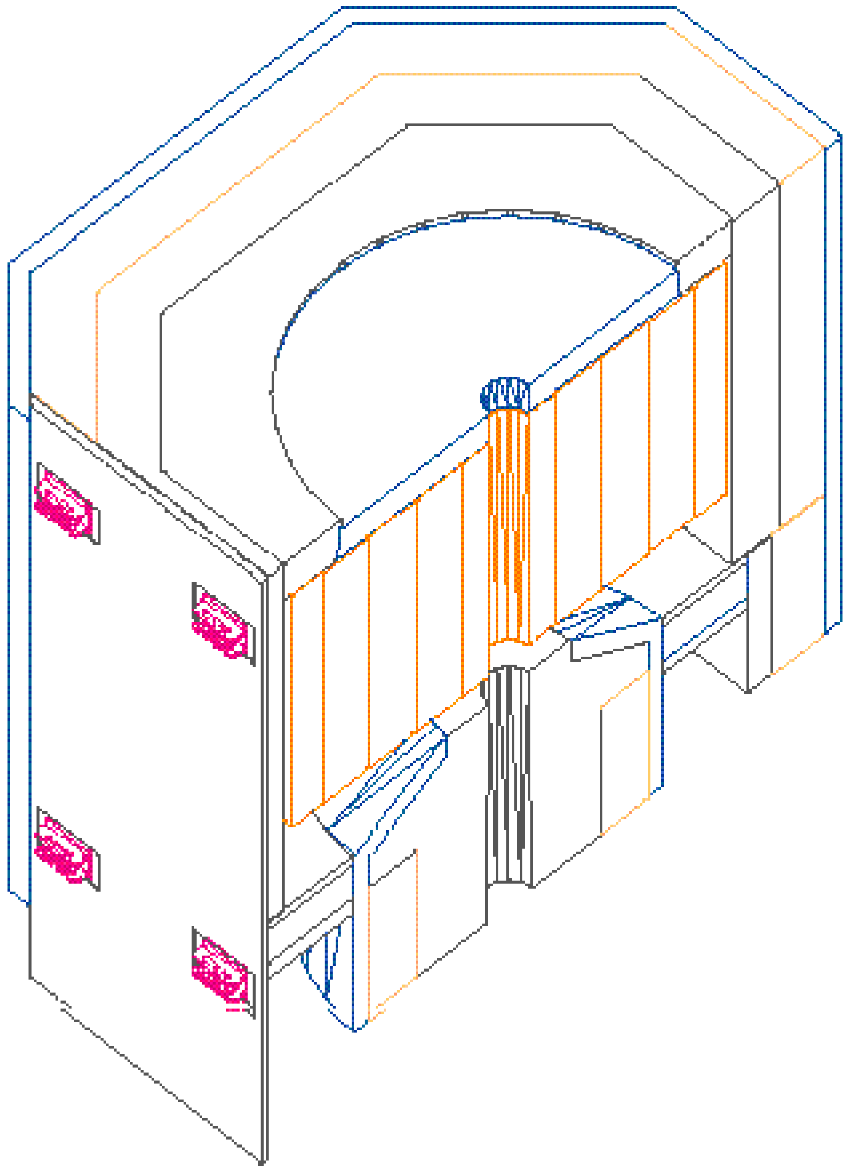

Fig. 5.11 (C. S.): Four heavy-duty rollers are located at the bottom of each detector half. These rollers move along the channels for left/right motion and also used in the assembly sequence.

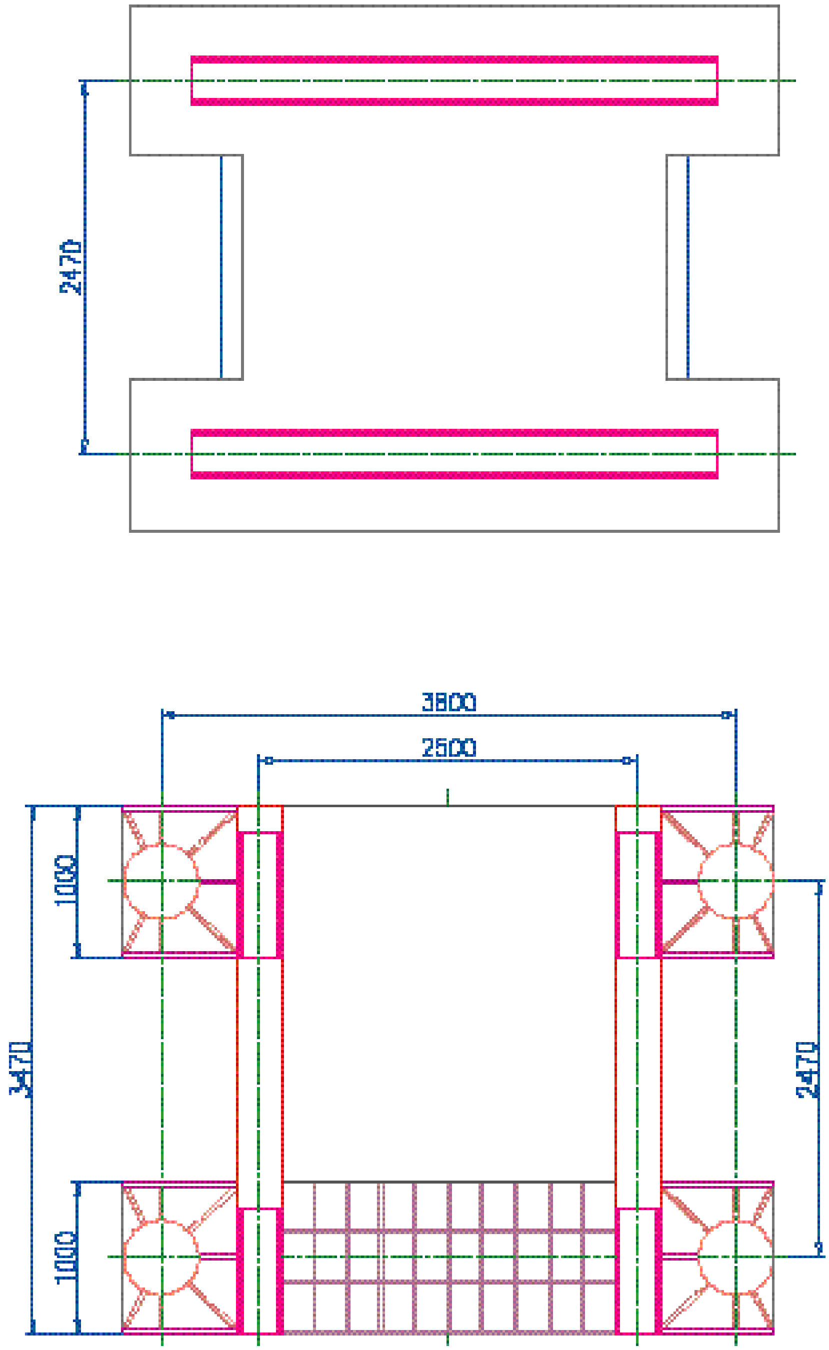

Fig. 5.12 (C. S.): The details of the transporter platform are illustrated above. The top drawing shows the top view and the bottom sketch illustrates the details of the airpad locations and the channels that assist in the z-motion.

5.4 HF ELEVATION SYSTEM

The beamline is ~8.6 meters above the floor level in the experimental area. The forward calorimeters need to be elevated and secured in position before data taking commences. Since the HF detectors are located outside of the main body of CMS, they will be installed into the beam position towards the end of the entire CMS assembly sequence. If access to the inner components of CMS is required during a shutdown, at least one of the HF detectors needs to be lowered and put in garage position. In order to make installation and deinstallation of the HF possible, an elevation system is designed as shown in Fig. 5.13. This system is required to handle the entire weight of HF including its shielding (310 tonnes), and to vertically position the detector within 1 mm of the beam center.

A set of four hydraulic jacks is located under the floor surface to raise the detector with the transporter table. Fig. 5.14 shows the locations at the corners of the platform where the jacks are located. This is the same location as the airpads. The detector is raised and a frame is slid under it. The frame would support the table on the flats shown at four corners. The rollers for the motion along the beam line are located just above these flats. The lifting flaps that are attached to the columns of the frames are used to further elevate the detector as shown in Fig. 5.13.

The raising and lowering operations will have to be performed by a team of crane and rigging operators. It is expected that it would take about a day to position the HF in the beam. A 10 cm thick lead shielding element is planned to be located in the front part of the HF during these operations to reduce the radiation background originating from the HF absorber. Further studies are underway to understand the nature of the activation radiation to facilitate optimal shielding.

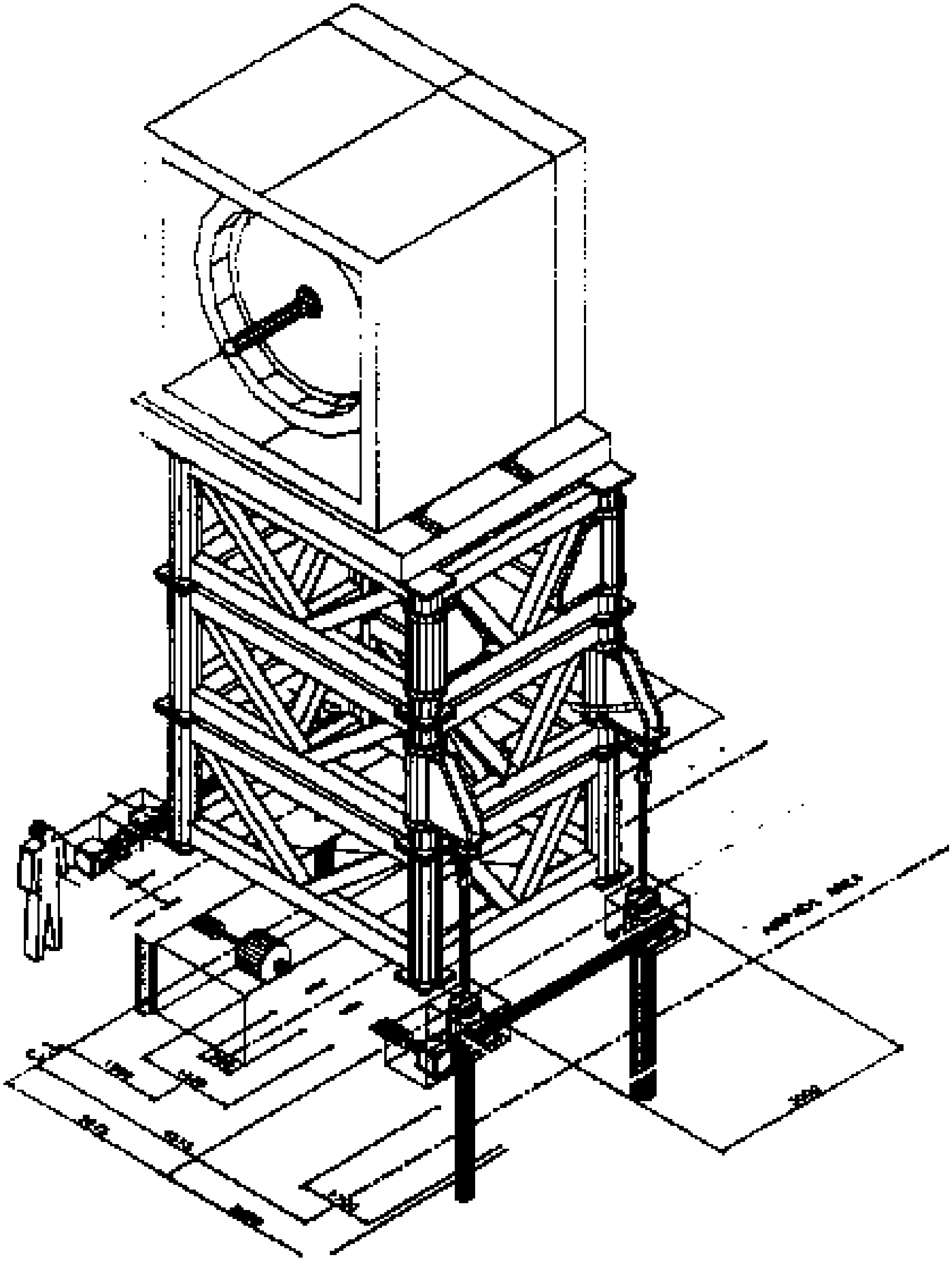

Fig. 5.13: The elevation system is shown above where three frames are used to support the weight of the HF and its shielding. The HF and the transporter platform are shown schematically.

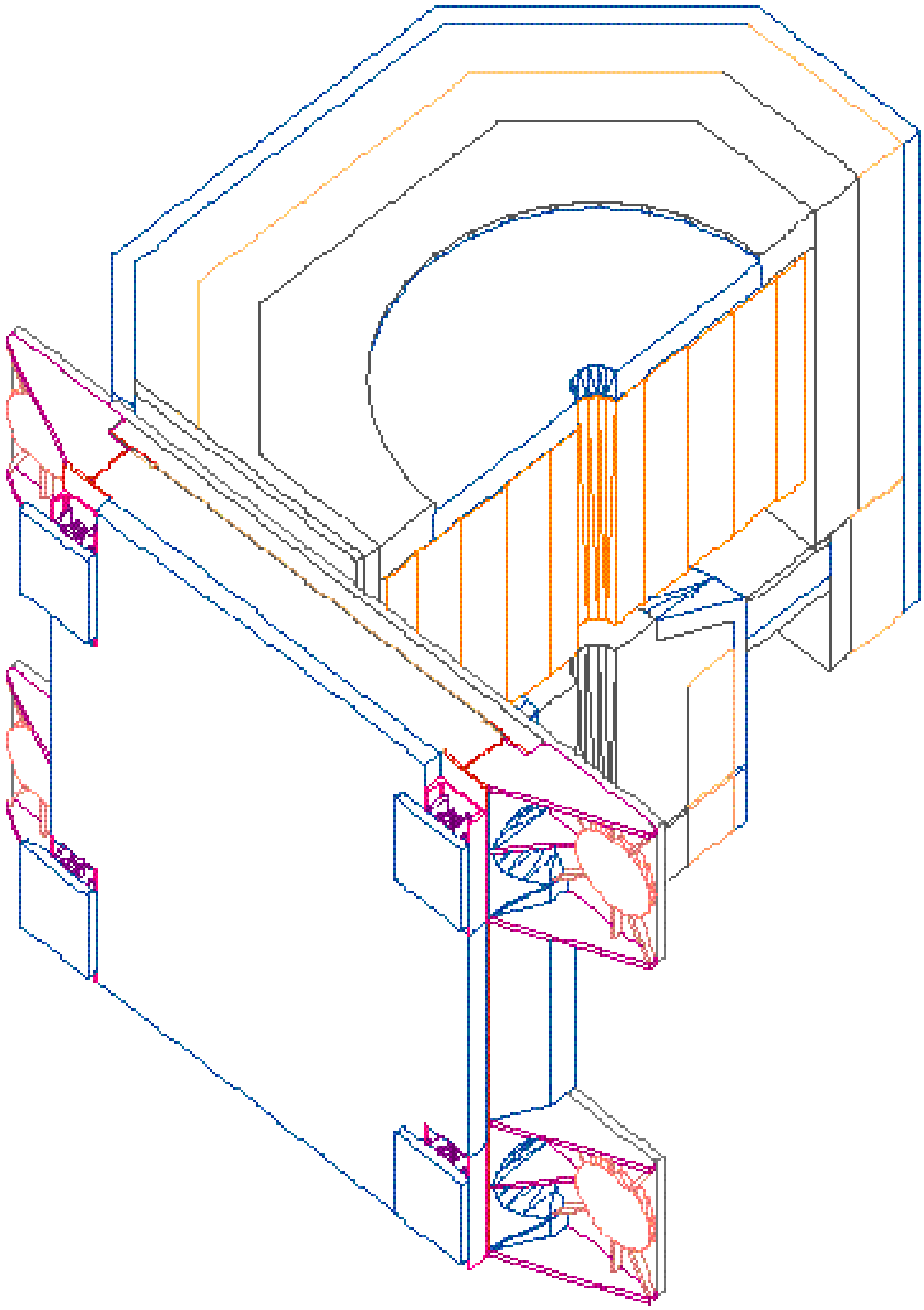

Fig. 5.14: Bottom view of the HF and the transporter table. Note that the airpads are removed and the four flats are shown where the upright columns of support frames mate the platform.

5.5 HF GARAGE POSITION

The HF garage is designed to meet multiple requirements and provide flexibility in HF manipulation and maintenance in general. A layout of the garage is shown in Fig. 5.15.

a) During the assembly and installation phase of CMS, the HF can be located away from the usable floor space of the experimental hall in the garage. This provides room for the endcap systems (muon chambers and calorimeter) to be fully retracted out of the barrel, e.g. for tracker installation in the beginning and later, for other maintenance needs.

b) HF PMT and electronics installation, testing and maintenance activities can be carried out in the garage position without interference with any other CMS subsystem.

c) The garage dimensions are 6.1 m high, 7.3 m deep and 7.1 m wide. The optimization of the transporter platform design, commensurate with the shielding requirements, provided minimization of the total height of the detector. This makes installation of a crane in the garage possible. The width of the garage is sufficient to open the two halves of HF by almost a meter apart for maintenance. The depth provides ample floor space for storage of spare modules, shielding elements and other equipment.

d) The entrance door to the garage from the side walls is at elevation of three meters which makes access to the upper electronics racks rather convenient. A walkway at this elevation is foreseen towards the back of the garage.

e) A 5-tonne crane is planned for the garage. This would enable us to manipulate the absorber modules (2.7 tonne max) and other shielding elements if it proves necessary.

f) A temporary lead shielding against the radioactivated HF absorber will be in place when the detector is in motion between the garage and the data taking position as pointed out earlier. In addition, when the detector is in its garage position, the sliding doors of the garage (15 cm concrete with a 5 cm thick lead insertion with a radius of 50 cm centered around the HF symmetry axis) will provide additional and adequate shielding.

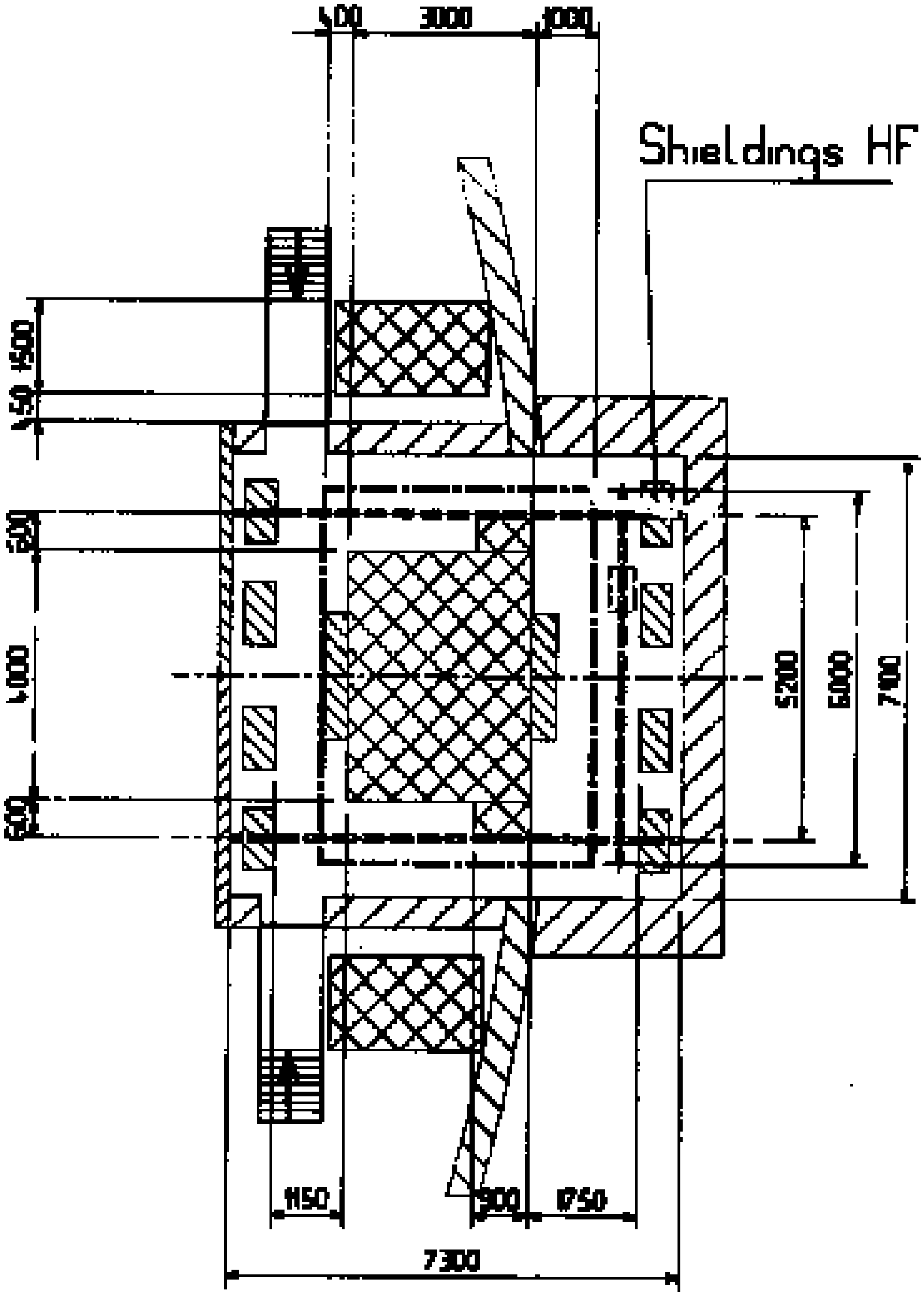

Fig. 5.15: The layout of the HF garage (top view).

5.6 FORWARD CALORIMETER DESIGN

5.6.1 Overview, constraints, specifications and requirements

The main requirements for the HF are the following:

a) Phase space to be covered by the HF spans =3 to 5 which is 40% of the available phase space of CMS. HF covers this region with good hermeticity, fine transverse granularity, adequate energy resolution and a sufficient depth. At z=±11.1 m, where the front face of the HF is located, the active radius is 1.40 m with a depth of 1.65 m or 10 nuclear interaction lengths, . The tower structure is chosen to be in a square geometry; for ||>4, the towers are 5 cm5 cm, and for ||<4, towers are larger, 10 cm by 10 cm square (see Fig. 5.16). The dead-zones are kept to absolute minimum in order not to adversely affect the missing energy measurement.

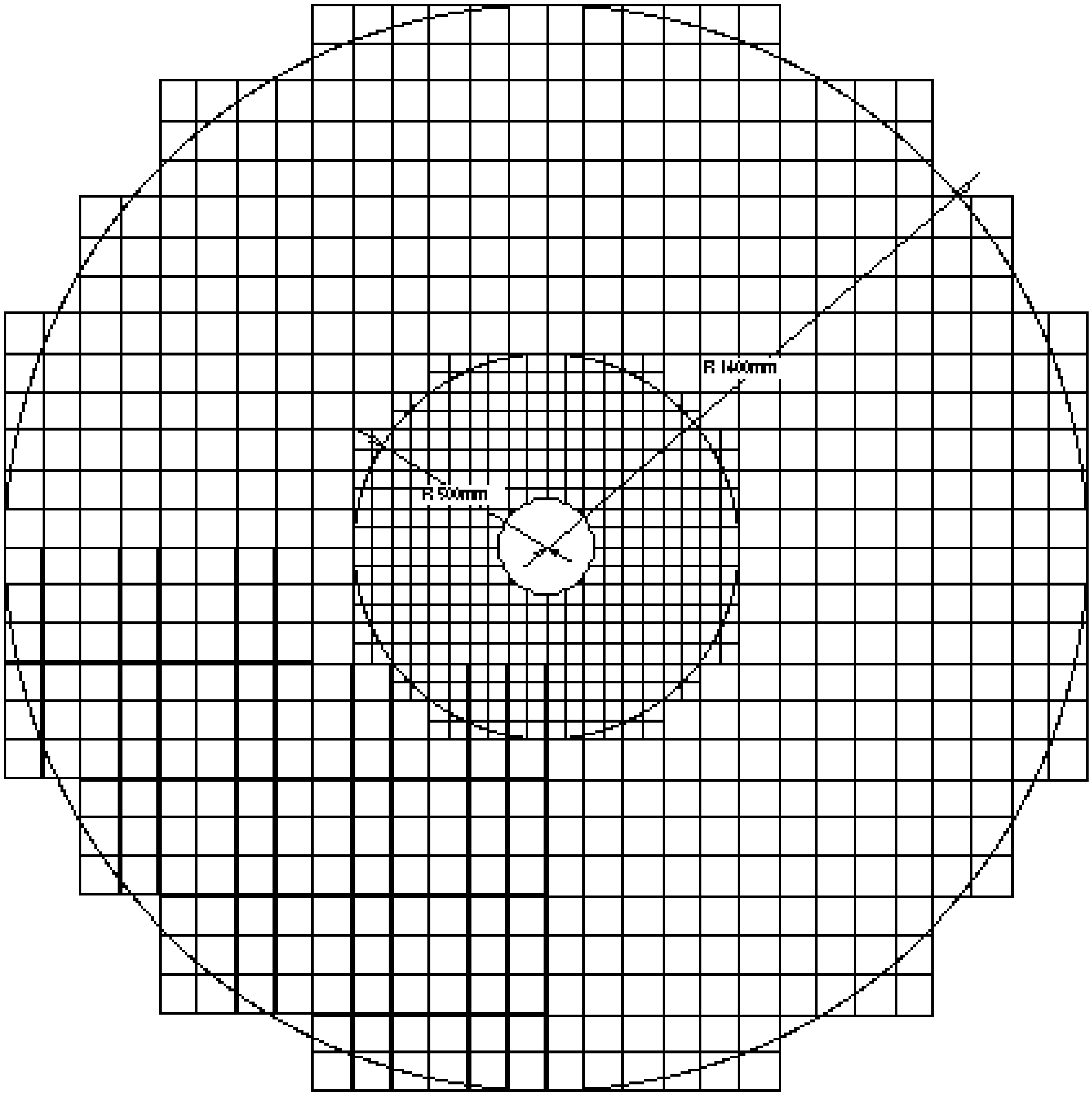

Fig. 5.16: The HF front face is shown with the tower structure as described in the text. The smaller (5 cm5 cm) are closer to the beam pipe region and the coarser towers are located at η<4. The inner radius is 12.5 cm.

b) The HF must maintain its intended functionality even at the exceptionally high levels of radiation expected at LHC. The radiation doses of up to a Grad over ten years are anticipated in the hottest region of the HF. The choice of quartz as the active medium serves this purpose well since it can withstand doses up to 30 Grad with only a few percent loss in transparency in the wavelength range of 300-425 nm[2].The accumulated dose from all sources and types of radiation at the PMT location does not exceed 10 krad/year, and at the electronics racks that are located outside the shielding elements, the total dose per year is about 3 krad. These doses are acceptable for satisfactory detector performance. Extensive radiation background studies resulted in the shielding configuration shown in Fig. 5.17.

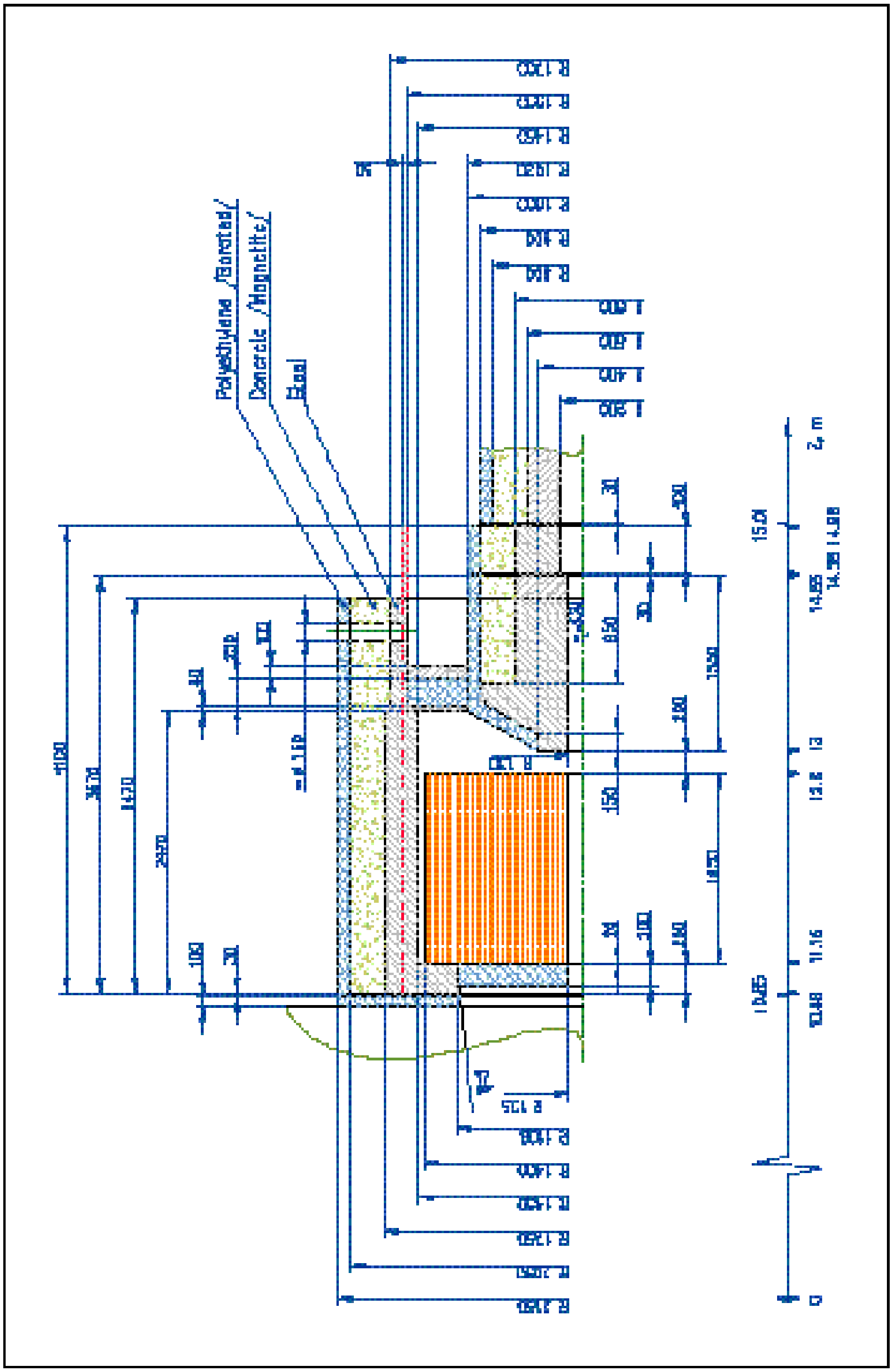

Fig. 5.17 (C. S.): The HF is surrounded effectively by 30 cm thick steel, 30 cm thick magnetite concrete and 10 cm thick borated polyethylene. In front, the HF is covered by a 20 cm thick polyethylene, and in the back, a plug structure shields the PMTs and fibre bundles. PMTs are located around a ring at 100 cm<*r* <140 cm.

c) The neutron rates in the vicinity of this detector will be exceptionally high. One of the fundamental features of this kind of a detector is that neutrons do not produce Cherenkov light and therefore do not contribute to noise in the detector. The total neutron fluence immediately behind the copper absorber and closest to the beam pipe, for $5\infty10^5$ pb^{-1}, is about $2\infty10^{15}$ n/cm^2. The fibre bundles will be located in this region. 140 cm away from the beam, the neutron fluence drops by an order of magnitude. The PMTs are well shielded behind a 40 cm thick matrix of steel and borated polyethylene slabs against the radiation emerging from the absorber region. Thus, the neutron fluence here is reduced to ~ $2\infty 10^{12}$ n/cm^2 for $5\infty 10^5$ pb^{-1}. The HF PMT window will be made of silica glass with superior radiation resistance properties. No appreciable transmittence loss is observed up to a total dose of $1.4\infty 10^{14}$ neutrons/cm^2 in the wavelength range of operation with these types of window materials.

d) The HF is being designed such that it integrates well with the rest of the CMS subsystems. These subsystems are:

- Endcap Muon System: The ME4/HF interface region is redesigned based on the results of the radiation background simulation results. The general difficulty has been to isolate the higher η regions of the ME4 muon systems from high neutron rates that originated from the HF and other sources. This problem is solved to a large extend by introducing a 25 cm thick steel and a 10 cm thick borated polyethylene in this interface region. The steel section is part of the HF shielding and radially covers from r = 110.8 cm to r=175.0 cm. A 10 cm thick polyethylene slab is attached to the backplane of ME systems such that it conforms to the HF projection onto the back of the muon system. This slab radially covers from r =110.8 cm to r=215.0 cm. A 3 cm air gap is foreseen in this region to facilitate the z-motion of HF when being installed/deinstalled in the beam position. In addition, a 20 cm polyethylene shielding is located in the front face of HF to reduce the backsplash albedo.

- Beam pipe and the vacuum pumps: A straight 20 cm diameter stainless steel beam pipe goes through HF. The thickness of the beampipe is about 1.5 mm. The current design of beam pipe calls for a change from 6 cm radius to 10 cm. This makes relocation or perhaps complete elimination of the vacuum pump in front of the HF possible. Further studies are presently carried out to simulate the vacuum conditions at the IP. Although a conical pipe inside HF might seem desirable at first sight, the background simulations do not indicate an appreciable difference between these two geometries. The HF is designed to separate in two halves such that it can envelope the beam pipe when installed in its final position. The beam pipe will remain in position when HF is installed/deinstalled. The HF design respects 2 cm stay-clear beam pipe zone.

- The rotating shielding: The rotating shielding is located in the back of the HF end-plug shielding. The rotating shield ends at z=14.96 m. A 40 cm long collar interfaces the rotating shielding with the back of the HF end-plug. This collar is the very last shielding element that is installed after the HF is positioned in its final beam position.

- Transporter: The transporter consists of two fundamental elements; the table that HF is mounted upon and the elevation mechanism. The details of these systems are already outlined in sections 5.3 and 5.4, respectively. The transporter table is designed such that each half of HF is able to move by ± 25 cm on the horizontal plane and that 30 cm motion along the beam is also required for final positioning of the calorimeter. The HF is elevated to the beam height by hydraulic jacks and frames and positioning tolerance of about ± 1 mm is expected. The total weight of the detector is 310 tonnes, including the shielding. The beam center is 8.6 m above the floor level.

e) In the location of the PMTs, the magnetic field at most is a few hundred gauss. The shielding material combined with a 0.5 mm thick μ-metal is adequate for this purpose.

f) The trace elements in the composition of the absorber material (C110, 99.5% Cu), should not contain elements that are readily activated. One such element is Co and the typical levels in industry produced plates are low, 0.005 to 0.006%.

The HF is constructed such that there are three different lengths of fibres inserted into the absorber as illustrated in Fig. 5.18. The long fibres that run the entire length of the absorber (165 cm) are called *long* fibres. The *medium* length fibres are shorter by 22 cm (15 X_o) from the front face of HF. The *short* fibres are inserted 30 cm (2 λ) from the back face of HF. Consequently, *long* fibres constitute the electromagnetic (EM) section, *medium* fibres, the hadronic (HAD) section, and *short* fibres, the tail catcher (TC) sections. Table 5. 2 summarises the HF tower structure parameters.

Fig. 5.18 (C. S.): Three different length fibres are located in the copper absorber in 2 mm square geometry. EM fibres that run the entire length of the absorber (165 cm) are schematically shown next to the TC fibres (inserted 30 cm into the absorber from the back of the calorimeter at every other plane) and the HAD fibres are shown as single fibres that are located at every other groove and plane and they are shorter by 22 cm with respect to the EM fibres.

Each section is readout by an individual photomultiplier. The tower structure is of square geometry. Close to the beam pipe ($\eta>4$) the tower size is 5 cm5 cm square and everywhere else it is 10 cm10 cm square as shown in Fig. 5.16.

Total HF depth is chosen to be ten interaction lengths, which is more than sufficient for the required physics performance. Increasing the absorber from eight to ten interaction lengths, a factor of two to three reduction is gained, on average, in all particle fluxes behind the calorimeter. A side view of the HF showing the shielding is given in Fig. 5.19.

Table 5. 2

The HF tower sizes and other parameters. The number in parentheses indicates the number of fibres for that tower.

Tower type	Size (cm cm)	Quan./Side	EM Length (cm)	HAD Length (cm)	TC Length (cm)
Small ($\eta>4$)	5 ∞ 5	320	165 (313)	143 (313)	
Large ($\eta<4$)	10 ∞ 10	564	165 (1250)	143(1250)	
TC Tower	20 ∞ 20	164			30 (2500)

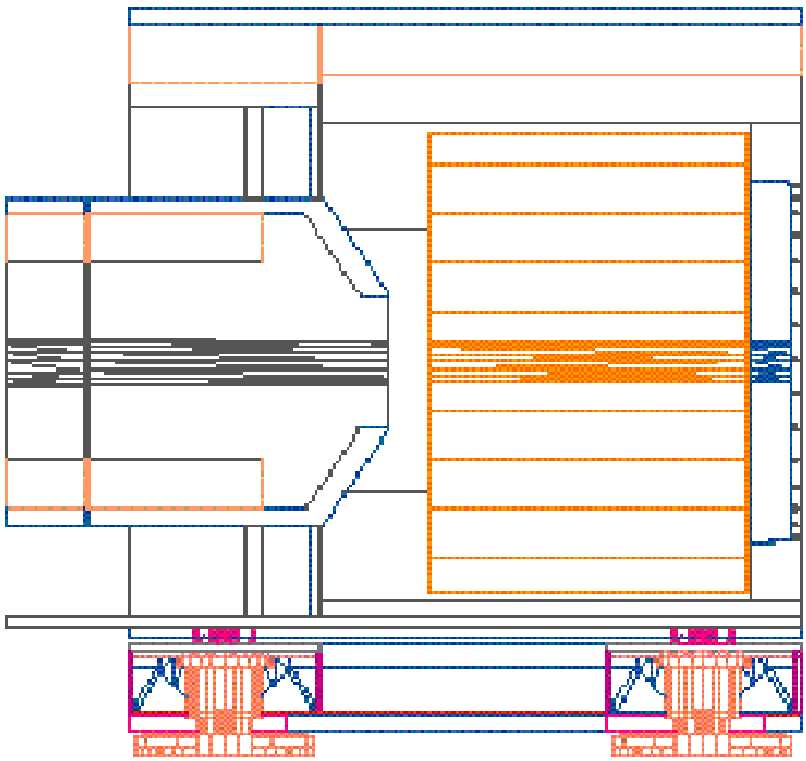

Fig. 5.19 (C. S.): The side view of the HF shows the absorber, the shielding end-plug and the transporter platform (IP on the right). The fibre bundles are arranged such that EM, HAD and TC fibres emerge in the back of the absorber and get connected to the right side of the back shielding (around the end-plug) via ferrules. PMTs are located to the left.

5.6.2 Absorber matrix

The basic construction element of the HF absorber is a module with holes for quartz fibres. The quartz fibres will laterally form a square matrix where the closest neighboring fibres are equidistant, 2 mm. Each hole will contain one (for EM section) or two (for HAD and TC sections) fibres of 345 micron diameter (including cladding and buffer thickness). Four different types of modules will be used in construction of the HF absorber. The main features of each of the module types are listed in Table 5.3.

Table 5. 3

Four different types of modules will be used in constructing the HF absorber. The main features of each of the module types are listed below.

Module Type	Size (w ∞ h) (mm ∞ mm)	Weight (tonne)	Quantity
I	600 ∞ 300	2.66	32
II	500 ∞ 300	2.22	32
III	300 ∞ 300	1.33	16
IV	600 ∞ 200	1.77	8

Modules will be made of copper plates with grooves. Plates will be stacked together using diffusion welding such that the modules will be self-supporting structures. The dimensions of the grooves are shown in Table 5.4.

Table 5. 4

Dimensions of grooves in the absorber plates.

Groove center-to-center (mm)	2.00 ± 0.10
Groove depth (mm)	0.5 + 0.2 - 0.1
Single groove width (mm)	0.5 + 0.2 - 0.1
Double groove width (mm)	0.9 + 0.2 -0.1

We have used photochemical etching to produce grooves in the copper plates of the prototypes. Our experience indicates that the required dimensions and tolerances can be achieved with this technique. The cold rolling seems more advantageous for mass production. Rolling technology is currently being refined for production of full size copper plates to the required groove dimensions and tolerances. This technique will be adapted for grooved plate production if it proves compatible with the construction procedures and requirements.

The module will be machined to size after the plates are welded. Top and bottom plates have allowance of 1±0.4 mm for achieving linear dimensional accuracy and surface flatness. After machining, the tolerances of ± 0.1 mm on the height and on the width is aimed for each block. The edges will be flat and parallel to within ± 0.1 mm. Dimensions and tolerences of the plates are given in Table 5.5 while modules are specified in Table 5.6.

The following inspections will be used for the quality control during the manufacturing cycle of the absorber modules:

a) inspection of copper plates -- dimensions and flatness of 5% of plates will be measured;

b) inspection of grooved plates -- dimensions of grooves for 5% of plates will be measured;

c) inspection of the welded modules -- the welding quality of each module will be tested at the vibration stand and with ultrasonic and/or X-ray techniques when appropriate. The dimensions of the holes will be checked using steel wire gauges.

d) inspection of machined modules -- outer dimensions and flatness will be measured using a rolling pass, the weight of the module will be measured to control the average density of the absorber.

Table 5. 5

Dimensions and tolerances of copper plates. The flatness tolerance is 0.1 mm and the edge -to-edge angle is 90_ ± 1.

Plate Type	Width (mm)	Thickness (mm)	Length (mm)	Quantity
I	602.0 ± 0.5	2.00 ± 0.20	1650 ± 0.5	5,600
II	502.0 ± 0.5	2.00 ± 0.20	1650 ± 0.5	4,800
III	302.0 ± 0.5	2.00 ± 0.20	1650 ± 0.5	1,200

Table 5. 6

The tolerances on the modules. The flatness is 0.1 mm, edge-to-edge angle is 90_±3, and parallelism is 0.1 mm.

Module Type	Width (mm)	Thickness (mm)	Length (mm)
I	600.0 - 0.5 + 0.0	300.0 - 0.1 + 0.0	1650 ± 0.5
II	500.0 - 0.5 + 0.0	300.0 - 0.1 + 0.0	1650 ± 0.5
III	300.0 - 0.5 + 0.0	300.0 - 0.1 + 0.0	1650 ± 0.5

The quadrant tolerances will be -0.5 mm for the width and the height. The flatness of the top, bottom and the side surfaces will be within 0.5 mm. The angle between the side and top/bottom surfaces will be within 3. The flatness of the side surfaces of the half of the HF is within 1 mm. The parallelism of the side surfaces for the entire HF is 0.5 mm.

5.6.3 Structural elements

The HF calorimeters are built in quadrants. It is convenient to assemble in quadrants both in terms of mechanics and, later, in terms of transportation, testing in a test beam, lifting/lowering and the final assembly in the assembly area.

One quadrant consists of 11 absorber modules, as described in the previous section, and mounted on a steel shell which provides structural support. The steel shell is also a part of the radiation shielding when installed. Before the assembly of a quadrant, the quality control of the necessary modules will have been performed and appropriate selections and modifications, if necessary, of modules will have been made in order to conform to the required tolerances for a given quadrant. A schematic of a quadrant is shown in Fig. 5.20.

The quadrant structure will be assembled in layers starting with the outer modules, *i.e*. those closest to the steel support shell. Possible gaps between the last absorber module and the support shell will be compensated for by shims. Several passes may be required in order to level the top and side of the quadrant. The expected deviation from the plane on the top and the outer side does not exceed 0.5 mm.

Fastening of absorber modules relative to each other is still being investigated. The absorber modules are not allowed to move with respect to each other or to the support structure while quadrants are transported, or a half of the HF assembled, or when the HF moves in and out of the garage. Among the options that are currently being considered are attaching the modules to the side wall of the shell with thin steel belts or bolting them together (at the expense of sensitivity loss) or epoxied together. Modules are held together from the side and top with 2 cm steel plates which encase the entire absorber matrix except the back where the fibres emerge.

The steel shell also serves as support for the segments in the back of the quadrant where the PMTs are located. The part of the shell which extends beyond the back face of the absorber is a separate unit. It is a structure with multiple pieces. This is necessary because of the fact that fibre insertion requires room behind the absorber and the pieces are attached and put together as the fibre insertion gets completed. The distance between the back of the absorber and the first 5 cm steel slab is 50 cm. The shielding matrix consists of 25 cm of polyethylene sandwiched by two layers of steel (5 and 10 cm thick, on either side of the polyethylene block). This matrix functions as a shielding component protecting PMTs and the experimental hall from background. The air-core mixers inside the through holes transport the light from the fibre bundles to PMTs located on the other side of the segments. The rear steel layer also shields the PMT against the magnetic field.

The entire structure (absorber and its steel shell) has rollers mounted on both bottom and side walls, so that it can be moved during assembly and installed onto the transporter platform. This design allows for the quadrants to be rotated by 90 and moved to assemble half of the HF as discussed in the next section.

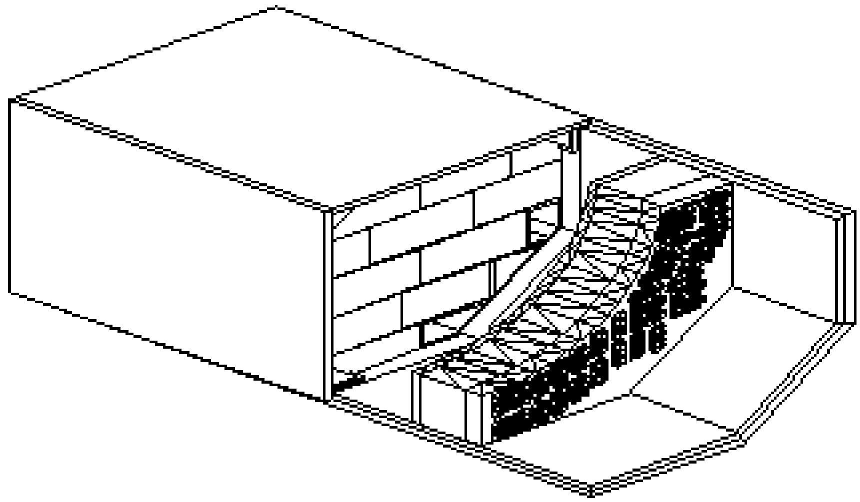

Fig. 5.20: One of the HF quadrants is shown schematically above. Steel plates cover the top and the side of the absorber. The back shielding and the through holes for the air-core light mixers are also indicated. The flanges that connect the back shell to the shell of the absorber can be seen around the inside periphery.

5.6.4 HF Assembly and installation

The HF and all of its shielding elements weigh 310 tonnes on the transporter platform. Naturally, assembly and installation of these massive components require adequate lifting and rigging capabilities. The construction, assembly and installation of these components need to be precisely planned in order not to exceed the limits of the existing cranes and other rigging equipment.

Static load due to the copper absorber alone per HF is 99.4 tons. The details are shown in Table 5.7. The detector must open in half to clear the beam pipe during installation. Thus, each half of the detector (~50 tonnes) must be structurally independent.

Table 5. 7

The static load due to the copper absorber per HF side is shown below.

Module Type	Weight/Module (tonnes)	Quantity/Side	Total (tonnes)
I	2.66	16	42.56
II	2.22	16	35.52
III	1.33	8	10.64
IV	1.77	4	7.08
TOTAL			99.4

Static load for shielding material is summarised in Table 5. 8 for each element. Note that each element is a sandwich of steel.

Table 5. 8

The static load due to the shielding elements per HF side is shown below.

Shielding Component	Weight/Block (tonnes)	Quantity/Side	Total (tonnes)
Top	9	2	18
Top-side	9	2	18
Side	15	2	30
Side-bottom	9	2	18
Platform+shielding	10	2	20
Endplug	5	2	10
TOTAL			114

The dynamic loads are small when the HF is in motion to and from the garage position. HF will be moved at a speed of ~ 5 mm/sec.

The installation plan calls for lowering the HF+ through the main shaft (PX56 with a 20.4 m diameter) when the 2500 tonne gantry becomes available in early 2003. This minimises the time spent on the experimental floor for assembly and shortens the general CMS assembly and installation schedule. The effective dimensions of the smaller shaft (PM54) are 3.8 ∞ 7.2 m^2 do not readily accommodate the entire HF on the transporter platform. We expect that at least one of the HF calorimeters (HF+) should be assembled/installed before other subsystems of CMS in the collision hall, *i.e.* YE/+3, +2, +1 and muon system.

A schematic illustration of the assembly plan is shown in Fig. 5.21 with steps (a) through (h) indicated. The absorber matrix (11 modules) and support structure are shipped to the assembly area (Building 168) in eight quadrants (a), each with mounted rollers on the bottom and side of the steel shell. Quadrants are rotated by 90 when a half of the HF+ or HF- needs to be put together. By this time, each quadrant has already been tested in a test beam and calibrated. Two quadrants are positioned relative to each other, and connected with two cm thick steel plates in the front and back.(b). The rear plate is auxiliary and can be removed as soon as the calorimeter is set into position on the transporter in the experimental hall. The half of the HF is rotated into vertical position (d) and, with the aid of rollers moved upon the transporter platform (e). The remaining half is also rigged on top of the platform at this stage as well (f). The shielding components are assembly tested (g and h).

All the steps shown in Fig. 5.21 are performed in the assembly area (Building 168). The shielding components after the assembly tests may be removed for transportation and lowering into the experimental all.

If either the HF construction schedule or the CMS general assembly is rescheduled, the lowering of HF into the experimental hall will be altered. There is a 80 tonne crane limit over the main shaft (PX56) which would require that HF be installed in pieces to the collision hall floor.

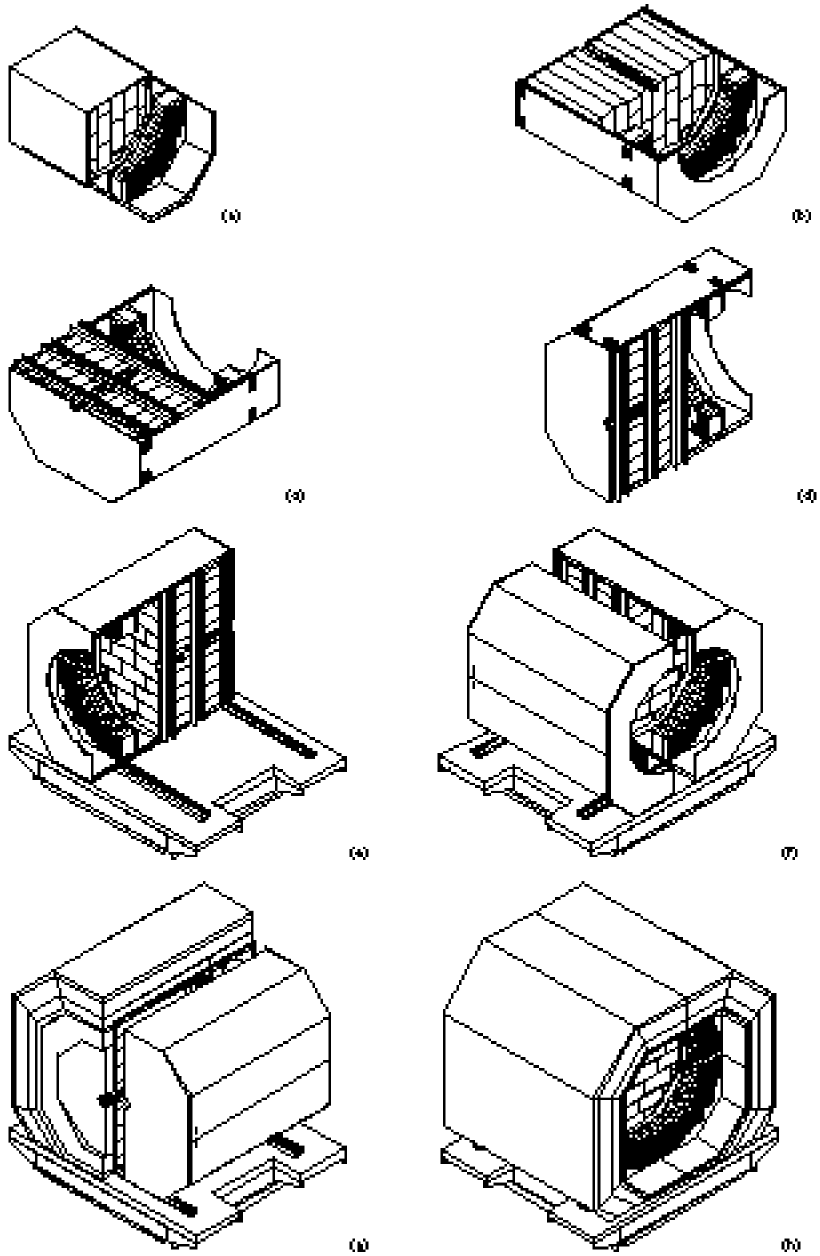

Fig. 5.21: The schematic illustration of the HF assembly is shown above.

5.6.5 Fibre layout

The fibre bundles that emerge from the back of the absorber are bundled into ferrules in order to couple to PMTs. The ferrules are connected to the 5 cm thick steel plate which is located in a ring structure between r =100 cm and r =140 cm. This connection is made using a pressure fitting. A conical hole is drilled into the steel plate and a slotted thin fitting over the cylindrical steel ferrule provides the necessary pressure to fix the bundle in place. The advantage of such a system is that the bundles do not need to be twisted during assembly and this mechanism provides sufficient strength, in addition to quick mount and dismount. We have tested this type of fittings up to 30 kg of force without failure. The expected force on the ferrules do not exceed a few kg.

Fig. 5.22 shows the coupling between the ferrule, steel plate and the light guides that transport light to the PMTs. 5 cm steel plate holds the ferrules. This piece will be made in sections to make room available for fibre insertion work. As the fibre bundle are made, they are attached and secured to the steel ring. The ferrules are stainless steel cylindrical tubes, 7 cm long with an outer diameter of 2.5 cm. The inside diameters of the ferrules are different for smaller and larger bundles, corresponding to the tower sizes. The largest ferrule ID is about 1.9 cm which holds the 2500 fibres for the tail catcher towers. The ferrules will penetrate through the steel plate into the borated polyethylene by one cm. A hexagonal cross-section air-core light guide is positioned inside this 25 cm thick shielding element to transport the light from the end of the ferrules to the PMTs. PMTs mounted on PMT boxes are located at the outer side of the second shielding (10 cm thick steel slab) and mate with the light mixer via plastic fitting washer.

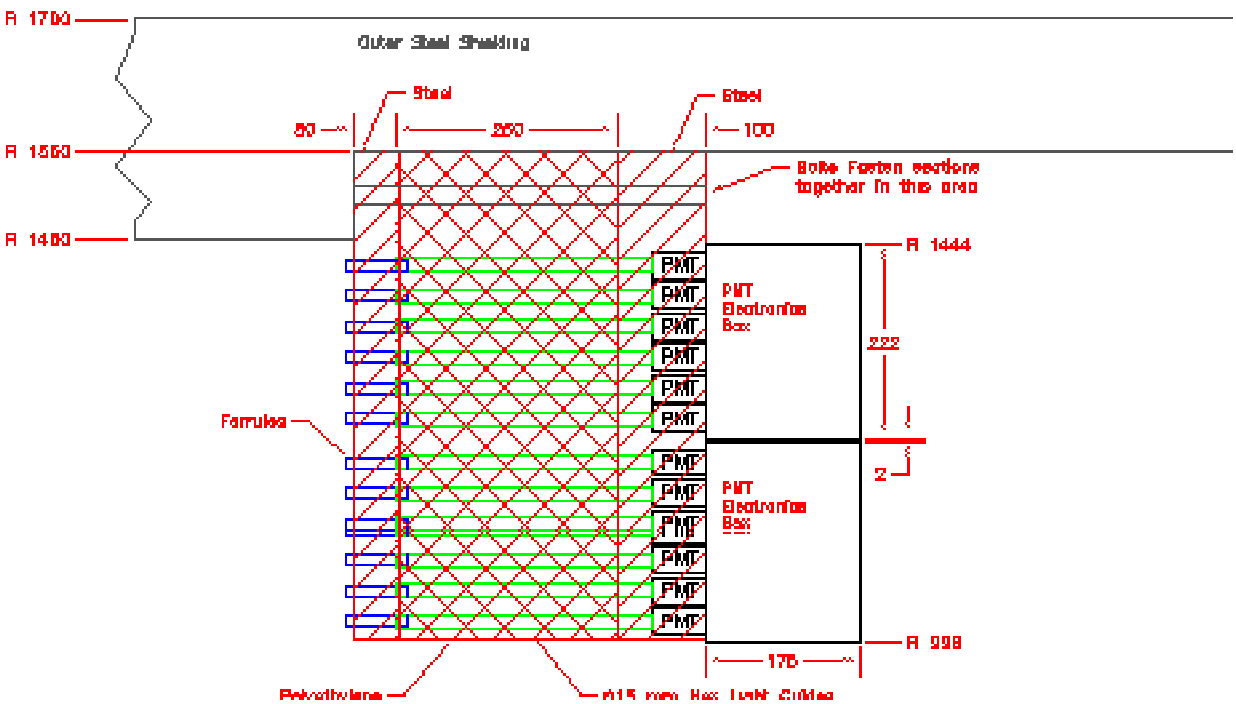

Fig. 5.22 (C. S.): The ferrules are coupled to steel plate via fittings as described in the text and light is transported through air-core light mixers to the PMTs located at the outer side of the second steel shielding slab.

There are 32 PMT boxes per quadrant as shown in Fig. 5.23. There are 16 PMTs mounted inside each box along with the calibration and monitoring components (laser and LED light distribution system and an input fibre for the quartz fibre radiation damage monitoring). The PMT boxes are located radially around the beam line between 100 and 140 cm and are geometrically arranged such that the quartz fibre bundle lengths from the towers are minimised and the available space is efficiently utilised. Each PMT box is identical and is mounted to the back of the steel shielding plane with the use of two quick release positioning screws. There is a 6 mm clearance space between the PMT boxes.

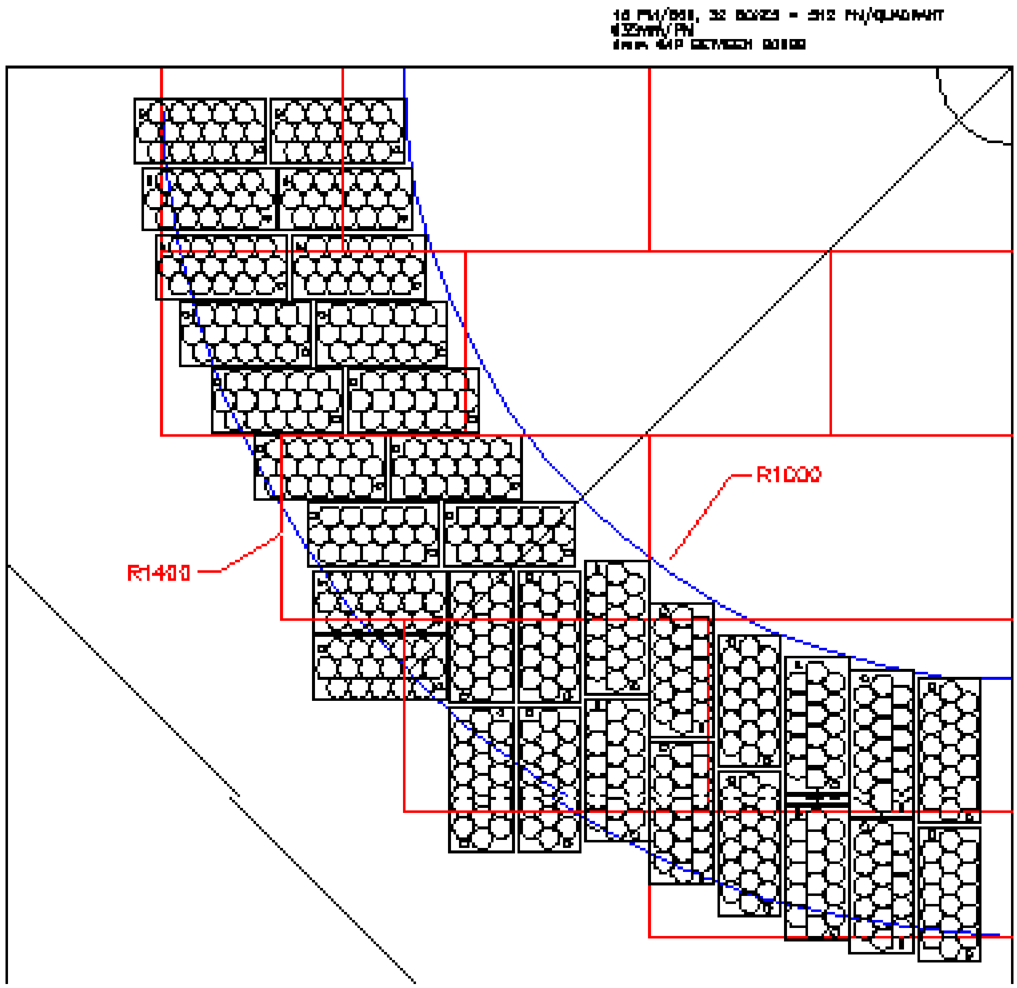

Fig. 5.23: The PMT boxes are arranged such that 512 PMTs are available per quadrant. Each PMT box is constructed identically and they are mounted to the back of the steel slab with the aid of two quick release screws for ease in installation and maintenance.

5.6.6 Photomultiplier layout/mechanics

The photomultipliers couple to the fibre bundles via air-core light mixers as described in the previous section. The PMTs are housed in a box as shown in Fig. 5.24. There are 16 PMT/box. Two quick-release screws attach the PMT box to the steel plate. Each PMT box is identical, and in addition to the PMTs, it houses the calibration and monitoring, Cockcroft-Walton high voltage components and nitrogen gas fittings.

The effective photocathode area of the PMT (dia 15 mm min) defines the dimensions of the light mixer and the fittings around the PMT head. A 0.5 mm thick μ-metal and a soft iron cylindrical housing extend 2 cm over the PMT photocathode (>2r) for magnetic field shielding. The soft iron housing is tapped outside at one end to be screwed into the faceplate of the PMT box. This minimises machining and cost while providing flexibility. Between the soft iron housing and the μ-metal shielding, a helical coil serves as a spacer and centers the PMT along the symmetry axis. This arrangement also allows the nitrogen to flow from the box volume towards the PMT head.

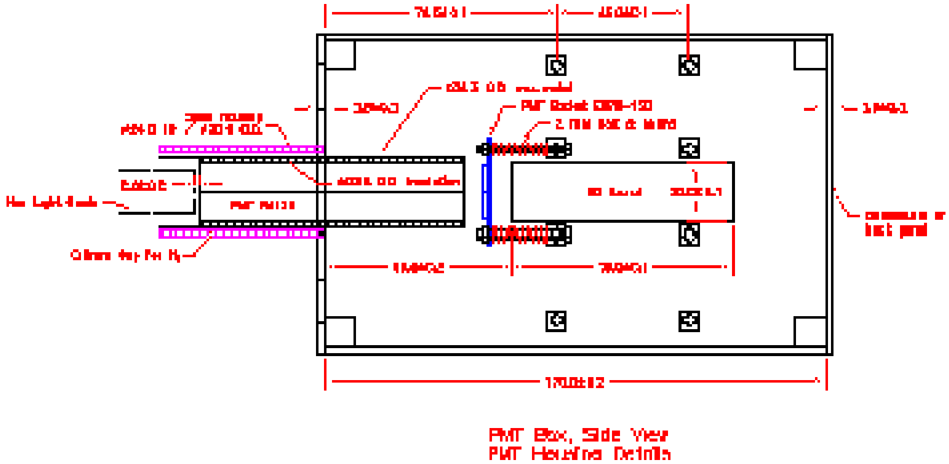

Fig. 5.24: The PMT and the PMT box cross section are shown above with mechanical details. The PMTs penetrate into the steel shielding by 4 cm. Connectors for signals and nitrogen are mounted on the back panel of the box.

Nitrogen is used to keep the He levels as low as possible around the PMTs since He permeability of silica glass window is higher compared to other standard glasses. This also protects the PMTs from catastrophic loss due to a possible He leak in the experimental area from cryogenic systems.

The PMT is connected via a socket to the circuit board (Cockcroft-Walton base). A spring loaded mechanism guarantees good contact between the PMT and the light mixer while maintaining electrical contact with the base. The signals and services are provided through connectors and feedthrough on the backplane of the box where they are easily accessible, as illustrated in Fig. 5.25.

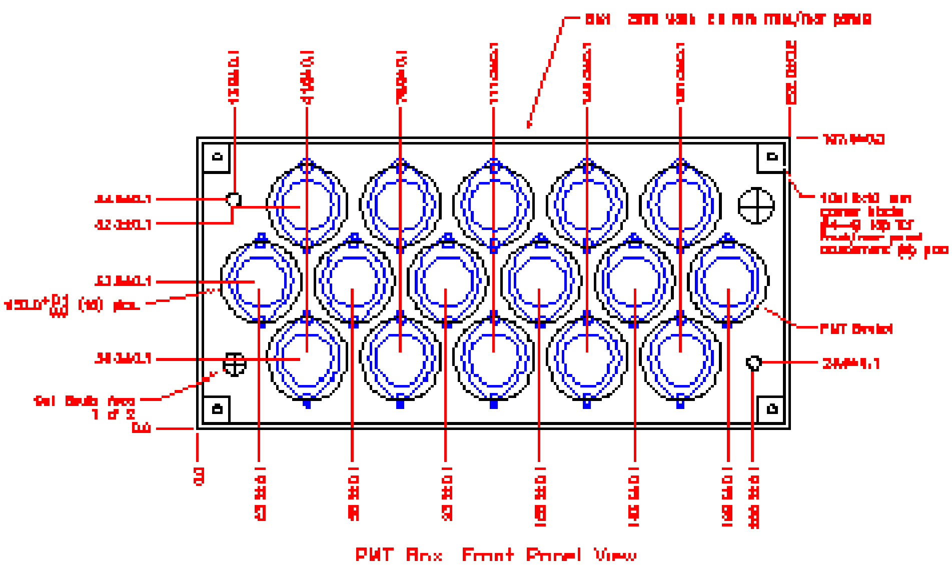

Fig. 5.25 (C. S.): The PMT box contains 16 PMTs and the Cockcroft-Walton high voltage generation components. The calibration and monitoring components for laser and LED are shown on the lower left and the upper right of the box. Two quick release screws position and mount the box onto the back of the steel shielding slab and are shown in upper left and lower right corners of the box.

5.7 ACCESS, MAINTENANCE AND OPERATIONS

5.7.1 Maintenance in the hall and garage

During assembly and periods of major maintenance or upgrade of the CMS detector, the HF calorimeters occupy garages at the experimental hall floor level at either end of the hall below the final focus quadrupoles. In the garage position the detector with its shielding rests on a transporter which is designed to move on airpads. The transporter consists of a steel structure mounted on four airpads with sufficient load bearing capacity to support the moving 310 tonne load of the detector and its shielding. Guide pins locate and secure the detector to the transporter. Locomotion between the garage and the location of the support structure is provided by winches. Guidance for the transporter in moving from garage to the support location is provided by steel cables attached to winches that are located in the garage.

The umbilical cord with the signal and power cables, the slow control cables, and the nitrogen purge and cooling water lines is constrained and moved in the 50 50 cm^2 utility trench by looping it in a pantograph arrangement similar to the UA2 detector at the SPS. At the detector the umbilicus splits into two bundles, one each for the left and right halves of the detector. The bundles enter the detector through the bottom front of the transporter platform and each bundle terminates at either of two racks (one high and one low) mounted on the shielding on either side of the detector.

A total of 15 cm is available below the platform and the floor. This space accommodates the cables, the main support structure, the components of the transverse drive mechanisms for the 25 cm motion of the two halves of the detector, and the vertical fine-tuning mechanism to center the detector vertically on the beam. The main support structure, which rests on the transporter when the detector is in its low position, is capable of supporting the 310 tonne load of the shielded detector from the four outboard jacking points which have a transverse separation of 4.4 meters and a longitudinal separation of three meters. Placement of the umbilical connection at the front of the detector clears the space below the main support structure for insertion of the stacked support modules in the operational configuration at beam elevation.

The height of the detector and shield is 3.5 meters including the mounting base for the detector halves. This leaves about 1.5 meter of vertical clearance in the garage position, sufficient clearance for a limited crane structure. Maintenance of photomultiplier tubes and other electronics will be done in the garage, but major mechanical assembly and maintenance requiring substantial crane coverage will be carried out using the EH bridge crane or a portable gantry of appropriate capacity.

When the muon chambers and end cap calorimeter are in their retracted positions, the HF calorimeter is shielded in its garage by massive doors. When the muon chambers and end cap calorimeter are in their operational positions, the HF calorimeter can be serviced by the hall crane or a suitable portable gantry.

Final shielding of the calorimeter is done at beam elevation using the hall crane.

While resting on the transporter in the low position, the main detector platform is less than 0.5 meter above the floor of the hall. This provides access to the lower electronics racks attached to the side of either half of the detector and to the PMT modules at the rear of the detector.

5.7.2 Radiation monitors

The HF will have to function in the worst radiation conditions of all CMS subdetectors. The estimated absorbed dose in the photomultipliers and read-out electronics during the lifetime of experiment is close to the upper limits for these devices. Therefore, the close monitoring of the background flux is extremely important. Based upon the results of Monte-Carlo simulation, we choose to monitor at the following locations as identified in below Table 5.9.

Table 5. 9

Location and measures of the HF radiation monitors

Point number	Coordinates z (cm)	Coordinates *r* (cm)	Energy (neutrons)	Neutron flux ($1/cm^2s$)	Hadron flux (E>15 MeV) ($1/cm^2s$)	flux (E=1-3 MeV) ($1/cm^2s$)
1	1320	100	<15 MeV >15 MeV	3×10^6 1×10^5	5×10^4	3×10^6
2	1400	100	<15 MeV >15 MeV	5×10^4 1×10^3	2×10^4	3×10^4
3	1320	230	<15 MeV >15 MeV	1×10^3 1×10^3	2×10^1	2×10^3

Point 1 is located in the area of fibre bundles (near the point where they enter the shielding). Point 2 is in the vicinity of the PMT boxes. Point 3 is at the electronics racks. This allows monitoring radiation conditions for all the critical HF elements. The same coordinates (*r* or z) will help to understand the efficiency of the radiation shielding of the calorimeter and give information on neutron, hadron, and containment. The measurements must be performed for both the HF+ and HF-.

These measurements are achieved using standard detectors manufactured by industry. The flux can be measured by small (0.8-1 cm diameter, 5.5-6.3 cm length) Geiger-Mueller counters. The possible choice is counters of SI series (SI-38G, SI-34G, SI-37G), which is sensitive to photons in the energy range 0.1-10 MeV with a rate up to 210^7 particles/cm^2 s. The Si semiconductor detectors are used to detect charged hadron background. They function well with hadron intensity up to 10^6 particles/cm^2 s.

Since neutrons (especially of the low energy) are the most damaging component of radiation background for PMTs and the read-out electronics, special attention must be paid to neutron flux measurements with the possibility to estimate the spectrum of neutrons.

The space inside radiation shielding is very limited. Therefore, detectors of the KNT series can be used for point 1. They are small (0.7 cm diameter and 7.1 cm length) fission chambers with 1-3 mg of fission material. These detectors work at the neutron rates up to 210^{10} neutrons/cm^{2}sec (KNT-8) with the lower threshold of neutron energy of 400 keV (KNT-7). In addition, B^{10} proportional chambers can be installed to the fission detectors for the points outside radiation shielding. The SNM-13 counters have a diameter of 0.8 cm and a length of 8.5 cm. These detectors work well neutron fluxes up to 510^6 neutrons/cm^2 s which exceeds the estimated neutron level in monitoring points 2 and 3 by at least two orders of magnitude. The bare counter is expected to detect thermal neutrons, but if equipped with polyethylene moderators of 5", 8", and 10" diameter, it will be able to detect neutrons up to energy 7, 20, and 30 MeV correspondingly. Polyethylene moderators will allow to evaluate the neutron spectrum. All quoted detectors are able to work in high fluxes which ensures the reliability of measurements.

References

[1] P. Gorodetzky et al, NIM A361 (1995) 161.

[2] P. Gorodetzky, Rad. Phys. And Chem. 41 (1993) 253.

TABLE OF CONTENTS

6. OPTICAL DETECTOR SYSTEM

6.1 OVERVIEW

The hadron calorimeter (HCAL) consists of three subsystems. A barrel calorimeter, HB/HOB measures particles with $\eta < 1.4$. An endcap calorimeter, HE/HOE, measures particles in the range $1.4 < \eta < 3.0$. A forward calorimeter, HF, measures particles in the range $3.0<\eta<5.0$. The barrel calorimeter part inside the coil is called HB (Hadron Barrel). The two layers of the calorimeter outside the coil use the coil and the muon iron as the absorber material and are called HOB (Hadron Outer). Similarly the Hadron Endcap calorimeter (HE) has a small one layer section using the muon iron as an absorber and is called the HOE calorimeter.

HB/HOB and HE/HOE are tile-fibre sampling calorimeters, i.e. they use scintillator tiles and fibre readout to sample the energy deposition of hadrons in the copper and steel absorber. Fig. 6.1 shows a generic diagram of the optical readout system of these calorimeters. The scintillation light is collected using wavelength shifting (WLS) fibre embedded in a groove in the tile. The groove follows a "sigma" (σ) pattern on the tile, as shown on Fig. 6.2. Outside the tile, the WLS fibre is spliced to a clear fibre. Clear fibres are connected the readout device via an optical cable using mass-terminated connectors.

This EPS image does not contain a screen preview.
It will print correctly to a PostScript printer.
File Name : ch6view3.eps
Title : C:\CH6VIEW3.EPS
Creator : AutoCAD PSOUT
CreationDate : 1997-05-12
Pages : 1

Fig. 6.1: Generic diagram of the optical readout system for HCAL Barrel and Endcap calorimeters.

6.1.1 HB design

For the HB, where the readout is located inside magnetic field of 4 tesla, the readout devices are Hybrid Photo Detectors (HPDs). The readout for the HO calorimeter is located in the region where the magnetic field is approximately 1 kG. Here either HPDs or shielded photomultiplier tubes can be used as a readout devices. The current default design calls for using HPDs everywhere to minimise the number of optical readout systems.

This EPS image does not contain a screen preview.
It will print correctly to a PostScript printer.
File Name : ch6sing.eps
Title : C:\SINGCH6.EPS
Creator : AutoCAD PSOUT
CreationDate : 1997-05-06
Pages : 1

Fig. 6. 2: Design of a single tile with a "sigma" fibre layout pattern.

The inner HB calorimeter consists of 18 sampling layers as shown in Fig. 6. 3 for the r-ϕ view and in Fig. 6.4 for the r-z view. The innermost layer (Layer 0) is located between the steel supporting plate of the ECAL calorimeter and the inner HCAL endplate, i.e. before any copper plates. The thickness of the scintillator for Layer 0 is 9 mm. The sampling layers between the inner and outer HCAL endplates (Layers 1 through 16) are placed every 5 cm of copper. They are instrumented with 4 mm thick scintillator, Kuraray SCSN-81. Layer 17 is placed between the HCAL outer endplate and the cryostat and will be instrumented with 9 mm thick scintillator. The outer HOB calorimeter consists of two sampling layers (three layers at η=0). The first layer of HOB is placed after the solenoid magnet and the second layer of HOB is placed after the first 20 cm thick muon steel absorber. The HOB layers are instrumented with 1 cm thick Bicron BC408 scintillator. All HB and HOB scintillator layers are read out by 0.94 mm Kuraray Y11 multiclad WLS fibres.

The HB/HOB calorimeter is segmented into three longitudinal readout segments. Layer 0 is separately read out as segment H1. This segment measures the hadronic component of the shower which was produced in the EM crystal calorimeter. Since hadronic energy in ECAL is undermeasured by the crystal, the ratio of energy in H1 to total Hadronic Energy (H1+H2+HOB) can be used in an algorithm to improve the resolution of the combined EM+HAD system. The second readout, H2, consists of 17 layers (1 to 17). The third readout, the HOB, consists of the two layers (or three layers at η = 0) located after the solenoid. The HOB segment corrects for the high energy tails measured by H1 and H2. The HOB and HOE calorimeters will also be used by the muon system to identity muons.

This EPS image does not contain a screen preview.
It will print correctly to a PostScript printer.
File Name : ch6cabc1.eps
Title : C:\CH6CABCH.EPS
Creator : AutoCAD PSOUT
CreationDate : 1997-06-04
Pages : 1

Fig. 6. 3: The r-φ view of the 20 inner HCAL wedge.

This EPS image does not contain a screen preview.
It will print correctly to a PostScript printer.
File Name : ch6sdv5.eps
Title : C:\CH6SDV5.EPS
Creator : AutoCAD PSOUT
CreationDate : 1997-06-04
Pages : 1

Fig. 6. 4: r-z view of a HB 20 wedge. The inner and outer steel plates are not indicated on the drawing. The dimensions are stated assuming the inner HB radius of 1806.5 mm.

The scintillators are inserted from the large η end of the HCAL wedge into the 9 mm gaps between the copper plates. Fig. 6. 5 shows a typical scintillator tray assembly for the a single layer of the HB calorimeter. Each readout layer consists of three elements: Side-Left, Middle and Side-Right scintillator trays which are inserted to separate copper slots. The neighbouring tiles in each tray are optically separated by grooves filled with white epoxy glue. The epoxied multi-tile sub-assemblies cut from a single piece of scintillator are called megatiles. Several megatiles are put together between two black plastic cover plates to form a scintillator tray. The bottom cover plate is 0.95 mm thick. The top cover plate is 1.9 mm thick. The routing of the fibres is inside the top cover plate.

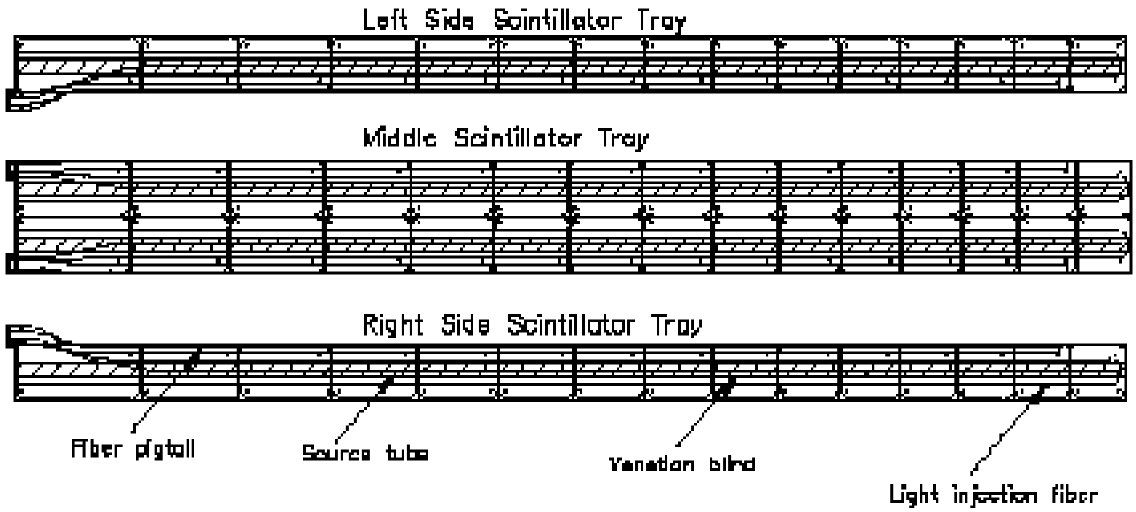

Fig. 6. 5: A typical scintillator tray assembly for the inner HB calorimeter.

The top cover plate has additional grooves. One of them is for a 1.3 mm diameter source tube where a remote motor will drive a pointlike radioactive ^{137}Cs γ source embedded in a tip of a wire. This source will be used for calibration both during construction and data acquisition. All layers will have "occasional" source tubes for use during checkout without a B field, while the endcaps are withdrawn. In addition, two layers in each tower (layer 0 in H1 and layer 9 in H2) will have a source tube permanently coupled to one of source drivers capable of operation with the magnetic field on.

Another groove is for a quartz fibre that will be used to inject either UV or blue light into the tiles. The quartz fibre will be inserted into the same two layers (one in H1 and one in H2) which will have permanently accessible source tubes. The light injection to tiles (or to photodetectors separately) can be done much more frequently. Light injection and g source calibration will allow us to monitor gain changes in the photodetectors as well as changes in the light output of the tile/WLS fibre system.

As a part of quality control each scintillator tray assembly will be scanned by a collimated radioactive γ source in a 1.6 m x 5.7 m megatile scanner. Following this measurement, the megatile will be scanned with the radioactive wire source. The collimated source provides an absolute excitation of each tile, and its ratio to the wire source excitation (which depends on tile size and other solid angle effects) provides a permanent data base to enable the accurate transfer of testbeam calibrations to the assembled calorimeter, via the wire source.

The HB/HOB calorimeter designs are close to the design of the CDF Plug Upgrade Calorimeter. Since all the components of the CDF Plug Upgrade Calorimeter are built and tested, many of the design and production issues for the CMS calorimeter are well understood. The HCAL group has built testbeam calorimeters using the tile-fibre method for 1994, 1995, and 1996 testbeam runs at CERN. Hence, the HCAL group is experienced in building tile-fibre calorimeters. The optical system of the HE calorimeter has similar design. Each scintillator tray covers a 10º wedge. There are 19 sampling layers in each Endcap module.

6.1.2 Design Requirements of the HCAL optical system

The testbeam results show that the HB calorimeter can attain the target energy resolution of $100\%/\sqrt{E} \oplus 5\%$. In terms of component performance, the 5% constant term requires that the variation of the tile-to-tile light yield be better than 10 % and that the rms of intra-tile transverse uniformity be better than 4% (even if the nonuniformity is the same for all tiles in a projective tower). An overall tile-to-tile light output variation of 10 % contributes approximately 3% to the constant term because the hadron shower is typically spread out over more than 10 layers. R&D on prototypes and QA/QC tests on completed calorimeter counters indicate that this performance level has been met.

The exact magnitude of the induced constant term depends on the calibration method. If all towers of the HCAL are to be measured in a test beam, or with a source/cosmic ray muon to sufficient accuracy, than a "local" calibration can be made, which means that all towers in HCAL have the same mean. If this cannot be accomplished, than the towers have means which vary due to the tile manufacturing tolerance. Clearly, in this "global" case, one has a larger induced error for HCAL taken as a whole, since the energy mean responses are not all the same.

The results shown in Fig. 6. 6 indicate that a 10% gaussian error on the individual towers induces a 2.5% local and a 3.2% global constant error in the fractional energy response. Since the H2 test beam data imply a 5% constant term, the additional error, folded in quadrature, causes a small and acceptable increase in the HCAL energy resolution.

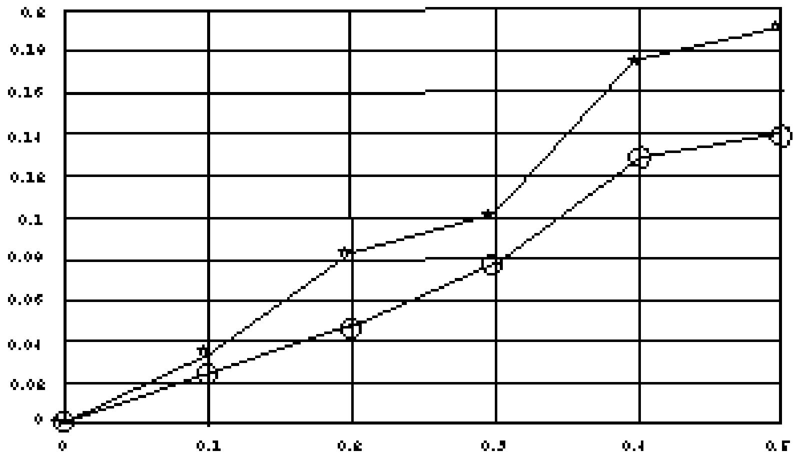

Fig. 6. 6: Induced constant term in the fractional energy error in the HCAL (y axis) as a function of tile manufacturing quality (fractional rms of light yield, x axis). The star symbols correspond to global calibration case and the open circles correspond to the local calibration case.

We require the calorimeter to have enough light to achieve $100\%/\sqrt{E} \oplus 5\%$ and to determine at 3 σ level if a muon traversed a tower. A minimum ionising particle going through 17 layers of the H2 readout section of the calorimeter with 5 cm copper sampling corresponds to an energy of 2 GeV. We require a minimum light yield of 1 pe/mip/tile. Therefore, the photostatistics contribution to the fractional resolution with a light yield of 17 pe/muon in 17 layers is $45\% / \sqrt{E}$, or half of the $100\%/\sqrt{E}$ expected from sampling.

Presently, electronic noise in HPD (at the gain of 2000) corresponds to approximately 2 photoelectrons. Thus 17 pe/muon is also the minimum number for the HPDs and electronics to see a muon. For a factor of 25% in safety, we should start with at least a level of 20 pe/muon. This light yield level has been achieved in CDF, which was able to get more than 1 pe/muon per tile, or more than 17 pe/muon in 17 tiles. In CMS initial tests show that we can achieve a light yield of 2 pe/mip/tile.

Fig. 6. 7 shows the radiation levels over the detector. The loss of light from radiation is another source of variation of the light yield of tiles. Since the maximum allowed tile to tile variation is 10%, we want the light loss from radiation to be less than 10%. For the HB calorimeter, the radiation damage (reaching 20 krad at radius of 198 cm at η=0 and 30 krad at η=1.1) is expected to be small over 10 year lifetime of the detector, assuming a total of 510^5 pb^{-1} of integrated luminosity. We will monitor the decrease to 2-3% as a function of time, which is much better than our margin of safety.

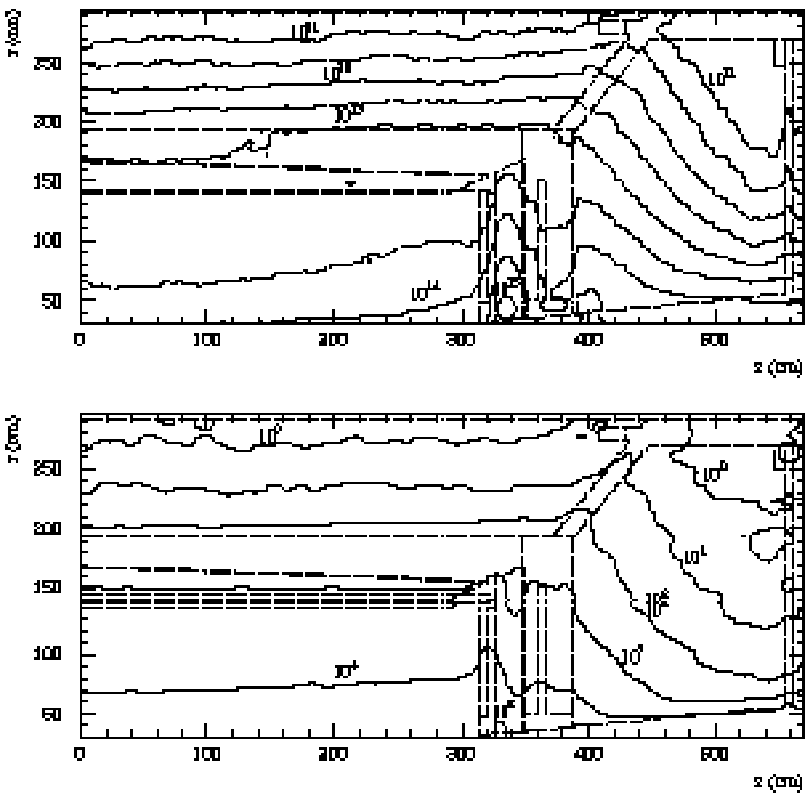

Fig. 6. 7**:** Radiation levels in the CMS detector. Fluence of hadrons E>100keV in cm^{-2} s^{-1} (upper plot) and radiation dose in Gy (lower plot) in the HB/HE region. The dose values have been smoothed by taking weighted running averages over neighbouring bins. Values are given for 5 x 10^5 pb^{-1}. The intermediate (dashed) contours in the fluence plot corresponds to 3.16 x 10^n. The dotted lines indicate the geometry.

The lateral segmentation must be fine enough for detection of narrow states decaying into pairs of jets. A segmentation of $\Delta\eta \times \Delta\varphi$ = 0.087 x 5º is sufficient for good di-jet separation and mass resolution. The calorimeter must have sufficiently good time resolution (σ_t < 5 ns) to determine the beam crossing of electrons and jets of physics interest. We require that 99% of the light generated by a particle going through a tower be collected in two beam crossings (each crossing is 25 nsec).

6.2 SCINTILLATOR SPECIFICATIONS FOR HB/HE/HOB/HOE

The length of the HB scintillator trays vary from 3.7 m to 4.3 m. The central tray vary in width from 33 cm to 50 cm and the side trays vary in width from 16 cm to 24 cm. The smallest tile in the HB calorimeter is 15 cm x 17 cm and the largest tile is 24 cm x 40 cm. The HE trays are 10º wedges called Pizza Pans that have the shape of a trapezoid with the tiles located 35 cm to 280 cm radially away from the beam.

The scintillators with the WLS fibres are the active medium of the hadron calorimeter. In order to attain the required resolution and maintain this value over the 10 year lifetime of the detector, the scintillators and WLS fibres have to meet stringent material specifications. Energy of the particles in the calorimeter is measured by the amount of light that reaches the photo detector. The criteria are developed so that a minimum ionising particle will produce nearly the same amount of light no matter where it crosses the scintillator in a tower. The baseline for the HB/HE detectors is the Kuraray SCSN81 scintillator (polystyrene based plastic) and the Kuraray Y11-250 double clad (WLS) fibre. The HOB and HOE tiles are substantially larger in size with the lower light yield. For these tiles, a higher light yield is required so that minimum ionising particles can be observed. The baseline is BC408, for which the plastic base is polyvinyl toluene (PVT) which produces a factor of two more light compared to SCSN81, and the thickness is 10 mm. The WLS fibres are the same as for the HB/HE calorimeters.

6.2.1 Scintillator specifications6.2.1.1

Material.

The scintillator material should have good mechanical and thermal properties. Its hardness and deformation temperature should be high to allow for fast sawing and machining with only cold air stream cooling with no lubrication. A minimum machining speed for a 0.88 mm groove 0.4 mm deep is 250 cm/minute with no signs of melting.6.2.1.2

Thickness (HB/HE).

The light yield is directly proportional to the scintillator thickness. The nominal value for layers 1-16 is 4.0 mm. Since the scintillator together with the plastic and other materials that form the scintillator tray has to fit inside the 9 mm slots in the calorimeter, the thickness cannot increase. A tolerance is: Thickness = 4.0 mm ±0.4 mm. Within a single scintillator sheet the thickness tolerance is better ± 0.2 mm. The thickness for layer 0 and layer 17 is 9 mm. The HOB and HOE are constructed from thicker scintillators and the nominal value is 10 mm ± 1 mm.6.2.1.3

Light Yield and Attenuation length of scintillator

The light yield should match WLS fibres doped with K27 dye (such as double clad Y11 or BCF91A), and produce light signal that is equal or exceeds the baseline scintillator and fibre. Fig. 6.8 shows an ADC spectrum of a photomultiplier tube signal from a minimum ionising particle traversing a 19 cm by 26 cm tile. The dimensions of this tile correspond to the size of HB tile in layer 7, tower 10. The light from the tile was collected with 0.83 mm WLS fibre spliced to 1.5 m long clear fibre. The fibre was then connected via a 65 cm long optical cable to a photomultiplier tube. Note that the light path included two optical connections and the WLS and clear fibres have length expected for the actual readout in the CMS detector. The light yield of this tile (4 mm SCSN-81) is approximately 2 photoelectrons/mip. The measurement was performed using a 2 MeV electron gun. We require that light yield of scintillator would be at least as high as of the sample used in this measurement.

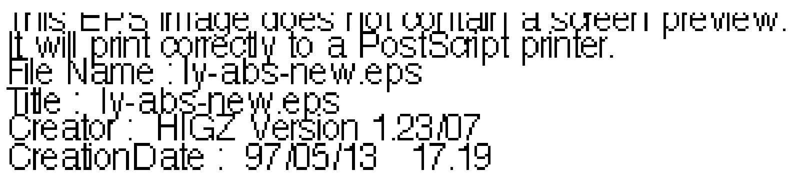

Fig. 6. 8: ADC spectrum of a PMT signal from tiles using collimated 2 MeV β source. The upper plot shows a spectrum for a calibration tile used to establish ADC-to-pe scale. The lower plot shows the spectrum of a 19 cm x 26 cm tile read out with optical cables corresponding to the actual length for the CMS. The light yield of the tile is approximately 2 photoelectrons/mip.

The attenuation length of scintillator must be long enough, so that the light yield of larger tiles (24 cm x 40 cm in HB) is not degraded relative to the light yield of smaller tiles (15 cm x 17 cm in HB). In addition, the uniformity of the light yield across the tile is also dependent on the attenuation length of the scintillator. In order to keep the uniformity of tiles within few percent, the effective attenuation length must be 80 cm or larger.

6.2.2 Radiation damage.

The typical irradiation dose in the barrel at shower maximum in 10 years of operation at design luminosity is about 300 Gy (30 krad) at η = 1.1. Most of the commercial scintillators and fibres will survive these rates with minimum degradation. The irradiation doses at shower maximum in the end caps are substantially higher reaching a value of about 0.4 Mrad (4 kGy) at η = 2.0 and about 2.4 Mrad (24 kGy) at η = 3.0. There are no commercially available scintillators that would survive the radiation dose in the region of 2<η< 3 without a loss of 50% in light yield.

Fig. 6. 9 shows the relative light yield of a 10 cm x 10 cm tile/fibre assembly as a function of radiation dose. The light yield versus radiation dose follows an exponential form [exp(-Dose/D_0)]. This light loss is due to the reduction of the scintillator and WLS fibre attenuation lengths. The D_0 values for the fibres are about 20 Mrad for a 40 cm fibre, while that of scintillators vary from about 3 to 10 Mrad for a 15 cm x 15 cm tile. In order to keep below the 10% damage limit, the combined (scintillator and fibre) D_0 should be greater than 6.5 Mrad for η <2. The only commercial scintillator that meets this value at this time is SCSN81.

Therefore to be able to partially correct for the radiation damage of HE scintillator trays, the HE calorimeter will have multiple readout sections in the η>2 region. Since most of the light yield is at shower maximum, where the damage is also maximum, a simple correction (first order) as a function of tower η can correct the light yield loss. As the light yield reduction is dependent on the tower depth, a full correction is not possible.

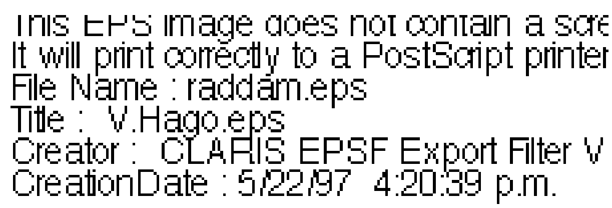

Fig. 6. 9: Relative light yield of tile/fibre assembly as a function of radiation dose. No radiation damage was noticed for doses below 0.1 Mrad.

In order to compensate the radiation damage of the scintillators the calorimeter must be divided longitudinally. The drop of light yield can be corrected by adjusting the weights for corresponding readout segments. In addition, the absolute light yield for minimal ionising particle must be at least 1 photo electron to minimise contribution of photostatistics to the HE calorimeter energy resolution.

Taking into account the longitudinal dose distribution after 10 years of operation for the most loaded scintillator presented in **Fig. 6. 10, and the scintillator SCSN81 degradation vs dose shown in Fig. 6.9, we have the longitudinal distribution of the scintillator light yield reduction after 10 years of operation, presented in Fig. 6. 11. The minimal number of the longitudinal divisions follows from a 20 % uniformity specification within each readout segment. Thus, the first read out is the first layer (after 8 cm plate), the second read out is the next 4 layers and the third read out is the last 14 layers.**

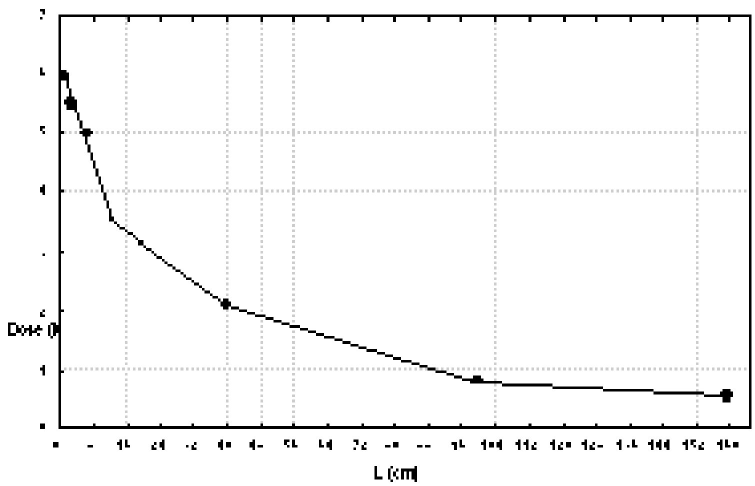

Fig. 6. 10: Radiation dose (in Mrad) in HE versus calorimeter depth for ten years of LHC operation (assuming $10^{34}/cm^2$ sec). Note that this level is twice that quoted for the first ten years of LHC operation.

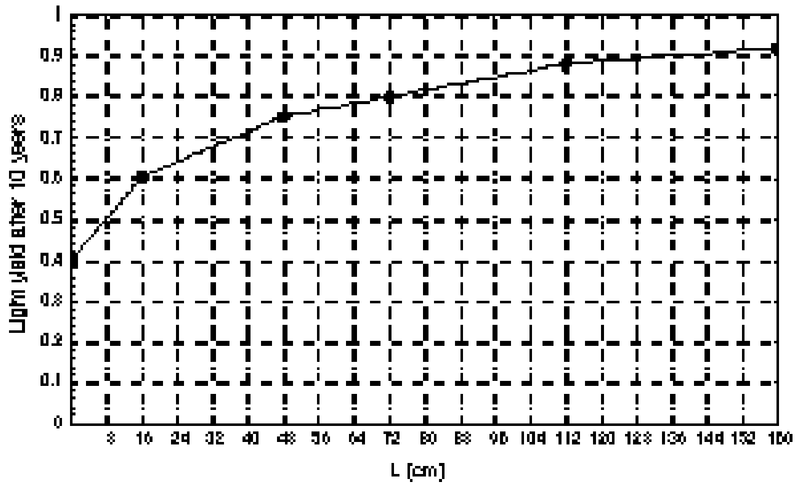

Fig. 6. 11: Reduction of light yield for HE scintillator versus depth layer for ten years of LHC operation at full design luminosity

The radiation doses for HOB and HOE are negligible and pose no problems.

6.2.3 Magnetic field

It has been known for some time that magnetic fields increase the light yield of scintillators. Fig. 6.12 shows the light yield increase of various scintillators that are commercially available. The light yield increase saturates at about 2 tesla. Therefore for the CMS detector, where the scintillators are within 2 to 4 tesla field, this corresponds to a simple overall correction term.

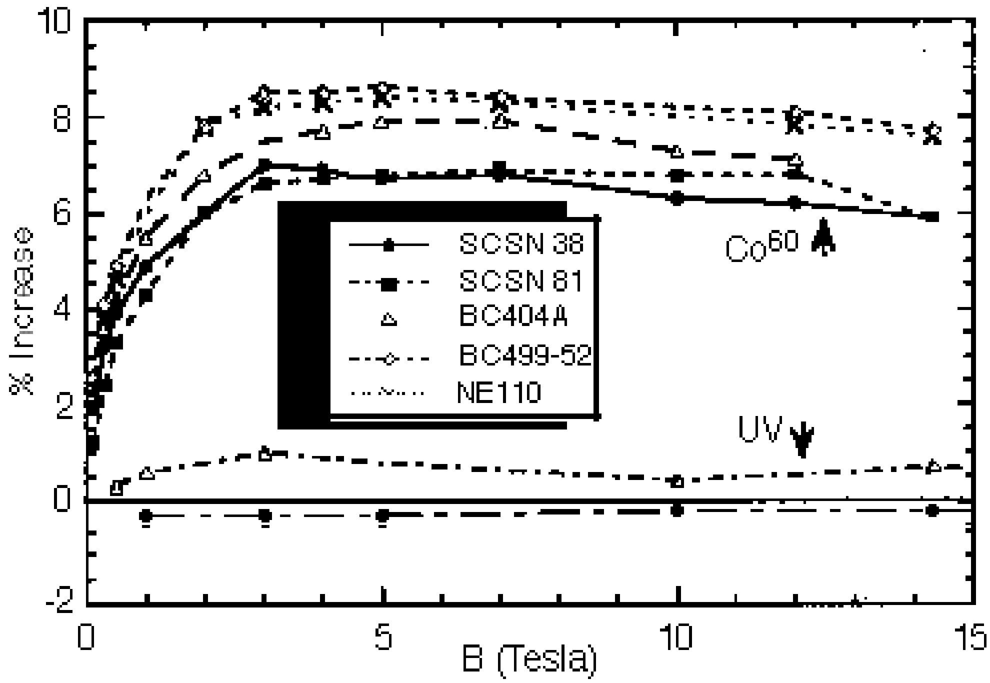

Fig. 6. 12: Light yield increase of various scintillators in magnetic fields.

6.2.4 Quality control.

This section addresses the quality control of scintillators produced by manufacturers. This section will form the basis of writing the scintillator specifications.

The scintillators are to be delivered in rectangular plates with saw cut edges. The two diagonals of the rectangle are required be of equal length with a tolerance of 5 mm. The plates are to be covered on both sides with adhesive, protective paper cover sheets. The cover sheets must be easy to remove and must not damage the scintillator. Samples of scintillators will be machine cut and grooved at the speeds specified above. The cuts must look clean and show no obvious sign of melting. The machined grooves should also show no melting or friction welded chips. The plate thickness will be sampled at uniformly spaced points to verify that it meets the thickness tolerance. The light output will be measured on various samples of grooved standard tile (such as 15 cm x 15 cm) with a standard WLS fibre to show that it produces at least sufficient light to meet or exceed the baseline elements of SCSN81 and that the light yield variation from plate to plate is within the tolerances described above. The attenuation length will be measured of sufficient number of samples to ensure that it meets the specifications. Several samples from each batch of plates will be irradiated by either electrons or photons to 0.5 Mrad (5 kGy). The light yield loss for this level of radiation should be less than 10%. For the lifetime requirement that the scintillator overall light yield does not degrade

in 10 years by more than 25%, the manufacturer should supply data that the type of scintillator has been used in high energy experiments, under conditions similar to this experiment and that the scintillators have shown no degradation, and are chemically, mechanically and optically stable and the surface crazing with time, if any does not reduce the light yield by more than a few percent.

Each plate from the manufacturer will be identified by a unique code and a data base will be produced that will identify each megatile as to the plate code, date delivered, date and machine that cut and grooved it, plus any other information that will be necessary to keep a lifetime history of each scintillator tray.

6.3 FIBRE SPECIFICATIONS FOR HB/HE/HOB/HOE

The baseline is a double clad 0.94 mm fibre doped with 250 ppm of K27 green dye. Each tile within a specific tower will have a WLS fibre of the same length, diamond cut at each end. This length corresponds to the green WLS fibre length required by the largest tile in each tower (i.e. layer 17). Note that tiles in towers 17 and 16, and some in tower 15 will have no splices since they are close to the connector at the edge and will have to be treated in a special manner. One end of the WLS fibre will be mirrored by aluminium sputtering and dipped in a clear coating for protection. The other end will be fused to a clear fibre of the same type and diameter. The second end of the clear fibres for one row of tiles in a scintillator tray will be placed in an optical connector and diamond cut polished. Two fibres produced by industry could meet these specifications, namely BCF91A-MC by BICRON Corporation and Y11-250 by Kuraray. The non-S type fibres of Kuraray are the default design. The non S type fibre is the simplest to polish and splice. However, the S-type fibre does have better flexibility. We will be doing R&D on getting and testing a slightly more flexible form of the non S-type fibre. Note that Kuraray can produce fibres with properties between S type and non-S type fibre. S-type denotes a slow extrusion process and non-S type is a faster extrusion speed.

6.3.1 Attenuation length

The current design for CMS uses 0.94 mm wavelength shifting fibres. We have measured transmission of splices, light yield and attenuation lengths for 1 mm fibres. These tests indicate that 1 mm fibres have similar performance to 0.83 mm fibres, which were used in the CDF Plug calorimeter. However, the ball groove can be cut much faster for 1 mm and 0.94 mm fibres. The design calls for 0.94 mm throughout the system from tile to connector to optical cables to the decoder box and the HPDs. This size was chosen because unlike the 1 mm case, the 0.94 mm option does not require any change in the current HPD design, as the 0.94 mm fibre can fit within the current active area of the HPDs.

The WLS fibre should have an attenuation length of at least 1 m and the clear fibre and attenuation length of at least 6 m when measured with a green sensitive (enhanced) bialkalai photo cathode. Fig. 6. 13 and Fig. 6. 14 show the measurement of light attenuation in Kuraray and Bicron multiclad WLS fibres. Fig. 6. 15 shows attenuation of light in a clear multiclad fibre.

The set-up consisted of a 8 m long piece of scintillator (similar to BC404). The tested fibre was inserted into a long groove extending through entire length of the scintillator, pushed up against a light mixer and connected to a R580-17, green extended tube. The length of the fibre outside the scintillator was 7.5 cm. The scintillator was excited using a movable strontium source rides in a plastic enclosure. The DC current from the photomultiplier tube was measured with a picoammeter.

Fig. 6. 13: Attenuation of light in 1.0 mm Kuraray multiclad WLS Y11. The fitted value of attenuation length in the range of 0.3 m < x < 1.0 m is equal to λ=2.3 m. The light yield ratio, LY(1.0m)/LY(0.3m)=0.71. Note that CMS will use 0.94 mm diameter WLS fibres.

Fig. 6. 14: Attenuation of light in 1.0 mm Bicron multiclad WLS Y11 fibre. The fitted value of attenuation length in the range 0.3 m < x < 1.0 m is equal to λ= 1.5 m. The light yield ratio,

LY(1.0m)/LY(0.3m)=0.65.

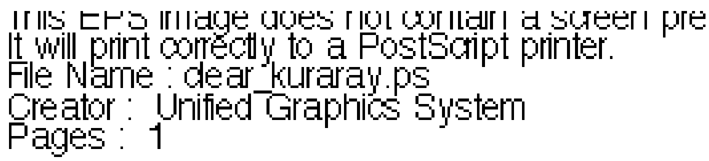

Fig. 6. 15: Attenuation of light in 0.83 mm Kuraray multiclad clear fibre used in CDF Plug Upgrade. The fitted value of attenuation length in the range 0.3 m < x < 3.0 m is equal to λ = 6.8 m. The light yield ratio, LY(3.0m)/LY(0.5m)=0.70.

The radiation damage, at levels encountered in the CMS detector, results in an additional reduction of the fibre attenuation length. For the HB, this is not a problem for the WLS fibres made by Kuraray and BICRON as levels are small and WLS fibre lengths are short. For the HE, the fibres in the high radiation area are short and the light loss is negligible.

6.3.2 Quality control

The light yield from WLS fibres coupled to scintillators have been measured to be roughly proportional to the diameter of the fibre. The specifications of the core diameter is 0.94 mm with the double clad adding 60 to 120 microns. The concentration of the K27(250 ppm) should be uniform enough for all batches to keep the variation in light yield and attenuation length to a minimum. The core diameter and K27 concentration variations should be small enough so that overall light yield does not vary by more than 3%.

The testing of fibres for light yield will be based on samples from various production batches to assure that it meets the 3% tolerance. These fibres will be cut a standard length of 80 cm, diamond cut each end and inserted inside the groove of a standard 15 cm x 15 cm scintillator and excited by a same radioactive source.

To check attenuation length of WLS fibres, fibres will be cut to 1.5 m length and diamond cut polished. Each end of the fibre will be attached to a green extended photomultiplier tube and placed in an attenuation measuring box. The fibre will be excited by the scintillator chosen for the detector. The DC current from the photomultiplier will be recorded as function of light excitation position. Most of the green light travels in the core of the fibre. A small portion of the light travels inside the clad (with a very short ~20 cm attenuation length), this causes the light yield as a function of distance to be a double exponential with a long and short components. The attenuation length, measured in the region. between 0.3 m to 10 m away from photodetector. should be greater than 1.0 m.

The attenuation length of clear fibre will be measured by splicing a WLS fibre to it and inserting it to a scintillator tile. By cutting pieces of clear fibre off (and resplicing it to the WLS fibre) we will be able to plot light yield at the other end of clear fibre as a function of clear fibre length and fit it to an exponential function. We will use the clear fibre length in the range 0.5 m to 4.0 m and require that attenuation length is greater than 6 m.

Both WLS and clear fibre samples will be irradiated and attenuation length measured. At 0.5 Mrad (5 kGy) the reduction of light yield for a typical tile at shower maximum should be less than 3%.

6.4 QUARTZ FIBRE SPECIFICATIONS AND REQUIREMENTS (HF)

There are two different types of quartz fibres in the HF detector. In the region $|\eta| > 4$, radiation-hard fibres with fused silica core and a fluorine-doped silica cladding are used. In the lower pseudorapidity region, $|\eta| < 4$, where the radiation levels are less severe, fused silica core and a plastic cladding fibres are planned to be utilised. Both types of fibres are 345 micron in outer diameter with 300 micron diameter core.

6.4.1 Dimensions

Fibre lengths will nominally vary from 2.5 to 3.5 meters depending on the location of the towers with respect to photodetectors. The optical transmission of <1 dB/m is required to minimise loss of light. Both end of the fibres will be polished. The OH^- level in the fibre core material is typically 1000 ppm. To avoid breakage during construction, we require short term mechanical stability at minimum bend radius of 1.5 cm or less. The tensile strength is required to be above 12 kg. The required fibre core noncircularity is less than 5% and the desired core concentricity error is 3%.

Table 6. 1 summarises the necessary dimensional characteristics for fused silica core fibres. Type I is identified as quartz-quartz (QQ) fibres in order to indicate the core and cladding materials. The core is fused silica and the cladding material is fluorine-doped silica. The buffer provides radiation hard coating

and structural stability, *e.g.* polyimide. Type II fibre has the identical core but the cladding is made out of a radiation hard synthetic material (polymer) and less costly and is identified as QP to indicate the core (quartz) and the cladding (polymer) materials. The numerical apertures of the fibres that are used in prototypes are 0.22±0.02 for QQ and 0.35±0.02 for QP for visible light.

Table 6. 1

The parameters for Type I and Type II fused silica-core fibres.

Fibre Type	Core dia (mm)	Clad thickness (mm)	Buffer thickness (mm)	Quantity (km)
Type I (QQ)	0.300	0.015	0.030	980
Type II (QP)	0.300	0.020	0.030	7812

6.4.2 Radiation damage

The extreme radiation levels where the HF will have to operate put stringent requirements on the acceptable levels of degradation in fibres. The expected total dose at EM shower maximum at $|\eta| = 5$ reaches few hundred megarads in ten years and in the body of the HF, the total accumulated dose varies by four orders of magnitude.

The single most important reason for choosing quartz as active medium is its inherent radiation resistance. High-purity quartz (suprasil) has been reported to withstand radiation levels up to 30 Gigarads with the transparency of small samples in the wavelength range 300-425 nm changing by less than 2%[2]. The radiation hardness of quartz fibres depends on its core material, in addition, on the properties of the low refractive index cladding material. With fluorine-doped silica cladding, the amount of light changed by less than 10% up to levels of 20 Gigarads[2]. Radiation damage studies with intense photon sources resulted in about 50% transmission loss in the visible band after 1 Gigarad of dose for 1 meter length fibres[3]. The performance degradation of the HF due to the expected radiation damage is addressed in detail elsewhere in this document. The radiation hardness of QQ and QP fibres are being carried out with protons, electrons, photons and neutrons by the members of HF group at different facilities. Fig. 6. 16 shows the radiation damage of QQ fibres under photon radiation.

This EPS image does not contain a screen preview.
It will print correctly to a PostScript printer.
File Name : fvp.eps
Title : fvp.eps
Creator : HIGZ Version 1.23/07
CreationDate : 97/04/22 21.07

Fig. 6. 16: Radiation damage characteristics due to photons of fibres with quartz core and fluorine doped quartz clad with polyimide buffer (Type I) as a function of total dose and wavelength is shown above.

6.4.3 Quality control and assurance

There are a number of quartz fibre vendors that can manufacture what is needed for the HF. Several standard measurements and tests are performed by some manufacturers.

a) Dimensional tests (clad and core): on-line using a laser micrometer. In the drawing stage, 100 % of the fibre is tested and continuously monitored.

b) Dimensional tests (core, clad and buffer: spool ends are viewed under a microscope to verify dimension. This test is carried out in sampling mode.

c) Proof test: 100 kpsi, 100% of fibre is tested as being drawn,

d) Proof test: 100 kpsi, 100% of fibre is tested while spooled,

e) Optical attenuation (100% of fibre).

A set of non-standard tests are also required to be performed by the manufacturer in sampling mode;

a) Tensile test/Weibul Plot. 60 m of fibre for test is needed,

b) Thermal cycling in the ranges of -50 C to 80 C,

c) Attenuation length *vs* bending radius,

d) Attenuation length *vs* temperature, and

e) Numerical aperture (NA) test.

Before fibre insertion into the absorber matrix, we plan to carry out our set of quality tests for physical dimensions, tensile strength, bend radius, light attenuation length and radiation damage for each draw batch and archive fibre samples in order to be able to trace back problems should they appear in a later stage. The total length of a batch depends upon the size of the preform and these sizes typically vary between 40 cm to 120 cm. For each batch, we will archive 100 m of fibre, in addition to the tests we plan to carry out per batch.

6.5 SCINTILLATOR TRAY DESIGN HB/HE/HOB/HOE

6.5.1 Hadron barrel scintillator tray design6.5.1.1

Tray layout

The HB/HOB barrel hadron calorimeter has a large number of towers: 2448. The 18 layers in the inner HB calorimeter consist of 42624 tiles. Each tile is 5 degrees in φ and 0.087 in η. The wedges are 20 degrees in φ (4 tiles each). There are 18 φ 20– segments and 36 wedges (2 wedges for each φ section, one for positive and one negative η). To simplify production and assembly into the copper absorber, the scintillator plastic for scintillator trays are packaged into a mechanical units called a scintillator trays. These scintillator trays contain the scintillator, readout fibres and optical connector at the end of the unit which the light can be accessed.

The HB scintillator trays are divided into two types of trays. One type is a side scintillator trays (Left and Right Side Tray) and the other type is a middle scintillator tray (Middle Tray) (see absorber).

A top view of the scintillator trays for layer 8 is shown in Fig. 6. 5 and the cross section of the scintillator tray is shown in Fig. 6. 17. The unit begins with a 0.95 mm thick, black polystyrene, Bottom Cover Plate. Then comes a sheet of black, opaque, .05 mm Tedlar which will wrap around the scintillator to provide an opaque layer of light tightening. Then the 4 mm SCSN81 scintillator plastic is covered on both sides with 0.15 mm thick, white, reflective Tyvek paper. The surface of the scintillator tiles are grooved to hold the WLS fibres. The black Tedlar sheet is wrapped completely around the scintillator and the top Tyvek. One side of the Tedlar sheet is taped onto the upper Tyvek sheet, and the other is taped to the Tedlar thus completing the wrap. Above the scintillator plastic is a 1.9 mm thick, black polystyrene, top cover plate (Fibre Routing Plate). Both the top and bottom plastic plates have the same transverse size as the scintillator. The fibres rise out of the scintillator through a 3.2 mm x 25.4 mm slot in the Fibre Routing Plate into 1.6 mm deep grooves on the top side of the same Fibre Routing Plate. The fibres are mass terminated at the edge of the tray into an optical connector. A mass terminated optical cable transports the light from the tray to the photomultiplier tube readout. At the photomultiplier tube readout, an equivalent of a cable "patch panel" assembles fibres from different longitudinal tiles of a tower onto the HPD designated for that tower. Source calibration tubes, 1.27 mm~O.D., are placed on the top of the Fibre Routing Plate. There is a calibration tube every 5^o, so that a calibration tube cross every tile. The megatile unit is held and compressed together by a set of 4.77 diameter screws and rivets (screw-nut). The top is a flathead 4-40 brass screw. The bottom currently is a commercial rivet (screw-nut). The rivets may need to be redesigned so that they need not be taped in, and snap in more easily by putting in a slight bevel. Each tile has two screws and rivets compressing the plastic sheets and pushing the Tyvek against the scintillator.

This EPS image does not contain a screen preview.
It will print correctly to a PostScript printer.
File Name : ch6cros2.eps
Title : C:\CH6CROS1.EPS
Creator : AutoCAD PSOUT
CreationDate : 1997-06-04
Pages : 1

Fig. 6. 17: The cross section of the scintillator tray.

Table 6.2 shows the thickness materials in the scintillator tray in the order which they appear in the cross section. The 0.15 mm black polyester tape hold the fibres in place. It also wraps around the sides of the pan and adheres to the bottom of the pan. Hence in the table it is shown twice. The top and bottom plastic cover plates will have maximum thickness of 2 mm and 1 mm respectively. The scintillator manufacturer can supply scintillator with thickness variation of 10%. The manufacturer can supply black plastic cover planes with a thickness variation of as low as 5%. Therefore, we specify that the top plate should be

1.9±0.1 mm and that the bottom plate should be 0.95 ±0.05 mm. The scintillator provides the largest thickness variation of the package. The nominal thickness of the total tray for HB is 7.6 mm. Table 6.2 below shows a maximum thickness of 8.31 mm to fit in a 9 mm gap. Note that 0.25 mm aluminium venetian blind type springs that hold the tray against the outer copper plate need to be added.

Table 6. 2

Thickness of materials in the scintillator tray.

	Thickness (mm)	Max Variation (mm)
Polyester tape	0.15	0.03
Top plastic	1.9	0.10
Tedlar	0.10	0.00
Tyvek	0.15	0.05
Scintillator	4.00	0.40
Tyvek	0.15	0.05
Tedlar	0.05	0.00
Bottom plastic	0.95	0.05
Polyester tape	0.15	0.03
TOTAL	7.6	0.71
Venetian blind alum	0.25	1.25
Available gap	9.00	

To reduce the number of separated scintillator tiles and to give the scintillator trays more mechanical rigidity, individual scintillator tiles for a scintillator tray are glued together. The scintillator for a scintillator tray is composed of two or three subassemblies, called megatiles. Each megatile consists of many η tile divisions bonded together by thin channels of opaque white-reflective epoxy that also provides optical isolation, as shown in Fig. 6.18. The cross section of the ball groove holding the WLS fibre is shown in Fig. 6.19.

This EPS image does not contain a screen preview.
It will print correctly to a PostScript printer.
File Name : ch6sepg1.eps
Title : C:\CH6SEPG1.EPS
Creator : AutoCAD PSOUT
CreationDate : 1997-05-27
Pages : 1

Fig. 6. 18: Separation groove between two neighbouring tiles.

This EPS image does not contain a screen preview.
It will print correctly to a PostScript printer.
File Name : ch6ball.eps
Title : C:\BALLCH6.EPS
Creator : AutoCAD PSOUT
CreationDate : 1997-05-06
Pages : 1

Fig. 6. 19: Cross section of the ball groove to hold WLS fibre.

Table 6.3 below gives the radial position, length and width of scintillator trays. The tolerances on the sizes of both, copper slots and scintillator trays were included, when defining the size of each scintillator tray. The wedges are 20 in φ. The φ boundary of the wedge is 1 mm away from the nominal 0 and 20 edge. The φ boundary of the wedge is covered by a 0.5 mm thick metal sheet. The φ edges of the trays are 1 mm away from inner edges of the copper slots. Hence, the outer edge of side scintillator trays are 2.5 mm away from the nominal 0 or 20 boundary. The inner edge of the side trays and the edges of the middle trays are 1 mm away from the nominal 5 and 15 boundary. The centre of the middle tray is in the nomial φ location. The θ = 90 degree line is 1 mm away from the edge of the wedge. The scintillator tray sits 1 mm inside the wedge at 90 line and 3 mm inside the wedge at the 53 line. Hence, each scintillator tray has at least 1 mm of nominal gap on all its edges.

Table 6. 3

The number of tiles in a given layer for both the Side and Middle Trays. The radial location of trays, and length and width of each tray are also shown. All dimensions are calculated under the assumption of the inner HCAL radius of 1806.5 mm.

Layer	Location in φ	# of η towers	Radius (mm)	Length in η direction (mm)	Width in φ direction (mm)
0	Side / Middle	17 / 17	1802 / 1839	3698 / 3726	109 / 319
1	Side / Middle	17 / 17	1873 / 1902	3752 / 3774	162 / 330
2	Side / Middle	17 / 17	1931 / 1960	3795 / 3817	167 / 340
3	Side / Middle	17 / 17	1989 / 2018	3839 / 3861	172 / 350
4	Side / Middle	16 / 16	2047 / 2076	3883 / 3905	177 / 360
5	Side / Middle	16 / 16	2105 / 2134	3926 / 3948	182 / 370
6	Side / Middle	16 / 16	2163 / 2192	3970 / 3992	187 / 380
7	Side / Middle	16 / 16	2221 / 2250	4014 / 4036	192 / 390
8	Side / Middle	16 / 16	2279 / 2308	4058 / 4079	198 / 401

9	Side / Middle	16 / 16	2337 / 2366	4101 / 4123	203 / 411
10	Side / Middle	15 / 15	2395 / 2424	4145 / 4167	208 / 421
11	Side / Middle	15 / 15	2453 / 2482	4189 / 4211	213 / 431
12	Side / Middle	15 / 15	2511 / 2540	4232 / 4254	218 / 441
13	Side / Middle	15 / 15	2569 / 2598	4276 / 4298	223 / 451
14	Side / Middle	15 / 15	2627 / 2656	4320 / 4342	229 / 462
15	Side / Middle	15 / 15	2685 / 2714	4364 / 4345	234 / 472
16	Side / Middle	15 / 14	2748 / 2782	4411 / 4345	239 / 484
17	Side / Middle	14 / 14	2859 / 2859	4345 / 4345	150 / 500

The light (collected by the Kuraray Y11(250 ppm) WLS fibre) is transported to the HPD using a series of clear fibres. Within the scintillator tray, the fibres are Kurarays 0.94 mm multiclad, non-S type fibres. The tip of the WLS fibre inside of tiles has been polished, aluminised, and protected with a thin polymer coating. The other end is spliced to a clear non-S-type multiclad Kuraray fibre. This splice is a heat fusion splice and is covered by a 2.54 cm long, clear plastic ferrule (FEP shrink tubing, 0.05" OD). The light transmission across this splice is 92% with a 2% rms. These optical fibres are routed from the tiles to optical connectors at the edge of the megatile via grooves in the black Fibre Routing plastic Plates. This groove is 1.6 mm deep. These grooves and fibres are covered with black polyester tape to secure and to protect the fibres. The grooving of the black plastic sheet is done with the Thermwood x-y milling table. The WLS-to-clear splice is kept in a straight section of the Fibre Routing Plate.

At the edge of the scintillator tray, the clear fibres from the tiles are terminated optical connectors. Fig. 6.20 shows the design of the optical connector. The fibres and optical connectors for the scintillator tray are constructed as one unit and tested before installation of the fibres into the tiles. These fibre-connector units are called pigtails. A pigtail consists of the WLS fibre which goes in the tile spliced to a clear fibre. A pigtail contains all the fibres for 5 degrees of a scintillator tray. The clear fibres of a pigtail are sandwiched by kapton tape make the pigtail easier to handle. The connectors are held on the outer edge of the black plastic cover plates. Fig. 6.21 shows a view of the layout of cables in the HB/HE gap.

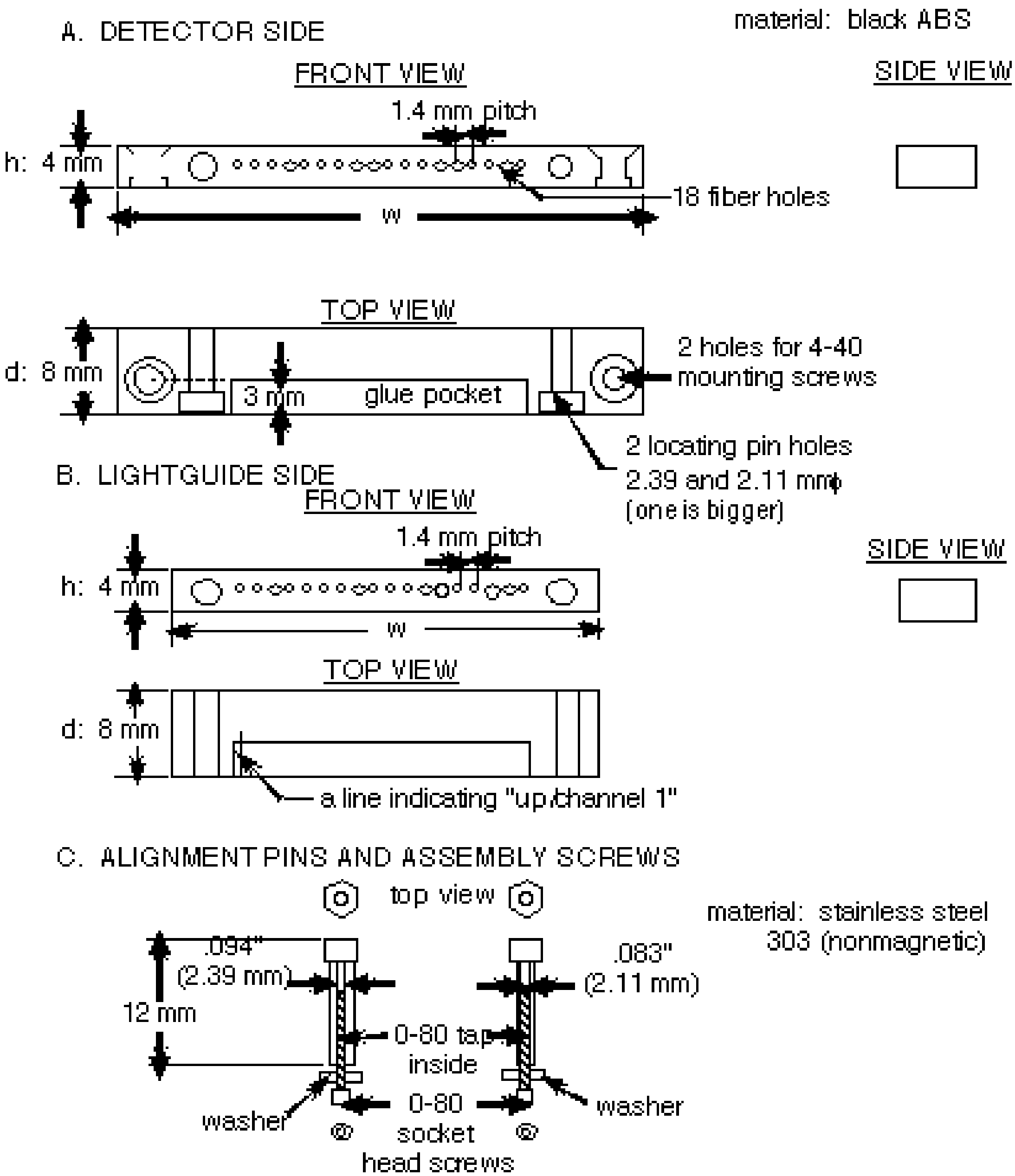

Fig. 6.8.1.1 Schematic drawing of the designed 18-channel connectors

Fig. 6. 20: Schematic drawing of the 18-channel optical connector.

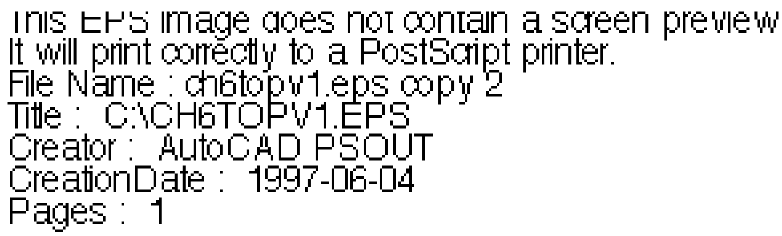

Fig. 6. 21: Top view of the megatile and connector layout.

Optical cables in the form of a flat, light-tight bundle of fibres (0.94 mm) carry the light from the tray's connectors to a router box near the HPDs. The optical cables consist of 18 optical fibres sandwiched by a Tedlar cover. The number of holes used for tile readout varies from 14 to 17. The eighteenth spare hole is used for optical light injection. The Tedlar cover seals the optical cables from light. The cables have the same optical connectors at both ends. Within the router (fibre patch panel) box, optical signals are sorted from layers into calorimeter towers. This sorting is performed using 0.94 mm fibres which connect fibres in layer connectors to tower based photomultiplier tube light mixers. The default fibres for the cables and descrambler are Kuraray, multiclad S type fibres. The use of the optical connectors allows for the segmentation of the optical path into three parts, the scintillator trays, cable, and router box. The design provides maximum protection for the fibres at all stages of assembly and installation. In addition different parts of the optical system can be assembled at various institutions and assembled at a central location.

6.5.1.2 Meeting design requirements

To achieve good intra-tile transverse uniformity, the tile's surface reflectivity is kept uniform and a uniform response fibre groove pattern is used. This avoids the use of a complex optical mask on the surface of the tile. To keep the tile's surface reflectivity uniform, its reflective wrapping material must be held evenly against its surface. Two rivets per tile performs that function. The transverse uniformity of the tiles is "tuned" by adjusting the depth of the fibre groove inside the tile. The optimal groove depth for 4 mm thick tiles is 1.5 mm. At this depth, the uniformity is fairly insensitive to the placement of the fibre groove relative to a tile's edge. The uniformity of individual tiles is expected to be better than 4%.

The light yield of tiles within a projective tower must also be kept reasonably uniform at the photomultiplier tube readout. The longitudinal front-to-back light yield variation must be kept below 20% for the variation not to effect the resolution of the tower. Several factors contribute to longitudinal light yield. Since towers are projective, the area of tiles in a tower increases from the front to the back. Larger tiles at the back have smaller light yields. We have built tiles which span the size of the tiles used in the CMS calorimeter and measured the light yield from these tiles. We have determined that the light is a function of L/A, where L is the length of WLS fibre in the tile and A is the tile area. Using this function we can predict the light from an individual tile. The clear fibres in the tray and the cables attenuate the light with attenuation length of approximately 7.5 m. The back tiles suffer less attenuation from clear fibre going from the connector at the edge of scintillator try to the HPD since length of the optical transmission cable decrease from the front to the back of the calorimeter. This effect partially compensates for the lower light yield (from L/A) of the larger back tiles.

Fig. 6. 22 shows an expected light yield (in number of photoelectrons per minimum ionising particle) of H2 readout section of Hadron Barrel calorimeter as a function of η tower number. The plot indicates that we the light yield exceeds the requirement of 20 pe/mip.

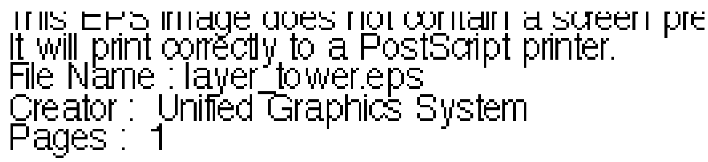

Fig. 6. 22: Expected light yield (in number of photoelectrons per minimum ionising particle) of H2 readout section of the Hadron Barrel calorimeter as a function of η tower number.

6.5.1.3 Magnetic effects

As stated earlier, variation in the radial position of the scintillator in the groove causes variation in the response of the tile. Hence, the scintillator tray should be pushed up against the upper edge of the copper slot. This will be done by a 5 cm piece of 0.3 mm brass venetian blind type section (acting as a spring) which is the length of the slot. The 5 cm cross section will be bent to form a venetian blind spring. The venetian blind spring will be slid in under the scintillator tray and push the tray up against the copper. The total force of the brass piece applies to the tray should be 2-3 times the weight of the pan. A middle pan weights about 20 kg. Hence, about 50 kg should be applied to the pans. As a middle pan will have two strips pushing on the pan each strip should apply about 25 kg.

6.5.1.4 HB quartz-fibre laser (or LED) calibration layout

This scheme requires some additional R&D and at the present time is only in the conceptual design stage. One extra fibre in a connector is used for laser calibration. UV laser light is sent through this plastic fibre to the connector at scintillator tray. One question is whether this plastic section will change its attenuation to UV light with radiation. At the tile, the HB design (which is different from HE) is for a 1 mm plastic clad quartz fibre to be put into the connector after the connector has been machined with the pigtails. The fibre will routed in a straight line to the opposite end of the tray in a groove in the top cover. It will turn around and go in a straight line close to the middle of the tiles (parallel to the source tube). There will be two 1 cm holes drilled in the black cover plates, Tedlar and Tyvek so the quartz fibre can enter the tile. The quartz fibre goes into one hole, passes through a 2.5 cm long groove on the top of the scintillator, exits out of the second hole and continues to the next tile. In the region of the hole, the cladding will be stripped from the quartz fibre, and the fibre etched with acid or scratched to form a diffuse surface. The length which is etched determines the amount of light injected to the tile. The UV light will exit the quartz fibre into the tile, and convert to blue light. If a blue LED is chosen instead of a UV laser an additional 1 cm white circle of paint must be painted on the bottom of the tile to reflect more blue light towards the green fibres. The quartz fibre's end is cut at 45º and painted black to avoid reflection. This geometry brings the UV light to all the tiles approximately at the same time as a real particle from the interaction point.6.5.1.5

HB Source tube layout

The source tubes are placed in the top of the 2 mm thick black plastic cover plate, in a groove nominally 1.52 mm deep. The source tube generally go at constant φ over the centre of each tile, but must make an S-bend (as gently as possible) to exit the edge of the pan near the optical connector and aimed purely in the z-direction (Fig. 6. 5 and **Fig. 6. 23).** The source tube groove drops gently to the bottom of the top plastic layer at the pan edge, and flares slightly in phi to provide tolerance where the source tube is inserted into a special cone coupler for transition from a 1/8" OD low-friction acetyl plastic tube. The metal tube is locked in place with a 2-56 nylon-tipped set screw; the nylon tube is locked by a paraxial 3-48 screw whose threads intrude into the 1/8" socket.

This EPS image does not contain a screen preview.
It will print correctly to a PostScript printer.
File Name : ch6sd.eps
Title : C:\CH6SD.EPS
Creator : AutoCAD PSOUT
CreationDate : 1997-05-06
Pages : 1

Fig. 6. 23: Side view of the radioactive wire source tube placement.

Most megatile layers in the assembled calorimeter will be accessible only when the endcap is retracted. At that time all layers of each tower will be measured, in order to check the integrity and uniformity of each tower and transfer test beam module calibrations to the main calorimeter. The occasional access tubes will be brought up in the channel which brings up the fibres to an access panel near the coil.

Layers 0 and layer 9 will be permanently coupled, via the acetyl tubing, to source drivers installed in the 8 cm gap at the back of a few wedges. One source driver, with a 35-foot (10.6 m) source wire can access up to 6 wedges, for a total of 6 installed source drivers in HB. The plastic tubes will make a gentle bend in the r-z plane rising no more than 5 cm from the end surface of the copper, and running in the same protected channel as the optical cables. The tubes will then, at the back of each wedge, bend (with radius no tighter than 12 cm) into the φ direction towards the source driver, which has a channel indexer to select one of 72 different tubes. There are 144 permanent tubes in each half barrel.

The compact source driver design using non-magnetic motors (most probably small commercially available air powered motors and piezoelectric air valves) is under development, and appears feasible at this time. The motors are claimed to have a long operating life and not to require a lubricated air stream. The extra-low-friction tubing and the NICOTEF-coated source wire have already been developed for the CDF endplug calorimeter upgrade. NICOTEF is a proprietary coating containing nickel-sulphide, ptfe, and phosphorus, with Rockwell hardness 40, chemically plated onto the source wire by the Nimet Corporation.

6.5.2 HE scintillator tray design

The HE calorimeter has a slightly different design of the optical system, as both the cost and machining capabilities are different in US and Russia. An HE scintillator tray covers 10– in φ. Each 10– wedge is subdivided into 20 towers. Each scintillator tray contains tiles as separate units. This simplifies the production of megatiles. The rigidity of the structure is provided by spacers placed at the edge of the megatile. This is possible due to staggered structure of the absorber plates. The tiles and covers are attached by pins through the scintillators. The cover plates are made of duraluminum because it is cheaper than plastic plates and provides better rigidity. Both the front and back cover plates have the same thickness, 1 mm. Between one of the plates and the scintillator there is 1.5 mm wide gap, fixed by spacers, for the optical fibres paths.

Fig. 6. 24 and **Fig. 6. 25 show the design of the tray. The tray layers are as follows: The first layer is 1 mm thick duraluminum cover plate, next a sheet of Tyvek reflective paper with holes cut in them for connecting screws. Brass spacers, 7 mm thick, are screwed along the edge of the duraluminum cover plate. The tiles are placed on the Tyvek paper and covered by another sheet of Tyvek with holes for screws, WLS fibres and quartz fibre reflectors. WLS fibres are inserted into scintillator grooves through the holes in the Tyvek and kept in the place by small spacers with holes. The edges of the scintillator plates are covered with reflective paint (BC 620). Insertion of Tyvek strips between the scintillators is an option we are considering. The optical connectors with glued fibres are fasten to the lower cover plate. The proposed QF light injection system is different from the HB system. Here the light injection fibre is fanned out to many small quartz fibres, separate one for each tile. In the gap between the scintillators (covered by Tyvek) and the upper cover plate is where the quartz fibres and stainless steel tubes are placed for the laser and the wire source calibrations respectively. To equalise the timing of the laser calibrations all fibres inside the tray have equal length. Therefore, reels with quartz fibres (delay lines) are also placed in this gap. The quartz fibres are glued to reflectors (to feed the UV light into the scintillators) which in turn are glued to the Tyvek. The upper cover plate has rivet nuts (1.5 mm thick) opposite the holes in the lower cover plate. The screws from the lower cover plate go between the scintillators and are screwed into the nuts. The surfaces of the cover plates are covered by resistive layer (galvanisation) to prevent chemical reaction with the brass plates. The trays are positioned on the absorber plates by screws on the outer surface of the HE.**

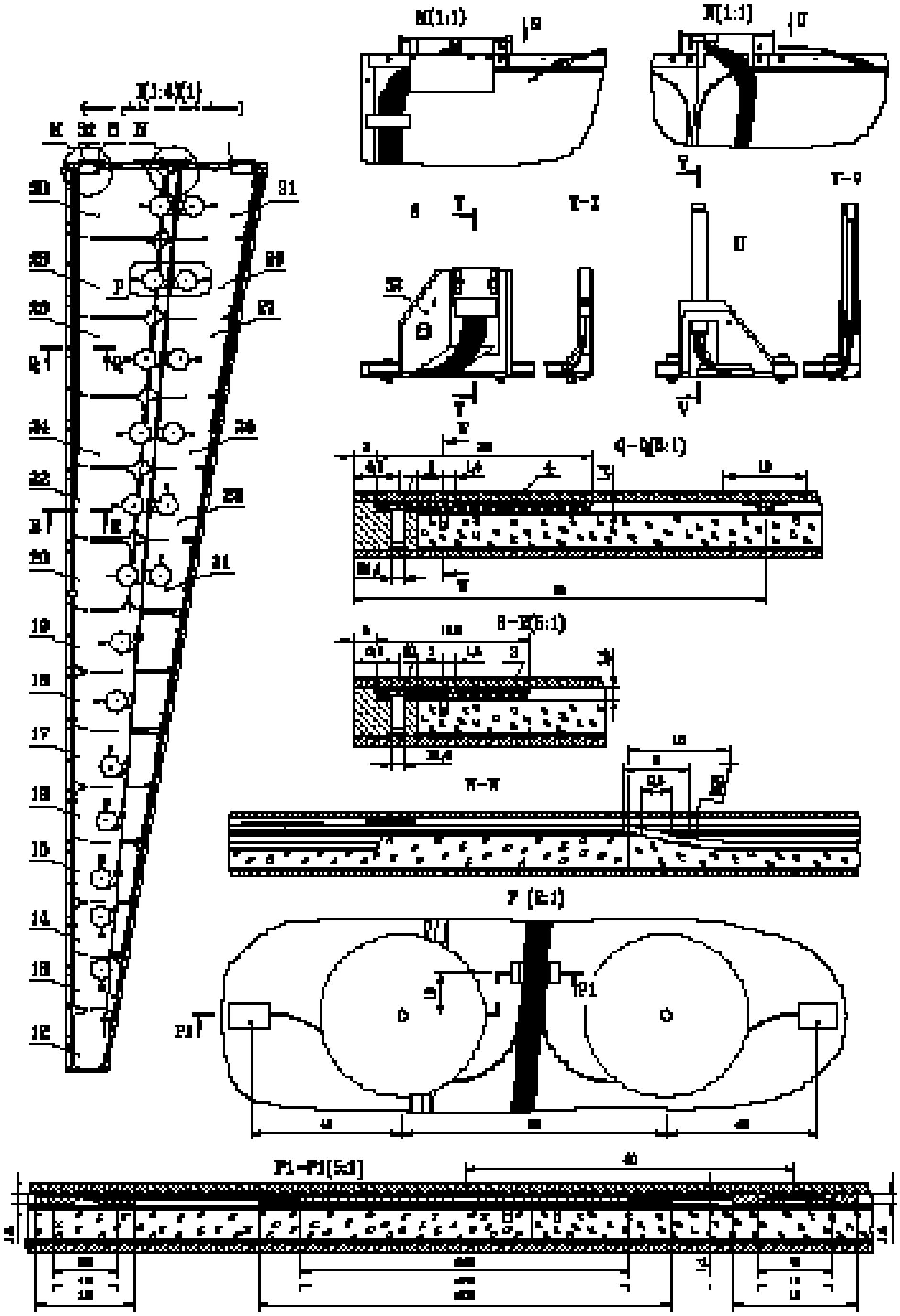

Fig. 6. 24: Design of the scintillator tray for HE; cross sections and front view without upper plate.

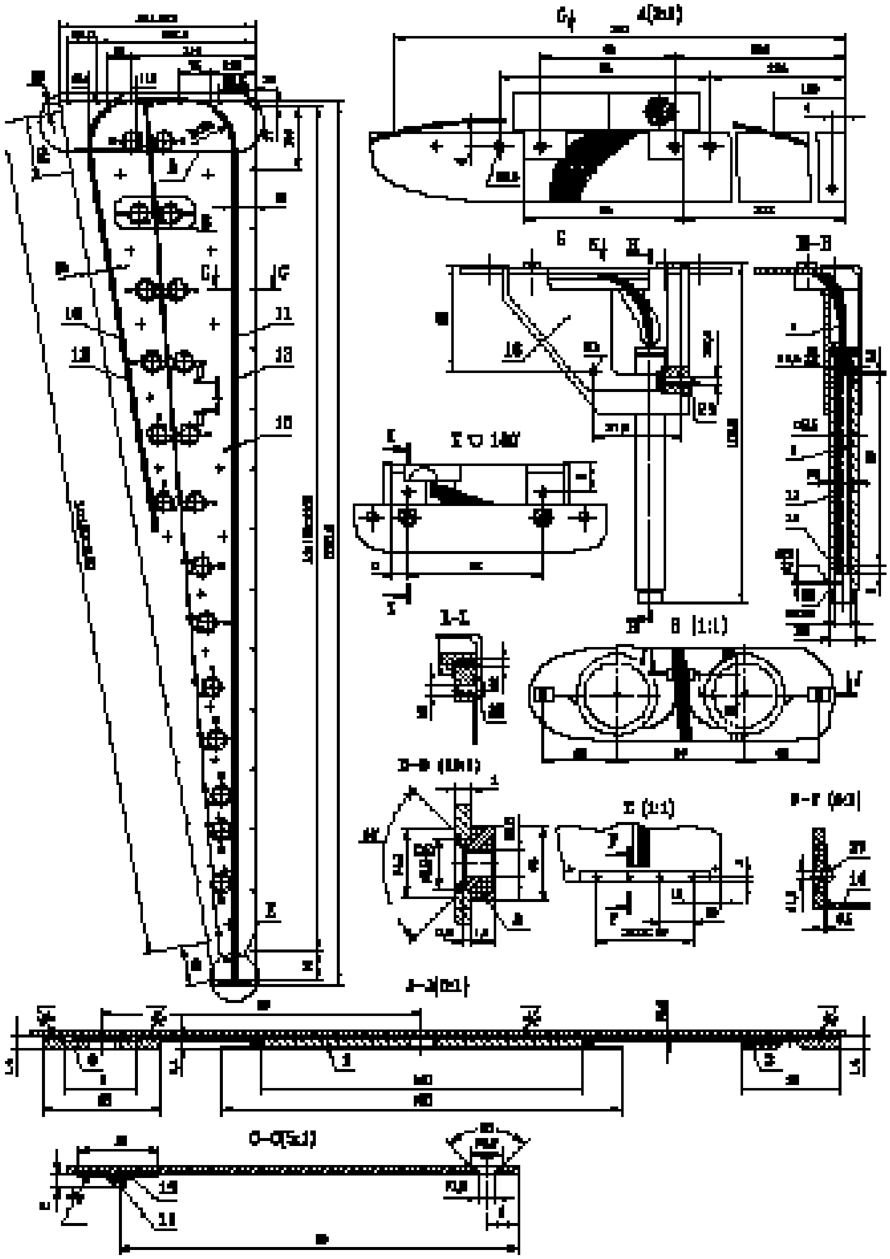

Fig. 6. 25: Upper cover plate with quartz fibres and radioactive source tubes.

The inner barrel calorimeter (HB) is only 5.12 interaction length (λ) deep and hence will be unable to contain the higher energy showers completely. The outer calorimeter is designed specifically to sample the tails of hadronic showers, in particular for those showers which developed deep inside the calorimeter. This is necessary to improve upon the missing E_T resolution and also to achieve the design resolution of 100%/E5%. Outer calorimeter can also be used in identifying and triggering on muons. In order to achieve these twin objectives, HO should have the capability to identify single muons. A light level of about 7 photo electrons (pe) due to 'single' muon may be necessary to identify muons at 3 σ level with the HPDs. Taking into account the long term degradation of the scintillator light yield due to the hostile radiation environment in which the detector will be located, it may be necessary to start with about 15 pe from 'single' muon using the two HO layers combined. Due to the large size of the scintillator tiles for the same $\eta-\phi$ segmentation as in the inner calorimeter and the limitation in the number of fibres that can be embedded in the tiles, we opted to use 1 cm thick BC408 scintillators for the two layers of outer calorimeters as a base line design. An additional 5 mm of space is needed for two plastic sheets on either side of the scintillators to anchor the individual tiles as well as to route the fibres and also to accommodate the stainless steel covers for the scintillators. Thus including the plastic and stainless steel covers, the thickness of the individual layers will be 15 mm.

Geometrical specifications: Constraints along ϕ

Each of the five muon rings have 12-fold symmetry along ϕ with each ϕ sector covering 30^0 in ϕ and 2.53 meters along z. One such 30 ϕ sector of the muon ring maps onto 6 calorimeter towers along ϕ. The ideal size of the tiles for the two outer calorimeter layers in the ϕ direction can vary between 0.40 m to 0.448 m depending on the location of the tower within the sector. These sizes are listed in the first row of Table 6. 4. However for a more realistic estimate of the tile sizes, we need to take into account the dead zones occupied by the stainless steel support beams. The two end tiles of the front layer are shortened and one end tile of the back layer has to be split into two trays due to the location of a support beam. The resultant sizes of the tiles along ϕ are given in row 2 of Table 6. 4.

There are additional constraints on the tile sizes along ϕ due to the frame structure needed to hold the scintillators in place. As will be described later, several scintillator tiles will be packed together into a single mechanical unit called a scintillator tray. A single tray will be one ϕ slice wide (5 in ϕ) and will cover the entire span of a muon ring along z i.e. 2.53 m. These trays will be resting on sheet metal C-channels welded to the inner and outer faces of the return yoke YB1. These C-channels will be of .5 mm wall thickness. An additional space of about 4 mm on either sides of the C-channels may be required for smooth insertion of the trays. To make these additional space for support structure, the tile sizes along ϕ direction will be constrained further. The final sizes of the tiles along ϕ are given in row 3 of Table 6. 4.

Table 6. 4

Tile lengths along ϕ.

	Layer 1	Layer 2
Tile length (m) (ideal case)	0.406 0.400 0.400 0.406 0.419	0.434 0.428 0.428 0.434 0.448

Tile length (m) (constrained by the return yoke support structure)	0.367 0.419 0.406 0.400 0.400 0.377	0.434 0.428 0.428 0.434 0.448 0.123
Tile length (m) (constrained by the return yoke and tray support structure)	0.354 0.408 0.396 0.391 0.391 0.367	0.257 0.426 0.419 0.419 0.426 0.559
Dead space along φ (%) # of tiles along φ	5.8 6	4.4 7

Constraints along z(η)

In the z direction we are constrained by the ring boundaries. The HO scintillators have to be terminated at these boundaries as the space between successive rings will be used as service path and will not be available for sampling. This will have the following constraints on the tile sizes along z.

- The tile size along z can vary from 34 mm to 661 mm.

- In layer 1, η tower # 4 will split between rings 0 & 1 (also 0 & -1) and η tower # 10 will split between rings 1 & 2 (also -1 & -2).

- In layer 2, η tower # 9 will split between rings 1 & 2 (also -1 & -2).

- η tower number 14 in layer 1 will be truncated at the outer edge of Ring 2 (and -2).

- η tower numbers 3, 4 and 13 in layer 2 will also be truncated at the edge of rings 0, 1 (-1) and 2 (-2) respectively. So these tiles will also be shorter along η.

Table 6. 5 summarises various tile sizes along z.

Table 6. 5

Tile sizes along z.

Ring	Layer 1	Layer 2

	Tower	η_{max}	Size(m)	Tower	η_{max}	Size(m)
0	1 2 3 4	0.087 0.175 0.262 0.274	0.400 0.402 0.408 0.058	1 2 3	0.087 0.175 0.262	0.427 0.431 0.410
1 & -1	4 5 6 7 8 9 10	0.349 0.436 0.524 0.611 0.698 0.785 0.791	0.160 0.430 0.446 0.465 0.487 0.514 0.034	4 5 6 7 8 9	0.349 0.436 0.524 0.611 0.698 0.747	0.274 0.460 0.477 0.497 0.522 0.306
2 & -2	10 11 12 13 14	0.873 0.960 1.047 1.134 1.171	0.390 0.578 0.617 0.661 0.290	9 10 11 12 13	0.785 0.873 0.960 1.047 1.116	0.124 0.582 0.619 0.660 0.551

Constraints along r

The radial position of the front faces of the two HO layers are 4.57 m and 4.89 m respectively. They are located on either side of the return yoke YB1. The radial thickness of each layer of outer calorimeter is only 15 mm. A "no go zone" of 5 mm separates the two HO layers from the either surface of the YB1. Similarly there is a 10 mm "no go zone" between inner face of layer 1 and outer face of MB1. A "no go zone" of 10 mm is also kept between the outer face of layer 2 and the inner face of MB2. The radial thickness of the HO layers should not exceed 15 mm allocated for them. It is however allowed to utilise the "no go" zone between the HO layers and the YB1 in order to fix the mechanical holding structure for the two HO layers.

Merging of Tiles

Fig. 6. 26 show one 30^0 ϕ sector for each of the two layers for the three rings with individual scintillator tile boundaries mapped onto it. It is clear that some of the tiles are very narrow as they were truncated due to location of supporting beams or due to inter-ring gaps.

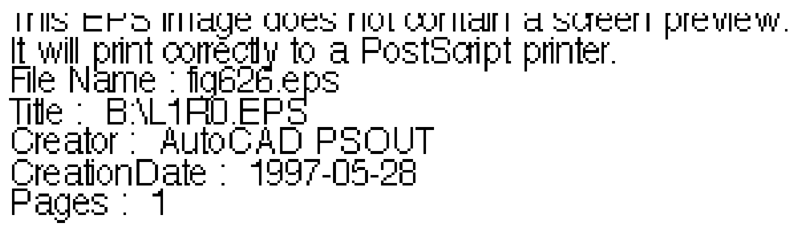

Fig. 6. 26: Example of a 32º φ sector for HOB megatile.

We have decided to combine these narrow tiles with their nearest neighbour as single tiles as follows:

- All the 12 tiles of 5.8 cm width on either side of ring-0 for layer 1 will be combined with their neighbours in the z direction.

- 6 tiles of 3.4 cm width on the outer edge of ring 1 and -1 will similarly be combined with their neighbours in the z-direction.

- All the 6 tiles of 12.4 cm width on the inner edge of ring 2 and -2 will be combined with their neighbours in the z-direction.

- All the 12.3 cm wide tiles along the ϕ edge of each 30 ϕ sectors in layer 2 will be combined with their nearest neighbour along ϕ in all five rings.

With these minor modifications and adjustments one requires 14 (2) different sizes of tiles for layer 1 and 13 (2) for layer 2 for each ϕ slice. The total number of tiles required for the two layers is 3888. Table 6. 6 summarises the number of different tiles required.

Table 6. 6

Required tiles for HO.

	Layer 1	Layer 2
# of tiles per sector	168	156
Total # of tiles	2016	1872
Max. tile size (mm × mm)	419 × 661	571 × 706
Min. tile size (mm × mm)	367 × 160	267 × 274

Based upon these estimates the total requirements of scintillators for the outer calorimeter are summarised in Table 6. 7.

Table 6. 7

Total requirement of scintillators for the outer calorimeter (HO).

	Layer 1	Layer 2

Position along R (m)	4.570	4.890
Width of a 30^0 ϕ sector (m)	2.449	2.621
Length of a ϕ sector along Z (m)	2.536	2.536
Area of a ϕ sector (sq m)	6.211	6.646
Total area of 5 x12 sectors (sq m)	372.65	398.74

Scintillator tray specifications

In order to simplify the installation of the two HO layers, several scintillator tiles will be packaged into a single mechanical unit called the scintillator tray. A scintillator tray will cover the entire length of a muon ring along z. In the ϕ direction, it will only be one tile wide. Each tray will contain 4,5 or 6 tiles depending upon its locations. These tiles will be wrapped completely first with TYVEK paper (for light reflection) and then with Tedlar sheets (to stop light leakage). This whole package will be sandwiched between a 1 mm thick plastic sheet on one side and a 2 mm plastic sheet on the other side. The 1 mm plastic is used to anchor the tiles in their respective positions using 6 BA countersunk screws passing through the tiles and bolts embedded inside the plastic. The 2 mm plastic on the other side will have channels grooved into it to route the fibres from individual tiles to an optical connector located at the edge of the tray to access the scintillator light. Finally, this whole assembly of scintillators, plastics and fibres will be placed in an tray of length 2.536 m and height 13.8 mm made of stainless steel plates of 0.3 mm thickness. This tray will be covered with a stainless steel plate of 0.3 mm thickness along the whole length of 2.536m. The bottom stainless steel tray and the top stainless steel plate of this assembly will be anchored to the plastic-sheet-covered scintillator detector by countersunk 6 BA brass screws and special form of nuts. These nuts will have a cylindrical shaft with 6 BA threads which ends in a thin circular plate. This thin circular portion will be projecting outside the stainless steel plate facing the muon chamber and the corresponding head of the holding screw will be outside the steel plate facing the magnet return yoke. we will need 360 scintillator trays for each of the two layers.6.5.3.1

Tray layout

Scintillator trays for the outer barrel calorimeter (HOB) will be one ϕ slice wide (5^0 in ϕ). However along z (η) direction , they will cover the entire span of a muon ring i.e. 2.53 m. Mechanical design for these trays and their support structure has already been discussed in detail in chapter 4. In brief, the trays would be resting on sheet metal C-channels of 0.5 mm wall thickness. An additional space of 4 mm on either side of the C-channels is required to ensure smooth insertion of the trays and also to account for the skin thickness of the trays. The actual separation between two successive scintillator tiles in the ϕ direction will therefore be about 8 mm. There will be six trays for a 30^0 ϕ sector , each ideally covering 5^0 in ϕ. Although all the trays will be of length 2.53 m along z, their width along ϕ will vary from one to other. There will be 9 different sizes of trays each containing either 4, 5 or 6 tiles along z. The actual inner dimensions and the number of trays required for each size are given in Table 6. 8. In total, there will be 720 trays corresponding to a total active area of 733 m^2 containing 3888 scintillator tiles of different sizes.

Table 6. 8

Required trays for HO.

Tray width (m)	Area of each tray in (m^2)	Number of trays	Total area (m^2)
Layer - 1			
0.359	0.90	60	54
0.411	1.03	60	62
0.397	1.00	60	60
0.392	0.99	120	119
0.367	0.93	60	56
Layer - 2			
0.259	0.65	60	39
0.426	1.08	120	129
0.420	1.06	120	128
0.563	1.41	60	85
Total		720	733

A top view of a typical scintillator tray is shown in Fig. 6. 27 and its cross sectional view is shown in Fig. 6.28. The trays are similar in design to those used for the inner barrel calorimeter and will be packed and assembled using similar techniques. However, unlike the inner barrel, the HOB scintillators are 10 mm thick, thereby increasing the overall thickness of the tray.Table 6. 9 shows the thickness of various materials in the order in which they appear in the tray.

This EPS image does not contain a screen preview.
It will print correctly to a PostScript printer.
File Name : fig621.eps
Title : sigma_tile3.fig
Creator : fig2dev Version 3.1 Patchlevel 1
CreationDate : Wed Apr 30 08:56:46 1997
Pages : 0

Fig. 6. 27: Top view of a typical scintillator tray for HOB.

This EPS image does not contain a s
It will print correctly to a PostScript prin
File Name : fig622.eps
Title : tile_section.fig
Creator : fig2dev Version 3.1 Patchle
CreationDate : Wed Mar 12 18:22:05
Pages : 0

Fig. 6. 28: Cross sectional view of a scintillator tray for HOB.

Table 6. 9

Thickness of materials in HO tray.

Material	Thickness in mm	Tolerance in mm
Polyester tape	0.15	.03
Top plastic	1.90	.10
Tedlar	.10	.00
Tyvek	.15	.05
Scintillator	10.00	1.00
Tyvek	.15	.05
Tedlar	.05	.00
Bottom plastic	.95	.05
polyester tape	.15	.03
Total	13.6	1.31

All the scintillator tiles in a tray will be made out of a single piece of scintillator by cutting a straight groove of 0.9 mm thickness and 9.5 mm depth between successive tiles. These grooves will be filled with an opaque, white epoxy to provide rigidity and optical isolation. At the bottom of these straight grooves is a bridge of 0.5 mm thick scintillator, which forms an enclosed area into which the epoxy will flow. In order to reduce the cross talk of light between the tiles , these bridges will be marked with a black marker on the outside. This technique is similar to that used for the inner barrel trays.

Groove design on a tile

Fig. 6. 29 shows the top view of a typical HOB scintillator tile. The light from the tile is read out using WLS optical fibres which are held inside the tile using circular grooves. The grooves are similar in design to that in an HB tile i.e. each with a circular part inside the scintillator of diameter of 1.35 mm and a neck of 0.86 mm width. The base line design is to use 0.94 mm double clad, non-S type, Y11 fibre of Kuraray. The HOB tiles are larger in size than the tiles in the inner barrel part of the calorimeter. As a result, they will give much less light if we use a single sigma groove running around the perimeter of the tile. The large length of the WLS fibre required for such a readout scheme will further reduce the light output as the attenuation length in WLS fibre is around 2m. In order to collect sufficient light from these large sized tiles, we plan to put 4 separate WLS fibres in a single tile in separate grooves. Each tile will be divided into 4 quarters. Each quarter will have a sigma groove as shown in Fig. 6. 29. Fig. 6. 30 shows a clasp of the sigma groove at the fibre insertion point. In a tile, the straight sides of the rectangular grooves are located at a distance of 2.5 mm from the edge as well as from the centre of the tile. The corners of the grooves are rounded and have 31.8 mm bend radius. This will prevent any damage to the fibre at the bend and also ease the process of fibre insertion in the narrow grooves. For smaller truncated tiles, instead of 4 fibres, we need only 2 fibres for equivalent light yield.

Fig. 6.31 shows the cross sectional view of an HOB tile for a better perspective of the groove design. It looks like a circular hole attached to a narrow neck. With such a design it will be possible to keep the fibre inside the groove provided the neck of the groove is narrower than the fibre diameter. Since the fibre diameter is 0.94 mm, the neck diameter is kept at 0.86 mm. In order to insert the fibre in the groove, one end will have a rounded shape of size 1.8 mm which will narrow down to 0.86 mm (neck size) within a distance of 9 mm.

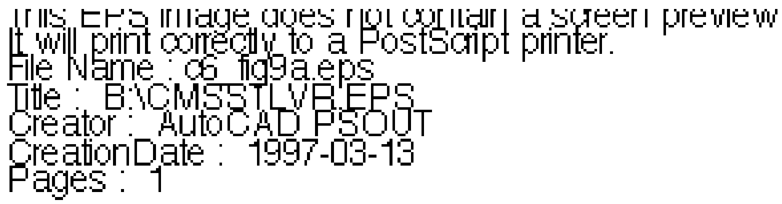

Fig. 6. 29: Design of the HOB tile. Each tile will be divided into four quarters.

This EPS image does not contain a screen preview.
It will print correctly to a PostScript printer.
File Name : c6_fig9b.eps
Title : B:\CMSSTR1.EPS
Creator : AutoCAD PSOUT
CreationDate : 1997-03-13
Pages : 1

Fig. 6. 30: Clasp of the sigma groove at the fibre insertion point.

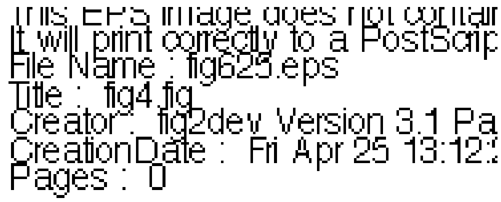

Fig. 6. 31: Cross section view of the HOB tile design including fibre groove.

Light transportation

The light collected by the WLS fibres inserted in the tiles will be transported to photo detectors located outside the muon rings using clear fibres. The captive end of the WLS fibres located inside the grooves will be polished, aluminised and will be protected with a thin polymer coating. The other end of the WLS fibre will come out of the tile through a slot (3 mm X 25 mm) made on the 2 mm thick black plastic cover sheet. This end of the WLS fibre will be spliced to a clear non-S type multiclad Kuraray fibre. The clear fibre will then be routed along the Z direction through 1.6 mm deep guiding grooves made on the outer side of the 2 mm plastic sheet to an optical connector located at the edge of the tray. Each tray will have two optical connectors mounted on either side of the tray. All the fibres from a tile will terminate on the connector located nearest to it. Since a tray will have a maximum of 6 tiles, there will be at the most 24 fibres per tray, 12 fibres per connector.

6.5.3.2 Meeting the design requirement:

The HOB calorimeter is designed specifically to sample the tails of hadronic showers, specially for those which develop deep inside the detector. This will enhance the energy

resolution of HCAL. In addition to this, it is expected to have the capability to identify and trigger on muons. A yield of 4 pe/layer is necessary to identify muons at 3 sigma level if HPD is used as the light readout element. Another consideration is to have uniform response within the tile. Both the requirements are fulfilled by

a) choosing higher scintillator thickness (10 mm) so as to have higher light output (higher photo electron yield)

b) 4 groove pattern for large tiles as shown in Fig. 6. 29 and 2 groove pattern for small tiles so as to have uniform response within the tile.

Light output from two layers of the same tower is pooled together at the decoder box and recorded by one readout element. Different response in the light output of these layers would affect energy resolution of the system. Responses of these layers are kept the same within 7 % approximately, using the techniques described in chapter 6.5.1.

6.5.3.3 Magnetic Field Effects:

Since HOB will be placed in a region where the magnetic field will be negligible, there will be no need to compensate for any field effects.

6.5.3.4 HB quartz-fibre laser (or LED) calibration layout

Though further R & D is required for this system, a spare hole would be provided on the optical connector to accommodate a quartz-fibre. Also, an additional groove would be made on the 2 mm black plastic as described in chapter 6.5.1.

6.5.3.5 Source tube layout

A radioactive source will move along the z-direction and scan the central portion of every tile on the tray. Data collected during this scan will be used for calibrating the tiles. A tube for the passage of the source will be laid on a groove on the 2 mm plastic sheet by the side of the fibre routing groove. There will be one source tube per tray.

6.5.4 HOE scintillator tray design

The HOE scintillator covers the pseudorapidity region of =1.2 to =1.5. It is meant to provide coverage for 7 (towers in the gap region between the HCAL Barrel, HB and the HCAL endcap, HE. Part of the HOE will be attached to the ME/1/2 muon chambers and be installed with the muon chambers while the rest will be attached directly to the YE/1 iron. The layout of HOE is given in Fig. 6.32.

The portion of the HOE scintillator that will be installed on the back faces of ME/1/2 (inside the muon chamber frames) covers 5.5 towers.

Due to the overlapping coverage of the ME/2, ME/-2 chambers, the same coverage is afforded to the HOE tiles in this region; nearly 100 percent. The muon chambers will provide the necessary structural integrity and support for the HOE tiles. An entire HOE package which covers the back of a muon chamber will be referred to as a megatile. Each megatile in this region will cover 10 degrees in ϕ or two ϕ towers.

In this scheme, the clear fibre that is spliced to the green Y-11 WLS fibre in the tile will carry the signal to the HPDs.

The construction of these megatiles will be the same as the construction of the HCAL barrel megatiles but the scintillator will be 10 mm thick BC 408 for greater light collection. An additional 5 mm of packaging will complete the megatile to give it an overall thickness of 15 mm, similar to the HOB tiles.

As the megatiles will be effectively trapped by the muon chambers, access will be limited to lengthy shutdowns and scheduled muon chamber maintenance periods.

In order to provide the remaining 1.5 (tower coverage over the "trough" of the HCAL barrel - endcap gap, additional tiles will be placed in the region between ME/1/2 and ME/1/3 where the "z-stops" for the endcap detector reside. These tiles will be fixed to the YE/1 iron before the muon chambers are in place. Due to the congested nature of this space, the tiles will only cover approximately 80 percent of the area. These additional tiles will be attached to the muon iron in a method similar to that of the HOB tiles.

Thin steel I-beams will be tack welded to the YE/1 iron which will hold the tiles in place. The supports and tiles must be placed on the YE/1 before the ME/1/3 muon chambers are installed. The reason for this is that the endcap cables go over this region of HOE tiles and under the ME/1/3 muon chambers. The complete effect of these cable paths has not yet been determined, but regardless of the layout, there will be some additional loss of coverage.

All the tiles in this region will be trapped by cabling from the inner detectors, so access will be limited at best. The HPDs will be accessible during shut down periods when the endcaps will be retracted.

Each tower in HOE will have 4 optical fibres going to a single pixel in a multi-pixel HPD which resides in the photodetector box of the HE Endcap. There are 4 fibres per tower for a total of 4032 fibres. There are 504 towers per end, 1008 towers total, with one readout per tower for a total of 1008 readouts.

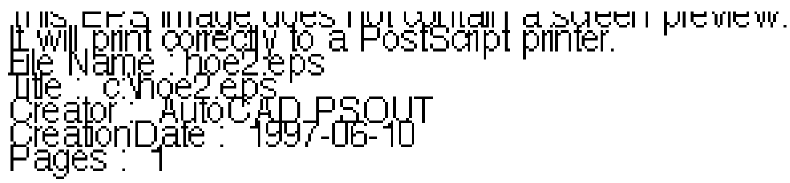

Fig. 6. 32: Layout of the HOE scintillator tray

6.6 HF OPTICAL SYSTEM

6.6.1 HF fibre insertion tooling

Fibre insertion into the absorber matrix is one of the critical parts of HF construction. The past experience in constructing the EM module suggests that about two man-years would be required for manual fibre insertion per detector. Fibre bundling for each tower and bundle installation behind the absorber would certainly require additional time. A programmable semi-automatic fibre insertion tooling is presently contemplated for this repetitive task. A robotic arm would pick an already cleaned fibre and insert it into a groove by the required length and move by groove-to-groove spacing to repeat the same task until a tower is completely finished. A manual intervention would be required if an insertion or another problem is encountered. The engineering aspects of this design are currently under study.

Fibre insertion will be done in a clean tent where a positive air pressure will be present to avoid dust particles accumulating in the grooves and on the fibre bundles over time.

One of the requirements for the absorber matrix is such that all the grooves are tested with a steel wire gauge for clear passage before the insertion of the quartz fibres. After this test, dry pressurised air is blown into the grooves to clean out possible burrs and dust particles. This procedure will reduce time consuming interventions if a robotic arm is used.

Once a tower is completed, a visual inspection from the far end (front face of HF) of the calorimeter will be conducted to make sure the uniformity of fibre insertion lengths. A light source will be used to inject light into each fibre from the same end to make sure that there was no fibre breakage during fibre installation. The acceptable rate of failure is one fibre in thousand.

6.6.2 HF fibre bundling, cutting and polishing

The fibres will be bundled to form towers at the back of the absorber. The fibre bundles will be made to form thin ribbons in order to minimise optical pickup noise from background radiation. At the very end of the bundle, fibres will be closely packed into cylindrical ferrules for mechanical mounting into the photodetector housing.

There are three types of fibre bundles that emerge from each tower; long fibres that run the entire length of the absorber (EM section) will be bundled separately from the medium length fibres (HAD section). The short fibres (TC section) will form yet another bundle. There are two different sizes of towers, the smaller ones (5 cm by 5 cm) and the larger ones (10 cm by 10 cm) depending on the eta region. For TC, superimposed towers will be formed in 20 cm by 20 cm square sections.

EM fibres will alternate with HAD fibres in the absorber, *i.e.* every other fibre will go either to EM bundle or HAD bundle. TC fibres will be inserted 30 cm into the absorber in the same groove as the EM fibres but at every second groove.

The experience with the previous prototypes has provided information in distinct ways; the fibres that constitute a tower are bundled at one end first and the free ends are inserted into the absorber as in the case of EM prototype that was built in 1996. During various stages of prototype construction, fibre bundles were glued, cut and polished several times and this experience proved extremely valuable. A new type of a wire saw that is recently introduced into the market makes cutting and polishing fibre bundles easier as shown in Fig. 6.33. The samples that are cut in this fashion require less time and effort to polish the bundle adequately.

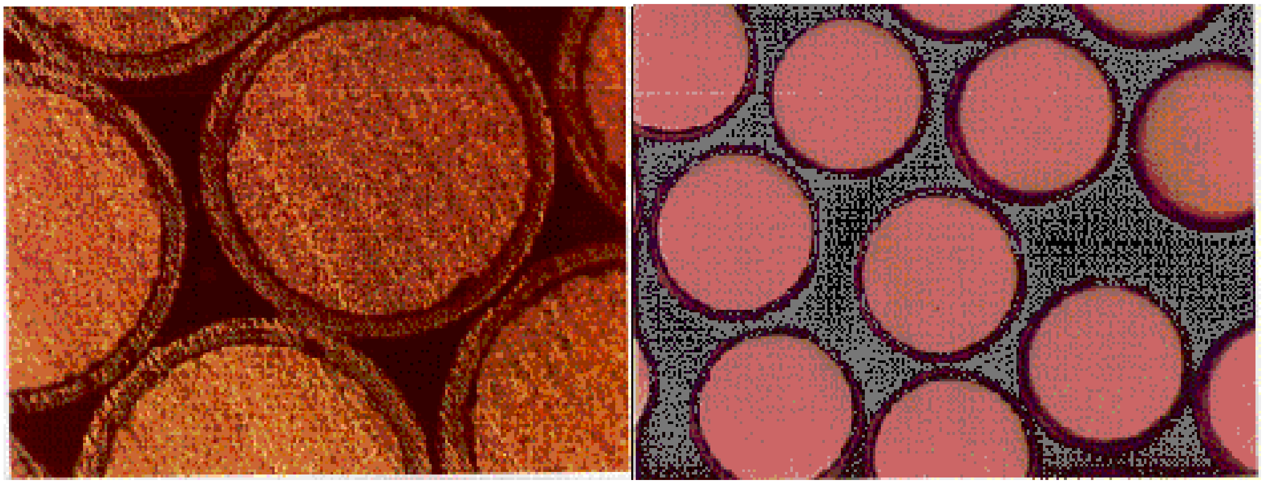

Fig. 6. 33: The top photograph illustrates the surface quality of the fibre ends after they have been cut with a diamond saw. Note that the core, cladding and the buffer are clearly visible. The bottom photograph the fibre ends after they have been polished.

Once a crack-free cut is established with the ferrule, wet polishing procedure starts with 33 micron grit silicon carbide. This is followed by a set of finer aluminium oxide polishing powders; *i.e*. 18, 12 and 3 micron grit sizes. The final polish is done using a 2 micron cerium oxide powder until the fibre ends are clearly reflective.

Before the ferrules are mounted into the holding grid, the polish will be visually inspected under magnification. In case of unacceptable polish (cracks, scratches, glue smears, *etc*.), the polishing procedure is repeated until an acceptable result is accomplished. After polishing, the bundle will be cleaned with a cleaning agent to remove small particles and dust and a protective cover will be placed over the ferrule. The failure rate of 1 cracked or deeply scratched fibre per hundred in a bundle is acceptable.

6.7 MANUFACTURING (HB/HE/HOB/HOE)

6.7.1 HB manufacturing6.7.1.1

Machining of scintillator and plastic covers

Each megatile sub-assembly is constructed from a single plate of scintillator. The processing of the scintillator plates is done over several steps. First, the protective paper removed from top side of the plate. The thickness of the plate is measured at two points at the edges using a micrometer. All machining operations are done on this top side only. The protective paper is left on the bottom scintillator until just before the scintillator pan is assembled. Since the separation grooves are cut so that only 0.25 mm of material remain, the scintillator plate with separation grooves machined onto it is fragile. However, as the protective paper on the other side is left intact on the bottom side, it gives additional structural support to the plate when it is handled. In addition, the paper prevents surface scratching when the scintillator is moved about.

The plate is positioned on the Thermwood x-y milling table. Next, reference holes are drilled along the edges for realignment in later operations. A "long reach" 0.90 mm end mill is then used to cut the tower separation grooves 3.75 mm into the scintillator (the last 0.25 mm is left uncut). The outer boundary of the megatile is not cut, just the inner tile separation grooves. The fibre grooves are not milled along with the tile separation grooves because of a risk of epoxy seeping into the fibre grooves from the separation grooves in the epoxying operation. This is because the fibre grooves are 3 mm away from the separation grooves, and a tape seal in such a small gap is not robust enough.

The scintillator plate is then removed from the milling table and white, opaque, epoxy is injected into the separation grooves. This is done by first taping over the grooves and then injecting epoxy into the channels. The epoxy is cured at room temperature for one day. The scintillator plate is put in a oven which is at 38 C for one day to harden the epoxy. The epoxy provides optical separation of the tiles, mechanical support, and a reflective surface at the tile edges. The plate is taken back to the milling machine and the megatiles are re-registered to the milling machine's co-ordinate system. The milling machine cuts the fibre groove routing, machines the rivet holes, and cuts the edges of megatile from the scintillator plate. The 1.52 mm deep fibre grooves are routed with a 1.35 mm end mill. The groove's circular shape, Fig. 6. 19, is cut with a 1.14 mm ball mill. Since the neck of the groove is smaller than the diameter of the fibre, the fibre is trapped in the groove.

The megatile is removed from the milling table. A fibre is inserted into each groove to insure that each fibre groove is clear. The megatile edges are painted with white TiO_2 paint to provide a reflective surface on the outside edges of the megatile. In addition, the side of the separation groove with the leftover 0.25 mm of scintillator is "painted" with a black marker pen. This reduces the adjacent tile-to-tile crosstalk to an acceptable 1 ±.6% per side. Fig. 6. 18 shows the mechanical configuration of the separation groove. The construction produces a large megatile that contains individual tiles which are optically isolated but are mechanically one unit.

Each scintillator tray consists of two or three scintillator megatile sub-assemblies. The largest piece of scintillator that manufacturer can supply is 2 m by 1.1 m. In order to minimise the total amount of scintillator used, the tiles are cut from the scintillator in the following way for layers 1-16. The scintillator plates are 2m long. We start with layer 1 tower 1 on the edge of a plate. Next the Thermwood goes to layer 1 tower 2. It continues sequentially until the next tile does not have enough space to fit on the plate. The next tower is on a new plate. At the end of the layer, the Thermwood goes to tower 1 of the next layer. If this tower fits on the old piece of scintillator, it puts it on the old piece of scintillator. Otherwise, it goes to a new plate of scintillator. The process proceeds to the last tower of layer 16. In this procedure, megatile sub-assemblies from separate layers can be cut from the same piece of scintillator. This procedure reduces the amount of scintillator we need to buy and reduces the cost. The thickness for layer 0 and 17 are different from the rest. Hence, a separate size plate is devoted to layers 0 and layer 17. The scintillator for 20º will be cut from a single plate. Each plate will have two side megatiles and one middle megatile cut from it.

The top and bottom black plastic plates are grooved on the Thermwood milling machine. The code for the milling machine is prepared from the database. Reference holes are drilled along the edges for realignment in later operations. Next the Thermwood cuts the grooves and holes on the black plastic. The Thermwood can cut plastic which is as long as 3.5 m. However, the longest scintillator tray is 4.5 m. Hence, after the cutting operation is over the plastic is repositioned on the milling machine using the reference holes. The rest of the plastic is machined to form a 4.5 m long single piece.

The milling of black polystyrene plastic cover plates are independent of the scintillator machining. However, the black plastic cover plates must be produced at the same pace at which the scintillator megatiles are cut. The scintillator, plastic (polystyrene), white paperlike reflector (Tyvek), light tightening black wrapping (Tedlar), and top and bottom black cover plates (black polystyrene) are assembled into a partially finished megatile-tray unit. This is the megatile-tray pre-assembly step. The fibre insertion is done later for the final finished scintillator tray pans.

Table 6. 10 shows the material needed to produce one wedge and the full calorimeter. 2052 scintillator trays are needed for the HB calorimeter. Note that before 36 wedges for HB are constructed, a single wedge pre-production prototype will be built.

Table 6. 10:

Summary of materials for the hadron calorimeter construction.

Material	1 wedge	36 wedges
Scintillator, SCSN81, 4 mm (m^2)	73.5	2683
Scintillator, SCSN81, 9 mm (m^2) (layer 17)	5.5	164
Scintillator, SCSN81, 9 mm (m^2) (layer 0)	4.2	110
Black plastic, 2.0 mm(m^2)	67.7	2170.0
Black plastic, 1.0 mm(m^2)	67.7	2170.0
Reflective paper: Tyvek 0.15 mm(m^2)	180.	4340.0
Black wrapping: Tedlar, 0.04 mm(m^2)	210.	4882.5
Y11 WLS multiclad fibre, 0.94 mm(km)	1.5	53.9
Clear multiclad fibre, 0.94 mm(km)	2.5	91.1

Clear 18 fibre cable, 0.90mm(1.2x15mm)(m)	53.	1900.0
Source calibration tubes, SS(0.050"OD)(km)	0.3	10.7
Epoxy: TiO2 loaded resin(kg)	15.	560
Rivets	2400	86400
Polyester tape, .15 mm(km)	0.5	16

The scintillator thickness of layer 0 is 9 mm. The scintillator thickness of layer 1-16 is 4 mm. The thickness of layer 17 is 9 mm. Since, the width of the scintillator pans is the smallest for the innermost layer and largest for the outermost layer, we can reduce cost by ordering plates with different width. We have decided to order scintillator plates of 3 different width for layers 1-16. Table 6. 11 lists the sizes of the plates and the number we need to order.

Table 6. 11

Scintillator Order. The sizes of the pieces of scintillator that are used to cut each layer.

scintillator	scintillator	scintillator	1 wedge	barrel
thickness(mm)	length(mm)	width (mm)		total
4	2000	1085	13	475
4	2000	930	14	514
4	2000	800	12	435
9	1600	860	4	119
9	2000	692	3	79

Times and manpower

The scintillator and plastic cover plates will be cut in Lab 8 at FNAL. The time to cut the scintillator and plastic cover plates for HB are based on the amount of time it took CDF to cut the scintillator and plastic cover plates for the CDF Hadron Plug Upgrade. We start by trying to estimate the amount of time CDF took to complete its Thermwood machining. These time estimates include both cut time and set-up time. The cut times were estimated form the total length of cuts and the cut speeds that were used. From the comparison of the CDF estimate and the actual CDF times we get a fudge factor. The fudge factor is an estimate of how much our time estimates are off. Next using the same methods, we estimate how much time it will take to cut the CMS plastic cover plates and scintillator. We have measured the machining speeds for the CMS grooves. We then multiply the CMS time by the fudge factor to get the CMS production time. The total times should be fairly accurate.

The actual time CDF spent was 1 calendar year. That calendar year consisted of 2 consecutive Thermwood shifts , 16 hours, on one Thermwood machine. The actual cut time available was 12.5 hours. The 3.5 hour overhead is due to turning the machine on, turning the machine off, cleaning the machines, and preparing the machines for the next day. Lab 8 has two Thermwood machines, and the technician had to prepare both machines for the next day. The CMS estimates will assume that we get the same machine time/day as CDF did.

We estimate that it should have taken CDF 0.58 years to cut the scintillator, 0.22 years to cut the plastic cover plates , and 0.13 years for set-up for each layer. We are off in our CDF estimate by 7%, as it took CDF one year of cutting time. Hence ,we multiply our CMS time calculations by 1.07. For CMS, we obtain the cut times of 1.44 years for the scintillator, 0.54 years for the top plastic cover plates and 0.34 years for the bottom plastic cover plates. We estimate 0.22 years for set-up time for each layer, for a total of 2.55 years of production cutting.

Next we estimate start-up times for the cutting. It took CDF 0.5 years from the time it tried to start cutting to full production. We give the same estimate, but we break it up into two components. We estimate 0.25 years of start-up for the preproduction wedge and .25 years for start-up for the full production. Hence, total barrel cutting time will be 2.80 years.

For the preproduction prototype we assume 0.25 years for start-up time. We also assume 0.22 years for the set-up time and transition between layers. These were the same times which we used to calculate the total production time. For the cutting time we take the total cut times and divide by 36. This gives us a total time of .55 years for the preproduction prototype.

Scintillator tray production cannot go faster than the Thermwood time, but with enough people hired it should go at the same rate. The assembly steps need to assemble the CMS megatiles are very similar to CDF. CDF needed about 3 people to do the assembly up to the fibre assembly. Hence, we estimate the 3 people are needed to do the preassembly up to the fibres. In addition we estimate this part of the project needs at least one full-time production manager.6.7.1.1.1

Quality control

An important quality control item in this step of the production is tracking the quality and uniformity of the scintillator plates used for each megatile. As part of the SCSN81 scintillator purchase agreement for CDF Upgrade project, Kuraray marked each plate delivered with an ID number that specified the production history of the plate. This information is included in the manufacturing protocol for the megatiles. Plates from different production batches are also tested and the results included in the protocol. Both the attenuation length and the light yield are monitored using tests described in the scintillator specification document. With this protocol, the megatile performance having to do with scintillator quality can easily be monitored as the megatile production proceeds.

Several checks of the scintillator plates are done. From each plate a 1 cm by 1 cm piece of scintillator is cut out of the sheet. This piece will be stored with the information as to which scintillator tray it is associated with. If a problem is found with the scintillator tray this piece can be retrieved and measured with a bismuth source. A fraction of the 1 cm by 1 cm pieces will be measured to determine the overall scintillator quality. The thickness of the plates will be measured in three places. Any plate with a the thickness outside the tolerance will be rejected. However, it is very important that the thickness of the plates not exceed 4.5 mm. To ensure they do not exceed 4.5 mm, a gauge with a 4.5 mm gap will be made. This gauge will be run down the edges of the plates. Any plate with a point that is thicker than 4.5 mm will be rejected.

After the scintillator is machined, a fibre is passes through each groove to insure each groove is clear. From knowledge gained from manufacturing the megatiles for CDF, we know that the dominate variation in the response of the scintillator trays is due to the variation of the fibre groove of the scintillator. The cutting of the scintillator gives a 5.5% rms for the light output and the distribution is gaussian with no tails. There are no manufacturing problems from cutting which give rise to low light yield tails. This information was determined by manufacturing 20000 tiles in 594 scintillator trays for CDF and measuring them. Hence, a visual inspection of the scintillator is sufficient to determine the quality of the megatile. The visual inspection determines the following: The scintillator is clean with no scratches, the edges are painted white, the fibre groove is clear, and the epoxy fills the separation groove.

The difference in grooves between low light yield tiles and high light yield tiles cannot by determined by inspecting the grooves. It can only measured when the trays is completely assembled with fibres. Hence, a sample of the preassembled pans will be stuffed immediately with fibres and measured. Production schedules will dictate whether all the pans can immediately stuffed with fibres.

The preassembly of the scintillator pan is done very quickly after that parts are available. This preassembly checks the whether the plastic is milled correctly.

Each scintillator tray will contain a traveller. The traveller will contain information about the tray at each step in production. It will contain information about the scintillator pieces used in the tray. Using the data from Kuraray, we can reconstruct information such as the thickness of the scintillator, the batch of the fluors, etc.6.7.1.2

Preassembly of megatiles

The preassembly of the scintillator pan done very quickly after the scintillator megatile sub-assemblies are prepared. This protects the megatiles from damage. First the rivets are snapped into the rivet holes in the bottom plastic plate. The plastic is laid on a table and the sheet of Tedlar is put down over the plastic. The Tedlar has holes in the position where the rivets are. Next the Tyvek is put down over the Tedlar. The scintillator is put down over the Tyvek and positioned with the rivets. a piece of Tyvek is placed over the scintillator. The bottom sheet of Tedlar has been cut big enough so that it can fold around the edge of the scintillator. The sheet on one side is taped onto the top sheet of Tyvek. The sheet on the other side is folded around the scintillator and is taped onto the Tedlar. This forms a light seal for the scintillator. Next the top black plastic cover is put on the Tedlar. 4-40 flat head screws are put through the holes in the black plastic and are screwed into the rivets. A electric screwdriver with controlled torque is used to tighten the screws. The optical fibres are not part of this assembly. After this assembly, the scintillator is well protected and can be safely stored or shipped anywhere. The preassembly trays are stored in boxes awaiting the fibres.6.7.1.2.1

Quality control

Quality Control of the preassembled tray is visual. We look at them to determine that all the tasks are performed. A traveller is checked off for the steps for the preassembly. The thickness of the scintillator pan must not exceed 8 mm. A special gauge will be made which has a air gap of 8 mm. The tray will be measured with the gauge along all edges to ensure the tray thickness does not exceed 8 mm. A sample of the preassembled trays have fibre installed and they are measured them with the scanner after the production.

The technology of production of the tiles was developed and tested for more then thousand tiles by SDC and CDF groups. New results were obtained during R&D at CERN by CMS collaboration. All the information and experience which we have give us confidence that the tile will satisfy the CMS requirements.6.7.1.3.1

Fibre cutting/polishing/splicing/assembly

The WLS fibres are cut to length. A template will enable to fibres to be cut to the correct length. Next both ends of the fibres are polished. Next the one end of the fibre is mirrored. The clear fibres are cut using a template to a length two inches longer than the length the fibre will be in the connector. The fibres are spliced together with an automated fusion splicer. The set of 17 polystyrene fibres + one quartz fibre are then assembled into a connector.

The pigtails are made using a plastic template with fibre grooves set to the correct length of the fibre run in the actual megatile. At one end of the template, a connector is

secured onto the template. The template for the side pigtail has location for the connector offset from the fibres. Fig. 6. 21 shows the curve the pigtail must make at the connector. First, each spliced WLS+clear fibre for a specific tower is inserted into its hole in the connector insert and then laid into its corresponding groove on the template. As there are tick marks in the template at the location of the splice for each fibre groove, it is clear if a fibre from a wrong tower is laid into a groove. After the fibres are in place, kapton tape is put on the bottom and top of the pigtail. This retains the shape of the pigtail and keep the pigtail flat. For the pigtails for the side trays another operation must be done to put in the curve near the connector. The kapton tape to hold the fibres is put on up to 30 cm (6 inches) away from the connector. A total of 15 cm of fibre away from the connector is left free of tape. The fibres are inserted in to connector. The connector and fibres are rotated to put in the bend that the pigtail fibres need for the side trays. The connector is then inserted into its position on the template and the fibres near the connector are taped in place. Hence, the fibres will easily follow the pattern they must follow in the scintillator tray. The fibres are secured with kapton to the connector and then glued. After the glue cures, the connector insert is faced off with a diamond cutter to form a clean, uniform optical surface. The combination of the fibre fusion splice, the WLS fibre mirroring, and the optical connector produce a light transmission rms spread of 3.5%.

We assume that the same steps that were needed for CDF to assemble the pigtails will be used by CMS. In order to estimate the assembly time for the pigtails we have used assembly times taken from CDF. The steps needed for building the fibres are the following: engraving the connectors, cutting the fibres, polishing the fibres, coating the mirrors with epoxy, splicing, cutting the protective tube used on the fibres, laying out the pigtail, gluing the pigtail, polishing the connector after gluing and testing the pigtail. Since the pigtails are bigger for CMS we estimate that it will take 20% longer to do the following steps: laying out the pigtail, gluing the pigtail, splicing the fibres, and testing the pigtail. We assume that it takes 10% longer to polish the pigtail. With the above estimates , we estimates it takes 4.9 man hours to make a pigtail for 5 degrees. This gives 350 hours needed to make the pigtails for a wedge. With 7 man hours in a day, this amounts to 50 days. For the entire barrel, it takes 12600 man hours. With 240 days in a year, this amounts to 7.5 man years of production

It took CDF about 6 months of start-up time for the pigtail production. During this period, one full time CDF physicist and 2 technicians worked on fibre R & D. We estimate that it will takes 0.30 years of start-up for the preproduction prototype and 0.30 years for the barrel.

For the preproduction prototype we estimate we need 1 production manager and 2 technicians. The time is 0.3 years of start-up + 0.2 year = 0.5 years of production. With 4 technicians and a production manager, it will take 0.3 of start-up + 1.9 years = 2.2 years to produce the pigtails for CMS.6.7.1.3.2

Quality control

Unlike the scintillator, low light tails in the tile response can come from bad fibres. Almost all of the problems in the tile/fibre assembly occur from bad splices or WLS fibre problems. Therefore, fibres are checked and tested prior to use. Several fibres from every batch of Kuraray are visually inspected for defects. If defects are found in these fibres then all the fibres of the batch are inspected. For WLS fibres, a sample is scanned with the UV scanner to assure that the light yield and attenuation length are within specifications. The fibres for each tower (fixed length green) are cut to length. The WLS fibres are cut in bulk,

polished, and mirrored on one end. Each batch of mirrored WLS fibres has several control fibres which are checked to assure uniformity in the mirroring. The reflectivity of the mirror is measured by measuring the mirrored fibre with the UV scanner. Next, for a small sample of test fibres, the mirror is cut off, and the fibre is remeasured. From these two scans the reflectivity is calculated. We expect a reflectivity of 0.85 ± 1.5%.

Each week the splicing quality is checked. This is done by taking a WLS fibre, cutting it in the middle of the fibre, and splicing it there. Next this fibre is scanned with the UV scanner. By measuring difference in light output across the splice the transmission across the splice is measured. The transmission across the splice expected to be 92% with an RMS of 1.8 %. In this measurement, the cladding light is removed by putting black tape on the fibre cladding before photodetector.

After the WLS and clear fibres are spliced and assembled into fibre-connector assemblies (pigtails), all fibres for all pigtails tested. They are tested in an automated UV-scanner box that is controlled by a PC. Those that are out of specifications are either reworked, or rejected outright. The results of these pigtail scans are saved in a data base for future reference.6.7.1.3.3

Quality assurance

The main quality assurance tool is the UV fibre scanner. The light yield of all the fibres in a layer is compared and all bad fibres are replaced.6.7.1.4

Source tube preparation and routing

The source tubes in the megatiles will be 18 gauge thin wall stainless steel hypodermic tubing, needle-grade fully hardened. The nominal OD is 1.27 mm to 1.32 and the ID is 0.965 mm. The source-carrying "wire" is 22 gauge stainless steel hypodermic tubing, 0.71 mm OD, with a bullet-shaped enlargement of approx. 0.833 diameter closing the active end of the tubing. As discussed elsewhere, the source wire is given a NICOTEF antifriction coating. All this is done before the active element is loaded and a keeper wire inserted, followed by closure of the inactive end of the source "wire".

The metal source tubes will be cleanly finished at one end, probably by EDM cutting. Each tube is crimped, or crimp-cut to length, and laid into the black plastic groove. The clean-cut end is secured in the pan-edge coupler with a nylon-tipped 2-56 set screw. The tubing is then taped in place with 0.1 mm thick polyester backed clear tape. The depth of the groove in the black plastic is nominally identical to the OD of the metal source tubing. The width of the groove is at least 0.065 mm to provide tolerance (especially against kinking) and the groove will flare near the edge of the pan to provide tolerance going into the pan-edge tube coupler.

The tube should end near the edge of the last tile (at η=0), but should end approximately 1 cm short of the end of the groove in the plastic, for tolerance and to accommodate some degree of thermal contraction of the plastic (the coefficient of thermal expansion of plastic is some ten times that of steel). The pans should be protected from large thermal excursions at all times.

6.7.1.4.1

Quality control

After cutting and before closure of one end, each metal tube will be flushed and/or blown-out, and probed with a 0.89 mm diameter wire to guarantee clearance for the source wire.

The tube must be securely fastened to the coupler. Tightening of the nylon-tipped set screw must be done firmly but not excessively, or the tube will be distorted or dimpled.

Test: The coupled tube must resist a pull of at least 3 kg-weight before being laid into the groove. If it fails, the set screw will be backed off and the tube recoupled more tightly.

Test: The tube and coupler must also still freely pass the 0.89 mm probe wire. Any tube failing this probe will be either repaired or replaced. Satisfactory repair can be made by carefully forcing an approximately full-diameter probe into the tube. The person doing the coupling will do the tests immediately. This will provide rapid feedback. The probe test will be repeated by another person, as a cross check.

It is important that the distance of the tube to the scintillator, and the degree of embedding of the tube in the plastic, not change with time, or the accuracy of the collimated source to wire source ratio will be degraded. We will rely on QC/QA of the depth of the groove in the plastic, and the tight manufacturing tolerance of the steel tubing. We believe that taping the tube into a nominally same-depth groove will locate it adequately. We will rely on QC/QA of the megatile assembly and riveting procedure. We will rely on the support-springs which locate the megatiles to the back of the copper slot, to help keep the megatile packages in a compressed state.

The coupling of the plastic tubes to the pan edge and to the indexer of the wire source driver will be checked by a 3 kg weight pull test.6.7.1.4.2

Quality assurance

Travellers will accompany batches of tubes, and will have checkout lists detailing procedural steps, including probing and testing. Similarly, tube installation and the testing thereof will be made part of the travellers which accompany megatiles.

The plastic tubes connecting pan source tubes to the source driver indexers will be colour coded at both ends, to help prevent scrambled couplings.6.7.1.5

Final scintillator tray assembly

In the megatile final assembly, the pigtails are installed and the connector piece of the pigtail is attached to the scintillator tray with rivets. The fibres in a pigtail are stuffed into their corresponding scintillator tiles, and the rest of the fibre laid and secured in its black plastic cover routing groove. The fibres are taped over with 6 mil polyester tape. To insure uniform compression, all rivets are torqued to fixed, specified level. 6.7.1.5.1

Quality control

After installation of the optical fibres in the scintillator tray, the tray is put through a QA/QC test to assure that the light yields from each tile are within specifications. Light yields from tiles are required to be ±20% of nominal. Those that are not within specifications typically have fibre damage in either the splice or WLS fibre. The QA/QC test is there to detect and correct these problems. Light yield results from these tests are also stored in a data base for future reference.

Each scintillator tray will be scanned by the Megatile Scanner using a photon source. If any individual tile light yield is outside of tolerance, due for example to broken WLS fibre, corrective action will be taken. The light yield information of each tile of each tray will be saved in computer files. There are 18 wedges in each half barrel of HB, so there are 36 identical wedges. Each layer in a wedge includes one two-φ wide middle (M) tray, and two singe-φ wide trays. Therefore, there are 36 identical middle, side-left and side-right trays for each layer. The mean light yield of all the layers can be matched by ordering each layer based on its mean light yield, and matching the lowest and highest mean light yield layers, respectively in corresponding wedges. Three megatile scanners will be constructed, one for HB, one for HE and the last one for HOB. The HOE tiles will be scanned by the HB megatile scanner. Each megatile scanner has a photon source that scans the megatile in x-y motion and stores the information in a computer. The HB scanner has a scan of 450 cm110 cm.

The relative tile-to-tile light yields from completed megatiles for CDF is shown in **Fig. 6. 34. As the plot is shown for large scale production, we expect the same result for the CMS tiles. The correlation between the light yield variations measured here and the pigtail light yield variations are shown in Fig. 6. 35.**

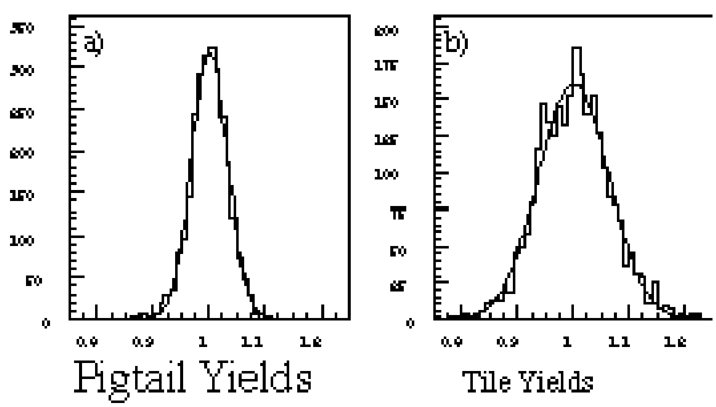

Fig. 6. 34: a) Relative light yield of fibre/connector assemblies (pigtails) before insertion into megatiles. The rms of this distributions is 3.5%. b) Relative light yield of individual tiles after the final assembly of fibres into megatiles. The rms of this distributions is 6.5%.[4]

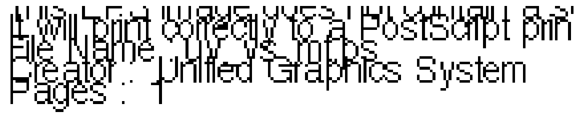

Fig. 6. 35: Correlation between average fibre light yield (x axis) and average tile light yield (y axis). CDF data.)

The light yield measurements are taken with a collimated ^{137}Cs γ source positioned over the centre of each tile. This is taken on an automated x-y scanning table controlled by a PC. The optical readout of scintillator trays, is done using mass-terminated optical cables which go to an optical patch panel which takes the light to a Hamamatsu R580-17 PMTs. The photomultiplier tube gains are monitored by two systems. One is a set of reference SCSN81 tiles (read out with Kuraray Y11 fibres) permanently connected to the PMTs. These are scanned by the γ source to provide a tile/fibre reference system. The second monitor is a set of NaI (with Am^{241} "light pulsers" directly mounted on the face of the PMTs. The megatiles, the x-y scanner table, and the optical system are within a large dark box. Measurement errors are 1% or less and the PMT gain monitoring system tracks the gain to better than 1%.

In addition to the collimated γ source measurements, pointlike source measurements are taken using the source calibration tubes and a ^{137}Cs wire source. The correlation between the collimated and point source measurements is good to ~1 % for a given size and shape of tile, indicating that the source tube locations, especially their heights above the scintillator, are very reproducible. There is a ~20% systematic variation of the tile response to the pointlike source as a function of tile size and shape. Large tiles have greater path lengths for the γ rays. On the other hand, the collimated γ source uses a lead cone such that the direct γ radiation falls entirely within a tile. This makes the collimated source response less dependent on source height and tile size. Since only the wire source can enter the assembled calorimeter, a data base is maintained of both the pointlike and collimated source responses.

Using a similar volume integral calculation for the pointlike source responses, the calculated pointlike to collimated response ratios (averaged, for each tile, over all megatiles in a layer) track the measured ratios with a rms of better than 2%. The calculation attempts to model the actual tile geometry in detail. For the final calibrations, the use of measured ratios is preferred because they should reflect any variations in source tube placement, etc., from one megatile to another.

Below are the measurements taken for quality control and quality assurance during production of the pizza pans.

a) Record information on each plate of scintillator from the manufacturer. Take and save samples of the scintillator as megatiles are made.

b) Measure the light yield of control samples from each batch of scintillator sheet. Measure attenuation lengths from batches.

c) Inspect each batch of optical fibres, and measure the attenuation lengths and light yield from samples of each batch.

d) Measure the combined light yield and transmission of each fibre-connector assemblies (pigtails).

e) Measure the light yield of each assembled megatile with a collimated and a wire (pointlike) ^{137}Cs γ source.

The key to production quality control is contained in Steps 4 and 5. Production information kept in a data base includes:

a) The information sent from the manufacturer about the scintillator pieces.

b) Measure of the light yield and attenuation of the scintillator control pieces.

c) The results of the UV pigtail scans.

d) The results of the collimated and wire source scan of the megatiles.

6.7.1.5.3

Final assembly manufacturing

The total calendar time for the final assembly is determined the amount of time it takes to cut the plastic cover plates and scintillator. Production can not go faster than this time. Hence, we will assume that enough technicians will be hired to keep up with rate of production of the preassembled trays and pigtails. We estimate the number of technicians need for final assembly by looking at what CDF needed. CDF needed one technician to put in fibres, one technician to test the pans and one technician to do the final assembly and do other jobs that were necessary. Hence we estimate we need a production manager and three technicians for the final assembly.

6.7.2 HE manufacturing

The end cap hadron calorimeter must have about 27500 scintillation tiles (4 mm thick) with different size and configuration. Only 1/36 part of them are identical. The mean size of the tile is about 15x15 cm^2. The total area of the plastic scintillator is about 620 m^2. The total length of the tiles edges and key shape grooves is about 16.5 km. Cutting and grooving of the tiles will be done with high speed milling machines. Technology tested ensures success of key shape groove production at revolution speed 20000 rpm and at the speed 20 cm/min via two milling passes. The edges cutting speed is 40 cm/min via one milling pass. So the mean size tile will be fabricated during 8 min. To finish all the 27500 tiles it will be needed about 1.3 year with one milling machine working 8 hours per day. We plan to use at least two milling machines.

6.7.3 HOB manufacturing6.7.3.1

Machining of scintillator and plastic covers

For HOB, as described earlier, there will be one tile per tray in the ϕ direction. But in the z direction, a tray will cover an entire muon ring. This means that one tray will contain 4-6 tiles. The individual tiles will be part of a big piece (similar to a megatile for HB). Deep grooves will mark the z boundaries of these tiles. Due to physical constraints there will be several different sizes of the tiles (see section 4.5.1 for the table of sizes). All these sizes will be kept in a data base, which will be referred to while machining the scintillator plates. The procedure of making the scintillator plates will be similar to that for HB, as described in section 6.7.1. However, since the thickness of the scintillator for HO is 10 mm, the grooves that separate the tiles optically will be 9.5 mm deep, leaving 0.5 mm material at the bottom. The scintillator plate is fragile at this point of the production and therefore has to be handled with care. A CNC machine of appropriate capacity will be used for milling the grooves. A vacuum bed will hold the scintillator in place with rubber gaskets during grooving. The position of the scintillator on the vacuum bed will be marked accurately. This way, the scintillator piece can be brought back to the same position if it is removed.

Grooving will be done in two stages. The deep, separator grooves will be milled first with a 0.89 mm(width) cutter. These grooves will be 9.5 mm deep leaving only 0.5 mm material at the bottom. The scintillator plate will then be taken out and the deep grooves will be filled with epoxy as described for HB in Section 6.7.1. Until the epoxy dries the scintillator plate will be fragile and has to be handled with care. After the epoxy dries, the scintillator plate will be put back on the vacuum bed again in the same position. Then the sigma grooves will be made with a keyhole type design and the procedure will be as described in 6.7.1.1. The length of the grooves will vary according to the sizes of the tiles. These lengths will also be kept in the data base.

The 2 mm piece of black polystyrene plates which will be used for routing the fibres coming from the scintillator tiles, will also be grooved by the CNC machine. There will be one 2 mm and one 1 mm polystyrene plate corresponding to each tray. Therefore these plates will also be of different sizes as given in section 6.5.3.1 Each of the 2 mm plates will be grooved for fibre routing, passage of source tube and quartz fibre routing. The sizes of grooves for each plastic cover plate will be kept in the data base. The CNC machine will be programmed for different grooving using the data base for both the cover plate and the scintillator. Holes will be drilled at regular intervals on the scintillators and the cover plates for rivets which will hold the whole assembly together.

Material needed

HOB will have 360 trays per layer, i.e. 720 in total. Each tray will be roughly 5 degrees in ϕ (0.41 m) and 2.536 m in the z (η) direction. Scintillators will be ordered in pieces having roughly the dimension of a tray i.e. 0.41 m by 2.6 m. Table 6. 12 below shows the material needed for the production of 720 HOB scintillator trays.

Table 6. 12

Material for HOB.

Material	Quantity
Scintillator, BC408, 10 mm (m2)	770
Black Plastic, 2.0 mm thick (m^2)	770
Black Plastic, 1.0 mm thick (m^2)	770
Reflective paper: Tyvek 0.15 mm (m^2)	1570
Black wrapping: Tedlar, 0.05 mm (m^2)	1650
Y11 WLS multiclad Fibre, 0.94 mm (Km)	15.
Clear Multiclad Fibre, 0.94 mm (Km)	30.
Clear 18-fibre Cable, 0.94 mm (1.2 x 15 mm)(m)	1600.0
Epoxy: TiO_2 loaded resin (Kg)	100
Kapton tape: 0.15 mm (Km)	4

Time estimate

In order to give a realistic time estimate for the production of the two layers of HOB, an estimate has to be made of the amount of grooving necessary. The following is an estimate of the total length of grooves in HOB for fibre laying.

If one assumes each groove to be roughly of the size 0.18 m x 0.25 m in layer 1 and 0.21 m x 0.28 m in layer 2 then the total groove lengths will be 6842 m and 6912 m for layers 1 and 2 respectively. Similarly, for the tiles with two grooves, the total groove length will be 126 m and 138 m for layers 1 and 2 respectively. Thus, we will have to mill about 14 km to make all the grooves in the scintillator. This will be the major portion of the production work.

The length of the separator grooves can be estimated similarly. Every tray has typically 6 tiles and hence 5 deep separator grooves. Therefore for 720 trays total number of deep grooves will be 3600. Each deep groove will be roughly 0.4 m long (φ length of a tile). Therefore, total length of the deep grooves will be 1.44 km.

The 2 mm polystyrene plate will have two wide pathways for fibre routing and one groove each for laser signal and radioactive source tube. This can be considered as four grooves, each of length 2.56 m. The total length of grooves on 720 such polystyrene plates will be about 7.4 km.

The following production times are based on simple calculations that break down the total operation into steps whose timing has been measured. The times are given for the machining of all the tiles in the two layers of HOB. A CNC day is one 8 hour shift. A year is 200 working days. A summary of the HOB labour time is presented in Table 6.13.

Table 6. 13

Time Estimate for HOB Production

Scintillator	One tray
0.94 mm ball groove	0.5 days
Separation groove	0.1 days
Total	0.6 days
Top black plastic	
Grooving	0.2 days
Total CNC time	0.8 days

Therefore for 720 trays we need 600 CNC days, i.e. 3 years in real time.

Quality Control during production of scintillator plates

The scintillator pieces will first be examined for any damage, like scratches or breaks. After some superficial cleaning it will be sent for grooving. Next will come fibre laying and packing. A quality control sheet will be filled at each stage of the production on each piece of scintillator. The information on these sheets will be then be entered into a data base in the computer.

The following steps will be taken to check the quality of the tiles.

- Record information on each plate of scintillator from the manufacturer.

- Measure the light yield of control samples from each batch of scintillator sheet. Measure attenuation lengths from batches.

- Inspect each batch of optical fibres, and measure the attenuation lengths and light yield from samples of each batch.

- Measure the combined light yield and transmission of each fibre-connector assemblies (pigtails).

- Measure the light yield of each assembled scintillator tray with a collimated and a wire (pointlike) ^{137}Cs gamma source.

The following production information will be kept in the data base.

- The information sent from the manufacturer about the scintillator pieces.

- Measurement of the light yield and attenuation of the scintillator control pieces.

- The results of the UV pigtail scans.

- The results of the collimated and wire source scan of the scintillator trays.6.7.3.2.1

Fibre cutting/polishing/splicing/assembly

Essentially the same steps will be followed for HOB as described for HB in chapter 6.7.1. Two fibre splicing machines will be set up along with a single fibre polisher. These will be used to polish the WLS fibres and splice them to clear fibres.6.7.3.2.2

Quality control

A UV scanner will be set up which will be able scan and measure the attenuation length of several fibres simultaneously. Fibres will be tested at regular time intervals to monitor the uniformity of their performance.

6.8 OPTICAL CONNECTORS AND CABLES (HB/HE/HOB/HOE)

6.8.1 Connector and cable design

All the connectors, one at each end of the optical cable, one at the pigtail exit and one at the HPD Box entrance have essentially the same design. Fig. 6. 20 is a schematic sketch of these connectors showing 18 fibre holes, the alignment pin holes, the dimensions w, the width, h, the height, d the depth and the location of mounting holes. The alignment of two joined connectors is maintained by two pin/screw elements within the alignment holes which bracket the 18 fibre holes. The alignment holes are different sizes to allow only one possible pin numbering. We have chosen to number the fibre holes 1-18 and require the 1 pin be next to the largest of the alignment holes. The overall arrangement is sketched in Fig. 6. 36. With this arrangement the two ends of the optical cable may be interchanged without danger of mixing up the fibre numbering.

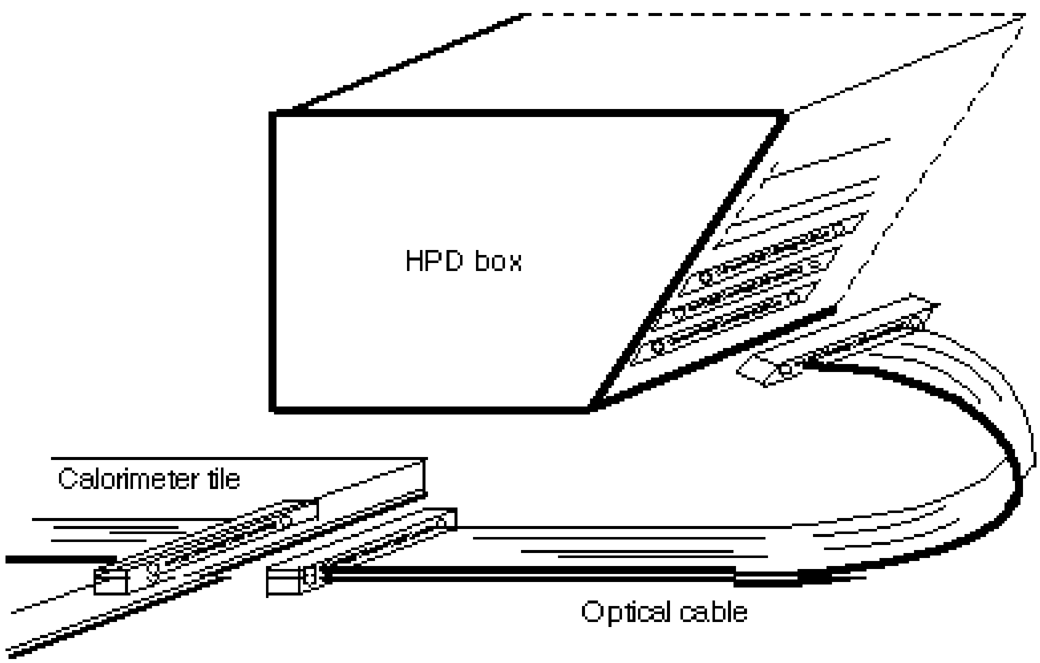

Fig. 6.8.1.2 Schematic drawing of the overall optical arrangement (for illustration only)

Fig. 6. 36: Schematic drawing of the overall optical arrangement.

The connectors on the ends of the cable will use the mounting hole region for attachment to a strain-relief boot and a light tight cable jacket. Similar optical connectors will be used for HB, HE, HOB and HOE calorimeters with only the channel count modified for HE and HOE. The overall sizes of the connectors for the other calorimeters vary according the mounting needs, but the basic design of the fibre holes and alignment holes will be the same.

After studying various prototypes and materials it was decided to have the connectors made by injection moulding. We could have a reliable, precise product (within tolerance) at a reasonable price. The material chosen was acrylonitrile-butadiene-styrene (ABS) plastic which has a shrinkage during injection moulding of less than 0.5%. Delrin, another possible candidate material, was found to have a shrinkage of 2% and was rejected.

In order to do the injection moulding a stainless steel mould is required. Aluminium moulds will not produce the required number of connectors. In the following we describe the tests that were made which lead to these decisions.

In the past we found that alignment tolerances have been met for moulded connectors as long as the moulds are initially calibrated and monitored occasionally throughout production. Measurements made on 1100 moulded connectors (with 0.835-to-0.835 mm fibre matching), produced for the D0 preshower detector determined light transmission to be 81% with sigma=3%. An air gap was used between connectors. Fibres were illuminated by green LED bargraphs with diffusers. The diameter step-up design would improve transmission slightly (85%) however light loss is dominated by a 9% transmission drop due the air gap. Transmission through connectors have been monitored for two years and found stable to ± 1%.

6.8.2 Connector production

The connectors will be injection moulded from a mould made of steel. The useful life of an aluminium mould is about 1000 pairs of connectors. The construction of the mould will be farmed out to an external vendor. Production of the connectors could take place at the vendor. However, we are also contemplating doing the production on an existing commercial quality moulding machine located at UIC.

Clear fibres and ribbons will be held in place with BC-600 epoxy and then fly-cut using a diamond to polish the ends at the P3 facility at FNAL. Approximately ten connectors can be polished simultaneously in one twenty minute run on the P3 facility.

6.8.3 Quality control

Transmission depends on careful fibre-to-fiber alignment. The holes for the fibres are fixed during creation of the mould and misalignment must be kept below 50 microns in order to keep the transmission high. Initial alignment will be checked with measurements of the mould and measurement of the first moulded pieces. Several connectors will be assembled with clear multiclad fibre and the transmission directly measured. Green LEDs are used as light sources and the output of silicon photodiodes are measured with a picoammeter.

Other quality factors which must be monitored include thin layers of plastic blocking holes and bubbles in the connector material which can affect strength and optical isolation characteristics. Both are obvious upon visual inspection.

The entire production run can take less than a week in a commercial facility so most monitoring throughout the production run will actually take place after the run and if a problem is discovered, a new run will be performed.

6.8.4 Quality assurance

We have produced injection moulded connectors for the D0 upgrade central fibre and preshower detectors. We have the expertise in mould design and injection moulding so connectors for the HCAL prototypes will be produced in house. However, commercial vendors with larger injection moulding machines will be required for production runs for the final detector.

6.9 HF AIRCORE LIGHT GUIDES

The quartz fibre bundle are formed by loosely gathering together the fibres emerging from the back of the calorimeter using PEEK plastic tie-wraps. The fibre bundle is turned between 75-90 and routed towards the outer radius of the calorimeter. The first row of PMT are located at about 100 cm in radius from the beam, whereas the first fibres emerge from the calorimeter absorber matrix at about 7 cm from the beam. The bend radius of the fibre bundle is at least 200 times the fibre radius, or ~8 cm minimum. The length of a typical bundle is about 1 m, including the bends. The fibre bundles terminate in a highly polished, hexagonally close-packed bundle held in place by a snugly-fitting stainless steel ferrule (cylindrical) collar (from 6 mm-18 mm in diameter, depending on eta) and about 7 cm long) which is epoxied in place. The fibre bundle light guide is bent a second time at the ferrule end, so that the fibre ferrule is oriented parallel to the collider beam (along z), pointing towards the photomultiplier windows, through mirrored air light guides. The ferrules all terminate in holes in a rigid annular plate, held by a pressure collet around the conical holes. The steel plate, about 1.4 m in outer radius, is oriented perpendicularly to the beam direction.

The purpose of the air-core lightguide is to:

a) mix the light,

b) save costs of fibres,

c) provide a method to enable heavy shielding around the PMT to be conveniently penetrated, and

d) avoid Cerenkov background generated by mips in a solid light guide.

6.9.1 Design description

The lightguide consists of a hexagonal cross-section hollow regular parallelopiped mirror which is at minimum 3.5 times longer than the useable photocathode diameter. This minimum length ensures that the meridonal light emerging from the fibres (NA=0.22=sinθ) centred in the hexagon illuminates the entire cathode with only at most 1 bounce, while only allowing the bulk of the skew rays to have only at most 2 bounces from the mirror. The major diagonal of the hexagon is 1.5 mm less than diameter of the photocathode (15 mm) for a tolerance. The maximal length of the light guide is <35 cm, chosen as a compromise between transmission and shielding.

The shape of the mirror - square or hexagonal - will be optimised before final design in order to maximise transmission, provide good mixing, and minimise needed photocathode area. In the test beam, hexagonal mirrors provided good performance and were a better match to round PMT photocathodes, as described below.

The mirror material has been tested and consists of Alzac (Alcoa Metals), an aluminium sheet material (75-1,000 µm typical available thicknesses). The purified aluminium substrate has been anodised with a special non-porous anodisation, designed for mirrors used in indoor and outdoor commercial lighting fixtures, which survive outdoors in temperate climates. The anodisation produces a sealed film of boehmite, a form of transparent amorphous sapphire (alumina) that is a typical alumina ceramic, and in film coatings highly resistant to radiation damage[5,6]. The total reflectance is guaranteed to be 95% at normal incidence in sunlight. (Note: this process is not normally used for optical mirror protection because the surface finish is not able to reach the wavelength tolerances necessary for high quality imaging - the reflectance has a small ~ few % diffuse component at normal incidence. In the quartz fibre transmission case, at nearly grazing incidence, this is largely irrelevant and contributes to the mixing.) In the HF case, the minimum angle to the normal is about 75°, where the reflectance in the blue (440 nm) averages above 98% in bench tests. These bench tests used a blue LED and the same quartz fibre used in the calorimeter. The light cone from the quartz fibre was oriented onto the mirror material at variable angles and the resulting light measured with Si photodetectors. The mirror materials were fashioned into light guides for bench and beam tests.

In test beam and bench tests, a 1 m long similar cylindrical mirror ~2.5 cm in diameter transmits 65% of the light injected at the emission angle of the fibres (about 15° max). It is because the emission from the fibres is <13° from the axis of the fibre that good light collection is possible using specular reflection. Fig. 6. 37 shows the design of a slightly tapered light guide used in the test beam with the prototype calorimeter. Fig. 6. 38 shows the measured transmission through these ~ 1m long guides. Fig. 6.39 shows the ADC distribution of the response to 80 GeV electrons in the test beam through a 1 m long air light guide, confirming the 65% measured in bench tests and calculated with ray tracing.

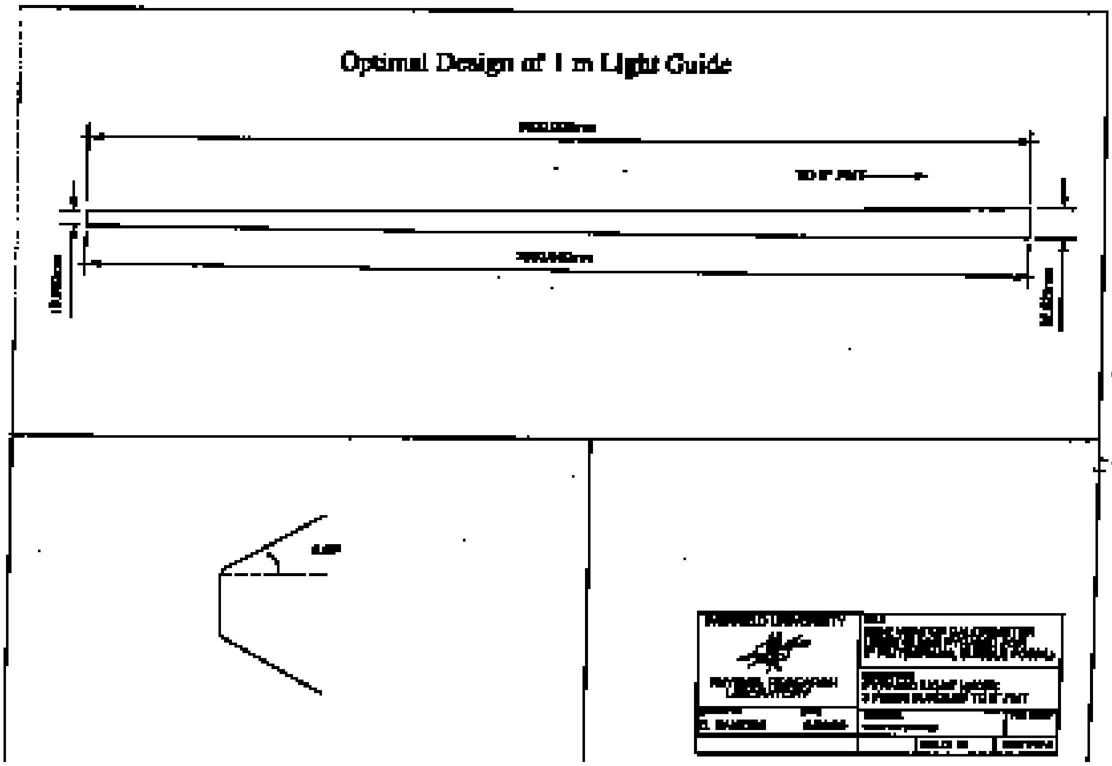

Fig. 6. 37: Tapered light guide design with a 16 mm and 32 mm aperture.

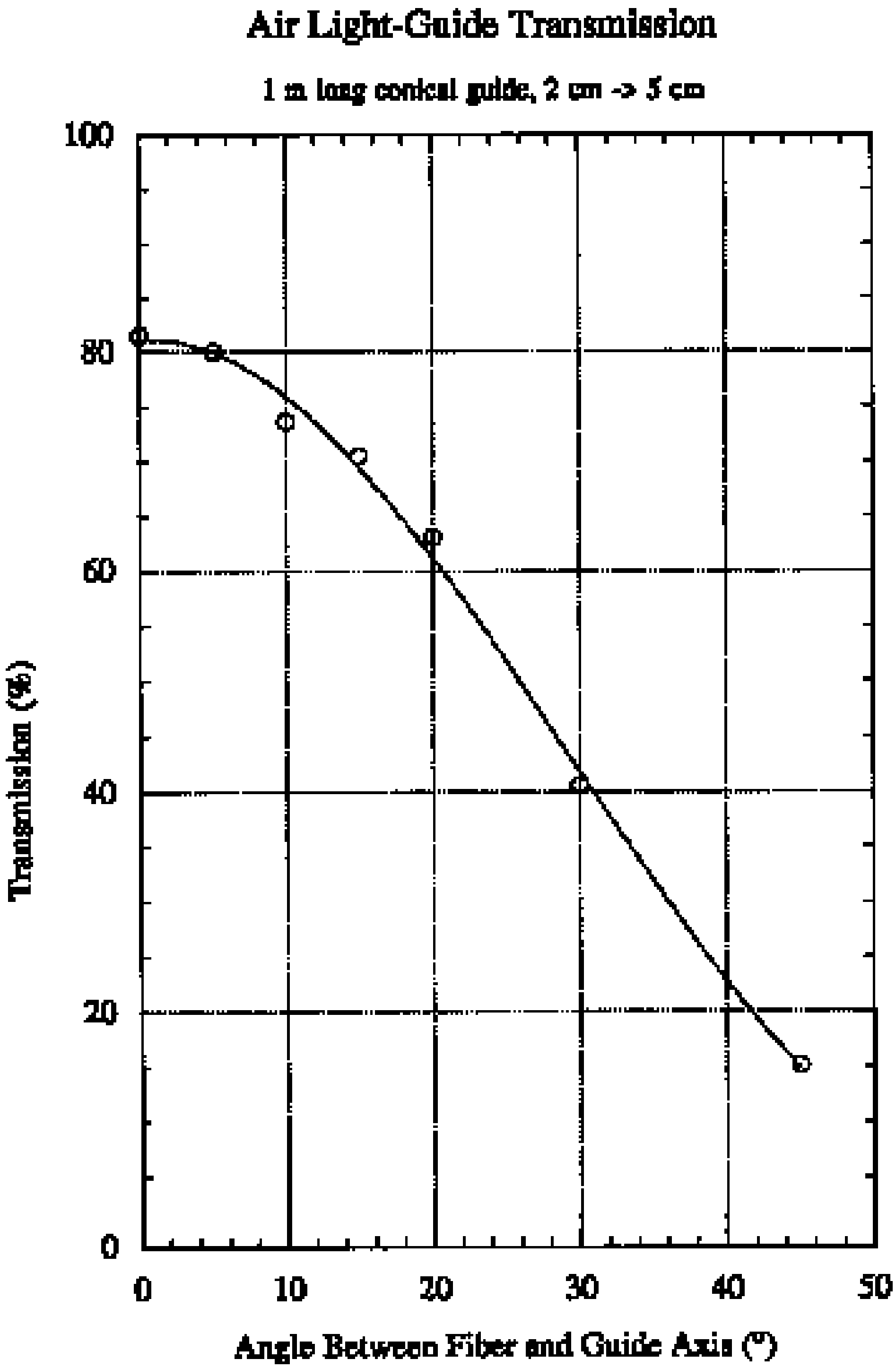

Fig. 6. 38: Measured light transmission through a conical 2.8 cm-> 4.5 cm aperture mirrored air light guide using a quartz fibre as the light source vs the angle of the fibre WRT the axis of the air guide. At ~12° (~78° to the surface) about 65% of the light is transmitted.

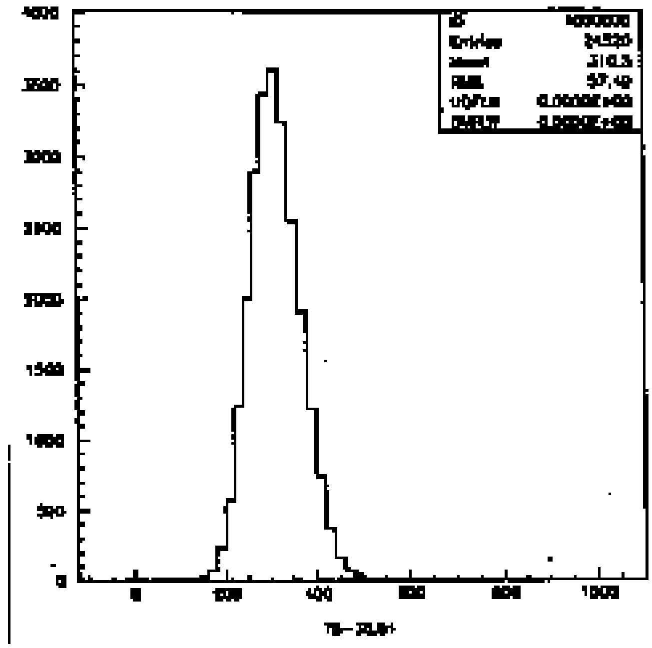

Fig. 6. 39: The ADC distribution of the response to 80 GeV electrons in the test beam through a 1 m long air light guide, confirming the ~65% transmission measured in bench tests and calculated with ray tracing.

For the test beam, hexagonal light mixers as shown in Fig. 6.40, were built using aluminised plastic. Measurements confirmed a reflectivity similar to the Alzac materials. The data shown for the test beam was taken mainly through these guides.

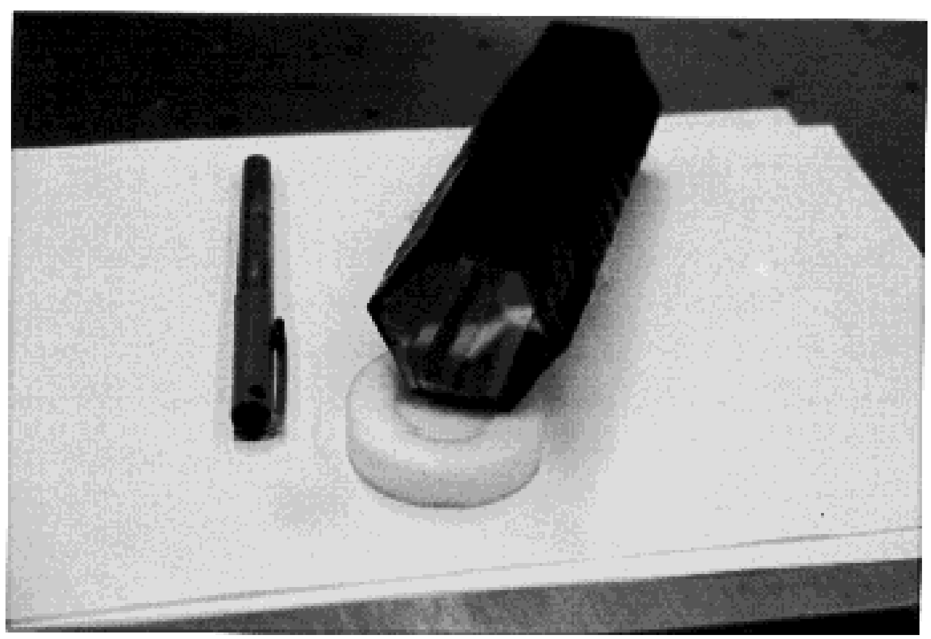

Fig. 6. 40: Photograph of a 13.2 cm long x 3.6 cm diagonal hex mirror.

For the HF design, we have specified a short air light guide. This guide is ~31 cm long and 15 mm in diagonal. A photon emitted from the compressed phase space of the fibre will bounce at most 5 times in this guide, and be transmitted at a level of 70% with 93% reflectivity; the average photon will have ~4 bounces and be transmitted at 75%. At 95% reflectivity, typical for the (grazing) angle of incidences >78 emitted from the fibre bundle, the average transmission is >80%.

Full radiation damage tests will be conducted over the next 2 years. If any reason should be found to reject these mirrors, aluminium mirrors overcoated with a film of radiation hard magnesium fluoride, silicon monoxide, or all-metal nickel or rhodium plated mirrors with a reflectance of >90%, are alternates which are known to survive high radiation levels[7,8].

6.9.2 Performance requirements

The minimum acceptable transmission requirement of the air light guides is 50%, which are met by the guides constructed heretofore. This requirement is set so that the least count in a hadronic physics tower is not greater than 5 GeV at η=3. The average energy of a particle at an average p_T of 0.5 GeV, low for LHC , is 5 GeV.

6.9.3 Quality control

The mirrors will be constructed in an assembly line with a precision slitting apparatus to cut the mirror material with a bevelled edge (60°). 3-sided halves of the hex mirror structural element are constructed from 3 mm thick bent and machine-finished steel. CERN-spec epoxy will be used to fasten the mirror skin to the structural elements. The non-reflective seam between the 6 mirror elements must be less than 250 µm in width. The manufacturing process will be designed to ensure that the mirror dimensions are the same with 1% from mirror to mirror, a tolerance of about ±0.15 mm. The flatness tolerance is ±0.1 mm across each panel of the hexagon. The design parameters are inherently not critical, as the number of mirror bounces is small, so that dimensional changes as high as a few % have negligible effect, so long as the output area is within the photocathode area.

6.9.4 Quality assurance

The first 10% of all mirrors will be tested fully with angle (0°-15°) and transverse scans using fibre light sources. Transmission less than 2% from nominal will be rejected. All others will be tagged for selection. If most of the first mirrors pass testing, all mirrors will be visually inspected, and put in a very simple go/no-go jig, made of fibre light sources and a photodiode array connected to a simple yes/no discriminator consistent with the 10% full testing. In any case, the mirror and PMT assembly will undergo a separate optical test later in the assembly process.

6.10 CABLE AND FIBRE LAYOUT

6.10.1 HB layout

The light from the scintillator pans are brought to the HPD box with optical cables. These optical cables consist of 18 clear 0.94 mm, s type Kuraray fibres with optical connectors at both ends. The optical fibres are covered with Tedlar to make the optical cables light tight. Nissei Opto Co. takes the clear fibre and makes the 18 fibre cables covered by Tedlar. Nissei made a 10 fibre cable consisting of 0.9 mm clear fibre for CDF.

Fig. 6. 3 is a view of the CMS hadron barrel at the large η boundary looking in the direction of the beam. It shows the routing of the optical cables from the scintillator pans to the HPD box. The optical cables and source tube are enclosed in a hadron cable channel consisting of 1 mm aluminium. The hadron cable channel surrounds the cables from layer 0 to the photodetector box. The channel protects the cables and forms a light tight seal for the cables and optical connectors.

The optical connectors and source tubes connectors protrude into the 53 degree crack. This is done for 2 reasons. If the optical connector were inside the copper, then the top of the optical connector must lie below the top of the scintillator pan. Since the optical connector is 4 mm high and the top plastic is 2 mm high, we would have to route out the scintillator where the connector is. The fibre for this tile would have to move in 4 cm way from the edge of the tile. The best location of the source tube connector is outside the copper. The source tube connector connects the source tube in the pan for the tube for the driver. Since the tube in the pan is on top of the plastic, the source tube connector must stick above the scintillator pan. Hence, if the connector is inside the copper the copper must be milled out where the connector is. The source tube connector must be 8 mm in depth. Hence, the scintillator must be removed where the source tube connector is if it is inside the copper. This degrades the uniformity of the edge tiles.

Fig. 6. 21 shows a top view of the scintillator tray at the end of the megatile. The figure gives a detailed view of the routing of the cables and source tubes at the pan.

Fig. 6.41 is a clasp of this region looking in the direction of the beam. The clear fibres for the pigtail for the middle tray are straight to the connector. while the clear fibres for the pigtail for the side tray are curved. The curve enables the optical connectors for the middle trays and side trays to overlap in phi. This reduces the amount of space need to route the cables in the 53 degree gap. The source tubes cannot cross the optical fibres on the pan. Hence, at the edge of the pan source tubes route out on both sides of the cables. As shown in the figure, the width across the optical connector and source tube connector is 6.05 cm. To further reduce the space needed to route the cables and source tubes in the 53 degree crack, the optical cables are offset with respect to each other, see Fig. 6.41. Therefore, the optical and source tube connectors take up 6.05 cm in the φ dimension for routing. The thickness of the hadron cable channel is 1.1 mm and 3 mm of tolerance separate the edge of the connectors from the inner edge of the hadron cables channel aluminium. The hadron cable channel is 7 cm wide at the lowest radial point. At the photodetector, the cables for the side and middle layers plug into different columns. The total φ width needed for 10 degrees is 11 cm at the photodetector box. Hence, the hadron cable channel will start out with a φ width of 6.85 cm and grows to a width of 11 cm at the photodetector box.

This EPS image does not contain a screen preview.
It will print correctly to a PostScript printer.
File Name : ch6confr.eps
Title : C:\CH6CONFR.EPS
Creator : AutoCAD PSOUT
CreationDate : 1997-06-05
Pages : 1

Fig. 6. 41: Front view of the optical connectors and wire source connectors.

Fig. 6.42 shows a r-z view of the routing of the cables along the 53 degree crack. The optical connector on the pan and connector for the source tube protrude into the 53 degree crack by 1.9 cm. A 0.7 cm cable connector connects to the pan connector. The total protrusion of the optical connectors is 1.9 cm. The 1.9 cm protrusion of the optical connectors is 1.5 cm normal to the 53 degree line. The optical cables bend to follow the 53 degree line. We have verified that the optical fibres are not damaged if their bend diameter is greater than 3.8 cm Taking the minimum bend radius for the optical cables as 3.8 cm, the optical cables bend to be a minimum of 2.9 cm normal to the 53 degree line. The cables are 0.11 cm thick. Near the photodetector box, the cable bundle will be about 28 cables high, and so the cable bundle is be 3.1 cm thick. 7.0 cm of space perpendicular to the 53 degree line will be needed to route the cables at the photodetector box.

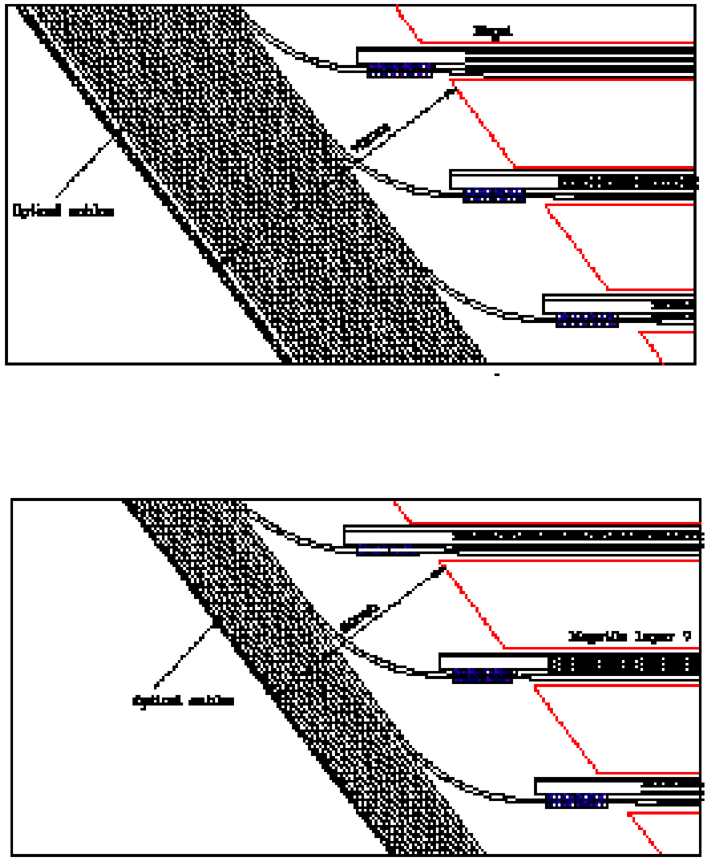

Fig. 6. 42: r-z view of the routing of the cables along the 53^{o} crack.

The permanent source tubes start bending approximately 1.5 cm (in z) from the pan and 1.2 cm (in the direction perpendicularly across the HB-HE gap) from the copper. With a minimum bend radius of 10 cm, these source tubes will rise to be 5 cm away from the HB copper perpendicular to the 53 degree line. Hence, the cover for the hadron cable channel will be 5 cm perpendicular away from the HB 53 degree line At layer 0 the channel contains both the optical cables and the source tubes, with the height of the channel determined by the source tubes. At layer 15 the channel will be 7 cm away from the 53 degree line, with the height determined by the optical cables.

6.10.2 HE layout

Each tray (covering 10^{0} in) has two optical connectors (10 fibres in each), two connectors-mixers for laser calibration and two connectors for radioactive source tubes. Optical cables from the trays go to decoding boxes. In each tray the optical connectors are shifted in such a way that all optical cables can be laid in four layers only not to exceed the space allocated for HE cables, as shown of Fig. 6.43. The quartz fibres in protective skin go from connectors-mixers on the trays to connectors-mixers where the laser light is fanned into 36 fibres corresponding to 36 trays in each layer, see Fig. 6.44. The plastic tubes from radioactive source tubes go around the HE in each layer and end up at the same (protruding from the HE cover plate. The basic idea is shown in Fig. 6.45 and Fig. 6. 46. In this way it will be easy to connect them to control system to check the performance of active elements without interfering with other cables when the calorimeter is moved outside of the magnet coil during a shut down period of collider run.

This EPS image does not contain a screen preview.
It will print correctly to a PostScript printer.
File Name : hfsector.ps
Title : From AutoCAD Drawing "E:\USERS\RONZHIN\HFSI
Creator : AutoCAD
CreationDate : 6697 8:48:2

Fig. 6. 43: Layout of the scintillator tray cables.

It will print correctly to a PostScript printer.
File Name : optic.ps
Title : From AutoCAD Drawing "E:\USERS\RO
Creator : AutoCAD
CreationDate : 6697 8:51:36

Fig. 6. 44: Layout of the optical cables (side view).

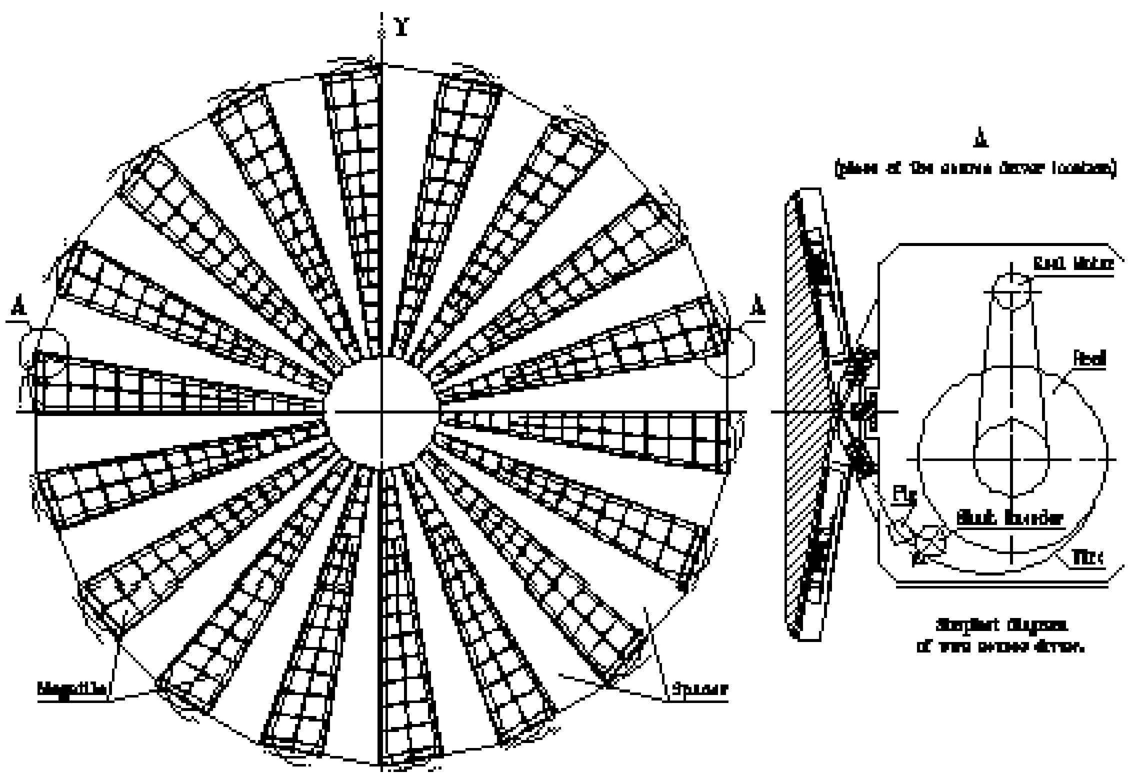

Fig. 6. 45: Layout of the radioactive source tubes.

6.10.3 HOB cable layout

Light from individual tiles in a tray is brought through optical fibre cables to the decoder box, located above the outer most layer of muon station. In each tray there are 4, 5 or 6 tiles depending upon its location. Generally there are 4 fibres per tile (some smaller tiles will have 2 fibres), making a maximum of 25 fibres per tray (24 fibres from the 6 tiles and an additional fibre for transporting laser light to the scintillator tiles). The standard HCAL optical connectors could accommodate 18 fibres. Thus two such connectors per tray will be used. These two fibre connectors will be fixed at one side. Since there are 6 trays in each 30º φ sector, 12 pairs of optical cables (6 pair from six trays of Layer 1 and remaining 6 pairs from layer 2) runs vertically upwards and transport the light to a decoder box located at the outer edge of the muon rings. A 30 mm wide and 5 mm thick corridor in the middle of every 5º φ sector on one side of each muon ring is required to route these cables from the tray edge to the decoder box. The total number of calorimeter towers in a 30º φ sector for ring 0, 1 and -1 is 36. For ring 2 and -2 the corresponding number is 30. There will be a maximum of 8 fibres for each tower (combining layer 1 and 2).

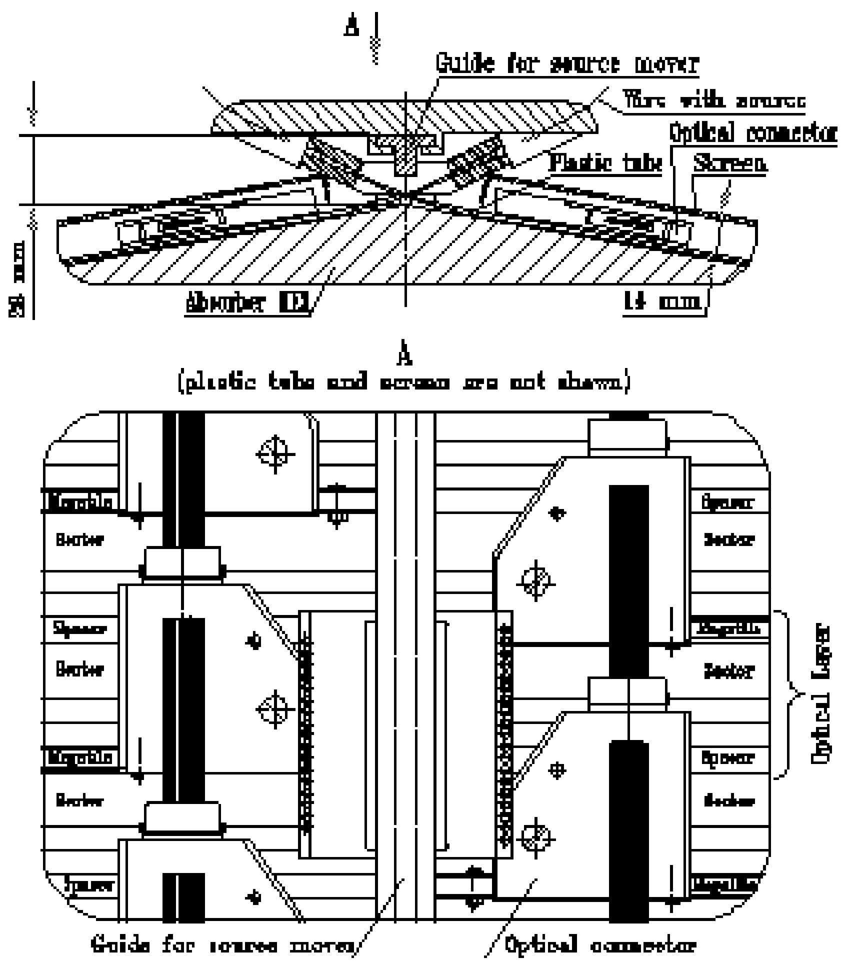

Fig. 6. 46: Layout of source tubes (side view).

6.10.4 HF layout

The umbilical cord of cables and cooling hoses is laid in the 50 cm by 50 cm trench between the transporter tracks. The cables are looped and bound into a bicycle-chain type cable tray. This avoids the triple depth trench which would be required if the bundle were folded back on itself beneath the detector in the running position.

In the garage position the cable bundles are fully extended, while in the operational position approximately 2 meters of slack must be accommodated. This extra 2 meters remains in the trench during beam operation. In intermediate positions 2-7 meters of slack must be accommodated. Since this amount of bundled cable cannot be accommodated in the trench, the trench will be uncovered and the cable bundle looped above it during horizontal moves of the detector. The flexible cable tray is attached to the support structure and will move with it during vertical moves.

6.11 SHIPPING/INSTALLATION

6.11.1 HB shipping/installation

The scintillator pans will be assembled and tested at Fermilab. They will be boxed in wooden boxes at Fermilab and shipped to CERN. The scintillator pan is fairly robust. We have shipped 2 testbeam modules to CERN with no damage to the pans or optical cables. The pans will be shipped to Building 168 where the pans will be installed in the wedges.

At CERN a small sample of pans will be tested with a megatile scanner. This will verify that no damage has taken place. If a small sample of pans are fine, then all the pans will not be scanned.

The pans will be removed from the box and the 'venetian blind', which pushes the pan up against the top of the slot in the copper absorbers will be taped on. The copper wedges will be in Building 168 with the slots for the pans parallel to the floor. The pans will be put on a stretcher and the stretcher will be put up to the slot of the wedge. The pan will be slid into the slot.

6.11.2 HE shipping/installation

HE modules will be manufactured in Russia and shipped by rail to CERN for installation.

6.11.3 HOB shipping/installation

HOB modules will be manufactured in India and transported by ship/rail to CERN for installation.

6.11.4 HOE shipping/installation

HOE modules will be shipped to CERN along with the HB modules.

6.11.5 HF shipping/installation

We anticipate that HF modules will be assembled in Hungary and shipped by rail to CERN.

6.12 ACCESS, MAINTENANCE AND OPERATIONS

6.12.1 HB/HE access, maintenance and operations

The optical system is sealed. Other services will be covering the optical system. Hence, we will have no access to the optical system. We anticipate that no access is needed. If we need to access optical system, other services can be removed and we can get at the optical cables and scintillator pans.

During the access period we will do a full source scan of all the tiles. This will determine whether any part of the optical system has deteriorated from radiation or other sources. The expected radiation levels are small enough that we expect the light output from the system to decrease no more than 7% over 10 year lifetime of the detector.

6.12.2 HOB access, maintenance and operations

One end of HOB modules will be untrapped, so trays could be removed, if needed.

6.12.3 HOE access, maintenance and operations

HOE will be attached to the Endcap muon chambers and could be only repaired when muon chambers are removed.

6.12.4 HF access, maintenance and operations

Alignment of the detector and maintenance of the optical systems will be carried out from the platform support of the detector or in the garage position. At beam height, access is provided by a portable scissors. This device is stored in the garage during beam operation to protect the hydraulics from radiation. The electronic modules in the racks are accessed and maintained easily in the garage position. In the case of a need to access the electronics racks when the detector is in the elevated beam position, the portable scissors will be used. The PMT boxes are protected by endplug shielding in operational position. Access to the PMT boxes requires no removal of heavy shielding elements.

References

[1] P. Gorodetzky, Rad. Phys. And Chem. 41 (1993) 253.

[2] J. B. Chesser, IEEE Trans. Nucl. Sci. 40/3 (1993) 307.

[3] V. Gavrilov et al., CMS TN/94-324.

[4] CDF End Plug Hadron Calorimeter Upgrade, P. de Barbaro at al, IEEE Trans. on Nucl. Science, vol 42, #4, p510-517.

[5] A. Holmes-Sidle and L. Adams, Handbook of Radiation Effects, (1994) Oxford U.P., Oxford, U.K.

[6] J. Wong and C.A. Angell, Glass: structure b y spectroscopy (1976) Dekker, Basel.

[7] Optical Radiation Corp., Azusa, CA, 91702, USA.

[8] Optic-Forms, Inc. Temecula, CA 92590, USA.

Table of Contents

7. OPTICAL-ELECTRONIC INTERFACE SYSTEM

7.1 OVERVIEW AND REQUIREMENTS

The front-end interfaces of the hadron calorimeter consist of a distributed set of units called "decoder" boxes, which are located strategically "on detector". While the name is derived from the optical function performed by these interfaces, in reality the units serve as a control point for a variety of functions, including: light collection and optical signal processing using fibre-optic light guides, operation of the phototransducers which are multi-channel Hybrid Photodiodes (HPDs) which detect and amplify the calorimetric signals, digitisation of the signals to 15-bit precision, and transmission of these digitised signals "off detector" to the Trigger/DAQ system. Additionally, the decoder boxes are the optical calibration interface, receiving input laser calibration signals and routing these to test HPD pixels and to test the scintillation tiles for response and ageing. An additional LED test feature for calibration of the HPDs is also provided which is independent of the Laser system and useful in the construction and assembly phase when the laser is unavailable.

To provide this functionality, decoder boxes support numerous interconnections. A schematic is shown in Fig. 7. 1. These include: input of optical signals from the detector; input of laser calibration signals from the counting room; input of HV to operate the HPDs; input of LV for HPD bias and separate LV inputs for operation of the preamps, digitisers, and line drivers; input of test pulses for the LED drivers; input of TTC (slow controls signals); connection to cooling water for temperature control; and connection to dry N_2 gas flow to protect the HPD cathodes from He poisoning. [Control and operation of the source tube driver is independent of the decoder box and is described elsewhere.]

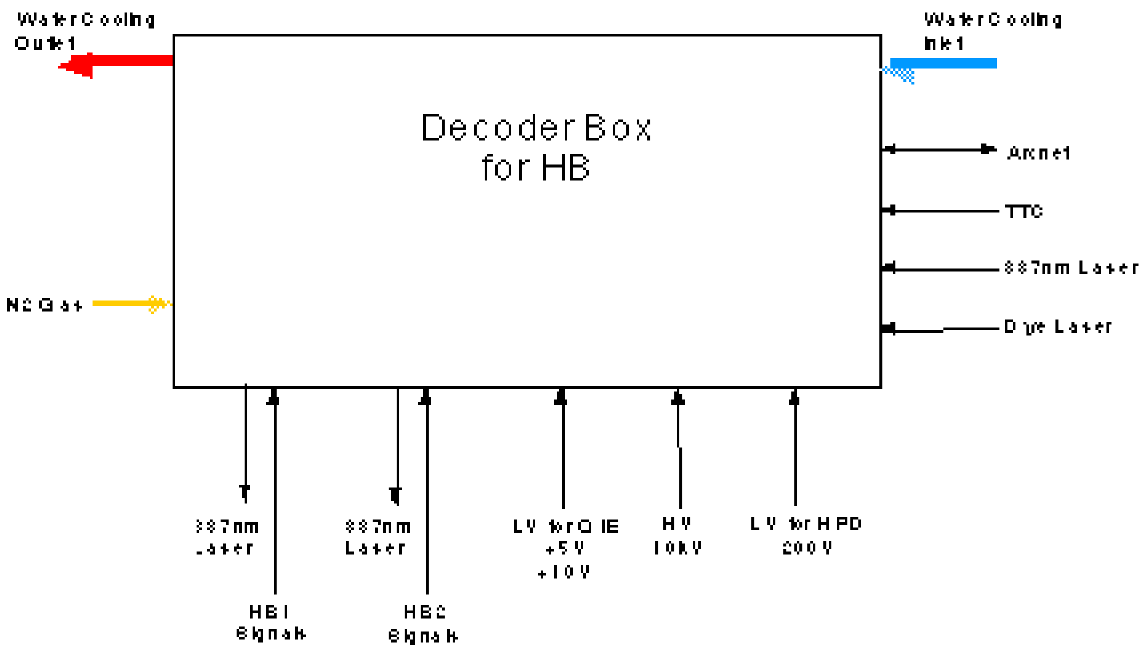

Fig. 7. 1: A system/interface schematic of a HCAL decoder box (or DBX). The example is for the HB subsystem, but is representative of all HCAL subsystems.

The actual configuration of the decoder boxes depends upon the HCAL subsystem involved: HB, HE/HOE, HOB-0, HOB1 and HOB2. While the global requirements for each detector are similar, there are regional differences in channel counts, configurations of sampling layers, numbers sampling layers to summed, and calibration requirements. Table 7. 1 summarises the number of decoder boxes and HPDs per HCAL subsystem. Overall there are 120 decoder boxes supporting a total of 456 HPDs. Table 7. 2 summarises the number of active pixels, calibration monitors (PIN diodes), and readout (QIE) channels for each subsystem. In the following sections we enumerate the design considerations appropriate to each subsystem.

Table 7. 1

Subsystem decoder box/hybrid photodiode summary.

HCAL Subsystem	[illegible]	[illegible]	[illegible]	[illegible]	Total [illegible]	Total [illegible]	Total HPD
HB+,HB-	[illegible]	[illegible]	[illegible]	[illegible]	[illegible]	[illegible]	[illegible]
HE+,HOE+	[illegible]	[illegible]	[illegible]	[illegible]	[illegible]	[illegible]	[illegible]
HOB-2,-1,+1,+2	[illegible]	[illegible]	[illegible]	[illegible]	[illegible]	[illegible]	[illegible]
HOB-0	[illegible]	[illegible]	[illegible]	[illegible]	[illegible]	[illegible]	[illegible]
Total [illegible]	[illegible]	[illegible]			[illegible]	[illegible]	[illegible]

Table 7. 2

Decoder box HPD pixel and readout electronics summary.

[illegible]

[illegible]	[illegible]	[illegible]	[illegible]	[illegible]	[illegible]	[illegible]	[illegible]	[illegible]	[illegible]	[illegible]	[illegible]	[illegible]	[illegible]
[illegible]	[illegible]	[illegible]	[illegible]	[illegible]	[illegible]	[illegible]	[illegible]	[illegible]	[illegible]	[illegible]	[illegible]	[illegible]	[illegible]
		[illegible]	[illegible]	[illegible]	[illegible]	[illegible]	[illegible]	[illegible]	[illegible]	[illegible]	[illegible]	[illegible]	[illegible]
		[illegible]	[illegible]	[illegible]	[illegible]	[illegible]	[illegible]	[illegible]	[illegible]	[illegible]	[illegible]		
						[illegible]	[illegible]	[illegible]					
[illegible]	[illegible]		[illegible]	[illegible]	[illegible]	[illegible]	[illegible]	[illegible]	[illegible]	[illegible]	[illegible]	[illegible]	[illegible]
[illegible]	[illegible]		[illegible]	[illegible]	[illegible]	[illegible]	[illegible]	[illegible]	[illegible]	[illegible]	[illegible]	[illegible]	[illegible]
[illegible]	[illegible]	[illegible]	[illegible]	[illegible]	[illegible]	[illegible]	[illegible]	[illegible]	[illegible]	[illegible]	[illegible]	[illegible]	[illegible]
[illegible]	[illegible]	[illegible]	[illegible]	[illegible]	[illegible]	[illegible]	[illegible]	[illegible]	[illegible]	[illegible]	[illegible]	[illegible]	[illegible]
[illegible]	[illegible]	[illegible]	[illegible]	[illegible]	[illegible]	[illegible]	[illegible]	[illegible]	[illegible]	[illegible]	[illegible]	[illegible]	[illegible]
[illegible]	[illegible]							[illegible]		[illegible]	[illegible]		[illegible]

7.2 HB OVERVIEW

HB refers to the hadronic calorimetry in the barrel region and within the 4 Tesla solenoid field. HB is constructed in wedge assemblies that are functionally divided at the midplane of the detector into two halves HB+ and HB-. For purposes of this discussion, we consider only one end of the detector and refer to it generically as HB. HB consists of 18 wedges, subtending 20 in , and each wedge is served by a decoder box which is located in the corner of the wedge at largest r and |z|. Additionally, HB is operationally divided into two longitudinal (depth) sections: HB1 which provides for up to three layers of initial sampling of a shower just at the exit of ECAL, and HB2 which consists of 17 sampling layers. Each sampling layer of HB1 and HB2 is subdivided into four intervals and up to 17 intervals. This planar unit of 68 elements is called a megatile.

Optical signals from the megatiles are conveyed via ribbon cables of fibre-optic waveguides up the 53 crack that delimits the barrel region to the decoder box for signal processing. Laser calibration signals are conveyed in the opposite direction from the decoder box to the megatiles via quartz fibre.

Low voltage power, high voltage services, cooling water, nitrogen gas, TTC and ancillary control signals are supplied via the radial crack (at |z| ~ 6.7 m) just beyond the end of solenoid, as are laser calibration signals. Digitised, optical signals destined for the DAQ system follow a similar routing.

7.2.1 HB front-end optical layout

Fig. 7. 2 shows a schematic of the mechanical and electrical layout of an HB decoder box (or DBX), and Fig. 7. 3 shows the optical layout. The DBX has external dimensions: 75 cm25 cm11.8 cm. The materials from which the box will be fabricated are non-magnetic: aluminium, copper, brass and plastics. The DBX is mounted onto the steel backing plate of the calorimeter wedge. It consists of two compartments which are optically isolated: a fibre-optic compartment and an electronics compartment. Five HPDs are mounted on the lateral interior wall between the two compartments.

Access to the fibre-optic compartment is via optical connectors at two optical patch panels, one at each end of the box. Each patch panel (Fig. 7. 4) is of 9.5 cm9.5 cm0.6 cm thick aluminium, and serves as the mounting surface for up to forty-two optical connectors arranged in two columns of twenty-one connectors. Each column corresponds to a 5 interval. Each connector (Fig. 7. 5) supports 18 multiclad fibres of 940 m diameter on a pitch of 1.4 mm, and each fibre within a connector corresponds to one of 17 subintervals within a megatile. The extra fibre is either a spare or a calibration fibre. Each of the optical connectors is surface finished by diamond flycutting - to provide for excellent optical transmission through the connector (>85%).

This EPS image does not contain a screen preview.
It will print correctly to a PostScript printer.
File Name : HB.EPS
Title : (Adobe Illustrator (R) Version 3.0 Full Prolog)
Creator : ImageMark Software Labs
CreationDate : (7/22/89) ()

Fig. 7. 2: Schematic of the mechanical and electrical layout of a HB decoder box.

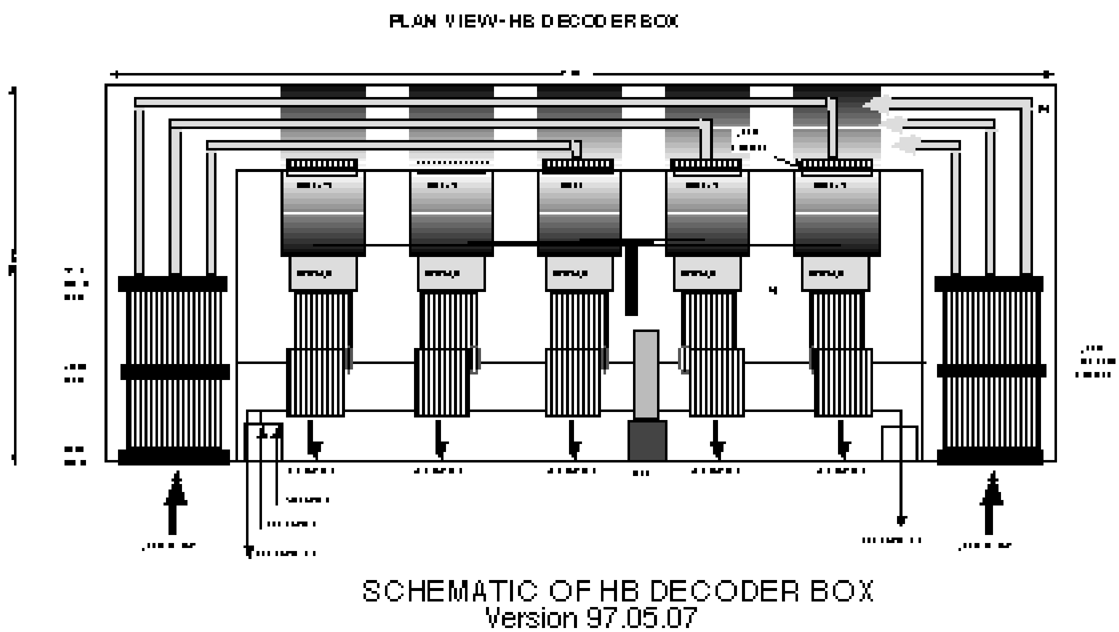

Fig. 7. 3: Schematic of the optical paths within a HB decoder box.

All optical signal fibres used in the overall HCAL system and within the decoder boxes are of 940 m diameter, multiclad construction, with polystyrene core, PMMA and fluorinated acrylic claddings. Because of the tight turning radii within the box (r~4 cm) and the need for flexibility, Kuraray S-type fibre is used for all interior optical interconnections.

Fig. 7. 4: Schematic of an optical patch panel for a HB decoder box.

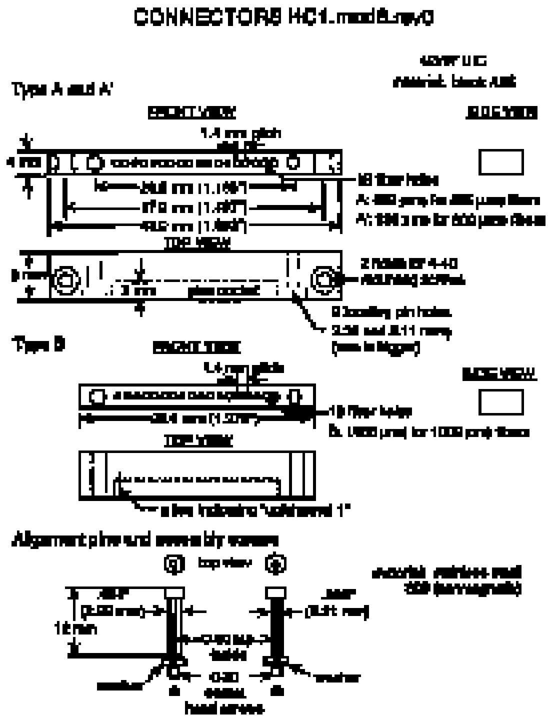

Fig. 7. 5: Optical connector design specifications for 18-fibre connector.

Certain of the megatiles of HB2 require special consideration in the placement and routing of their optical waveguides, because they are located either directly behind or immediately beneath the decoder box, and hence optical connectors would be trapped (or blocked) as is the case for layers 13-16, or because they are located on the outer surface of the wedge and are mounted to the back of the stainless steel plate (layer 17). These special waveguides will have identical optical connectors to the normal flat-ribbon waveguide connections, but the fibre bundles of the guides will be of cylindrical cross section over most of their length and hence will be more flexible than are the standard, flat ribbons.

Additionally on the optical patch panel, there are four connectors each supporting a quartz optical fibre for transmission of laser calibration signals to selected megatiles, to monitor timing and scintillator/waveshifter ageing.

7.2.2 HB fibre decoder structure and mapping7.2.2.1

HB formation of tower geometry

Within the optical compartment, and ~10 cm behind the optical patch panel (Fig. 7. 6), is a Delrin "sorting" plate through which the interior optical fibres are organised into HB1 and HB2 subgroups and also into tower geometry. A plate schematic is displayed in Fig. 7. 7. For HB1 there are 34 "tower bundles" of up to three fibres, and for HB2 there are 34 tower bundles of 17 fibres. The holes in the sorting plate are oversized, so that the fibres simply pass through with no constraint. The bundles are then inserted into tubes held in a tube holder plate and routed to the HPDs. Additionally, a pair of multiclad fibres of 300 m diameter are inserted into each bundle. These are optically connected to the Y11 mixers of the dye laser/LED calibration system to provide an independent monitor of the sensitivity and gain of the HPD pixels. Fig. 7. 6 also displays schematically this implementation.

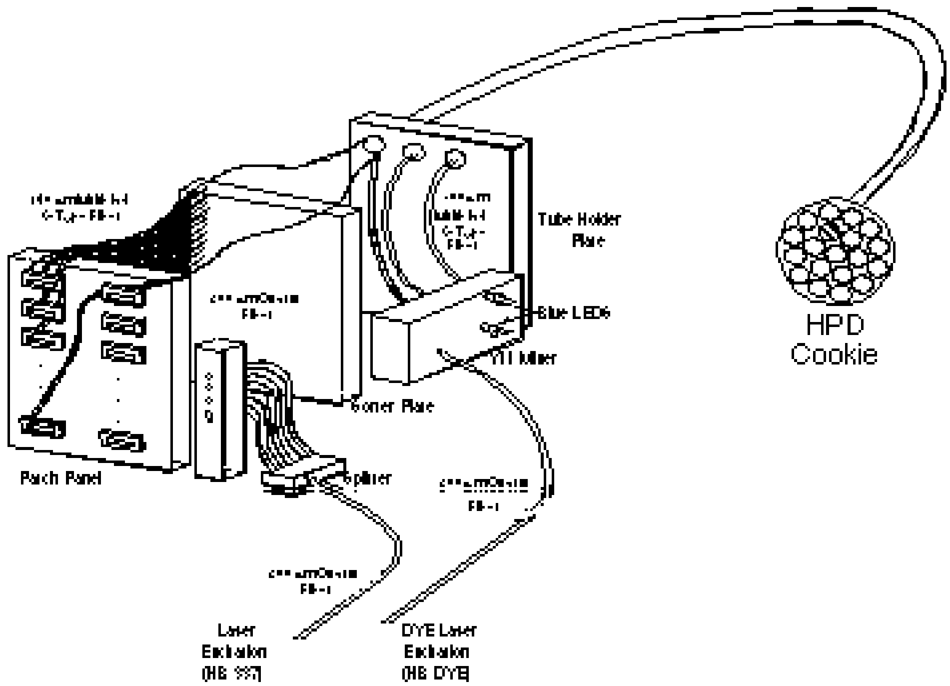

Fig. 7. 6: Decoder box optical compartment elements.7.2.2.2

HB mapping to hybrid photodiodes

The HB2 bundles from one of the patch panels are mapped onto two 19-channel-format HPDs, designated HPD19-1 and HPD19-2 in Fig. 7. 3. Note that these are located on the far side of the optical compartment from the patch panel to allow for more adiabatic routing of the fibre bundles. The HB1 bundles from the patch panel are mapped onto half of the available pixels of a 73-channel-format HPD, designated HPD73 and positioned centrally relative to the optical compartment.

In a similar fashion, the HB2 bundles from the opposite-side optical patch panel are mapped onto the two remaining 19-channel HPDs (HPD19-3 and HPD19-4), and the HB1 bundles from that side are mapped onto the remaining pixels of HPD73.

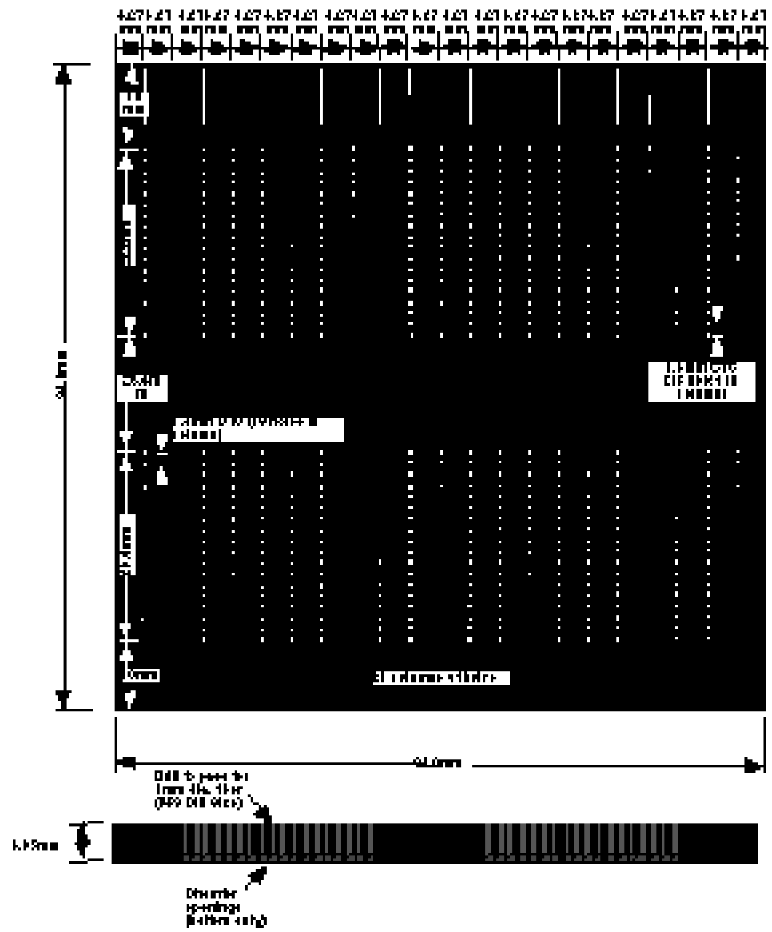

Fig. 7. 7: Delrin sorting plate format.

A mapping scenario is presented in Fig. 7. 8, which indicates a pixel mapping for one of the four = 5 intervals onto the HPDs within the HB decoder box. Choices of HPD location and pixel position are driven by the need to keep fibre bend radii as large as possible within the space constraints and for "simplicity" of the pattern of fibre routing.

To provide accurate alignment of the fibre bundles to the pixels of the HPD tubes, the fibre bundles are gathered into thin-wall sleeves (100 m thick wall), that are routed from the sorting plates. The sleeves stop short of the cookies. Only the fibres are inserted and glued into holes in 1.5 cm thick Delrin cookies. (See Fig. 7. 9.) The faces of the cookies are optically finished by diamond flycutting and are held in proximate contact with the HPD fibre-optic entrance windows by 50 m thick spacers. The cookies are physically mounted onto the interior lateral dividing wall that separates the optical and electronic compartments of the decoder box. The HPDs are spring loaded into sockets to hold them in alignment with the cookies.

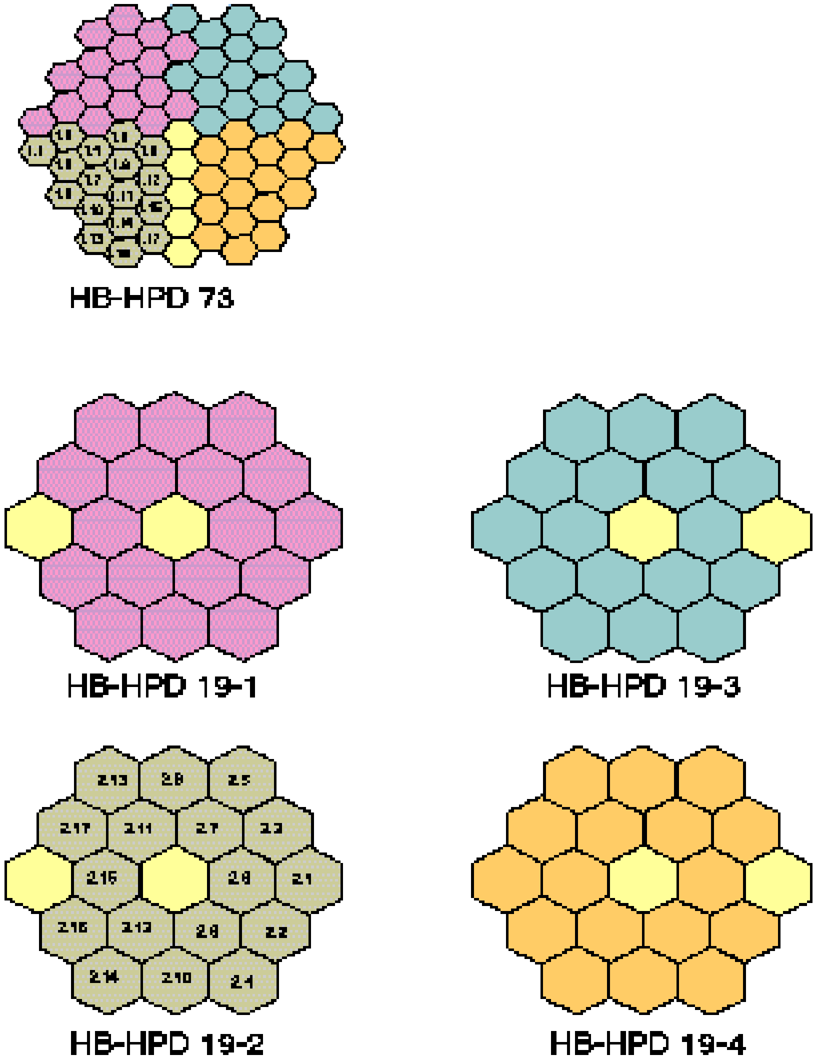

Fig. 7. 8: HB Fibre/pixel mapping scenario. The mapping of 1/4 of the channels within the decoder box is indicated, corresponding to 17 towers in a = 5 interval. The HB1 towers are mapped to the HPD73 tube; the HB2 towers are mapped to one of four HPD19 tubes.

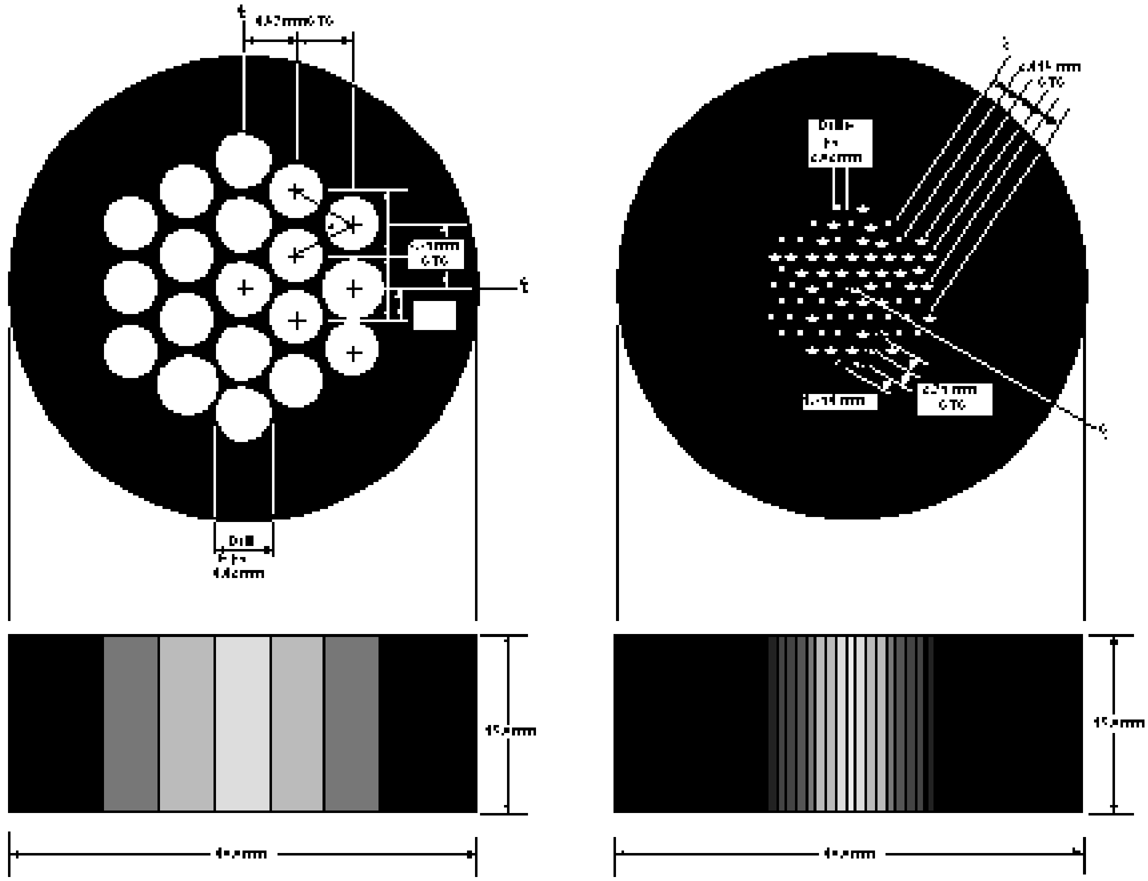

Fig. 7. 9: Delrin cookies which provide alignment of fibre bundles to the HPD faceplates in HB decoder boxes. Schematics for 19-channel and 73-channel HPDs are indicated. The 19-channel design supports up to 17 fibres of 940 µm diameter plus one or two 300 µm diameter calibration fibres per hole. The 73-channel plate supports up to three fibres of 940 µm diameter plus one or two 300 µm diameter calibration fibres per hole. [Holes for alignment pins and mounting bolts are not shown.]

Alignment concerns include: misalignment of fibre bundles relative to the HPD pixels; effects of numerical aperture of the light exiting the fibre bundles; and misalignment of tube axes relative to the direction of the local magnetic field direction.

Mechanical: The cookie is registered with alignment pins provided on the HPD which will allow for a placement tolerance of <100 µm between fibre bundles and HPD pixels.

Optical: Because of surface imperfections (surfaces of the cookies are not optically flat), the light exiting a fibre bundle will diverge according to the numerical aperture of the fibre as it passes through an airgap between the cookie and the fibre-optic faceplate of the HPD. To compensate for local surface imperfections, the Cookies and HPD faceplates will be shimmed apart by a 50 m spacer. Crossing this gap this will lead to an "expansion" of the optical image by ~50 µm in radius, as the exit angle is slightly larger than 45.

Magnetic: The mounting structures for the HPDs are expected to hold the HPD symmetry axes in alignment with the magnetic field direction to within 3. Every 3 of misalignment of the HPD axis relative to the B-field will lead to a 100 µm offset of the photoelectron image in the HPD.

The 27.5 mm format HPD is tolerant of misalignments: up to 485 m in the 19-channel tube for HB2 (Fig. 7. 10) and up to 570 m in the 73-channel tube for HB1 (Fig. 7. 11). In the event that three layers of HB1 must be combined, the misalignment tolerance is 330 m in the 73-channel tube (Fig. 7. 11).

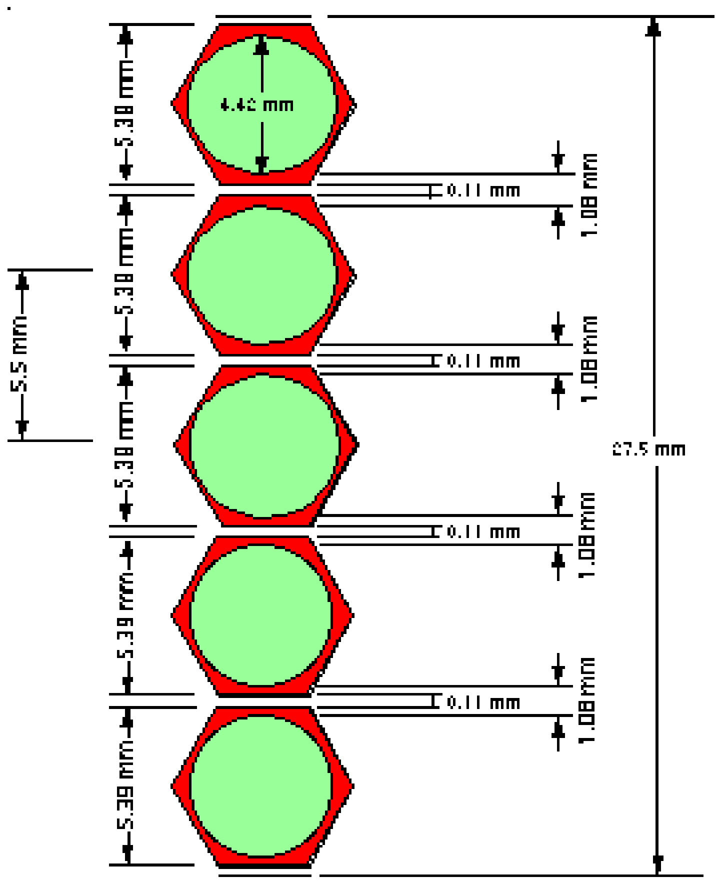

Fig. 7. 10: Flat-to-flat pixel layout across a 27.5 mm format HPD for a tube design supporting 19 channels. The circular area is the region within which a perfectly aligned optical image of a bundle of 17 fibres of 940 µm diameter is located. This is representative of the HB2 configuration. This optical image can be shifted by mechanical misalignments, optical effects, and magnetic field effects. There is 485 µm of tolerance to the edge of a pixel. This includes room for one or two 300 µm calibration fibres.

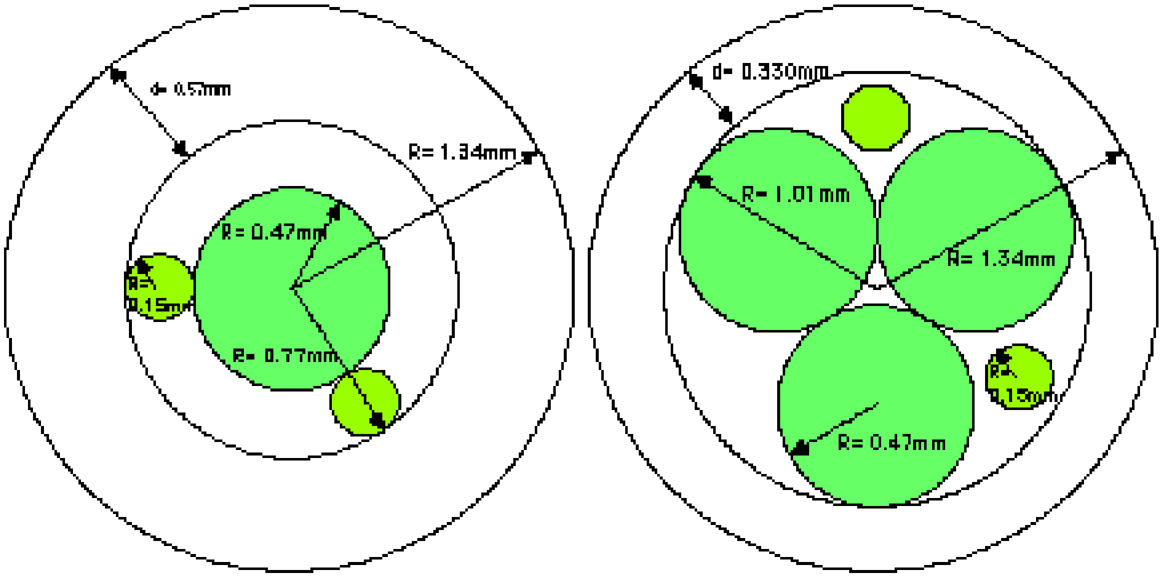

Fig. 7. 11: HB1 fibre configuration presented to a pixel of a 73-channel HPD, in the baseline case where a single layer is imaged per pixel, and for a hypothetical case of three layers combined per pixel. Small diameter fibres are for calibration signals. Here the outer circle indicates the position of the nearest edge (or flat) of the hex-shaped pixel. An alignment tolerance of 570 µm is indicated for the single-fibre configuration, and 330 µm for the three-fibre configuration.

7.2.3 HB front-end electronics layout

Approximately half the decoder box volume is allocated for electrical and support services for the HPDs, for signal amplification, digitisation, and optical signal drivers, for calibration and slow controls functions, and for water cooling and thermal monitoring. The output signals from the active HPD channels (136 of the available 149 channels are associated with active detection elements) are routed to readout boards located in an internal custom crate structure, with signal lead lengths kept as short as possible. The ceiling and floor of the electronics compartment are water-cooled copper plates to maintain all regions of the decoder box at or below a temperature of 26 C.

Services to the HPDs include: Photocathode high voltage (-10 kV), bias voltage to the silicon (typically 100 V), and supply voltages for the QIE preamp/digitiser/driver boards (+5 V and +10 V). These are supplied to the decoder box via a panel on the "front face" (Fig. 7. 2).

All HPDs used in HB will be operated at a photocathode voltage near -10 kV. These will be fed individually from outside the detector over minicoax to each HPD. Similarly, LV bias (~100 V) for the silicon substrates of each HPD will also be supplied individually via minicoax from supplies located outside the detector. These electrical power services are routed to the decoder boxes through the radial crack (|z| ~6.7 m) at the end of the solenoid magnet.

Water temperature and flow sensors are placed on the entrance and exit ports of the water lines outside the detector.

The electronics layout (Fig. 7. 2 and Fig. 7. 3) includes HV distribution, two LV systems, and ancillary controls, calibration, and monitoring systems. Each HPD channel is amplified and digitised in a QIE chip. HPD outputs are multiplexed (three channels per optical link) and driven via laser diodes off-detector to the trigger and data acquisition system. Forty-eight optical cables are required to transfer the digital signal information. Water cooling is required for the electronics compartment because of power dissipation in the QIE chips and the laser diodes which are used to drive the digital signals off-detector..7.2.3.1

HV layout

Five commercial minicoax cables import the required 10 kV photocathode voltage to each HPD within the decoder box. Power supplies are located outside the detector.7.2.3.2

LV layout

There are two distinct LV systems supplied to the decoder box. One provides bias to the HPD silicon substrates and is supplied by minicoax. The other involves high current feeds for amplification, digitisation and signal processing, and for calibration and monitoring.7.2.3.2.1

LV for HPD bias

Five commercial minicoax cables import the required 100 V bias to each HPD substrate in the decoder box. The cables should be rated to supply 200 V max. at a very small (nanoamps) standing current. Power supplies are located outside the detector.7.2.3.2.2

LV for signal processing and monitoring

The low voltage requirements for the QIE, FADC, DBC and drivers are based upon the experience of KTeV and work done for CDF on the new QIE6. We estimate that the requirements for each crate would be 75 amps at +5V and 15 amps at +10V. The high current will require the back plane of the electronic compartment to be supported with adequate bus bars to distribute and handle the supply and return current paths.

The backplane located in the decoder box will have a connection to the slow control network via a J-TAG which will use a low speed (1 MHz) serial link to send and receive data. Implemented on the backplane will be voltage and current monitors to sense low voltage supply status. This information can be read back to the control room every few minutes for monitoring purposes. A micro-controller on the backplane could shut down the system in the event of excursions in voltage, current or temperature limits are exceeded. Note: It is expected that individual boards within the crate will be protected by "poly-fuses" which open on an overcurrent and close once power is removed.

As in the case of supply voltages and currents above, the backplane will also support temperature sensors, four in the electronics compartment and two within the optical compartment. These will allow the system to monitor the decoder box temperature and to shut power services down if limits are exceeded.

Due to the large currents involved in the low voltage supply, it is assumed that the supply leads will be hardwired to the crate using adequate cable for the currents specified.

The connection to the slow control network would be via a 3- or 5-wire serial link which could be daisy-chained from crate to crate or supplied directly to each crate. In either case, the connector would likely be very small and captive locking so that it would not disconnect accidentally.

The water supply for the cooling system needs to provide about 1.0 US gal/min of cooling water. This could be made via hard connections or quick disconnects. We prefer the hard-line connections since the quick disconnects might leak or come uncoupled. Once in position, the decoder boxes are essentially permanently fixed and, should a Box need to be removed, unsoldering the water lines would be a minor addition to the complexity of the task.

The cooling of the circuitry in the electronics compartment is performed primarily via conduction through PC boards and air to copper plates in physical contact with the cooling water. The volume of the electronics compartment is basically divided into < 100 separate compartments, each of which is surrounded on six sides by copper walls which provide a low thermal impedance to the cooling water. Each compartment dissipates about 1.0 W. This scheme should keep the entire heat load away from the fibres which are heat sensitive and should keep the chips cool enough to keep lifetimes long. We estimate the maximum chip package temperature to be 40 C.

The readout scheme uses a QIE chip followed by a commercial five bit FADC and a DCS (digital clocking synchroniser) chip. The QIE is a pipelined chip which has no dead time and basically provides two outputs which are valid four clock cycles after the cycle of interest. Its pipeline length is four ticks plus one for the output. In every clock cycle, the QIE outputs a three bit digital number which corresponds to the exponent of the input current and an analog voltage which corresponds to the mantissa of the input current. The exponents go directly to the DCS while the analog voltage is sent to the FADC. The QIE also sends to the DCS a two bit capacitor ID number which corresponds to the capacitor (one of four) which tells the user which cap in the pipeline was used. Since capacitors can differ slightly in value, this number is needed for calibration and correction of the data off-line. Experience with KTeV has shown that the caps are equal to within a few percent without any correction, and that the value can be measured to ~ 0.1% off-line.

One clock tick later, the FADC has produced a five bit digital mantissa for the analog input from the QIE. This mantissa is sent to the DCS which receives it and synchronises it with the exponent data from the QIE. The synchronisation takes another two clock ticks and with one tick for the FADC, the total latency of the pipeline is eight ticks.

At this point the DCS has a complete data word: a two bit Cap-ID, a three bit exponent, and a five bit mantissa. The data is then sent to a parallel-to-serial converter chip and a laser diode driver which drives the data from the decoder box to the counting room. There the data is split: part to make a trigger, the other part stored locally awaiting a trigger decision. Every clock tick, another full data word is sent from the decoder box. Note: since the speed of the laser optical link is 1.2 Gigabits/sec, it is possible to multiplex three channels of HCAL data onto one optical link. Thus the number of laser drivers needed is 1/3 the number of active channels in the decoder box.7.2.3.3

Calibration layout

Two optical calibration systems, laser and LED, are supported within the DBX. A schematic is indicated in Fig. 7. 6. These, together with a source-tube calibration system, are used to correlate absolute calibration measurements from the test-beam with signals from in situ calorimeter megatile layers and to monitor and maintain the relative calibration of these calorimeter elements over time.

Laser calibration of scintillation elements is provided for selected megatile layers HB1.1 and HB2.9 only: the first, because it is the primary (and presently the only) layer of the first sample and near shower maximum; the second, because it provides a monitor deep in the calorimeter, relatively far from shower max, yet which samples most of the towers in .7.2.3.3.1

Nitrogen laser calibration at 337 nm

Laser pulses from the CMS calorimeter laser calibration system are input into each DBX. (Refer to Fig. 7. 12). Two 200 m diameter quartz fibres are utilised. One set of laser pulses excites the megatiles directly, to monitor scintillator and waveshifter ageing. This excitation wavelength is 337 nm and is derived from the primary (nitrogen) laser. This calibration pulse is supplied to two selected layers of the HB at selected depths within the tower structure: HB1.1, the first sampling layer of HB, and HB2.9 which is located approximately midway in depth in a tower. An additional requirement of this link is to set and monitor the relative timing of the megatiles. The incoming 337 nm laser lightguide is divided into nine individual quartz waveguides on a receiver card located within the electronics compartment of the DBX. Eight of these waveguides are exported via the patch panels (four through each) to megatile layers HB1.1 and HB2.9. The remaining waveguide is coupled to a photodiodes situated on the receiver card to monitor the laser timing and light intensity.

The optically-induced pulses in the megatile scintillator will be used to cross-check source tube measurements in the same megatile layers and to facilitate time-slewing corrections for each channel.7.2.3.3.2

Dye laser and LED calibration at 430-450 nm

The second laser link (Fig. 7. 12) transmits pulses from a dye laser at a wavelength of 430-450 nm, which will activate two Y11 waveshifter mixers located within the DBX. The Y11 mixers are fibre-optically coupled directly onto each HPD pixel. (Refer to Fig. 7. 6.) These pulses measure the HPD cathode responsivity and provide a monitoring measurement independent of the characteristics of the megatiles.

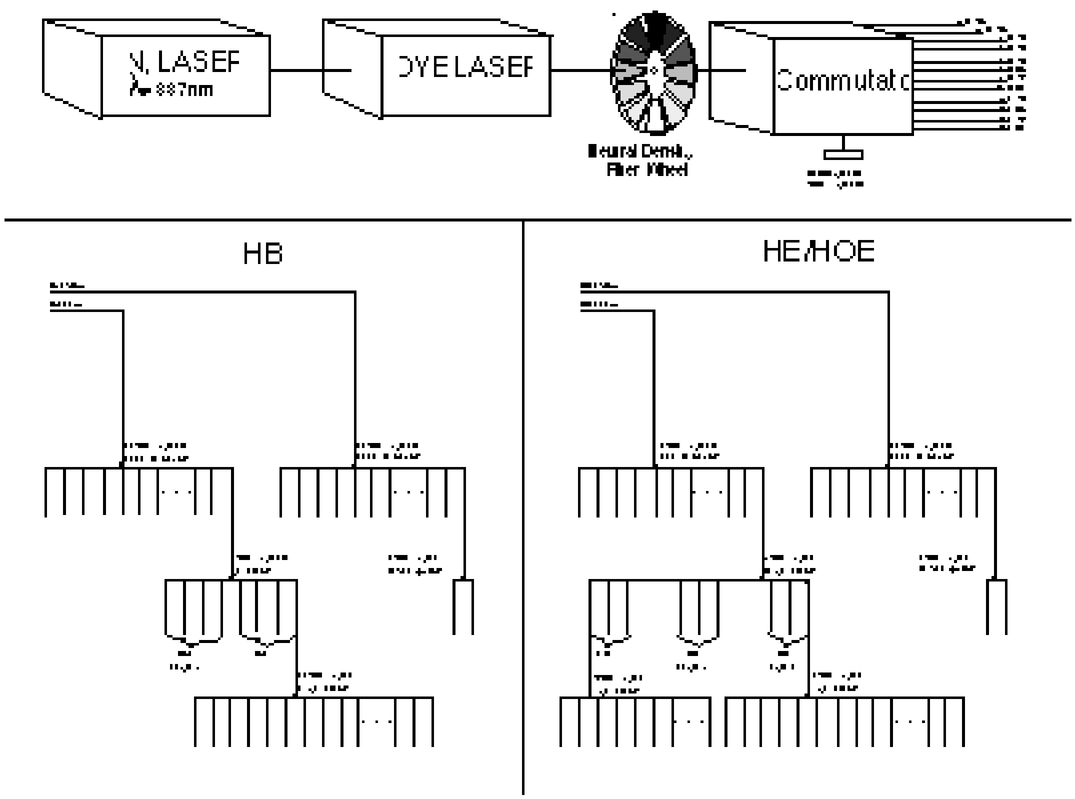

Fig. 7. 12: HCAL laser calibration system, as it applies to HB and HE subsystems.

This calibration task of the HPD pixels is also shared with a blue LED (430-450 nm) pulser system. Test pulses received from the counting room via a twisted pair driver can excite the LEDs which are optically connected to the same Y11 mixers as the laser system. This provides an independent measure of the single photon response of the HPDs and, additionally, provides for a full test capability of the DBX during fabrication and bench testing, when there will likely be no laser access.

7.2.4 HB system interfaces

The decoder boxes must maintain appropriate operating voltages, temperature controls, and diagnostic information to monitor and maintain stable operation of HB1 and HB2 elements. A TTC interface is included in each DBX.

7.2.5 HB monitors and controls system

Numerous monitor and controls functions are required in every DBX. It is expected that these will be served via the TTC.7.2.5.1

Temperature monitor

Temperature monitoring is required to protect the electronics and especially to prevent temperature excursions which could damage the optical fibres resident in the optical compartment. Six temperature sensors will be provided per DBX: two in the optical compartment and four in the electronics compartment. Temperature excursions would result in a shutdown of the LV feeds to the QIE boards. A similar shutdown would occur if temperature indicators or flow indicators on the return lines of the cooling water show an excursion.7.2.5.2

HPD HV and LV monitors

The photocathode high voltage, low-voltage silicon bias and associated currents will be independently controlled and monitored for each HPD from crates outside the detector. For HB, five individual HV lines and five individual LV lines will be supplied to each decoder box. Voltage or current excursions or faults will result in the shutdown of the offending HPD from the system.7.2.5.3

LV monitor

Low voltage (+5 V and +10 V) will be supplied from outside the detector by two separate input lines to the bus of the crate structure within the DBX. These services will be used to support the QIE preamp/digitiser/driver cards, for the LED drivers, and for photodiode operation. Current and voltage values will be controlled and monitored from the outside the detector. The bus lines in the electronics compartment which provide LV internally to the QIE boards, will be fused with resettable polyfuses. Individual QIE boards will be similarly fused.7.2.5.4

Optical fault/DBX closure

Monitors will be provided to assure that HPD high voltage cannot be activated when any of the decoder box covers are removed. This essential safety requirement will be provided by three distinct systems: light sensing using photodiodes: current monitoring of spare HPD pixels: and by sense switches to assure continuity of material (box closure).7.2.5.5

Gas monitor

To prevent helium gas poisoning of the HPDs, dry nitrogen gas at slight overpressure will be circulated within the DBX.7.2.5.6

Water flow monitor

Water flow indicators and temperature sensors will be located outside the detector in the return lines.7.2.5.7

Laser and LED monitors

For the 337 nm laser, a photodiode will be used to monitor laser timing and laser power. For dye laser and blue LED excitation of the Y11 mixers used in direct tests of HPD photocathodes, photodiodes will be used to monitor the light directly in the Y11 mixer, and will be common to both systems. A photodiode will be used to monitor each individual Y11 mixer block, of which there are two for each HB decoder box. These photodiodes will be read out via the same readout boards (QIE boards) just as other data signals.7.2.5.8

QIE controls

Interfacing capability is required to download thresholds and timing trims to the QIE circuitry. This will be accomplished via the TTC network.

7.2.6 Access, maintenance, and operations

The decoder boxes will be designed to be maintenance free. However, currently the actual effective "lifetime" of an HPD tube (time to failure) is unknown. Eventually, one might expect some tubes to be replaced over the lifetime of the experiment. Because of the large array of electrical, optical, plumbing and other services which are routed up the 53 crack, and which effectively obscure any substantial access to the decoder boxes, only simple adjustments can be made without functional disassembly of services in front of the boxes. Service to the boxes could be effected when an endcap is withdrawn and "easier" access is available.

7.3 HE/HOE OVERVIEW

7.3.1 The inner endcap calorimeter (HE) layout

HE refers to the hadronic calorimeter in the endcap regions that is situated within the 4 T field. There are two such structures, one at each end of the CMS detector and labelled HE+ and HE-. Here we consider only one end of the detector and refer to it generically as HE. HE consists of 36 sector assemblies, each subtending 10 in , and every three sectors are served by a decoder box (DBX) which is located at the outer radius of the sector (large r and small || region). Sampling layers comprise HE, and the individual layers (or megatiles) are mechanically subdivided into 5 or 10 intervals in and up to 14 intervals in . HE is also logically divided into longitudinal (depth) sections. HE1 consists of a single layer of sampling of a shower just at the exit of the endcap ECAL. The sampling in depth behind HE1 is more complex than for the barrel calorimeter (HB) case, because of the increased radiation field. In the high || region where integrated radiation levels are expected to reach several Mrads during the course of the experiment, additional sampling in depth is required to correct for the effects of radiation damage to the scintillator over time. This applies particularly to the six intervals covering the kinematic region 1.98<||<3.0. Specifics are presented in Section 7.3.4 below.

Optical signals from the megatiles are conveyed via ribbon cables of fibre-optic waveguides up the 53 crack that delimits the barrel/endcap region and/or through the horizontal opening between the magnet and the endcap to the DBX for signal processing. Laser calibration signals are conveyed in the opposite direction from the DBX to select megatiles via quartz fibre.

Power, cooling, high voltage, and low voltage services are supplied via the radial crack just beyond the solenoid (near |z| ~6.7 m), as are laser calibration signals. Digitised, optical signals destined for the DAQ system follow similar routing.

7.3.2 The outer endcap calorimeter (HOE) layout

HOE refers to the hadronic calorimeter in the endcap region that is situated beyond the coil and on the inside face of YE/1. There are two such assemblies, one at each end of the CMS detector and labelled HOE+ and HOE-. Here we consider only one end of the detector and refer to it generically as HOE. HOE consists of 72 sector subassemblies, each subtending 5 in . Every six sectors (= 30) are served by an HE/HOE decoder box. Each HOE sector assembly consists of a single megatile layer, a portion of which is mounted onto the back (large |z|) face of a ME1/2 muon chamber and the remainder of which is mounted directly onto the YE/1 face. Each megatile is subdivided into seven intervals, with four waveshifter fibres to reach out each interval.

Optical signals from the megatiles are conveyed via ribbon cables of fibre-optic waveguides inward along YE/1 to the HE decoder boxes. Laser calibration signals are conveyed in the opposite direction from the DBXs to the megatiles via quartz fibre.

Power, cooling, and high voltage services are supplied from outside the detector and via the HE DBXs.

7.3.3 HE/HOE front-end optical layout

Fig. 7. 13 shows the layout of an HE/HOE decoder box, with dimensions 80 cm25 cm11.8 cm. This structure is functionally identical to HB decoder boxes, except that an additional 73 channel HPD must be accommodated, and the electrical and optical patch panels must account for a different orientation of access in the endcap region. The materials from which the box will be fabricated are non-magnetic: aluminium, copper, brass and plastics. Each decoder box is mounted to the steel backing flange of the calorimeter wedge. The DBX consists of two compartments which are optically isolated: a fibre-optic compartment and an electronics compartment. Six HPDs are mounted on the lateral interior wall between the two compartments.

Access to the fibre-optic compartment is via optical connectors at two optical patch panels, one at each end of the box. Each patch panel is of 9.5 cm9.5 cm0.6 cm thick aluminium, and serves as the mounting surface for eighty optical connectors arranged in four columns of twenty connectors. Each connector supports ten multiclad fibres of 940 m diameter on a pitch of 1.4 mm, and each fibre within a connector corresponds to one of the elements within a megatile. Each of the optical connectors is optically finished by diamond flycutting.

All optical signal fibres used in the interior of a HE/HOE decoder box are of 940 m diameter, multiclad construction. Kuraray S-type fibre is specified because of its flexibility.

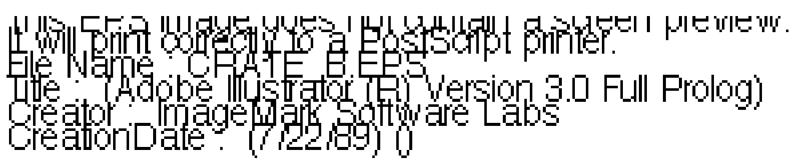

Fig. 7. 13: Schematic of the mechanical and electrical layout of a HE/HOE decoder box.

Certain of the megatiles of HE2 require special consideration in optical routing, because they are located directly adjacent to or beneath the decoder box, and hence optical connectors would be trapped or blocked. Layers 15 through 18 are those affected. For these, as in the case of the trapped layers of HB2, special fibre-optic cables will be prepared which are of cylindrical cross section and more flexible than the standard, flat ribbon connectors.

Additionally, on each optical patch panel there are nine connectors for quartz fibres that provide transmission of laser calibration signals to selected HE megatiles (layer 1 corresponding to HE1 and layer 9) and three signals to HOE megatiles.

7.3.4 HE/HOE fibre decoder tower structure and mapping

A HE/HOE decoder box receives the information from 30 in azimuth (three 10 sectors). There are a total of 12 HE/HOE decoder boxes at each end of the CMS detector and 24 in all. Within these boxes, the layer sums are formed corresponding to tower geometry. The summations in the HE region are more involved than for the HB (barrel) case, because for ||>1.98 multiple depth samplings are required to correct for radiation damage effects over time. For ||<1.98, there are two depth samples, HE1 and HE2. For ||>1.98, there are three or four depth samples: HE1, HE2-HE4. HOE consists of a single plane in depth, but four waveshifter fibres are used to read out a given component tile within the plane. The HOE elements are labelled HE5. The basic readout structure for a 10 sector is indicated in Fig. 7. 14.

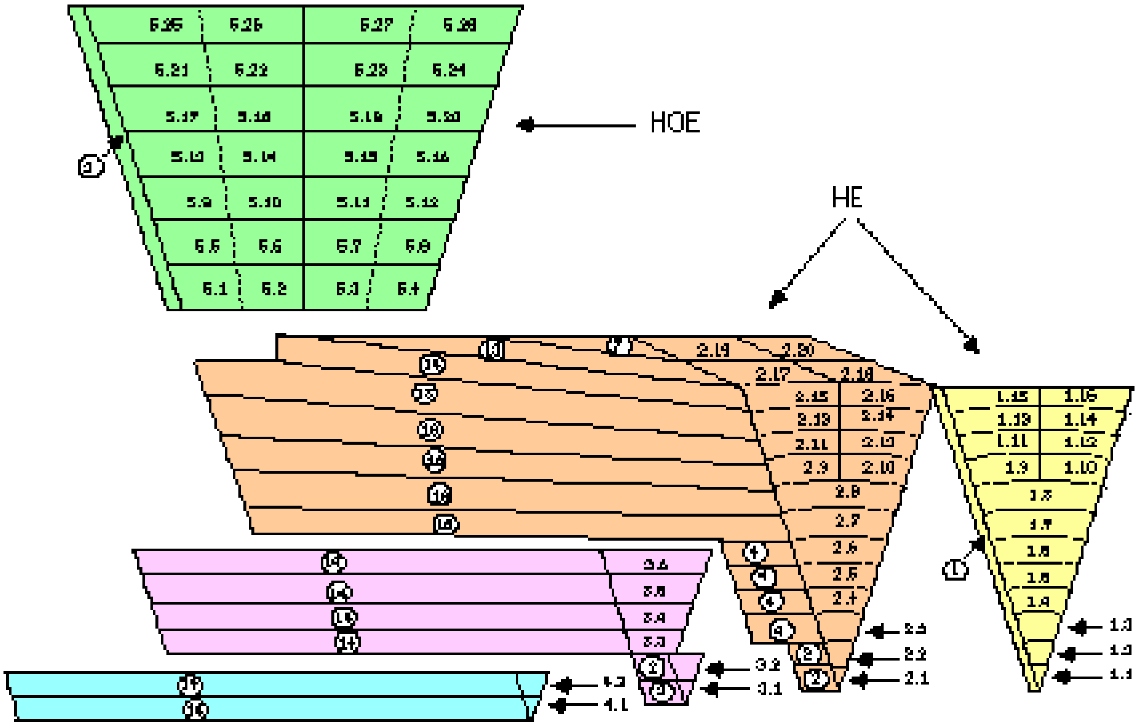

Fig. 7. 14: Schematic "exploded" view of a HE/HOE = 10 calorimeter sector, indicating the sampling subsections. The tower labelling is indicated on the front face of each section. These labels correspond to HPD pixels displayed in Fig. 7. 15. The numbers in circles indicate either the number of layers combined per HPD pixel (for HE) or the number of fibres per tile combined onto a HPD pixel (for HOE). Additionally, for the HE case the number of independent depth samples is a function of , to compensate for radiation damage effects. For ||<1.98 (bin number greater than 6) there are two samples in depth; for 1.98<||<2.5 (bins 3-6) there are three samples in depth; and for ||>2.5 (bins 1-2) there are four samples in depth.7.3.4.1

Formation of HE tower geometry

Within the optical compartment of the decoder box and ~8 cm behind the optical patch panel is a Delrin "sorting" plate through which the interior optical fibres are organised into HE1 and HE2-HE4 subgroups and also into tower geometry. The elements of a = 10 calorimeter sector are now described.

For HE1 there are 16 "towers" of single-layer sampling. These towers are labelled HE1.1 through HE1.16 and are mapped onto the pixels of a HPD73 tube, labelled HPD-73-1 in Fig. 7. 15.

For HE2-HE4, the number of layers summed in depth (and mapped to a given HPD pixel) depends upon the bin.

For ||<1.98 (corresponding to bins 7-20), there are 14 towers formed by summing up to 18 available samples over the full depth of HE. These towers are labelled HE2.7 through HE2.20, and are mapped onto a 19-channel HPD labelled HPD19-2 in Fig. 7. 15.

For 1.98<||<2.5, the layer summation is provided over two samples in depth, so that radiation damage effects can be compensated for by reweighting of the samples. For mapping to HPD tubes, refer to Fig. 7. 15.

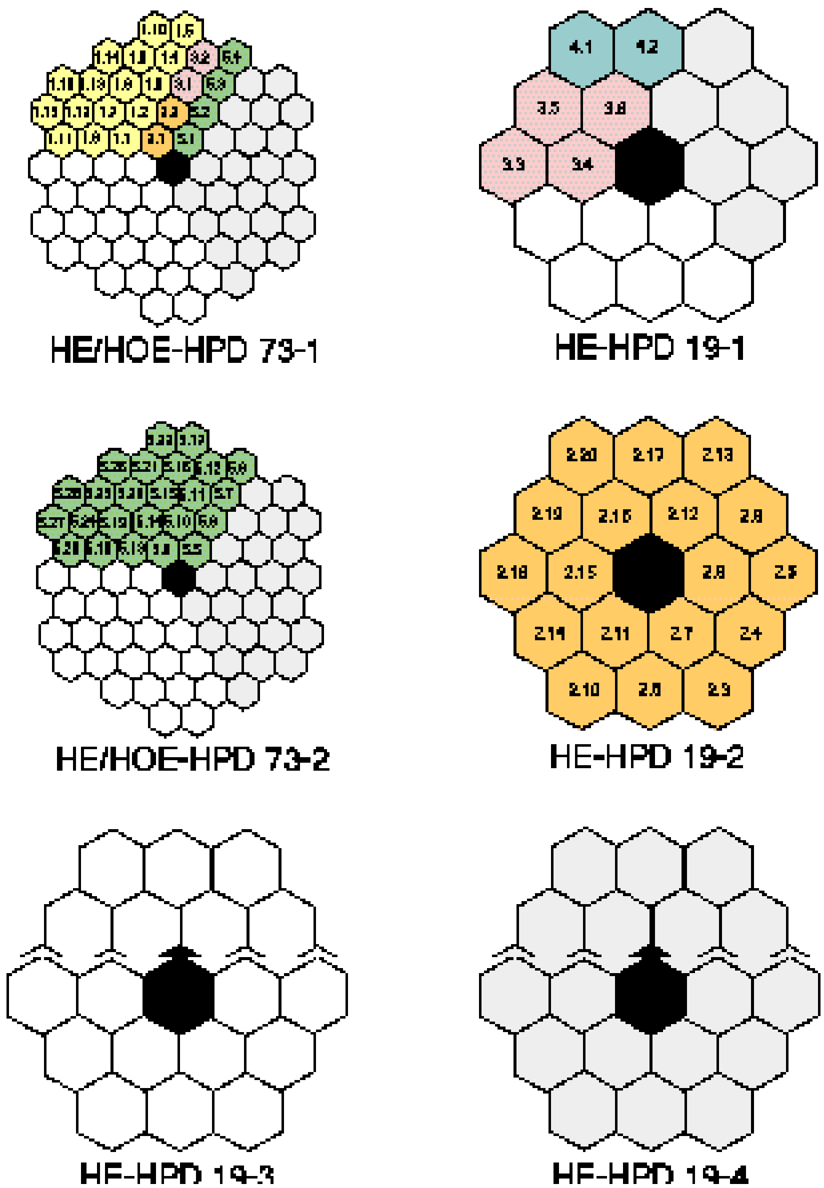

Fig. 7. 15: Fibre/pixel mapping scenario for an HE/HOE decoder box. Towers from 1/3 of the channels are indicated corresponding to a =10 section. A schematic of the corresponding tower positions are indicated in Fig. 7. 14.

- 4 tower sums over 4 sampling layers - labelled HE2.3 to HE2.6. These are mapped onto the HPD19-2 tube.

- 4 tower sums over 14 sampling layers - labelled HE3.3 and HE3.6. These are mapped onto the HPD19-1 tube.

For 2.5 < || < 3.0, the layer summation is provided over three samples in depth.

- 2 tower sums over 2 sampling layers - labelled HE2.1 and HE2.2. These are mapped onto the HPD73-1 tube.

- 2 tower sums over 2 sampling layers - labelled HE3.1 and HE3.2. These are mapped onto the HPD73-1 tube.

- 2 tower sums over 14 sampling layers - labelled HE4.1 through HE4.2. These are mapped onto the HPD19-1 tube.7.3.4.2

Formation of HOE tower geometry

A =10 calorimeter sector of HOE consists of a single plane megatile composed of 14 individual tiles. There are two bins in and seven bins in . Because of their physical size, each tile is read out with four waveshifter fibres. However because of the small pixel size available in the HPD73 tubes, it is inadvisable to map four 940 µm diameter fibres to a single pixel. Instead, pairs of fibres are mapped to an HPD73 pixel, and then pairs of pixels are connected electrically and read out through a single electronic channel. To illustrate this, Fig. 7. 14 displays a HOE sector. Elements 5.1 and 5.2 are readouts from the same HOE tile. Element 5.1 consists of two fibres mapped to an HPD-73-1 pixel. Element 5.2 consists of two fibres mapped to another HPD-73-1 pixel (Fig. 7. 15). The electrical signals derived from these pixels are electrically combined prior to amplification and digitisation by a single QIE channel. Hence the 28 pixels elements of HOE indicated in Fig. 7. 14 are readout by 14 QIE channels.7.3.2.3

Mapping to hybrid photodiodes

To implement the mapping scenario presented above, fibres are routed from the patch panels through sorting plates in the optical compartment of the decoder box (Fig. 7. 16). The holes in the sorting plates are oversized, so that the fibres simply pass through with no constraint. The bundles are then inserted into tubes and routed to the HPDs. Additionally, an extra pair of multiclad fibres of 300 m diameter are inserted into each bundle which are optically connected to the Y11 mixer block of the Dye Laser/LED calibration system to provide an independent monitor of the sensitivity and gain of the HPD pixels. Choices of HPD location and pixel position are driven by the need to keep fibre bend radii as large as possible within the space constraints and for "simplicity" of the pattern of fibre routing.

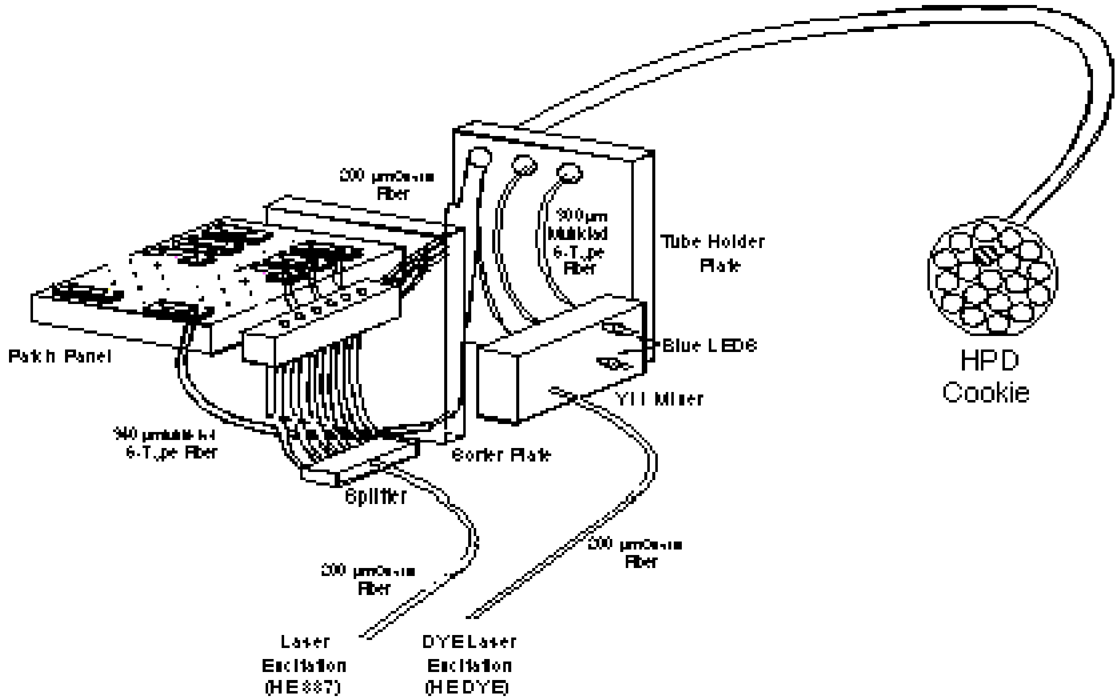

Fig. 7. 16: HE decoder box optical compartment elements.

Registration of the fibre bundles to the HPD pixels is performed in a similar fashion to the HB decoder boxes. As for HB, alignment concerns include: misalignment of fibre bundles in the cookies; misalignment of the cookies relative to the HPD pixel structure; numerical aperture effects in the air gap between the cookie and the fibre-optic window of the HPD; and misalignment of tube axes relative to the direction of the local magnetic field direction.

Mechanical: The cookie is registered to the HPD faceplate with alignment pins provided on the HPD which should allow for a placement tolerance of ~100 m between fibre bundles and HPD pixels.

Optical: Because of surface imperfections (surfaces of the cookies are not optically flat), the light exiting a fibre bundle will diverge according to the numerical aperture of the fibre as it passes through an airgap between the cookie and the fibre-optic faceplate of the HPD. To compensate for local surface imperfections, the Cookies and HPD faceplates will be shimmed apart by a 50 m spacer. Crossing this gap this will lead to an "expansion" of the optical image by ~ 50 µm in radius, as the exit angle is slightly larger than 45.

Magnetic Field: Assuming a 2 mm gap between the photocathode and the silicon in the HPD, 3 of axial misalignment of the HPD axis relative to the local field direction would lead to a systematic shift by 100 µm of the photoelectron image on a given pixel.

If up to 18 fibres are imaged per pixel (as is the case for HE2.7 to HE2.14), we can accommodate a total misalignment of <405 m in the 19-channel HPD tube (Fig. 7. 17). For HOE (HE5.1-HE5.28), two fibres are imaged per pixel per 73-channel HPD tube (Fig. 7. 18). Here a similar misalignment tolerance of 400 µm is indicated. Hence the HE/HOE decoder boxes must maintain the alignment of the HPDs to within a 3.0 angle of the field, to fit safely within the allowed alignment tolerances.

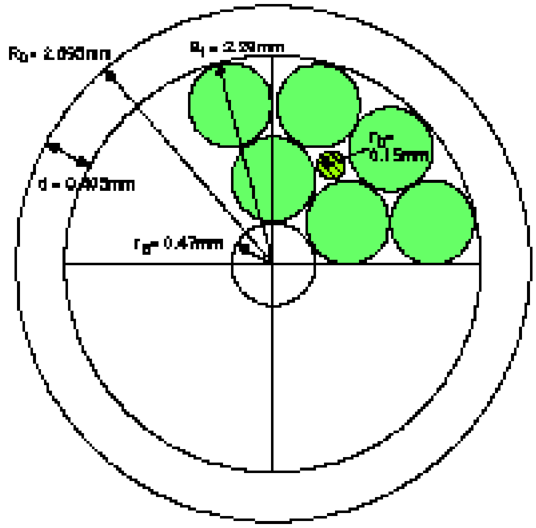

Fig. 7. 17: HE2 fibre layout presented to a pixel of a 19-channel HPD, for a case where 18 fibres of 940 µm diameter are mapped to a pixel. The small 300 µm diameter fibre is for calibration. Here the outer circle indicates the position of the nearest edge (or flat) of the hex-shaped pixel. An alignment tolerance of 405 µm is indicated for this configuration. Note that this is 80 µm less than for HB2, where 17 fibres are mapped to a pixel (Fig. 7. 10).

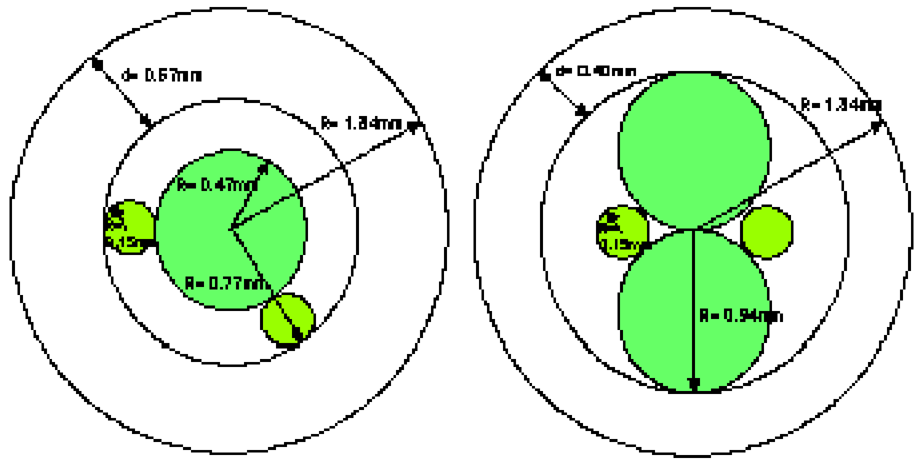

Fig. 7. 18: HE1 and HOE fibre configurations presented to pixels of 73-channel HPD tubes. For HE1 one fibre is imaged per pixel; for HOE two fibres are imaged per pixel. Small diameter fibres are for calibration signals. The outer circle indicates the position of the nearest edge (or flat) of the hex-shaped pixel. An alignment tolerance of 570 µm is indicated for HE1 and 400 µm for HOE.

7.3.5 HE/HOE front-end electronics layout

The HE front-ends are functionally identical to those of HB. Approximately half the decoder box volume is allocated for electrical and support services for the HPDs, for signal amplification, digitisation, and optical signal drivers, for calibration and slow controls functions, and for water cooling and thermal monitoring. All of the output signals from the 168 available HPD channels (162 of which correspond to active detection elements) are routed to readout boards located in a internal custom crate structure, with lead lengths kept as short as possible. The ceiling and floor of the electronics compartment are water-cooled copper plates to maintain all regions of the decoder box at or below a temperature of 26 C.

Services to the HPDs include: Photocathode high voltage (-10 kV), bias voltage to the silicon (typically 100 V), and supply voltages for the QIE preamp/digitiser/driver boards (+5 V and +10 V). These are supplied to the decoder box via a panel on the "top face" (see Fig. 7. 13).

All HPDs used in HE will be operated at a photocathode voltage near -10 kV. These will be fed individually from outside the detector over a minicoax to each HPD. Similarly, LV bias (~100 V) for the silicon substrates of each HPD will also be supplied individually via minicoax from supplies located outside the detector. These electrical power services are routed to the decoder boxes through the radial crack (near |z| ~ 6.7 m) at the end of the solenoid magnet.

Water temperature and flow sensors are placed on the entrance and exit ports of the water lines outside the detector.

The electronics layout is similar to HB decoder boxes and includes HV distribution, two LV systems, and ancillary controls, calibration, and monitoring systems. Each HPD channel is amplified and digitised in a QIE chip. HPD outputs are multiplexed (three channels per optical link) and driven via laser diodes off-detector to the trigger and data acquisition system. Water cooling is required for the electronics compartment because of power dissipation in the QIE chips and the laser diodes which are used to drive the digital signals off detector.

7.3.6 HE/HOE system interfaces.

Identical with HB. The decoder boxes must maintain appropriate operating voltages, temperature controls, and diagnostic information to monitor and maintain stable operation of HE1 and HE2-HE5 elements. A TTC interface is included in each DBX.

7.3.7 Monitors and controls system

Identical with HB. Numerous monitor and controls functions are required in every DBX. It is expected that these will be served via the TTC.

7.3.8 Access, maintenance, and operations

Similar to HB, the HE/HOE decoder boxes will be designed to be maintenance free. Because of the large array of electrical, optical, plumbing and other services directly over the top of the decoder boxes, only simple adjustments can be made without functional disassembly of services atop the boxes. Extensive servicing of the boxes could be effected when an endcap is withdrawn.

7.4. HOB OVERVIEW

HOB refers to the hadronic calorimeter in the central (barrel) region that is situated outside the coil and attached to the inner and outer faces of the five muon steel "rings", YB/0/1, YB/1/1, YB/2/1, and on the inside face of the steel absorber at r ~ 3.8 m, which we label YB/0/0. One hundred thirty-two megatiles comprise the system.

On each muon ring, HOB is divided into twelve =30 sectors (matching the muon steel segmentation). The number of intervals covered (5, 6 or 8) depends upon the ring. Each sector is served by a decoder box (DBX) which is located radially outside the last muon chamber station in each ring (MB/0/1, MB/1/1, MB/2/4 at r ~7.43 m).

Optical signals from the megatiles are conveyed via ribbon cables of fibre-optic waveguides up the radial cracks at |z| ~1.27 m and 4.0 m between rings to the DBX for signal processing. Laser calibration signals are conveyed in the opposite direction from the DBX to the megatiles via quartz fibre.

Power, cooling, and high voltage services are supplied from outside the detector, as are laser calibration signals. Digitised, optical signals destined for the DAQ system follow similar routing. These services are assumed to be located adjacent to those supplying HB, HE, and HOE subsystems.

7.4.1 HOB front-end optical layout

Fig. 7. 19 and Fig. 7. 20 show the layouts for HOB decoder boxes, with dimensions of 50 cm25 cm11.8 cm and 40 cm25 cm11.8 cm. These structures are functionally similar to HB/HE decoder boxes, except that the box size is reduced since either two or three 19-channel format HPDs need to be supported per box. Also the electrical and optical patch panels are modified to account for orientation differences, and magnetic shielding of the boxes are required to screen out the leakage field from the muon steel. Structures within the interior of the box will be fabricated of non-magnetic materials: aluminium, copper, brass and plastics. Each DBX is mounted onto the radially-outer surface of an MB chamber module and consists of two compartments which are optically isolated: a fibre-optic compartment and an electronics compartment. The two or three 19-channel HPDs are mounted on the interior wall between the two compartments.

Access to the fibre-optic compartment is via optical connectors at one optical patch panel. The patch panel is of 9.5 cm9.5 cm0.6 cm thick aluminium, and serves as the mounting surface for optical connectors arranged in two columns of twelve connectors (for YB/1 and YB/2 rings), and two columns of eighteen connectors (for the YB/0 ring). Each connector supports up to 18 multiclad fibres of 940 m diameter on a pitch of 1.4 mm, and typically twelve of the 18 fibres within a connector correspond to active elements within a megatile. Two connectors are required to read out a =5 "tray" of a megatile. Each of the optical connectors is optically finished by diamond flycutting.

All optical signal fibres used within the HOB decoder box are of 940 m diameter, multiclad construction. Similar to HB, HE, and HOE, Kuraray S-type fibre is specified for all interior optical interconnections.

Additionally, on the optical patch panel there are six connectors supporting six quartz fibres of 200 micron diameter for transmission of laser calibration signals to each megatile.

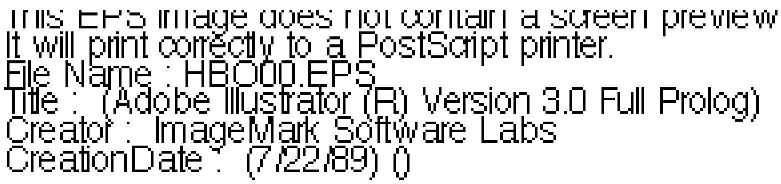

Fig. 7. 19: Schematic of the mechanical and electrical layout of a HOB-0 decoder box.

This EPS image does not contain a screen preview.
It will print correctly to a PostScript printer.
File Name : HBO12.EPS
Title : (Adobe Illustrator (R) Version 3.0 Full Prolog)
Creator : ImageMark Software Labs
CreationDate : (7/22/89) ()

Fig. 7. 20: Schematic of the mechanical and electrical layout of a HOB1 or HOB2 decoder box.

7.4.2 HOB fibre decoder tower structure and mapping

There are 12 HOB decoder boxes per barrel muon ring and 60 in all.7.4.2.1

Formation of HOB towers

Within the optical compartment and ~8 cm behind the optical patch panel is a Delrin sorting plate through which the interior optical fibres are organised into tower geometry. For HOB, the number of these tower "bundles" depends upon the ring.7.4.2.1.1

Ring HOB2:

There are 30 tower bundles of up to eight fibres, covering five intervals of and six intervals of . The bundles are sorted and then inserted into tubes and routed to the HPDs. Additionally, two extra multiclad fibres of 300 m diameter are inserted into each bundle which are optically connected to the Y11 mixer block of the laser/LED calibration system to provide an independent monitor of the sensitivity and gain of each HPD pixel. The 30 tower bundles are mapped onto two 19-channel HPDs.7.4.2.1.2

Ring HOB1:

There are 36 tower bundles of up to eight fibres, covering six intervals of and six intervals of . The bundles are sorted and then inserted into tubes and routed to the HPDs. Again, two extra multiclad fibres of 300 m diameter are inserted into each bundle which are optically connected to the Y11 mixer block of the laser/LED calibration system to provide an independent monitor of the sensitivity and gain of each HPD pixel. The 36 tower bundles are mapped onto two 19-channel HPDs.
7.4.2.1.3

Ring HOB-0:

There are 48 tower bundles of up to 12 fibres, covering eight intervals of and six intervals of . The bundles are sorted and then inserted into tubes and routed to the HPDs. Again, two extra multiclad fibres of 300 m diameter are inserted into each bundle which are optically connected to the Y11 mixer block of the laser/LED calibration system to provide an independent monitor of the sensitivity and gain of each HPD pixel. The 48 tower bundles can be mapped onto three 19-channel HPDs or onto two 25-channel HPDs. The difficulty with mapping onto the 25-channel option is that it would allow only 40 microns of alignment tolerance, which is unrealistic. Hence the option of three 19-channel HPDs is specified.7.4.2.2

Mapping to hybrid photodiodes

Registration of the fibre bundles to the HPD pixels is performed in a similar fashion to the HB decoder boxes. Choices of pixel position are driven by the need to keep fibre bend radii as large as possible within the space constraints and for "simplicity" of the pattern of fibre routing.

As for HB, alignment concerns include: misalignment of fibre bundles in the cookies; misalignment of the cookies relative to the HPD pixel structure; optical effects at the cookie/fibre-optic faceplate interface; and offset of the photoelectron image due to stray magnetic field. The cookie is registered with alignment pins provided on the HPD which will allow for an alignment tolerance of ~100 µm between fibre bundles and HPD pixels. Numerical aperture effects lead to an additional ~50 µm. Magnetic shielding of the boxes will be essential to eliminate any leakage fields from penetrating within. However, given the small fibre count being mapped to a given HPD19 pixel, alignment issues are less critical for the HOB decoder boxes than for the other HCAL subsystems.

7.5 HF OVERVIEW

7.5.1 Layout of optical fibre bundles

The quartz fibres will be bundled to form towers at the back of the absorber. The fibre bundles will be made such that they form thin ribbons in order to minimise optical pickup noise from background radiation. At the very end of the bundle, fibres will be closely packed into cylindrical steel ferrules for mechanical mounting to photodetectors.

There are three types of fibre bundles that emerge from each tower; long fibres that run the entire length of the absorber (EM section) will be bundled separately then the medium length fibres (HAD section). The short fibres (TC section) will form yet another bundle. There are two different sizes of towers, the smaller ones (5 cm5 cm) and the larger ones (10 cm10 cm). Especially for TC, superimposed towers will be formed in 30 cm30 cm square sections.

EM fibres will alternate with HAD fibres in the absorber, *i.e.* every other fibre will go either to EM bundle or HAD bundle. TC fibres will be inserted 30 cm into the absorber in the same groove as the EM fibres but at every third groove/plate. Table 7. 3 below summarises the main features of these fibre bundles.

Table 7. 3

Number of fibres required for each of the towers and bundles. The numbers in parentheses indicate the internal diameter of ferrules when 30% packing fraction is assumed for 0.345 mm diameter fibres.

Type of Bundles	No. Fibres 5 5 cm^2	No. Fibres 10 10 cm^2	No. Fibres 30 30 cm^2
EM Bundle	313 (7)	1250 (14)	-
HAD Bundle	313 (7)	1250 (14)	-
TC Bundle	-	-	1406 (15)

Manufacture, QC/QA, installation, monitoring

Fibre are inserted into the absorber as described in Section 6.6.1. The fibre bundles are glued into the ferrules, cut and polished. The polishing is performed using the industry techniques and equipment. The final polish is accomplished with one micron grit size.

Each end after being polished will be inspected under magnification for obvious scratches and cracks in the fibres before connections to the light guides are made.

7.5.2 Layout of light guide/tower

Aircore light guides are used to transport the light generated in the calorimeter to the photodetectors.

Light guides are mechanically attached at one end to the fibre bundles and at the other to the photodetectors. The beam tests show that 65% of the light can be transported over 1.1 meters with an aircore light guide that is constructed out of aluminised mylar. The optimisation of this system is still being studied since it affects background radiation shielding, photodetector matrix design, maintenance, etc.7.5.2.1

Manufacture, QC/QA, installation, monitoring

Light guides are manufactured using a polycarbonate shell with a enhanced reflective aluminium surface interior. A hard single dielectric layer of halfwave optical thickness will provide better than 90% reflection on average for all incidence angles and wavelengths and will increase resistance against abrasion, tarnish and oxidation.

Each light guide will be tested before installation for light transportation performance on a test bench using identical NA fibre bundles at some fixed wavelengths.

Each light guide will be installed individually. It will be mechanically connected to the ferrule and the PMT box structure. A fixture will position and fix the light guides in position. In order to monitor their reflectivity in time, a calibration fibre and an LED will be installed at the far end of the light guides.

7.5.3 Layout of transducer/preamp

The packaging of the PMT and HV bias circuit are described in chapter 8. A radiation tolerant preamplifier is also packaged within the PMT shield, and drives a coaxial cable to the electronics racks.

7.5.4 High voltage services

No high voltage is delivered externally to the HF. The biasing for the PMTs is accomplished locally using a Cockroft-Walton type voltage multiplier. Radiation levels inside the shield may require that the Cockroft-Walton generator be located outside in the electronics racks.

7.5.5 Low voltage services

The LV power requirements for on-detector HF electronics are summarised in Table 7.4.

The total power dissipated by one PMT and it's associated front-end electronics is about 5 watts. This corresponds to a total of 9 kW per detector end. We propose to distribute 350 VDC from the underground electronics area to the detector, then use DC-DC converters to supply the required voltages locally.

Table 7. 4

LV power requirements for HF front-end electronics.

PMT (Cockroft-Walton HV)	250 mW
dual QIE+ADC	3.0 W
control ASIC	100 mW
laser serialiser	500 mW
laser	500 mW
Total Per PMT	5.0 watt

The DC-DC converters are mounted in the electronics racks on the detector platform. The converters (typically in flat packages about 1 cm thick) are mounted on heatsinks, which are installed vertically in a crate. A single rack-mount crate of dimensions equal to a 9 U Eurocard enclosure will suffice for one half of an HF detector end.

7.5.6 Cooling

The total power dissipated by the PMT with Cockroft-Walton generator is about 250 mW. This heat must be removed from inside the shielding. The total power dissipated by one channel of front-end electronics is estimated at 5 W per channel. This power is dissipated entirely outside the HF calorimeter shielding in the electronics racks, which are water cooled in a conventional manner The total power dissipation for the FE electronics is about 4.5 kW per rack.

The baseline transducer is a Hamamatsu R5380 and the power consumption is about 9 kW per end as enumerated in Section 8.5.5. For the tubes:

a) PMT temperature coefficient for bialkali <600~nm is -0.4%/C whence for a 10C temperature change only 4% change in PMT gain; to get a 10% change, T=25C.

b) HCAL is to be cooled by chilled water at 18C held to 1C; thus, there is no problem with PMT gain change; the temperature of the electronics and the PMTs are routinely measured.

c) The thermal conductivity of iron is about 0.2 kcal/cm-s-C and copper is 1.7 in the same units. Assuming, for a worst case, we leak 1 kW on the inner diameter (0.3 m) along the EM compartment (0.3 m) and conduct the heat to the outer radius, then the T inner face to outer face is 5.6 C (assuming the inner area as the conduction area).

d) The quartz fibres have a thermal conductivity of 3210^{-4}cal/cm-s-C, so no power is conducted down/along the fibres. Consequently, no discernible thermal effects on the quartz fibres and none on the PMTs.

7.5.7 Slow controls

An extensive set of conditions must be monitored in the HF system. All sensors will ultimately be treated in a similar way; connected to multiplexed ADC inputs which are read out by a local microprocessor and transmitted to the CMS detector control and monitoring system. A Field Bus standard (i.e. CAN) will hopefully be adopted CMS-wide, and will be used for HF. A small crate dedicated to control and monitoring will be mounted in each electronics rack.

A summary of HF control and monitoring requirements is given in Table 7. 5.

Table 7.5

HF slow controls requirements.

Item	Count	Notes
High Voltage	100 per end	set V, monitor I, V
Low Voltage	80 per end	monitor I, V
Temperature	100 per end	

TABLE OF CONTENTS-----

8. PHOTODETECTORS

The Hadron Calorimeter is composed of several subsystems. HB and HE are situated directly in the 4 T solenoid field, and to keep the detected light yields at a reasonable level, the phototransducers must be located within the field volume. The Outer Calorimeter systems, HBO and HOE, are located within the barrel and endcap muon systems, and photosensors can be placed at the outer perimeter of the CMS muon yokes and rings. Hence residual and leakage fields from the muon steel can be screened out for these photosensors by careful attention to magnetic shielding. The HF subsystems are located forward and backward along the beam, beyond the endcap muon detectors. Here radiation damage is the principal concern, and magnetic shielding is a minor issue.

These issues, plus the substantial channel counts per subsystem, and the need to maintain a reasonable per channel cost, impose the requirement of commonality (where possible) among system elements - particularly the phototransducers and associated front-end electronics. In the long term, the fewer distinct systems to maintain the better. For HB and HE, the photodetector is the Hybrid Photodiode (HPD), a proximity-focussed photomultiplier tube with a silicon target, which can operate effectively in high magnetic field. Because the HPD is a pixel device (19-, 25-, 61-, and 73-channel HPDs are under consideration), the cost per channel can be reduced substantially. For HBO and HOE, the magnetic field issues do not apply, but the channel count for these systems is large. Commonality with HB and HE systems dictates that the appropriate photosensor for these subsystems is also the HPD. For HF, where quartz calorimetry is utilized to provide excellent physics (shower) measurement in the presence of a significant radiation field, higher gain is required. Here conventional photomultiplier tubes with quartz or boron-free glass windows are the preferred solution.

8.1 HADRON CALORIMETER PHOTODETECTORS

8.1.1 HB/HE requirements

There are several important requirements imposed on the photosensor used in the inner barrel (HB) and inner endcap (HE) calorimetry.

Magnet Field: The HB/HE photodetectors must operate in a 4 tesla field.

Linearity of Response: The transducer must be linear over a range of signals from minimum ionizing to 3 TeV hadron showers. The need to detect muons via their small, minimum-ionizing signal, specifies an excellent signal to noise ratio.

Leakage/Dark Current: The scintillator towers must be calibrated to 1% using a radioactive source mounted on a remote-controlled retractable wire.

Lifetime: The photodetector must operate adequately for at least 10 years of LHC operation, which corresponds to an integrated output charge of ~ 3 Coulombs and to an integrated neutron dose of ~ 5×10^{10} n/cm^2.

Results from studies performed both in laboratory bench tests and at the CERN test beam have shown that HPDs meet the above criteria.

The HPD consists of a photocathode followed by a gap of several millimeters over which a large applied electric field accelerates the photoelectrons onto a silicon target. (See Fig. 8.1) The gain of such a device is therefore given by the acquired kinetic energy of the photoelectrons (above some threshold energy which depends on the surface treatment of the diode) divided by the 3.6 eV required to release an electron-hole pair in the diode. For an applied voltage of 15 kV, a gain of approximately 3000 is realized. The response curve and extracted absolute gain curve are shown in Fig. 8.2 for a commercially available 7 channel HPD from DEP[1]. The photocathode is S20 with a fiber optic window and effective quantum efficiency of 12% in the green (λ ~ 500 nm). The ability to measure to 1% a small DC current above background fluctuations imposes an additional requirement on the transducer.

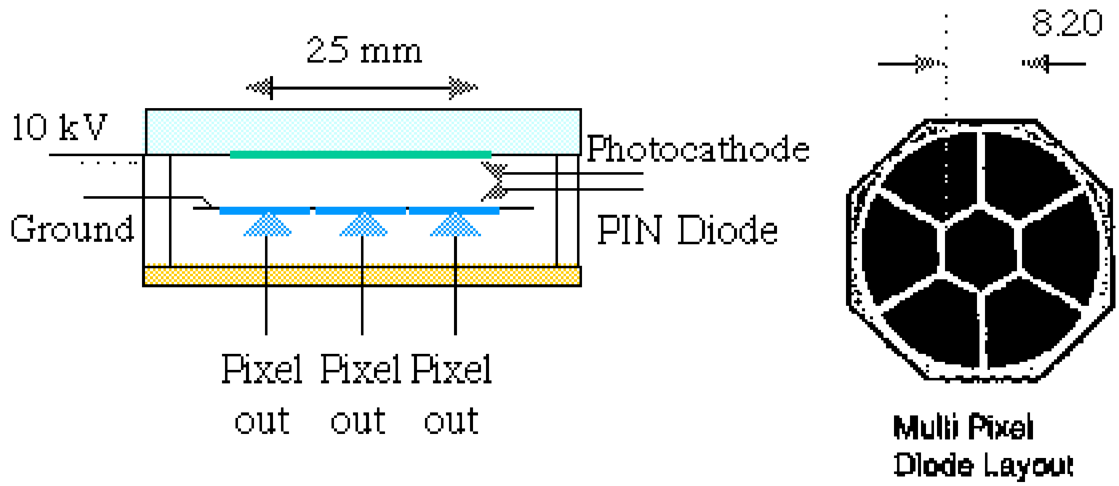

Fig. 8.1: HPD Schematic and tube structure.

Fig. 8.2: Response and absolute gain for a 7-channel HPD.

8.1.2 HOB and HOE photodetector requirements

The Outer Calorimeter systems HOB and HOE are expected to supply approximately 10 p.e./m.i.p. if a PMT were used. Since the function of the HO detectors is to tag muons and to tag and measure late developing showers, there are not very stringent requirements on the photo-transducer. Indeed, since the HPD has sufficient performance to meet these requirements, and since the commonality arguement is compelling, we also chose HPDs for the HO detectors as the baseline.

8.2 HPD MEASURED CHARACTERISTICS

Several characteristics of DEP HPD's were measured on the bench. Transducers with 1, 7 and 25 pixels were used. The photocathode uniformity was measured by scanning a light beam across the 7 pixel device. The uniformity observed was excellent , as shown in Fig. 8.3. The Si layer of the 25 pixel device is shown in Fig. 8.4. The gain uniformity as a function of high voltage and at fixed high voltage for all 25 pixels is shown in Fig. 8.5 and Fig. 8.6. Clearly, the linearity and gain uniformity requirements are met by the DEP device.

The resolution of response to a fixed amount of light (7 pixel device) is shown in Fig. 8.7. Clearly, no long tails are observed and the response is very well represented as a Gaussian over 4 orders of magnitude. The resolution of the 7 pixel device at fixed incident light intensity and PIN diode bias, but variable high voltage is shown in Fig. 8.8. At very large voltages a high level tail appears. We ascribe it to secondary charge liberated from the residual gas in the tube. These and other observations caused us to place a strict requirement on residual gas in the device.

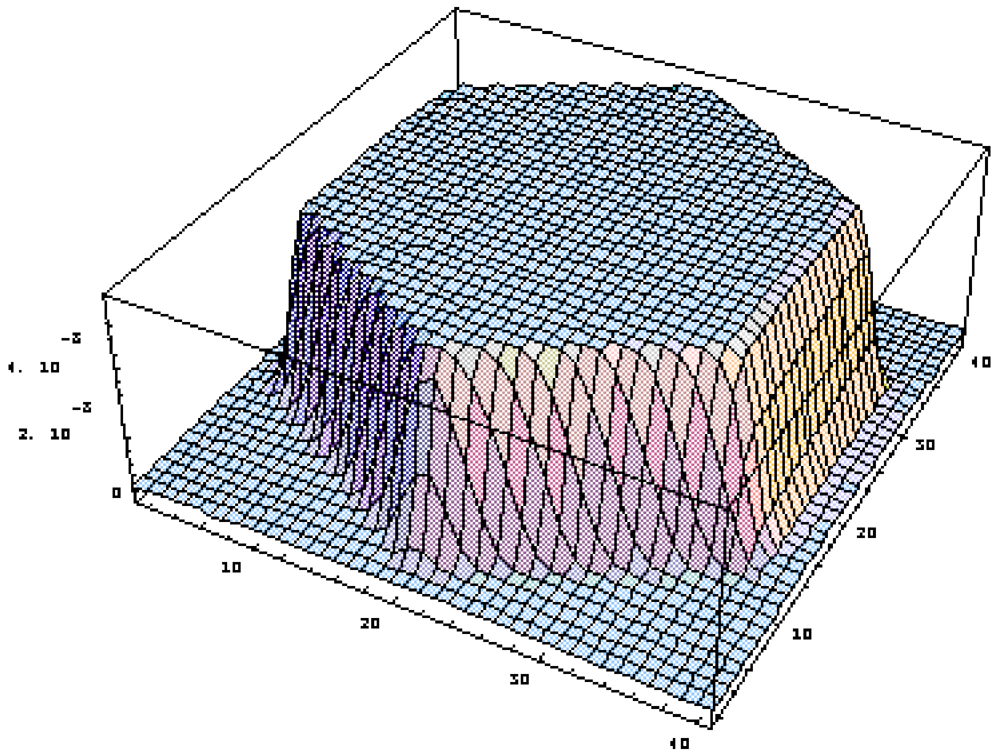

Fig. 8.3: The result of a scan of the central pixel . This plot shows current in nA for the central pixel *10^{-1} versus position on the face of the HPD (in 250 m increments).

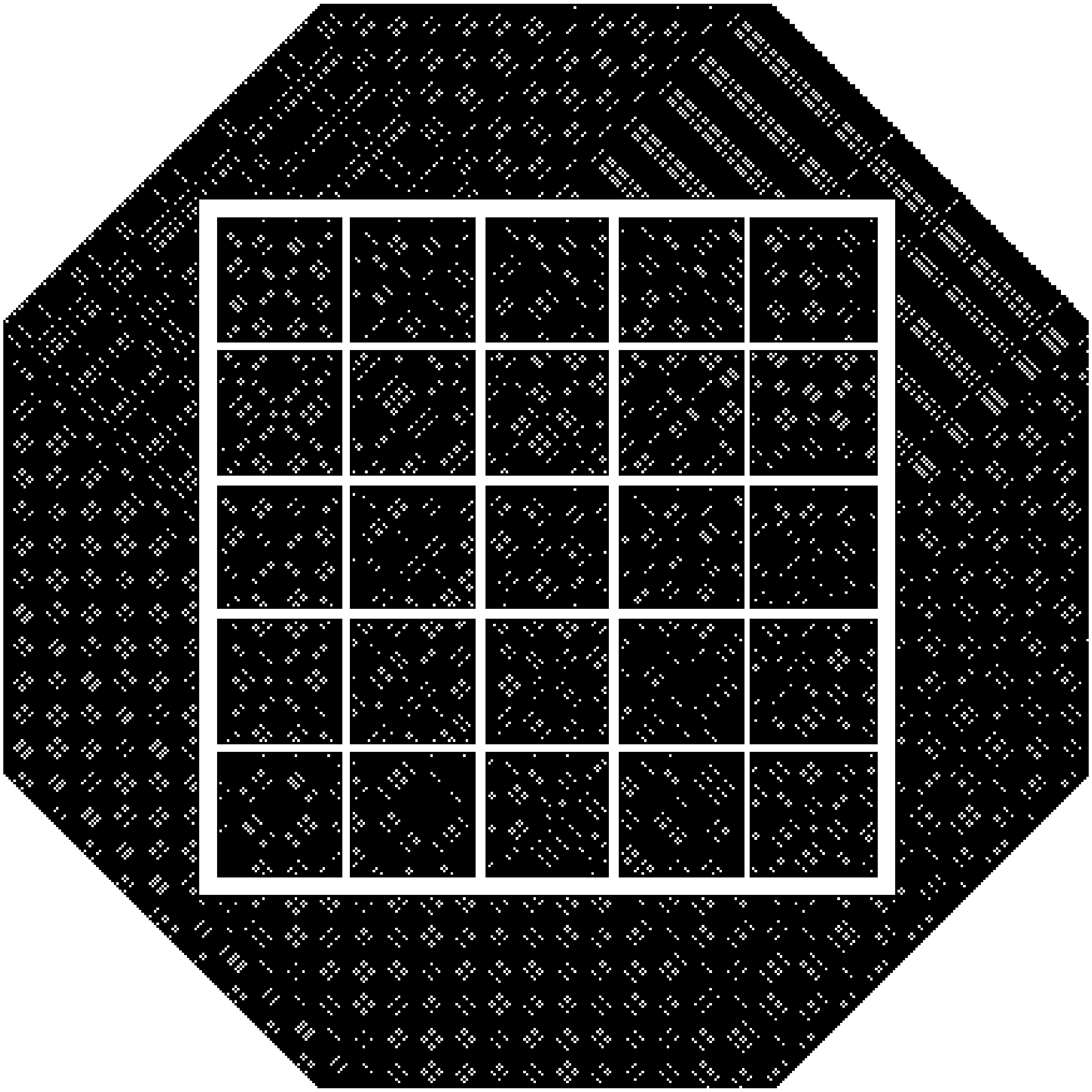

Fig. 8.4: Layout of the 25 pixel device.

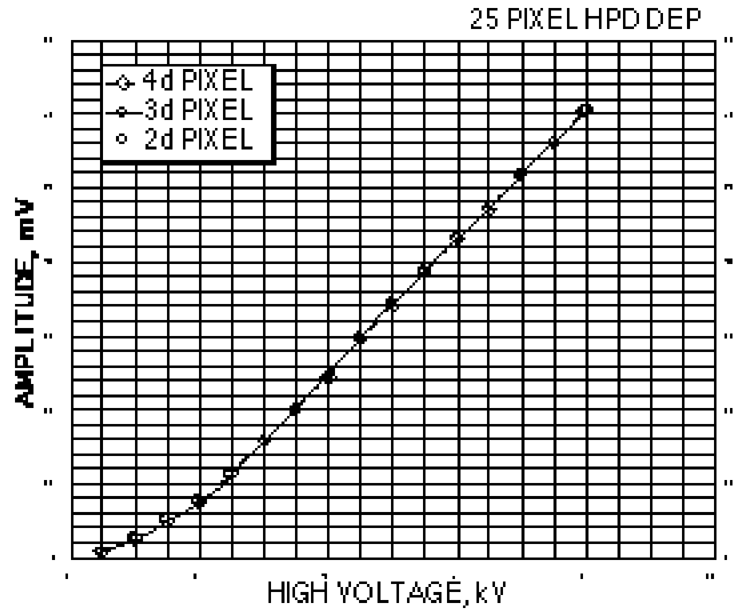

Fig. 8.5: Pixel to pixel response of gain vs. high voltage.

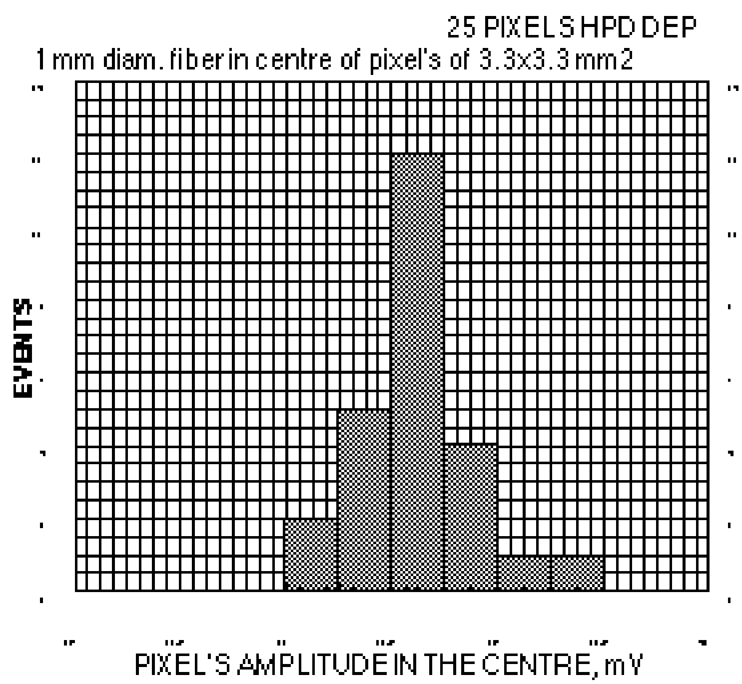

Fig. 8.6: Mean gain for each pixel (25 pixel HPD) at fixed high voltage.

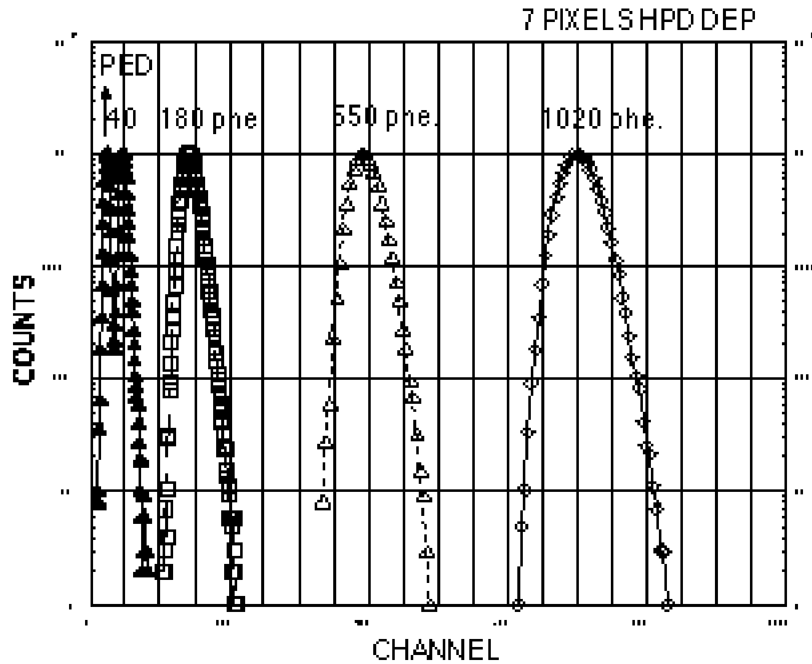

Fig. 8.7: Pulse response of 7 pixel device to different light levels at fixed high voltage

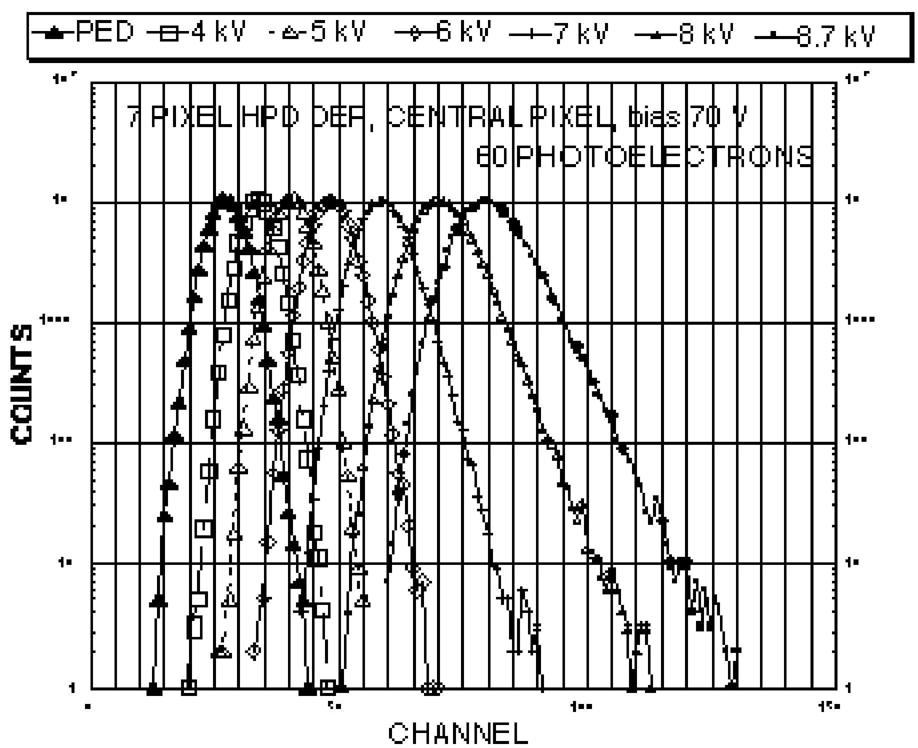

Fig. 8.8: Pulse response of the 7 pixel device at fixed light level and fixed diode bias as a function of high voltage

We have also studied the pulse shape of the device. For technical reasons the diode is backside illuminated, which means that we collect holes at the grounded anode of the PIN diode. The physics event rates involved require d.c. coupling. Hence we have a rise time set by the hole drift across the 300m depth of the diode, since the bombarding 10kV electrons have only about a 15m range in silicon. The observed rise and fall times of a 25 pixel device (minimum source capacity) are shown in Fig. 8.9 as a function of diode voltage. Full depletion occurs at approximately 70V, so that the device must be run heavily overdepleted to achieve a rise time which is less than the 25ns bunch spacing.

Since the scintillator tile + WLS fiber time constant is about 12 ns, it is unacceptable to have such a slow device with an intrinsically fast technology. The diode can be thinned to 150m, which halves the rise time. We are negotiating with DEP to have thinned prototype devices as soon as possible.

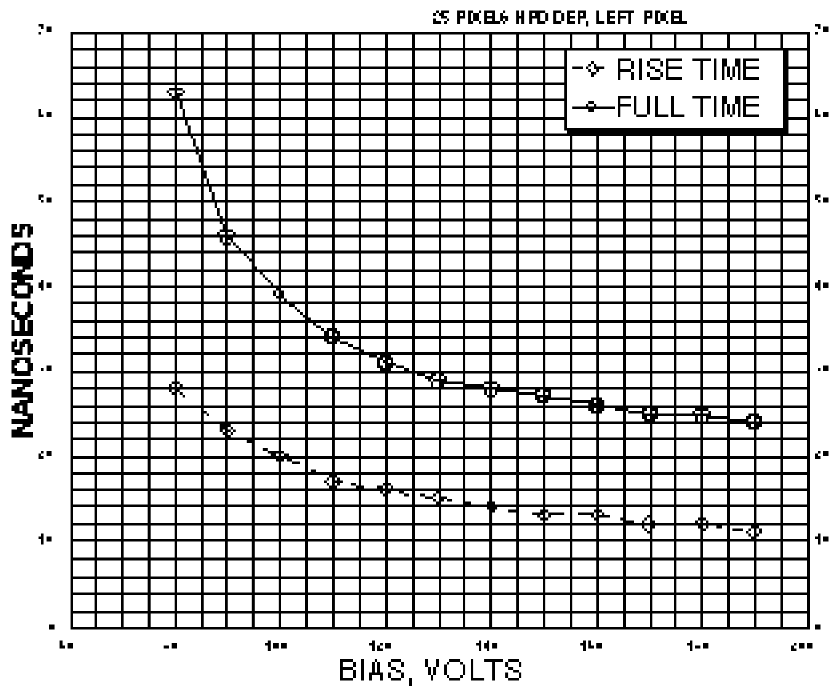

Fig. 8.9: Rise and fall times as a function of the diode bias.

8.3 HPD CHARACTERISTICS FROM TEST BEAM AND RADIATION EXPOSURE

8.3.1 Response to particles - muons

A prototype HB stack was read out by both APDs and HPDs in several beam tests at CERN in 1995 and 1996. Electron and hadron energy resolutions were the same as measured with standard phototubes, and were determined only by the sampling fluctuations of the shower and the calorimeter design. On the other hand, the low-light performance was found to be distinctive dependent upon the choice of phototransducer. A high energy muon (m.i.p.) recorded in 10 layers of scintillator produced a mean signal of 7.5 p.e. for a standard PMT, 6.5 p.e. for a HPD, and 45 p.e. for a silicon APD (as confirmed by LED studies). However, this mean signal was detected with a signal-to-noise ratio (defined as the mean of the signal divided by the pedestal width) of 59 for the PMT, ~ 8 for the HPD and ~ 2.4 for the best APD channel. The muon results are shown in Fig. 8.10. Note that the data confirm the observation that HPDs meet the requirement of clean muon detection for the HO transducers.

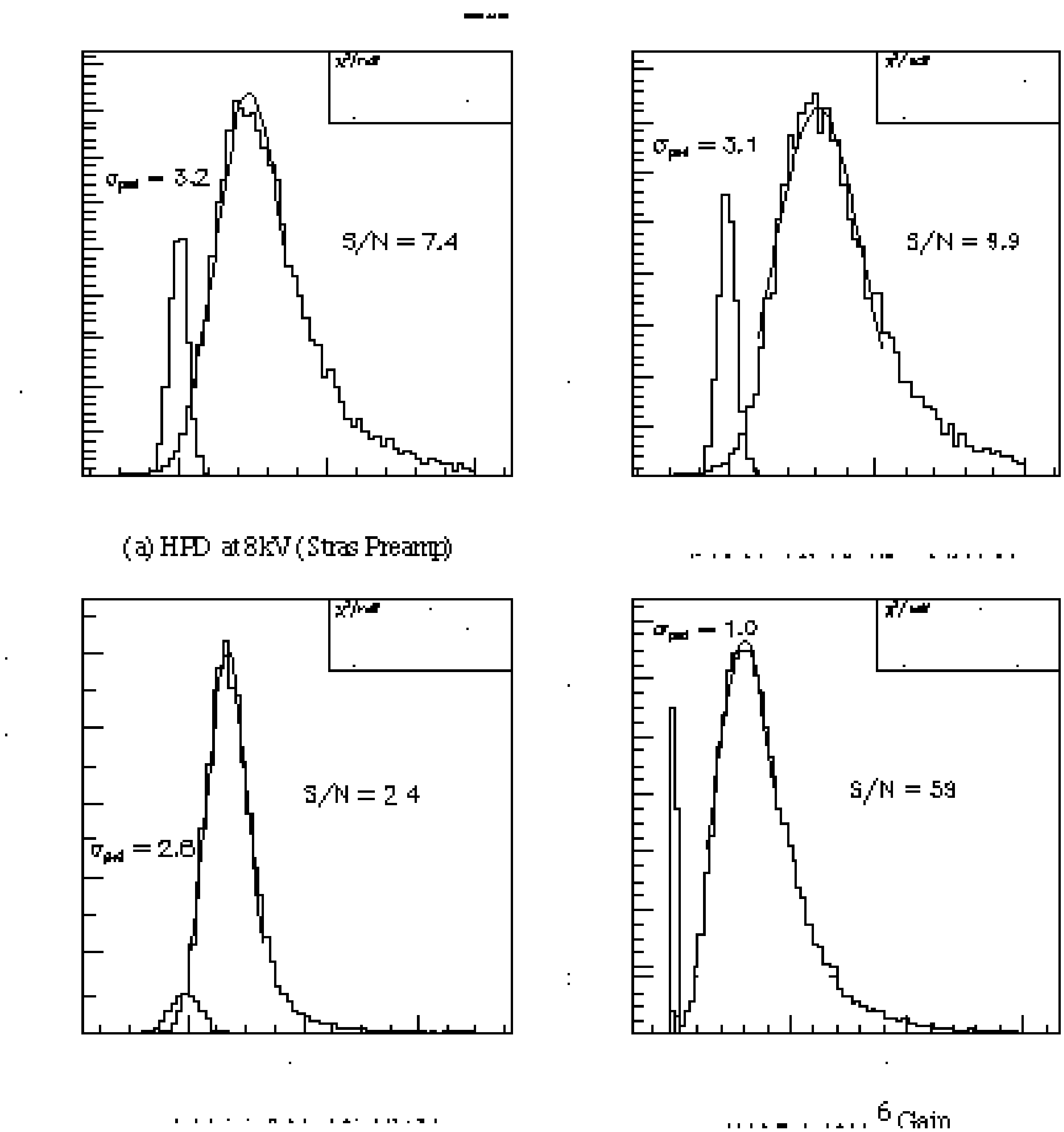

Fig. 8.10: Photodetector comparison for minimum ionizing particles: ADC signal and pedestal for muons.

8.3.2 DC response and calibration to Cs source

Source current measurements were also made at the test beam. As the 5 mC source passed across each tile in the calorimeter stack, custom 7-channel op-amp conditioning circuits mounted directly on the electronics box in the beamline converted the HPD current to a voltage which was read out by a peak-sensitive scanning ADC. Trim pots on each channel zeroed out the leakage current (5-10 nA) which was of the same order as the expected DC signal. Since it is the fluctuation on the background current rather than its level that determines the signal-to-noise, the ratio rms/I_{source}(%) gives the percent sensitivity that can be achieved. A comparison of PMT and HPD results for the same two towers (first 4-layers) is compiled in Table 8. 1. On average, one can make current measurements to 0.7% with the HPD and none are larger than the 1% specification.

Table 8. 1

Comparison between HPD and conventional PMT during radioactive source calibration

at the 1995 CERN test beam. Source current (I_{source}), dark current (I_{bkgd}), and fluctuations

in dark current (rms) measured in nanoamps

	Tower 5	HPD		Tower 6	Tower 5	PMT		Tower 6
Layer	I_{bkgd} ± rms =		I_{bkgd} ± rms =		I_{bkgd} ± rms =		I_{bkgd} ± rms =	
	-0.3192 ± 0.0369		-0.1753 ± -0.0316		3.095 ± 0.1719		2.992 ± 0.1814	
	I_{src}	rms/I_{src}(%)	I_{src}	rms/I_{src}(%)	I_{src}	rms/I_{src}(%)	I_{src}	rms/I_{src}(%)
1	4.9	0.753	5.3	0.596	-	-	-	-
2	5.8	0.636	4.7	0.672	314.	0.055	251.	0.072
3	4.3	0.858	5.8	0.545	294.	0.058	298.	0.061
4	5.8	0.636	4.8	0.658	342.	0.050	249.	0.073

8.3.3 Lifetime and radiation damage

The photodetector lifetime is affected by both the intensity of the signal itself and by radiation damage. The maximum integrated charge collected at the output (assuming an operating gain of 3000) is expected for an HE tower which samples shower maximum at highest jet energies ($|\eta| = 3$) and is 15 Coulombs over 10 years. Two HPDs have been operated under monitored illumination at DEP for 6 months and their gain as a function of time is shown in Fig. 8.11. Tube E18 is an electrostatically focused tube (with a getter) operated at 15 kV and Tube P25 is a 7-channel proximity focused tube (without getter) operated at 11 kV. The reverse diode bias in both cases is at 25V. At present, no change in gain has been recorded after 0.44 C of integrated charge in the tube with the getter. The tube without getter has a 30% loss in signal. A getter is therefore required for the CMS tube. We will continue to observe these tubes for another year in order to insure that at least 15Coulombs can be pulled off the anode.

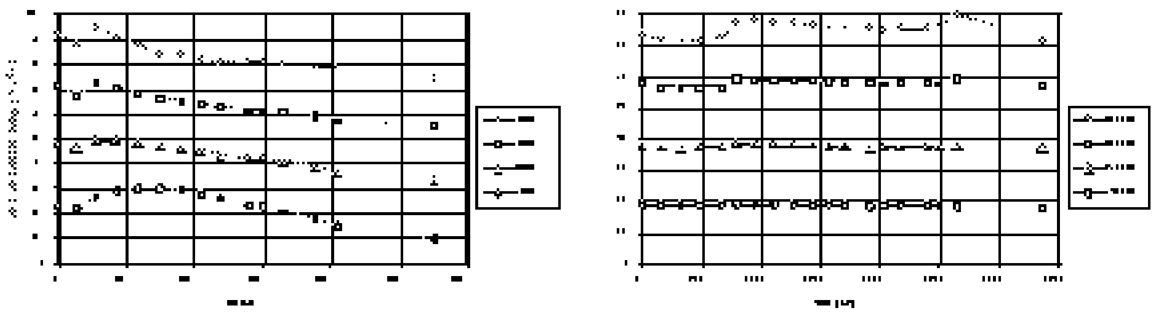

Fig. 8.11: Lifetime of DEP HPD under constant illumination: Gain vs. integrated charge at output. Left side is P25 and right side is E18.

The maximum integrated radiation dose of neutrons is expected to be 5 x 10^{10} n/cm^2 for photodetector boxes of HB/HE. To measure the effects of integrated dose, a 7-channel DEP tube was irradiated by moderated (1 MeV) neutrons from seven distributed ^{252}Cf sources at Oak Ridge National Laboratory with a total fluence of (3.5 ± 0.3) x 10^{10} n/cm^2/hour at the surface of the photodetector. The HPD was operated at high voltage and bias during the irradiation, and both a center and side pixel were monitored by blue light piped through rad-hard fused silica optical fibers. As can be seen from Fig. 8.12, both pixels reacted to neutron irradiation with a monotonically increasing leakage current typical of silicon. When normalized to the area of the pixel (58 and 72 mm^2 for central and side pixel respectively), this corresponds to a rate of increase of 20 nA /10^{10}n /cm^2. For CMS HPDs with pixel areas of 6.25 and 25 mm^2, the leakage current would rise to 6 and 24 nA after an integrated dosage of 5 x 10^{10} n/cm^2. When exposed to doses an order of magnitude larger than expected (as high as 10^{13} n/cm^2), the HPDs continued to operate properly, although photocathode damage resulted in a 30% reduction in the signal and leakage currents rose to µA. The rms fluctuations in the leakage current, however, were still measured to be 16 pA, meaning that a 1% DC source current calibration should still be possible.

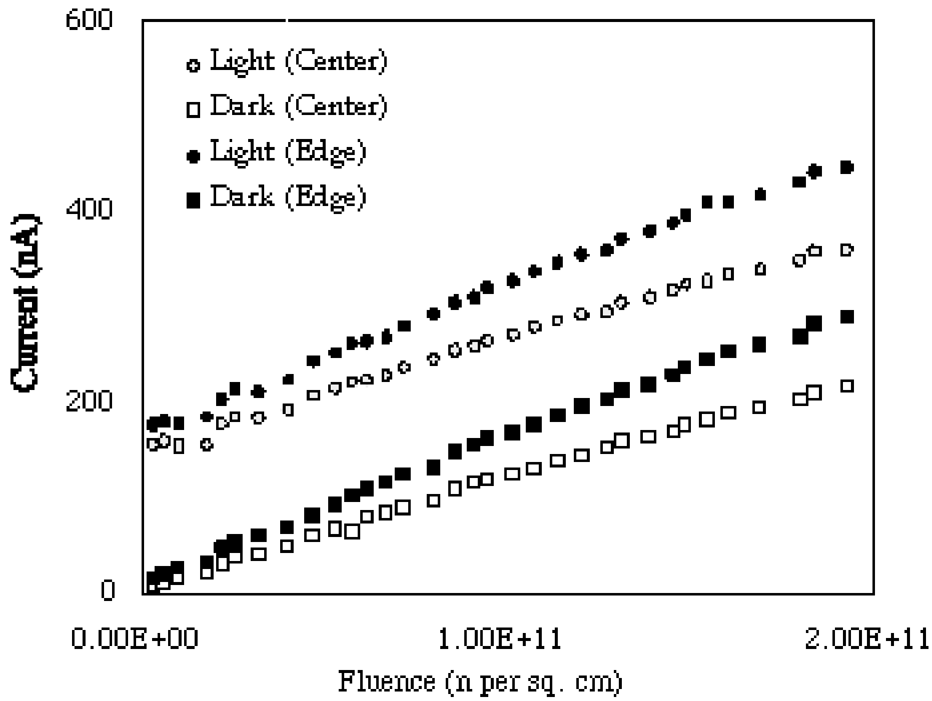

Fig. 8.12: Light and dark currents measured in 7-channel DEP HPD as a function of neutron dosage.

8.3.4 Magnetic field studies

During the 1996 CERN test beam, the 7-channel DEP HPDs read out the prototype HCAL while in the 3 tesla field of the H2 magnet. The response to muons improved consistent with a combination of scintillator brightening and focusing (the tube used in the 1996 run had a glass window and therefore some crosstalk at zero field). No reduction of gain or performance was measured, nor was mechanical stress a problem during cycling of the magnet current.

Both a 7-channel tube and a 25 channel tube were placed in the bore of a 5 tesla NMR magnet and their response to a light pulse (piped through a 1mm diameter fiber) was measured as a function of angle, accelerating voltage and bias. Since the B-field is so large, the photoelectrons rapidly gain energy and approach the regime where magnetic forces dominate over electric forces. The velocity $u=(1/B^2)E \times cB$ applies and the electrons follow the B field direction, making tight helical orbits with very small radii of curvature around the field axis. When the axis of the tube is at an angle θ_B to the B-field, the motion of the photoelectrons corresponds to a sideways shift of $\Delta y \tan \theta_B$ superposed on their acceleration to the target, where Δy is the gap between photocathode and target. The cross field drift is only ~50 μm at this point. As the angle is increased, the signal in the center pixel diminishes as the centroid moves off-center. By offsetting the input light to reestablish the maximum, and plotting offset versus θ_B, one can deduce the accelerating gap from the slope of the resulting straight line (Fig. 8.13). The fitted slope of Δy=5.3 mm is consistent with the vendor's value of 5 mm. At zero degrees, the gain in the tube with a glass window actually increased with magnetic field, due to focusing effects. The smallest accelerating gap consistent with safe application of a 15 kV accelerating voltage is 2 mm. Assuming this gap, and requiring a positioning of the HPD tube axis to within 5^0 of the B-field axis, the fiber bundles should be 400 μm apart to eliminate any crosstalk and gain shifts due to the B-field. Note that the dead region between pixels shown in Fig. 8.4 serves this purpose.

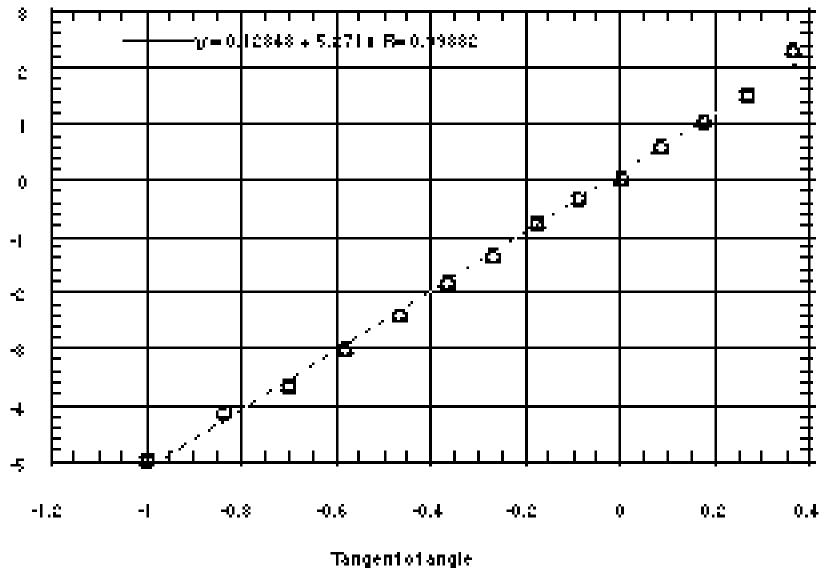

Fig. 8.13: Offset vs. tan θ_B for a 7-channel DEP HPD in a 4.5 tesla field.

8.3.5 Crosstalk and uniformity

Since the target cost is $100/channel, multi-pixel devices look promising. Crosstalk and uniformity were therefore measured in the lab for several different pixel configurations. Boundary scans such as Fig. 8.14 show that there is no dead space between pixels and that pixel to pixel uniformity is 2% or better. This high uniformity, coupled with the reproducibility of tubes with identical gain, means that there is no need for gain balancing either in the HV or in the readout electronics. Since the current required is very low, the HV distribution system can service multiple tubes with no problem. Optical crosstalk between pixels (with fiber optic window) will be less than 1% for the fiber bundle configurations and dead spaces between pixels planned for CMS. Capacitive crosstalk has been bench tested to be less than 2%. It can be reduced even further, by a thin aluminized layer and a drain structure between pixels. These improvements are being made in the new set of CMS diodes.

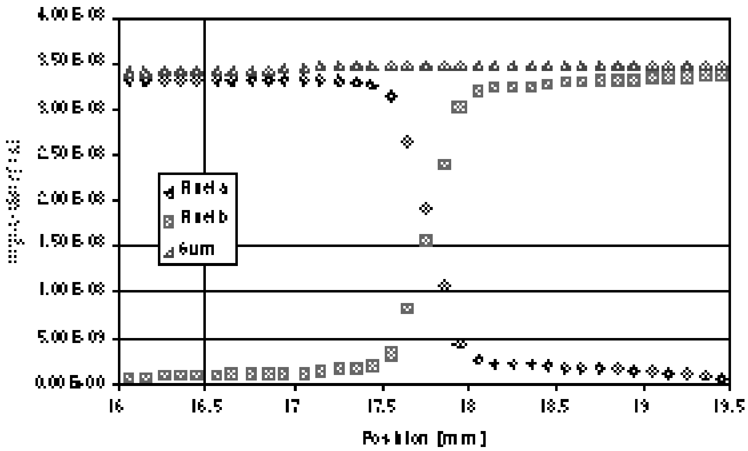

Fig. 8.14: Scan across pixel boundary of 25-pixel DEP tube using green light focused to a 250 micron diameter spot.

8.4 HPD DESIGN AND SPECIFICATIONS FOR CMS

Once HPDs were selected as the readout technology, specifications were drawn up and delivered to potential vendors. The specifications are listed in Table 8.2.

Since the longitudinal segmentation of HB and HE is so asymmetric, two different multipixel tube configurations are envisioned, one with fewer pixels which can accommodate bundles of up to 18 fibers and another with four times as many pixels, each of which services only up to 4 fibers per bundle. The latter will also be used for HB1/HE1 and HOB/HOE channels. In order to keep the total photodetector cost low, the ceramic carrier design will be the same for both types of tubes, as will the tube envelope. The proposed design for the two tubes is presented in Fig. 8.15. They are both on 25 mm diameter format. Each HCAL wedge consists of 4 φ-partitions and 2 depth-partitions, each with 16 η towers. Since each photodetector box is associated with a wedge it contains four 16-channel devices for the HB-2 section and one 64-channel device for all the HB1 channels.

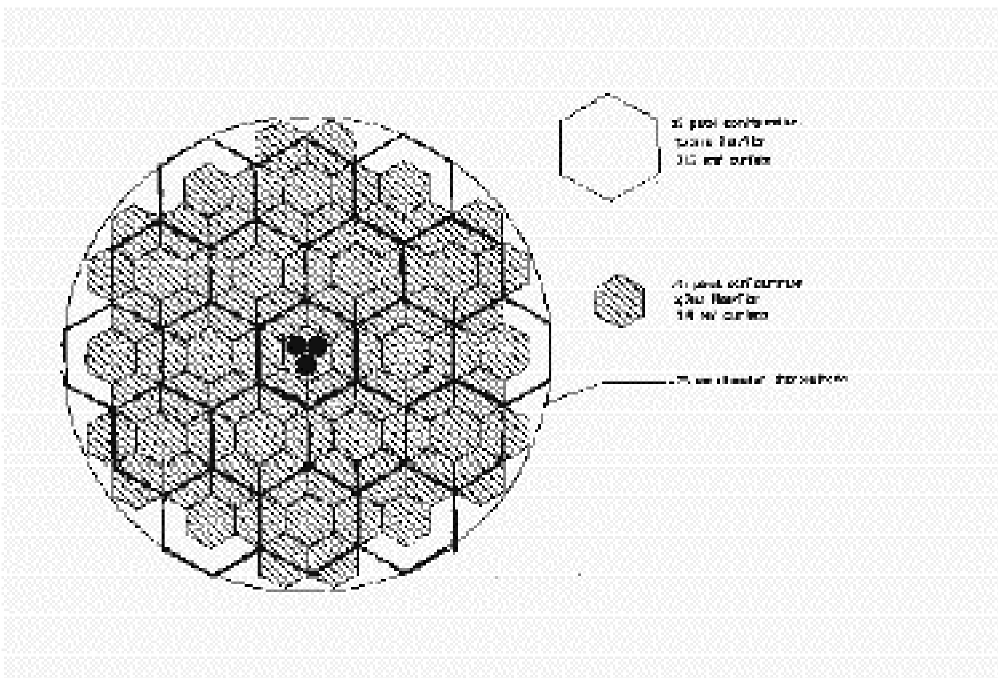

Fig. 8.15: Pixel configuration and tube outline of HPDs for CMS HCAL.

Table 8. 2

CMS HCAL Photodetector Specifications

1. Photocathode:	Fiber optic window with S20 photocathode	
	Quantum efficiency:	>12% at 520 nm
	Radiant sensitivity:	>50 mA/W at 520 nm
	Dark counts:	<250 cnts/s/cm**2
	Photocathode uniformity:	better than 8%
2. Diode	Reverse current:	<20 nA at all bia voltages
	Pixel capacitance:	4 pF
	Channel and lead capacitance:	<25 pF
	Thickness uniformity	5 microns
	Inter-pixel resistance:	<100 ohms
	Junctions:	solder bump-bonding
3.Overall Tube Performance		
3.1 Gain	Operating gain:	>2000 electrons per photoelectron
	Gain variation channel/tube:	<2%
	Gain variation tube/tube:	<5%
	Min signal (muon)	10 photoelectrons (1 GeV equiv)
	Max signal (500 GeV hadron)	5000 photoelectrons
3.2 Linearity	Linear to 2% over this range:	(1 pe - 5000 pe or 12 bits)
3.3 Noise	Noise floor:	2000 rms electrons equivalent to 1 pe response
3.4 Crosstalk	Optical crosstalk:	<1%
	Capacitive crosstalk	<2%
3.5 Timing	Rate dependent gain shift:	<1% in all pixels
	Step input : rise time	<8 ns

	fall time	<8 ns
	Transit time spread	<1 ns
3.6 Magnetic Field	Resistant to magnetic field to	4 tesla
	Crosstalk	<2% at 5 degrees off-axis (0-4T)
	Gain reduction	<5% at 5 degrees off-axis (0-4T)
	Implications:	accelerating gap < 3mm used pixel perimeter plus interpixel gap > 400 microns
3.7 Pixel Size	Two types of tube required: Pixel size (with B-field allowances a specified by 8.3) must allow for bundles of:	a) 19 0.94-mm-diam plus thin calib fibers b) 3 0.94-mm-diam plus thin calib fibers plus B-field allowance as specified by 3.6.
3.8 Lifetime	After integrated radiation dose of 10^{11} n/cm2 and 15C of integrated charge.	leakage current < 100nA fluctuation in - PC response <5% - dark counts <5% - uniformity remains as specified in 1. And 3.1

3.9 Pixel Failure	Number of pixel out of specifications:	zero
	Number of pixels failing over 10 years due to leakage current: due to internal flaws:	1 or less 2 or less
Cost Schedule	Final cost needs to average to under $100/channel	$100/channel

8.5 QUALITY CONTROL AND INSTALLATION

Quality control stations will be established a several locations. Three parallel processes will occur simultaneously. A few tubes will be left in the lifetime testing station for accelerated lifetime testing under various conditions. The rest will move through two other stations, one of which will concentrate on gain, rate dependence, signal-to-noise, and capacitive crosstalk in pulsed mode with the appropriate preamp connected. The second station will do DC scans of the photocathode and diode to determine uniformity and crosstalk. It will also do a trending histogram of the leakage current from all pixels for both long-term stability and short term rms fluctuations relevant to the source measurement. All phototubes go through both test stations.

8.6 HF PHOTOSENSOR SPECIFICATION

The HF photomultiplier specification is based on test beam performance of prototypes which used common low cost PMTs. During the test beams in 1994-6 with 3 different prototype modules, standard 5 cm (2") bialkali glass window PMTs (Hamamatsu R329[1], Philips XP2020, Philips XP2020Q) were used with no difficulty despite the low signal levels from the quartz fiber calorimeters. Fig. ADC distributions for high energy hadrons showed no tails from radiation punch-through induced pulses in the large PMTs, which were placed behind and 10 cm radially away from the edge of the back of the calorimeter, oriented with their axis perpendicular to the beam axis.

The specifications for the PMT, therefore, follow closely the specifications of the tubes used in the prototype work, with the some added requirements for operation in the LHC environment and the HF design.

In general, the selected tubes will be smaller than the PMTs used in the test beam to match the size of the fiber bundles and minimize the projected area of the PMTs to background radiation. Lower gain, will be utilized as well to match the low input noise afforded by the readout electronics and to increase the lifetime of the PMT (total charge drawn from the anode). However, in the main, the PMT are similar to most calorimeter PMT used in existing experiments. The basic HF phototube properties are determined by requirements of:

a) dynamic range;

b) area of fiber bundles;

c) average and peak currents;

d) tube lifetime;

f) counting rates;

g) gain sufficent for 1 p.e. as a least count separated from pedestal in the readout;

h) operation of HF in a hundred Gauss of magnetic field at most.

The latter requirement allows standard low cost focussed dynode PMT when sufficiently shielded with iron cylinders and μ-metal. The high neutron flux at the location of the HF PMTs places a requirement that they are radiation resistant. For this reason we chose quartz (synthetic silica) window PMTs.

The maximum dynamic range of 1 p.e.- 1,500 p.e is modest, corresponding to ~2 GeV - 3 TeV for jet energies in one tower, a very unlikely occurrence but possible. Thus, the linear dynamic range required in HF is for the PMT is no more than ~3,000 and should present no difficulty for most dynode-gain technologies.

An η=5 tower may be exposed to as much as 100 GeV/crossing at 40 MHz, requiring a long-lived PMT (~30-40 C/year of operation at a gain of 10,000), generally achieved by operation at lower PMT gains followed by very low noise electronics. The gain requirement depends on the noise level of the electronics. If the noise level is ~10,000 electrons for the readout at the end of a 2 m cable connecting the PMT to the readout electronics, a gain of $> 8 \times 10^4$ is sufficient for a S/N of 8 at the 1 p.e. level essential for the low energy response of the HF. The S/N level of ~8 is chosen so that 1/4 p.e. level can be discriminated and counted at least a 1:1 S/N level, and so that there is an additional factor of 2 in gain possible if the gain sags during the experimental conditions or if additional gain is needed for cable driving and to overcome additional electronic noise. The 1/4 p.e. discrimination is necessary to:

a) determine accurately the shape of the 1 p.e. ADC spectrum which corresponds to ~1(2) GeV electromagnetic (hadronic)energy;

b) to have some additional safety margin in case of a loss of PMT gain during operations or in case of unanticipated electronic noise (widening the pedestal to a few channels for example), and

c) to enable both ~ 1 MeV source calibration photons and possibly muon signals to be recorded in the test beam and off-line. Note that ~ 1 MeV source calibration photon can generate on average at most a 1 p.e. pulse when a Compton electron fully crosses a fiber at 42°. A higher noise level in the electronics will necessiate a higher gain PMT.

The very short optical pulse from the Cherenkov light, co-temporal with the relativistic part of the shower, and only 7-8 ns wide pushes up peak current linearity requirements, but the low light levels keep peak currents at modest levels, < 25 mA, easily realized by commercial PMT. If the fibers were bundled as $\Delta\eta$ x $\Delta\phi$ physics towers, the largest fiber bundles (low η) are matched by PMT with photocathode diameters of about 20 mm. If the fibers are bundled together from the fibers collected from 10 cm $\times$ 10 cm and 5 cm $\times$ 5 cm bricks, the tube diameters with areas equal to the fiber bundle diameter are 14 (7) mm respectively. It is of some advantage to standardize on the maximum or larger PMT diameter. Since the higher η tower PMT's receive more light by nearly an order of magnitude over the η = 3 towers and require a higher level of charge drawn per unit area of anode, it is reasonable to select a PMT in the diameter range of 15-20 mm for the photocathode for all towers, reducing complexity and lowering cost due by economies of scale.

After- and pre-pulsing at typical levels from commercial PMT will not be a problem for this experiment, and will be less than the noise pulses at the few p.e. level from ambient radiation (neutron, photon), inducing on average 0.5 p.e. noise per tower on each gating.

The risetime requirement derives mainly from the desire to reserve the potential to separate beam-gas and interactions in the quadrupoles from genuine beam-beam events by timing, but long enough so that peak currents are not a problem for the PMT. Rule-of-thumb dictates timing at ~ 20% of the risetime is reasonable. Combining requirements gives a risetime < 2.5 ns, and > 1 ns.

An important requirement is that the transit time through the PMT be less than the bunch interval time, in order to minimize hysteresis effects in the PMT. We have demonstrated (Fig. 8.16) that a PMT with a transit time of 8.5 ns (Hamamatsu R5900) can easily reproduce a 40 MHz optical pulse train generated by a blue LED, at a level of ~30 p.e. (about 60 GeV jet energy in HF) at a gain of ~1 x 10^5. This is thus an important requirement, and the baseline PMT chosen has a maximum transit time specification of 16 ns.

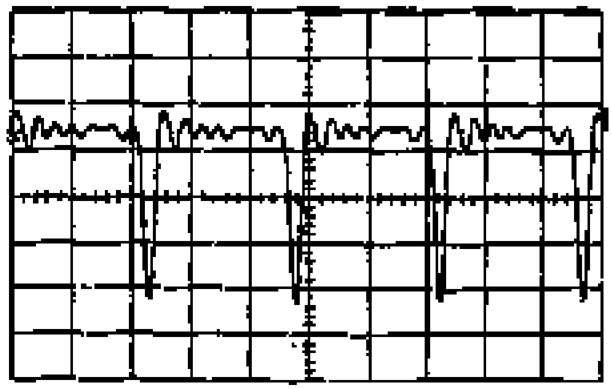

Fig. 8.16: 40 MHz optical pulse train using an R5900 (20 mV/div x 10ns/div).

The PMT lifetime requirements are derived from the rates induced at high η by the beam. At |η| > 5, we anticipate that a PMT at a gain of 10,000 will deposit ~32 C/year on the anode. The anode lifetimes are typically ~350 C. We have demonstrated pulsed current lifetimes of the miniature PMT in excess of > 300 C. Fig. 8.17 shows such a lifetime test.

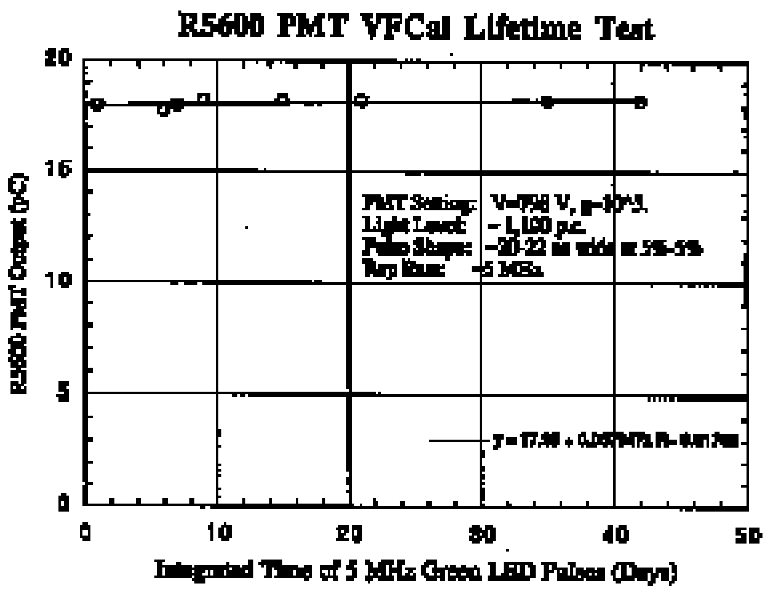

Fig. 8.17: PMT lifetime test at 1,100 p.e./pulse (~2 TeV/pulse) at 5 MHz.

Thus the PMTs on the towers of highest pseudorapidity, accounting for ~104 PMTs, may have to be changed on an annual basis, if the design specification for the QIE noise is greatly exceeded. Alternatively , one could accept a S/N level of 1 in the highest η towers. Lowering the gain to ~10,000 (i.e. by a factor of 10) would increase the lifetime to 10 years.

Basic PMT requirements derived from the above considerations are summarized in Table 8.3.

Note that the PMT requirements include:

1) Reduced Radiation-Induced Pulses: Where possible, compact vacuum envelope, compact dynodes, opaque envelope, and thin photocathode window PMT will be selected, in order to minimize the amount of false pulses from neutrons, gammas and muons crossing the PMT itself. Additionally, materials in the PMT should be chosen to minimize neutron activation and fast neutron reactions. Alternative glasses (especially fused quartz) to boron-containing ones are preferred.

These background pulses associated with the particles incident on the calorimeter are not anticipated to be large in any case. Test beam data show that the background pulses induced on an XP2020 5 cm diameter PMT placed directly behind the calorimeter prototype have an average value of ~1.3 GeV with an rms of ~1 GeV with 350 GeV pions incident. Note that the ADC gate was 60 ns during this testing. Similarly, a miniature R5600 (8 mm cathode) had negligible induced pulses when similarly placed behind the prototype calorimeter in the test beam.

Table 8. 3

HF PMT Specifications.

Diameter:	$\phi_{cathode}$ > 13 mm
Q.E.	15% 400-500 nm; 25% @ 400 nm
Cathode Uniformity	<±10%, ±2 mm point, within 0.9 dia.
Photocathode lifetime:	>10 mC drawn from cathode, with $g>0.9g_{initial}$
Gain:	>5 x 10^4 per 10,000 e- noise
Single p.e. Resolution	rms/mean of single p.e. peak <50%
Linearity, Pulse	±2% from 1-3,000 p.e.
Peak Current	Ip 25 mA ±2% (per 2 ns t_{rise})
ttransit	< 25 ns
trise	2.5 ns (10%-90%)
Pulse Width t_{FWHM}	8 ns
Gain (1/2) Lifetime:	320 C/year (g=105, 100 GeV per 25 ns)
Average Current:	60 µA
Stability:	<±3% 24 hours; <2% short term
Tube-Tube Uniformity:	Gain*QE within ±1% by HV adjustment
Window	Quartz, thickness: < 2 mm

Window Coatings	Transmission: >90% 400-600 nm, <10% 300 nm He Permeability: borosilicate glass
Envelope	Opaque & Conductive coating
Radiation Dose	10 KRad/year: <90% QE*G loss 3 x 10^{12} n/cm^2 /year: <50% QE*G loss

The radiation background calculations indicate that about 2.7 $\times$ 10^{-5} mip/cm^2/crossing will be at the front face of the PMT, or about 5 $\times$ 10^{-5} per PMT per crossing. A study of background induced in PMT by mips and photons through the front window of PMT was carried out by the ITEP group in HF[2]. Fig. 8.18 shows the probability as a function of $N_{p.e.}$ to obtain $N_{p.e.}$ for mips passing through a 1mm thick PMT window (R5600). The mean response to a mip is 6.06±3.58 p.e. This would correspond to a noise of 1.2 p.e/crossing, or about 2.5 GeV/crossing in noise from mips. Note that this noise floor may soften the gain requirements on the PMT.

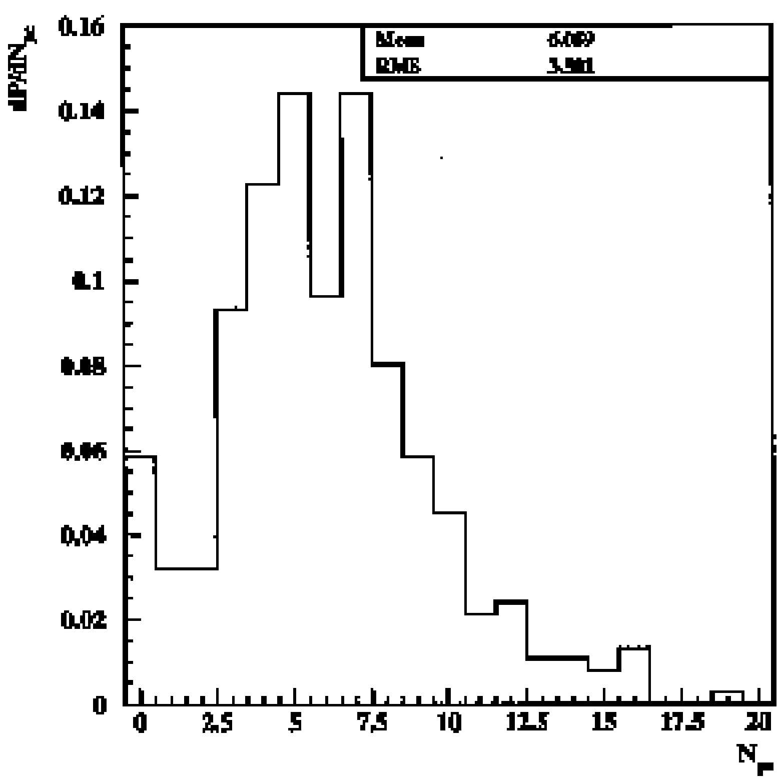

Fig. 8.18: The probability as a function of $N_{p.e.}$ to obtain $N_{p.e.}$ for mips passing through a 1mm thick PMT window (R5600)[2].

The probability for a ~1 MeV (^{60}Co) photons to induce pulses in an 8 mm diameter, 1mm thick window

PMT (R5600)[2] has a mean is 0.25 p.e./photon, and the efficiency (probability of 1 p.e. or greater) for counting a photon is 15%. The radiation dose calculations indicate that there will be ~10^{-4} photons per PMT/crossing impinging on the PMT windows, or a noise floor, of 0.33 p.e. per crossing from photons.

2) Helium Partial Pressure: Envelope and coatings to reduce the permeability to He are essential. The photocathode window may be overcoated with a thin low index silicone polymer, both for antireflection coating and for He permeability resistance, if it can be proven for radiation damage. This may be demanded by He partial pressures anticipated in the hall. Alternatively, a CVD coating of MgF or CaF may be specified in the PMT bid. Permeability to He in quartz is 1-2 orders of magnitude larger than in glass. The PMT housing and gas system will reduce ambient He pressure by more than 10^{-3}.

3) Removable of UV component: Because the UV light generated in the quartz fibers is subject to degradation by radiation damage, the UV light is cut-off by a filter system. This system will either use a Schott glass filter of 1 mm thickness[2], or dielectric coatings with short wavelength cutoffs. These may include an ITO (indium tin oxide) conductive coating at the HV of the photocathode which will protect the cathode also from electrostatic effects when connected to tthe cathode voltage.

The ITO coating and the antireflection coatings are resistant to He diffusion. Thin-film coatings are generally known to be radiation hard[3,4] because (a) a coating thickness <~1-2 µm requires an enormous dose to create a large optical density on such a thin film, (b) it is difficult to change the electron density and hence the index *n* by radiation, and (c) dielectric coatings with high resisitivity on the order of 1 wavelength have low absorption. The magnesium fluoride and/or silicon monoxide films likely to be selected for the HF PMT.

The PMT requirements outlined above are met with a 19 mm (15 mm cathode OD) PMT from Philips and Hamamatsu, and by the 25 mm (21 mm OD cathode) R5800Q. The desired baseline PMT is a 10 stage, in-line dynode Hamamatsu PMT, the R4125, with a typical (maximum) gain of about 10^5 (10^6), developed for high linearity. This tube is available with a special coating to make the walls black and impermeable, and with a quartz window only 2 mm thick[5].

In test beams, the very lowest background PMT is the metal envelope, metal-mesh dynode PMTs from Hamamatsu [Table 8. 4], the R5600, with an 8 mm diameter photocathode, and the R5900 (18 mm square cathode). The diameter of the R5600 is matched to the size of the bundles from the highest η towers. The window material may be made as thin a 0.8 mm, greatly reducing Cherenkov light. Additionally, the metal channel mesh dynode stack is only 6 mm thick for 8 stages of gain (up to 10^5), which reduces the cross-section for induced pulses from radiation backgrounds. The metal mesh family of Hamamatsu PMT are also preferred because of the short transit times (< 9 ns).

Refinements in the choice of baseline PMT may be made at the time of order, depending on development efforts by commercial manufacturers. There are clearly a number of reliable alternatives, and performance is not a serious issue. It is likely in order to decrease the transit time further, and to increase the linearity and lifetime, we may specify PMT variants of the R4125 or XP1918 with 8 stages rather than 10 stages. The transit time should decrease to ~13-14 ns in the R4125. At present, the best compromise between price and performance is the R4125/XP1918 types, while the best price is the R5800Q.

Table 8. 4

Photomultiplier tube summary.

	R4125	XP1918	R5800	R5600
Diameter	15 mm	15 mm	21 mm	8 mm
Gains	10^5 /1,100 V	10^5 /900 V	10^5 /800 V	10^5/900 V
Q.E.:	27% /400 nm	26% /400 nm	27%/400nm	27%/400n
t_{rise}:	2.5 ns	2.4 ns	1.5 ns	0.7 ns
$t_{transit}$:	16 ns	23 ns	21 ns	<8 ns
Pulse Linearity	±2% 100 mA	±2% 80 mA	±2% 100mA	±5%,30 mA
I_{ave}:	100 μA	200 μA	100 μA	100 μA

8.7 RADIATION DAMAGE

The HF PMTs are sufficiently shielded by the HF itself, the HF shielding, and by the bulk of CMS that radiation damage will be minimal. The HF PMT are located at over 1 m in radius, from the beam pipe and over 14 m from the IP, and are enclosed in a robust shield to absorb neutrons. Radiation calculations indicate that the HF PMT should receive a radiation dose of about 1 krad/year, with about 10^{10} n /cm^2/year.

The dynodes are intrinsically radiation hard[6]. A study of the dynode radiation hardness up to 10 Mrad of ^{60}Co indicates no change to the dynode gain (ibid). The photocathode materials, a bialkali photocathode (NaK_2Sb or Cs_2KSb), is classed as a very loosely bound amorphous semiconductor; *i.e.* a simple stochiometric ratio of materials made by alkali diffusion into a thin amorphous Sb at temperatures well-below that needed to form crystalline materials. This structure is not affected strongly by dislocation defects from radiation bombardment. The principle cause for radiation damage failure is the darkening of glass envelope windows, activation of the window material producing phosphorescence (thermal luminescence), and insulation failure. Fig. 8.19 shows the radiation-hardness of 3 major types of glass used in PMT, from the Hamamatsu handbook, for photons (left) from 144 krad- 44 Mrad, and neutrons (right) from ~4 x 10^{13} - 2.5 x 10^{14} n/cm^2[7].

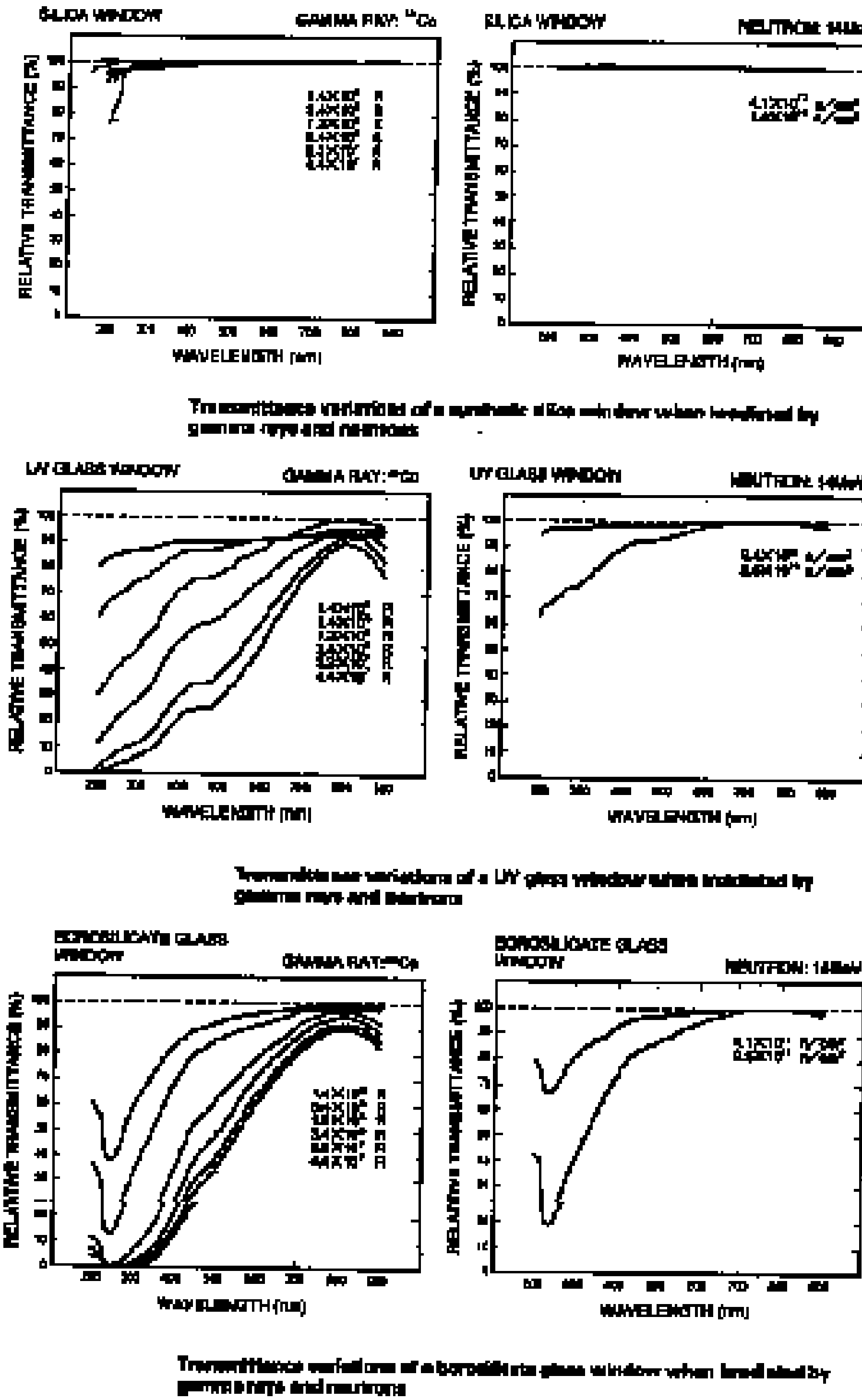

Fig. 8.19 : The radiation-hardness of 3 major types of glass used in PMT, from the Hamamatsu handbook, for gammas (left) from 144 KRad- 44 MRad, and neutrons (right) from ~4 x 10^{13} - 2.5 x 10^{7} n/cm^{2}.

Additionally, induced fluorescence, phosphorescence and "scintillation" occurs with radiation on standard glass photocathode substrates. Fig. 8.20 from the Hamamatsu PMT Handbook shows the increase in dark current with a very low dose of radiation (10.5 rad) in borosilicate glass[8].

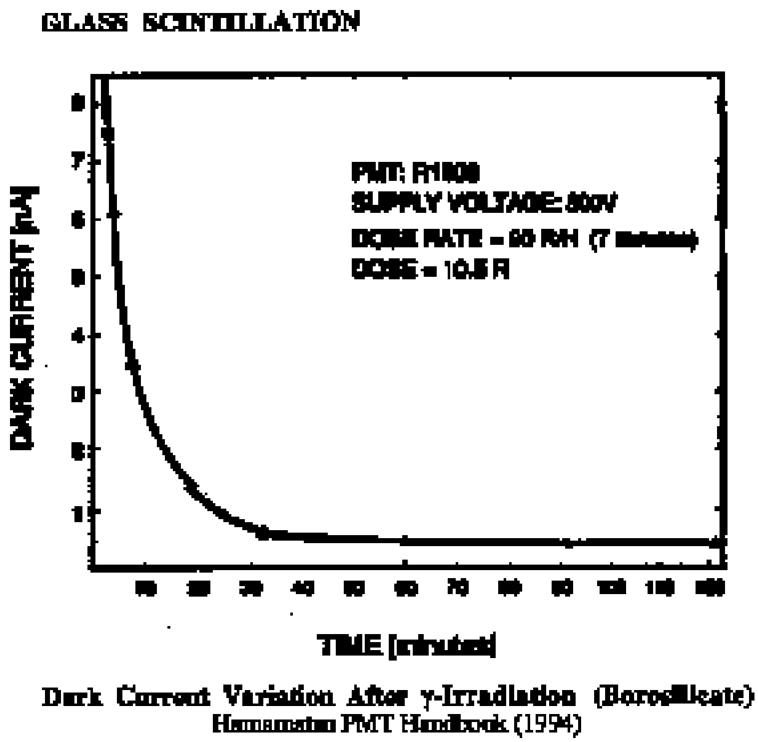

Fig. 8.20: The increase in dark current with a very low dose of radiation in borosilicate glass.8

The PMT candidates are undergoing tests in Hungary to determine the extent and properties of radiation damage. They operate at up to 10^{14} n/cm^2 with little effect on gain. However, PMT radiation damage occurs first in the glass window. The glass of the envelope may turn black, with little effect on the PMT gain operation. We have observed low levels of induced phosphorescence in the window using UV-glass from Hamamatsu. We anticipate that the high purity synthetic quartz version will not have this effect. Other quartz window PMTs have been shown to operate at levels of exposure up to 50-100 Mrad of ^{60}Co radiation. For example, EMR Photoelectric, Princeton, NJ, has demonstrated operation of quartz window PMT up to 100 Mrad (type 730N-01-13, 1" end-on PMT) for operation in the cosmic ray environment of space which uses a thinned silica glass window and a standard bialkali photocathode[9]. Additionally, some PMT may use insulator materials which are not fully radiation-hard for the connector pins or for dynode standoffs. Alumina- and lead-oxide-based ceramic dynode standoffs are specified, and used in the PMT selected.

8.8 QUALITY ASSURANCE

The PMT quality for HF will be assured by a test cycle that occurs in 3 forms: at the manufacturer, testing and preselection as they arrive, and beam and calibration tests during the installation period. The purpose of these specifications and tests is to assure that a PMT can be replaced with the confidence that any PMT will function within 2% of any other PMT, with control of the HV alone. Spare PMT will be ordered (10%) to allow for preselection matching, breakage, and failure.

For the manufacturer, a detailed set of specifications, similar to the ones shown above, will be proposed in the bidding process, but with an appropriate negotiation so as not to increase the price inordinately due to very extensive manufacturer testing or pre-selection. Because of the low light levels of the HF signal, the quantum efficiency and cathode uniformity are key issues in the specification. At present, the industrial capability is available to guarantee a point-point uniformity over 2mm x 2mm areas of ±5% out the the edge of the usable photocathode. This uniformity is sufficient, because the light from each fiber will be pseudorandomized by a light mixer in such a fashion that each fiber will illuminate more than 50 % of the photocathode area.

The PMT will be delivered half each to 2 identical test stations for testing, with duplicate measurements for comparison made on 10% of the PMT. These stations will utilize pulsed light systems (laser and LED), radiosource-scintillator constant light sources, and data acquistion to measure: (a) gain vs HV, (b) pulse shape, (c) single photoelectron level, (d) PMT noise at the 1/4 p.e. level, (e) the linearity of the response from 1-2,000 p.e., (f) relative gain changes at 0.1, 1, and 40 MHz. A fiber scanner will quantify photocathode non-uniformities on a 5 mm scale. The quantum efficiency at several wavelength pass-bands (in a range from 300-600 nm) will be measured with temperature controlled scintillators + alpha source (NaI, BGO, CaF_2 and BaF_2) with optical filters, which serve as constant light sources.

The PMT can be delivered at a rate of about 200/month, requiring a 6 month lead time to start delivery, 17 months for the PMT fully delivered order, or 2 years to complete the PMT acquisition and testing. We budget a total of 1 hour each to unpack, test, label, repack, and enter, merge publish & archive data for ~4000 PMT. The selection database will be maintained for each PMT together with the base and front end electronics.

References

[1] Hamamatsu Photonics Corp. Bridgewater NJ.

[2] V. Gavrilov et al., Sensitivity of Photomultipliers to Protons and Gammas, CMS TN/95-146 (15 Nov., 1995).

[3] Schott Glass Inc.

[4] A. Holmes-Sidle and L.Adams, Handbook of Radiation Effects, (1994) Oxford U.P., Oxford, UK.

[5] J. Wong and C.A.Angell, Glass: structure by spectroscopy (1976) Dekker, Basel.

[6] S.Belianchenko et al., Study of PMT Radiation Hardness, IHEP 96-90 (1996) (submitted NIM).

[7] Photomultuiplier Handbook, Hamamatsu Corp., 176 (1994).

[8] Photomultuiplier Handbook, Hamamatsu Corp., 177 (1994).

[9] M.M.Birnbaum, R.L.Bunker (JPL, Pasadena, CA), J.Roderick, and K.Stephenson (EMR Photoelectric, Princeton NJ), "Development of a Radiation-Hard Photomultiplier Tube" (1984) EMR Photoelectric Publication, Princeton, NJ, and published in the American Institute of Aeronautics and Astronautics (AAIA) Guidance and Control Symposium Proceedings, AIAA-84-1852, (Aug. 20-22, 1984).

Table of Contents

9. FRONT END ELECTRONICS

9.1 INTRODUCTION

9.1.1 Readout electronics overview

Readout of the CMS hadron calorimeters is realized through a chain of system elements beginning with photodetectors coupled to light produced in the calorimeter detection media and ending with memory storage of digitized results in an on-line processor farm. Electronics systems are located in three different areas of the Point 5 experimental complex: (1) the control room at grade level 150 meters above the accelerator tunnels and caverns, (2) the shielded underground service room about 100 meters radially inward from the beam line, and (3) on or adjacent to the detector in the underground cavern centered around the beam line.

Signal processing functions required of the calorimeter readout electronics chain during colliding beam operations can be summarized as follows:

a) Analog signal conditioning of photodetector responses

b) Digitization of conditioned analog signals at the beam crossing rate of 40 MHz

c) Transmission of digitized values from the detector to the adjacent service room at 40 MHz

d Linearisation and conversion of front end results into deposited energy values at 40 MHz

e) Generation and transmission of filter-extracted first level trigger information at 40 MHz

f) Pipeline storage of linearised energy values during the first level trigger decision interval at 40 MHz

g) Buffering of linearised time samples at the average first-level trigger accept rate of 100 kHz

h) Generation of second level trigger information at 100 kHz

i) Formatting, organizing and transferring of trigger and linearised time sample data to the event builder at 100 kHz

All of the 40 MHz signal processing operations at the very front end of the system are synchronous with accelerator operations and are phase locked to the beam crossings. The higher levels of the readout system operate at an average "interesting event" rate of 100 kHz and are decoupled from the synchronous, pipelined front ends by a set of derandomising buffers.

Other modes of operation of the readout system, e.g. data acquisition for the light flasher calibration system or determination of pedestal values, are far less demanding. The requirements are easily met by a subset of the capabilities needed for data taking.

9.1.2 System configuration

Partitioning of the readout chain is subject to several important global architecture and space constraints, and is impacted strongly by considerations of maintainability. Environmental aspects associated with placing electronics in the collision cavern or inside the detector are discussed in chapter 9 below. In summary, access could be possible to the regions along the side walls of the cavern on a twice a month basis. For the inner part of the detector access could be possible on a yearly basis with difficulty. The CMS first level trigger system cannot be located on the surface because of the time delays introduced; it is located as close to the detector as possible in the adjacent underground service room. Sufficient shielding is planned so that this area can be accessed during accelerator operations. The remainder of the data acquisition and trigger system is located on the surface due to the limited size of the shielded underground service room.

The configuration selected for readout of the hadron calorimeter has electronics systems located on the detector, along the side walls of the collision cavern, in the underground service room, and on the surface. Analog signal conditioning and digitization electronics are located at the photodetectors attached to the calorimeter elements, trigger and data acquisition electronics are located in the underground service room, and readout control, formatting, and interfaces to higher levels of the system are located on the surface. High speed data links connect the front end digitisers on the detector to the trigger and data acquisition systems in the underground room at the 40 MHz beam crossing rate, and standard communications links bring the digitized data up to the surface at the reduced rate corresponding to first level trigger accepts. Low voltage power supplies and other utilities are located along the side walls of the cavern.

9.1.3 Front end electronics overview

There are a total of 15,096 readout channels in the system; the breakdown by subsystem is given in Table 9. 1 below.

Table 9. 1

Readout Channels

SYSTEM	SECTION	CHANNELS	TOTAL
	Front	1768	

Forward	Main	1768	
	Outer	328	3864
	Front	2448	
Barrel	Main	2448	
	Outer	2160	7056
	Front	1152	
End Cap	Main	2016	
	Outer	1008	4176

The front end electronics system comprises those components located on the detector in close proximity to the calorimeter photodetectors as shown in Fig. 9. 1 and Fig. 9. 2. These components provide the functions of analog signal conditioning, digitization, synchroni-zation/control, and data transmission. A functional block diagram of the system elements for a three-channel subsystem is shown in Fig. 9.3. A later section of this chapter provides details on the individual components. Performance and reliability risks associated with placing the digitiser portion of the readout electronics directly on the calorimeter, where routine service is problematic, have been evaluated and incorporated into the requirements for reliability.

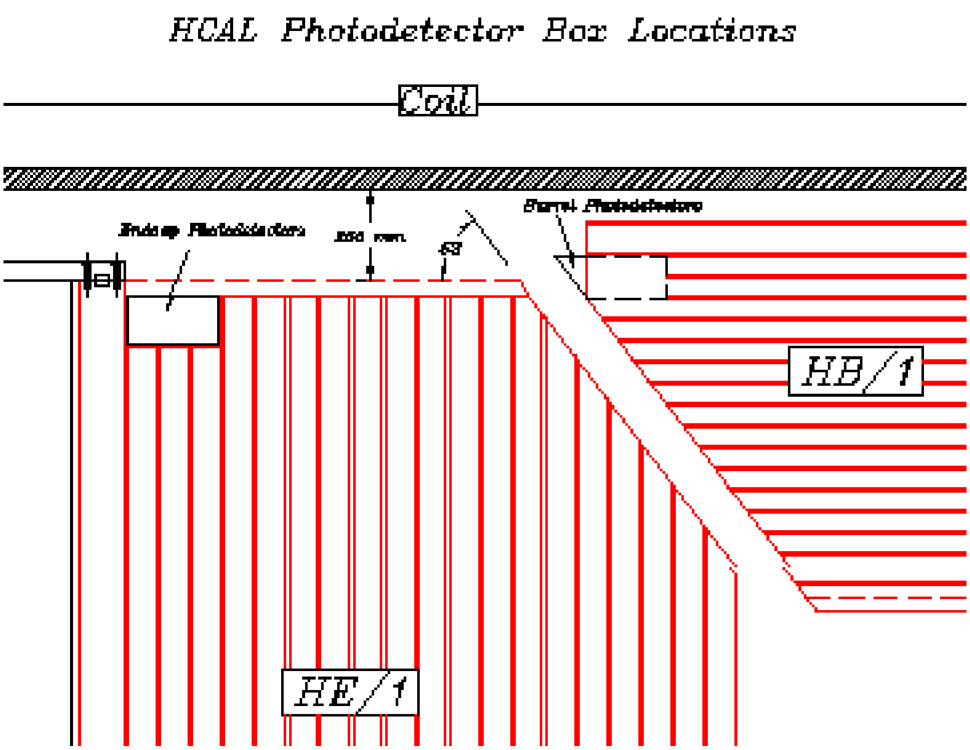

Fig. 9. 1: Barrel and End Cap front end electronics locations

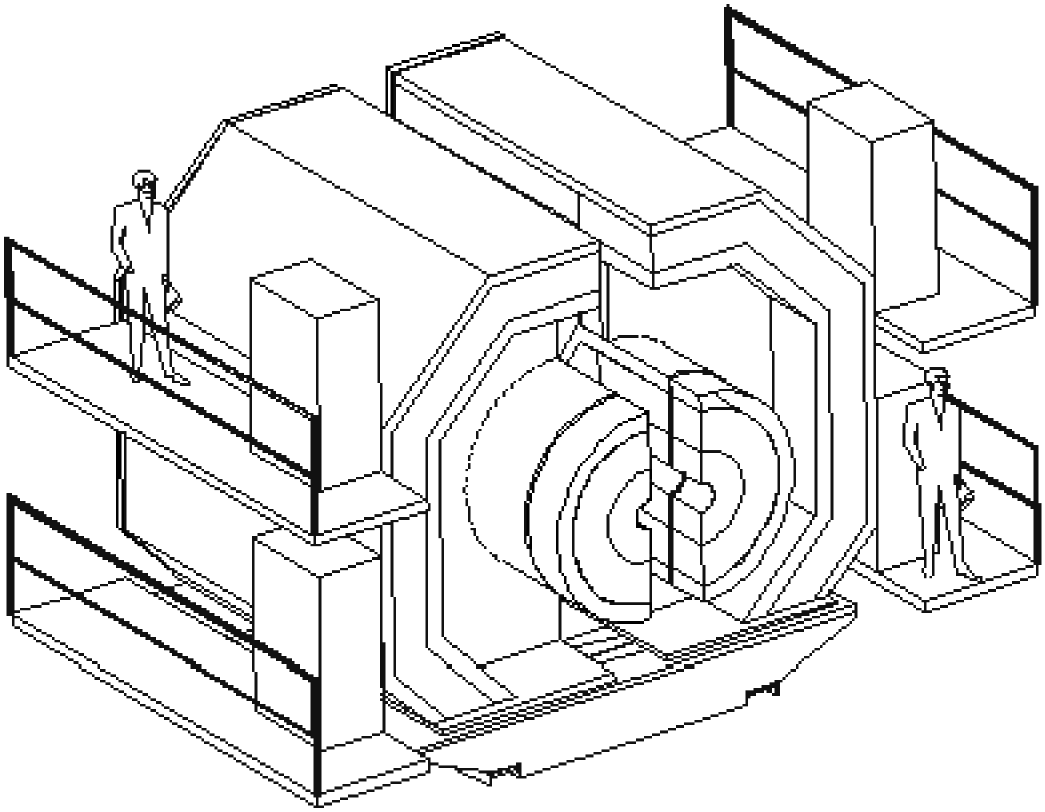

Fig. 9. 2: HF electronics rack locations.

Analog signal conditioning is done using a multi-range current splitter and gated integrator, the QIE (Q for charge, I for integrating, and E for range encoding) ASIC. The outputs of this ASIC are 3 bits of range information and an analog level corresponding to the integrated charge on the encoded range. After conversion of the analog level by an ADC, the digitized result is in a eight bit pseudo floating-point format with 3 bits of range (or exponent) and 5 bits of charge (or mantissa). A separate digital ASIC is needed to control and synchronize the QIE channels and to transfer the results over a high speed link to the trigger and data acquisition electronics.

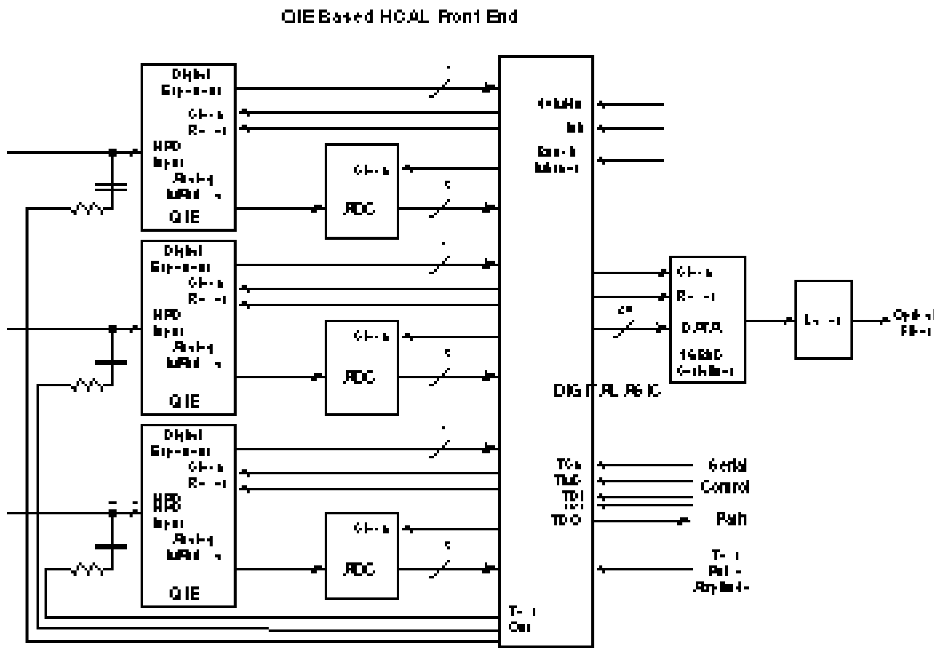

Fig. 9. 3: Front end electronics block diagram.

The front end system operates continuously and synchronously with the accelerator r.f. time structure, 25 ns between beam crossings. Operations are completely controlled by an external clock. A digital value for the energy deposited in every calorimeter channel for each 25 ns interval is transmitted from the front end electronics to the trigger and data acquisition electronics. This 40 MHz clock is provided by a sophisticated distribution and receiver system[1] and includes a synchronization marker which occurs once per orbit of the beam. The marker occurs during the gap in the collider fill reserved for the beam abort function and is used in conjunction with a bunch counter to provide an important check of data validity.

A serial fieldbus, described in chapter 13, is used for communication with and control of the front end systems. Monitor and alarm functions are provided for photodetector high voltages and currents, electronics low voltages and currents, synchronization validity, and temperature values. This fieldbus is also the pathway for exercising test and diagnostic functions, downloading control and parameter data, and selecting operational modes.

Packaging requirements vary according to the location of given calorimeter system. For the inner barrel and end cap systems, custom packaging is needed due to the space constraints as shown in Fig. 9. 1. Small cutouts or pockets are placed into the absorber at the outer radius to accommodate these packages or readout boxes. There is sufficient space for standard crate-based electronics packaging at the forward calorimeter and at the photodetector locations for the outer barrel and end cap calorimeter compartments.

9.2 REQUIREMENTS

Calorimeter requirements vary over the different regions of phase space in accordance with the physics processes of interest. Missing energy signatures are important for performance requirements in all of the calorimetry, whereas high energy dijet processes mainly challenge the central region calorimeter, and high rate situations are the province of the forward calorimeter. In this chapter, the hadron calorimeter readout requirements are presented in detail over the whole region to define the parameters which set the performance limits. The goal is to define a single set of requirements appropriate to all of the hadron calorimetry and to define a single set of electronics which meets those goals. Considerations driving a single choice involve maintenance and support, stockpiling parts to protect against process obsolescence, economies of scale, and duplication of effort.

9.2.1 Performance 9.2.1.1

Analog signal conditioning

In the central region, the calorimeter detection elements are scintillators readout with wavelength shifting plastic fibers and the photodetectors are hybrid photodiodes (HPD). The shape of the light pulse produced is an initial step followed by an exponential decay corresponding to the fluorescence characteristics of the combined scintillator-waveshifter system. This time constant, using a single exponential approximation, has been measured to be 11.3 ns. Thus the expectation is that 89.1% of the light signal occurs in the first 25 ns, 9.9% occurs in the next 25 ns interval, and 1.0% occurs in the third 25 ns interval on average. The signal is stretched further when the 5 to 10 ns impulse response of the photodetector and differences in optical path lengths of the elements of a tower are taken into account and convoluted with the light signal; 68% is in the first interval, 29% in the second, and 3% in the third on average. Finally, statistical fluctuations on these average values are significant, especially for the case of low light levels where only tens of photoelectrons are involved.

Since the signals from at least two following beam crossings after the one of interest must be added to obtain the true value, the current produced by the photodetectors must be integrated (and digitized) over each 25 ns interval separately. This is also the case when there is pile up of signals from adjacent crossings as estimating the baseline shift requires charge integral results for several early crossings. Therefore, the central systems require a gated integrator which is reset every crossing, has a precise aperture as close to 25 ns as practical, and suffers negligible charge loss at each 25 ns boundary.

In the forward region, the calorimeter detection elements are quartz fibers directly viewed, and the photodetectors are photomultiplier tubes. The signal produced is due to Cerenkov light from relativistic shower particles, and, as such, is very fast. Test beam results with small, fast phototubes indicate that the entire signal can easily be made to occur in less than 25 ns. Pile up of signals from adjacent crossings thus does not occur, and the pedestal (or baseline depends only on the amount of out-of-time background. Fig. 9. 4 shows a multiple trace oscilloscope picture of calorimeter signals produced by 350 GeV protons.

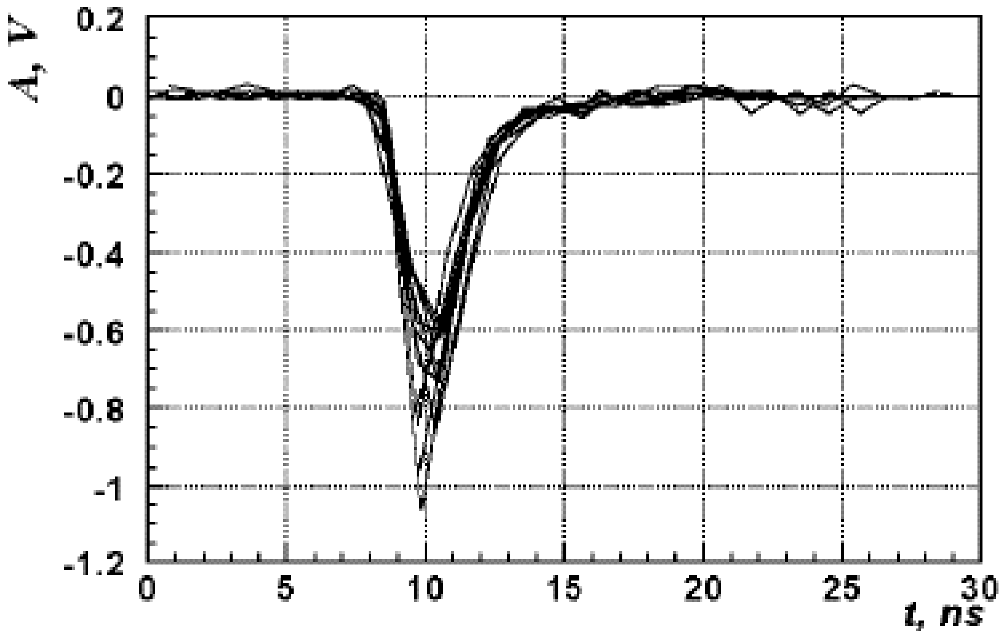

Fig. 9. 4: HF Response to 350 GeV Protons

Given that the signal duration is smaller than the bunch crossing interval, a gated integrator which is reset each crossing is also appropriate for the forward calorimeter. The requirement on aperture precision is modest, 10% is adequate, and the issue of charge loss at the 25 ns boundaries is not relevant to the principal measurement.9.2.1.2

Dynamic range

The main compartments of the barrel and endcap calorimeters, HB2 and HE2, are required to respond reliably to minimum ionizing particles in order to contribute to the muon trigger and for off-line identification of muons. This situation determines the details of the low end of the dynamic range and is described below in the chapter on signal to noise considerations. At the high end, studies[2] have shown that the largest energy deposition expected in a central or end cap calorimeter main compartment over 10 years of operation at full luminosity is of order half the beam energy, or 3.5 TeV. Actual jet energies could be higher, but the energy in a jet is spread over several towers spatially and is shared between the electromagnetic and hadronic depth segmentations. In terms of photoelectrons, these requirements correspond to a dynamic range of 1 to 35,000 or 15 bits.

The outer compartments of the central and end cap calorimeters, HOB and HOE, are required to be sensitive to minimum ionizing particles. However, the highest energies seen are significantly lower than those in the main compartments due to the depth at which these layers are located. The physics dynamic range necessary is from minimum ionizing to a rare 1 TeV occurrence. When the photoelectron yield and the low end granularity considerations are taken into account, the requirement is for a 16,000 to 1 dynamic range or 14 bits.

For the forward calorimeter, the single photoelectron signal is extremely important as it corresponds to more than a GeV of energy. Cerenkov light, even when directly viewed, is quite weak in intensity. Test beam studies[3] show that the calibration for the main compartment is approximately 0.4 photoelectrons per GeV. Allowing the upper end to extend to the full beam energy gives a dynamic range of 1 to 3000 photoelectrons, or slightly less than 12 bits. Providing an extra factor of 4 granularity for single photoelectron performance then gives an overall dynamic range requirement between 13 and 14 bits.9.2.1.3

Precision

The precision of measurement requirement, or the granularity of digitization, is set by the energy resolution performance of the calorimeter systems themselves. Resolution is an energy dependent characteristic resulting from statistical fluctuations in shower development and measurement sampling coupled with energy independent effects due to systematic variations in calorimeter response as a function of point of impact or depth of shower initiation. A special case occurs, as noted in the previous chapter on dynamic range, in which the granularity of digitization requirement is determined by a need to measure signal-to-noise values with precision at the low end of the scale.

Energy resolution characteristics of the different calorimeter regions are listed in Table 9. 2 below. A certain functional form is assumed where two terms are folded in quadrature to get the resolution σ:

$$\sigma/E = {}^{a}/_{\sqrt{E}} \oplus b$$

where, *E* is the energy in GeV, *a* is the stochastic term coefficient, and *b* is the energy independent term to be taken in quadrature with the stochastic value. The values listed are taken from test beam measurements of representative calorimeter structures[3]2.

Table 9. 2

Energy Resolution Coefficients

Calorimeter	*a*	*b*
Central	85%	5%
End Plug	90%	5%
Outer	150%	3%
Forward	200%	3%

The precision of measurement required is therefore an energy-dependent quantity. At very high energies, the resolution limit is about 5% for all calorimeter regions. At very low energies, the requirement for minimum ionizing response or single photoelectron performance also needs a few percent of reading precision. Similarly, for the middle ranges, a few percent of value provides adequate resolution. Precision needed is a parameter that is relative to the size of the signal. Small signals require an appropriately fine precision while for large signals, there is no need for such fine granularity.

Accordingly, the two aspects of precision and range can be separated making the actual requirement one of fixed precision anywhere in the larger dynamic range. The granularity of digitization increases the resolution as the bin size divided by $\sqrt{12}$ must be added in quadrature. For the case of a 10% increase in resolution, from 5% to 5.5%, only 3.5 bits of precision are necessary. At 4 bits precision, the resolution change is 5% to 5.3%, and at five bits the change is only 5% to 5.08%. Thus selection of a 5-bit precision requirement results in negligible increase in resolution (performance) from the effect of digitization granularity and provides considerable margin against possible degradation of differential linearity.

The least count requirement is set by the photodetector with lowest gain, the HPD (chapter 8). With gain 2000, one photoelectron becomes 2000 electrons, or 0.32 femtoCoulombs (fC) establishing the minimum granularity.

9.2.1.4 Noise floor

The signal-to-noise figure of merit is derived from considerations of performance at the low end of the scale. Two different aspects are seen in the calorimeter systems. For the scintillator based devices, the issue is separation of the minimum ionizing particle signal from electronics noise. For the Cerenkov light device, the issue is separation of the single photoelectron response from electronics noise.

The most difficult case for minimum ionizing response occurs in the central region outer detectors where the response is 10 photoelectrons per minimum ionizing particle. High detection efficiency, > 99%, results from achieving a useful threshold at 4 or fewer photoelectrons. A low probability, < 1%, for electronics noise to give a false positive result results from the threshold being 2.33 sigma above the zero photoelectron level. Defining the threshold as 3.5 photoelectrons then sets the noise floor at 3.5/2.33= 1.5 photoelectrons. For a photodetector gain of 2000, the noise floor needed is then 3000 electrons rms.

Single photoelectron response is required in the forward detectors. High detection efficiency, > 99%, results from achieving a useful threshold at 2.33 sigma below the mean. For a signal-to-noise ratio in excess of 10:1, this threshold should correspond to 1.5 sigma on the noise. Thus, the single photoelectron response should be 2.33 + 1.5 = 4 sigma above the zero photoelectron level implying a noise floor of 1/4 photoelectron. At the maximum photomultiplier gain of $4 \infty 10^4$ (chapter 8), the noise floor requirement is 10,000 electrons rms. For the expected noise figure of 3000 electrons, the photomultiplier gain could be lowered to $1.2 \infty 10^4$.9.2.1.5

Cross talk

Cross talk between readout elements can come from several sources; optical cross talk at the photocathode, capacitive cross talk between HPD pixels, and electrical cross talk in the digitisers. Since the signals generated by the coupling mechanisms listed are constant fraction in nature, it is possible to correct the data off-line. Correction is not possible in the trigger systems and a cross talk limit of 2% has been agreed upon. The HPDs have fibreoptic windows which eliminates all optical crosstalk making the cross talk requirement for the readout 2% or less.9.2.1.6

Summary

Table 9. 3

Requirements Summary

Parameter	Value
Operation	Gated Integrator
Frequency	40 MHz
Aperture	~25 ns
Aperture Stability	less than 2%
Charge Loss	less than 2%

Range	15+ bits or 35000:1
Precision	5 bits or 0.9% rms
Least Count	2000 electrons or 0.32 fC
Noise Floor	3000 electrons rms
Cross Talk	less than 2%

9.2.2 Calibration9.2.2.1

Laser system

A tree-structure of clear fibers is used to distribute laser light from a central station to each of the photodetectors in the calorimeter system. The principal functions are gain calibration of the readouts and synchronization of the individual channels. Laser light is also sent to a sample of the scintillators to track aging and radiation damage. The frequency with which the laser is pulsed is more than three orders of magnitude lower than the 40 MHz required for beam crossings. No special front end performance requirements are needed over those necessary for event data readout.9.2.2.2

LED system

Light emitting diodes are included in each photodetector enclosure for simple viability checking purposes. The frequency of pulsing is arbitrary and could be set high enough to verify the readout capability at the beam crossing rate. The requirements on the front end appear in the area of control functions and are presented in chapter 9 below.9.2.2.3

Radioactive source system

A radioactive source traveling in guide tubes can be moved across each of the scintillators in the central calorimeter and is used to establish the calorimeter absolute energy scale. The signal produced in the hybrid photodiode readout is a current of approximately 5 nA. Dark current in the device sets the baseline. Initially this current is in the 3 to 5 nA range, but will increase linearly with radiation exposure to 20 to 30 nA after ten years of operations. The requirement is to measure the source current to 1% of its value on a background that could be as high as 30 nA. The dark current arises from leakage current in the bulk silicon of the diode. It is ohmic in nature (negligible fluctuations) and quite constant in time. In contrast, the signal from the source is quite granular; it is composed of individual photoelectron emissions each amplified by the HPD gain factor of 2000. 9.2.2.4

Charge injection

Charge injection directly into the front end of the analog processing ASIC is planned for quality assurance and monitoring purposes. The absolute accuracy of the injection network is not important, but the stability over time is very important. The components involved should be stable at the 2% level for both the ten year planned useful lifetime and the approximately 10^{11} photons and neutrons per square centimeter exposure predicted over that span. Control requirements are discussed in chapter 9 below.

9.2.3 Environment9.2.3.1

Magnetic field

All photodetectors and front end electronics are affected by the 40 kG solenoidal magnetic field to some degree. The inner barrel and end cap detectors are immersed in the full field, and are in a region where the field is very uniform. Electronics designs, therefore, cannot use magnetic components such as inductors, relays, fans, power supplies or transformers. In addition, care must be taken to minimize the dipole moment of power leads or to properly brace them against magnetic forces. Testing of electronics prototypes in a 40 kG field is required.

The photodetectors for the outer calorimeter compartments in the central and end cap region are outside of the main detector structure attached to the steel of the return yoke. Fringe fields in this location vary from 500 to 1500 gauss depending on proximity to the service gaps in the return yoke. The field is non-uniform on the scale of meters, but is locally uniform on a scale of centimeters. Unlike the inner detector case, the field strengths are low enough to allow magnetic shielding options to be considered. Magnetic field testing of prototypes is required.

At the location of the forward calorimeter electronics, the fringe field strength is down to a few hundred gauss. Standard crate and power supply systems can be used, although oscilloscopes and other CRT devices will not function there.9.2.3.2

Radiation

The radiation environment is most severe in the forward calorimeter system (chapter 5). At the location of the photodetectors, a fully radiation hard chip fabrication process would be required. However, since the electronics is to be located on the outside surface of the shielding encasing the calorimeter, some two meters away from the phototubes, the radiation exposures are expected to be very similar to those predicted for the barrel region electronics. Over a ten year period, the neutron fluences are predicted to be 10^{11} per centimeter squared in both locations. The charged particle dose is negligible by comparison, and the photon fluxes are of the same order of magnitude as the neutrons.

All front end electronics systems are required to withstand this radiation environment and maintain performance levels which meet the specifications in chapter 9 above. Periodic replacements of components over the ten years of operations is not foreseen. Validation of components and/or prototype systems with neutron and photon exposures is required.9.2.3.3

Service access and reliability

Forward calorimeter systems are completely separated from the central detector. Access to the electronics mounted on the outer surface of the calorimeter radiation shield is not limited by the CMS detector configuration. The same holds true for HCAL power supply and utility systems located along the side walls of the cavern and for the barrel and end cap calorimeter components mounted on the outer surface of the magnet return yoke (HOB, HOE). No special provisions are required as service access is straightforward.

The inner barrel and end cap electronics are mounted on the outer radius of the calorimeters inside the superconducting coil. At best, service access could be possible on a yearly basis; a long and difficult disassembly sequence must be executed to gain access to these systems. Even then, repairs are difficult as many layers of cables, cooling pipes, and power leads for the tracking detectors and the electromagnetic calorimeter "trap" the front end electronics boxes and deny straightforward, ready access. These conditions lead to a reliability requirement for the electronics such that single channel failures should be less than 0.1% per year. Also, coupled failure modes which lose an entire box of channels should either be reduced in probability to less than one such failure in the whole system over ten years or be eliminated by engineered mitigations and redundancy.9.2.3.4

Cooling

All CMS detector systems in the cavern are required to be cooled; waste heat cannot be dumped into the air. The cooling requirement includes power supplies and power leads as well as the electronics. A large chilled water plant is envisioned. For those cases where it is impractical to remove 100% of the heat generated by water cooling, e.g. a crate of electronics or a power supply, the water system will be operated somewhat below ambient temperature. The subsequent refrigeration of the room air combined with direct heat removal can satisfy the cooling requirement in aggregate.9.2.3.5

EMI and EMC

Since the entire electronics plant in the cavern will be operated synchronously at 40 MHz, the potential for EMI problems is great. Second, essentially all of the low voltage power supplies will use switching technologies. And last, ground loops can couple in 50 Hz "hum" and harmonics thereof especially when the loop involves the metal of the detector. Accordingly, the electronics designs shall be compliant with the following guidelines:

1) Interconnections of data cables, signal cables or power sources shall not create ground loops,

2) AC signal currents, analog or digital, shall not flow through the metal structures of the detector,

3) Low voltage power supplies must meet or exceed the European "Electromagnetic Compatibility IEC 1000 - 1-4" specifications for conducted and radiated EMI, plus such additional requirements as developed by the CMS working group on low voltage supplies and grounding,

4) The frames (cases) of low voltage power supplies shall be isolated from local detector metal structures with safety grounding provided by the safety conductor of the power cord,

5) The techniques used for transmission of digital signals over cables must be approved by the CMS working group on low voltage supplies and grounding,

6) Digital circuitry shall be designed in accordance with good engineering practices for control of EMI[4].

7) Documentation shall be provided describing the system configuration, interconnects, and grounding.

9.2.4 Control

9.2.4.1 Event data

During collider operations, the front end electronics runs continuously at 40 MHz under the control of an external clock. Because of differences in time-of-flight, fiber lengths, and photodetector transit times, each channel will require an adjustable phase delay of 64 steps of 0.5 ns size. The fieldbus connection to the Detector Control System will be used for downloading this information to the channels.

9.2.4.2 Calibration data

Charge injection is foreseen for every channel. The control functions required are:

1) Amplitude. The magnitude of the signal should cover the full dynamic range.

2) Shape. Two different time structures are needed, a short ~10 ns impulse for the forward calorimeter and a longer RC = 11.3 ns signal for the barrel and endcap calorimeters.

3) Rate. The frequency of charge injection pulses should be selectable from 40 MHz down to 4 kHz.

4) Mask. Each channel should have an off/on function

5) Phase. The phase for charge injection can be varied using the phase delay control already needed for event data.

6) Synchronization. The signal shall be synchronized to the 40 MHz system clock.

Laser light calibrations and scintillator quality monitoring operations will not be synchronized tightly to the 40 MHz system clock due to the jitter in timing of the flashes. Given that beam operations will be off during calibration periods, the transient recorder character of the free running front ends can serve to extract the results. Similarly, the signal produced by the traveling radioactive source is not correlated to the system clock, and higher levels of the readout chain will extract the information from the front end data stream. No special control features are needed.

The LED's used for general viability testing purposes are controlled locally in each readout box. Individual channel controls are not required, except for the phase delay which is already present for event data. Control of the frequency and amplitude of the LED driver are needed.

9.2.5 Error detection and handling

Detection of synchronization slips is needed to guard against misaligned data streams. A 40 MHz counter, reset every beam orbit by the marker pulse, and a comparator should be used for establishing data synchronization validity. Detection of an error results in an appropriate message being sent over the fieldbus to the front end controller in the corresponding trigger and data acquisition crate.

The data links between the front end electronics and the trigger and data acquisition electronics are required to detect and correct loss of synch occurrences. During the interval over which synch is gone, the receiver shall raise an error flag to indicate a bad data condition to the higher levels of the system. The readout pipeline never halts; when corrupted data conditions are detected, the pipeline output is directed to the wastebasket instead of the processor farm.

Sending of test patterns on demand is also a system requirement. The frequency with which this validity check is done has not yet been decided; it will require some operating experience with the links to decide. Possibilities range from once every beam orbit during the abort gap in the fill to only when needed as a diagnostic tool.

Bit error rates on the links may be such that an unacceptable false first level trigger rate is generated. The solution is to add syndrome bits to each transmission to allow error detection. Such error codes increase the bandwidth requirement for the link and could conceivably increase the bit error frequency. As with test patterns, experience with the links is necessary before the decision can be taken.

9.3 COMPONENTS

9.3.1 Overview

The requirements for the front end electronics detailed in chapter 9 above call for a low noise, high frequency, wide dynamic range digitiser system. In particular, the combination of 3000 electrons rms noise, 0.32 fC least count, 40 MHz clock frequency, and 16 bits dynamic range is unique to the LHC conditions. In the particle physics community, the system which comes closest is the digitiser recently developed for the KTeV experiment at Fermilab[5]. The performance achieved was 15000 electrons rms noise, 8 fC least count, 53 MHz clock frequency, and 16 bits dynamic range. Unlike the LHC case, there were no special requirements on reliability, radiation tolerance, magnetic field immunity, cross talk, and capabilities for DC current measurement.

The front end electronics design is based on an improved version of the analog processing ASIC developed for the KTeV experiment. As shown in Fig. 9. 3, the building blocks are the analog ASIC, a 40 MHz digitiser, a control ASIC and an optical link. Because of the extreme space constraints present in the barrel and end cap regions, a three channel format has been selected as indicated in the figure. Each of the components is described in the following chapters.

Analog processing is done through a multi-range gated integrator. An example of range and resolution performance using a 5 bit ADC and an eight range integrator is shown in Fig. 9. 5. The resolution of the central calorimeter is plotted versus energy along with the contribution from electronic noise at the 1.5 photoelectron level and the contribution from the multi-range front end digitiser system with range parameters as given in Table 9.4.

This EPS image does not contain a screen preview.
It will print correctly to a PostScript printer.
File Name : Figure 9.6.eps
Title : /usr/people/rvidal/cms/gie_scale/hcal5_32.ps
Creator : HIGZ Version 1.19/16
CreationDate : 97/05/01 13.41

Fig. 9. 5: Resolution performance

Table 9. 4

Range and Resolution Example

Range	Current	Min E GeV	Max E GeV	#Bins	bin size GeV	bin size fC	Resolution Increase
1	I	0	2.8	28	0.1	0.32	1.001
2	I/3	2.8	11.2	28	0.3	0.96	1.002
3	I/9	11.2	36.4	28	0.9	2.88	1.004
4	I/27	36.4	112.0	28	2.7	8.64	1.010
5	I/81	112.0	338.8	28	8.1	25.92	1.024
6	I/162	338.8	792.4	28	16.2	51.84	1.020

7	I/324	792.4	1699.6	28	32.4	103.68	1.020
8	I/648	1699.6	3514.0	28	64.8	207.36	1.020

9.3.2 Analog conditioning ASIC - QIE9.3.2.1

Requirements summary

- 40 MHz operation

- 16 bits dynamic range

- 2000 electrons or 0.32 fC least count

- 3000 electrons rms noise

- 5 bits precision

- Systematic errors small enough to measure a few least count source current

- Charge loss at sample boundaries less than 2%

- Cross talk less than 2%9.3.2.2

QIE overview and experience

QIE is an acronym for the functions of the ASIC, Q (charge) I (integration) and E (encode). A large dynamic range is accomplished[6] through a multi-range technique. The input current is simultaneously integrated on all ranges, and comparators are used to select the lowest range that is not at full scale. The outputs are a voltage representing the integrated charge plus a three-bit gray code indicating the range. Operations are time multiplexed and pipelined to allow signals to settle and to make the reset interval the same as the integration interval. Latency is 100 ns as the pipeline is four clock cycles deep.

The QIE contains multiple sets of eight capacitors of a uniform value. Attached to this structure is a current splitter. Matched transistors in common base configuration and connected in parallel will share the current driven through them equally. This property is exploited in the QIE design to apportion a fixed fraction of the input current to a given capacitor in the array. Each capacitor receives a fraction of the current of its lower range neighbor. For example, if the splitting was simply by powers of two, the capacitor for range n would receive $1/2^n$ of the input current. Fig. 9.6 shows the pattern of transistors for a single-stage binary-weighted splitter with eight ranges.

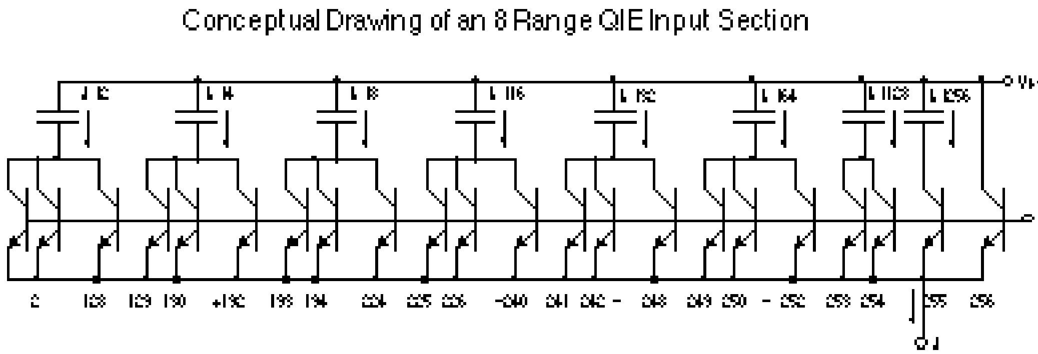

Fig. 9. 6: Input section example for an 8 range QIE.

One set of capacitors integrates the input current for one beam crossing interval; the clock frequency is equal to the beam-beam collision frequency. While one set of capacitors is collecting charge, others are being read out and reset. There are four sets of capacitors. At any given point in time, one set is collecting charge, one is settling, one is being read out, and one is being reset.

A DC bias current is added to the input current. One of the functions of the bias current is to provide a minimum current in the splitter to ensure that the transistors are in a good operating region. The current is then adjusted so that the analog output on the range of interest matches the input requirements of a single-range ADC. For a given charge deposition over one clock interval, no more than one capacitor in the set will have its voltage within specified limits. The voltage on this capacitor is connected to the analog output of the device and digitized by an external ADC. The priority encoded address of this capacitor make up the exponent bits. The voltage on the capacitor is the mantissa and the address of the capacitor is the exponent.

The QIE is presently in service on the 3100 channel KTeV cesium iodide crystal calorimeter. CsI has an intrinsic energy resolution approaching 0.5%, which requires very high performance electronics to make full use of this capability. The KTeV device has 8 ranges with a factor of two gain change between ranges giving a dynamic range of 16 bits. Fig. 9. 7 shows the results of a laser calibration of a QIE chip carried out at 53 MHz; the scatter in the points is due to photostatistics. There are a number of distortions in the transfer function of this device. The main contributions to the non-uniformity in the overall charge to voltage slope are variations in the size of the capacitors and accuracy of the splitter. Although this is a less than 0.7% effect, KTeV keeps four sets of calibration factors for each QIE, which amounts to 64 constants, four sets of 8 slopes and 8 offsets.

This EPS image does not contain a screen preview.
It will print correctly to a PostScript printer.
File Name : Figure9.7.ps.eps
Title : (Adobe Illustrator (R) Version 5.0 Full Prolog)
Creator : Adobe Illustrator(r) 6.0
CreationDate : (3/7/1994) ()

Fig. 9. 7: Laser calibration of a QIE chip.

9.3.2.3 HCAL design

For HCAL, a modified and improved version of the QIE is planned. The radiation tolerance requirement, the need for extreme reliability, and the operational advantages of a low power design all argue for migrating away from the present 2.0 micron CMOS process. A deep submicron BiCMOS process is under consideration, but the radiation effects are not fully understood at this time. As is the case for all electronics located deep inside the detector, validation of the appropriate level of radiation tolerance is required.

Modifications to the input stage to achieve lower impedance are necessary because of cross talk concerns. The individual anodes in the multi-anode hybrid photodiode detector are capacatively coupled to their neighbors. A signal on a given element will cause a voltage excursion on the adjacent elements that is determined by the QIE input impedance and the inter-element coupling capacitance. Overall, cross talk to adjacent elements is to be less than 2%.

The noise specification of 3000 electrons rms requires approximately a factor of five improvement in performance. The source capacitance for the CMS HPD and the KTeV photomultiplier tube are roughly the same, ~ 5pF. Thus the improvement must come from circuit design and process technology.

At the time the modified QIE design begins, consideration will be given to bringing the ADC onto the ASIC. The advantages include; lower power as analog drivers and receivers are eliminated, increased reliability from reduced component count, and possibly a lower noise figure. Information will soon be available from a QIE chip designed for the CDF upgrade shower maximum detector which has a 5-bit ADC on board. The noise and frequency specifications are more relaxed than needed for LHC, but the feasibility issues will have been addressed.9.3.2.4

Vendor aspects

The practicality of the KTeV QIE is limited by the relatively crude 2 micron CMOS process used for fabrication. The promise of a high performance BiCMOS process for fabrication of the next generation device should simplify using the QIE from a system point of view. KTeV suffered through a series of fabrication quality assurance problems, something that should not occur if a good foundry is used. Nevertheless, KTeV is achieving remarkable performance even with this less than ideal device. They have equivalent dynamic range to that required by CMS HCAL and operate at 53 MHz rather than 40 MHz. Further, system problems have been solved, and 3100 channels is a substantial fraction of the 15000 needed for CMS. The running experience of KTeV brought to light many mundane system issues that are only obvious in hindsight.

As discussed above, the fabrication process selected must maintain performance specifications for an integrated flux of 10^{11} neutrons per square centimeter where the kinetic energies are greater than 100 keV. Also, the photon flux is of the same magnitude and the energies range from 400 keV to 2 GeV.

9.3.3 ADC9.3.3.1

Requirements:

The digitiser connected to the QIE analog output must be capable of digitizing the stepped output voltage with full accuracy in one clock cycle. Full span slewing occurs frequently, specifically every time a range boundary is crossed. This puts a premium on the input analog bandwidth of the ADC. It should be greater than 40 MHz in order to accommodate this slewing. If we require that the input section settles to 1/4 of an lsb in one 25 ns clock interval, and further, naively assume a two coincident pole response, that implies about 9 time constants are needed. That is 2.7 ns or about a 60 MHz bandwidth for the components in the analog signal path.

Since the radioactive source calibration current is to be measured by simply reading a large number of samples, it is important that the ADC bin widths remain constant for the duration of the measurement[7]. In any one measurement interval, the signal is small, only 2 or 3 least counts. It is likely that the ADC bin widths around pedestal will have to be mapped using the laser calibration system to meet the accuracy specifications for the source readout.9.3.3.2

Vendor aspects

The critical issues are power consumption and radiation tolerance. There are several commercial ADCs on the market that potentially fulfill the requirements. All candidate devices will have to be carefully evaluated and tested for irradiation effects.

9.3.4 Channel control ASIC9.3.4.1

Functionality

Data synchronization

The exponent bits come directly from the QIE, while the mantissa comes from the QIE and goes into the ADC and is then digitized. Exponent and mantissa data appear at different times and need to be re-synchronized before being sent on to the data transmitter. 9.3.4.1.2

Clock phasing

The channel control ASIC supplies clock signals to the QIE and ADC. An adjustment is needed for each channel to synchronize operations to the beam generated calorimeter signals. This phase adjustment can remove differences in photodetector transit times, timing differences in the QIEs and ADCs, and differences in light arrival times down the fibers. There is sufficient range to time in all HCAL channels using only these electronics delays.9.3.4.1.3

Initialize

The QIE is a synchronous, pipelined device which contains state machines. After power up, it is necessary to place all the QIEs in a known state with a precision of one 40 MHz clock cycle. The channel control ASIC is required to receive an essentially asynchronous system reset pulse and synchronize this signal to the local clock before sending it on in order to meet the set up and hold times for the reset input of the QIEs.9.3.4.1.4

Data formatting

The QIE + ADC pair produces 3 + 5 or 8 bits of data at the 40 MHz rate. Standard high speed data serialiser chips typically operate on 16 bit data at 66 MHz. This bit rate is a good match to three channels' worth of data. The ASIC can multiplex the incoming 24 bit data into a 16 bit stream at 1.5 times the collision rate or 60 MHz. Should CRC error codes prove necessary, the link frequency can be set to 66 MHz affording enough additional bandwidth to include two syndrome bits. It should only be necessary to protect the exponent bits. Three exponents are nine bits with two bits of error correction. One word at a time, two bits cannot be used to detect more than single bit errors. If the correction algorithm spans five words, that is, ten CRC bits are applied to 45 exponent bits, the majority of 2 bit errors and all 1 bit errors are detected. Error correction should be implemented only if it can be convincingly shown that there is any net improvement in system reliability.9.3.4.1.5

Interface with serial links

The channel control ASIC is the logical place to implement test and control functions by means of a serial link. These functions would include data test patterns, clock trim values, charge injection control, and the control of operating modes. Internal states of the device can examined as part of a power up diagnostic for example. The widely used CAN standard has been selected for the serial path.9.3.4.1.6

Event synchronization

It is important to identify the crossing from which an event originated. A counter clocked at the crossing rate and reset with the beam turn marker can detect synchronization errors. Subsequently, an error message is sent using the serial link. It is also important to reset, globally, all crossing counters to a known value, and the system must be fast enough to achieve this in one clock cycle on receipt of the bunch marker.

The crossing counter along with a turn counter could be used to specify the time of a test injection pulse. A pair of registers in the ASIC could be loaded with turn and crossing values. If test pulse injection is enabled, then every "n" turns at crossing "m" a test pulse could be issued.9.3.4.1.7

Charge injection and LED trigger

Charge injection and LED test and calibration operations are synchronized to the 40 MHz clock. A DAC and clock counter can provide the signal, and the counter can also serve as a way to turn individual channels on and off.

9.3.5 Data links9.3.5.1

Requirements

The CMS trigger system needs information about every crossing. At 40 MHz x 8 bits, 320 Mbit/s per channel is required. This data must be sent 100 meters to the trigger system. An initial comparison of the cost of copper ribbon cable with parallel data transmission at 40 MHz with that of serial optical transmission at 1 Gbit/s shows the ribbon cable to be approximately twice the cost of the serial transmission scheme. It must be noted that data transmission technology is rapidly evolving. Both copper and optical fiber transmission technology are dropping steadily in price while the available bandwidth is increasing. Three channels produce 960 Mbit/s of data which is a good match to present day 1 Gbit/s links. We will carefully watch commercial developments in order to use the trends which develop.9.3.5.2

Laser transmitter

There are a number of 1Gbit/s serialiser chips available. It may be for reasons of radiation hardness that GaAs devices are to be preferred. Most of these chips take in a 20 bit word at a 66 MHz rate. The 20 bit word is the result of applying an 8b-10b encoding scheme for 16 bits of data. Clocking the serialiser at 60 MHz or 1.5 times the crossing rate gives the necessary bandwidth to send three eight bit channels on one link. If additional status or error detection bits need to be added to the data stream, it is possible to insert one additional word out of 10 if the link were run at 66 rather than 60 MHz. TEL or GTL I/O levels would be preferable to ECL or PECL levels for reasons of power consumption.

There are a limited number of commercial sources of packaged units which include the laser driver, mounting of the laser and the mechanical housing which enables the coupling of the optical fiber to the face of the laser. For distances of 100 meters, lower cost multi-mode fibers can be used. Their larger diameter also makes the installation into the drivers somewhat easier, although in comparison to copper connections, optical terminations are more difficult. The transmitter is the single most expensive item on the front end boards. If past history is any guide, transmitters will cost substantially less in three or four years' time.9.3.5.3

PIN diode receiver

Typically, the firms making the laser module also make the companion fiber optic PIN diode receiver module. Though less costly than the laser, the receiver is still expensive. It too can be expected to come down it price at a rate comparable to the laser modules.

As with the laser and PIN diode modules, most vendors of serialisers make the de-serialisers. It would make sense to use a transmit/receive pair by the same vendor to make sure the serial data stream is compatible.9.3.5.4

Link error handling

The 8b-10b encoding scheme which ensures the proper link duty factor also provides some degree of error detection for the integrity of the link. Illegal bit patterns can be detected at the receiver. Commercial modules using this protocol provide a link error output signal which can be used by the data acquisition system to discard events.

9.3.6 Quality control, assurance and monitoring9.3.6.1

QA/QC process

The electronics design and development process follows a well known and often used QA/QC process. A complete set of requirements are developed first and then formally approved by technical management. Subsequently a design proposal is developed and reviewed against the specifications. Some R&D is usually part of this step in order to demonstrate feasibility. The design proposal is accompanied by a high level estimate of the cost and schedule impact. Third, a detailed plan of work, a full schedule with appropriate milestones, and a very detailed cost breakdown are prepared. These last items are used to monitor and guide the project to completion and for reporting to oversight groups.9.3.6.2

Components

During wafer fabrication of the final designs, there are test structures placed on each wafer for verification that process specifications have been met. It is not clear what sort of tests will be made available to us by the foundry, in light of the small numbers of devices we are having made. Low frequency digital test vectors may be the only tests available. Perhaps more sophisticated tests, including analog voltage profiles will be available because of our participation in CMS.

During the design phase, particularly for the mixed signal devices, several test structures will be needed. The current splitter is an obvious example of something that will need to be characterized. Other structures for tests of radiation hardness will also be needed. Presumably representative structures from many CMS sub-systems can made on one wafer. This wafer can then be irradiated.

A comprehensive, turnkey test setup was built for KTeV. At least two sets of 3000 QIE chips were run through these testers. Tests were run on the chips before and after their assembly onto a PC card.

Analysis of the impact of die yields shows that for yields of less than 98% component level testing is required. The initial yields from Orbit Corp. on the KTeV QIE were of order 70%. It is unlikely any vendor can provide dice with 98% yield.

Commercial components have the advantage of comprehensive testing prior to delivery. Board level testing should be sufficient.

After initial assembly, but before operations with beam begin, the readout system can be monitored and tested in several ways. The most useful are charge injection and the LED's. With charge injection, the full dynamic range can be tested, and the LED's can test viability at the beam crossing rate. Many commercial ADCs have built in test features such as bit pattern generation. This feature is useful for monitoring the data links by running through all possible bit patterns.

9.4 ASSEMBLY AND INSTALLATION

9.4.1 Barrel and endcap readout boxes9.4.1.1

Three channel PCBs

The front end digitisers for the HPD signals will be implemented as three channels on a single PCB with 3 QIE chips, 3 FADC chips, digital channel control chip, and an optical link transmitter (Fig. 9.3). Digitized results for the three channels are sent to the trigger and data acquisition system using a serialiser chip and fiber-optic data driver. The 3-channel board must be laid out with no components on the back side and will have to be made as 2 species, a right and a left, as the boards will be laminated to a copper plate which provides a primary cooling path for the electronics. The present estimate for the size of these PCBs is 9 x 9 cm and a nominal FR-4 thickness of 0.157 cm (.062 inches). (FR-4 is used since it is a fire retardant PCB assembly material.) The PCBs will likely be 6 layers with internal power and ground planes for noise reduction. All components on these boards will be surface mounted to facilitate the lamination. It is likely that the boards will be tested for conductivity and then laminated prior to installation of components.9.4.1.2

Six-Channel modules

The six-channel modules will be made by laminating a right and left 3-channel PCB to a 0.157 cm (.062 inches). copper sheet which becomes the board support and heat sink. After lamination the assembly will have its connectors for the back plane and other components added. Note: depending on the PCB layout requirements, the lamination may or may not be electrically conductive. It must, however, be thermally conductive. These 6 channel modules are the minimum replaceable unit for on-detector servicing, having a connector to the digital back plane and to the analog input back plane as well as optical data driver connectors on the front of the module.9.4.1.3

Backplane interconnections

It seems most likely that there will be 2 separate back planes, (they may be physically the same FR-4 material but will be electrically separated by some amount of space in the layout.) The Digital side of the back plane will provide power distribution, clock distribution, connection to the slow control system, and monitoring services for voltage and temperature. The "analog" back plane will simply provide a connection from the HPDs, which will have short soldered wire leads from their pins to the back plane to the analog inputs to the QIE chips. Communication along the digital back plane is serial data using the "CAN" bus protocol.9.4.1.4

Photo detector interconnects

The HPDs have an array of pins on the back which must be connected to the inputs of the QIEs. A socket which matches the pins on the HPD provides a solid ground plane with the appropriate signal return and bypass capacitors. Short twisted pair runs are soldered to appropriate points on the analog section of the back plane. This method allows the removal and replacement of an HPD without having to do any unsoldering. The reason for using discreet wires and keeping them short is to minimize the input capacitance to the QIE and to avoid the crosstalk that a ribbon cable might introduce. It is here that we need the full dynamic range, and care must be exercised. After the QIE splitter, noise level constraints are less severe.9.4.1.5

External interconnects.

The largest number of external interconnects by far are the fiber-optic data cables, 1 for every 3 channels, which connect the front-ends to the trigger and DAQ system. These connections are made directly to the front of the 6 channel modules using a bayonet style fiber connector. There are also 2 fiber optic cable inputs to the box bringing in the clock and the slow control network. These connect to a special 9x9 cm laminated board structure where the signals are received, processed and distributed on the digital backplane.

Power is brought into the box and onto the back plane using ridged copper bar and threaded stud and nuts with locking washers. These bars must be able to stand the forces experienced due to the magnetic field.

The high voltage for the HPDs is brought onto the HPD socket using a captive bayonet style connector which may be made of molded polycarbonate material and will have mounting screws to prevent accidental disconnection. This connector will also carry the low voltage bias for the HPD.

The last external connection is for the cooling water to the crate. The water lines will be separated from the bundle locally and will be mated to the crate water cooling connectors using a barb and clamp system suitable for use at the flow rates and pressures needed to deliver the 1 liter per minute of cooling water needed to cool the electronics.9.4.1.6

Installation.

The readout boxes will be installed on each wedge as the wedge is assembled in Building 168 and will have a full compliment of readout modules installed. This allows for each wedge to be fully tested as a unit prior to installation in the detector. All optical connections from the scintillator tiles are made to the box and each fiber's integrity may be checked using the source system or laser system, thus assuring that all fibers are routed and connected correctly before the wedge is even shipped to the assembly hall.

The mounting of the box and the mounting of the back plane within the box must be of such a design as to withstand the forces due to the magnetic field. Once the wedge is installed in the detector, the real power cables must be installed and appropriately anchored to the wedge. Water lines will then be connected and the final assembly fully tested prior to being sealed up in the detector.9.4.1.7

Quality control, assurance and monitoring.

In general, all assemblies will be specified to the vendor to meet the requirements of the final design. PCB manufacturers must meet minimum de-lamination force testing and all PCBs will be "bed-of-nails" tested to assure correct conductivity prior to being accepted. Commercial electronic components will be required to pass needed minimums for voltage tolerance and for radiation tolerance. Sample parts from vendors must be radiation hardness tested before being selected for final assembly.9.4.1.7.1

Custom integrated circuits

It is expected that the full custom chips which will be designed for this application will have a multilevel evaluation process. The first part of this will be to qualify the foundry which will be making the parts for radiation hardness and for process stability. The vendor which will be packaging the parts must also be qualified, although this is somewhat less critical as the choice of packaging vendor may be changed easily, where as the choice of ASIC foundry is much more difficult to change.

The next level of assurance will be to have a series of prototype parts made and tested in parallel with a design review using impartial but interested engineers to make sure that no design flaw is missed. Prototype parts will also be subjected to stresses of radiation and thermal cycling to assure that the part can stand the stresses placed upon them in normal and extreme operating conditions. Note that the cooling system as designed will operate at a temperature slightly below ambient which will keep the parts quite cool and add reliability. Of course, there will be test structures present on each wafer of chips produced; these will be used to monitor the process and quality at the foundry.9.4.1.7.2

Chip testing

Once production parts begin arriving, we will be using the ASIC/Board test system developed at Fermilab to do production testing of the chips. All chips will be tested at speed and will be required to pass stringent cuts on the performance of the part as well as the total current draw. Once parts have passed the chip testing stage, they are shipped to qualified assembly houses which mount the parts to the PCB modules and ship these back for testing. (Note: the vendor MUST adhere to correct ESD protection procedures, as failure to do so may damage or weaken parts which will then fail prematurely.) It is expected that the time to test each chip will be about 20 sec., this includes installing the chip in the test fixture and removal and sorting of good and bad chips.9.4.1.7.3

Board testing

The 6 channel modules will also be tested using the ASIC/Board test system and will again be tested at speed. Also in this test, the cross talk between channels is measured and each channel is required to pass the same performance test as the chips passed. The current drawn by the board will be measured and boards which do not pass the test will be returned for re-work/repair.

It is expected that the time to test each board will be about 2 minutes. This is in part due to the optical connections which must be made by hand to allow for the full testing of the board. The test fixture will have a pseudo-back plane which the board will be installed in during testing.

It is further expected that some number of boards will be subjected to thermal cycling and extended running to elicit expected infant mortality and longevity numbers. It is also likely that all boards will be installed into a burn-in fixture and will be run for several weeks and then be re-tested, again to catch infant mortality of components.9.4.1.7.4

System testing

Since the only active components which are part of the readout box are the HPDs and since they will be tested separately, it is assumed that testing will be done on the wedge as it is assembled. Any additional testing would be redundant and would not add to the reliability of the system.

9.4.2 Forward readout electronics9.4.2.1

VME readout crates

The digitisers for the PMT signals will be implemented on 32-channel boards, 9Ux400mm Eurocard format, with VMEbus signals on the P1 connector (referred to as "VME modules" for simplicity). Each module will consist of a PCB of conventional design, fabricated of 0.157 cm (.062 inches) thick FR-4 material, with SMT components on both sides. It is likely that groups of 3 digitiser channels will be assembled on a small "daughtercard" for ease of assembly and testing, and that 10 daughtercards will mount on a VME module. All components except connectors will be surface-mounted. Front panel hardware and board stiffeners will be Eurocard standard.

Assembly will be performed by an outside vendor, using conventional pick-and place component installation and infra-red reflow soldering. Mechanical components will also be installed by the vendor.

A 9U crate of standard size will house up to 16 VME modules. A standard VME-16 P1 backplane will be installed, along with a power distribution backplane and coaxial ribbon connectors for PMT input signals. An existing standard such as the CERN V430 specification will be chosen for power distribution. The crate will be custom-manufactured to our specifications by an outside vendor.9.4.2.2

PMT bases and interconnects

The PMTs are housed in individual shielded enclosures, with a simple PCB soldered to each. The PCB contains the voltage-multiplier portion of a Cockroft-Walton generator as described in chapter 8. Each PMT base has two connectors, a coaxial signal output connector, and a multi-pin control connector for the high-voltage generator. The high voltage is generated inside the PMT base, so the interconnections themselves are low voltage.

The PCBs for the PMT bases will be assembled and conformably coated by an outside vendor using standard techniques. Final assembly of the PCB to the PMT and installation in the base enclosure will be performed in-house at a collaborating institution's shop.

Interconnection cables will be manufactured by an outside vendor to CMS specifications, and tested in-house.9.4.2.3

External interconnects

This chapter refers to all off-detector connections which leave the HF platform. The majority by number are the fiber-optic data cables. Each 32-channel module has 11 data cables, which are identical in function to those used in HB and HE.

The 220 VAC power is supplied to each rack in a conventional manner. Low voltage is generated in each crate using a conventional power supply. Cooling water is also supplied to each rack. Two fiber-optic connections are required for each rack for the clock (TTC system) and detector control.9.4.2.4

Installation

The PMTs with bases will be installed while the detector final assembly is done in the experimental hall.

Electronics racks containing VME readout and high voltage control crates will be installed on the exterior of the detector. Cables will then be run from the PMTs to the racks.9.4.2.5

Quality control, assurance and monitoring

In general, the same procedures will be followed as for the remainder of HCAL. The custom ICs will be processed as described there. The VME modules will be tested in a dedicated test station in-house after assembly. Each VME crate will be similarly tested in-house.

9.5 EXPECTED PERFORMANCE

9.5.1 Event data

The front end electronics system is based on a multi-ranging integrator and encoder called the QIE. The system is fully pipelined producing digitized values synchronously with the beam crossings after a latency of 100 ns corresponding to the pipeline length of 4 clock cycles. It is designed to meet the requirements described in detail in chapter 9. Based on the successful experience of the Fermilab KTeV experiment which uses a QIE and a very similar front-end electronics design, the HCAL system is expected meet all of the goals.

The most demanding requirement is the noise floor, 1/2 of a fC or 3000 electrons rms is the requirement, resulting from the low gain figure of 2000 for the HPD. There are three environmental factors which lend credibility to achieving a 3000 electron noise floor system; (1) the HPDs and the readouts are in fully enclosed copper boxes, (2) the connections to the HPDs are only a few cm long and the bypass network for the silicon diode pixels has a good ground plane, and (3) the only external copper connections to a box are the high voltage and low voltage power leads which are configured with a single point ground at the box.

9.5.2 Calibration data

Light flasher operations, whether from the laser system or the LED system, only occur when beam is off. Thus, there is no baseline shift or pileup correction to be made. Also there is no requirement that the flasher be synchronized to the clock as the front ends function as digital wave form recorders. The higher levels of the trigger and data acquisition system are fully capable of extracting flasher responses. However, it is convenient to synchronize the flashers to the clock to set repetition rates by counting and simplify generation of trigger accepts at the proper time. Synchronization also makes programming of the higher system levels that much easier.

Charge injection calibrations are fully synchronized to the clock in each individual channel control

ASIC. As such, operations are identical to those for event data except that the trigger accepts are synchronous.

The requirement to measure the current produced by a radioactive source illuminating the scintillators is challenging. The induced current is about 5 nA after amplification by the HPD. There is a DC leakage current in the silicon diode pixel which starts out also at about 5 nA but increases linearly with radiation exposure and is predicted to be 20 to 30 nA after 10 years of operations. This silicon leakage current is ohmic in character so that the fluctuations are negligible.

Due to the noise floor requirement, adding switches at the very front end to allow for a separate DC current transducer readout path is essentially ruled out. A second negative is the added system complexity and cost and reduced reliability introduced. The choice is to operate the system in its normal mode at its normal clock speed and measure the small source current through extreme over-sampling[7]. By using the noise in the system and the photoelectron fluctuations of the current to "dither" the signal, it is possible to measure the current to a few tenths of a percent of a least count by averaging over a large number of readings.

Five nA corresponds to an average of 0.4 photoelectrons per measurement. This value also corresponds to 0.4 of the least count as the system granularity on the most sensitive range is one photoelectron per ADC bin. The Poisson probabilities for the number of photoelectrons per measurement are: P(0) = 67.0%, P(1) = 26.8%, P(2) = 5.4%, P(3) = 0.7%, and P(4) = 0.07%. Chapter 11 describes the control functions and configuration of the higher levels of the readout system needed to accumulate and average the readings. The pulse-height spectrum built up by a large number of measurements will be the 0.4 photoelectron Poisson distribution convoluted with a gaussian noise distribution which has a sigma of 1.5 least counts (3000 electrons). The calibration value extracted by fitting the spectrum is the average number of photoelectrons per measurement interval.

9.6 SERVICES AND UTILITIES

9.6.1 Cables, wires and connectors9.6.1.1

Barrel and end cap

Front end electronics for the barrel and end cap are contained in readout boxes attached to the detector. There are 120 boxes distributed as shown in Table 9. 5.

Table 9. 5

Number of Readout Boxes

System	No. of Boxes
Inner Barrel	36
Outer Barrel	60
End Cap	24

Each box has power cables, cooling water hoses, 50 data fibers (to be determined), a fieldbus duplex fiber cable, a TTC fiber cable, and a twelve pair high voltage cable.

The power and cooling services are described in chapter 12. Selection of the data fiber interconnects will be done following CMS-wide discussions of commonality between different detector systems. The fieldbus interconnect is a commercial Arcnet hardware, and the TTC link follows the recommendation of the RD-12 group. The high voltage cable has silicon rubber insulation for the pairs, a nonscintered PTFE tape 50% lap, a tinned copper spiral shield, and a halogen-free thermoplastic elastomer jacket.

Connectors for the power leads are bolted copper flags with Belleville tensioning washers. Connectors for the data fibers are to be determined. The Arcnet and TTC links have off-the-shelf connectors which are predetermined by the TX/RX hardware. High voltage cables will use custom multi-pin molded connectors as commercial catalog products are limited to 14 kV. Deep wiping contacts similar to those of "banana jacks" are planned.9.6.1.2

Forward

Front end electronics for the forward calorimeters reside in VME crates in relay racks attached to the calorimeter outer shield. Coaxial cables bring the phototube signals out from the interior of the detector through penetrations in the shielding. The high voltage cables (also routed through these passages) are multi-conductor with an overall shield made of the same materials as those for the barrel and end cap systems. Ethernet and TTC services use optical interconnects and commercial technology. Selection of the data fiber interconnects will be done following CMS-wide discussions of commonality between different detector systems. Table 9.6 below gives the count and routing for the interconnects.

Table 9. 6

Cables Required for HF

Count	Function	From	To	Length	Type
3900	PMT HV	HV PS	PMT Box	2m	custom multi-conductor
3900	PMT Signal	PMT Box	FE Card	2m	coax

1300	Digitized Data	FE Card (Rack)	Service Room	100m	optical fiber
16	DCS	Service Room	Crate	150m	optical fiber
16	TTC	Service Room	Crate	150m	optical fiber

9.6.2 Cooling9.6.2.1

Barrel and end cap

Cooling water for the readout boxes is brought in via hoses described in chapter 12. A water temperature rise of about 4 °C is expected for the 210 watt heat load with a flow of one liter per minute. If the supply temperature is set 4 or 5°C below ambient temperature, the system provides some degree of refrigeration to the cavern environment.9.6.2.2

Forward

The crates for the forward calorimeter front end electronics are located in relay racks. Standard CMS infrastructure cooling is planned with air-water heat exchangers and forced air circulation. The electronics dissipates 1.1 W per channel. For 500 channels in one 9U VME crate, this is 550 W. An additional 250 mW per channel is needed for the high voltage supplies giving another 125 W for a total of about 800 W when control and processor cards are included. A flow of about 6 liters/min. would give a temperature rise of 5 °C. For the full system then, a flow of 50 liters/min. is required. Because heat is not removed effectively in rack based crate and power supply systems (getting 60 to 70 % into the water is doing well), the entire system will be operated below ambient to provide extra refrigeration to compensate.

9.7 ACCESS, MAINTENANCE AND OPERATIONS

9.7.1 Inner barrel and end cap electronics

The inner barrel and end cap electronics along with the photodetectors are located in water-cooled readout boxes mounted on the outer surface of the calorimeter structures. These locations are inside of the cryostat for the solenoidal coil as shown earlier in Fig. 9. 1. Access is not possible without a long and difficult disassembly of the detector involving the forward calorimeter, the end cap muon detector and return yoke, and the end cap calorimeter. At best, service access could be possible on a yearly basis. Stringent reliability requirements derive from the lack of repair access. Failures at the single channel level must be less than 0.1% of the channels per year, no more than 7 of the 7500 trapped channels. At the system integration level, the relevant time interval is the ten year operating period foreseen. Loss of an entire readout box of 128 channels should occur no more than once in the ten year period.

Repairs and maintenance operations, even after the detector has been opened up, are very difficult as many layers of cables, cooling pipes, and heavy power leads prevent straightforward, ready access to the boxes. Additional time will be needed to disassemble whatever portion of these services are blocking access to that area of the box where the repair is to be done. Simple service activities, changing an electronics card or repairing a high voltage problem could take months to execute. Accordingly, the design of the readout boxes is such that no maintenance is required. All parameter adjustments are made using a fieldbus connection, there are no hand-setable adjustments. The power supplies are in accessible locations in the cavern and the service room. There are no moving parts to wear out. All interconnections are threaded or locking, and the power connections use Belleville tensioning washers to eliminate any need for periodic retightening.

9.7.2 Outer barrel and end cap electronics

The outer barrel and end cap electronics along with the photodetectors are located in water-cooled readout boxes mounted on the outer surfaces of the return yoke. These locations are directly accessible during any routine access into the cavern. There is no issue of residual radioactivity at those locations, but the magnetic field strengths expected, 500 to 1500 gauss, would call for proper procedures, training, and equipment should a service access be made with the solenoid energized.

Having relatively unimpeded access to the equipment makes these electronics systems readily serviceable. However, there are many advantages to using identical readout electronics systems to those designed for the inner detectors. Thus, the outer calorimeter electronics system, like the inner one, would have no maintenance requirements. The reliability goals of the inner system are such that repair accesses should be minimal, once per year or less.

9.7.3 Forward electronics

Electronics for the forward calorimeter are mounted in conventional racks and crates on the detector support platform on the outer surface of the HF shielding. High voltage and signal cables penetrate through the shielding to minimize cable lengths. Fig. 9.3 shows the approximate rack locations. When the detector is in the garage position, the racks are easily accessible for any required maintenance or repair operations. Access is somewhat more difficult in the cavern as the calorimeter is some 8 meters above the floor level centered on the beam line. Specific personnel access techniques, stairs, catwalks, and lifting devices, have not been designed at this time, but are straightforward applications of well-known hardware. The magnetic field strengths expected, a few hundred gauss, would call for proper procedures, training, and equipment should a service access be made with the solenoid energized.

The residual radioactivity activity levels discussed in chapter 5 refer to the end of a ten year operating period. During commissioning and the early years of accelerator operation, activation will not be a problem and no restrictions on access to the electronics are expected. As the system grows more and more activated, there could be need for placing time limits on access or for temporary local shielding during maintenance operations. Therefore, the forward calorimeter front end electronics system should feature good remote diagnostics to pinpoint problems and allow for simple replacement as the preferred method of repair.

References

[1] Timing, Trigger and Control Distribution for LHC Detectors, B.G. Taylor, ECP Division, CERN.

[2] Dynamic Range of the CMS HB @ HF Electronics, W. Wu and R. Vidal, CMS Group, Fermilab.

[3] HF Test Beam Report showing calibration in pe/GeV and Resolution HB & HE Test Beam Reports showing the resolution.

[4] Printed Circuit Board Design Techniques for EMC Compliance, Mark I. Montrose, IEEE Produce No. PC5595-QMC.

[5] Beam Test of a Prototype CsI Calorimeter, R.S. Kessler et al, NIM A368 (1996) 653.

[6] A Pipelined Multiranging Integrator and Encoder ASIC for Fast Digitization of Photomultiplier Tube Signals, R. Yarema et al, Fermilab-Conf-92/148.

A Second Generation Charge Integrator and Encoder ASIC, T. Zimmerman and M. Sarraj, IEEE NS V43#3, June 1996.

[7] Source Current Calibration of HCAL using Noise and Extreme Over-Sampling, A. Baumbaugh, CMS Group, Fermilab.

10. CALIBRATION

10.1 OVERVIEW

The calorimeter calibration and monitoring is designed to determine the absolute energy scale and monitor the calorimeter system for changes during the lifetime of the detector for offline corrections. Parts of this system will also be used for the relative timing of each calorimeter tower and to measure the linearity of each tower readout. Other parts of this system will be used during construction and assembly for quality control.

The HCAL has five distinct complementary systems for the calibration and monitoring. These are:

a) Megatile scanner: focused gamma source to measure light yield of each tile of every megatile.

b) Moving radioactive wire source: source tube(s) installed in every megatile that crosses every tile.

c) Light injection (UV laser and blue LED): UV laser light injection into two layers of each wedge. UV laser and blue LED light injection into the decoder box which has the photodetectors.

d) Test beam calibration: several individual wedges with muons and hadrons versus moving radioactive wire source for absolute energy calibration scale.

e) Physics events in the completed detector including jets and muons.

The megatile scanner will measure the relative light yield of each tile to better than 1%. The moving wire source will track changes of each tile to better than 0.7%. The laser light injection into the tiles is complementary to the moving wire source. In the decoder box, it will also be used for the timing of the individual calorimeter towers and for linearity measurement. Both the moving wire source and laser light injection will track changes in signal strength. The radioactive source will transfer absolute single-hadron test beam calibrations to the calorimeter. The test beam and physics events will provide the ultimate jet energy calibration.

Magnetic field brightening of scintillator light is well determined for the HE modules where the only effect is due to the increase in the signal due to the increase of light yield of the scintillator. For the HB, the effect is more complex and will be computed by using both the test beam results (initial) and physics jet events (final).

Light yield changes are expected due to ageing of the scintillators, radiation damage and changes in the photodetector response. Due to lack of space the moving wire source will be permanently attached to only two layers of each wedge where measurements can be performed during off beam times. These two layers are the first one after the electromagnetic calorimeter and one in the middle of the wedge, layer 10 for HE and layer 9 (or the last layer of tower 17, in eta) for HB. No permanent wire source will be needed for HO. In addition, during periods when the CMS detector is open, each megatile (including HO) will be scanned by the moving wire source. Radiation damage of scintillators in HB and HO are minimal, but for 2 < $|\eta|$ <3 in HE, the light yield will degrade by as much as 50% during the lifetime of the detector. To monitor and apply corrections to this eta region, each tower has four longitudinal segments and each segment has laser light injection to follow degradation. In addition one 20 wedge will have permanent wire source access to all four longitudinal segments for absolute measurement.

The calibration and the monitoring of the calorimeter wedges is a multi-step process as follows:

a) The measurement of light yield of each tile of every megatile before insertion into the calorimeter wedges. This step will use the megatile scanner that will measure each tile by a collimated narrow spread gamma source driven by a computer controlled X, Y motion. In addition each megatile will also be measured by the moving gamma wire source in a steel tube inside the megatile assembly.

b) After insertion inside the calorimeter wedge, each megatile will again be scanned with the moving wire source. The two layers that have the UV laser connection will also be excited by the laser.

c) A small fraction of the calorimeter wedges will be placed in the test beam for the absolute calibration.

d) After assembling the calorimeter segments, but before closing the CMS, each megatile will again be scanned by the moving wire source. The two layers per wedge will also be checked with the UV laser. During this period each decoder box will be excited by both the UV laser and blue LED for timing as well as monitoring. The procedure with the moving wire source will be repeated (about once a year) during the periods when the detector is opened.

e) After the start of taking data, but during the off beam times, the layers that have light injection and the source tubes permanently connected, will be scanned by the UV laser and, occasionally, by the moving wire source. These will track the radiation damage, as well as other damages. Also, the decoder box will be flashed with UV laser and LED for monitoring purposes.

Calibration of HO-B and HO-E is via the continuous flow of energy across boundaries, and by muons, as well as by occasional-access wire gamma source, LED light injection to the prototubes, and we are considering laser light injection to the tiles for timing calibration.

10.1.1 Calibration and monitoring systems

Below is a brief description of each calibration and monitoring system.

THE MEGATILE SCANNER: This system is described in chapter 6 where a pure Caesium-137 gamma source moves under computer control a few millimetres above the megatile assembly. Phototubes connected to various tiles via optical fibres will read and store the signal strength of each tile.

THE MOVING WIRE SOURCE SYSTEM: As described in chapter 6, each megatile has four built-in source tubes where a Caesium 137 radioactive source at the end of a "wire" can be remotely inserted all the way across every row of tiles. Since each tile is in a different tower, each tile can be read independently. Inside the detector, only the first and middle layer of each HB and HE wedge will connect permanently to the moving source driver. The rest of the layers (including HO) can only be scanned when CMS is opened up. In HE one wedge will have permanent source tube connection to all four longitudinal segments to monitor the radiation damage at high eta and to cross check the light injection into tiles.

UV LASER and LED INJECTION: On the megatile layers with laser option, one quartz fibre per ϕ segment will bring in the UV pulse. It will then be fanned out to every tile by 200 micron quartz fibres. In the decoder box, both the laser and the LED will be used to excite a Y11 wave shifter. From this wave shifter, 200 micron quartz fibres will be fed to each pixel of every photodetector. This allows monitoring of the gain of every pixel as well as timing of the towers.

TEST BEAM CALIBRATION: A small number of wedges will be placed in a test beam at CERN where hadron and muons of various energies will be used to determine absolute calibration between beam energy and light yield response to the moving wire source.

PHYSICS CALIBRATION: In the CMS detector, single tracked hadrons from taus, jet balancing and dijet resonances will be used for in situ calibrations, as discussed in chapter 10.7. Muons will be used to determine the response to minimum ionising particles, and to link the HO to the rest of the calorimeter.

The HF calorimeters made of quartz fibres and read by photomultiplier tubes are in a much harsher radiation environment and require continuous monitoring of the radiation damage. As described in chapter 10.4.7, the calibration and monitoring system for HF uses the UV laser, test beam and physics events. The laser pulse is wavelength shifted and fed into each PMT to monitor the gain. In addition, the wavelength shifted laser pulse is also fed into the back end of a test fibre near maximum irradiation dose area. The front end of the fibre is then curved back into another nearby slot and read at the back end by a PMT. This system will follow the radiation damage accurately. The absolute calibration is by means of test beam data of several modules. During data taking, jets produced in conjunction with known particles (e.g. Z's) will also be used to further improve the calibration. We are investigating the option of moving Co-60 gamma sources at the front face of the HF calorimeter and in longitudinal source tubes (parallel to the quartz fibres) to provide tower-to-tower relative normalisation, transfer testbeam calibrations, and provide direct scans of the fibre radiation damage profiles.

10.1.2 Discussion of choice of calibration techniques

The energy resolution of the CMS Hadron calorimeters is expected to have a constant term of ~5%. In order not to degrade this significantly, it is important that the tower-to-tower energy scales be known to better than 3%, and that any changes in calibration with time can be monitored quickly and frequently, with an accuracy of 1% or better. The absolute initial calibration will be accomplished using moving radioactive sources to transfer testbeam calibrations of a few wedges to the rest of the calorimeter. Eventually, absolute calibrations will be refined, and the jet energy scale more precisely established, by use of various in situ physics signals. Frequent gain monitoring will be accomplished by systems for injecting light to the phototransducers and to a few selected layers of scintillating tiles, and verified occasionally by use of the moving radioactive source system.

Additional functions of the light injection system include: to provide timing calibration signals for all towers, and to provide a series of light intensities to check or calibrate the linearity of each calorimeter channel. The proposed light injection system is uniquely suited to perform these two functions.

The use of the moving source system for Quality Control/Quality Assurance of the optical systems at construction and assembly time is discussed fully in chapter six. The technique of visiting every tile with a moving source is essential to QC/QA of the optical systems at all stages, from megatile construction to the initial assembled calorimeter. Later, the moving source can check in detail whether the response profile of a tower has changed, permitting an accurate recalibration.10.1.1.1

Moving source capability to transfer absolute testbeam calibrations

It is important to have an initial absolute calibration which is independent of collisions, in order to set uniform trigger thresholds and collect collision data optimally. The moving radioactive source is uniquely suited to do this. The initial absolute calibration is also important because in situ physics HCAL calibration using collider data will take time to collect, analyse, and understand. Initially equalising all towers in the HCAL to an accuracy of 2% for single particles also dramatically simplifies and speeds up the in-situ calibrations, since there are 144 towers at each location in η. Since collision-related data are expected to be azimuthally symmetric, only 17 different η values need to be studied in HB, for example, and data from all 144 towers at a given η can be lumped together.

The moving source strategy allows us to put only several wedges into the testbeam. The method requires measuring the source response of every tile in the calorimeter ("fingerprinting" each tower) and making a suitably shower-weighted sum over the tile source responses of each tower. The method has demonstrated a systematic accuracy of ~2% in source-beam comparisons, and permits not only the relative normalisation of all towers in the calorimeter, but also the absolute normalisation of the calorimeter relative to a few towers which have been calibrated in testbeams. Recent preliminary analysis of the CDF endplug EM calorimeter testbeam module, from which beam calibrations will be transferred to the rest of the calorimeter, shows rms agreement of ~1.8% between the electron beam response and the EM-shower-weighted sums of the source responses of tiles within towers.

The first link in this calibration chain is discussed in chapter six. At the QC/QA stage of megatile construction, we measure the response of every tile to a collimated Cs-137 gamma source and also to the uncollimated wire gamma source. The ratio is preserved in a calibration data base, and is used whenever a wire-source fingerprint is taken.

The wire source response depends on the lateral size of the tile, the location of the source tube, and in a nonlinear way on the thickness of the scintillator, whereas the collimated source excites all tiles in an essentially absolute way. The collimated gamma source excites all tiles in an equal amount, independent of position and lateral tile size. With the collimated source, tiles are excited in direct proportion to their thickness. This tracks the excitation of the tiles by shower particles.

Care has been taken in the design to ensure that the source tubes do not move relative to the scintillator when the megatiles are installed in the calorimeter. Thus the collimated/wire ratio will still be valid. We use the collimated/wire ratios to calculate an effective "collimated source fingerprint", which is then convolved with the average depth profile of hadronic showers to predict the relative response of every tower, and to relate the testbeam wedges to the rest of the calorimeter.

Variations in absorber thickness could, in principle, lead to shower response variations. The moving source technique does not address this source of variation, which could contribute to the rms seen in source/beam ratios for a set of towers, for example the above mentioned 1.8% rms seen at the CDF testbeam. For CMS HB and HE such absorber variations are not expected to cause significant degradation of the testbeam/source calibrations.10.1.1.2

Magnetic brightening of scintillator in magnetic field

One essential link to complete the testbeam/source calibrations is to understand, and where possible measure in situ, the magnetic brightening effects at 4 Tesla[1]. The radioactive source has been shown to follow accurately the magnetic brightening of scintillator. Light injection cannot measure this brightening. The brightening curve for a particular type of scintillator is measured in advance, and can in principle be applied to zero-field calibrations if it proves too difficult to run moving sources with the field on. The magnetic field is expected to be very uniform over all parts of HB and HE. In HO the field is less than 4 Tesla, but known, and corrections will be applied. We are pursuing the engineering development of a source driver using non-magnetic motors to permit direct field-on source measurements of one tile in every tower.10.1.1.3

Magnetic shower energy steering in HB

The last link in the absolute calibration chain, relevant only for the HB configuration where the magnetic field is parallel to the HCAL plates, is the magnetic steering of extra shower energy into the scintillator. As discussed in chapter one, this effect has been predicted by GEANT and confirmed in the 1996 H2 testbeam measurements at CERN. The effect is predicted to be, and measured to be, absent in the HE configuration where the plates are perpendicular to the magnetic field. The radioactive gamma source is, of course, unable to measure this effect which involves the steering of charged particles. The effect depends on the placement of the scintillator package in the gap, and is minimised by placing the scintillator in the (radially) outer location in the gap. As discussed in chapter 1, there is a relatively large variation if the front and rear air gaps both change due to motion of the scintillator package in the slot. The present HB design uses venetian-blind springs to support the scintillator packages firmly to the outside of the 9 mm gap in the brass. For a 7 mm thick scintillator package in this location, GEANT calculations for 50 GeV pions show less than 2% increase in response at 4 Tesla the HB baseline geometry happens to be rather close to optimal.

Tolerances in machining and in scintillator thickness are estimated to give an air gap of approximately 1.5 to 2 mm in front of the megatile package. GEANT calculations indicate 4%/mm change in response as a function of front air gap, for pions at 4 Tesla. Thus we expect an rms scatter of (4%/mm)(0.5mm)/ $\sqrt{12}$ or less than 1% in the pion shower steering factor at 4 Tesla, globally for all tiles in the HB. Therefore, we believe that the magnetic steering factor can be applied globally to the radioactive source calibration of HE, and that the resulting absolute single-hadron calibration will be accurate within the desired 3% systematic accuracy.

A further possible redundant cross-check of magnetic field effects can be done by collecting various classes of collider HCAL signals with the magnetic field on and off. Magnetic steering of the copious lower- momentum charged particles in jets (curl-up of tracks with p_T < 800 MeV/c in the tracking volume, oblique incidence of other charged particles onto the ECAL, and magnetic steering of showers between ECAL and HB) would need to be understood in order to use this technique. These issues relate to the field-on jet energy scale and will therefore need to be studied and understood in any case.10.1.1.4

Source monitoring

The moving source system has a repeatability (as distinguished from systematic accuracy) of approximately 0.5%, and can be used, at relatively infrequent intervals, in the permanently accessible layers to monitor changes in the response of each tower. This will also serve to monitor and calibrate the more frequently used light injection to the phototubes and to the special megatiles.

10.2 SPECIFICATIONS AND REQUIREMENTS (HB/HE/HO/HF)

The calibration and monitoring system should be capable of establishing the initial calibration of every tower to an accuracy of 3%, and of maintaining calibrations to 1% accuracy. The initial calibrations are necessary, among other reasons, to permit clean trigger thresholds at the start of collisions, to permit immediate use of the calorimeters for physics analysis, and as a cross check of possible in-situ calibrations done using physics signals from the collisions.

The light injection system should be capable of determining the relative timing of towers to a few ns. This system will also use a series of selectable neutral density filters, with a dynamic range of four orders of magnitude covering the dynamic range of the photodetectors and DAQ, to measure the linearity of each tower.

10.3 SOURCE CALIBRATIONS

Source calibrations involve, first, the use of movable collimated radioactive gamma sources in three megatile scanner boxes, in conjunction with the use of three CDF-style wire source drivers. Then, at the testbeam, one or more further wire source drivers will take data for the transfer of testbeam calibrations to the HB, HE and HO (and possibly HF). Further wire source drivers will be used at the wedge assembly area and in the detector hall for late-stage QC/QA and then for "occasional access" sourcing of every tile.

Finally, three dedicated slimline wire source drivers will be installed on each half-barrel and each endcap, and coupled permanently to one scintillator layer in every tower of each HCAL depth compartment, thus permitting calibration monitoring by the sources when the detector is closed. This is a total of 12 permanently installed non-magnetic slimline source drivers for HB and HE. Prototype slimline source drivers are being developed in 1997, capable of fitting in the space between the back of a barrel wedge and the magnet cryostat. Development is also underway of piezoelectrically switched air motors capable of operating in a 4 T magnetic field, to permit field-on source calibrations of at least one tile in every tower, and thus measure directly the magnetic brightening of tiles in a variety of locations.

10.3.1 Design specifications

The design and use of wire source drivers and the associated systems are described[2,3,4,5,6,7,8]. The radioactive source is mounted inside the tip of a long flexible stainless steel "wire": a point-like Cs-137 gamma source, with active length typically 5 mm and activity in the range 0.5 to 5 mCi, is contained at one end of a sealed 22 gauge stainless steel needle-grade fully-hardened hypodermic tube, of 0.71 mm OD and with a length of up to about 11 m. The active element in future sources, manufactured by the Isotope Products Laboratory of Burbank, California, will be a set of ion exchange beads which have been sealed and hardened by heating in a Hydrogen atmosphere. An internal keeper wire holds the active element at one end of the sealed tube, which is a second level of source encapsulation. Further details are given in Chapter 6. The source is garaged in a cylindrical lead pig when not in use. The wire is coiled in a storage reel of radius 12.7 cm, which can push or pull the wire with a force up to about 11 N. A schematic of the Model III source driver is shown in Fig. 10.1. The driver uses two small motors to direct the wire source into the calorimeter. One motor controls the source tube selection via a spiral indexer which can select one of up to 380 different channels, and the other motor drives the storage reel to extend or retract the wire, which travels in 3.2 mm OD low-friction acetyl plastic tubing to the calorimeter. Inside the calorimeter, the source wire travels in thinwall stainless steel hypodermic tubing of 1.3 mm OD and 0.97 mm ID.

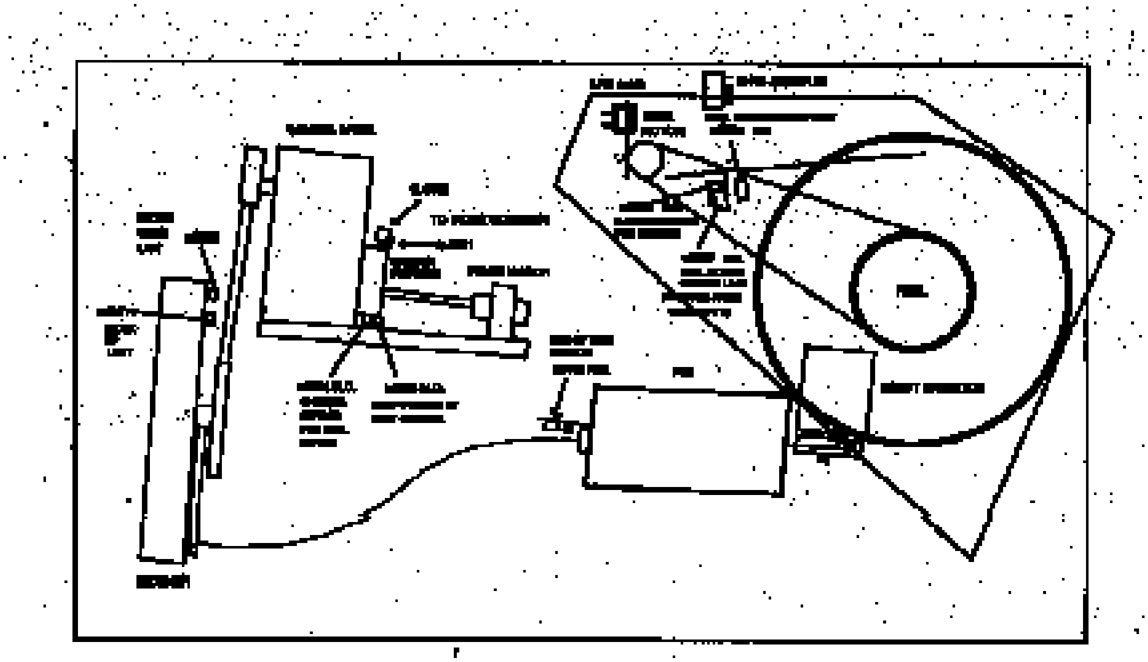

Fig. 10. 1: Schematic of a wire source driver which uses a storage reel.

Typical wire speeds are 5 to 10 cm/sec using the CDF Model III source driver with reversible DC electric motors. The wire speed is switchable to about one-half of the above speed if desired inside the calorimeter. The wire position is read out with a least count of 0.1 mm, and the indexer location is read in counts of one unit per channel, by batch counters which can be remotely interrogated and which also have visual readouts. The wire driver is controllable either by panel switches located on the electrical control box, or by a computer. The control box will be located within about 3 m of the computer, but can be located over 100 m away from the source driver.

The Model III source driver design used for CDF and for SDC, and proposed for most uses at CMS, has been described above. The design for the permanently installed drivers has two major changes: (1) to fit into the space at the back of a wedge, the indexer will be linear and will have fewer selectable channels (48 channels), and the wire driver motor and other elements will be confined to a maximum height of 7.5 cm, and (2) piezoelectrically switched "oil-free" air motors will be used, to permit operation at 4 T. The motors are made by the E2 Corporation, Model LZB 22 LR, and are readily available. The time between field servicings of these motors is claimed by the manufacturers to be approximately 1500 hours. Extensive tests of these motors will be done to determine the actual useful running time before maintenance is required. One calibration run into one scintillator layer in six HB wedges, at approximately five minutes per channel into 24 source tubes, would require two hours of running, and another two hours to monitor a second HCAL depth compartment.

A design using pinch rollers has been prototyped (Figs. 10.2 and 10.3) and is presently undergoing extended multi-cycle "torture testing". The pinch roller design is also well-suited to a slimline layout, although the prototype shown makes use of many Model III parts and is not yet arranged compactly. The pinch roller design, by almost everywhere confining the wire to a tube, eliminates the possibility of the wire's buckling, and also permits pushing the wire with more than 11 N of force if needed. However, it is believed that the reel drive, with 11 N of force, would be sufficient for the proposed tube layouts; the recently-found low-friction acetyl tubing is very helpful in reducing the overall friction on the source wire.

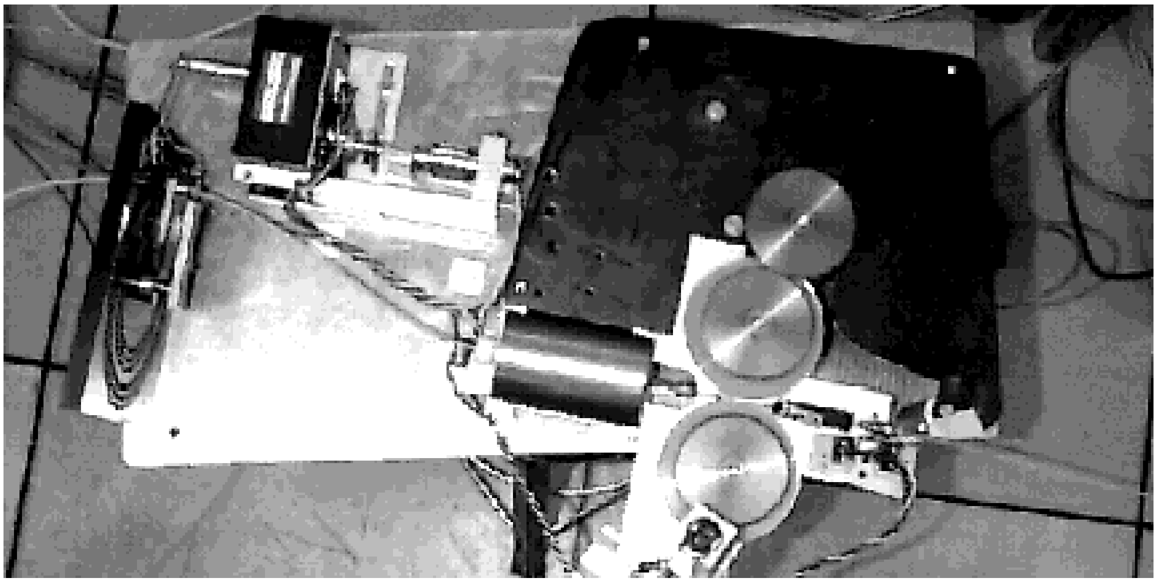

Fig. 10. 2: Top view of prototype pinch-roller variant of a wire source driver. The layout is not yet optimised.

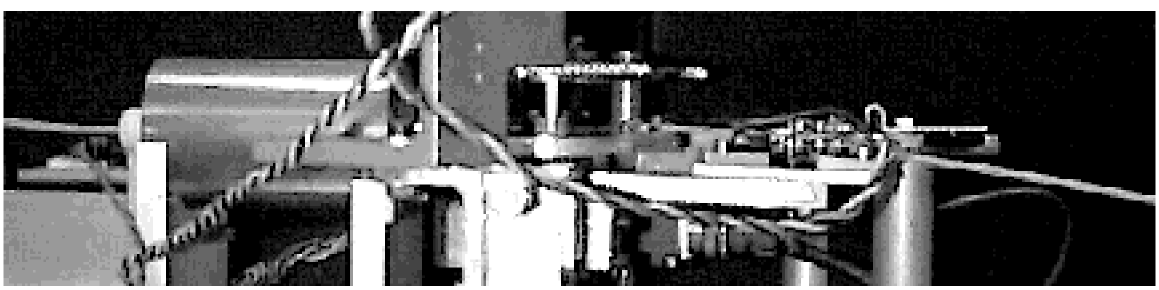

Fig. 10. 3: Side view of the prototype pinch-roller wire source driver.

The choice of permanently-accessible source tubes to only two layers of each HB tower and most HE towers is a compromise. There may be room for a longer linear indexer, or a modified indexer design, which could accommodate more than the planned numbers of source tube channels. We will investigate whether the number of index channels can be cheaply and easily increased. A few more permanently-accessible layers would provide more complete initial field-on sampling of the calorimeter, better redundancy of source access to the towers, and more complete sampling of radiation damage whenever desired. The extra cost and labor of installing more plastic tubes to the indexer is not large, since every pan-edge coupler will at least receive a short plastic tube. Because the air motor lifetime between servicings is not yet proven, extra permanent tubes might be used rather infrequently, but could provide useful options. Open access fingerprinting would still be by the Model III source drivers which use small electric motors.10.3.1.1

Quality control

Source drivers of the final design for permanent installation will be extensively tested through many wire insertion cycles into a mock-up of the calorimeter tube layout. One such source driver will be exercised on the Pre-Production Prototype wedge, first at Fermilab and later at testbeams at CERN.

Tube couplings will be installed under strict protocols, and the security and integrity of the couplings will be double-checked after installation. All source channels in the assembled calorimeter will be probed with a dummy source wire to check that their full length is accessible. (As discussed in chapter six, similar checks will be made on individual megatiles at production time.)

10.3.2 Layout

The layout of the source tubes is discussed in part in the Optical Systems chapter six. The metal source tubes run the full length of the megatiles, crossing near the centres of tiles except at the end of the megatile, where the tubes make an S-bend to exit the pan as close as possible to the optical connectors. The bend radii are kept as gentle as possible to minimise friction and to minimise flexing of the source wire. The S-bend radii of the present design are 12 cm and 20 cm. Fig. 10.4 shows a plan view of a megatile with source tube routing.

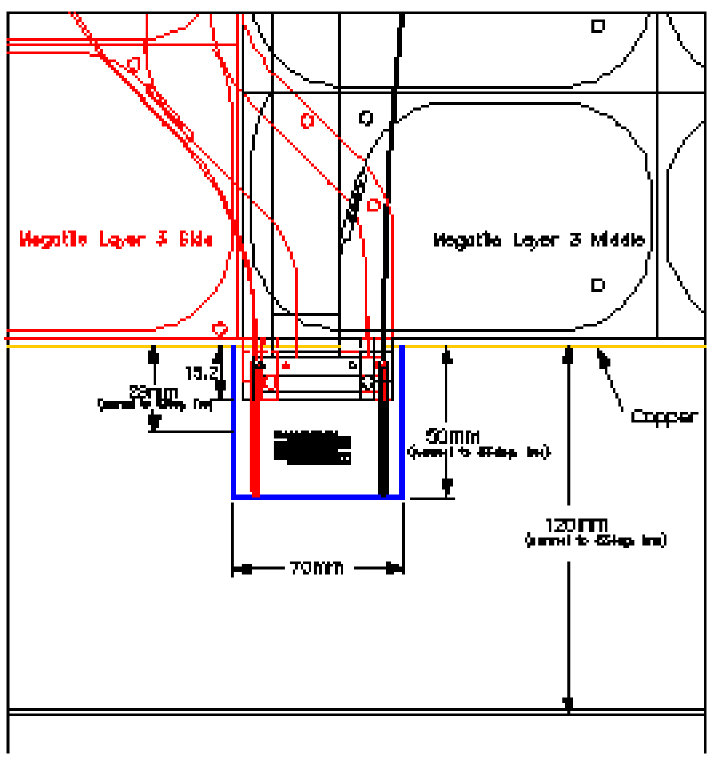

Fig. 10.4: Top view of the megatile and connector layout.

At the pan edge, a brass transition coupler locks onto the metal tube with a 2-56 nylon-tipped set screw, and locks onto the 3 mm (1/8") diameter acetyl tubing with a paraxial 3-48 screw whose threads bite into the plastic. A cone of 18.5 full angle guides the tip of the wire into the narrower metal tube. Both the optical couplers and the source tube couplers protrude a short distance, (of order 1.8 cm beyond the edge of the megatile, or 1.5 cm beyond the copper, for the source tube couplers), into the protected channel dedicated to them. Front and side views of the couplers are shown in Fig. 10.5, Fig. 10.6 and Fig. 10.7. A more panoramic view of the end of a wedge, showing the dedicated channels and source driver, is in Fig. 10.8. One source driver, with a 35-foot (10.6 m) source wire can access up to 7 wedges. For symmetry, both HB and HE will use one source driver per 6 wedges (or per 120 degrees in azimuth).

Fig. 10. 5: End view of HB megatile-edge source tube coupler.

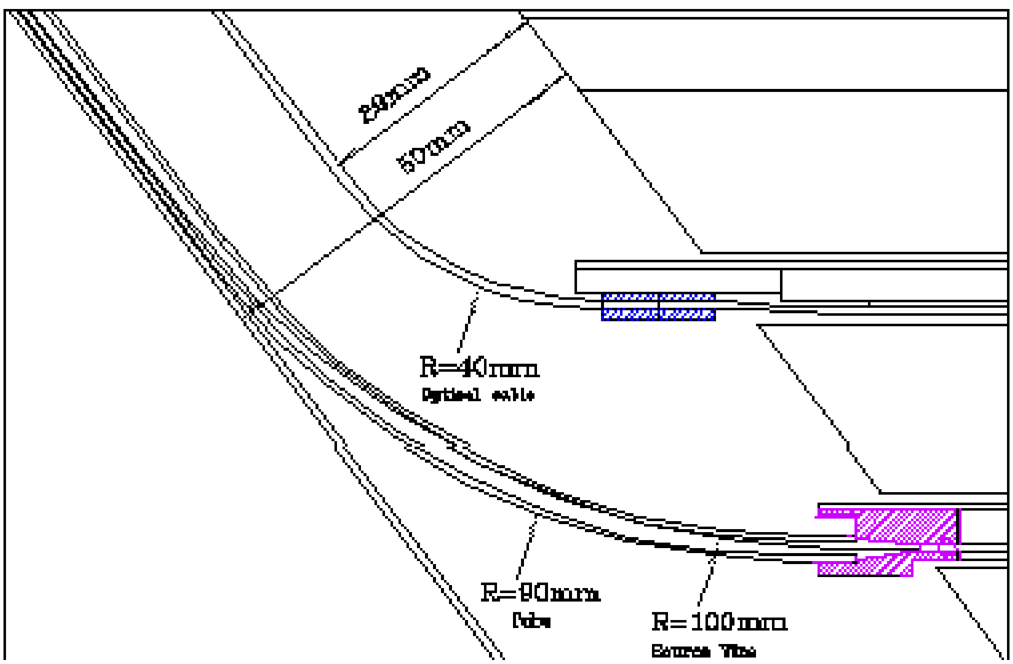

Fig. 10. 6: Side view of the edge of an HB megatile showing the source tube coupler and the direct R-Z bend of a permanent plastic source tube.

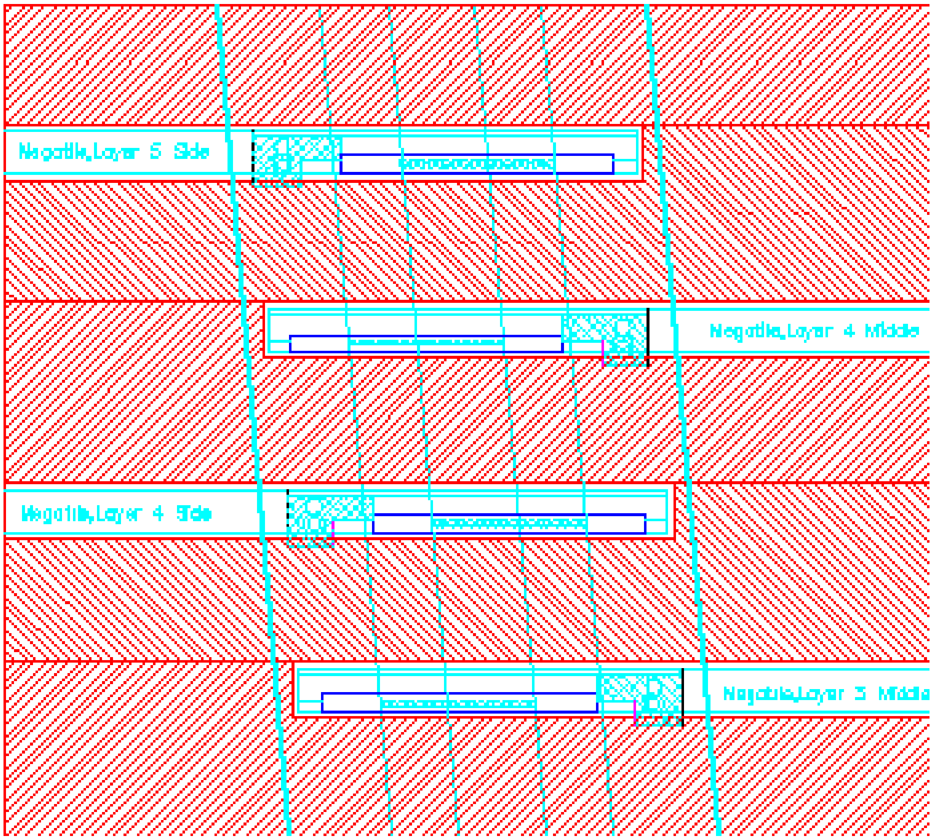

Fig. 10. 7: End view of HB megatile optical and source tube couplers.

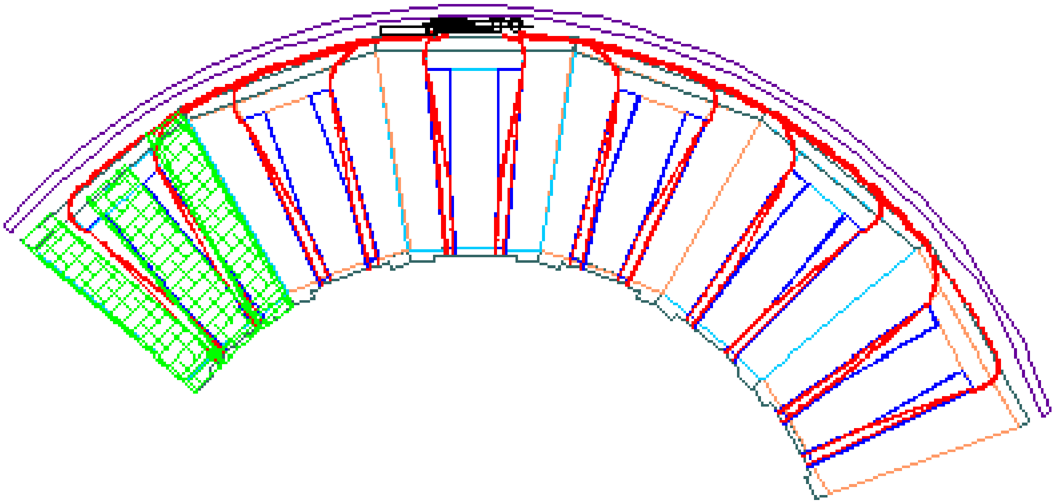

Fig. 10. 8(C.S.): Panoramic view of the end of six HB wedges, showing the channels dedicated to the optical cables and source tubes, source tube routing, and a slimline source driver. The leftmost wedge also indicates (hatched) a possible routing of the overlying services from HE and Tracking.

Most of the layers will be coupled to a source driver only on occasions when the endcaps are retracted. For HB, if the innermost 40 cm of the channel is buried under other services, the plastic tubes will be conducted out beyond a radius where the overlying services have fanned out away from covering the HCAL channel. A possible routing of the overlying services is shown hatched in the leftmost HB wedge in Fig. 10. 9. As soon as possible towards the back of the wedge, the HCAL channel height should increase to more than 5 cm above the copper, to ease the wire bending radius when entering the outer calorimeter layers.

All plastic tubes will be permanently attached to the couplers at the edge of the megatile. Quick-release barrel connectors will be used occasionally to couple, via 3 mm (1/8") plastic tubing, a roving source driver to all of the source tubes in a tower, to repeat the "fingerprinting".

One layer of tiles in each depth compartment will have light injection fibres and will also have source tubes coupled via plastic tubing to permanently-installed source drivers. The plastic tubes will run from the pan edge to the back of each wedge, in the HB channels shown in Fig. 10.8. The tubes turn and run azimuthally just inside the cryostat towards the source driver. One slimline source driver will serve 6 wedges. A radial view of the driver and associated plastic source tube routing is shown in Fig. 10. 10.

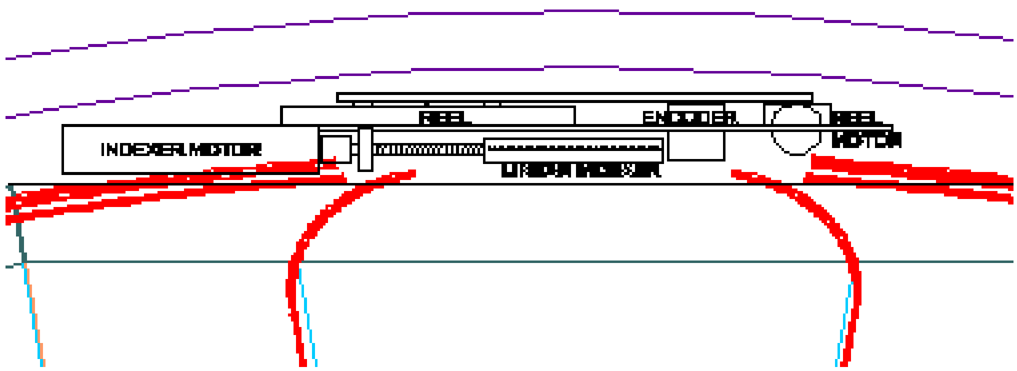

Fig. 10. 9: Z-view of a slimline source driver. For clarity, the 90 bends of the plastic tubes into the Z-direction are not shown.

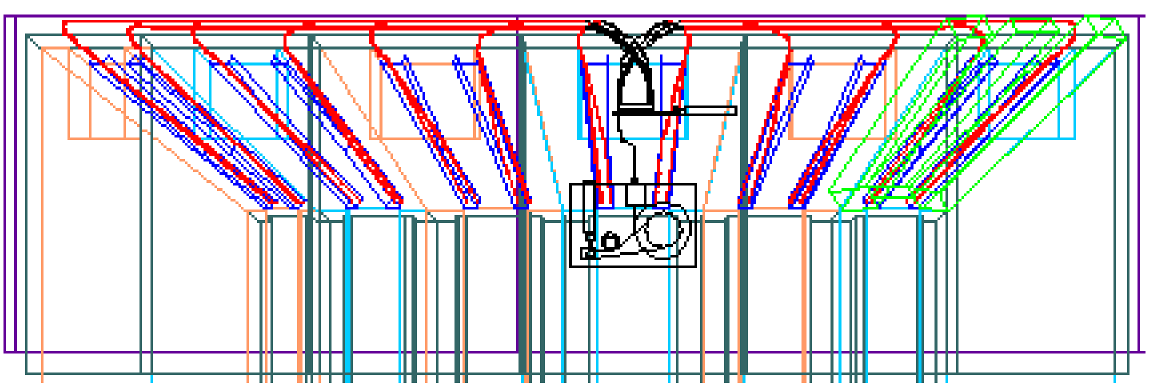

Fig. 10. 10: Plan- or R-overview of source tubes and slimline source 4,5,5,6, driver at the back of an HB wedge.

Each driver will require a 90 psi air supply, with one air hose per half-barrel, and one hose per endcap, coming from outside the detector. Each installed driver will require a separate multi-wire cable running to its electrical control box located in one of the control rooms in the cavern wall or at the surface.

For HE, the space constraints in the 12-cm crack are quite different: the source tube routing is not constrained to narrow phi intervals, but on the other hand less space may be available above the metal calorimeter plates. The solution is to bring out the source tubes at the edge of the megatile pointing in the phi direction, via a 90 bend. At that point, quick-disconnect CDF-style transition couplers are installed on the ends of the metal source tubes and mounted securely to the edge of the megatile. These couplers are specially modified brass Parker fittings, with a steep internal cone leading to a socket for the steel source tube. The steel tube is permanently locked in with a 2-56 nylon-tipped set screw. Occasional-access sourcing by roving source drivers is via the 1/8" plastic tubing into these quick-disconnect couplers. Permanent plastic source tubes routed to selected tile layers will couple into the same type of quick-disconnect couplers. These permanent plastic tubes will make 90 turns to run generally in the Z direction to the rear of the calorimeter and then turn toward the source driver.

10.3.3 System interfaces

The primary source driver system interface is: (1) at the front panel of the electrical control box, via a 25-pin D connector to the TTL digital logic expansion card in the PC. The traffic consists of motor control signals and status signals; (2) the RS485 interface between the two batch counters (wire position and index channel counts) and a serial Communications port.

The control computer contains software to control the motion of the source wire and the selection of channels. The PC will communicate with the host computer which does the run-control and the DC source current data acquisition from the HPDs.

10.3.4 Data acquisition and processing

During source calibration operations, the calorimeter readout system will be operated in its normal mode at the normal clock speed with the calibration established through extreme oversampling. For the case of a 10 cm tile and a source speed of 5 cm/sec, averaging data samples over 10 msec intervals provides 200 data points across the surface of the tile. Since the majority of the source data will be acquired before installation in the cavern or at times when the CMS TriDAS system is not expected to be operational, the Detector Control System (DCS) has been selected to acquire and process the data. This system also provides control, display and database services for the calibration process and acquires the source position readings needed for the calibration algorithm.

Each readout crate in the system contains a DCS processor. During source runs, this processor becomes the master and the crate is disconnected from the normal data path to the farm. The trigger and data acquisition cards continuously receive the data stream from the front end digitizers into the first-level trigger pipelines. A first-level trigger accept, generated by the DCS processor, causes 8 groups of 16 consecutive readings to be moved into the derandomizing buffers. Subsequently, each group of 16 is sent through the second level filter which performs a sum operation. Finally the 8 summed results are readout over the VME bus into the DCS processor for further averaging and histogramming. Only those channels for the set of tiles in the calorimeter layer being scanned are read out, but all of them (up to 34 for the longest tile tray in the barrel) are readout for each first-level yes independent of the source position.

Finally, the processor executes the calibration algorithm on the histograms for each tile. Since the number of photoelectrons expected in each measurement interval is small, the calibration amounts to fitting the data to a Poisson photoelectron distribution convoluted with a Gaussian noise distribution and extracting the average number of photoelectrons per measurement interval. The measured spectra are available to the operator at any time during the run and particularly at the end for diagnostics if the algorithm reports a calibration failure. There are 14 source systems in total, and using crate based processors allows for parallel operations without a rate penalty.

10.3.5 Access, maintenance and operations

The initial fingerprinting and calibration will require access to the "occasional-access" source tubes with the detector open, and also requires measuring the source response of selected scintillator layers with the magnetic field on.

Subsequent monitoring by the moving source, of gains and of light injection to the special layers, can be done as often as desired. It is envisioned to take place at one to two month intervals, or as dictated by our experience with the stability of the light injection monitoring and of the various light injection paths to HPDs and to individual tiles.

Access to the source drivers and their associated tube manifolds will be only when the endcaps are retracted, which is expected to be at very infrequent intervals of perhaps one year. Access to the installed source drivers, for possible maintenance, must be feasible. This is an important integration issue involving the pipes and cables which run in the crack between HB and HE and then along the inside of the magnet cryostat.

10.4 LASER CALIBRATION AND OTHER LIGHT INJECTION

The HCAL calorimetry systems necessitate a precise calibration scheme. Calibration systems are needed to:

a) Monitor the performance of PMTs and front-end electronics, for each channel (laser)

b) Maintain calibrations from a test beam or collider data. Both absolute and tower to tower gains need to be tracked in time.

c) Set timing offsets for each channel

Monitoring of the system has to be far more frequent than the in "in situ" absolute calibration with collider data. Monitoring will be accomplished with the help of well-controlled light sources (laser and blue LEDs) which will be externally generated and distributed throughout the system. The light injection can be done several times per day (during nonfunctioning of the collider). These systems will be used for photodetector gain and linearity monitoring and for radiation damage monitoring. In principle the light injection response data can be made available very quickly to an operator to check the performance of all the calorimeter channels. A number of quartz and plastic-scintillator-tile hadronic calorimeter prototypes were monitored during the 1995/1996 test runs using various combination of LED and laser systems. Our data indicate that these systems can deliver monitoring of photodetectors better than 3% under realistic experimental conditions. We expect that with further optimisation, this precision could be improved to 1% which is adequate for HCAL systems.[9]

10.4.1 Specifications

DYE LASER: A pulsed nitrogen dye-laser can be tuned both in wavelength (337-500 nm) and intensity (neutral density filters) remotely for multiple purposes. At a few Hertz repetition rate, a commercially available pulsed N2 laser with 4 mJ energy at 337 nm can provide 225 μJ if a dye is used. This corresponds to 510^{14} photons at 450 nm. If we assume that one million p.e. per channel are needed for monitoring and that a conservative estimate of quantum efficiency, light losses at splitters and connectors is made, then we need about 310^{12} photons per one side of HF, for example. The dye has the virtue that a tuneable frequency light source is possible over a range of 350-500 nm. The tuning requires about 1 second to reach any given wavelength. The manufacturers indicate that a command jitter of less than 1 ns is possible with modest development. In test beam work, we have experience with sealed (open TEA) nitrogen pulsed lasers which provided 3 ns (0.6 ns) wide pulses.

LED: LEDs serve as an additional information source, namely: to extract a gain and single photoelectron level via the statistical method. LEDs are also logistically useful at times or places where the laser is unavailable, such as in the HO-B and HO-E.

- Superbright blue LEDs based on GaN grown on SiC substrates are newly available in the market. We have already used these LEDs in the test runs.

- The typical brightness for these LEDs is now about 1000 mcd.

- They have a remarkably low dependence on temperature, due the large direct bandgap in GaN.

10.4.2 Design

LASER: A 4 mJ laser will be suitable for the purpose of monitoring HB, HE and HF simultaneously. This laser will be housed in the counting room.

In the test beam work, we have used a sealed nitrogen pulsed laser which provided a 3 ns wide pulse at frequencies from 1 to 20 Hz. Each pulse was about 120 μJ at the nitrogen wavelength of 337 nm with a 5% variation in power from one pulse to the next. The beam size at the exit of the laser cavity was 3 mm by 8 mm and the beam divergence was 5 mrad by 8 mrad. This laser can be externally triggered with a minimum of 1 μs wide TTL pulse. Our present system and related optics are shown in Fig. 10. 11 through Fig. 10. 14. The system contains vertical and horizontal slits which reduce the intensity of the light in x and y directions respectively. There are 4 beam splitters that reflect some small fraction of the light to the photodiodes and the transmitted light is captured by a 1 mm inner diameter quartz fibre.

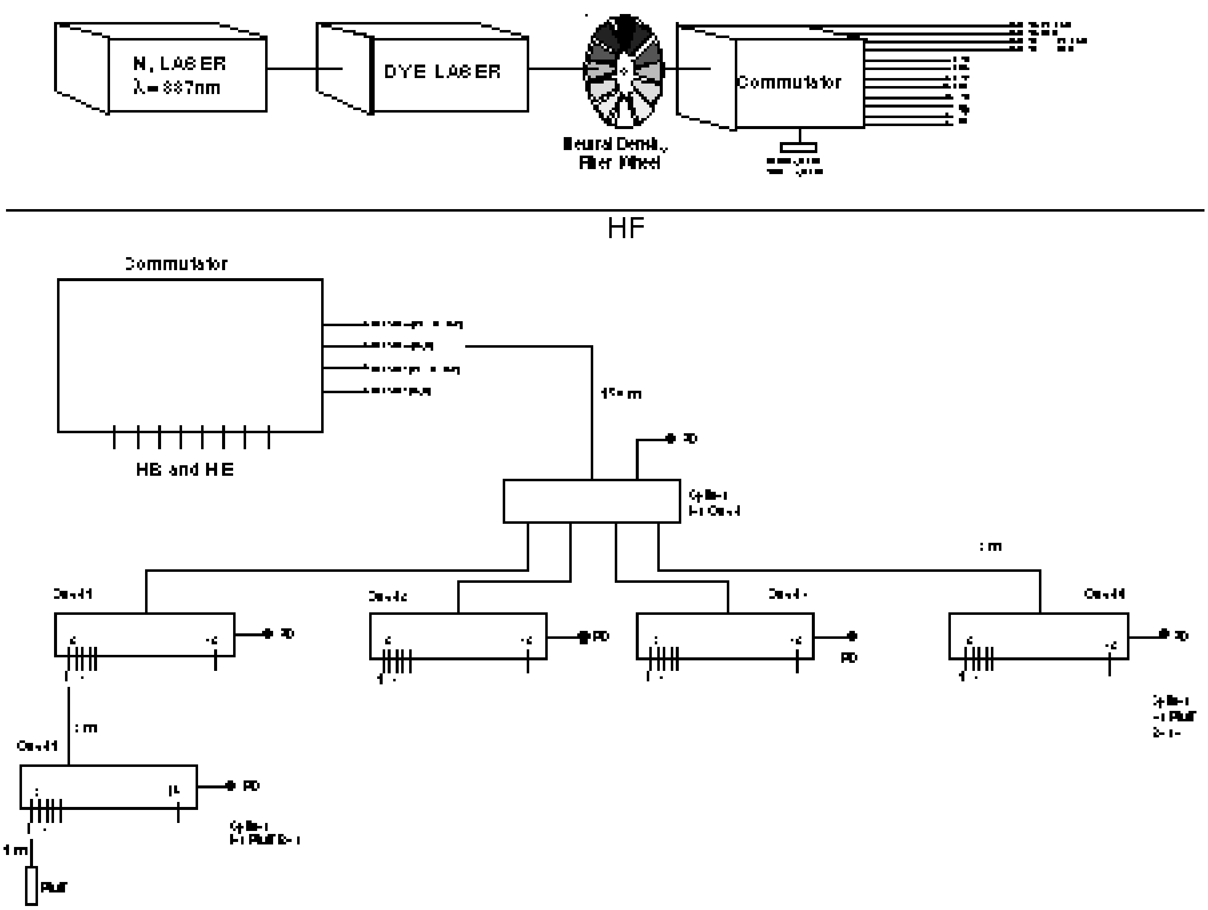

Fig. 10. 11: The layout of the HF laser light distribution system. The HB, HE system is shown in chapter 7.

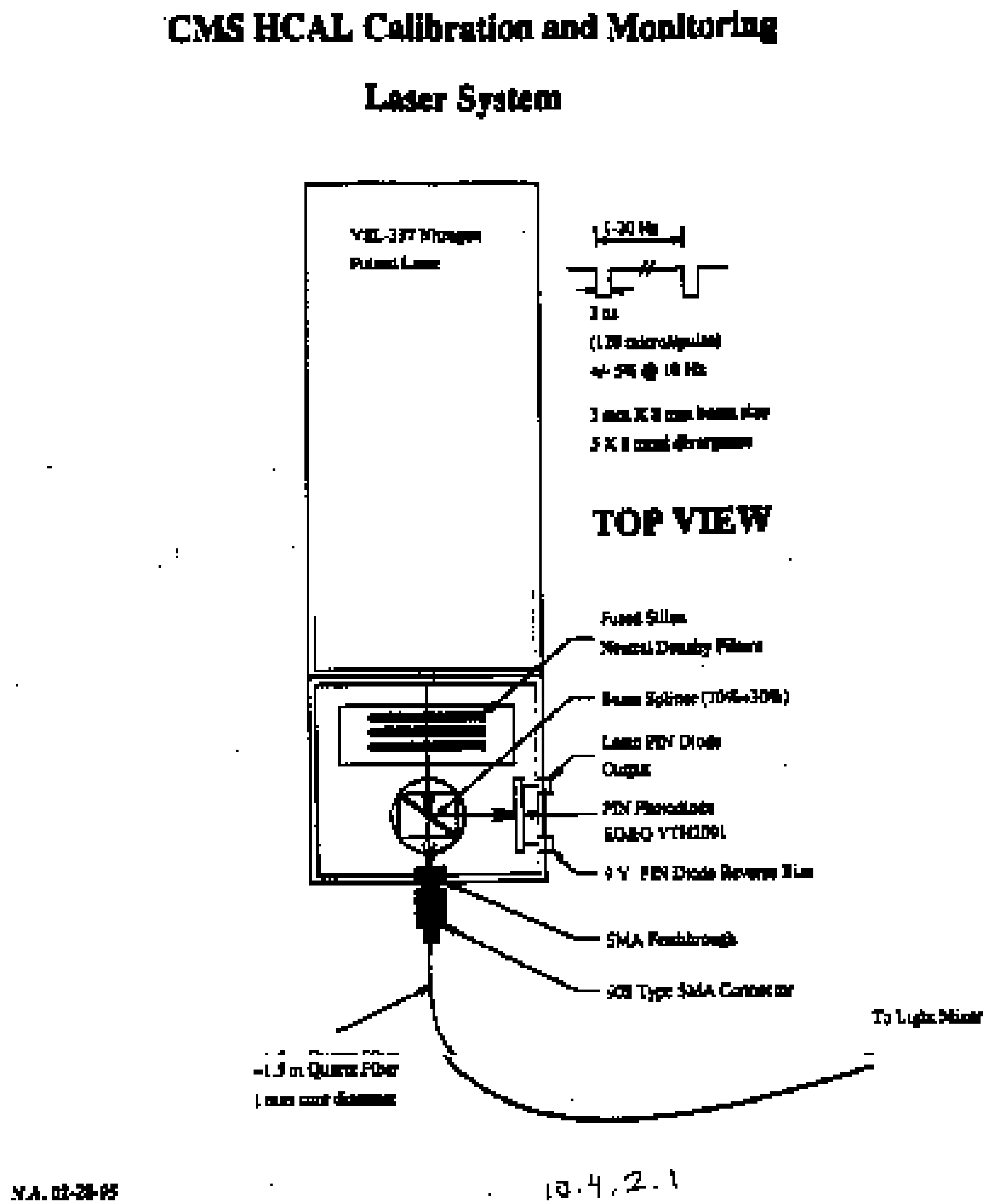

Fig. 10. 12: Laser light injection system and related optics. The box attached to the laser source houses necessary components for pulse-to-pulse monitoring of the laser.

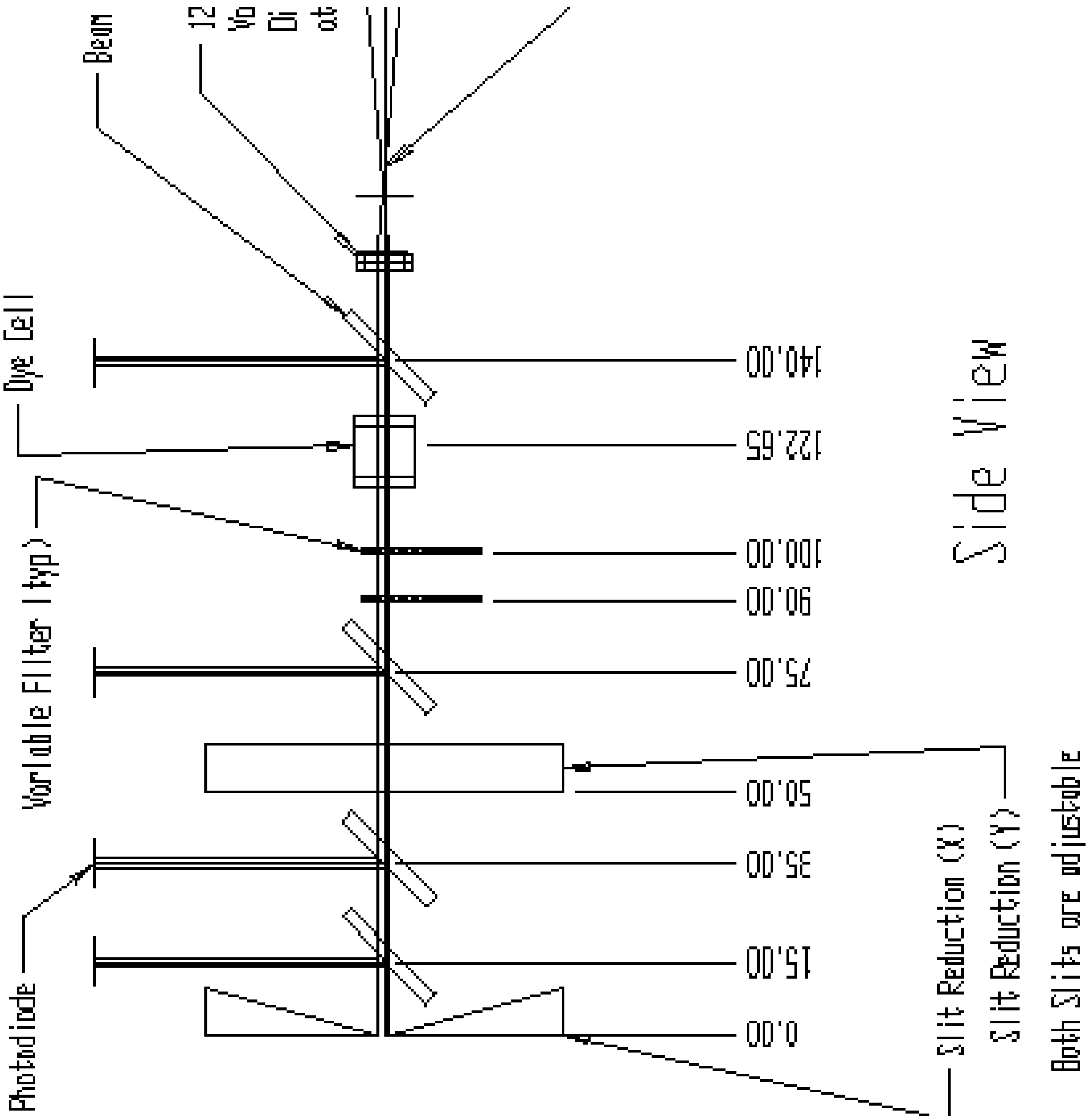

Fig. 10. 13: Laser light injection system and related optics.

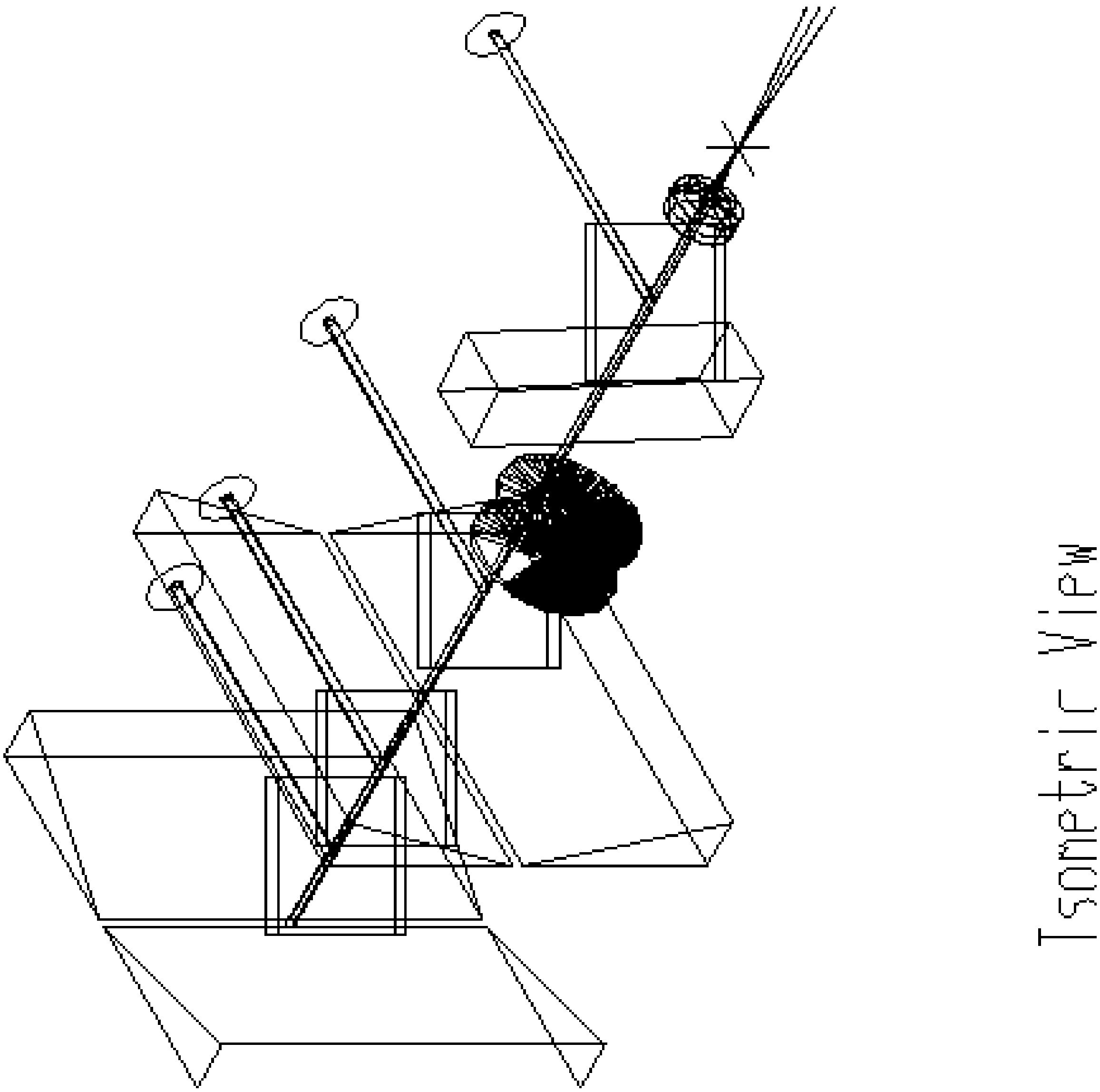

Fig. 10. 14: Isometric view of laser light injection system.

The system would have the nitrogen laser triggered by a programmable module. The laser light pulse is split, part of the light is fed to a PIN diode to control the pulse amplitude (about 10^6 photons to avoid the use of an amplifier). The other part of the light is fed to a filter wheel to change the light intensity in steps to cover four orders of magnitude (about eight steps) to control the dynamical range of photodetectors and ADC. The position of the wheel is controlled by a programmable module. The programmable module allows the introduction of a fixed delay between the laser trigger and the ADC gate (with few ns step) to measure pulse position within the gate for each channel.10.4.2.1

Quality control

For the HB, HE and HO we will build a LED system (blue LEDs) into the decoder box to be used in stand-alone mode. We also have an independent LED system for the HF. This HF LED system is foreseen to be used for tuning the readout chain (PMTs, FERMI Boards, cables, connectors) and for setting/monitoring the PMT gains. We propose to use blue LEDs. In this system, we will have a VME controller for the LED drivers. The LEDs will be connected to bundles of short fibres with 100 micron diameter and each fibre is connected to a particular PMT. A LED driver has four channels (one channel per LED). There are 20-30 fibres in a bundle and 5-10 LED drivers will be sufficient for one half of each HF calorimeter. The LED driver scheme is shown in Fig. 10. 15. Fig. 10. 16 shows the complete LED test system.

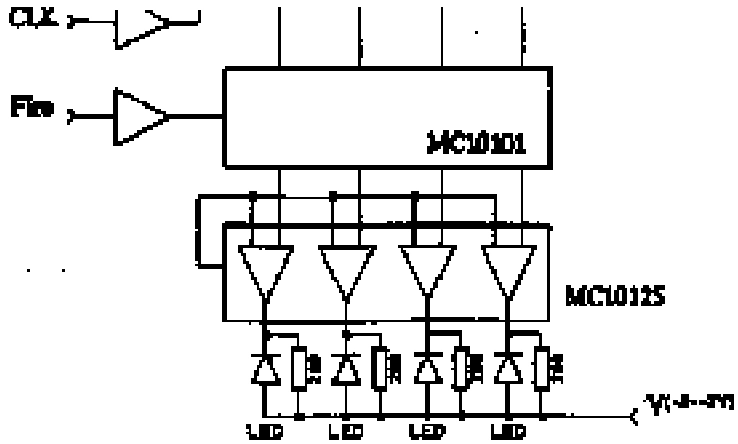

Fig. 10. 15: LED driver scheme.

Stability of quartz fibres is an important issue for small angle tiles. A measurement of the radiation hardness of the quartz fibres shown that there are available fibres which can satisfy the required measurement precision without degradation up to 50 kGy (5 Mrad).

A second reference monitor, for redundancy, consists of a CDF-style temperature-stabilised PMT which simultaneously views one of the fibres and an 241Am-loaded NaI scintillator. The stability of the PMT response is monitored using the 5.4 MeV 241Am alpha particle peak. The temperature dependence of the NaI response, ~0.2%/K, requires controlling the temperature of the PMT and the NaI to better than about 3 K. Use of this reference phototube is contingent upon being able to locate it in a sufficiently magnetic-field-free region, with suitable magnetic shielding.

A third reference monitor is an HPD which views a light-injection fibre as well as a temperature-stabilised scintillator tile which can quickly be exposed to a small dedicated ^{137}Cs source. This monitor would be installed outside the calorimeter and probably close to the laser/LED light source. A somewhat similar system, but with a manually-moved ^{137}Cs wand source, was used at the H2 testbeam in the summer of 1996.

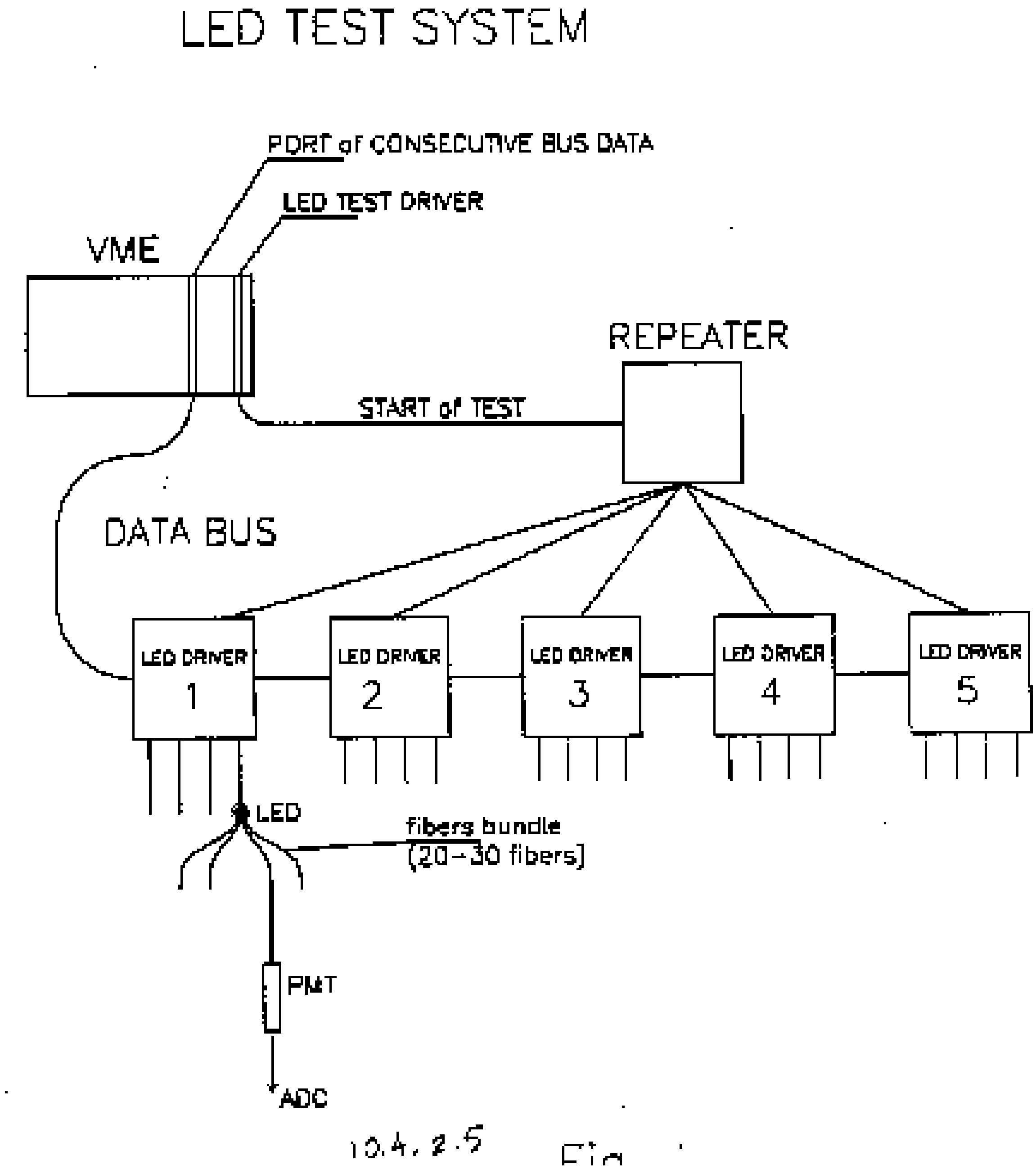

Fig. 10. 16: LED system.

10.4.3 Layout for HB, HE, HO and HF

The single laser light system uses quartz fibres, where the diameter starts with 1 mm and after all the splits ends up with 200 micron quartz fibres. First, the laser pulse passes through a filter wheel where the intensity can be varied by four orders of magnitude. Next the light is sent to a commutator that can send the light to any one of 12 outgoing fibres. These are as follows: four to HB, four to HE and four to HF. The HB fibres are routed as follows: 2 to each side, one of each side for the decoder boxes and the other to the scintillator layers. The light splitting is as follows. The decoder box fibre is split 18 ways, one for each decoder box. Inside each decoder box, it is split again so each pixel of every photo detector gets a 200 micron fibre. At this split the blue LED is also attached to the splitter so a light signal from the LED can use the same fibres to illuminate the photo detector pixels. The other fibre for the scintillator is also split 18 ways, one for each wedge. For each wedge, each fibre is again split 8 ways, where four fibres each are connected to the two tile layers that have the laser system. Each tile layer receives 2 fibres for the central megatile and one each to the edge megatiles. At the tile trays, the light is fanned out from the input fibre through a small mixer to the 16 tiles by 200 micron quartz fibres.

The HE fibre divisions are very similar to HB, except that there are 12 wedges instead of 18[10]. The HF is also similar where one fibre on each side is split 4 times, one for each quadrant and split again 32 times, one for each photo detector. The other fibre on each side is used to determine radiation damage by routing the light through a fibre near maximum irradiation as explained in more detail below.

The HOB and HOE only have blue LED in each decoder box, where plastic fibres send this light to each photo detector. Since HO will see very little radiation damage, plastic fibres are sufficient.

For the HF, we are also considering a design with a separate laser and LED calibration and monitoring system to provide an alternative system which could be more suitable for the needs of HF, and would simplify the logistics of monitoring HF quartz fibre radiation damage while the other laser does the routine monitoring of HB and HE. The laser system for the HF is very similar to the one used in the central calibration system, namely a pulsed nitrogen laser with trigger system, selectable colours, wide dynamic range intensity filter wheel with reference PIN diode for intensity monitoring and timing. Another reason why we might need an independent laser system for the HF is to monitor the radiation damage to the quartz fibres. In this radiation damage monitor, a number of fibres from the distribution system will traverse the entire length of each tower and return back to the photodetector. In this system the laser and attenuator are connected through a 300 micron diameter quartz fibre which is about 10 m long. The function of the attenuator is to change the intensity of the light output over a wide range (100) by changing the distance between input and output fibres. The diameter of the output fibre is 1 mm and it is about 15 m long. Both fibres going into the attenuator are matted. The output fibre is then put into a distribution system which is 0.5 m long fibre of 2 mm diameter. This distribution system has 20-25 fibres of 130 micron diameter. These 130 micron fibres are then distributed to the calorimeter tower bundles and light guides

10.4.4 HF normalisation

In HF, the absolute and relative tower-to-tower calibration will have to come from the collider data as di-jet Et balancing and photon-jet Et balancing. Monte-Carlo studies of Z+jet events as a function of missing Et indicate that the necessary calibration precision is 5%. The HF can be calibrated using the entire sample of di-jet events. By requiring one jet detected in the HF and the other in another part of the calorimeter system (HB/HE), the intercalibration between these systems can be verified by Et balancing. Similarly, gamma-jet events can be used for calibration using Et balance but in this case a single photon real energy measurement is necessary from the ECAL. There are other possibilities and these are also under study. For example there are low cross section processes that possess jets of well understood energy, a high Pt Z recoiling off of a single jet. The high energy and luminosity of the LHC may supply enough of these events for quantities useful for calibration. Another interesting process is $t\bar{t}$ production. Here both top quarks decay into W+b. If one requires one W to decay leptonically, this provides our trigger. The other W decays into quarks that form jets. These two jets, which will reconstruct to the W mass, provides our means of calibration. To eliminate the combinatorial confusion, we require that both b s are tagged by the tracker.

10.4.5 HF radiation damage monitoring

Radiation damage affects light transmission in quartz fibres mostly below 425 nm and above 460 nm. The possibility of tuning the laser to various frequencies provides a handle to monitor radiation damage to fibres. For this purpose, we will have fibres that traverse and then return the entire length of the calorimeter modules for each tower. In order to monitor the photodetectors, light from the source will be split and cascaded to the PMTs with quartz fibres. With similar systems, long term stability of 1.4% was achieved in large experiments over a few years.

10.4.6 Other HF normalisation

We recently started investigating the possibility of using a moving gamma or beta source system similar to the gamma source system that will be used in the HB and HE systems. If sufficient light is generated in the quartz fibres, this could provide a useful cross-calibration of HF towers, as well as providing a standard illumination to check the light injection monitoring of photodetectors and of individual tiles. A 0.9 mCi ^{90}Sr beta source inside a standard 18 gauge source tube next to the same four quartz fibres gave a DC current of roughly 15 pA. Stronger ^{90}Sr wire sources will be difficult to obtain, and the radiation is probably too local. ^{60}Co gamma radiation, much of which is above 1 MeV, will be investigated soon, and is expected to excite the quartz fibres efficiently via Compton electrons which are above the Cherenkov radiation threshold in quartz. This radiation will also penetrate the copper calorimeter matrix to illuminate a greater volume of quartz fibres.

As another method of normalisation, the long term response of each calorimeter channel can be monitored using energy flow. This can be achieved by measuring the photodetector dc-current as a function of luminosity. The dc-current will be integrated with a few microsecond integration time and this functionality will be designed into the front-end electronics, and is also necessary for source calibrations. As a function of eta, we expect to monitor relative calibration and to detect nonuniformities in the detector when normalised with the luminosity at CMS.

10.4.7 Data acquisition and processing

During light injection operations, a large number of channels are illuminated. Readout requirements range from the full system of about 16,000 channels to one of six possible partitions corresponding to the two halves of the HB, HE and HF detectors where 2,000 to 3,500 channels are involved. Because of the volume of data and the need to cover the full dynamic range during a calibration, the normal TriDAS system has been selected for data acquisition and processing. The exact division of control and data archiving functions between the on-line processor farm and the DCS general purpose computing services has yet to be determined.

Pulsing of the laser or the LED's is controlled by presetting a counter on the 40 MHz system clock. For the LEDs, this counter is in the channel control chips for the front ends; for the laser, the counter is incorporated into the laser controls. The front end digitizers operate in the normal mode at the normal clock rate and send a continuous data stream to the first-level trigger pipelines. A first-level trigger accept is generated with the proper timing and distributed to all channels through the normal Timing and Trigger Control mechanism. An automatic second-level trigger accept than causes the data to move through the derandomizing buffers into the second level filter which extracts the total signal from the time frame and places the result into the readout FIFO. The full block of data, 2,000 to 16,000 channels, is then moved into the farm for processing.

Readout of the HCAL is done through 16 Front End Drivers each capable of 200 Mbytes/sec. For the case of the whole detector, the maximum event rate is then 100 kHz. Data processing in the farm, initially to accumulate the histograms and then to extract the mean and sigma and prepare for the next point, will certainly reduce the event rate. Taking a one-to one correspondence between farm nodes and readout drivers gives a work load of 1000 channels per processor. Allowing for 10 operations per data word in a 200 MHz farm processor gives an event rate of 20 kHz. For the case of 8 ranges (chapter 9.3), 5 different points on each range, and 10,000 events per data point, the complete calibration could be done in 20 seconds.

Sixteen calibration constants are determined for each channel, a slope and an intercept for each of the eight ranges. This 512 Kbytes is to be archived through a bridge to the DCS database services. At the beginning of a run, downloading of the calibrations into the readout lookup tables can be accomplished either through the DCS path to the front end crates or through the bridge to the farm and the data acquisition system path.

Usage of the 3.17 microsecond gap in the machine fill is problematic at this time. The time needed to switch from physics data to calibration mode, take one light flasher event, histogram the results, and switch back to physics data mode is poorly known and estimates have a large uncertainty. Also, the stability of the calorimeter system is expected to be such that calibrations are only needed between fills of the collider, once or twice per day. On the other hand, it is possible that unexpected luminosity-dependent effects may require that calibrations be taken during a store. Thus, development of the relevant systems will be followed until a definitive answer can be established as to the viability of interleaved data and calibration operations.

10.4.8 HF calibration and monitoring

In the following, we describe the hardware calibration and monitoring system for the HF.10.4.8.1

Hardware tools of calibration and monitoring of HF

The calibration of individual towers directly affects the overall energy scale of the HF and the effective energy resolution at high energies due to the internal tower-to-tower calibration uncertainties. The requirement on the HF resolution implies that the calibration uncertainty for tower-to-tower response of 3% and on the overall energy scale uncertainty of 3% are acceptable.

The hardware system for the calibration and monitoring should address the following:

- light response of the quartz fibres in a high radiation environment and the efficiency of a light collection system

- the light signal amplification (PMT gain)

- the performance of the entire chain of front-end and read-out electronics

As the HF calorimeter systems will have to function in a severe radiation environment, one should take special care as to the reliability of the hardware monitoring system and should build in redundancy and flexibility into its components. The control and monitoring of the above ingredients will be realised by the following hardware and procedures :

- quality control of the technology at the mass production stage

- beam tests

- calibration *in-situ*, using physics event signatures

- light emitting diode (LED) monitoring system

- laser gain monitoring system charge injectors for noise, gain, non-linearity monitoring and for timing adjustments of the chain from PMTs to the front-end electronics.10.4.7.2

Quality control at fabrication

Control at various stages of mass production is necessary in order to ascertain adherence to the optical and mechanical specifications. Here, we foresee:

- an effective procedure for the identification of possible assembly faults in the calorimeter towers;

- incoming control of both optical and mechanical properties of quartz fibres - the homogeneity of the active media in individual towers have to be kept at the level of 1%;

- control of mechanical tolerances of the copper-quartz fibre matrix - here we keep the copper-to-quartz volume ratio at the level specified.

10.4.7.3 Beam tests

The test beam runs serve as the final step of the mass production and as the first estimate of light yield. The following points should be addressed:

- uniformity of the tower responses;

- response to electrons and corresponding light yield, Np.e./GeV per tower;

- intercalibration of tower-to-tower;

- response to hadrons;

- a first approximation to the calorimeter absolute energy scale.

We are investigating the use of moving Cobalt ^{60}Co photon sources to link test beam calibrations to the installed calorimeter in the collision hall.

10.4.7.4 Physical Calibrations

The next iteration of a calibration after the beam tests are the analysis of the LHC data samples taken *in-situ* using select event signatures. Such methods afford us calibration of the light yield of every tower and equalization of the relative responses of towers. These changes are expected come from:

- radiation damage - the most dominant factor;

- aging of quartz fibres;

- deterioration of various optical contacts;

- other similar effects.

The nice possibility for a calibration of long term changes is provided by the recent study of the energy spectra of the minimum bias events. The requirement of the similar slopes for the energy deposited in individual towers constrains the relative tower-to-tower calibration factors. The final calibration of the overall scale will exploit several physical processes and will rely on the redundancy of the CMS detector. Among the possible candidates are two-jet events with one jet to be detected in other CMS calorimeters and the second one in the HF with balanced transverse missing energy, and the QCD Compton process with the photon to be measured with ECAL and the balancing hadron jet flowing to the HF section.

10.4.7.5 Laser Gain Monitor

The HF calorimeter employs the global laser system of CMS HCAL. This system enables us to simulate the light pulses similar to the ones that are generated in the HF in time, spectrum and amplitude characteristics. It serves for:

- linearity test of PMTs, front-end and read-out electronics chain in a wide dynamical range,

- fast signals for timing measurements and adjustments on channel-to-channel basis,

- the short term monitoring and the measurement of the PMT gains.

The principal scheme has been successfully tested with an HF prototype of during the 1996 test runs. The analysis of the data collected has proved the feasibility to reach good light injection uniformity, better than 5%. The pulse to pulse variation of laser light is monitored by a series of PIN photodiodes.

10.4.7.6 LED System

The monitoring redundancy for the HF calorimeter is a necessity since it is located in an extremely harsh radiation environment. The LED system not only provides a low cost redundant system but also brings a set of advantages. This system is:

- technically simpler and more versatile than the laser system,

- relatively inexpensive,

- stable and provides good pulse-to-pulse amplitude stability,

- easy to construct fast triggers, and

- easy to monitor using stable photodiodes.

We plan to use the fast and bright blue LEDs. The system will be used for:

- a number of tests during the assembly and installation period as a stand-alone tool,

- determination of PMT gains using the method of photo-electron-statistics and to equalise the gains; and we expect to reach the uncertainty of less than 3%,

- monitoring short term gain drifts of every tower.

The PMT gains can be checked and the HV adjusted during the short breaks in the collider. In addition, the timing properties and the behavior of the whole readout chain from PMTs up to the front-end electronics can be tested at high rates, 40 MHz. The LEDs can fire during the regular data taking and can be timed with empty bunches. This makes monitoring of short term gain variations and almost on-line correction of the data possible.10.4.7.7

Laser monitoring of the quartz fibres

This system is a tool for monitoring of the long term radiation damage of quartz fibres. It exploits the same laser light pulser as laser calibration system. The light is injected to a control quartz fibres embedded in selected calorimeter towers. With the possibility to tune the laser wavelength, we will be able to measure the light attenuation as a function of wavelength in fibres due to the long term radiation damage.10.4.7.8

Moving radioactive sources

We will investigate the use if ^{60}Co gamma sources in two systems:

a) moving a collimated source across the front face of the calorimeter (*x*-*y* remotely controlled motion), and/or

b) wire sources moving in longitudinal channels within the calorimeter.

The former system could provide tower-to-tower relative normalization and carry testbeam calibrations to the collision hall. The motion of the radioactive source is accomplished by a remotely controlled *x*-*y* translator where the precision of motion is required to be within a millimeter in both horizontal and vertical directions. Two *x*-*y* motion devices are planned per HF side, each serving a half of the detector. The latter system could provide direct scans of the longitudinal distribution of radiation damage to the quartz fibres. Two remote controlled motors per HF side will service the selected source tubes that are embedded throughout the HF absorber. The necessary source strengths need to be determined. Very intense ^{60}Co sources carried inside the standard 0.7 mm diameter "wires" can be obtained, relatively inexpensively, from the North American Scientific Company, North Hollywood, CA. These investigations are important since we can transfer the calibration to each tower with the aid of a source as in the HB and HE systems. This will therefore eliminate the need of a test of each tower in the beam.10.4.7.9

Charge injectors

The Q-injection system will be used for the noise, gain and non-linearity studies of the QIE5 structures to be used as charge sensitive ADCs for the calorimeter signal digitization and readout. We expect also that the system will provide us with the possibilities to trace the time properties of the front-end electronics.

10.5 OTHER SYSTEMS

It is assumed that the magnetic field will be mapped. Nonetheless, three-axis Hall probes should be installed in a variety of locations in HB and HE, especially to keep track of any residual magnetic fields when the magnet current is turned off, as well as to measure the full field. The reason is to provide a redundant way (in addition to field-on radioactive source calibration) to track the brightening of scintillator, which is quasi-logarithmic in the magnetic field. Thus, a field-on calibration could be based on bench-top measurements of the brightening curve, known starting and ending values of the magnetic field, and magnet-off source calibrations.

This system of Hall probes might be categorised along with other slow- controls items such as temperature probes, and read out like other environmental variables. However, it is anticipated that the Hall probe data will be needed only occasionally, mainly to provide field "on versus off" information. Hence a more primitive readout system could also be acceptable.

No explicit design exists for the layout of the probes. It is assumed that they will be connected by cables to a multiplexing readout located somewhere outside the detector.

10.6 HADRON CALORIMETER TIMING

The whole calorimeter will be timed using a single laser system so that every signal from every tower will arrive at the same time for an event that occurs at the centre of the CMS detector. Timing corrections will be performed at two places. The first is in the decoder box where the clock phasing can change the timing in 64 steps of 0.5 nsec each.

This will be used to synchronise the timing within a calorimeter unit, such as a wedge in the barrel calorimeter. The second adjustment place is in the DAQ where different modules can be timed to each other. The plan is to keep the optical readout fibres and other cables to a minimum length and apply the corrections electronically.

10.6.1 Time variation within a calorimeter wedge

The first step of the synchronisation process is to compute the time difference between various towers in a single module. This is accomplished as follows:

a) Compute the time secondary particles will take to reach the layer of shower maximum for HB and HE , the first layer for HO and the front of HF. Here assume that the particles travel at the velocity of light (c).

b) Compute the time the light signal takes to reach from the active region to the photo detectors. For this part the velocity of the signals in the fibres is measured to be about 0.5 c.

The sum of step a and b will be stored within the computer so timing corrections can be applied in the decoder box to compensate for this difference.

The time variation inside a tower for HB and HE, from the various layers is of the order of 2 ns. This is due to the fact that particles travel at the velocity of light within the calorimeter, while the light signal travels inside the fibre at half that speed. The layers closest to the interaction point get the particles first, while their light signals takes the longest. This difference over the thickness of the calorimeter of one meter is about 1.5 ns. The time variation from tower to tower inside a single wedge is substantial. In HB the signal from = 0 arrive about 15 ns later than the signal at = 1.5. For HF the maximum time difference is smaller, of the order of 10 nsec. This difference in timing will be compensated in the decoder box as explained below. Similar timing correction will be applied for HO-B and HO-E. This time difference for HF is negligible, as the fibre cable length of each tower is about the same length.

10.6.2 Timing correction within a decoder box

Each decoder box gets one laser signal. Each tower is read by one photo detector pixel, where the output time of the signal can be varied inside the amplifier in 64 steps of 0.5 ns each for a total of 32 ns. This clock phasing is performed remotely by downloading the information via the field bus. This correction is applied so that the amplifier signals of each tower, if this was a real event, will come out at precisely the same time. This is where the photo detector timing variation will also be compensated. This means that the signal from the tower within a wedge that arrives the earliest will have the most delay by this clock phasing. The digital waveform decoder will read each tower so that each tower signal arrives at the appropriate delay as computed in chapter 10.6.1.

10.6.3 Overall timing

The same laser signal is sent to each decoder box. The laser fibre lengths will be cut to the required lengths, so that if the laser mimics a real event, every signal of each decoder box will arrive in synchronisation. This means the laser signal to all the HB and HE decoder boxes will arrive at the same time. The laser signal to all the HF decoder boxes will also arrive at a common time, but later to account for the difference in particle travel time. By adjusting DAQ clock phasing, the signals from every component will be synchronised. The blue LED will also be timed to be similar to the laser, so its signals will arrive at the decoder boxes at the same relative time as the laser.

10.6.4 Data acquisition and processing

During laser timing operations, a large number of channels are illuminated. Readout requirements range from the full system of about 16,000 channels to one of six possible partitions corresponding to the two halves of the HB, HE and HF detectors where 2,000 to 3,500 channels are involved. Because of the volume of data and the need to take numerous different timing settings, the normal TriDAS system has been selected for data acquisition and processing. The exact division of control and data archiving functions between the on-line processor farm and the DCS general purpose computing services has yet to be determined. The laser trigger and the first-level trigger accept are derived from a counter on the 40 MHz system clock. An automatic second-level trigger accept forces readout at the same rate.

The operation of timing the 16,000 calorimeter channels with respect to each other will be done during the detector commissioning phase, before collider operations begin. Thus, there is no premium on achieving a high event rate. Most of the work will be done using the partitions corresponding to the two halves each of the HB, HE and HF detectors. For each event, a time frame of 16 consecutive readings is readout from each channel giving event records of 64 to 112 Kbytes (512 Kbytes for the whole detector). In the farm, histograms are accumulated and processed, and the operation is repeated for a different laser delay setting. The data set of results versus laser delay is then processed to determine the relative timing of the readout channels to each other.

This timing calibration is crucially dependent on the Timing and Trigger Control system stability. Using a sampling of channels, the stability of the results will be monitored continuously. Initially, this will be done many times per day to establish the size of diurnal variations. Subsequent monitoring intervals will depend on the outcome. Finally, it is anticipated that monitoring will continue into the operations phase and be done routinely between fills of the collider as one of a set of standard calibrations performed at the end of each store. Using 25 time settings and accumulating 1000 events per setting at a 1 kHz event rate requires 25 seconds. An event rate of 1 kHz for a small sample of channels (of order 256) allows 99% of the time between events for processing in the farm as the readout is capable of 100 kHz.

10.7 CALIBRATION WITH COLLIDER

DATA

Proton-proton collider data taken in situ at the LHC will provide an additional calibration tool.

10.7.1 Calibration using taus

We may most simply use the pp collisions as a source of isolated hadrons whose energy may be measured in the magnetic field. This will enable the hadronic response of the calorimeter to be determined. One such source of isolated hadrons is taus from W and Z decays. Using a single hadron + missing E_T trigger, about 180 pions may be recorded for each HCAL tower in 10 fb^{-1} of data. Cuts on shower width and profile are required to select charged pions without accompanying π^0s, but the resulting precision of the calibration is estimated to be 2% in each tower.[11]

10.7.2 Jet energy scale

Because pp interactions provide the only available source of jets, the jet energy scale must be determined from collision data. This can be done using a family of jet-balancing techniques.10.7.2.1

Photon+jet balancing:

In this technique photons (or EM clusters from electromagnetically-fragmenting jets) are used to fix the jet energy scale relative to the EM scale (which can be determined from the Z resonance). Events with a single jet recoiling against the photon are selected, either by requiring that the photon and jet be almost back to back in azimuthal angle or by a veto on additional jets above some minimum E_T. The jet scale may then be determined as a function of the EM object E_T by minimising the projection of the missing E_T along the jet axis (the Missing E_T Projection Fraction or MPF). This is the primary jet calibration technique used by DØ, who have demonstrated 3% accuracy. It is also used as a cross-check by CDF. One disadvantage is that the maximum E_T photon which is attainable for any given luminosity is only about one third of the maximum jet E_T reached, since the photon cross section is much lower that that for jets. Consequently some extrapolation is always required at high E_T.10.7.2.2

Z+jet balancing

We have looked at the possibility of extending this technique to Z+jet events. This will provide a cleaner signal than photons (though restricted to lower E_T). CDF have found that, with 100 pb^{-1} of data, Z+jet balancing gives a 5% check on the jet scale for E_T<50 GeV. We found[12] that 700 k Z+jet events (only one jet above 40 GeV E_T) could be accumulated per month at a luminosity of 10^{33} cm^{-2} s^{-1} sufficient to calibrate up to many hundreds of GeV in jet E_T.10.7.2.3

Dijet balancing

This technique is used in DØ to transfer the calibration to very forward jets; a central jet (calibrated by one of the above techniques) is balanced against a forward jet whose calibration is to be determined. A similar procedure may be needed in CMS to calibrate the HF calorimeters.

Probably some combination of all the above techniques will be needed to determine the jet energy scale in CMS. All are demonstrated to work in a hadron collider environment, but all require Monte-Carlo to understand the possible biases (e.g. from jets below the minimum E_T cut or unclustered energy), since in all cases the entire mismeasurement is ascribed to the "probe jet".

10.7.3 Dijet resonances

For direct verification of multijet mass reconstruction, e.g. for W ∅ jj in high mass Higgs search and for H ∅ $\bar{b}b$, it will be useful to have direct calibrations of dijet resolution and response using resonances of known mass.10.7.3.1

W ∅ jj in top decays

A proof of principle for this possibility is already present in CDF and DØ data, where the dijet mass of untagged jets in top events shows a clear peak near m_W. We find[12] that 45,000 double-tagged top events would be recorded each month at a luminosity of 10^{33} cm^{-2} s^{-1}. A clear W-peak is visible when events consistent with top decay are selected, as was shown in chapter 1.5.1. The reconstructed $\langle m_W \rangle$ depends on the level of minimum bias pileup: it moves from 70 GeV∅60 GeV when <n>=30 pileup events are overlaid and a 1 GeV clustering threshold is added. This is not a problem with the calibration technique - it is exactly the kind of effect we wish to calibrate.10.7.3.2

Z ∅ $\bar{b}b$

This will provide a handle on the energy scale of $\bar{b}b$ jets (should it prove to be different from light quarks). This signal should be visible in CDF/DØ data at the Tevatron by Run II and the rate at the LHC will be very large.10.7.3.3

Z ∅ t+t-

Similarly, to determine the energy scale for tau-jets, the Z will provide a large signal at known mass.

References

[1] Bertoldi et al, NIM 386 (1997) 301.

[2] Virgil E. Barnes and Alvin T. Laasanen, "Proceedings of the First International Conference on Calorimetry in High Energy Physics", ed. D. F. Anderson, M. Derrick, H. E. Fisk, A. Para, and C. Sazama, World Scientific, (1991) 189.

[3] Virgil E. Barnes, Alvin T. Laasanen and James A. Ross, "Proceedings of the Second International Conference on Calorimetry in High Energy Physics", ed. Antonio Eriditato, World Scientific, (1992) 195.

[4] Qifeng Shen, "Proceedings of the Fifth International Conference on Calorimetry in High Energy Physics", ed. Howard A. Gordon and Doris Rueger, World Scientific, (1994) 302.

[5] Virgil E. Barnes, "Proceedings of the Fifth International Conference on Calorimetry in High Energy Physics", ed. Howard A. Gordon and Doris Rueger, World Scientific, (1994) 338.

[6] Solenoidal Detector Collaboration, "Technical Design Report", SDC Note SDC-92-201 (April, 1992).

[7] "The CDF II Detector Technical Design Report", Fermilab-Pub-96/390-E (November, 1996).

[8] Nural Akchurin, Virgil E. Barnes, James Freeman, Alvin T. Laasanen, Yasar Onel, Qifeng Shen and W. Wu, "CMS HCAL Calibration System -- Conceptual Design" CMS TN/96-040 (May 1996).

[9] Nural Akchurin and Yasar Onel,"The PMT readout and Calibration issues for the SSCintCAL detector" GEM TN 92-184.

[10] V.I.Kryshkin, L.K.Turchanovich, V.G.Vasil'chenko. Nucl. Instr. And Meth. A 381 (1996) 573.

[11] R. Kinnunen, CMS HCAL meeting 3/15/97 and CMS-TN in preparation.

[12] J. Freeman and W. Wu, Fermilab-TM-1984, 1996

TABLE OF CONTENTS

11. TRIGGER AND DATA ACQUISITION ELECTRONICS

11.1 INTRODUCTION

11.1.1 Overview

Digitised results arriving from the on-detector electronics on optical fibre links are converted to electrical signals and applied, channel by channel, to the readout system. The first step in the process is to linearise the data by means of a Look-Up Table (LUT) containing the inverse function of the QIE compression and the detector response. This linearised data provides the first-level trigger with time and energy information per trigger tower and is also stored in a pipeline for later readout according to the first-level trigger decision. Fig. 11.1 shows a simplified block diagram of the chain. The implementation is making full use of modern assembly techniques e.g. Multi-Chip-Modules (MCM) and Chip-on-Board technologies. Also, fault tolerance and error detection architectures are used throughout the system thus creating a highly reliable system. The HCAL readout electronics is based on the developments done within the RD16-FERMI project [1,2].

All electronics in the counting room are implemented as 9U VME modules making use of the rear transition card for interfacing purposes. A Detector Dependent Unit (DDU), being part of the Front End Driver (FED), supervises the read out of a VME crate or part thereof. A total of 14 memory modules (RDPMs) are envisaged for the HCAL at the entry of the Farm switch.

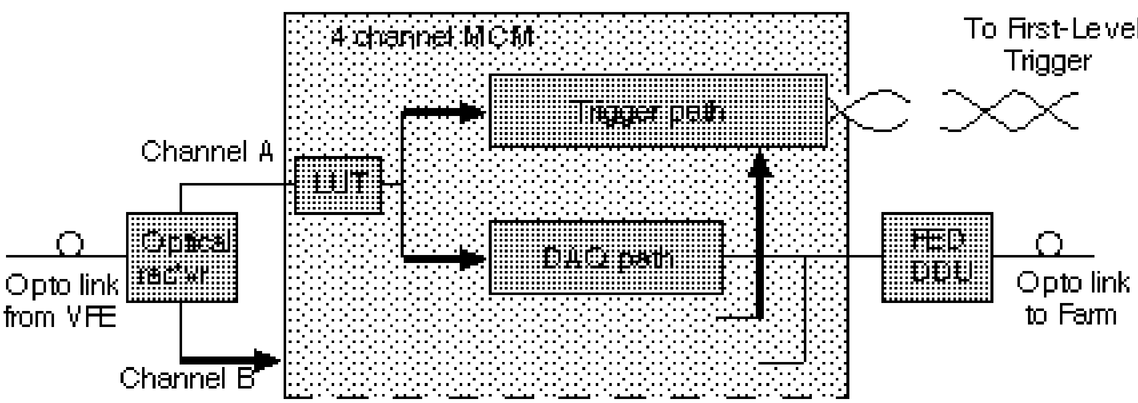

Fig. 11.1: Simplified block diagram of the HCAL readout system

11.1.2 First-level trigger system

The linearised data is taken, immediately after the LUT, through individual thresholding circuits and applied to an adder circuit where the information from HAC1 and the corresponding HAC2 are combined to form a trigger tower. This data is applied to a dual FIR filter circuit which extracts the energy and Bunch Crossing information and formats the data according to the trigger system requirements (trigger primitives). Also, a Trigger Feature Bit is generated as a function of the energy relation between HAC1 and HAC2 and included into the trigger primitives.

The information from two trigger towers is multiplexed onto one high-speed copper link and transferred to the first-level trigger system. In parallel, the individual primitives are stored in pipeline circuits of programmable length for subsequent readout together with the corresponding data from the individual channels. Fig. 11.2 shows the main functions of the trigger primitive extraction circuit.

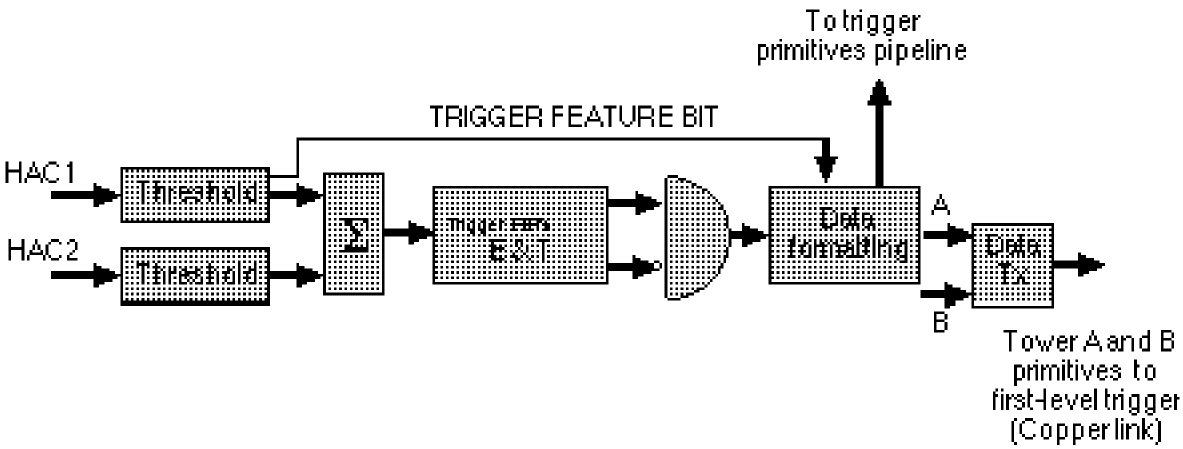

Fig. 11.2: Functional diagram of the trigger path.

11.1.3 Data acquisition system

The expanded and linearised channel data and the corresponding trigger primitives are stored in pipelines consisting of individual dual-port memories implemented as circular buffers with individually programmable length (4 to 256 positions). A temporal environment, a time frame of programmable length (max. 16), is associated with each event accepted by the first-level trigger. These time frames are, upon a positive first-level decisions, transferred into a set of derandomisers for later processing and readout.

The Readout controller supervises the extraction of data, from the derandomisers, either in the form of complete time frames or as digitally filtered values of the energy. In the latter case the information contained in a time frame is extracted using an adaptive non-linear digital filtering techniques optimised for extracting a precise value of the energy even in the presence of noise and jitter. It is envisaged that the filtered readout should be default when pushing data to the virtual second-level trigger process. This process could, however, return for selective readout of full time frames, which might be necessary in order to resolve specific conditions. Currently, it is envisaged to transmit full time frames to the third-level trigger and subsequent off-line analysis.

It should be noted that, as the linearisation constants are known, the off-line analysis can, at any moment, retrieve the raw data generated by the front end digitiser electronics.

Fig. 11.3 shows the functional diagram of the DAQ path.

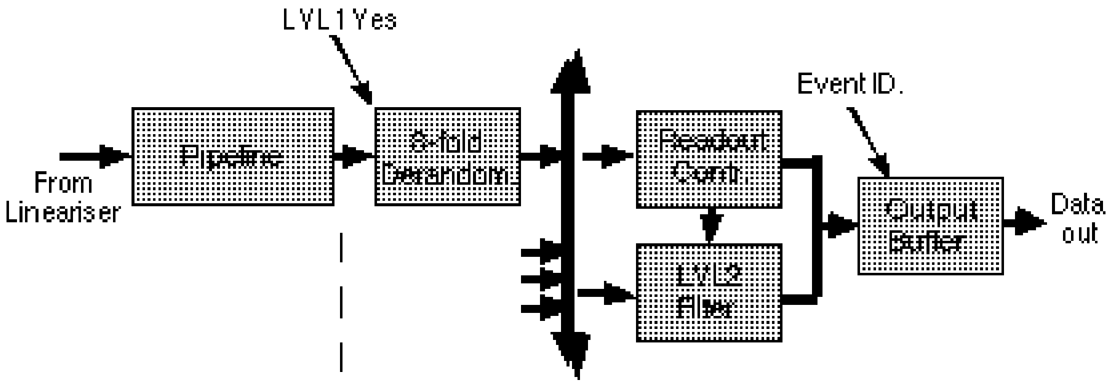

Fig. 11.3: Functional diagram of the DAQ path.

11.2 ARCHITECTURE AND FUNCTIONALITY

11.2.1 System layout

The HCAL readout system is divided into two main parts, the on-detector electronics and the off-detector electronics. The first part consists of the Hybrid Photo Detector, the QIE compressing function with eight ranges, 5 bit ADC and a Control ASIC per channel and the latter consists of the feature extraction and storage elements which will be discussed in detail below (see Fig. 11.4).

Each on-detector channel produces 8 (5+3) bits of information at every Bunch Crossing clock and this allows three channels to be multiplexed onto one high-speed optical link. These links arrive in the counting room where the data is demultiplexed and routed to the digital part of the readout system.

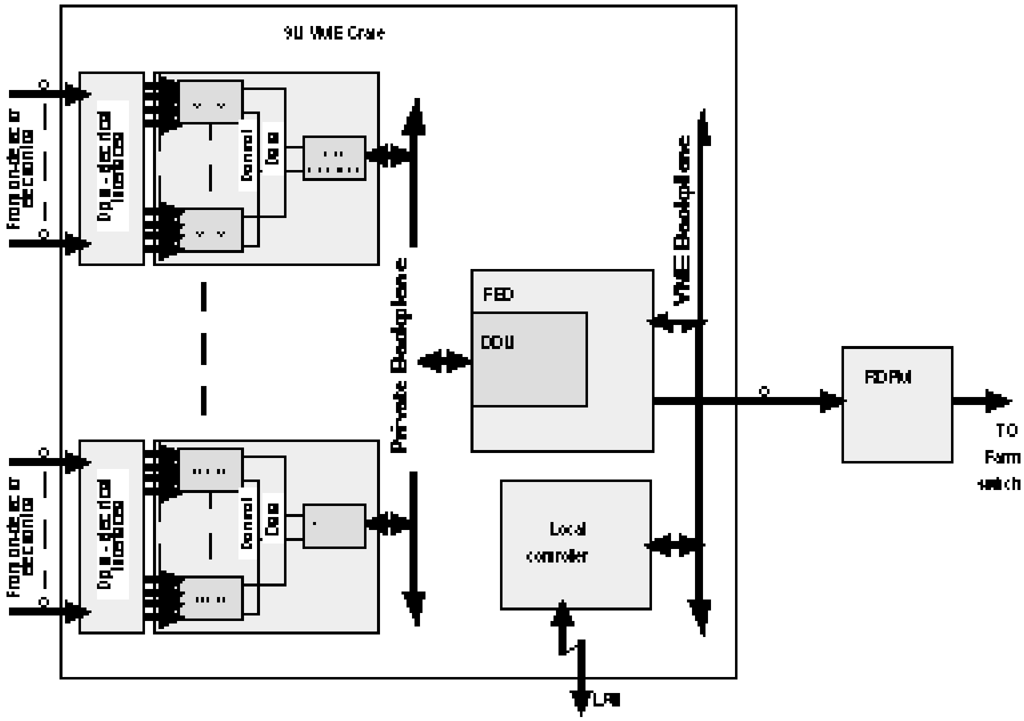

Fig. 11.4: Overview of the digital part of the readout system.

The Board Controller, see Fig. 11.4, organises the transfer of all information belonging to a particular event from the derandomisers of the individual channels in the MCMs to the DDU. In the DDU the information is formatted according to the requirements of the subsequent stages in the DAQ chain.

11.2.2 Data Links between detector and counting room

On the detector the compressing and digitising front ends are combined three-by-three and applied to the input serialiser of the optical link. This combined information is transported over a single fibre at a rate of 1.2 Gbit/s. At the other end, in the Counting Room, the link receiver will demultiplex the data, retrieve the clock, synchronise the data to the local phase of the 40 MHz acquisition clock and perform a Data Integrity Check, see Fig. 11.5. The Data Integrity Bit accompanies the sample(s) throughout the system and is used to, in the trigger path, to zero the data at the level of the threshold function (see below) and will be read out together with the associated data by the DAQ system for later use.

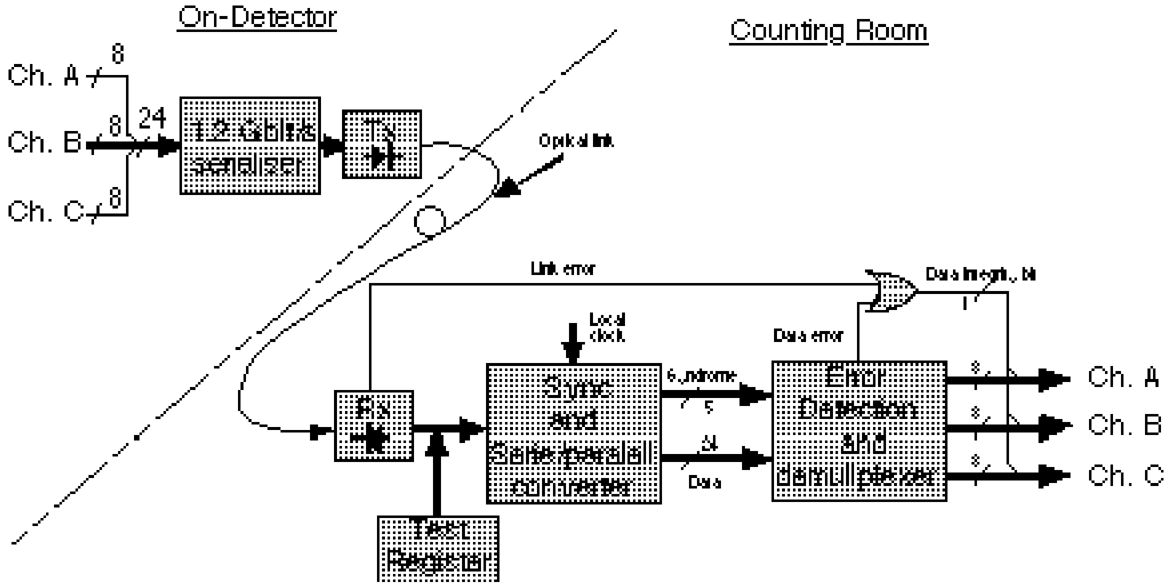

Fig. 11.5: Front end optical links.

11.2.3 Linearisation of the data

The data arriving from the Front End link receiver circuit is applied to a Look Up Table while the Data Integrity Bit is passed around with the appropriate delay. Despite that the data requires only 256 locations (8 bits) a 2 kWord x 17 bit LUT is being used. The LUT is serving two different purposes, linearise and restore the full dynamic range of the acquired data and, for test purposes, being a programmable source of 2048 consecutive samples allowing a full test of all feature extracting functions and readout procedures. Fig. 11.6 shows the functional diagram of the LUT.

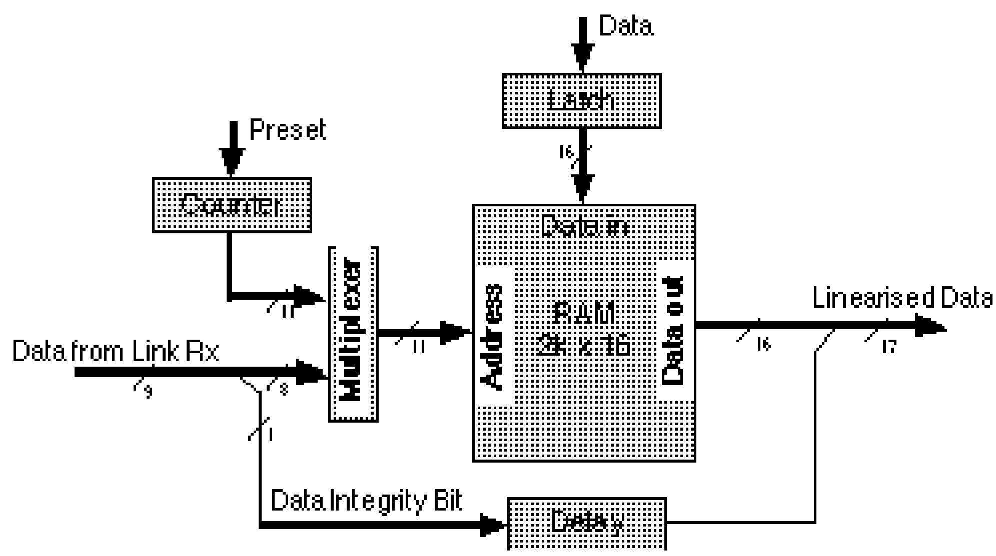

Fig. 11.6: The look-up table.

Once the behaviour of the detector and the QIE-ADC combination is known and the LUT has been loaded with the proper correction constants, the data used for subsequent processes are absolute i.e. no correction constants are required at any stage. However, as the LUT content is known the original data can be restored at any moment during both the on-line and off-line analysis.

In order to preserve synchronism the Data Integrity Bit is routed around the LUT and through a delay corresponding to the access time of the LUT.

11.2.4 First-level trigger data

Requirements

The HCAL first-level trigger information, as seen by the trigger [3], shall have a programmable quad-linear format with a width of 8 bits per tower. This solution was chosen to allow the tailoring of the energy response in order to be able to send information both on very low energy depositions like muons as well as having a reasonable resolution over the required range. This range is set to 500 MeV - 500 GeV.

A Feature Bit has been included to indicate high energy deposition in HAC1 in order to help resolve problems induced by the dead zone between ECAL and HCAL and improve pion-electron separation.

Two towers should be sent over one serial connection.

Data, that has been corrupted either by the link or any other function ahead of the trigger feature extraction, should be set to zero.

Special care must be taken to extract the correct energy and time taking into account the statistical fluctuations of the detector response. A schematic of the feature extraction is shown in Fig. 11.7.

Implementation

Linearised data from the outputs of the LUTs are applied to individual and programmable threshold functions. These functions suppress data below the programmed values as well as providing zero output data if either the loaded value is FFFFh (switch off the channel) or if the Data Integrity Bit indicates that the information has been corrupted at a preceding stage.

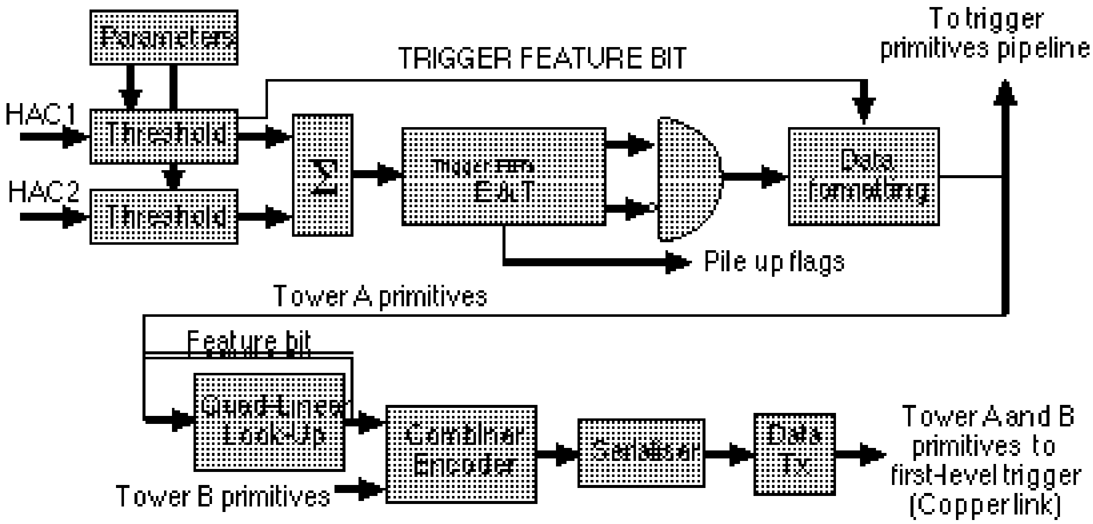

Fig. 11.7: First-level trigger feature extraction.

Within the threshold circuit a Feature Bit is generated as a function of the relation between the energy depositions in HAC1 and HAC2. The simplest implementation is to set the bit when the HAC1 energy is above a specified value.

The thresholded data from HAC1 and the corresponding HAC2 compartments are added to form a Trigger Tower sum. This addition is performed with full 16-bit precision in order to avoid truncation errors. Also, the adder function is protected by a 3-code residue coding to assure the quality of the operation.

The tower sum is applied to two 6-tap finite impulse response (FIR) filters, one optimised for the energy extraction and one for the time identification. These filter functions are using data with full 16-bit resolution and 7-bit signed coefficients. Both the coefficients and the length of the filters are programmable. The Time Flag conditions the energy information giving an output value of zero except at the bunch crossing that corresponds to the origin of the information. Both filters are protected by 3-code residue coding to assure the quality of the results. Also, flag bits, called pile up flags, are generated by the timing filter to tag events where the distance in time is below a programmed minimum value. Two such flags are generated, one for severe pile up and one for light pile up. The definition of light and severe is done by programming the number of bunch crossings required for each case.

Thereafter, a sliding window with a width of 10 bits is applied in order to truncate the data to the required range of 500 MeV to 500 GeV and the above mentioned Feature Bit is included at the output. The place of the window is programmable.

A 1k x 8 bit programmable Look Up table is used to convert the 10-bit linear representation to the required Quad-Linear format which is combined with the corresponding information from another identical trigger tower processing circuit. To this combined information an Error Detection Code (EDC) is added in order to preserve the quality of the information sent to the trigger.

The data with its EDC envelop is serialised and transmitted over a high-quality copper link to the Local Trigger Crate which is placed close to the HCAL electronics.

To cope with the large differences created by the response fluctuations in the detector, two methods have been developed. One is to program the time filter to be edge sensitive, and the other makes use of the total energy sum seen in the timing filter. As both filters are individually programmable in length, the correct energy will coincide with the time tag produced by either method. It has been decided to ignore the true baseline behaviour which, on average, is exponential and simply use the mean of the two presamples as the baseline for the pulse. This means that the two FIR filters use five samples, two for the baseline and three for the pulse information giving another tap free for future implementations.

11.2.5 Second-level trigger data and event data

Requirements

Events accepted by the first-level trigger shall, for the second-level trigger process, generate a single word per channel. The current solution with a non-linear filter consisting of 3 FIR banks and an Order Statistics operator, called Filter 2, fulfills the requirement as the filter algorithm can be controlled by external conditions such as pile up, luminosity and signal amplitude.

Events passing the virtual Second-level trigger shall, per channel, provide the Third-level and subsequent processes with Event Data consisting of a time frame containing the five samples corresponding to the pulse. (See also [4].)

Implementation

The data path (see Fig. 11.3) is common for the second-level- and the event-information as the second-level trigger is a virtual process within the DAQ farm.

The linearised data from the LUT is sent into a pipeline of individually programmable length (4 to 256 locations) where the data is stored during the first-level latency. Each positive decision by the first-level process initiates a transfer of a time frame of programmable length (max. 16) to one of eight derandomising buffers. If a second Level-1-Yes arrives during the transfer of a time frame a second derandomiser is opened and the overlapping data is written to the two destinations thus creating individual time frames even in cases of severe pile up. A Read Out Controller (ROC) within the MCM supervises the extraction of the data and the processing by the Filter 2. For each channel the ROC extracts both the individual time frame values and the result of the Filter 2 operation where the Filter 2 value will be used by the virtual second-level trigger and the time frame by the subsequent processes. Formatting of the event block is done in the DDU (see 11.3.6). This formatting creates one block for the second-level trigger, containing only the filter values, and one block for the third-level and data storage containing the time frames.

The pipeline is based on a dual-port RAM and implemented as a rotating buffer of programmable length. It contains the data samples and corresponding information i.e. Data Integrity Bit and Pile Up flags. As the Pile Up flags are created with a certain latency compared to the samples they will be stored at a location corresponding to the last position of the time frame in the pipeline.

In case of a positive first-level decision the corresponding time frame is transferred to one of the eight Derandomising Buffers together with the bunch crossing number (BCID) from the TTC system and eventual additional status information . At this level a time frame always has the length of 15 samples and the write sequence will be (in Buffer addresses) 1,2,3,4,5,6,.....,15,0 ; which will force the flag, status and BCID information to be stored in the first location of the buffer. At read out the ROC will see, as the first word, the flag information and set the proper working conditions for the Filter 2. In case of overlapping time frames, i.e. Pile Up conditions, a particular sample might be stored in more than one Derandomising Buffer thereby creating, in each buffer, a complete time frame.

The ROC will, for each first-level Yes, extract the information from the Derandomising Buffer corresponding to the event and read a number of samples corresponding to the programmed time frame length. The first word, containing the BCID, flags and Status, is used by the ROC to set up the working conditions for the Filter 2 and as an event data synchronise check. Subsequent words in the time frame are applied both to the filter and to the Output Buffer creating a data block consisting of the individual time frame samples followed by the result of the Filter 2 operation.

Filter 2 consists of three FIR filters combined through a Order Statistics operator (OS). As the samples and the coefficients are applied in sequence a single FIR tap, used in a pipelined mode, is implemented per filter function. The coefficient memory contains eight banks of 16 coefficients, each being a 10-bit signed value. This gives a total of 24 filter combinations and the ROC, with help of the OS operator can, according to flag and status information as well as externally loaded conditions, chose the proper filter for each event. This can be seen as similar to "IF' or "LOOP" statements in an algorithm for optimum pattern recognition.

In the output buffer, event data from the individual channels, together with the Event ID from the TTC system, as well as the corresponding data from the Trigger Primitives pipeline, are merged into a MCM event block. A Board Controller, on the VME module, supervises the transfer of all MCM-blocks to the DDU/FED module, see Fig. 11. 8, where the data is reformatted into one block containing the filtered values tagged with their address and one block with the time frames tagged in the same way. Zero skipping is also performed at this level thus minimising the data volume sent to the DAQ system.

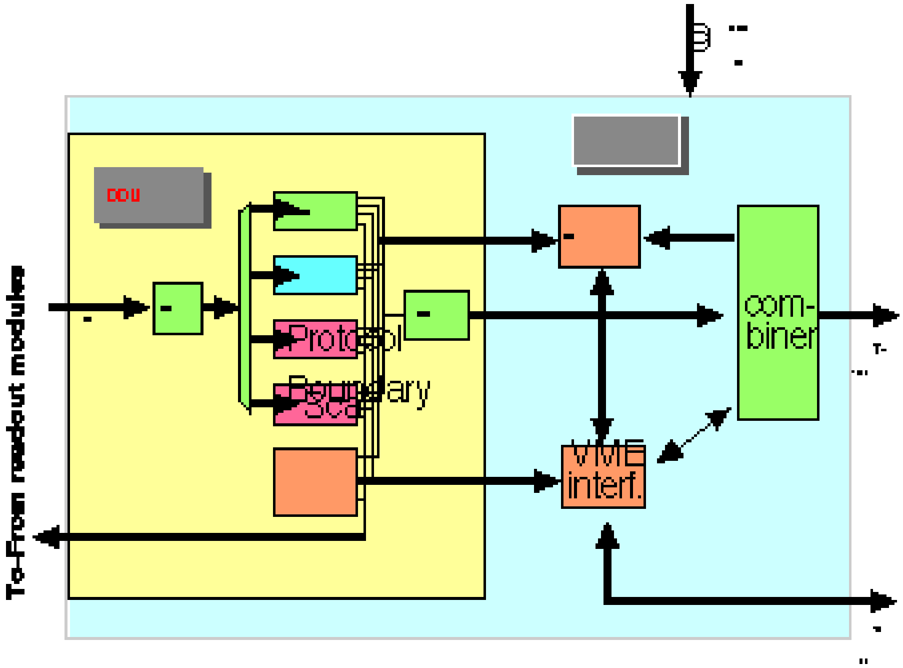

Fig. 11.8: The DDU/FED module.

The detector dependent unit (DDU), which is part of a standardised front end driver (FED) module, controls a set of Readout Modules and performs all required operations on the data, executes hardware functional tests, downloads the required status and coefficient information. It also acts as the interface to the first unit in the central DAQ system, the readout dual port memory (RDPM).

11.2.6 Calibration data

Calibration data is generated either by the laser, the LEDs or the radioactive source. In all three cases, the LUT is programmed for unity transformation. For the pulsed calibration, the front-ends are operated in the normal 40 MHz mode and a properly synchronised first-level trigger accept is sent to the derandomising buffers and the ROC. Here, the filter 2 transformation required is to extract the total signal deposited by a laser or LED pulse.

The source calibration requires readout of many contiguous time frames of sixteen samples each, stored in consecutive derandomiser buffers. First-level trigger accepts occur at a rate determined by processes operating in higher levels of the system. The subsequent Filter 2 operation generates the sum of these time frames (without thresholds) which is then transferred to the RDPM for histogramming in a farm processor.

11.2.7 Control

The control of the entire read out system is supervised by a Local Controller in the VME crate. This will be a commercial CPU which is driving the VME backplane in the crate and also is connected to the LAN

Control link system. It will delegate standard operations to the DDU and the Board Controllers, like downloading LUTs, filter coefficients, etc. The Local Controller is responsible for the continuous control of the system behaviour through a "Spy" connection to the Readout Modules. It monitors the data and creates statistics on number of signals per
channel and their energies. Also, it will be the point where all error information from the downstream system arrive. Actual actions on errors will be specified together with the DAQ group.

The DDU has provisions to execute repeated and standard actions like setting pipeline lengths and loading coefficients and configuration parameters into the Readout Modules. To minimise transfer time the Board Controllers handle, in parallel, the loading of identical parameters to all MCMs.

11.2.8 Testing and diagnostics

All ASICs have the IEEE 1149-1 Boundary Scan circuits implemented with a MCM-wide structure. The Board Controller acts as the local scan controller with a TAP controller on each MCM. Through this function the DDU can request contiguity tests and some functional tests of the system.

A very powerful test is to load the LUTs with simulated data which is sent out at the 40 MHz clock rate into the DAQ and Trigger paths. As the data is known the results can be compared, in real time, with the expected values and a complete diagnosis of all functions can be done under control of the DDU.

Each functional block, links, LUTs, etc. controls its own process and provides one or more error bits of two different classes, Fatal and Non-Fatal errors. Non-Fatal errors, like data being corrected by an Error Correction Code, are histogrammed and an alarm will be given only if the error rate exceeds a predefined level. Fatal errors, like loss of sync in a link, might require the intervention of a higher-level process.

Finally, there are a number of strategically placed "SPY' registers that can be read over the control path at any time to assure proper functioning of a specific block.

11.3 COMPONENTS

11.3.1 Lineariser ASIC

Description

The Lineariser ASIC is built around a 2k x 24 bit RAM whereof 18 bits are available for the data, 5 bits for ECC syndrome bits and 1 bit is the address parity. A multiplexer at the input, together with a counter-latch, allows the downloading of the LUT content over the MCM control bus. A schematic of the lineariser ASIC appears in Fig. 11.9.

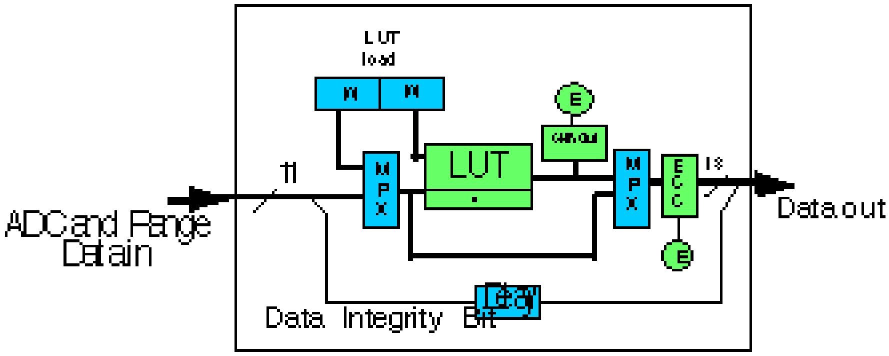

Fig. 11.9: The lineariser ASIC.

A hardwired address parity bit is, for each operation, compared with the calculated parity of the input data which acts as address for the RAM and creates a Fatal error in case of mismatch. The ECC decoder at the output of the ASIC corrects eventual transient faults and generates a Non-Fatal error.

The Data Integrity Bit from the detector to counting room link is passed through a delay to compensate for the memory delay.

Results

This function was an integrated part of the two first versions of the so-called Channel ASIC, and different versions have been produced using different technologies, AMS 1.2 µm, ES2 0.7µm and AMS 0.8 µm CMOS, starting with a large surface 3-channel ASIC. It contained all the functionality now split between the Lineariser, Adder and Pipeline ASICs.

The second version of the Channel ASIC was extensively used, together with a 10-bit ADC and the original RD16 dynamic range compressor, during the 1996 ECAL H4 beam test runs.

To cope with the difference in requirements between, e.g. ECAL and HCAL, the lineariser is now being implemented as a separate ASIC. Functionally, the HCAL lineariser is identical to the one in the prototype Channel ASIC.

11.3.2 Adder ASIC

Description

The Adder ASIC is a joint ECAL-HCAL development capable of generating trigger sums over 2 to 6 channels. For HCAL, two sums of two channels (HAC1 + HAC2) is generated on the "Partial Sum out" outputs. A block diagram of the adder ASIC is given in Fig. 11.10.

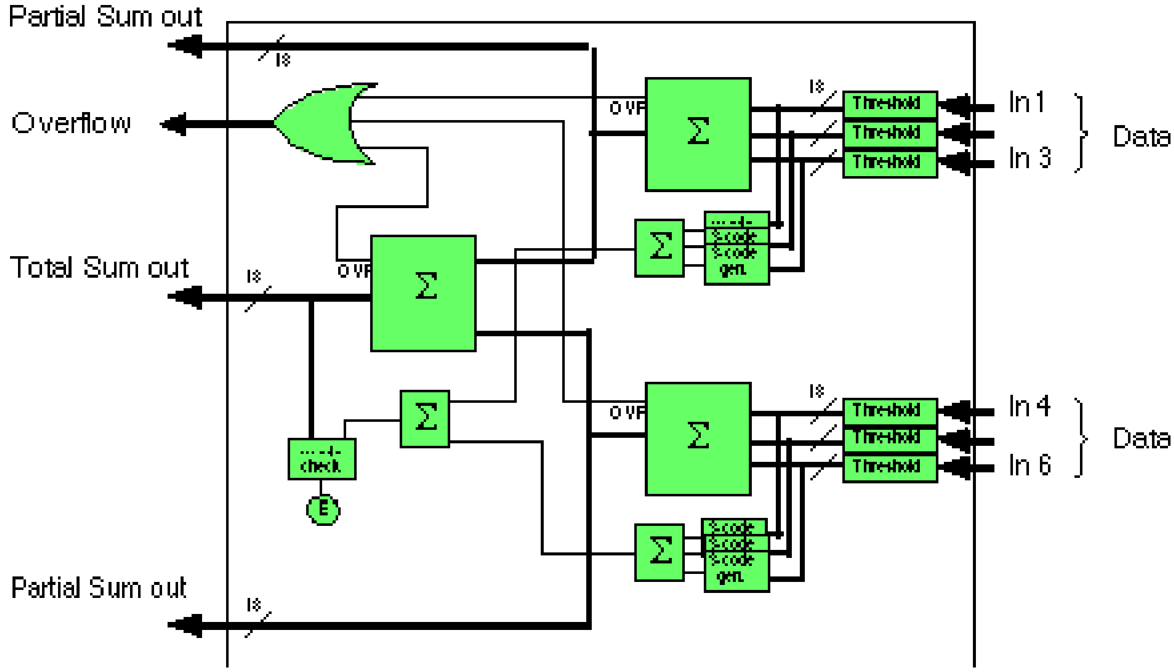

Fig. 11.10: Adder ASIC.

Each input has a individually programmable "Threshold" function which zeroes data below the loaded value and in case of a data error flagged by the Data Integrity Bit. Also, when the value FFFFFh is loaded the channel is switched off, i.e. the value is always zero. The adder is protected by a residue 3-code process which generates a Fatal error in case of mismatch between the reside sum and the encoded 3-code of the output value.

Results

The two first versions of the above mentioned Channel ASIC also contained the adder function but to improve flexibility and adaptability the function has been extracted and is now a separate ASIC. The above described version is implemented in AMS 0.8 µm CMOS, and, as can be seen in Fig. 11.11, the surface is not optimised as it was required to use classical wire bonding into PGA packages for the first prototypes. Final version will be adapted to flip-chip bonding thereby eliminating all unnecessary surface. The ASIC is fully tested in the packaged version.

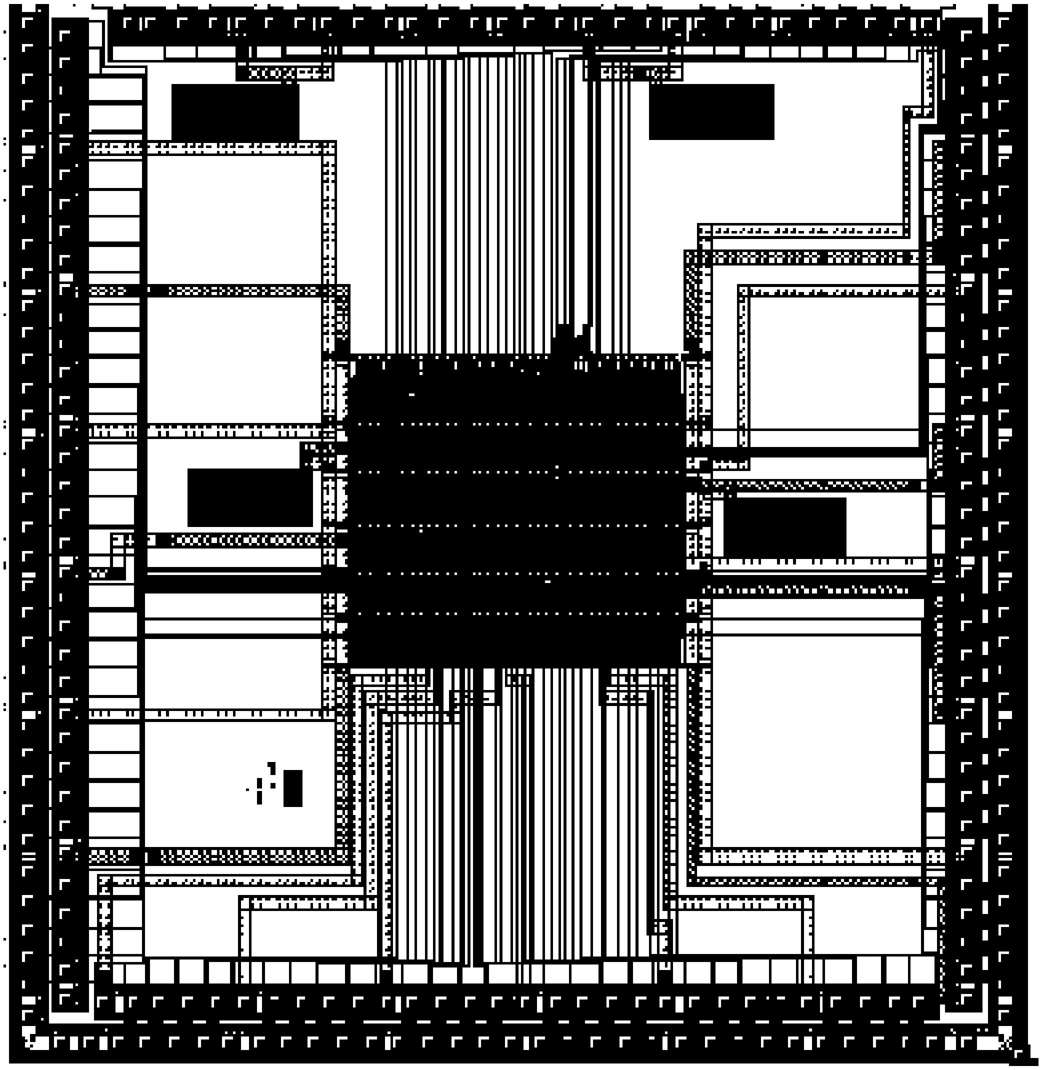

Fig. 11.11: Adder ASIC layout.

11.3.3 Pipeline ASIC

Description

The Pipeline ASIC consists of a programmable length Pipeline, built as a rotating buffer,

and a set of derandomising buffers. A schematic of the pipline ASIC appears in Fig. 11.12.

Data from the LUT is combined with the flags from the Filter 1, encoded in a ECC envelope and written into the buffer at each machine clock. The length, i.e. the delay, is programmable between 4 and 256 clocks. A bypass path is built in for test purposes.

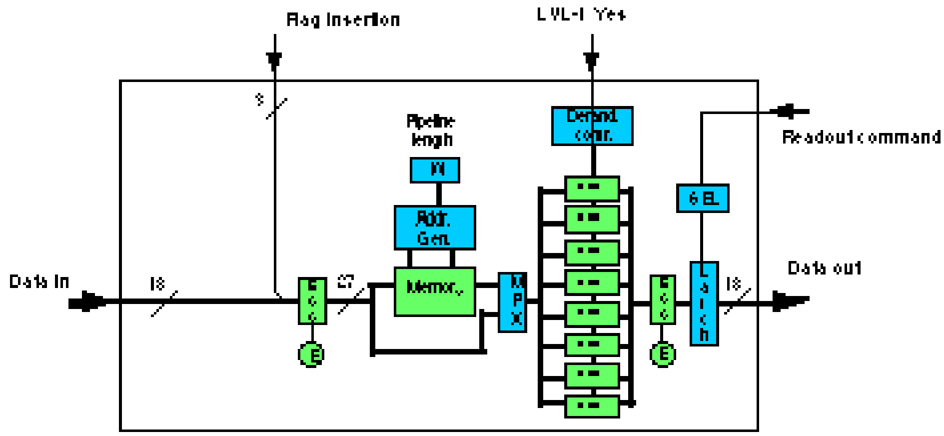

Fig. 11.12: The pipeline ASIC.

At each first-level Yes a time frame, 16 samples long, is written into the next free Derandomising Buffer. It a new Yes arrives within the 16 clocks a new buffer is opened and another time frame is written into it. This creates complete frames for each trigger even in cases of severe pile up.

At the output, the data passes a ECC decoder which will correct any transient bit error occurring within the storage elements. In case of a correction the ECC decoder will issue a Non-Fatal error.

Results

The current version of this ASIC contains the pipeline preceded by a lineariser function which will be disabled in the HCAL application.

A final prototype version, as described above but also including the HCAL lineariser circuit, has been implemented in the AMS 0.8 μm CMOS. The ASIC is currently under test and will be used in the first complete MCM (see chapter 11.4.1). A microphoto of the ASIC is shown in Fig. 11.13.

Fig. 11.13: Microphoto of the pipeline ASIC.

11.3.4 Filter 1 ASIC

Description

The Filter 1 ASIC, see Fig. 11.14, consists of two 6-tap FIR filters, one optimised for energy extraction and the other for time (BC) identification. Each tap in the two filters has loadable coefficients with a width of 7 signed bits. The Energy FIR is processing with full resolution in order not to bias the results while the Timing FIR truncates two LSBs. At the input of each filter is a 3-code generator followed by a 3-code filter and, at the output, a 3-code comparison between the results of the filter and its 3-code filter. In case of mismatch a Fatal error is generated. Also, the corresponding 3-code coefficient and a parity bit is added to each tap coefficient, the latter to assure that no transient errors have occurred in the storage.

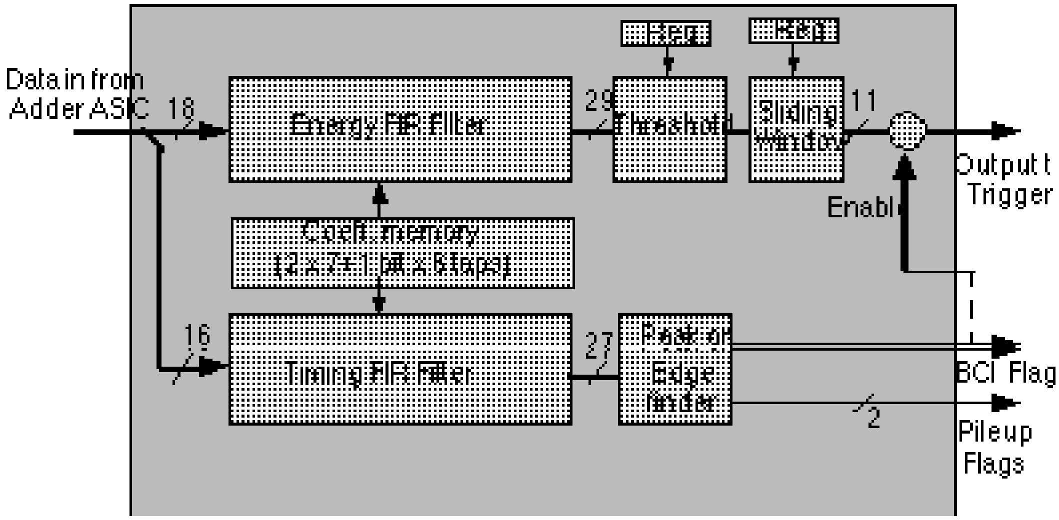

Fig. 11.14: Filter 1 ASIC.

Following the Energy filter is a programmable Threshold and a equally programmable Sliding Window which selects up to 11 bits of the energy. The timing FIR is followed by a Peak or Leading Edge finder that identifies the time origin of the signal, called BCI flag. Also, this circuit detects possible Pile up conditions by checking the number of clocks between two BCI flags and two values can be loaded to define Pile up and Severe Pile up. The corresponding flags are generated for insertion into the Pipe line. The BCI flag is also used to conditioning the energy output in order to produce zero energy except at the correct bunch crossing.

Results

A first version of the Filter 1 ASIC was implemented in the ES2 0.7 µm technology and used extensively in the ECAL H4 beam tests together with the above mentioned Channel ASIC. A second version has been submitted to foundry and is expected to be delivered in August 1997. Fig. 11.15 shows the lay out of the ASIC, while Fig. 11.16 shows some representative test data illustrating possible filter 1 functions.

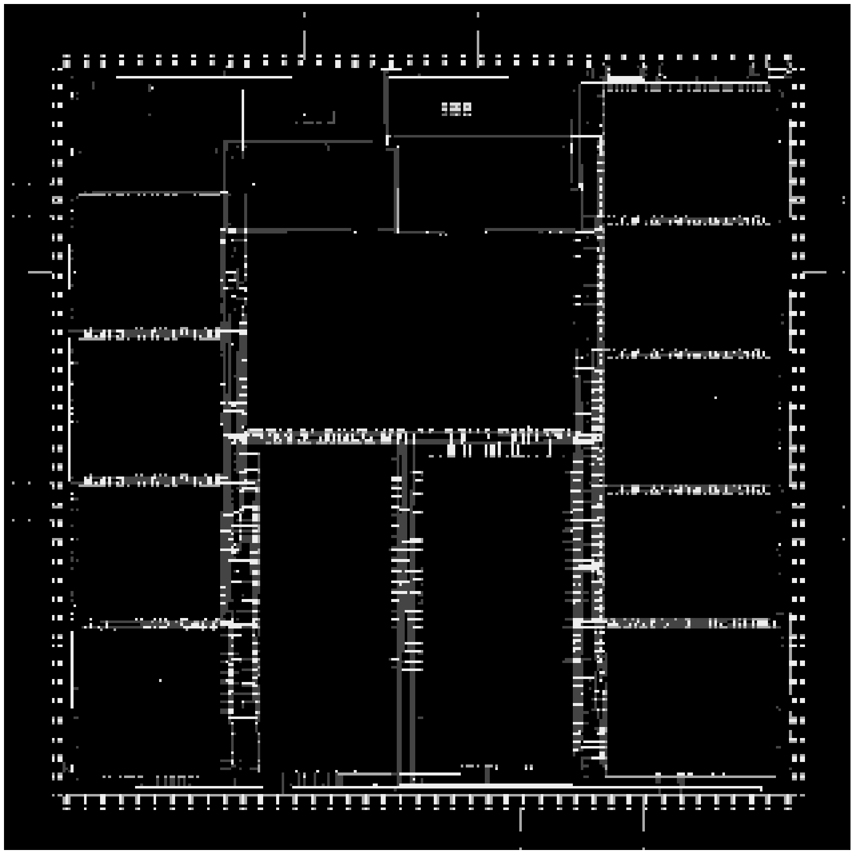

Fig. 11.15: Layout of the Filter 1 ASIC

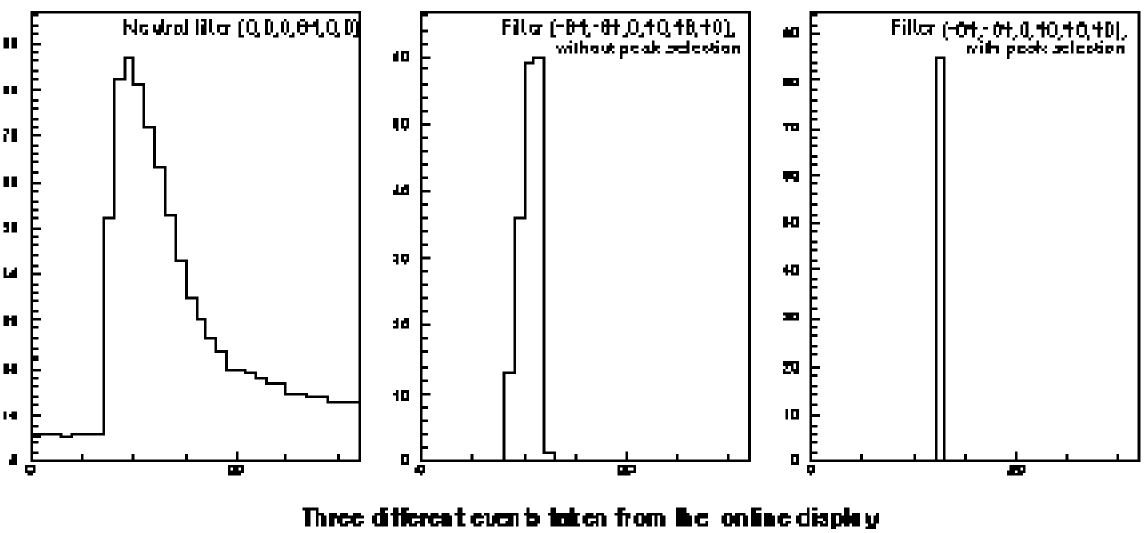

Fig. 11.16: The Filter 1 function

11.3.5 Filter 2 ASIC

Description

The Filter 2 ASIC, see Fig. 11.17, consists of three pipelined FIR taps and an Order Statistics operator supervised by the Read Out Controller. Each FIR filter has an associated coefficient memory consisting of eight banks of 16 locations which can be selected according to

event conditions (flags) or by external commands. From the insert it can be seen that the coefficient word contains a 10-bit signed FIR coefficient, the corresponding 3-code coefficient and a parity bit.

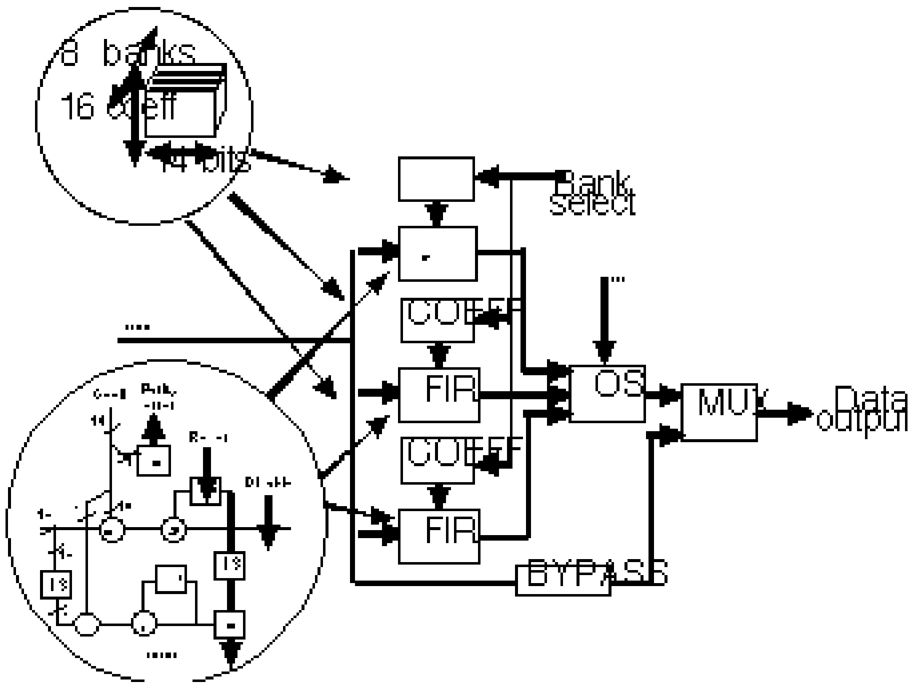

Fig. 11.17: The Filter 2 ASIC

Each FIR is, by its coefficients, optimised for a particular condition, like low signal-to-noise ratio, pile up conditions or, in the case of HCAL to the fluctuations in detector response. The OS operator selects the FIR giving the best result by sorting them according to max. min. or median criteria [2]. This creates a similarity with "loops" or "case" statements in a pattern recognition routine.

Two different error checks are done, parity check on the coefficients and a 3-code check of the filter function, both giving Fatal errors.

Results

The Filter 2 ASIC is being laid out and is expected to come back from foundry in November 1997.

11.3.6 Read out controller ASIC

The Read Out Controller (ROC) will be implemented using a programmable array of the XILINX or ALTERA families. The reason is that the functionality cannot be fully defined at this moment as it is closely related to the central DAQ in particular system design, transfer protocols and error handling.

The functions currently envisaged are, apart from moving data and controlling the Filter 2, to act as the interface between the board wide field bus and the internal control bus, to act as the TAP controller for the MCM wide Boundary scan tests, to gather and transfer to the Board Controller the error bits generated within the MCM and to house the MCM I/O buffers.

Once the final functionality is determined a mask programmed version will be ordered to improve the reliability of the ASIC.

11.3.7 Data links

There are three types of links within the readout system, the optical connections with the on-detector electronics, see 11.2.3, the copper links between the readout system and the first-level trigger system and the links to the Farm switch.

For the link from the on-detector electronics the environment in the detector forces the use of rad-tolerant implementations while at the counting room end a standard technology can be used. The bandwidth must allow to pass three channels, each with 8 bits of raw data, plus the EDC envelop indicating that a 1.2 Gbit link is required. Severe demands on inter-link synchronisation exist as all samples generated by a particular bunch crossing MUST be retrieved with the same clock edge in the Readout Modules and any loss of sync results in a Fatal error report.

The link to the Trigger will be a 1.2 Gbit serial link using a high-quality copper cable. All links will of the same length, currently estimated to 20 m, and commercially available serialisers and drivers will be used. Also, the sync requirement is severe for the same reason as above.

For the link to the Farm switch we assume that a common CMS solution will be developed.

11.3.8 Front end driver/detector dependent unit

The FED/DDU module, see Fig. 11.8, is a 9U VME module where the FED part is common to all sub-detectors and the DDU part is tailored to each sub-detector requirements. It contains the necessary interfaces to the VME backplane and to the RDPM which is a dual-port memory where the DDU stores the formatted event blocks for later access by the Farm switch.

For HCAL, and ECAL, the DDU contains the necessary processes to handle the Readout modules. These processes, as understood today, are Data formatting, Calibration and parameter generation and loading as well as in-situ functional tests of the system . The DDU is built around a commercial CPU-DSP chip set and is fully reconfigurable to adapt to the final requirements of the total system.

11.4 PROTOTYPE TEST RESULTS

A set of VME modules were constructed using an analogue dynamic range compressor, a 10-bit ADC, the 3-fold Channel ASIC (see chapter 11.3.1) and the first Filter 1 prototype. These units were, together with the ECAL trigger primitives generator built by Lisbon and Ecole Polytechnique, used to read out a 3x3 ECAL crystal matrix during 1995 test beam period.

Both the trigger information extraction and the detector resolution was tested and Fig. 11.18 and Fig. 11.19 show the results. It should be noted that the compressor was NOT perfectly adapted to the detector and that ONLY 10-bit ADCs were used thus creating a situation where the full performance of the readout system could not be explored.

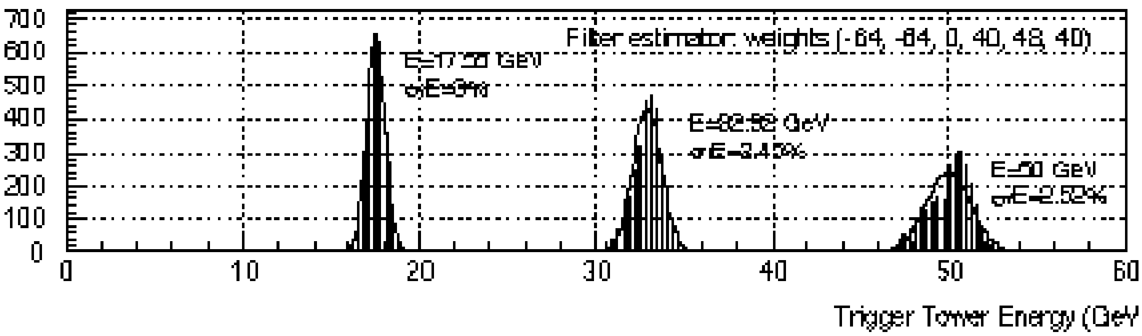

Fig, 11.18: The Trigger energy resolution

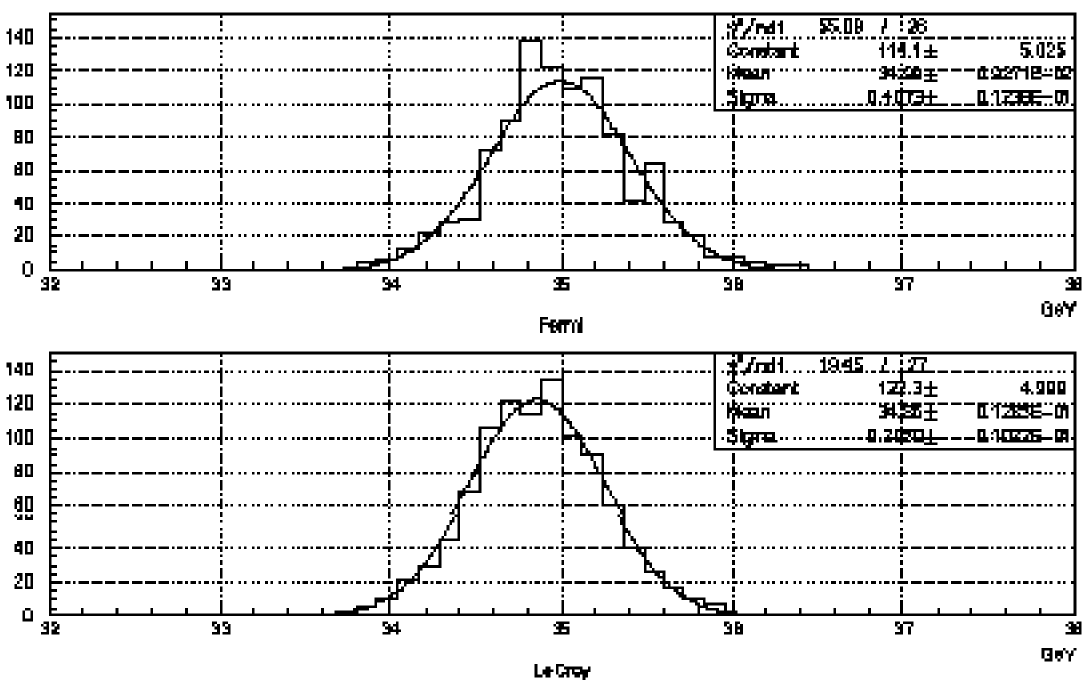

Fig. 11.19: Resolution at 35 GeV with the FERMI readout vs. Charge ADC readout.

11.5 ASSEMBLY AND INSTALLATION

11.5.1 Multichip module

Within the RD16-FERMI project, developments of modern assembly techniques have been one of the goals. As a result, a method of producing MCM-D substrates which can use the flip-chip mounting technique has been evaluated and found very reliable. This assembly method eliminates the classical bond wires for the connection of the individual dies to the substrate which contains all the interconnections. Instead, solder spheres with a diameter of 100 μm, are deposited onto the I/O pads of the dies which are then place upside-down on the substrate and the solder is reflowed, see Fig. 11.20. In this way the MCM becomes an extremely compact and reliable subsystem.

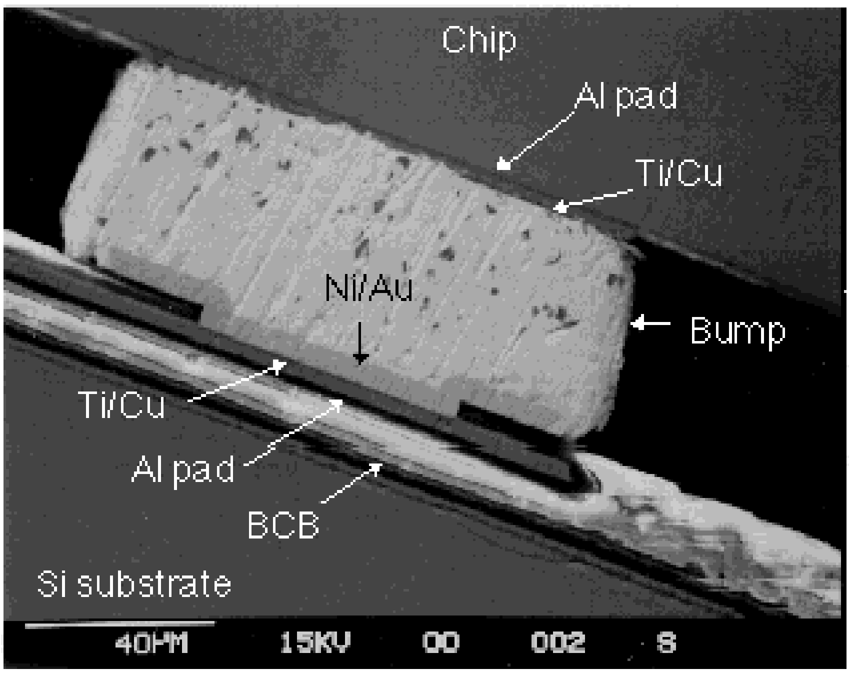

Fig. 11.20: Scanning electron microscope cross-section of a flip-chip mounted die.

The HCAL MCM contains a set of the above described ASICs capable of processing four channels and to generate two trigger tower information including the trigger primitives pipelines. The goal is to get the dimensions of the MCM down to less than 45 x 45 mm by migrating the existing ASICs, now in 0.8 μm and 0.7 μm technology, to a high-performance deep sub-micron technology, e.g. 0.5 μm or better with three metal layers. This is possible as the environment in the counting room allow the use of classical CMOS technologies i.e. no radiation problems.

Fig. 11.21 shows a prototype MCM system produced by the RD16-FERMI project which was used to evaluate the reliability of the technology. Extensive temperature cycling have been done without any sign of fatigue.

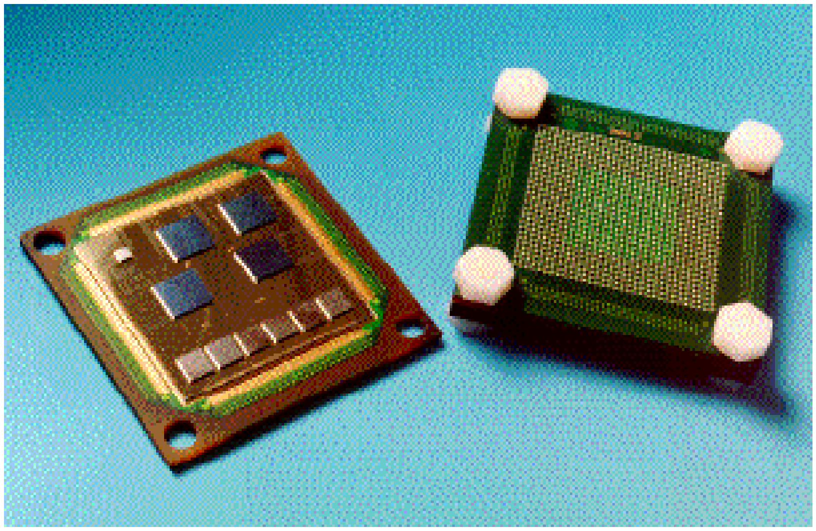

Fig. 11.21: A prototype FERMI MCM in a BGA package.

The MCM has been developed within the EUROPRACTICE programme thus allowing access to multiple industries for the production. The MCMs will be delivered tested and guaranteed by industry.

11.5.2 Readout VME module

A Readout Module, built as a 9U VME module, contains 15 MCMs and associated functions like Board Controller and interface to the DDU and trigger. This gives 60 channels or 30 trigger towers per module. The Board Controller will be in the form of a FPGA or EPLD. Estimated power dissipation is around 50 W per module.

The Readout Module will be produced by industry and delivered tested and guaranteed. A total of 250 modules are needed to read out the HCAL detector

11.5.3 Crate system

The type of crate to be used will be the standard CMS 9U VME crates.

Each crate houses 18 Readout Modules, the DDU/FED module and a Local Control module or an interface to a shared Local Controller. A custom backplane is used for the Data path connections inside the crate and the Transition module at the back of the crate will be used for the optical connections and interfacing.

A total of 14 crates are foreseen for the total system which corresponds to the data volume requirement of 14 RDPMs.

11.5.4 Quality control, assurance, and monitoring

The totality of the items will be produced by industry and a ISO 9000 compatible follow-up process will be used. This guarantees the best possible quality control, assurance and monitoring during the total production chain. All items will carry at least a 1 year guarantee by the manufacturer which should be followed by maintenance contract to be renegociated at regular intervals.

11.6 ACCESS AND MAINTENANCE

11.6.1 Access

All electronics, except the on-detector front-end part, is placed in the counting room and therefore, is continuously accessible.

11.6.2 Maintenance

As stated in chapter 11.5.4 all items will be covered by an initial guarantee period followed by set of maintenance contracts. A set of spare items, around 10%, will be made available.

References

[1] H. Alexanian et al; "FERMI: a Digital Front End and Readout Microsystem for High Resolution Calorimetry", NIM A 357 (1995) pp 306-317

[2] H. Alexanian et al; "Optimized digital feature extraction in the FERMI microsystem", NIM A 357 (1995) pp 318-328

[3] CMS Calorimeter Trigger Group; "CMS Calorimeter Trigger, Preliminary Specifications of the Baseline Trigger Algorithms" CMS TN/96-10

[4] S. Cittolin et al; "Front End Logical Model in CMS", CMS TN/96-015

Table of Contents

12. HIGH AND LOW VOLTAGE SYSTEMS

12.1 HIGH VOLTAGE SYSTEMS

12.1.1 Barrel and endcap photodetectors12.1.1.1

Requirements

Photodetectors for the barrel and endcap calorimeters are hybrid photomultiplier tubes (HPD). HPDs are a specific variant of image intensifier technology in which an array of silicon diode pixels is placed in close proximity to the photocathode. As described in chapter 8, gain is due to the kinetic energy gained by photoelectrons from the applied acceleration field between the photocathode and the silicon anode. High voltages in the range 12 kV to 15 kV result in photoelectron gains in the range 2000 to 3000.

The photoelectron current drawn by the tube is extremely small. In the region with the highest energy particle flux, close to the beam pipe in the endcap calorimeter, this current amounts to only 20 pA per pixel or about 400 pA for a 19 pixel tube. At the quietest point, the midpoint of the barrel calorimeter at 90 polar angle, the photocurrent is a factor of 8 lower. The maximum current needed is 2 nA when all five HPD tubes in a given readout box are connected to a single high voltage power supply.

Since gain in an HPD device is linear with the applied high voltage, gain stability does not impose severe requirements on power supply stability. The requirement is that gain variations due to high voltage power supply changes should be less than 1% . The linear gain-voltage relationship implies a corresponding power supply voltage stability that is also good to better than 1%.

The HPD diode pixel array must be reversed biased into full depletion in order to collect the ionisation each incident photoelectron. Depletion occurs for a back bias potential of 50 to 70 volts. Applying a higher field improves the timing response, and values in the 100 to 150 volt region are typically used with these photodetectors, since the signal comes from hole motion.

At a gain of 2000, the HPD diode current resulting from beam-beam interactions is significantly smaller than the current produced by the device itself in the absence of photon irradiance. This dark current is 1 to 5 nA per pixel initially and comes entirely from bulk leakage processes in the silicon. Neutron irradiation creates defects in the bulk material leading to an increase in leakage current which is linear with dose, 20 nA/10^{10} neutrons/cm^2 has been measured (chapter 8.2). For the largest diode area, 24 square mm, and a worst case predicted lifetime neutron exposure, $5x10^{11}$ per cm^2, the leakage current increases to some 24 nA. Allowing for uncertainty in the radiation exposure estimate, the bias power supply maximum current requirement for a 19 pixel tube is 2 μA.

Bias voltage only depletes the silicon and influences the impulse response behaviour. It is not involved in determining the gain. Consequently, voltage stability is not an important parameter.

For both the high voltage and the bias voltages, noise and ripple are very important parameters. Any AC signal on the voltage supplies is capacitively coupled directly into the readout and is coherent over the entire pixel array. For this reason the voltages are well bypassed right at the HPD pinouts. Overall, the noise floor goal is 3000 electrons rms, or 0.48 fC, per pixel (chapter 9). This requirement implies a bias voltage noise floor smaller than 100 μV rms for the 5 pF pixel capacitances involved. For high voltage, the coupling capacitance between the photocathode and an anode pixel is a factor of 30 smaller making the noise floor limit 3 mV rms. The noise floor requirements apply to the overall system; power supplies, power leads, and local filter stages. Essentially, whatever noise level is introduced by the power supplies and through pickup in the connections must be reduced to acceptable levels by filter stages at the photodetector interfaces.

Overcurrent protection is necessary to protect the system. A fast voltage trip function triggered by a sudden increase in current should shut down the supply and discharge the cable. This type of protection is found on all wire chamber high voltage supplies. For HPDs, the fast trip is needed on both the high voltage and the bias supplies. The HPD voltage supply requirements appear in Table 12. 1.

Table 12. 1

HPD Power Supply Requirements.

	High Voltage	**Bias Voltage**
Voltage	12-15 kV	100-150 V
Stability	< 1%	< 10%
Current	2 nA	2 μA
Noise	< 3 mV	< 100 μV
Fast Trip	yes	yes

System overview

Power supplies for the high voltages and bias voltages are located in the shielded service room adjacent to the detector cavern to eliminate concerns about radiation exposure effects and accessibility. However, noise considerations dictate the system grounding and return path parameters. A single point safety ground connection for the power supply and readout systems is envisioned to eliminate any possibility of a DC ground loop vulnerability. This configuration rule must also include the low voltage power supplies for the front-end electronics which are located along the side galleries of the detector cavern. Supply outputs are differential and have a single-point, common safety ground at the readout boxes.

One high voltage supply and five bias sources are packaged as a 6U VMEbus card; one such module is needed for each HPD readout box. VME was selected to make the interface to the Detector Control System as natural and simple as possible. The VME crate(s) are located in the underground service room where repair and maintenance access is straightforward; the cable runs are then about 150 meters long.

High voltages are brought to the photodetectors using twisted-pairs with an overall shield. The shield is hard grounded at the readout box and AC terminated at the supply to minimise EMI. A single high voltage supply services all of the HPDs in a given readout box for cost reasons. However, each photodetector is connected individually; there is one pair in the cable per HPD to avoid a single point failure which could take out an entire readout box. To be in compliance with CERN policy on the use of plastics in underground enclosures, the pairs will have silicon rubber insulation. Derating the dielectric strength of silicon rubber to 30 kV/mm
implies an insulation thickness of 0.3 mm for 16 kV service. Thus, the cables are quite small and flexible. A custom connector is planned which has wiping contacts similar to banana jacks.

Additional pairs in the cable bring the bias voltage to each HPD in the readout box. In this case, individual supplies for each HPD are necessary to allow for the (potential) individual characteristics and ageing behaviour of the diode arrays.12.1.1.3

Assembly and installation

The high voltage supplies are based on commercial DC-to-DC converters; night vision devices use such converters making them readily available. At this time, it is not known whether a commercial noise filter unit exists or whether development is required. A custom fast trip circuit is needed as none are available for the 16 kV operating point. An adaptation of one often used trip circuit design involving sensing the return current will be undertaken. The same custom connector used at the load end of the cable will be used at the supply end.

Bias voltages will be derived from a DC-to-DC converter also; at a working point of 150 volts, commercial noise suppression devices are available. Subsequent individual regulator stages allow for separate control and monitoring of the bias for each HPD separately.

Whether assembly is done commercially or at one of the collaborating institutions is not yet decided. The system comprises 120 modules plus spares and 7 VME 6U powered crates; 120 high voltage cables are also needed. Installation involves placing crates and racks in the service room and laying cable from there to the cavern and the individual readout boxes.12.1.1.4

Quality control, assurance, and monitoring

The QA/QC process that will be followed has three steps. First, the set of requirements is developed and approved by technical management. R&D is then carried out to develop a design proposal and a rough cost and schedule outline which are reviewed against the requirements. Third, a detailed plan of work, a complete schedule with appropriate milestones, and a very detailed cost breakdown are prepared. These items are then used to monitor and guide the manufacture and for reporting to oversight groups.

For fabrication of power supplies, especially high voltage units, testing of completed assemblies is not sufficient. Acceptance testing of the critical elements is necessary before assembly, and corresponding test stands are part of the project. Cable assemblies are tested twice, first at the fabricator and then after installation but before connection to the equipment.

Having the supplies packaged as VME modules makes monitoring a simple task. The Detector Control System extends to the VMEbus using an in-crate Input-Output-Controller. This processor continually monitors the voltage and current readings and transmits error messages for out of tolerance conditions or trips to higher levels of the system.12.1.1.5

Access, maintenance, and operations

The high voltage supplies are VME modules located in the underground service room. Access for authorised personnel is straightforward should repairs be required. There are no maintenance requirements. Operations are controlled and monitored remotely using the Detector Control System.

12.1.2 Forward photodetectors HF12.1.2.1

HF requirements

The HF uses standard dynode-multiplication photomultiplier tubes of at most 10 stages. The PMTs require high voltages (HV) up to at most 1.8 kV. In order to control the stable gain of the photodetectors, and to detect faults in the system, the HV system must provide the ability to: (a) control or "set" the voltage, (b) read back the voltage actually delivered to the devices, (c) monitor the current drawn, (d) provide overcurrent protection, and (e) provide sufficient current in such a fashion that the PMTs maintain high linearity.

An individual PMT requires at most 60 µA of anode current at 1.8 kV or 110 mW of HV power for direct amplification of photoelectrons for the HF. Additional power loss occurs as electrons in the dynode stages strike the dynode elements, a loss which appears in the form of heat. Typical upper limit for this loss is estimated at about 60 µA 100 V at the anode, or 60 mW lost to heating. This is the case where HV power is used only to directly to bias the PMT dynodes.

The PMT must maintain current linearity within 2% from 0-60 µA average current, and from a peak pulsed current of 0-25 mA. Therefore, the PMT HV supply must maintain a current linearity similarly; i.e. it must maintain a linear current to 2% during the 1.5 ns risetime of the PMT and be able to support discharges at the 40 MHz rate of crossings without loss of linearity. To maintain these levels using a resistive dynode biasing circuit, the currents maintained by the HV supply must be 100 larger.

For gain stability, since the gain $g \sim V^D$, where D = number of dynodes, then $\delta V/V \sim 1/D\ \delta g/g$. We impose a requirement that the gain g is stable to ±1%. Thus the voltage must be stable to <0.1% for a ten stage PMT. The HF PMT power supply requirements appear in Table 12.2.

Table 12. 2

HF PMT Power Supply Requirements.

High Voltage Max	1.2-1.8 kV
High Voltage Steps	#dynodes+1
Current, Average	100 µA
Current, Peak	25 mA
Slew Rate	100 V/µs
Ripple/Noise, p-p	100 mV
Stored Energy/Dynode	4 µJ
Current Monitor	yes, ± 1 µA
Current Trip	yes, <10 ms
Current limit	yes, 120 µA
Specific Power	>50 mW/cc
Voltage Setting Error	±1V
Stability	<0.1%

System description

The HF PMT will be negatively biased with a Cockcroft-Walton (C-W) type voltage capacitive multiplier which provides an individual fixed voltage ratio output for each dynode and the photocathode via the successive stages of the capacitive full-wave rectifier voltage multiplier ladder.[1-6] Fig. 12. 1 shows a typical C-W circuit produced commercially by Hamamatsu and used in HF testing. The circuit for HF would be similar to this. In this example of a C-W circuit, a self-oscillating sine-waveform power generator (180 kHz) is boosted by a transformer to up to 100 V, and fed into the multiplier. The feedback regulation uses a 1:1000 laser trimmed precision divider to compare the opposite sign reference control voltage to the generated HV to control the voltage applied to the power oscillator through a pass resistor. Typically the circuit consumes 100 mA @ 15 V to deliver 600 µA at 2 kV. The control voltage is 1 V/kV. The volume is <20 cc and the specific power >75 mW/cc. A typical temperature coefficient can be maintained at 100 ppm/C°.

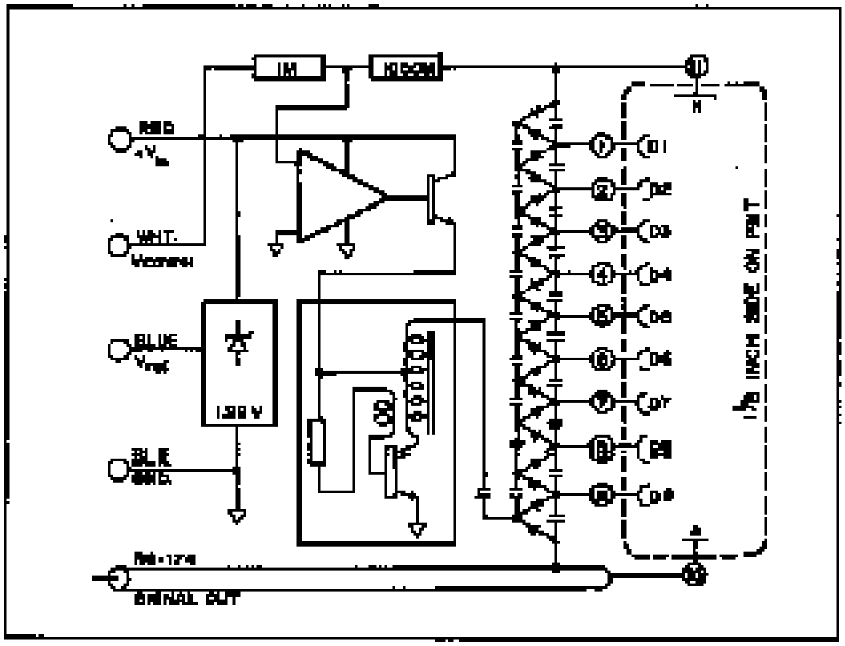

Fig. 12. 1: Cockcroft-Walton type active base/power supply.

These C-W base/supplies have been successfully used in experiments and have become commercially available. The great advantage in a C-W base is the large increase in linear dynamic range provided, due in part to the ability to isolate the voltages on the dynode chain from dynamic effects during the amplification process. It is this aspect that leads to the proposal of this type of bias circuit for the PMT in the HF calorimeter. Fig. 12.2 shows the increase in the linear PMT current possible with a C-W base, compared with a similar resistive base. Typically a factor of 10-20 in linear dynamic range can be obtained, and that helps to match an ordinary PMT to the task of the HF calorimetry at high rates. Additionally, power and ancillary heating of the PMT/base assembly is saved due to the absence of a resistive dynode chain.

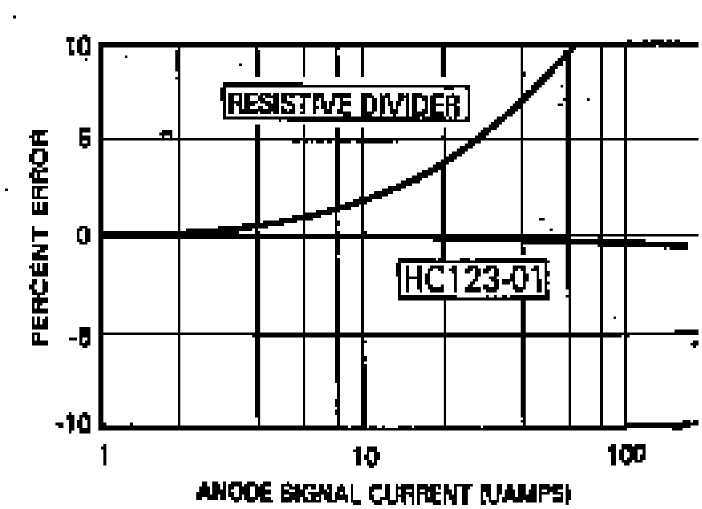

Fig. 12. 2: The linear PMT current possible with a C-W base/HV supply.

In a C-W base, the voltage level is determined by a low voltage oscillator which typically operates up to a few hundred kHz. Feedback circuitry is used to maintain voltage level. Careful attention to reducing pickup of the switching transients by the data signals will be needed.

A possible provision of the base/HV would be that the cathode-D1 voltage will be separately controlled from the voltage across the dynode chain, in order that the electron optics be separated from the gain section. At present this does not seem to be a necessity, but will be kept open as an option.

In an attempt to limit active components inside the HF shielding, to reduce cooling requirements at the PMT, and to increase the available space for shielding we plan to generate the HV for each dynode remotely from the PMT in a rack outside of the shielding. A bundle of 11 (# dynodes+cathode+ground) wires carry the HV for each dynode and cathode from HV crates located a few m from the HF itself. The "base" would thus consist only of a PMT socket, bypass capacitors for high frequency performance, a multipin HV connector, and at most a passive matching network for the anode signal coax. The current on each dynode HV cable is less than 1 mA, with the power at most a few mW on each conductor. With silicon rubber insulation, radiation hard to the ~Grad level, the HV multiconductor cable would be about 6 mm in diameter.12.1.2.3

Assembly and installation

It is likely that the HV units will be based on commercial products. The individual components and sub systems are assembled as 32-channel VME modules in the 9U by 400 mm format. this modularity matches that of the 32-channel front end electronics VME modules. A semi-custom VME crate is required to provide the output connections to the photomultiplier tubes.

Whether assembly is done commercially or as one of the collaborating institutions has not been decided. The system consists of 128 high voltage modules plus spares and 8 powered VME 9U crates. Installation involves setting racks and crates on the detector platform, and connecting 2 meter-long cables from the back planes to the photomultiplier tube sockets through small openings in the HF shielding.12.1.2.4

Quality control, assurance, and monitoring

The QA/QC process will be similar to that for HB and HE in that pre-assembly testing of certain components is needed. In addition to testing of completed asemblies before installation, a combined photomultiplier tube - high voltage unit longer term test is planned. This burn-in period is as least 48 hours and uses operating conditions at 100% of the voltage and current limit as established by a LED light flasher source operated at 40MHz.

Monitoring is straight forward as the Detector Control System extends to the VMEbus using a standard Input-Output-Controller. this processor continually monitors voltage and current values and transmits errors messages for out of tolerance conditions or trips to higher levels of the system.12.1.2.5

Access, maintenance, and operations

The access to the HF high voltage system is straight-forward, since all of the racks are external to the shielding and readily accessible by authorized personnel during a routine access to the cavern.

12.2 LOW VOLTAGE SYSTEMS

12.2.1 Barrel and endcap electronics12.2.1.1

Requirements

The front-end electronics for the barrel and endcap calorimeters described in chapter 9 are contained in individual readout boxes located on the outer surface of the absorber. Local power supplies or DC-to-DC converters cannot be used as the magnetic filed strength is 40 kilogauss at that location. Also, any components placed at the readout boxes must meet a difficult reliability requirement as described in chapter 9 for the electronics.

Each readout box requires +5 volts at 40 A and +10 volts at 6 A. Specifications for ripple and EMI/EMC (to be worked out during prototyping) will be very tight because of the low noise requirement on the electronics. Components of the low voltage system inside the readout box should introduce minimum additional heat load.

Radiation conditions at the location of the readout boxes is estimated at 10^{10} neutrons per square centimetre per year with about the same flux of gamma rays. Charged particle doses are negligible. Components for this location must be shown to withstand this level of irradiation. At the side galleries of the cavern, fluxes are about two orders of magnitude lower. Because of the well-known lack of radiation tolerance for some power supply components, validation is required for those systems as well.12.2.1.2

Low voltage system

The topology for low power distribution is to use local low voltage, low drop-out linear regulators at the front-end electronics and place switching power supplies 30 meters away where the magnetic field is about 500 gauss. It is quite possible to shield the power supply transformers from such a field. Because of the reliability and noise floor requirements, each three channel module is equipped with two regulators, one for the digital section and one for the analog section. The power required for the three channel group of ASICs and optical link on each front-end board is estimated to be 3.25 W. The total power per box, including 48 boards and the regulators, is estimated to be about 210 W. Fig. 12. 3 and Fig. 12. 4 illustrate the proposed system.

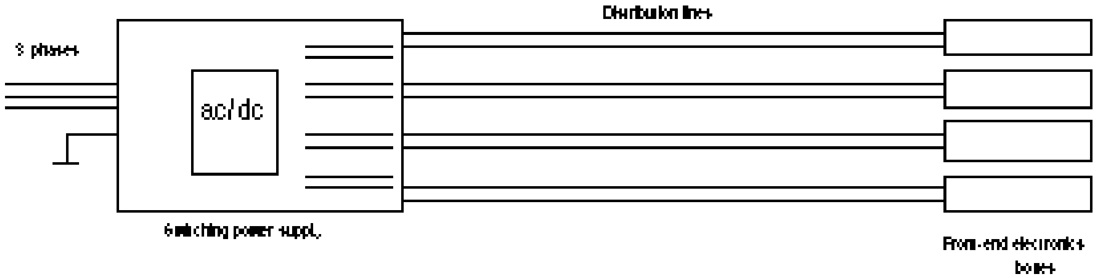

Fig. 12. 3: System Layout.

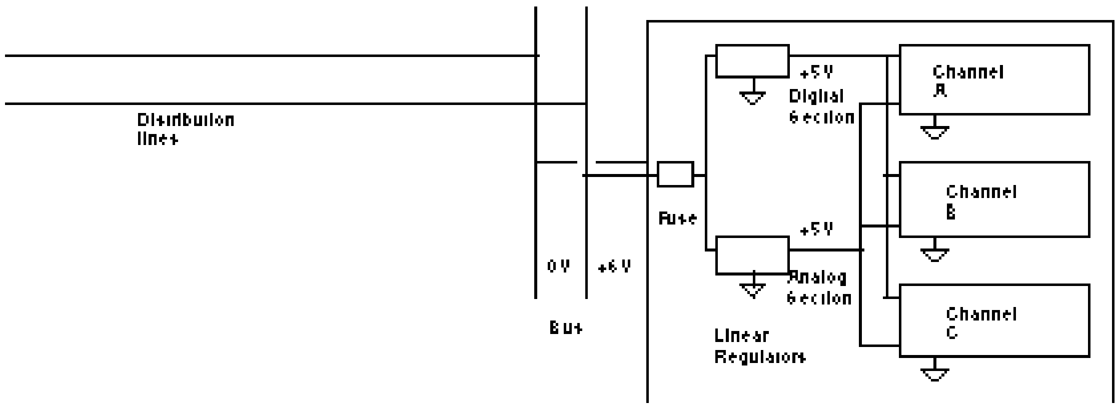

Fig. 12. 4: Front-End Module Power.

Each channel of front-end electronics is expected to have a single +5V power supply. Low drop out linear regulators are used to regulate this input voltage from a bus located in each box. A box is connected to 1/4 of a switching power supply main frame using water cooled copper conductors. Switching power supplies are configured as multiple modules connected in parallel to reach the current level required by the front-end electronics. They have a three phase input, a built-in AC-DC converter and eight modules rated up to 200 W. Two of them are connected in parallel at the output to feed the distribution cable. This commercial package has to be shielded from magnetic fields for proper operation.

The current required per front-end board is about 0.65 A. Linear regulators can be connected between the internal power bus and the analog and digital sections of the board separately. By using low drop out devices it is possible to keep the power dissipation in the regulator to a minimum. There are commercial devices with 5 V/0.75 A output which are appropriate for this application. They can handle input voltages up to +26 V and have a minimum input to output voltage drop of 600 mV. The output voltage of these devices is in the range +4.75 V to +5.25 V. Under these conditions, the minimum input voltage for proper operation of all devices is +5.85 V. These regulators have fold-back output current protection. Fuses rated at I > 0.85 A are necessary at each distribution point of the bus to protect the connector and input traces of each board. Snap-action resettable Poly-Fuse devices are proposed, but the radiation tolerance and magnetic field sensitivity parameters of these devices are not yet established.

The nominal current flowing through the distribution lines is about 35 A These lines are designed to avoid large voltage drop across them, which means the cross section is over-designed for such a current. These lines do not need current protection supplemental to that built in into the switching power supplies. Under any plausible fault condition, the maximum current that the power supply delivers is lower than the rated current capability of the wires. The voltage drop estimated for these conductors is about 0.8 V, or a total power loss of 600 W for HB and HE.

The switching power supply configuration consists of AC/DC converters at the input and DC/DC modules at the output. The output voltage required is about 7 V. The AC/DC converters take the three phase AC input power and performs filtering and rectification. The DC/DC converters plug into a high voltage back plane and provide low-noise, independently regulated and fully isolated outputs. The AC/DC converters are fully protected against loss of a phase, excessive loading, etc. This commercial package is cooled by a fan. It is necessary to include an air-water heat exchanger to avoid conducting heat into the cavern environment. Additionally, a magnetic shield has to be designed to protect those power supplies from the 500 gauss stray magnetic field.

Each power supply is connected to the three phase system and the chassis and the input ground is connected to the safety ground of the main AC distribution. Outputs can float allowing for a single point ground configuration for the readout boxes. This ground connection is made locally at each box.12.2.1.3

Power cable and cooling

Power and cooling water services for the readout boxes have the following requirements:

a) No net heat into the local environment from cabling or electronics

b) Water flow of 1 liter/min

c) Water and power lead lengths about 30 meters

d) Nominal current of 40 A at +5V and 6 A at +10 V

e) Conductors are in a 4 T field

f) Voltage drop less than 1 V

g) Very high reliability inside the detector

Power and cooling water is brought to each readout box individually to avoid coupled failure modes. The configuration where a large supply is brought in and services are distributed locally through manifolds was not selected for reasons of reliability, ground loops and electrical protection. Flexible components have been selected to facilitate installation; multi-filament #3/0 AWG welding cables for the 5 volt supply and return and fibre reinforced power supply hose for the cooling water supply and return. The 10 volt service uses a pair of #10 AWG copper wires.

The power conductors will be twisted periodically and tied together at suitable intervals to accommodate the 4 T field forces present over the last few meters of the run.

The copper leads are pre-terminated at each end with high compression "copper only" cable lugs. At the ends, torqued connections will be made using belleville washers for high reliability and zero maintenance. The water lines are also terminated during manufacture with appropriate fittings for the supply and readout box couplings. There are several overpressure protection devices to prevent hose failure and subsequent leaks.

The line drop for the #3/0 copper cables is approximately 0.8 V which is within the specified requirements, and the drop on the #10 cable is about 0.2 V which is again an acceptable number. The heat dissipated by the leads is less than 8 watts; and no special cooling system is required. Inlet water temperature is set sufficiently below ambient temperature to have the return flow exit at ambient temperature. The net refrigeration to the cavern provided by this operating condition more than compensates for any heat dissipation into the air.12.2.1.4

Acquisition and installation

Power supplies will be purchased by going to tender with appropriate specifications. These supplies will be semi-custom commercial units because the voltage needed is not very common in industrial applications. For economic reasons, we anticipate a CERN coordinated quantity acquisition which involves other subdetectors. Service, installation, and repair functions are simplified by such commonality as well. Installation into the relay racks is straight forward and can take place any time after the racks are installed and powered. Installation and connection of the conductors takes place quite late in the schedule. The central wheel muon detector system must be completed before any cables can be installed; and it is prudent to wait until the corresponding calorimeter assemblies have been installed to avoid damage.

Low voltage drop-out linear regulators are off-the-shelf commercial components. The specifications are for maximum and nominal electrical ratings and reliability. Installation is described in chapter 9 for the front-end modules.

Both the regulators and the power supplies must operate in a neutron and gamma ray radiation environment. In addition, there is a magnetic field present. The resistance of the product to this environment is typically information that industrial producers do not supply. Testing and validation is necessary before final selection can be made.12.2.1.5

Quality control, assurance, and monitoring

The low voltage supplies are commercial units, the result of preparing a specification and going to tender. A semiautomatic test stand is needed for incoming inspection and verification of capabilities and EMC compliance. Sampling is not anticipated, all supplies will be checked.

It is probable that assembly of the water hoses and power leads will be put out for tender. In that case, QA/QC provisions will be included in the specifications. It is likely that QC for the materials used to construct the leads will be left to the vendor, but the QC plan will be required in the bid response. QA measures for the completed assemblies are part of the specifications in the bid package. Testing of both electrical and hydraulic characteristics is necessary, and the method of testing and the criteria will be specified by experienced engineers in the Fermilab magnet power supply and leads group.

After installation but before first use, the leads are to be rechecked for possible induced damage. A simple pneumatic test identifies leaky cooling hoses, and measurements of continuity, isolation and ground impedance identifies electrical faults.

Voltages, currents and temperatures are continuously monitored using the Detector Control System capabilities. Each power supply rack contains a local processor running a monitor and control task; ethernet is used for communication with the higher levels of the system. A fieldbus connection to the readout boxes brings back similar information from the far end of the power leads. Specific monitoring for EMI/EMC compliance is not necessary; the sensitive front-end electronics for the calorimeter and muon detectors will easily identify a noisy power supply condition.

The Detector Control System is also interfaced to the site utility plant, in particular to the chilled water system. Control and monitoring of the supply and return cooling water conditions is accomplished using this interface.

Commercial voltage regulator components have a yield of better than 99%. Therefore, tests of these devices will be at the board level as failure modes, even an input to output short, do not lead to damage of the other components on the board. Testing requires only that the output voltage is within specified limits.12.2.1.6

Access, maintenance, and operations

Low voltage power supplies for the front-end electronics are located in racks along the side galleries of the cavern. Access by authorised personnel is possible, but is normally a scheduled activity due to the interruption in accelerator operations. Maintenance is not an issue; the supplies do not require servicing. Operations of the power supplies are controlled remotely using the capabilities of the Detector Control System.

For one third of their length, the water hoses and power leads are as accessible as the power supplies. For the remaining two thirds of the length, a major disassembly of the detector is required to provide a repair access. The majority of the trapped run calls for disassembly not only of the forward and endcap systems, but two of the return yoke wheels as well. The power lead terminations are designed to be maintenance free, and the water connections do not use quick-disconnect technology. The power leads are completely passive and have no operational impact.

12.2.2 Forward electronics 12.2.2.1

Requirements

The front-end electronics are packaged on printed circuit boards and housed in 9U VME crates. Standard VME power supply assemblies are required, and standard relay racks are used.

The stray magnetic field in the vicinity of HF is a few hundred gauss. Shielding of the power supply transformers may be necessary, but this is a standard procedure, e.g. the L3 experiment at LEP.

At the HF electronics racks location, the neutron fluence is predicted to be 10^3 per square centimetre per second. This corresponds to 10^{10} neutrons per square centimetre per year. The flux of gamma rays is of the same order of magnitude. Ionising doses are negligible, amounting to 100 rad per year. Power supplies must withstand these irradiations for the ten year operating period foreseen. Because of the well-known lack of radiation tolerance for some power supply components, validation is required. 12.2.2.2

Acquisition and installation

Power supplies will be purchased by going to tender with appropriate specifications. For economic reasons, we anticipate a CERN coordinated quantity acquisition which involves other subdetectors. Service, installation, and repair functions are simplified by such commonality as well. Installation into the relay racks is straight forward and can take place any time after the racks are installed and powered. Connection to cooling water systems will determine the schedule. 12.2.2.3

Quality control, assurance, and monitoring

The low voltage supplies are commercial units, the result of preparing a specification and going to tender. A test stand is needed for incoming inspection and verification of capabilities and EMC compliance. Sampling is not anticipated, all supplies will be checked.

Voltages, currents and temperatures are continuously monitored using the Detector Control System capabilities. Each crate contains a local processor running a monitor and control task; ethernet is used for communication with the higher levels of the system. Specific monitoring for EMI/EMC compliance is not necessary; the sensitive front-end electronics for the HF calorimeter will easily identify a noisy power supply condition.

The Detector Control System is also interfaced to the site utility plant, in particular to the chilled water system. Control and monitoring of the supply and return cooling water conditions is accomplished using this interface.

12.2.2.4 Access, maintenance, and monitoring

When the detector is in the garage position, the racks are easily accessible for any required maintenance or repair operations. Access is somewhat more difficult in the cavern as the calorimeter is some 8 meters above the floor level centered on the beam line. Specific personnel access techniques, stairs, catwalks, and lifting devices, have not been designed at this time, but are straightforward applications of well-known hardware. The stray magnetic field strengths expected, a few hundred gauss, would call for proper procedures, training, and equipment should a service access be made with the solenoid energised.

The residual radioactivity activity levels discussed in chapter 5. refer to the end of a ten year operating period. During commissioning and the early years of accelerator operation, activation will not be a problem and no restrictions on access to the electronics are expected. As the system grows more and more activated, there could be need for placing time limits on access or for temporary local shielding during maintenance operations. Therefore, the power supply system should feature good remote diagnostics to pinpoint problems and allow for simple replacement as the preferred method of repair.

References

[1] Purschke, M.L. "A new HV supply for large PMT systems", 3rd Int. Conf. on Elect. for Future Colliders, Chestnut Ridge, NY US (1993) LeCroy Corp.

[2] Hubbeling, T., HIVOC: a VME HV control card for large PMT systems, CERN ECP 93-2.

[3] Bin Lu, "The Cockcroft-Walton PMT base and the ethernet HV controller", Virginia Poly. Inst. State Univ. VPI IHEP 91-1 (1 Jun 1991).

[4] S. Neumaier et al., A new VME-based HV power supply for large PMT systems, GSI-95-06 (Jan. 1995).

[5] V. Astakhov, Multichannel HV system for PMT arrays, JINR preprint (1995). (astakhov@sunhe.jinr.dubna.su)

[6] "R329 Cockcroft-Walton Base" (Authors' names not translated from Kanji script) Inst. for Nuclear Study, U. Tokyo, INS-T-536 (June 1995). Also documented as KEK electronic scan preprint library 95-9-

134.

TABLE OF CONTENTS

13. CONTROLS AND MONITORING

13.1. OVERVIEW

Control and monitoring functions for all CMS detector subsystems are co-ordinated by the Detector Control System (DCS) Group in order to design and implement a single control system to operate the detector. Using guidelines provided by DCS, each of the sub-detector groups are to define and design the data acquisition and control function needs for their sub detector. Data from these sub-detectors is available to the global control system which provides console hardware and software, as well as display, archiving and other higher level services. This section describes the control and monitoring of the HCAL sub-detector.

Parameters to be measured by the control system exist in three locations, the counting room, the side galleries of the cavern, and inside the detector itself. Physically, the electronics in the counting room and attached to the forward calorimeter are housed in VMEbus crates. Inside the detector, electronics resides in the readout boxes distributed throughout the HCAL detector. Access to data in the readout boxes will be via a network connection from dedicated DCS crates in the counting room to controller cards in the readout boxes. All VMEbus crates include a DCS processor with a network connection to the higher system levels. The DCS architecture is shown in Fig. 13.1.

13.2 DCS OVERVIEW

13.2.1 Design principles13.2.1.1

Hardware architecture

The DCS hardware architecture consists of three principal layers. At the top are operator workstations and general purpose computers which provide access to all of the DCS services. The front-end or bottom layer consists of large number of distributed front-end processors (VME-based). The middle layer is a dedicated local network interfacing the previous layers. This network is segmented for availability purposes, and is connected to the general CERN network by a filtered access. The general CERN connection provides for world wide access by authorised persons. The front-end layer connects to detector systems and equipment through direct I/O or through field buses shows the architecture of the DCS network.13.2.1.2

Software architecture

The software architecture is a co-operating network of dedicated control applications, DCS general services and gateways to other CMS and CERN systems. The dedicated control applications are the distributed controls for CMS detectors which are composed of real time process control components and supervision components.13.2.1.3

Operations

DCS services are needed for all operational phases of the experiment, from construction and commissioning to physics data taking runs, calibration tests and monitoring during shutdown periods. According to the operational phase, one or more operators will concurrently operate the CMS detector. These operations will be done from control rooms, equipment rooms, or remotely under the filtering of the DCS access control.

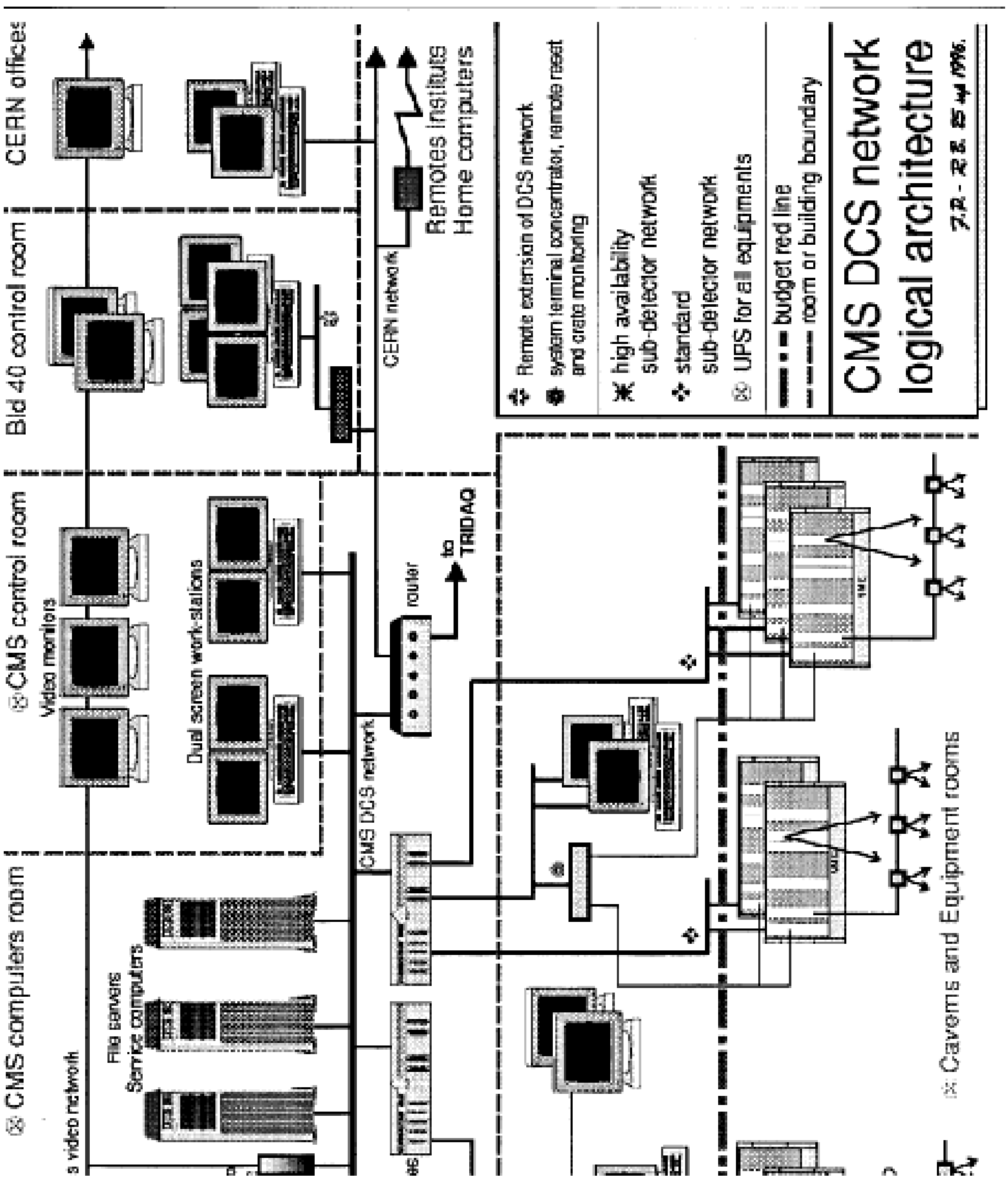

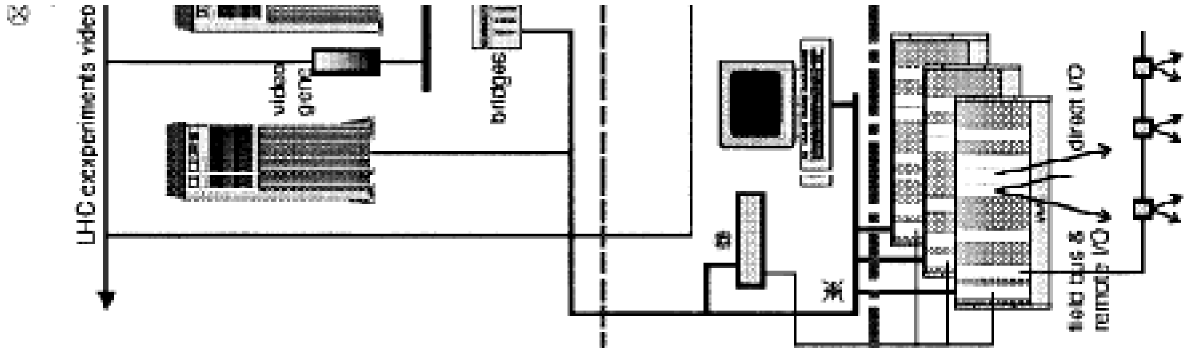

Fig. 13.1: DCS architecture.13.2.1.4

DCS toolkit

DCS provides general services; Archiver, Logger, Alarms, Access controls, Central Repository and a manager for the overall DCS activities. A toolkit is provided to build the dedicated control applications at the individual system level. The kit consists of drivers for the commanded I/O hardware, a control kernel, generic applications and a set libraries for specific applications.

13.2.2 Controls software system

The CMS collaboration has decided to implement a common general services software approach using an existing controls package. Commonality among all four LHC experiments is presently under discussion as well. In CMS and ATLAS, the respective DCS groups are evaluating EPICS as a possible general software system and have demonstration projects underway. EPICS is a highly developed software controls system that is widely used in the high energy and nuclear physics community and is supported by many laboratories.

To have a specific configuration and software environment, the remainder of this chapter is based on the use of EPICS in its current VME implementation. In this context, the starting point for the individual detector sub-groups is the EPICS Input-Output-Controller (IOC), a VMEbus based front-end crate containing a single-board computer running EPICS compatible software. At the present time, IOCs use the VxWorks real-time operating system running on Motorola processor boards. The data request protocol, Channel Access (CA) allows upper level processors to read and set parameters in the IOC. At start-up, each IOC is downloaded with the programs and database entries needed to acquire and process locally, the parameters associated with that particular IOC.

Because EPICS is used at many laboratories, software drivers are available for most commercial modules. The DCS group has indicated that they will recommend modules to use for standard analog and digital control system signals. This standardisation goal is intended to minimise the software effort required to implement sub-detector control and monitoring systems.

An important feature of the total EPICS/IOC software package is an extensive system for alarms monitoring and reporting of analog and digital alarm conditions. Included in the alarms task is the provision for two-tier analog alarms, with independent settings for high and low values, plus high-high and low-low values to distinguish severe from off-normal alarm conditions. Using this capability, less severe out-of-tolerance conditions can be reported, allowing preventative maintenance to be performed before real hardware failures occur. Alarm system values are part of the data that is downloaded to each IOC at initialisation time.

In EPICS, the database is a key element that allows the system to be adapted to different applications. Database records that are downloaded to the IOCs are processed at a rate dictated by that record. Processing the record may be as simple as reading an analog value, but other operations such as state machines and PID control loops are also implemented by configuring parameters of predefined database entries rather than writing special programs.

13.3 DISTRIBUTED DATA IN THE HCAL DETECTOR

The majority of the remote data for HCAL consists of readings and settings associated with the HF phototube high voltage supplies and the data channels in the HB and HE sections

of the detector. There are 11,232 data channels distributed over the readout boxes for the barrel and endcap calorimeters. For each of the channels in a given readout box, there are eight bytes of test data, two bytes of timing trim setting data, and a byte of miscellaneous control and mode settings. Also for each readout box, there are about ten voltage and temperature readings to digitise.

To accommodate the above requirements for HB and HE, a small controller card will be added to the card cage used to support the photodetector electronics. This controller card is interfaced to the individual channel ASICs via CAN bus. Support for CAN bus will be included in the channel ASIC. Communication between the readout boxes and the EPICS nodes in the counting room will be by way of fibre optic Arcnet, a small network that can easily provide the necessary data communication requirements. A processor such as the MC68376 can provide the local processing, the CAN bus node interface, the AD converter and operate the Arcnet protocol chip. Inside a readout box, the CAN bus connection could be duplicated or segmented to minimise the effects of any potential single point failure.

From the EPICS VMEbus crates in the counting room, the readout boxes will be star-connected using a commercially available Arcnet copper to fibre optic hub. For convenience, the network cable is to be bundled with the other cables connected from the counting room to the individual readout boxes.

13.3.1 Arcnet

Arcnet is a small local area network that is well matched to the requirements for accessing data in the HCAL readout boxes. Protocol interface chips and network hardware for this LAN are readily available. Arcnet adapters for the counting room nodes are available as VMEbus boards and as IndustryPack modules. Because the readout boxes are inaccessible, the controller cards there should be as simple as possible. One of the important reasons for selecting this network is that very little software is required to support the communications. The protocol supplies secure, acknowledged, collision-free transmission of data frames between nodes with little software overhead.

13.3.2 CAN bus

To conserve backplane space and minimise pin connections, some sort of serial connection is needed to communicate with individual channel ASICs. Instead of developing a non-standard serial connection, the established commercial standard CAN bus will be used. Support for the CAN bus interface can be included in the design of the channel ASIC. During normal operation of the detector, no control system access to the individual channels is needed. At start-up time, the timing delay setting and the mode setting bits are downloaded. For testing purposes, several bytes of test data can be downloaded to each channel. The size of the CAN bus frame is a good match to the needs of the individual channels. A standard CAN bus interface transceiver is used to connect with the backplane of the readout box.

13.3.3 Processor for the readout box controller

The Motorola MC68376 microcontroller will be used for the controller board. This device includes a CAN bus module and a 1-channel 10-bit A-D converter to read the voltages and temperatures within the readout box. These readings will be returned to the EPICS crates in the counting room once a second.

13.3.4 Crate based systems

Control and communication functions for distributed data from detector systems that use standard electronics crates are implemented by providing an EPICS IOC node in each crate.

In the case of readout channels where the CAN protocol is used for communications with the channel ASICs, VME 9U crates are used. The P3 user defined area of the backplane is used for CAN bus lines to each module. Connections back to the higher levels of the DCS are through its standard LAN interfaces.

13.4 VOLTAGES AND CURRENTS

13.4.1 Photodetector high voltage

High voltage supplies for the HCAL photodetectors are commercially available units that reside in the counting room in the case of HB and HE, and in local relay racks for HF. VMEbus-based controllers allow voltage values and maximum current values to be set, read, and alarmed as normal EPICS devices. Control functions for the high voltage channels will include ON, STANDBY, OFF, and the RESET of over-current trips conditions.13.4.1.1

Hybrid photodetectors

Hybrid photodetectors (HPD) are used in the barrel and endcap sections of HCAL. There are 36 readout boxes for the barrel section, 36 boxes for the endcap sections, and 72 boxes for the outer calorimeter compartments. The HPDs require an accelerating voltage in the range of 10-16 kV plus a diode bias voltage of 150 volts. There are 144 high voltage supplies, one per readout box, and about 500 bias supplies, one per HPD. These voltages will be cabled separately to each of the boxes. Each supply includes a fast over-current trip. The controllers for the high voltage supplies reside in an EPICS IOC crate. Operating parameters are downloaded as normal EPICS settings.13.4.1.2

Photomultiplier tubes

The forward detector uses photomultiplier tubes that require high voltage in the 1-2 kV range. Controllers for the high voltage supplies reside in EPICS IOC crates that are located in racks near the detector. Each supply includes a fast over-current trip. The total number of PMT high voltage channels is 3744. Operating parameters are downloaded as normal EPICS settings.

13.4.2 Front-end electronics power supplies

Voltages are distributed to each readout box separately (chapter 12) where local regulators are used for each channel. Low voltage bulk power supplies, +5V and +10V, for the front end electronics in the readout boxes are located on the side galleries of the cavern. Voltage and current readings for these supplies, both at the source and at the load, along with measurements of the lead temperatures will be returned to IOC crates in the counting house. The forward detector uses standard crate and rack based electronics, and the DCS infrastructure for rack systems can be applied.

13.4.3 Crates and racks

Electronics in the counting room will be implemented in the 9U VME64x format. The design, manufacture, installation, and cooling of the racks and crates is the responsibility of the

CMS infrastructure group. Monitoring and control functions are the province of the DCS group.

The space required to house electronics in the counting room depends on the allowed power dissipation per card. For the case of 16 channels per module and 18 usable slots per crate, the 14,000 readout channels in HCAL will require about 50 crates located in 16 racks. Monitoring operating parameters for each crate is necessary as well as two-tiered alarming on overtemperature, overvoltage or overcurrent conditions.

13.5 TEMPERATURES

Within each of the boxes in the detector, the ambient temperature of the air and the cooling plates will be monitored for alarm conditions. In this case, no additional control is needed, because the reason for an alarm condition can usually not be corrected by the HCAL group. Temperature readings would be returned to the IOC crates in the counting room using the Arcnet connection to the individual boxes. Temperature monitoring and alarming for the forward calorimeter rack systems are included in the standard rack protection package.

13.6 SOURCE CALIBRATION

A source calibration system is integrated into the HCAL sub detector. A radioactive source attached to a wire is guided by a small tube through portions of the detector while the DC response of the scintillator, light pipe, and photodetector system is recorded using the normal fast data collection system. Control is needed to select between several tubes and to drive the wire out and back during this calibration process. Twenty four such calibration systems are needed to cover all parts of the HCAL system. The source motion can be controlled either by the processor in the IOC crate, or by a companion processor board in the IOC crate. To interpret the calibration data, the source position must be correlated with the response data from the photodetectors. Even without a special timing system, measurements in separate EPICS IOCs can be correlated to a few milliseconds.

For the calibration process, the front-end electronics will be downloaded with parameters such that 16 consecutive readings are summed by the FIR filter of the second level trigger electronics. Then several hundred such sums will be averaged and the results correlated with the position of the source. Both the front-end electronics crate and the source controller crates will contain an EPICS CPU card. The reading of source calibration data will be controlled by the EPICS processor in the front-end crate which is able to cause the Level_1_Accept trigger needed to control the second level filter. This EPICS node will request and receive time-stamped values of source position from the EPICS CPU in the source controller crate. It is desirable to have the calibration system independent of the Data Acquisition System and so the processing of the calibration data is done by the EPICS system in the front-end electronics crate. It is not necessary for the trigger and DAQ systems to be operating during source calibration operations, only the system clock is needed. Details of the source controllers, the mechanism for moving the source and the readout of source position are described in chapter 10.

13.7 LUMINOSITY MONITOR

Part of the Luminosity monitor instrumentation includes several Roman Pots which contain devices that measure small angle scattered particles near the beam. In addition to the front-end electronics used to process the detector data, the Roman Pots need slow controls support for motor drivers, position readouts, high voltage control and readout, and downloading operating parameters and test patterns. Front-end data processing electronics will reside in two VMEbus crates, and to provide the slow controls support, an EPICS IOC processor will also reside in each of these crates. These processors are also used to read and monitor the parameters for the Roman Pots and provide an access filtered path for authorised personnel (in the accelerator control room) to read and control the position of moveable devices near the beam.

13.8 ARCHIVES

The upper levels of DCS will provide archived information for HCAL. Two types of archives are needed; constants used for calibration and configuration of the detector, and values of monitored parameters. Values include voltage and current readings, temperature measurements, and results of calibration runs.

13.9 TESTING FACILITIES

Test capability will be needed for the front-end DAQ and trigger electronics located in the counting room. It is expected that boundary scan testing will be incorporated into the design of the digital electronics. All electronics in the counting room will reside in VMEbus crates, so test data and readback will be possible over the DCS network. Test events can be written to and read back from the DAQ buffers using EPICS software in a processor located in each crate.

Operational testing and troubleshooting should be possible to accomplish from a remote workstation, located anywhere. Real-time, or pseudo real-time, correlated displays of accelerator data, detector data, and DCS parameter values are essential for diagnostics and troubleshooting. Gateways to the data acquisition processor farm and to the accelerator Controls System should offer this functionality.

TABLE OF CONTENTS

FACILITIES 504

14. SAFETY

14.1 OVERVIEW

The safety requirements for experimental activities are described in SAPOCO/42 which defines the safety policy at CERN. As a first step toward implementation of the provisions of the codes and instructions which emerge from this policy, the CMS collaboration has established a Safety Working Group with membership mainly drawn from the technical design staff of the major subsystems. Coordination with the TIS Commission is ensured as three individuals from Technical Inspection and Safety (TIS) are members of the working group. As defined in the booklet "Safety Guide for Experiments at CERN", the goal is initiation of safety hazard analysis activities during the earliest phase of the life cycle of the detector, the conceptual design stage, to facilitate early hazard identification and elimination or control.

The hazard identification process involved a review of the HCAL technical designs by the CMS GLIMOS and an individual from the TIS Commission. The design concepts for the calorimeters were discussed and evaluated with the HCAL engineers, safety working group representative, and technical management. Hazards could arise from the design choices themselves or follow from the operational conditions implied by the designs. The process was called an Initial Safety Discussion. A detailed worksheet was filled out, and used also as a guide to ensure that the scope of the process covered all aspects of hazards at accelerator facilities. Hazards which could cause death, injury, or occupational illness, or damage to facilities, systems, equipment or the environment as well as those not routinely encountered by the public were the focus of the identification step.

The purpose of this chapter is to summarize the results of the initial hazard identification process for the hadron calorimeter (HCAL) systems, and to present the mitigation strategies used to reduce or eliminate the risks.

14.2 ELECTRONICS

14.2.1 Introduction

Electronics refers specifically to the three major signal processing functions necessary to acquire event data from the detector: front-end electronics, trigger electronics, and data acquisition systems. In addition, the high voltage systems needed for operation of photodetectors are included under electronics.

14.2.2 Overview

Conventional electrical systems for power, lighting, convenience outlets, etc. are not discussed here as the safety issues are well covered by CERN practice, Safety Instructions IS23, IS24, IS26, IS28 and IS33 and Safety Code C1. For electronic systems, there is no analogous code or handbook of good engineering practice. Despite the fact that electronics systems are characterized by low voltage DC power systems, typically 15 volts and lower, there is still a significant fire and thermal damage hazard because of the possible high current capability of the supplies. Low voltage power supplies in the several hundred ampere range are becoming commonplace.

Detector electronics system designs will make use of a variety of packaging strategies, location optimizations, and low-voltage power distribution techniques as dictated by the signal processing requirements and physical locations. Standard VME crate systems installed in racks are used on the surface, in the underground service room and on the forward calorimeter platform. Highly specialized front-end digitiser electronics systems will be mounted directly on the barrel and end cap calorimeters to optimize the signal to noise figure. Unique mounting, packaging, and cooling designs are necessary to meet performance within the available space as described in chapter 7 and Figs. 7.3 and 7.13. Chapter 12.2 provides details regarding the low voltage power system.

Power sources are typically low-voltage high-current types; switching supplies instead of linear supplies are used for reasons of cost, size, efficiency, weight, and cooling. For VME systems, the power supplies are located in the same rack as the crates, in some cases mounted directly on the back of the crate and in others connected to the crate by short, flexible high current conductors.

14.2.3 Overcurrent protection

World HEP experience has shown that lack of adequate overcurrent protection and temperature monitoring in low-voltage high-current distribution networks and electronics systems were the most frequent causative factors in fires in experimental facilities. The same is true for high-tech facilities in general, from research laboratories to telephone switches

From the point of view of ease of installation, cooling, and maintenance, the simplest implementation for low voltage power supplies is to mount them physically separate from but nearby to the loads. Although this is quite natural for non crate-based systems, it can also be true for crate-based electronics when weight and cooling requirements are considered. Such a separation, while optimal for operations, introduces a low voltage distribution network between the supplies and the loads. High currents coupled with lack of adequate overcurrent protection and/or undersized conductors could lead to overheating of the conductors between the source and the load - thus presenting a fire or thermal damage hazard.

The HCAL group has elected to implement an overcurrent protection policy to ensure that designers and users of low-voltage high-current electronic systems shall take all reasonable steps to assure safe operation under foreseeable fault conditions. The underlying concept is that all current carrying conductors shall be protected in accordance with their ampacity. The policy calls for mandatory design criteria with reviews and inspections prior to initiating operations. The accompanying review and inspection procedures will be developed in conjunction with other similar controls to maintain a coherent oversight situation.

Design and Implementation Criteria for Low-Voltage High-Current Power Distribution Systems - April 1997 Draft:

1) Power Source Overcurrent Protection

A power source may or may not be overcurrent protected. The nature and level of protection, if any, shall be determined so as to properly specify the source to load conductors. Power sources may be internally or externally modified to exhibit a known safe level of overcurrent protection. The external addition of overcurrent protection shall be as close to the source as possible.

2) Power Source to Single Load Conductors

Conductors supplying power to a single load shall be adequately terminated and sized to carry the load current under all anticipated load conditions. A short circuit at any point to ground or between conductors shall not lead to overheating or damage to the conductors or the insulation. These criteria shall also apply to sense conductors, when present, between the source and the load.

a) Overcurrent Types

A short circuit may or may not result in an overcurrent trip condition at the source depending on the particular overcurrent protection at the source and the impedance of the conductors.

i) If a trip condition does occur, the conductors shall safely support the fault current necessary to cause a trip. If the overcurrent trip value is adjustable, the conductors shall be designed for the highest adjustable value.

ii) If a trip condition does not occur, the conductors shall be sized to safely support the fault current.

b) Multiple Conductors

Where several conductors are wired in parallel to provide sufficient current carrying capability as well as reduce the series impedance, the failure of a single conductor may not reach the necessary fault condition or may result in unsafe current levels in the remaining conductors. In such cases, each of the conductors shall be reasonably protected against inadvertent shorts at any point. Connections to the source and the load shall be sufficiently robust to prevent overheating, inadvertent disconnection, and failure. Special circumstances may require overcurrent protection on each of the parallel conductors in an installation.

3) Connection to Multiple Load Conductors

Connection of a single high current supply to multiple loads can result in hazardous conditions if due consideration is not given to the criteria delineated for single loads. The criteria presented in chapter 2. above shall apply to each conductor between the single source and the network of loads separately.

Use of fuses and circuit breakers between the source power bus and the individual load taps is often the most practical solution to the safe powering of multiple loads. Such measures allow the safe utilization of conductors more appropriately sized to each individual load.

Printed circuit boards and modules that are powered from a bus on a backplane that is connected to a high current source are best protected by interior fuses or current limiting devices.

4) Connection of Source to Load Conductors

Mechanical connections shall be properly tightened and lock nuts, lock washers, or Belleville washers shall be used where appropriate. Fastening hardware such as bolts or screws shall not be used as current conductors unless specifically designed for such purpose. Special caution is advised when the connection is made between dissimilar materials.

Connection of conductors between source and load shall be clearly labeled using standard colors and keyed or polarized so as to prevent any reasonable possibility of misconnection or shorting. Ribbon cables where used in part or whole for distribution of power shall be keyed or polarized.

5) Selection of Source to Load Conductors

The selection of conductor type and size is an engineering problem that has no simple answer. The designer, following good engineering practice, shall consider the overcurrent characteristics of the power source, conductor impedance, length of conductor, conductor/termination impedance, rating of the conductor insulation, the nature of the conductor path and raceways, ambient temperature and packing density. Proper consideration of these and other applicable factors is necessary for selection of a conductor size and type that will assure safe operation.

14.2.4 Rack and crate protection

The standard NEMA relay rack is designed as a stand-alone cabinet for installation of chassis mounted electronics and crate systems. Before modification by users, the rack is fully contained with three sides, a top and a bottom; the front is closed by electronics assemblies and blank panels. Cable penetrations and cooling requirements are the usual reasons for modification. Such rack units then only present hazards in accordance with the character of the installed equipment; the most significant of these is thermal damage and fire exposures from high power density systems. Removal and control of waste heat is a primary performance and safety design concern.

CMS planning calls for removal of waste heat from rack-mounted equipment by means of embedded air-water heat exchangers and forced ventilation. It is anticipated that some racks in the data acquisition system could contain up to 9 kW of electronics and corresponding low voltage power supplies. This air/water choice is not only the most effective in controlling the operating temperatures of the equipment, but is also the most efficient when considering the alternate of adding this load to the HVAC plant. A properly designed rack cooling system could even contribute to the total air conditioning requirement by operating slightly below ambient temperature.

Although not explicitly called out in code specifications or safety orders, CMS has identified such high power rack systems as presenting significant risk. Rack protection, designed to mitigate against the inherent fire and thermal damage risks of 9 kW rack power densities, is included in the engineering design requirements. The mitigating strategy is based on an extension of the existing requirements for process monitoring: detection of off-normal voltages, currents, and temperatures through the Detector Control System. Detection of a minor fault would result in an off-normal condition alarm; detection of a major fault would result in complete shutdown of the rack. Among the process conditions presently planned to be monitored for operational integrity, the following have been identified as being of potential significance for automatic shutdown:

- Smoke detection in the rack air stream

- Temperatures above and below each crate

- Temperatures of power supplies

- Cooling water flow through heat exchangers

- Cooling water supply and return temperatures

- Cooling water leaks

- Overcurrent conditions in power supplies

- Overvoltage conditions in power supplies

- Ventilation fan failure

14.2.5 High voltage

High voltage, greater than 1 KVDC, is required for operation of photomultipliers, and the hybrid photodiode devices require up to 16 KVDC. To achieve a set of practical design requirements and mitigation measures, usage of high voltage has been divided into two classifications based on life safety:

those which can be directly lethal as measured by the threshold for onset of ventricular fibrillation, and those which cannot. The electrical parameters related to shock severity are the current and duration of a fault condition, and the stored energy. The duration time limit parameter is especially relevant to installations with active fault detection and shutdown (or trip) capability. The suggested limits for these parameters to distinguish between the two classes of hazard have been taken from the data on human effects contained in International Electrical Commission publication 479-1, Effects of Current Passing Through the Human Body (also see IS28). The limits presently recommended by IEC for this distinction are:

- Safe Current Limit 10 mA

- Safe Duration Limit 20 ms

- Safe Stored Energy Limit 10 joules

For installations characterized by parameter values less than the above limits, there is still the possibility for secondary accidents, e.g. falls, caused by electrical shock, and mitigation measures can be deployed to minimize such exposures. In these installations, the design shall ensure that no live parts are accessible without using tools when voltage is on. Any work on energized systems shall be controlled by a hazardous activity permit procedure, and conspicuous labeling shall be used. Finally, special care shall be taken in the selection of external high voltage connectors to ensure that the neutral/return conductor engages first, and that an unplugged energized cable cannot spark to an external object or person.

For installations with any one parameter in excess of the above limits, the following measures are required in addition to those described above. During operation, total inaccessibility of the high voltage shall be assured by physical barriers and interlocks. Access for repairs, modifications, etc. shall be controlled by a mandatory lockout/tagout procedure. In the case of stored energy hazards, remotely actuated discharge systems shall be used to make the installation safe prior to access. Each element of the installation shall be clearly labeled with adequate warnings.

The high voltage systems described in chapter 12 for the calorimeter photodetectors all have operating parameters more than two orders of magnitude below the operating parameter limits listed above

14.2.6 Cooling

Pressurized water systems present a direct damage risk to nearby equipment, especially energized electronics. Designing with a large safety margin and installing so as to avoid induced damage vulnerabilities are essential mitigation measures against the occurrence of leaks. Parameters of the water system, mainly pressure, flow, and temperature values, shall be monitored for off-normal conditions. Shutdowns of the water system due to serious leaks shall be carefully interlocked to power shutdowns for the affected systems to preclude overheating.

14.3 MECHANICAL

Structural integrity of the hadron calorimeter detector and it's components is essential to safe and reliable operation during the life cycle of the experiment. The policy adopted by the HCAL engineering team requires that supports, components, and the principal structure of the calorimeter shall be designed and engineered with a factor of safety equal to 2 to ensure overall structural integrity. This safety factor of 2 requirement was derived from considerations of the guidance found in codes applicable to buildings and structures such as AISC "Manual of Steel Construction", ANSI A58.1 "Minimum Design Loads for Buildings and Other Structures", and Aluminum Association "Specifications for Aluminum Structures". Lifting fixture code requirements are given in ANSI/ASME B30.20 "Below-the-Hook Lifting Devices" and the HCAL fixtures will be in compliance.

In general, the adequacy of more conventional detector structure designs will be reviewed as part of the hazard analysis process for each individual subsystem. In contrast, the size and scope of the central calorimeter assemblies encompasses very large scale structural components and supports that are also complex, procedure oriented, and structurally critical. Verifying the adequacy of the design calls for a peer review.

Preparation of design criteria, calculations and documentation is considered essential for all structural systems associated with HCAL. The adequacy of design criteria shall be the domain of the safety review process, now initiated by the Initial Safety Discussion process. The accuracy of design calculations shall be the domain of peer reviews through the CMS technical review process. Such design criteria and calculations shall be prepared, reviewed, and approved prior to commencement of fabrication or installation activities. In addition, conventional safety reviews are required to assure that non-structural safety concerns associated with assembly, detector operations, and detector maintenance have been addressed by the designs.

The technique for review of calculations is expected to vary depending on the details of the individual component design. These will range from hand calculations for relatively simple configurations to execution of a fully independent finite element analysis for a complex critical joint or bolting pattern. The working criterion for the latter, at present, is that such numerical cross checks shall deal with potential input errors, modeling errors, or math errors by using a completely different finite element analysis code or by changing both the boundary conditions and the modeling on the same code package.

Finally, the design criteria shall not be limited to static situations. A very important additional requirement follows from a determination of dynamic situations and deflections/stresses set up by the movement of extremely heavy loads during assembly and maintenance or resulting from probable failures such as that of one jack in a multijack system. Design criteria shall be developed such that supports and structures are engineered to accommodate such anticipated local dynamic deformations, including that of the floor itself, in addition to the static operational loadings. The dynamic requirement for earthquake situations in the Geneva, Switzerland area calls for resistance to 0.15 g accelerations in all three dimensions.

14.4 FIRE PROTECTION

14.4.1 Overview

In fire protection at accelerator facilities, emphasis is placed on four principal areas; life safety, program continuity, property protection, and releases to the environment. The size and scope of the CMS detector presents some very important challenges to fire protection engineering. By its very mission, the detector is not capable of being partitioned into physically separate fire risk zones of lower value. Also, the deep underground location compounds problems of providing for emergency egress and smoke ejection. The situation is much like that found in many high-tech, high-value facilities where the probability for a fire incident is very low intrinsically, but the consequences could be catastrophic in the absence of protection and mitigation measures.

14.4.2 Combustible material

The most significant combustible loading in the detector is plastic scintillator in the calorimeters and muon trigger layers. Approximately 22 tonnes of polystyrene plastic scintillator is used in the end cap and barrel calorimeter systems. For the outer calorimeters, the scintillators are enclosed in metal trays (chapter 4) and attached to both sides of the inner layer of the steel return yoke. The inner calorimeter scintillators are encased in plastic trays and slid into small slots in the massive copper absorber (chapters 2 and 3) and covered by a metal skin. Readout fibers are covered by a metal protective cover. Because of these placements, the scintillator is not available as fuel in the early stages of a fire incident. It becomes available only after the temperature of the polystyrene (and the attached heat sinks) reaches the melting point and containment is no longer certain. The fuel loadings external to the calorimeter structures are not sufficient to cause such a temperature rise even if completely combusted.

The other significant combustible loading is the cable plant. The most important of the mitigation measures planned is to use cable types that comply with CERN Safety Instruction IS 23, "Criteria and Standard Test Methods for the Selection of Electrical Cables, Wires, and Insulated Parts with respect to Fire Safety and Radiation Resistance". These requirements deal with corrosive and toxic emissions as well as flame spread. The goals are to ensure that all cable fires are self-extinguishing once the heat source is removed and to minimize emissions. Essentially all fire accidents in HEP and similar high-tech facilities have had the same experience; secondary damage resulting from generation of corrosive smoke significantly can exceed the direct thermal damage of the fire itself.

14.4.3 Detection

Incipient detection is planned for all interior spaces within the detector and the overhead space immediately above it. An aspiration, sample-draw smoke detection system is envisaged for the different internal layers with modularity appropriate to the natural openings, maintenance accessways, and combustible loadings.

Multitiered alarming is used to take maximal advantage of the early warning from incipient detection. A low level alarm condition is responded to by local operations center personnel attempting a diagnosis of the off-normal condition. An system of TV surveillance cameras is planned to facilitate remote investigation of pre-alarms. At the high level, it is a fire alarm; all appropriate actions and annunciations are triggered.

14.4.4 Suppression

Given that incipient detection will be installed, suppression equipment should be designed to allow for a staged response that provides for any scale incident. The goal is to allow for localized fire control appropriate to the scope of the incident that would minimize the induced damage of the fire control method. In the past, such systems have used extinguishment equipment that ranged from standard portable carbon dioxide units, to wheeled tanks of halon 1211 with hand hose lines, to water standpipes with hose cabinets, to total flooding halon 1301 systems, to full sprinklering of the collision hall. With the ban on the use of halon in new facilities, this broad range of low damage highly effective fire control agents is no longer available. Consequently, the suppression agent(s) for the inner HCAL regions of the detector cannot be identified with certainty at present.

In the event of a fire incident during accelerator operations, immediate access for human intervention is not possible. The beam can be aborted, but the residual radioactivity of the air can be such (depending on the beam intensity) that a cooling down period of up to an hour is necessary. Also, powering down the large solenoid coil using the fast dump takes tens of minutes. Thus, the emphasis with regard to suppression systems is on remote application techniques. Such systems should still allow for a staged response and localized application to gain maximal advantage from incipient detection.

14.4.5 Prevention and loss control

A series of significant prevention and loss minimization measures have been identified during the Initial Safety Discussion process. These are listed and briefly described below. Decisions on these and other measures will be taken in the course of engineering and planning of fire protection for the CMS complex.

Automatic shutdowns

Fire alarms will automatically shut down all electrical power in the affected zone. For HCAL, this implies the capability to shut down high voltage systems in the service room in the event of an alarm from the cavern.

Smoke ejection

A fire alarm causes the HVAC equipment to switch into an active smoke ejection mode. Dampers will switch the intake to 100% outside air and the return to 100% exhaust, and the supply flow is doubled and directed to the lowest level only.

Response procedures and training

On-site support personnel will be trained to execute investigation and mitigation procedures for both pre-alarms and fire alarms.

Overcurrent protection policy

Mandatory engineering and inspection standards are being developed for overcurrent protection of HCAL low-voltage high-current electronics systems.

Rack protection

A rack protection system automatically shuts down individual racks based on local sensor information including smoke detection.

Process monitoring

A very extensive system of process monitoring is planned using the Detector Control System Those off-normal conditions that are directly relevant to fire risks will be separately alarmed as potential fire risk warnings requiring mandatory investigation.

Housekeeping policy

For many reasons, including fire prevention, a strict housekeeping policy is envisaged.

14.5 RADIOACTIVE MATERIALS

Radioactive materials will be found in two areas of the HCAL detectors and the collision hall. First, the calorimetry uses a system of permanently installed ^{137}Cs sources to maintain energy response calibrations. The activity of these sources will be less than 5 mCi. As described in chapter 10 each of the

16 separate sources planned is attached to the end of a flexible wire which is normally stored on the back of the calorimeter structure with the source itself inside of a lead storage container/shield. During calibration operations, a wire source is pushed through one of numerous small tubes which serve to guide it to precisely located calibration positions deep inside the calorimeter stack. Because of the frequency with which calibration data is taken, the source mover system is automated for remote operation.

Both Fermilab and CERN source inventory and control policies govern acquisition, packaging, personnel protection measures, and dosimetry aspects regarding the calibration sources. Design of the lead storage container shall use criteria limiting radiation fields in potential personnel access or work areas to the specified standards. Shipment of the sources or source mover assemblies is governed by these and appropriate over-the-road regulations.

Secondly, over a period of time, the steady exposure to secondary particles produced in beam-beam collisions will cause radioactivation of materials in the forward calorimeter area. This is particularly true for the part of the structure closest to the beam pipe, as well as the beam pipe itself, where significant activation levels are predicted, chapter 5. At the radius of the beam pipe in the forward/backward calorimetry regions, ionizing doses of 1000 Mrad per year are estimated at design luminosity. Dose levels decrease dramatically with distance from the beam pipe, varying as the third power of the radius, thus there is a naturally defined zone of radioactivation.

Designing for maintainability is of crucial importance to keep worker exposures as low as reasonably achievable by minimizing the frequency and duration of maintenance tasks and by maximizing the worker separation distance and self shielding potential of the structures. Portable and semi-portable shielding assemblies will be required for temporary protection in highest radiation field areas as any permanent shield would itself become activated. Use of passive and real-time dosimetry is planned both to provide a record for the exposure received by calorimeter components and to provide situation awareness information to personnel making an access.

Table of Contents

1. INSTITUTIONAL RESPONSIBILITIES, COSTS AND SCHEDULE

15.1 SCHEDULE AND PLANNING

The HCAL project has a planning methodology embedded in the overall CMS planning. A summary of the CMS general planning is given in theTechnical Design Report for the Magnet Project []. A summary outline of CMS planning as regards HCAL, extracted from the general CMS planning, is shown in Fig. 15.1. This schedule refers to the experimental halls, the magnet, and the Muon, ECAL, and Tracking subsystems as well as HCAL. Since HB is supported off the cryostat vacuum tank, HE is supported off YE, and HB in turn supports ECAL and the Tracker, these subsystem milestones are also indicated in the summary.

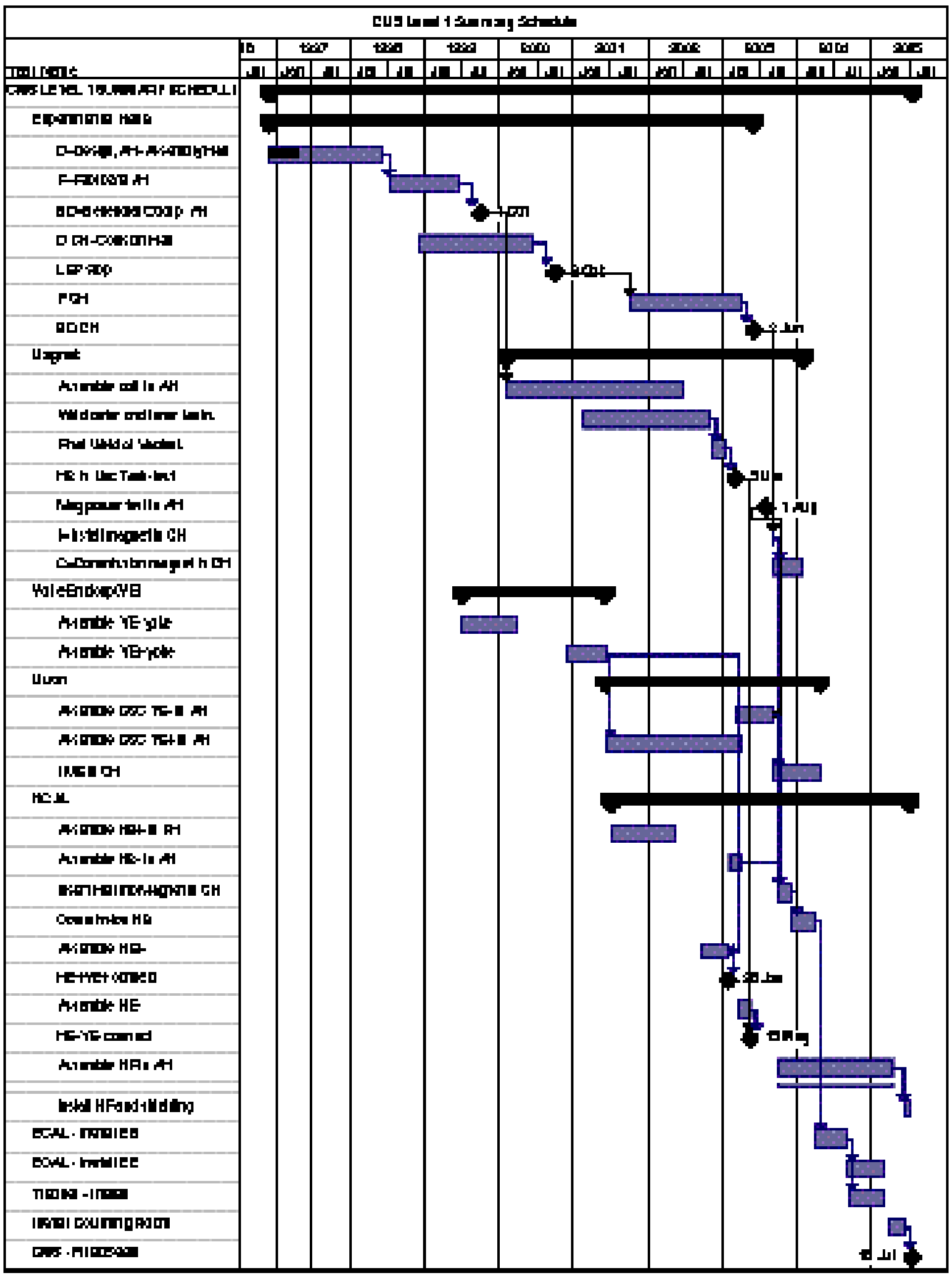

Fig. 15.1: CMS summary schedule relevant to HCAL.

The required schedule for HCAL which is needed to meet the level 1 schedule shown in Fig. 15.1 is given in Fig. 15.2 (a) and (b). Note that these milestones summarise the planning for HB, HO, HE and HF. The relevant level 1 schedule and the HB level 2 schedule are shown in Fig. 15.2 (a), while the HO, HE, and HF level 2 schedules appear in Fig. 15.2 (b). The HB, HO, HE, and HF activities are linked to the level 1 summary schedule, as shown in the figure. The planning which appears here must still be made consistent with the funding profiles of all the contributing HCAL institutions as they become known and understood. This task will begin with execution of the Memoranda of Understanding (MOU). The details of the level 2 schedule will undoubtedly require adaptation as more is understood about the funding profiles.

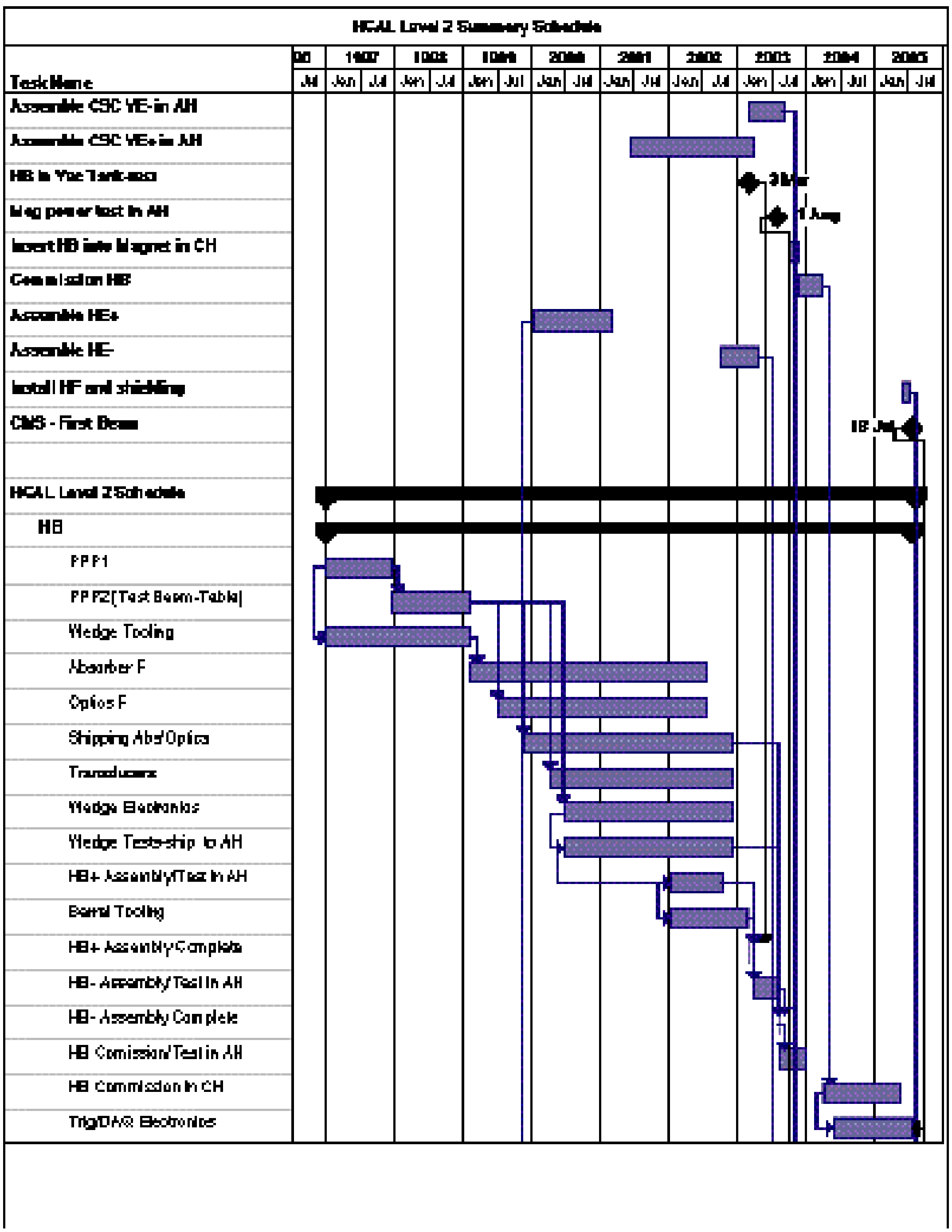

Fig. 15.2 (a): HCAL level 1 and HB level 2 summary schedule.

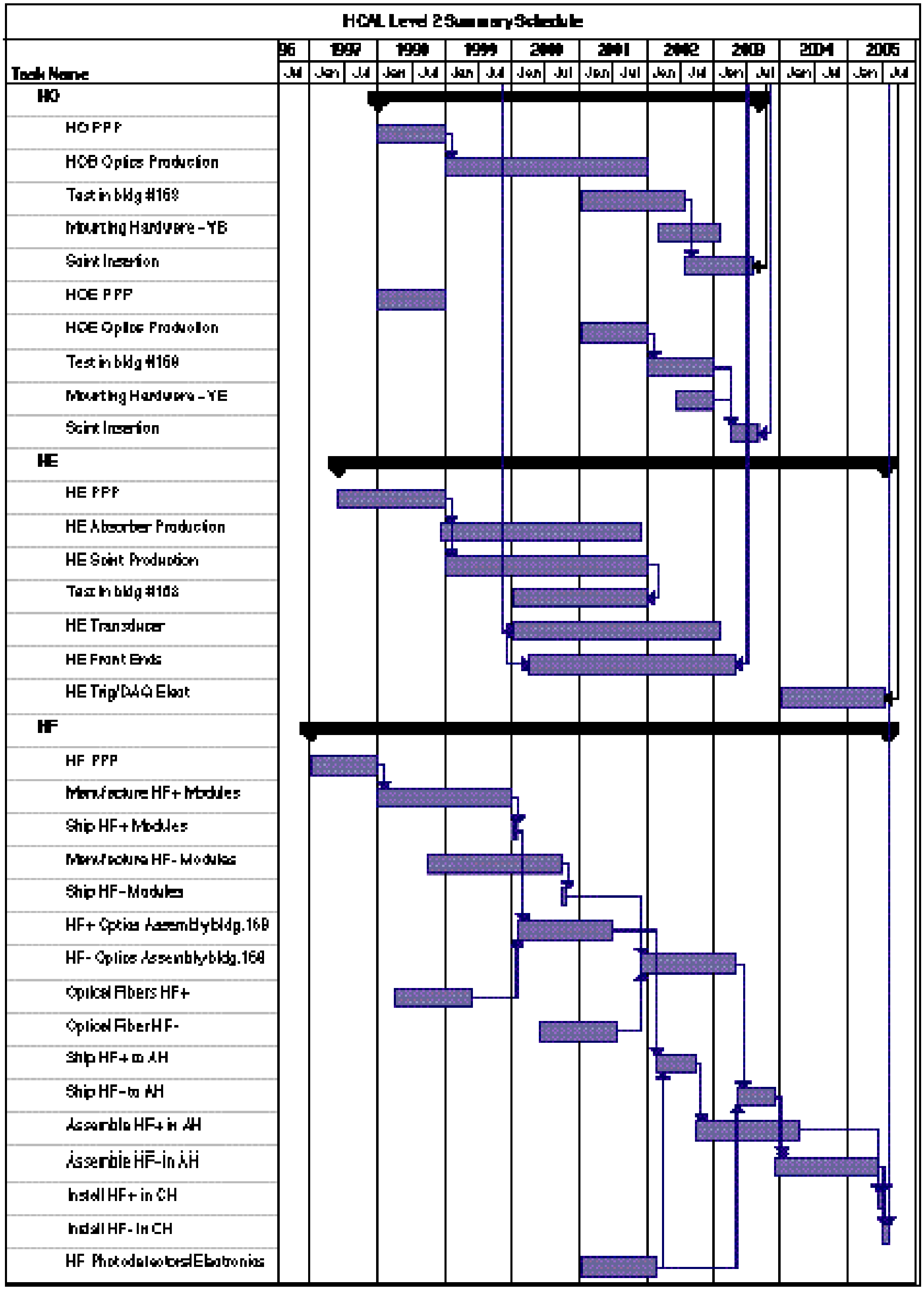

Fig. 15.2 (b): HO, HE, and HF level 2 summary schedule.

15.2 COST ESTIMATES

As is explained below, the cost estimates for HCAL are made in great detail. A summary is shown in Table 15.1. The HCAL costs are given using CERN accounting methods, and the full costing for HCAL is available in the CMS Cost Estimate Version 8 []. We reproduce here only a higher level rollup of the costing, suitable for a single page summary.

Table 15.1: Summary of the HCAL costs, in kCHF, from CMS Cost Book Version 8.

No.	Item	Total Cost
4	**Hadron Calorimeter**	44490
4.1.1	**Barrel**	20007
4.1.1.1	Mechanical Structure	8409
4.1.1.2	Optical System	2102
4.1.1.3	Phototransducers	2694
4.1.1.4	Electronics	1040
4.1.1.5	Tooling	3707
4.1.1.6	Shipping	304
4.1.1.7	Prototypes (2 wedges)	1490
4.1.2	**Outer Barrel**	5827
4.1.2.1	Mechanical Structure	280
4.1.2.2	Optical System	2118
4.1.2.3	Phototransducers	959
4.1.2.4	Electronics	490
4.2.1	**Endcap**	12761
4.2.1.1	Mechanical Structure	7103
4.2.1.2	Optical System	1590
4.2.1.3	Phototransducers	2333
4.2.1.4	Electronics	891
4.2.1.5	Tooling	260
4.2.1.6	Shipping (included in Mech. Structure)	
4.2.2	**Outer Endcap**	1001
4.2.2.1	Mechanical Structure	26
4.2.2.2	Optical System	249
4.2.2.3	Phototransducers	481
4.2.2.4	Electronics	245
4.3.1	**Forward Electromagnetic Section**	1974
4.3.1.1	Detectors and Components	1360
4.3.1.2	Electronics	615
4.3.2	**Forward Hadronic Section**	3415
4.3.2.1	Detectors and Components	2800
4.3.2.2	Electronics	615
4.3.3	**Forward Tailcatcher**	1119
4.3.3.1	Detectors and Components	947
4.3.3.2	Electronics	171

4.3.3	**Forward Calorimeter**	111.9
4.3.3.1	Detectors and Components	94.7
4.3.3.2	Electronics	17.1
4.3.4	**Forward Common Systems**	33.4
4.3.4.1	Mechanical Structure and Support	8.5
4.3.4.2	Assembly/Installation	10.5
4.3.4.3	Calibration/Monitoring	11.1
4.3.4.4	Service Systems	3.3

15.3 COST PROFILE - TENTATIVE

A first attempt has been made to integrate the cost items shown in Table 15.1 with the level 2 schedule for HCAL. The resulting cost profile is shown in Fig. 15.3. This exercise has only begun. The full realisation of this planning exercise requires a good knowledge of the funding profile of the integrated total funds available from each of the countries participating in HCAL and the subsequent linking of the cost profile to the composite funding profile. This is a work in progress, and has just begun at this time.

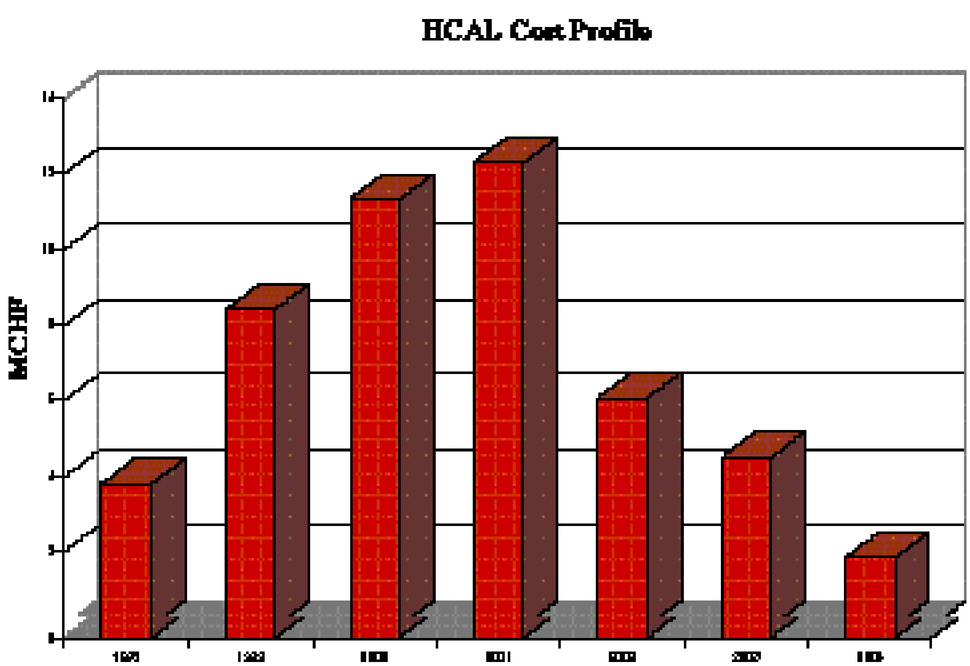

Fig. 15.3: Tentative HCAL Cost Profile.

15.4 MONEY MATRIX

There are several groups participating in the HCAL system. It is of paramount importance to first see if the resources thought to be available to these groups match the expected costs of the HCAL system. In Table 15.2 we give the HCAL "money matrix" showing the resources available to the groups participating in HCAL. Within the uncertainties attached to this table, there is a good match of costs and resources. Note that the design of HF has yet to be fully defined and that new groups may join that effort. Within the uncertainties and the flexibility allowed in the final definition of the scope, HCAL costs match the available funds. At this time it is premature to attempt to match the cost profile shown in Fig. 15.3 with the funding, even though the time integrated "money matrix" appears to be sufficient to cover the total HCAL costs, as estimated in Table 15.1.

Table 15.2: The financial resources, in MCHF, of groups participating in HCAL.

16 May 97

HCAL Money Matrix (MCHF)

	China	Hungary	India	RDMS	Turkey	US DOE	US NSF	Total Income	Cost Estimate version 3
HCAL Income	**1.4**	**0.3**	**1.1**	**11.1**	**0.6**	**24.4**	**4.4**	**43.3**	**44.5**
HCAL Cost	**1.5**	**0.3**	**0.9**	**11.1**		**24.4**	**4.4**	**43.3**	**44.5**
Barrel	1.4		0.9			19.8	1.9	23.9	23.9
Endcap	0.1			9.1		1.4	2.5	13.2	13.8
Forward		0.3		2.0	0.6	3.2		6.1	6.8

There is the additional issue of the funding profile for the financial resources shown in Table 15.2. At present our knowledge of the funding profile is somewhat rudimentary. However, the US groups have been given a funding profile by their funding agencies. A first attempt to match costs and funds to schedule for the US groups in HCAL appears to indicate no major difficulties. This statement should be tempered by the fact that it is not yet clear if industrial firms involved in major purchases will require full payment at the start, or if a schedule of phased payments is possible, and if so the details of the obligation profile.

15.5 MANAGEMENT CONTROL

The HCAL project of CMS is headed by a project manager appointed by the CMS spokesperson with full consultation of the CMS collaboration. As explained in detail in the CMS Constitution [], the HCAL project manager represents the HCAL system to the full CMS management as a member of the CMS

Management Board. The organization of the HCAL effort is summarised in Fig. 15.4.

The groups participating in the HCAL project form the Institution Board of HCAL. All decisions are ratified by that board. The project has a single project manager and resource manager, who carry overall responsibility for the project. The geographic sectors, HB, HE and HF each have a project manager or coordinator and a technical coordinator. They report to the HCAL project manager. The HE Project manager is also a member of the CMS Management Board. The HB, HO, HE, and HF geographic sectors also have persons responsible for the engineering aspects of those sectors who report to their respective project coordinators.

There are a variety of tasks which apply to all subsystems. Indeed, the structure of this TDR reflects that fact, as does Fig. 15.4. The commonality of HCAL, for example electronics, is built into the structure of the HCAL project. Leaders for efforts common to HCAL are indicated in Fig. 15.4.

The overall governance of CMS is explained in the CMS Constitution [3]. The HCAL subsystem of CMS is governed in the same general fashion as are all CMS subsystems. In the HCAL case the three distinct geographic sectors (HB, HE, HF) are recognised as such, while the common efforts are also recognised and mirrored in the form shown in the HCAL organisation chart, Fig. 15.4.

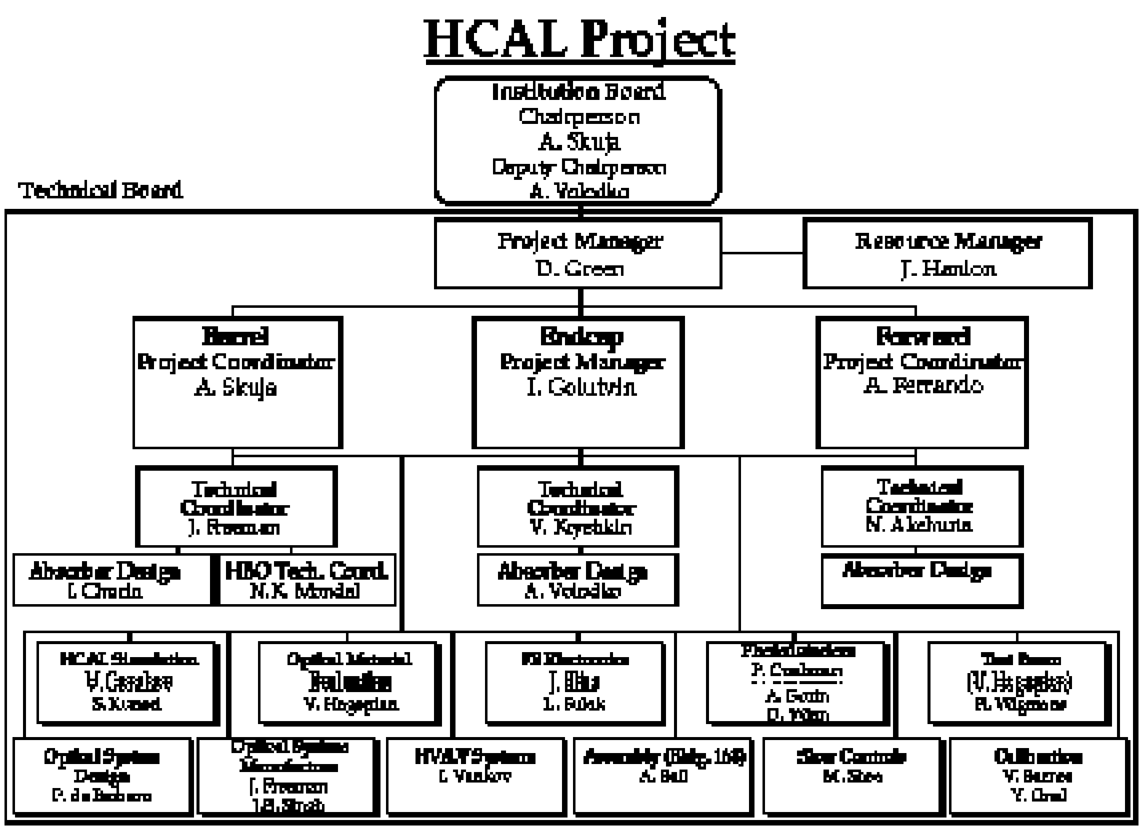

Fig. 15.4: The organisation chart of the CMS HCAL Project.

15.6 INSTITUTIONAL RESPONSIBILITIES

The tentative responsibilities of the countries involved in HCAL follow from the interests of the groups. Basically, the US groups are responsible for the HB mechanics and optics and for the electronics of all of HCAL. The RDMS groups are collectively working on the mechanics and optics of HE, while the combined Indian groups are responsible for the mechanics and optics of the samples made outside the solenoid in HB. A group of RDMS members, most notably ITEP, is responsible for the HF mechanical design and the absorber construction. The Hungarian and Turkish groups take the lead in the mechanical assembly of the HF quartz fibre active elements, while the US groups will supply transducers and front end electronics for HF. Of course, the exact elements of HCAL for which each group is ultimately responsible can only be defined when the MOUs are signed by the relevant funding agencies. At present, we simply indicate the broad outlines of the proposed responsibilities of the groups.

A single page summary of items rolled up from the version 8 Cost Book [2], together with the responsibility by country for that task, is given in Table 15.3. The cost for the task, at a very high level, is also indicated in the table.

Where available and agreed upon, the responsibilities of individual groups for HCAL items are shown in Table 15.4. As events progress, and as CMS negotiates the MOU with each collaborating institution, these areas of responsibility will change, and are shown here as indicative of the tentative assignment of tasks.

Table 15.3: CMS Cost Book items and the associated responsibility by country for HCAL.

No. Item	Responsible Groups	Total Cost (kCHF) - V8
4. HCAL		44,498
4.1 Barrel - HB		23,895
4.1.1 Barrel		20,067
4.1.1.1 Mechanics	US, (China)	
4.1.1.2 Optics	US	
4.1.1.3 Phototransducers	US	
4.1.1.4 Electronics	US	
4.1.1.5 Tooling	US	
4.1.1.6 Shipping	US	
4.1.1.7 Prototypes	US	
4.1.2 Outer Barrel		3,827
4.1.2.1 Mechanics	India	
4.1.2.2 Optics	India, US	
4.1.2.3 Phototransducers	US	
4.1.2.4 Electronics	US	
4.2 Endcap - HE		13,762
4.2.1 Endcap		12,761
4.2.1.1 Mechanics	RDMS, US	
4.2.1.2 Optics	RDMS, US	
4.2.1.3 Phototransducers	US, RDMS	
4.2.1.4 Electronics	US	
4.2.1.5 Tooling	RDMS	
4.2.1.6 Shipping	RDMS	
4.2.1.7 Prototypes	RDMS	
4.2.2 Outer Endcap		1,001
4.2.2.1 Mechanics	US	
4.2.2.2 Optics	US	
4.2.2.3 Phototransducers	US	
4.2.2.4 Electronics	US	
4.3 Forward - HF		6,841
4.3.1 EM section		1,974
4.3.1.1 Detectors	Hungary, RDMS, Turkey	
4.3.1.2 Electronics	US	
4.3.2 HAD section		3,415
4.3.2.1 Detectors	Hungary, RDMS, Turkey	
4.3.2.2 Electronics	US	
4.3.3 TC section		1,119
4.3.3.1 Detectors	Hungary, RDMS, Turkey	
4.3.3.2 Electronics	US	
4.3.4 Common Systems	Hungary,RDMS,Turkey,US	334

Table 15.4: CMS Cost Book categories and the associated responsibility by institution.

No.	Item	Cost (kCHF)	Responsible Group(s)
4.1.1	**Barrel**	**20,067**	
4.1.1.1	Mechanical Structure	8,469	
4.1.1.1.1	Barrel Design		FNAL, Maryland, Miss
4.1.1.1.2	Barrel Wedges		FNAL
4.1.1.1.3	Bolted Assembly		FNAL, Maryland
4.1.1.2	Optical System	3,162	
4.1.1.2.1	Tile Trays (20 degree)		FNAL, Rochester, FSU
4.1.1.2.2	Optical Cables		UIC, Notre Dame
4.1.1.2.3	Pig Tails		UIC, Rochester, Notre Dame
4.1.1.2.4	Installation		FNAL, Maryland, Rochester
4.1.1.3	Phototransducers	2,694	
4.1.1.3.1	Photodetectors and Bases		Minn, FNAL, Virginia Tech
4.1.1.3.2	Cables and HV Power Supplies		Virginia Tech
4.1.1.3.3	Stabilization System		Notre Dame, Iowa, Iowa State, Purdue
4.1.1.3.4	Temperature Control		FNAL, Notre Dame
4.1.1.3.5	Decoder Boxes		FNAL, Notre Dame
4.1.1.4	Electronics	1,040	
4.1.1.4.1	Electronics EDIA		FNAL
4.1.1.4.2	Electronics mfg. labor		FNAL
4.1.1.4.3	Fermi Channels		CERN, FNAL
4.1.1.4.4	Crates, cooling, low voltage, drivers		FNAL, Miss
4.1.1.4.5	Preamps		FNAL
4.1.1.5	Tooling	3,767	
4.1.1.5.1	Scintillator Tooling		FNAL, Rochester
4.1.1.5.2	Fiber Tooling		UIC, Notre Dame
4.1.1.5.3	Phototransducer Testing		Minn, FNAL
4.1.1.5.4	Other Tooling and Testing Apparatus		FNAL
4.1.1.5.5	Absorber Fabrication Tooling		FNAL, Maryland, Miss
4.1.1.5.6	Installation Tooling		Maryland
4.1.1.6	Shipping	504	
4.1.1.7	Prototypes (2 wedges)	1,430	
4.1.1.7.1	Test Beam Stand		FNAL, IHEP
4.1.1.7.2	Wedges (pre-production)		FNAL
4.1.2	**Outer Barrel**	**3,827**	
4.1.2.1	Mechanical Structure	260	
4.1.2.1.1	Hangers onto Solenoid		TIFR, BARC, IOP, Panjab
4.1.2.2	Optical System	2,118	
4.1.2.2.1	Tile Trays (30 degree)		TIFR, BARC, IOP, Panjab
4.1.2.2.2	Optical Cables		UIC, Notre Dame
4.1.2.2.3	Pig Tails		TIFR, BARC, IOP, Panjab
4.1.2.2.4	Installation		TIFR, BARC, IOP, Panjab
4.1.2.3	Phototransducers	959	
4.1.2.3.1	Photodetectors and Bases		Minn, FNAL, Virginia Tech
4.1.2.3.2	Cables and HV Power		Virginia Tech
4.1.2.3.3	Temperature Control		Notre Dame, FNAL
4.1.2.3.4	Decoder Boxes		FNAL, Notre Dame, Iowa, Purdue, Miss
4.1.2.4	Electronics	490	
4.1.2.4.1	Electronics mfg. labor		FNAL
4.1.2.4.1	Fermi Channels		CERN, FNAL
4.1.2.4.2	Crates, Low Voltage, Cooling		FNAL, Miss
4.1.2.4.3	Preamps		FNAL

Table 15.4 (cont.): CMS Cost Book categories and the associated responsibility by institution.

No.	Item	Cost (kCHF)	Responsible Group(s)
4.2.1	**Endcap**	**12,761**	
4.2.1.1	Mechanical Structure	7,163	
4.2.1.1.1	Endcap Design		JINR, NCPHEP (Minsk)
4.2.1.1.2	Endcap Wedges		NCPHEP (Minsk), INRNE (Sofia), JINR
4.2.1.1.3	Bolted Assembly (included above)]		JINR, NCPHEP (Minsk)
4.2.1.1.4	Interface to endcap steel		JINR
4.2.1.2	Optical System	1,590	
4.2.1.2.1	Tile Trays (10 degree)		IHEP, FNAL, INR, KIPT, YERPHI
4.2.1.2.2	Optical Cables		UIC, Notre Dame
4.2.1.2.3	Pig Tails		Rochester, Notre Dame, IHEP
4.2.1.2.4	Installation		IHEP
4.2.1.3	Phototransducers	2,333	
4.2.1.3.1	Photodetectors and Bases		Minn, FNAL, Virginia Tech
4.2.1.3.2	Cables and HV Power Supplies		Virginia Tech
4.2.1.3.3	Stabilization System		Notre Dame, Iowa, Purdue, IHEP
4.2.1.3.4	Temperature Control		FNAL
4.2.1.3.5	Decoder Boxes		FNAL, Notre Dame, IHEP
4.2.1.4	Electronics	891	
4.2.1.4.1	Electronics manufacturing labor		FNAL
4.2.1.4.2	Fermi Channels		CERN, FNAL
4.2.1.4.3	Preamps		FNAL
4.2.1.4.4	Crates, Cooling, Low Voltage		FNAL, Miss, Notre Dame
4.2.1.5	Tooling	260	
4.2.1.5.4	Other Tooling and Testing Apparatus		JINR
4.2.1.5.5	Absorber Fabrication Tooling		JINR, NCPHEP (Minsk)
4.2.1.5.6	Installation Tooling		JINR
4.2.1.6	Shipping (included in Mech. Structure)	0	JINR, IHEP, INR, NCPHEP (Minsk)
4.2.1.7	Prototypes (30-degree sector)	524	JINR, IHEP, INR, NCPHEP (Minsk), INRNE (Sofia)
4.2.2	**Outer Endcap**	**1,001**	
4.2.2.1	Mechanical Structure	26	
4.2.2.1.1	Hangers onto MF1		Maryland
4.2.2.2	Optical System	249	
4.2.2.2.1	Tile Trays (30 degree)		FNAL, Rochester, PSU
4.2.2.2.2	Optical Cables		UIC, Notre Dame
4.2.2.2.3	Pig Tails		UIC, Rochester, Notre Dame
4.2.2.2.4	Installation		FNAL, Maryland, Rochester
4.2.2.3	Phototransducers	481	
4.2.2.3.1	Photodetectors and Bases		Minn, FNAL, Virginia Tech
4.2.2.3.2	Cables and HV Power Supplies		Virginia Tech
4.2.2.3.3	Temperature Control		Notre Dame, Iowa, Iowa State, Purdue
4.2.2.3.4	Decoder Boxes		FNAL, Notre Dame, Miss
4.2.2.4	Electronics	245	
4.2.2.4.1	Electronics mfg. labor		FNAL
4.2.2.4.2	Fermi Channels		CERN, FNAL
4.2.2.4.3	Crates, Low Voltage, Cooling		FNAL
4.2.2.4.4	Preamps		FNAL, Miss, Notre Dame

Table 15.4 (cont.): CMS Cost Book categories and the associated responsibility by institution.

No.	Item	Cost (kCHF)	Responsible Group(s)
4.3.1	**Forward Electromagnetic Section**	**1,974**	
4.3.1.1	Detectors and Components	1,360	
4.3.1.1.1	Absorber		ITEP, METU, MSU
4.3.1.1.2	QQ Fibers + 5%		ITEP, METU, MSU
4.3.1.1.3	QP Fibers + 5%		METU, Iowa
4.3.1.1.4	Optical System		KFKI-RMKI
4.3.1.1.5	QC&A		KFKI-RMKI
4.3.1.1.6	Prototype		all HF groups
4.3.1.1.7	Assembly of EM		ITEP, KFKI-RMKI, METU, MSU
4.3.1.1.8	Installation of EM		all HF groups
4.3.1.2	Electronics	615	
4.3.1.2.1	Photodetectors		Fairfield, Iowa
4.3.1.2.2	Front-end Electronics		FNAL, Boston
4.3.1.2.3	Cabling		Boston
4.3.1.2.4	Power Supplies		Boston, Fairfield, Iowa
4.3.1.2.5	Monitoring		Iowa
4.3.1.2.6	Prototype		all HF groups
4.3.2	**Forward Hadronic Section**	**3,415**	
4.3.2.1	Detectors and Components	2,800	
4.3.2.1.1	Absorber		ITEP, METU, MSU
4.3.2.1.2	QQ Fibers + 5%		ITEP, METU, MSU
4.3.2.1.3	QP Fibers + 5%		METU, Iowa
4.3.2.1.4	Optical System		KFKI-RMKI
4.3.2.1.5	QC&A		KFKI-RMKI
4.3.2.1.6	Prototype		all HF groups
4.3.2.1.7	Assembly of HAD		ITEP, KFKI-RMKI, METU, MSU
4.3.2.1.8	Installation of HAD		all HF groups
4.3.2.2	Electronics	615	
4.3.2.2.1	Photodetectors		Fairfield, Iowa
4.3.2.2.2	Front-end Electronics		FNAL, Boston
4.3.2.2.3	Cabling		Boston
4.3.2.2.4	Power Supplies		Boston, Fairfield, Iowa
4.3.2.2.5	Monitoring		Iowa
4.3.2.2.6	Prototype		all HF groups
4.3.3	**Forward Tailcatcher**	**1,119**	
4.3.3.1	Detectors and Components	947	
4.3.3.1.1	Absorber		ITEP, METU, MSU
4.3.3.1.3	Plastic Fibers + 2%		METU
4.3.3.1.4	Optical System		KFKI-RMKI
4.3.3.1.5	QC&A		KFKI-RMKI
4.3.3.1.7	Assembly of TC		ITEP, KFKI-RMKI, METU, MSU
4.3.3.1.8	Installation of TC		all HF groups
4.3.3.2	Electronics	171	
4.3.3.2.1	Photodetectors		Fairfield, Iowa
4.3.3.2.2	Front-end Electronics		FNAL, Boston
4.3.3.2.3	Cabling		Boston
4.3.3.2.4	Power Supplies		Boston, Fairfield, Iowa
4.3.3.2.5	Monitoring		Iowa
4.3.3.2.6	Prototype		all HF groups

Table 15.4 (cont.): CMS Cost Book categories and the associated responsibility by institution.

No.	Item	Cost (kCHF)	Responsible Group(s)
4.3.4	**Forward Common Systems**	**334**	
4.3.4.1	Mechanical Structure and Support	65	
4.3.4.1.1	Engineering		ITEP, MSU
4.3.4.1.2	Tooling for table		ITEP, MSU
4.3.4.1.3	Jigs		ITEP, MSU
4.3.4.1.4	Test beam supp. str		ITEP, MSU
4.3.4.1.5	Optic. readout jigs		ITEP, MSU
4.3.4.1.6	Alignment		ITEP, MSU
4.3.4.1.7	Horizontal table		ITEP, MSU
4.3.4.1.8	Prototype		ITEP, MSU
4.3.4.2	Assembly/Installation	105	
4.3.4.2.1	Transportable mods.		ITEP, KFKI-RMKI, METU, MSU
4.3.4.2.2	Surface Assembly		all HF groups
4.3.4.2.3	Inst at Exp Beams		all HF groups
4.3.4.2.4	Table design		ITEP, KFKI-RMKI, METU, MSU
4.3.4.2.5	2-axis table		ITEP, KFKI-RMKI, METU, MSU
4.3.4.2.6	2-axis table		ITEP, KFKI-RMKI, METU, MSU
4.3.4.2.7	Table manufac.		ITEP, KFKI-RMKI, METU, MSU
4.3.4.2.8	Cabling (undergrd.)		all HF groups
4.3.4.2.9	Checkout		all HF groups
4.3.4.2.10	Load transf. system		all HF groups
4.3.4.2.11	Inst. manpower		all HF groups
4.3.4.3	Calibration/Monitoring	111	
4.3.4.3.1	System design & integ		Iowa, Purdue
4.3.4.3.2	Housekeeping (temp..)		Iowa
4.3.4.3.3	In situ calib.		Texas Tech, ITEP, MSU
4.3.4.3.4	Test pulses		Boston
4.3.4.3.5	Slow controls (HV ...)		Boston
4.3.4.3.6	Slow controls		Boston
4.3.4.3.7	Table remote cont.		ITEP, MSU
4.3.4.3.8	Table remote cont.		ITEP, MSU
4.3.4.3.9	Prototype		all HF groups
4.3.4.3.10	LED, optical comp.		Notre Dame, Iowa, ITEP, MSU
4.3.4.3.11	Manf. Light calib sys.		Iowa
4.3.4.3.12	Inst. manpower		all HF groups
4.3.4.3.13	Installation		all HF groups
4.3.4.3.14	Pulsed N2 lasers		Iowa
4.3.4.3.15	ND Filter wheels		Iowa
4.3.4.3.16	Laser dyes		Iowa
4.3.4.3.17	Optical couplers		Iowa
4.3.4.3.18	Transport fibers		Iowa
4.3.4.4	Service Systems	53	
4.3.4.4.1	Cooling		Boston
4.3.4.4.2	Cooling		Boston
4.3.4.4.3	Crates		Boston

References

[1] The Magnet Project Technical Design Report, CERN/LHCC 97-10, May 2, 1997.

[2] CMS Cost Estimate Version 8, 1997-003, Feb. 3, 1997.

[3] The CMS Constitution, CMS/D-CB/1996-1, Sept. 13, 1996.